DEVELOPMENT OF A CRYOGENIC DRIFT CELL SPECTROMETER AND METHODS FOR IMPROVING THE ANALYTICAL FIGURES OF MERIT FOR ION MOBILITY-MASS SPECTROMETRY ANALYSIS

A Dissertation

by

JODY CHRISTOPHER MAY

Submitted to the Office of Graduate Studies of
Texas A&M University
in partial fulfillment of the requirements for the degree of

DOCTOR OF PHILOSOPHY

August 2009

Major Subject: Chemistry

DEVELOPMENT OF A CRYOGENIC DRIFT CELL SPECTROMETER AND METHODS FOR IMPROVING THE ANALYTICAL FIGURES OF MERIT FOR ION MOBILITY-MASS SPECTROMETRY ANALYSIS

A Dissertation

by

JODY CHRISTOPHER MAY

Submitted to the Office of Graduate Studies of
Texas A&M University
in partial fulfillment of the requirements for the degree of

DOCTOR OF PHILOSOPHY

Approved by:

Chair of Committee,	David H. Russell
Committee Members,	Simon W. North
	Robert R. Lucchese
	David A. Church
Head of Department,	David H. Russell

August 2009

Major Subject: Chemistry

ABSTRACT

Development of a Cryogenic Drift Cell Spectrometer and Methods for Improving the Analytical Figures of Merit for Ion Mobility-Mass Spectrometry Analysis.

(August 2009)

Jody Christopher May, B.S., University of Central Arkansas

Chair of Advisory Committee: Dr. David H. Russell

A cryogenic (325-80 K) ion mobility-mass spectrometer was designed and constructed in order to improve the analytical figures-of-merit for the chemical analysis of small mass analytes using ion mobility-mass spectrometry. The instrument incorporates an electron ionization source, a quadrupole mass spectrometer, a uniform field drift cell spectrometer encased in a cryogenic envelope, and an orthogonal geometry time-of-flight mass spectrometer. The analytical benefits of low temperature ion mobility are discussed in terms of enhanced separation ability, ion selectivity and sensitivity. The distinction between resolving power and resolution for ion mobility is also discussed. Detailed experimental designs and rationales are provided for each instrument component. Tuning and calibration data and methods are also provided for the technique.

Proof-of-concept experiments for an array of analytes including rare gases (argon, krypton, xenon), hydrocarbons (acetone, ethylene glycol, methanol), and halides (carbon tetrachloride) are provided in order to demonstrate the advantages and

limitations of the instrument for obtaining analytically useful information. Trendline partitioning of small analyte ions based on chemical composition is demonstrated as a novel chemical analysis method. The utility of mobility-mass analysis for mass selected ions is also demonstrated, particularly for probing the ion chemistry which occurs in the drift tube for small mass ions.

As a final demonstration of the separation abilities of the instrument, the electronic states of chromium and titanium (ground and excited) are separated with low temperature. The transition metal electronic state separations demonstrated here are at the highest resolution ever obtained for ion mobility methods. The electronic conformational mass isomers of methanol (conventional and distonic) are also partially separated at low temperature. Various drift gases (helium, neon, and argon) are explored for the methanol system in order to probe stronger ion-neutral interaction potentials and effectuate higher resolution separations of the two isomeric ions. Finally, two versatile ion source designs and a method for axially focusing ions at low pressure (1-10 torr) using electrostatic fields is presented along with some preliminary work on the ion sources.

DEDICATION

This dissertation is dedicated to my family: my parents, Chom and Earl, and my siblings, John and Karen. Not only have they been highly supportive in my pursuit of higher education, they have tolerated my long bouts of silence between phone calls home and numerous conversations marked with my incoherent science babble for when I did pick up the phone.

Graduate school can be as little or as much as you make of it. It can be dredging through late nights of experiments and sentences, or it can be a springboard for discovery about yourself and the world around you. For me, graduate school was my creative outlet and my chance to embrace opportunity and engage the world in dialect. It was there I learned from artisans, gained new life perspectives, and met my future wife, Stacy. My final dedication is to her and the sepia toned inspiration that she brings me. Stacy is now my creative outlet.

ACKNOWLEDGEMENTS

I would first like to thank my research advisor, Dave Russell, for allowing me the opportunity to spend my graduate years in his laboratory tinkering with all of his instruments and indulging me as I built my own. He presented me with an undeniable opportunity to learn hands-on instrumentation development with a full laboratory of equipment and tools at my disposal. In the end, I had fun and gained an array of marketable skill sets.

I am also thankful to my committee members, Dr. North, Dr. Lucchese and Dr. Church for their support and the insight they have bestowed upon me whenever I needed a bout of clarity.

I am grateful to the department machine shop staff, who have changed faces over the years but share the common denominator that all of them had worked on a piece of the instrument which is described in this thesis: Ken Greer, Tony Montalbano, Rick O'Neill, Will Seward and Carl Johnson. A good machinist is an instrument builder's best friend.

An equally good friend to a builder is a good electrical technician, and I was fortunate to have worked with one of the best, Greg Matthijetz. Without Greg, my instrument would be nothing more than a shiny mass of stainless steel.

Rounding off my associations with highly skilled artisans is my gratitude to Tom Egan of Ionwerks, Inc. whom for the past decade or so has developed an incredibly powerful and impressive data acquisition and visualization software package for the ion

mobility-mass spectrometry experiment. All data acquisition and 2-dimensional visualization of the mobility-mass data was made possible by the Ionwerks software package.

My former research advisor, Dr. Bill Taylor, introduced me to the ion mobility technique and instrument development research, and encouraged my continuation in the field. He is a highly skilled instrument builder, instructor and mentor and I would not be in this area of research had it not been for him.

I acknowledge the first person I met in Dave Russell's group, Dr. Guido Verbeck, who became my friend and mentor and acclimated me into the world of ion mobility instrument development.

I also acknowledge those who came after me, the incoming graduate students and postdoctoral researchers whom I taught and subsequently learned from more than I had learned from my mentors.

I recognize the many avenues of financial support that provided the momentum to see our ideas to fruition: the National Science Foundation, the Welch Foundation, Ionwerks, Inc. of Houston and the Department of Chemistry at Texas A&M University.

My time at Texas A&M has been marked with numerous milestones in my life, but none more committed to my memory as the time I spent there with my future wife, Stacy. To her I owe my deepest thanks and gratitude. *Meta non est, iter est*.

NOMENCLATURE

CAD	Computer Aided Design
cryogenic	referring to very low temperature (typically below 100 Kelvin)
DC	Direct Current (*i.e.*, an electrostatic potential)
desorption	the transfer of molecules from a condensed phase to the gas phase
duty cycle	the time interval in which an instrument is doing useful analysis
dynamic range	the linear response range of an instrument or detector.
ESI	Electrospray Ionization
EI	Electron Ionization (synonymous with Electron Impact)
grid	a transparent array of thin wires used in charged particle optics
IMS	Ion Mobility Spectrometry
LDI	Laser Desorption/Ionization
longitudinal/axial	the direction parallel to the transit of the ion beam or swarm
MALDI	Matrix Assisted Laser Desorption/Ionization
MCP	Microchannel Plate
MS	Mass Spectrometry
m/z	mass-to-charge ratio, the standard unit of measure in MS
PEEK	polyetheretherketone, a high temperature thermoplastic
PMT	Photomultiplier Tube
ppb	parts per billion (1 part in 10^8)
ppm	parts per million (1 part in 10^6)

RF	Radio Frequency (*i.e.*, a temporally dynamic potential)
swarm	a (usually low) density of ions within a neutral gas
throughput	an instrument's measurement rate, quantified in spectra/sec.
TOF	Time-of-Flight (in reference to the mass analysis technique)
transverse/radial	the direction orthogonal to the transit of the ion beam or swarm
TWIMS	Traveling Wave Ion Mobility Spectrometry

TABLE OF CONTENTS

Page

Page

Page

Page

LIST OF FIGURES

Page

Page

Page

Page

LIST OF TABLES

1. INTRODUCTION AND OVERVIEW OF METHODS

1-1 An Overview of Ion Mobility Spectrometry

Ion mobility spectrometry (IMS) is an electrophoretic gas-phase separation technique [1,2] that has been applied to a wide range of analytical applications from the trace level detection of chemical warfare agents [3] to the size measurement of nanoparticles and aerosols [4], the differentiation of molecular species in complex matrix environments such as biological medium (*e.g.* buffers, salts & other non-analyte concomitants) [5] and structural determination of hydrocarbon molecules in crude oils [6]. Ion mobility has seen the greatest success as a chemical analyzer for military and homeland security applications, evident by the over 50,000 standalone IMS instruments (as of 2003) used to screen travelers daily in airports throughout the world [7,8]. The widespread acceptance of IMS for routine analysis is attributed to several favorable figures of merit for the technique, including i) the exceptionally high speed at which IMS can acquire experimental measurements (throughput can exceed 10,000 measurements per second) ii) the high degree of response (sensitivity) of IMS instruments to a given sample input (detection limits reported at ~0.1 fmol [9]), iii) the flexibility of operating IMS as either a narrow bandpass filter or broadband chemical analysis tool, depending on the specific technique used, and iv) the relatively simple operational principles of IMS which makes it easy to use (see **Section 1-2**) v) combined

---

This dissertation follows the style of The International Journal of Mass Spectrometry.

with its relatively low cost, portability and robustness[1]. Despite these impressive attributes, ion mobility has historically been slow to develop as a discovery driven analytical technique, falling upon its more pragmatic role as a fast chemical filtering device [12]. This is perhaps most evident by the fact that over a century has passed since Langevin published the first fundamental papers on ion mobility [13,14] yet only within the last decade has significant steps been made towards commercializing a research quality ion mobility instrument platform[2]. Indeed, a stigma existed around ion mobility for many years due to the early attempts to compare it with solution phase chromatography and time-of-flight MS methods. IMS cannot compare analytical with either of these techniques in terms of separation power, however there are specific analytical areas of merit in which IMS excels, and from which IMS has enjoyed a renewed interest (*vide infra*).

1-1.1 The Analytical Scope of Ion Mobility Coupled to Mass Spectrometry

Ion mobility has seen a growth of renewed interest in the last decade, particularly the coupling of ion mobility to mass spectrometry (MS), which provides a means of mass identifying ions separated by IMS. Hyphenating ion mobility to mass spectrometry (IMS-MS) enhances the information content of the technique by providing data across

[1] As an example the SABRE 4000 portable IMS (Smiths Detection) has the dimensions 36.3x11x13 cm, weighs ~7 lbs, and about 10 seconds of response for chemical detection. Cost is ~$20,000 USD [10]. It is estimated that a working IMS can be built using off the shelf parts purchased from a local hardware store and analytical grade IMS spectrometers will in short order cost as little as $1000 USD to end users [11].

[2] In 2006, Waters Corporation released the first large scale ion mobility research platform, the Synapt High Definition Mass Spectrometer (HDMS) which utilizes IMS for characterization and extends the ion mobility technique beyond its utility as an ion filtering method. Other instrument vendors have similar projects in the works and their subsequent release of ion mobility instrumentation is anticipated.

two dimensions of analysis [15]. When the coupling of two techniques yields different molecular information regarding the analyte, the dimensionality is referred to as being orthogonal— the extent of orthogonality is governed by the amount of additional information that can be learned from the combined analysis [16]. In the IMS-MS configuration, the analysis yields information regarding the analyte ion's size (IMS) and mass (MS). Because mass scales near linearly with analyte size, the orthogonality of IMS-MS is low as compared with other separation techniques coupled to MS such as liquid chromatography (LC-MS) and capillary electrophoresis (CE-MS)[3]. Peak capacity, as defined as the number of resolved peaks in the two-dimensional analysis space, will be low for IMS-MS as a result of the low degree of orthogonality, since analyte signal is not dispersed across the full area of analysis, but rather clustered about a size-mass correlation line [18]. This effect can be readily seen in **Figure 1** which contains a 2-dimensional mobility-mass plot of carbon clusters, with the data being isolated to a relatively narrow trendline from lower left to upper right representing the scaling of molecular size with mass. While the peak capacity is comparatively low for the IMS-MS technique, it is the speed of the separation and the potential for information driven analysis *viz.* size-mass correlation that lends IMS-MS its greatest strength as an analytical tool. For comparison, fast LC separations take place on the scale of minutes to hours [19] while ultra fast GC based on sample prefocusing methods can separate on

[3] The peak capacity of IMS-MS is estimated at 5.5×10^3 using time-of-flight mass analysis. For comparison, the peak capacity of LC-MS has been reported as high as 6×10^7 for Fourier transform ion cyclotron resonance (FTICR) based MS—over 4 orders of magnitude higher owing to the ultra high resolving power of FTICR, which can exceed 500,000 (as measured full width at half the peak's maximum). The record for FTICR resolving power stands at somewhere over 200,000,000 (two hundred million) for $^4He^+$ [17].

the scale of several seconds [20]. Neither compare in separation speed to IMS, which can disperse ions across mobility space within 10^{-6} to 10^{-2} seconds [21]. Additionally, the performance of condensed phase separations is highly dependant on the chemical characteristics of the analyte (*e.g.* sample volatility, column affinity). Because IMS separations occur following sample ionization and are based on a fundamental physical parameter of the analyte, the ion cross-section, the performance of IMS is comparable across a wide range of analyte classes, that is to say, if it can be ionized, it can be analyzed by IMS-MS.

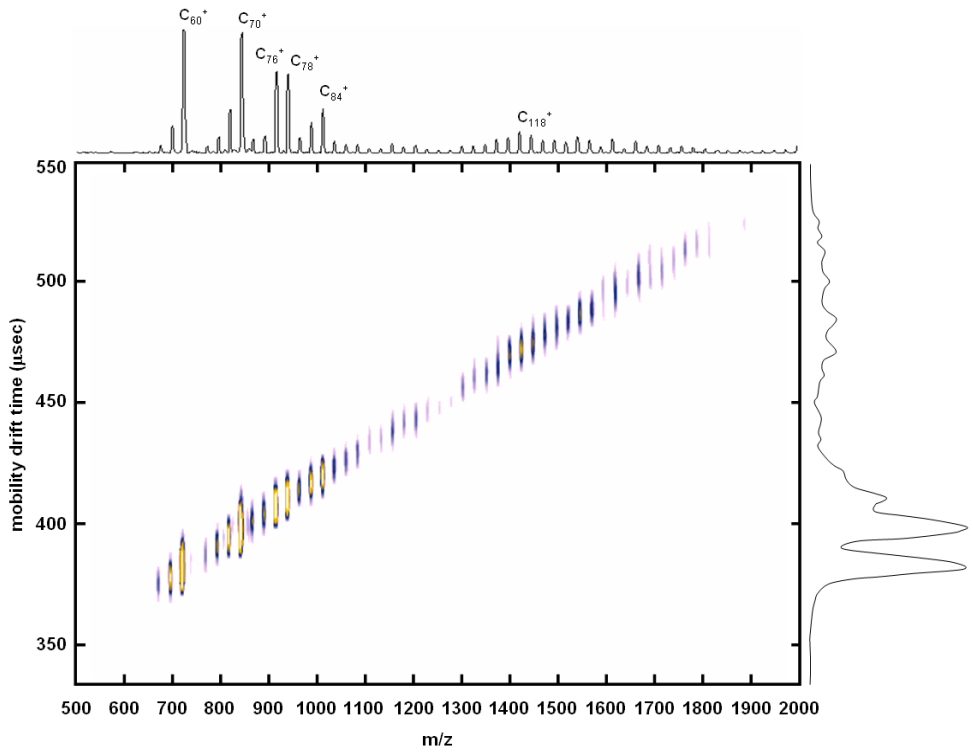

Figure 1 – A 2-dimensional (2D) ion mobility-mass spectrum of carbon cluster ions (fullerines) formed from laser ionization. Here and elsewhere, the IMS data is projected on the y-axis and the MS data is projected along the x-axis. Because the correlation between ion cross section and ion mass are closely related, data in the 2D projection will fall along a trend line relating these two parameters. The ratio of mass and size (trend line slope) are molecular class specific and relates to the gas-phase packing efficiency of the analyte, thus different analyte classes will exhibit different trend lines in the 2D analysis.

1-1.2 The Various Ion Mobility Techniques and Their Defining Features

There have recently been introduced several variations of the ion mobility technique, all of which have been coupled with mass spectrometers and each offering their own analytical advantages and limitations. An overview of the major ion mobility techniques and their defining features is provided in **Table 1** and these techniques are conceptually illustrated in **Figure 2**.

Table 1 – A summary of ion mobility techniques and their characteristic features.

Ion Mobility Technique	Type	Drift Region Geometry	Nature of Electric Field Used	Ion Motion to Electric Field	Ref.
Ion Mobility Spectrometry (IMS) Plasma Chromatography	dispersive in time	Radially Symmetric	Axial DC	parallel	[22]
Traveling Wave IMS (TWIMS)	dispersive in time	Radially Symmetric	Axial DC; Radial RF for Ion Focusing	parallel	[23]
Overtone Mobility Spectrometry	scanning / filtering	Radially Symmetric	Electrodynamic DC	parallel	[24]
Cyclic Drift Tube Mobility Spectrometry	scanning / filtering	Radially Symmetric; Cyclic Ion Path	Electrodynamic DC	parallel	[25]
Differential Mobility Analysis (DMA) Gas-phase Electrophoretic Mobility Molecular Analyzer (GEMMA)	scanning / filtering	Parallel Electrodes; Planar	Orthogonal DC Field	orthogonal	[26]
High-Field Asymmetric IMS (FAIMS) Differential Mobility Spectrometry (DMS)	scanning / filtering	Parallel Electrodes; Planar or Curved	Orthogonal RF (or electrodynamic DC); High Field Component	orthogonal	[27] [28]

Four of the most commonly encountered IMS techniques are i) traditional drift tube ion mobility utilizing a uniform electric field formed by direct current (DC) electrostatic potentials, which here and elsewhere is referred to simply as IMS (**Figure 2A**), ii) traveling wave ion mobility spectrometry (TWIMS) [29] which uses a radio frequency (RF) electrodynamic potential across an otherwise traditional geometry drift cell to carry analyte ions through the buffer gas (**Figure 2B**) iii) filter type ion mobility

instruments where ions are introduced orthogonal to a neutral gas flow and separated based on their differential mobility across two parallel electrodes, referred to as an aspiration ion mobility spectrometer or more commonly called a differential mobility analyzer (DMA, **Figure 2F**) [26,30], and iv) filtering ion mobility techniques utilizing electrodynamic potentials across parallel electrodes which induces differential ion migration to one electrode as the gas carries the ions between them (**Figure 2E**). In the latter ion filtering device which incorporates the electrodynamic potentials across two parallel electrodes, stable ion motion between the electrodes is mobility dependant and so only ions possessing a narrow distribution of gas-phase electrophoretic mobilities will be stable through this device. This type of ion mobility is referred to by several names; the two most commonly used are high-field asymmetric ion mobility spectrometry (FAIMS) and differential mobility spectrometry (DMS) [27,31]. Techniques i) and ii) (IMS and TWIMS) are *dispersive*, meaning all ions can theoretically be observed in the same experimental sequence while iii) and iv) (DMA and FAIMS/DMS) are *scanning* devices, meaning only ions possessing a narrow distribution of mobilities will have stable trajectories through these devices and be observed in any single experimental sequence, requiring systematic retuning of electrode potentials in order to generate a complete mobility spectrum.

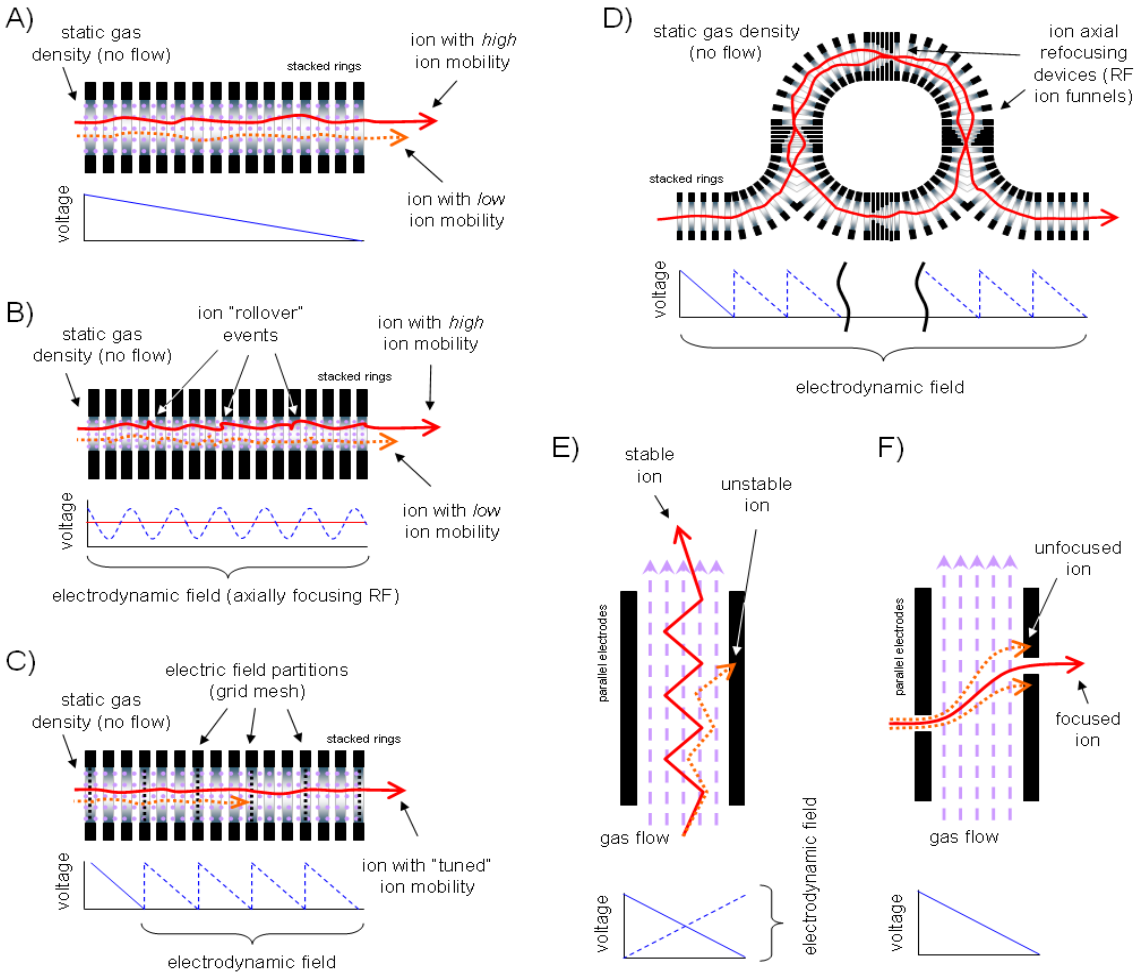

Figure 2 – Several ion mobility techniques and their principles of operation. Left and down: **A)** Conventional drift tube ion mobility spectrometer (IMS). **B)** Traveling wave ion mobility spectrometer (TWIMS) utilizing an RF field to drag ions through the gas filled cell. **C)** Overtone mobility spectrometry which takes an otherwise conventional IMS and applies an electrodynamic field to direct ion motion much like TWIMS. **D)** Cyclic drift tube mobility spectrometer which is a circular geometry IMS allowing ions to travel multiple cycles through the device, enhancing the resolving power, at a cost of sensitivity. **E)** Differential mobility spectrometer (DMS) which uses high and low fields across two parallel plates in the presence of a gas flow to selectively pass ions of a particular ion mobility value through the device. **F)** Differential mobility analyzer (DMA) which introduces ions orthogonal to the gas flow through a narrow aperture. The ion's mobility will determine whether it will exit another aperture at the far end electrode. Ion focusing can be accomplished by varying field and gas flow conditions.

The primary advantage of the scanning ion mobility instruments is that these devices can analyze a continuous stream of sample ions which is particularly useful for applications benefiting from single analyte monitoring and/or high instrument sensitivity

and response (due to the attenuation of chemical noise) such as chemical detectors. In contrast, dispersive ion mobility techniques require a narrow pulse of ions be periodically introduced into the spectrometer, which limits the analytical throughput and overall sensitivity of these types of instruments, however dispersive methods allow the entire mobility spectrum to be acquired in a single experimental sequence, greatly benefiting the dynamic range of analysis [32]. A new technique called overtone mobility spectrometry has been very recently described, which operates a dispersive IMS instrument configuration in a scanning mode by substituting the static DC potentials with electrodynamic potentials such that only a narrow distribution of ion mobilities follow the dynamic electric field and are allowed to traverse the drift region (**Figure 2C**) [24,33]. While very analogous in operational principle to the traveling wave IMS, the primary distinguishing feature of the overtone technique is the observation of ion signals at higher order (overtones) frequencies of the fundamental applied frequency. Ion signals at these overtone frequencies exhibit narrower peak widths than those found at the fundamental frequency, which offers the advantage of increasing the resolving power in a traditional IMS geometry, but at a cost of decreased sensitivity and dynamic range. Spectral interpretation of these overtone ion signals can also be more difficult than deciphering a conventional dispersed drift time spectrum and the dynamic range remains low. The temporally dynamic DC fields utilized in the overtone mobility method has established the foundations for operating a drift cell in a cyclic geometry for multi-pass IMS experiments (**Figure 2D**), which holds promise for enhancing the resolving power of IMS instrumentation even further [25]. Other exciting

areas of high resolution IMS development focus on drifting the ions against a counter-flow of buffer gas to increase the dampening forces and thus the retention time [34,35] and sampling ions orthogonally from a conventional IMS drift tube to minimize the deleterious effects of lateral ion diffusion on the temporal spread of ions in the swarm to further increase instrument resolving power [36]. The latter is analogous to orthogonal acceleration time-of-flight mass spectrometry methods, which is discussed in **Section 1-6.2**.

The decreased sensitivity of dispersive instruments is considered a reasonable compromise for other advantageous analytical figures of merit for dispersive techniques such as a broad dynamic range and high separation efficiencies in the mobility dimension. Conventional drift tube IMS instruments still perform with the highest obtainable ion mobility resolutions [37-39] and is the only ion mobility technique where the experimentally measured data can be directly correlated to the ion's gas-phase collision cross section—structural information which is desirable particularly in the analysis of nanomaterials, peptides and proteins [40-42]. In this sense, IMS transcends the traditional function of a separation device, lending itself also as an analytical identification and characterization tool, which sets it apart from condensed phase separation sciences (where the focus is traditionally on the separation rather than analytical information) and makes drift tube IMS an ideal platform for fundamental studies in research applications. The lowered sensitivity resulting from the introduction of a duty cycle in the pulsed IMS experiment can be compensated for by the additional observation time afforded by the high speed of the separation [21]. Hyphenating IMS

with a high performance MS technique such as time-of-flight (TOF) MS offers a fast and information rich, high peak capacity analysis afforded by the enhanced resolution and broad dynamic range across both dimensions (mobility and mass) of data [43]. The scope of this dissertation henceforth will concern only conventional DC uniform field drift tube IMS, which is the most commonly encountered and theoretically developed ion mobility method and upon which the work detailed in the subsequent sections is based.

1-2 Basic Operational Principles of Ion Mobility Spectrometry

In qualitative terms, ion mobility refers to the velocity of an ion through a neutral gas under the influence of an electric field. The vector direction of the ion with reference to the electric field (either parallel or orthogonal), the field's magnitude (either high or low field), and whether or not the field is static (DC) or dynamic (RF) in time defines the various analytical techniques which are presented under the name ion mobility (refer to **Table 1** for a list of the various ion mobility techniques). The first, simplest and most widely encountered ion mobility spectrometry technique is that which operates on the basis of ion motion parallel to a low magnitude, electrostatic field through a buffer gas experiencing little or no flow (*i.e.*, under static pressure conditions). The basic instrumentation features and operational principle of this type of ion mobility referred to here and elsewhere simply as IMS, is illustrated in **Figure 3**.

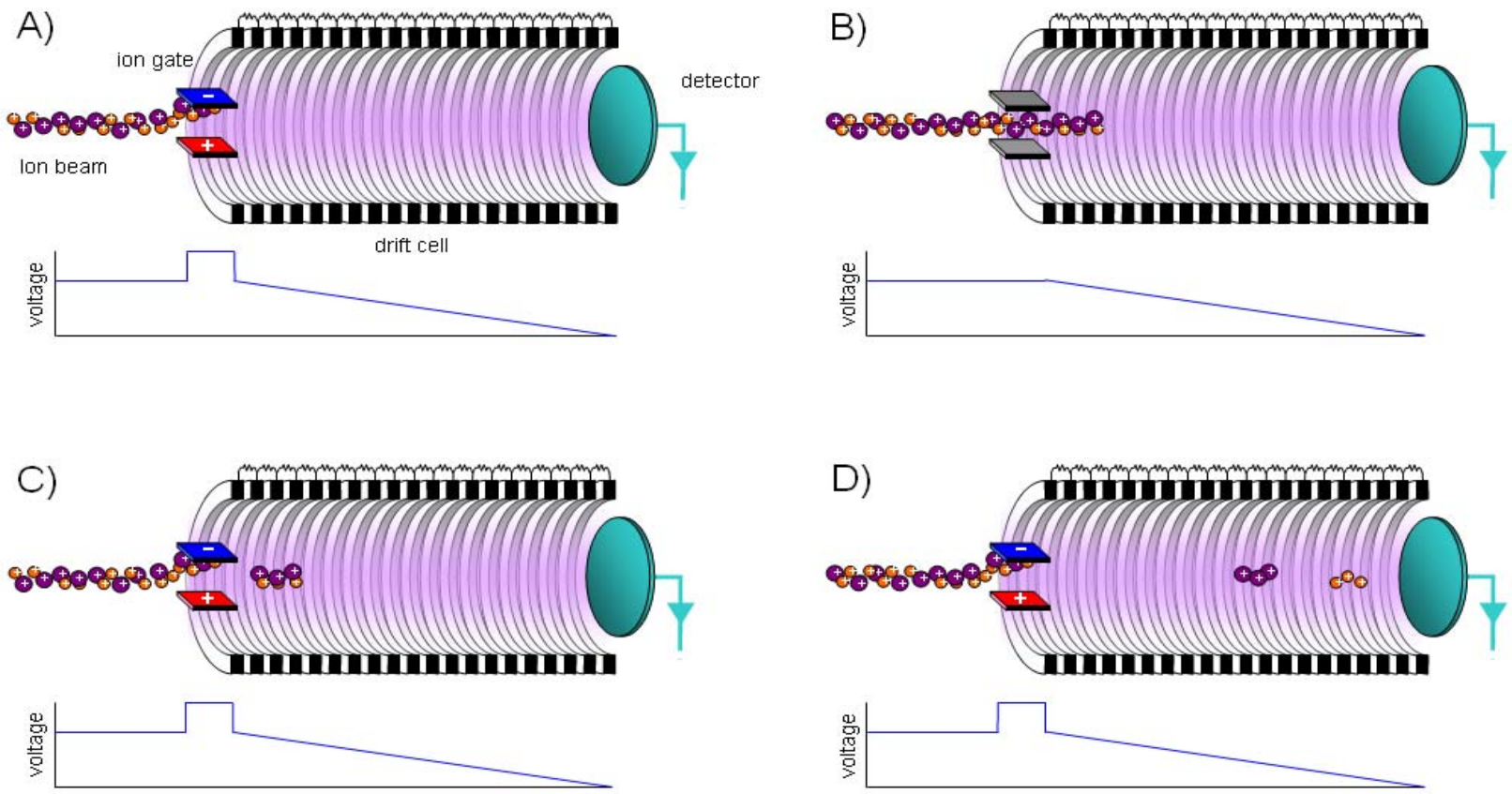

Figure 3 – The basic operational principles of the drift tube ion mobility experiment. **A)** The ion gate (shown here as a two element ion deflector) blocks ions from entering the drift region most of the time. **B)** The gate opens for a brief period of time (~10-100 μs), allowing a narrow pulse of ions to enter the drift region. **C)** The ion gate closes and the ion swarm is allowed to traverse the drift cell (pulled through by the electric field gradient) and experiences collisions with the buffer gas. **D)** As the ion swarm drifts through the neutral gas, ions within the swarm will separate based on their different ionic mobilities.

The ion mobility experiment begins with the creation of a pulse of ions, which can be accomplished either from a pulsed ionization source (*e.g.*, desorption/ionization from a pulsed laser) or through gating a continuous ion beam as depicted in **Figure 3** (refer to **Section 1-4.2** for an overview of ion gating methods). This distribution of ions is then introduced into a drift cell which contains an (ideally) fixed pressure of a pure, nonreactive gas and an electric field gradient that directs ion motion forward through the drift region. During their transit through this drift region, the distribution of ions (traditionally referred to as an ion swarm) experiences many dampening collisions with the bath gas—different ion species present in the swarm can drift at different velocities depending on their ion mobilities. The ion mobility experiment is a time-of-flight measurement between the time the ions are introduced into the drift cell to the time these ions take to traverse the drift region and elute out the other end. During this gas transit time, ions partition into their species dependant ionic velocities (mobilities) and so arrive at a detector in different time intervals. Specific experimental details of the IMS technique are presented in **Section 2**.

1-2.1 Electric Field Considerations for IMS Experiments

The ion motion through the drift region can be described by simple kinetic theory, where the electric field (acceleration) and collisional dampening (deceleration) of a distribution of ions is balanced at a "steady state" through the proportionality constant, K (the mobility constant) by the following relationship:

$$v_d = KE \tag{1}$$

Where v_d is the drift velocity of the ion swarm and *E* is the magnitude of the electric field (measured as volts per unit distance). **Equation 1** is a first approximation of the ionic mobility. *K* is only constant at low electric field conditions where the ion-neutral interaction is characterized by nonreactive, elastic diffusional scatter [44]. At conditions where the ion swarm gains a significant amount of energy between collisions (high field conditions), the relationship between the drift velocity and the electric field is no longer linear, that is, *K* is no longer a constant, predictable value and the proportionality constant of **equation 1** must then consider higher (cubic) order terms [45,46]. High field conditions have been utilized in IMS to introduce selectivity in the separation by inducing nonuniform behavior between specific ions with the bath gas [47,48]. This strategy relies on the principle that specific ions in a mixture analysis will separate due to increasing differences in their ion mobilities as the electric field is raised, though this approach is not useful when analyzing ions of a similar chemical class since differences in their ion mobilities are not expected to change significantly relative to one another [49]. Aside from these special analytical applications, IMS is normally operated at or below low field limits, since under these conditions the relationship between the electric field and the arrival time is linear and predictable. **Section 1-3.3** discusses in more detail the measure and experimental conditions which influence high and low electric field in the IMS experiment.

1-2.2 Measurement of Mobility Constants and the Gas Phase Collision Cross Section

The value of the mobility constant, *K*, will scale with the drift velocity, v_d, which for the same ion will change depending on the temperature and number density of the drift gas. In order to compare IMS data across different instrument platforms, it is customary to normalize the mobility proportionality constant (K) to standard temperature and pressure, through the following conversion [50]:

$$K_0 = K(\frac{273.15}{T})(\frac{P}{760}) \quad (2)$$

K_0 is referred to as the standard or reduced mobility value and *T* and *P* are the buffer gas temperature (in units of Kelvin) and pressure (in units of torr), respectively. The units of both *K* and K_0 in **Equations 1** and **2** are in $cm^2 \cdot V^{-1} \cdot s^{-1}$. Strictly speaking, the reduced mobility (or any analogous normalized mobility parameter) should be based on the number density rather than the pressure particularly when varying the temperature of the experiment, but standards have already been established and remain usable for the vast majority of experimental purposes currently encountered in the IMS research community (refer **to Section 1-3.3** for more insight into this issue) [51].

The above relationship underscores a key piece of information that the IMS experiment can provide: mobility coefficients that are reproducible at low field and can be compared across different IMS instrument platforms [52,53]. An additional piece of information which can be derived from low field IMS experiments is the ion swarm's average gas-phase collisional cross-section, Ω, which is related to *K* by the simplified Chapman-Enskog kinetic theory [50,54]:

$$K = \frac{3}{8}\frac{q}{N}\left(\frac{\pi}{2\mu k_b T}\right)^{\frac{1}{2}}\frac{1}{\Omega} \quad (3)$$

The values q, N, μ, and k_b are the ionic charge, buffer gas number density, ion-neutral reduced mass term, and the Maxwell-Boltzmann constant, respectively. When all other conditions of the ion mobility experiment are known (ion charge and mass; buffer gas temperature, mass, and pressure), the ion collision cross-section can be directly calculated using **Equation 3**, and this Ω value can be compared with results from theoretical simulations involving the structural dynamics of higher order molecular systems in order to arrive at a reasonable value for the ion's gas-phase structure [41]. Further refinements of the theory have been made which incorporate higher order ion effective temperature terms since the relationship in **Equation 3** does not factor in ion heating effects due to the electric field, but these refinements account for only a 2% change in the cross-sectional values obtained using the generalized theory above, and so are not widely used for deriving structural data from the ion mobility measurements [46]. While the work detailed in this dissertation makes no explicit use or derivation of Ω from experiment, it is instructive to note that such information can be obtained from the IMS experiment, and constitutes a significant motivation of the current state of IMS research today [5,42].

1-3 Separation Efficiency of Ion Mobility and High Resolution Considerations

By large the widest and most successful application of the IMS technique to date has been its use as a separation device. Analyte separation in IMS relies on the principle

that different analyte ions in the swarm will interact with the neutral buffer gas differently as the swarm traverses the drift region of the instrument. While the predominant mechanism that governs ion retention in the IMS experiment is the ion's physical size and shape via the ion's hard sphere collisional cross-section [55], ion-neutral long-range interactions can become significant [56], particularly if more polarizable buffer gases (as compared with helium, *e.g.,* argon, carbon dioxide) are used in the experiment [57]. Ion-neutral gas affinities have been exploited advantageously to introduce selectivity to the IMS experiment and separate ionic species which are very similar and cannot be differentiated by conventional MS analysis alone, such as chiral molecules [58], structural [59,60] and electronic state isomers [61].

1-3.1 The Measure of Separation Efficiency in IMS

In terms analogous to those used in optical spectroscopy [62] and mass spectrometry [63,64], separation efficiencies in ion mobility instrumentation are reported in two primary means, as either *resolution* [65] or *resolving power* [66]. These two terms are oftentimes erroneously used interchangeably in the ion mobility and mass spectrometry literature—the currently accepted convention in the mass spectrometry community is to refer to resolution when dealing with empirically measured separation of two peaks and resolving power when measuring the width from a single peak [67]. While it is the *resolution* that is most informative metric when dealing with the ability of an analytical technique to differentiate two closely spaced signal peaks, it is a difficult quantity to compare across instrument platforms since so many different classes of

samples are analyzed from one instrument variation to another. Numerous chemical standards have been proposed for use in IMS instrumentation in order to facilitate the accurate and comparable measurement of IMS resolution [68-70], however the wide variance of operational conditions currently utilized in IMS instrumentation (*e.g.,* buffer gas, ionization methods) has made it difficult for the IMS community to come to a consensus on any single standard or class of standards. Thus, *resolving power* has emerged as the accepted "performance parameter" measurement of IMS separation efficiency and is based on a single-peak quotient which is calculated from experimental data as follows [66]:

$$R = \frac{t_d}{t_w} \tag{4}$$

where t_d is the analyte signal's measured drift time and t_w is the measured peak's full width at half of its maximum height (FWHM). The fundamental problem with this definition, however, is that the quotient value has no interpretable meaning in ion mobility regarding an IMS instrument's ability to resolve out specific analyte features. This becomes clear when one considers that unlike optical spectroscopy and mass spectrometry where resolving power refers to the ability of the instrument to resolve out specific features of the measurement (*i.e.*, quantized levels of the electromagnetic spectrum for the former, units of exact mass for the latter), there are no quantized features in mobility space which can be resolved out by IMS[4]. A more proper definition

[4] Consider also that in mass spectrometry, resolving power values have physical meaning. For example, at a mass spectrometer resolving power of 100, the instrument will be capable of separating signals of two ions with m/z values 100 and 101. The same resolving power of 100 for an ion mobility instrument cannot

of separation ability in ion mobility has been provided by Hill and coworkers in terms of the number of theoretical plates, the separation efficiency performance parameter commonly used in fractionation and chromatography [71], but has yet to gain acceptance in the ion mobility community [72]. An additional concern regarding the resolving power measurement described by **Equation 4** is that since the peak widths are compared across half height measurements, band broadening below half height is ignored, that is, a peak of non Gaussian shape (*e.g.,* Lorentzian[5] or irregular peak shape) may be much broader at its base than at its half height, which can result in favorable calculated resolving power values but poor observed separation ability [73]. Thus, despite questions regarding the analytical meaningfulness of the single-peak based quotient value calculated by **Equation 4**, this resolving power value remains today the most widely accepted measure of an IMS instrument's separation ability, due to the ease at which the value can be calculated from virtually any piece of experimental IMS data and the possibility for direct comparison of instrument performance across ion mobility instrument platforms. With these appropriate *caveats* in place, this dissertation will make use of the resolving power method to discuss and compare IMS separation power in order to facilitate likeminded discussion.

---

be directly interpreted into a meaningful performance criterion, thus it remains useful primary as a metric for comparison.

[5] Lorentzian peaks are observed when data deconvolution algorithms are used following IMS data acquisition, specifically in Fourier or Hadamard transform IMS.

1-3.2 Factors Limiting IMS Resolving Power

Revercomb and Mason described four factors which contribute to band broadening (t_w) and ion drift time (t_d) [46]. These include: i) lateral (axial) *diffusion*, ii) *Coulombic repulsion* between mutual ions in the swarm (space charge) iii) the *initial temporal spread of the ion swarm* introduced into the drift region and iv) *ion-molecule reactions* between the ion and the neutral buffer gas and/or impurities in the gas. Experimentally, these factors have been observed to reduce the observed resolving power in IMS. For example, significant band broadening in a miniature IMS equipped with a laser ionization source was observed and attributed to space charge effects, that is, under experimental conditions where high ion densities were admitted and confined to a small drift volume [74]. Ion molecule reaction chemistry can have a substantial impact on lowering the observed resolving power in IMS even when special care is taken to remove impurities in the drift gas [75]. Water impurities are particularly invasive and can distort mobility measurements if steps are not taken to reduce or quantify the presence of moisture in the IMS drift cell [76]. Hill and coworkers also identified an *inhomogeneous electrostatic drift field* and ion *detector response times* as factors contributing to peak broadening, but conclude these factors have a small contribution to the overall resolving power measured in ion mobility [66]. Recent theoretical treatments of ion drift in the presence of elastic collisions support the idea that nonuniform electric fields will broaden ion distributions and lead to a decrease in resolving power [77]. We have also concluded in our own laboratory that field inhomogeneity does contribute to peak broadening particularly for the extreme case where relatively strong focusing fields

are utilized across the entire length of the drift region [78], which results in about a 20% reduction in the maximum obtainable IMS resolving power. Detector response times have been shown to have a significant contribution to peak broadening when using direct ion current measurement detectors (Faraday plate) due to current induction effects[6] [79]. Finally it should also be mentioned that structural or conformational isomers will also contribute to peak broadening and reduced resolving power values, though the occurrence of these isomers is expected to be uncommon.

If a sufficiently narrow packet of ions is admitted into the IMS such that the temporal spread of the ions does not contribute to the observed peak widths after ion migration through the drift field (that is, diffusion is the predominant band broadening mechanism), then factor iii) *initial temporal spread*, can be considered negligible as well as factor ii) *Coulombic effects*, since the ion densities under these conditions would be low [80]. Factor iv), *ion-molecule reactions*, can also be ignored if a neutral drift gas such as helium or nitrogen is used with very little impurities present and ions do not gain an appreciable amount of energy during their transit through the drift gas to initiate reaction chemistry (that is, ion energies are maintained close to thermal) [65,81]. The probability of reaction chemistry occurring is also much lower at reduced pressures (*e.g.,* 10 torr) than at ambient pressure due to the decreased number of collisions, though care must be taken in reduced pressure IMS to ensure ion energies are kept low since the decreased number of collisions will in turn lead to an increase in the ion energy at

[6] Standalone IMS instruments, such as those used in airport security checkpoints and military weapons screening devices, use ion current detection methods. This is both to reduce cost and for practical reasons that electron multiplication methods do not work effectively under elevated pressure environments.

elevated electric fields. Inhomogeneity in the electric field can be minimized by taking special care in the design and fabrication of the IMS cell. Finally, since hyphenated IMS-MS instruments utilize electron multipliers in high ($<10^{-5}$ torr) vacuum to detect ions, detector response times are low as compared to Faraday plate current detection meaning that very fast electron multiplication detectors for time-of-flight measurements will have virtually no contribution to IMS band broadening in the experiment [82,83].

When these minor contributions to reduced resolving power are considered and taken into account in the experimental setup, the *predominant contribution to observed signal peak widths in the ion mobility experiment is lateral ion diffusion and the initial width of the ion swarm* introduced during each experimental measurement. A practical relationship has been derived by Hill *et al.* between resolving power, R_d, and experimental conditions which considers only diffusion as the limiting factor for observed peak widths [65]:

$$R_d = 0.3\left(\frac{Vq}{k_b T}\right)^{\frac{1}{2}} \tag{5}$$

No straightforward relationship such as the one in **Equation 5** has been derived between resolving power and the initial ion pulse width, however one can conclude intuitively that the width of the measured signal peak cannot exceed the initial time width, t_w, of the swarm, thus the initial pulse width-limited resolving power, R_w, can be expressed by the following inequality:

$$R_w \leq \frac{t_g}{t_d} \tag{6}$$

A cursory examination of **Equation 5** reveals that resolving power can only be increased by increasing the drift voltage, V, increasing the number of charges, q, on the ion, or decreasing the temperature, T, of the ion and surrounding neutral gas. **Equation 6** suggests also that these conditions will affect resolving power only if the initial pulse width of ions is sufficiently small as to not affect the measured peak widths, that is, the experimentally limited resolving power is governed by the lower of the two values, R_d or R_w. These effects have been verified experimentally for practical IMS instrumentation [84] and experimental results are in good agreement with theory.

1-3.3 The Influence of Pressure, Length and Voltage on IMS Resolving Power

While much of the current literature dealing with resolution in ion mobility makes the above distinctions regarding the resolving power dependencies on V, q, T, and t_w, there remains some confusion as to the roles that the drift cell length, L, and the drift gas pressure, P, play in measured resolving power values. Indeed, the highest recorded resolving power values have been achieved on IMS instruments incorporating long drift regions [39], high pressures (760 torr and above) [38,85], or both [37], yet **Equations 5** and **6** do not make mention of these experimental parameters. This is due to the fact that **Equation 5** is derived from the Einstein diffusion relationship, which is valid only for ions with near thermal energies [86]. At sufficiently high electric field conditions, diffusion no longer describes the motion of ions in the IMS experiment because ions gain an appreciable amount of energy between collisions with the neutral gas to where

scattering processes dominate ion motion. Ion energy gained in the presence of the electric field and neutral gas can be expressed by the parameter,

$$\frac{E}{N} \tag{7}$$

classically measured in Townsend units (Td, which is equivalent to 10^{-17} V·cm^2) but oftentimes expressed as *E/P* in units of V·cm^{-1}·torr^{-1} for ease of calculation [87]. Low field threshold values of *E/N* are mass and chemical class dependant and can vary anywhere from ~2 V·cm^{-1}·torr^{-1} for atomic species to more than 40 V·cm^{-1}·torr^{-1} for peptides and protein ions[7] [88,89]. The important consequence of the *E/N* expression is that the parameters, *L* and *P* play significant roles in maintaining diffusion only ion motion in the IMS experiment, specifically, low field conditions are maintained by using sufficiently long drift regions and/or high number gas densities (*i.e.*, proportionality of the first order approximation of **Equation 1** is valid). Since **Equation 5** suggests higher voltages are needed in order to achieve higher resolving powers in the ion mobility experiment, a careful balance must be achieved in IMS instrument designs in order to maximize *V* while maintaining the low field requirements of *E/N*, that is, as *V* is increased, either *L*, *P* or both must also be increased in order to gain the resolving power benefits of high voltage operation [90].

[7] These numbers assume room temperature. It is important to note that the Townsend unit accounts for temperature variance in the IMS experiment, since it is based on *N* rather than *P*. The result is that at low temperature, *E/N* values would be much lower than at higher temperature, for all other parameters (*P*, *V* & *L*) being equal.

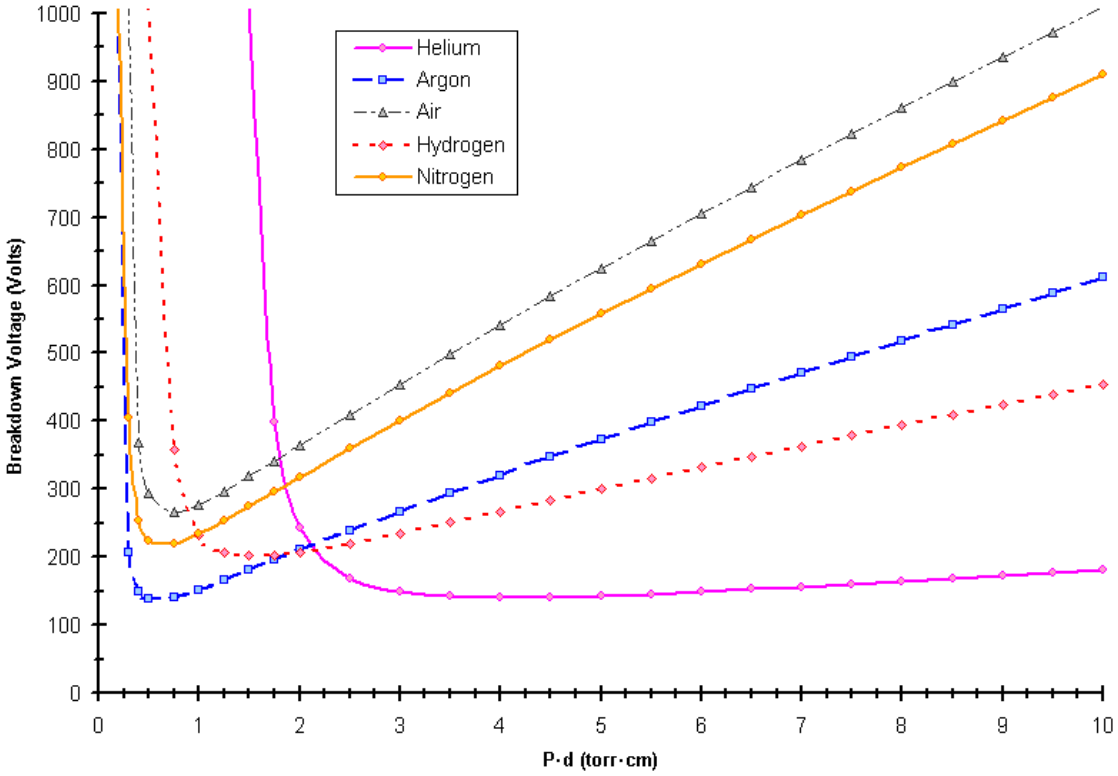

Figure 4 – Paschen breakdown curves for several dielectric gases. Data is for breakdown between iron electrodes (the primary component of stainless steel alloys). The experimentally determined Paschen coefficients were obtained from reference [91] and plotted using the method described by A. L. Burm [92]. Paschen curves are visually useful for estimating maximum operating voltages for electric fields in the presence of a dielectric gas, if values such as the operational gas pressure and the highest potential applied across the shortest conductor distance are known. Note that helium (blue squares) possesses the lowest tolerance to electrical breakdown and is relatively insensitive to pressure changes above ~3 torr. Air (black triangles) is among the most tolerant gases for resisting electrical breakdown.

There remains a practical limit to the magnitude of the voltage which can be applied across the drift region. At sufficiently high values of *V*, gas breakdown will occur, the voltage threshold for breakdown is governed in DC fields by many factors, including the potential drop across two electrodes, the spacing between these electrodes, the material and shape of the electrodes [93], and the type and density (pressure) of the dielectric gas present in the electric field [94,95]. Low pressures in the 1-10 torr regime

are particularly susceptible to gaseous breakdown due to the favorable gas velocities at these gas densities for initiating a secondary electron cascade [96]. Such breakdown affinities can be characterized through experimentally derived plots known as Paschen curves. Paschen curves for several common dielectric gases used in the IMS experiment (*e.g.*, helium, nitrogen, air) are provided in **Figure 4**. These curves provide a useful means of estimating the highest practical voltage one can obtain in a given IMS experimental setup. For example, the Paschen curve predicts that two electrodes spaced 1 cm apart in ~2 torr of helium gas will experience breakdown at ~250 V—reducing the electrode spacing by half (1/2 cm) or increasing the pressure by a factor of 2 (4 torr) will have the effect of lowering this breakdown voltage to ~150 V. An interesting point to note is that for helium, the highest probability of discharge occurs in the range of 2-8 torr cm [97], which is the pressure regime of the majority of drift cells operating in an IMS-MS configuration [15]. Increasing the gas density or electrode spacing for helium gas has little practical effect on this discharge probability—a factor of two increase in pressure, from 4 to 8 torr for example, will only raise the maximum operational voltage of the IMS experiment by ~10% due to the high discharge affinity of helium gas [92]. An examination of the curves in **Figure 4** suggests that discharge limited operational voltages can be dramatically increased by utilizing drift gas other than helium such as N_2. In practice, more massive bath gases compromise ion mobility resolving power and ion transmission due to increased ion diffusion and scatter losses [98] and particularly polar bath gases (*e.g.*, carbon monoxide) severely broaden ion signals due to the extended ion-neutral interaction, and so helium remains the bath gas of choice for

research IMS instrumentation. Still, a common practice for overcoming this discharge limit in gaseous dielectric applications is to add a small fraction of an electronegative gas, such as SF_6, which suppresses the initiation of an electron cascade [99]. In our own laboratory, we have found that introducing a small impurity of air into the helium gas will raise the discharge limit and allow us to operate the IMS experiment at higher voltages. It should be noted that the addition of any gas impurity will perturb the mobility measurement due to the added collisions with the ion and impurity, causing a broadening and shift in observed mobility times even for low impurity concentrations in the sub ppb range [75] which amounts to only 1 impurity molecule for every 10^{10} atoms of helium! Undesirable ion chemistry in the drift region is particularly problematic in the analysis of small molecular ions [100]. Practical considerations can be utilized when designing the initial electrode geometry for the drift region in order to maximize operational voltages which can be achieved. A simple and straightforward design criterion to minimize the likelihood of electrical discharge for routine experimental conditions is to maximize the distances between high potential electrodes, or by the same approach minimize the voltage drop across closely spaced conductors of high potential difference. Another simple strategy to overcome discharge voltage limits is to break the line of sight between electrodes possessing a high potential between them, since discharge is an electron propagation phenomenon. Another strategy for controlling gaseous breakdown has been to coat electrodes with a thin layer of dielectric material, such as fluorocarbon polymer [101], though this approach has limited practical utility in IMS since dielectric materials dissipate surface charge poorly and can adversely

influence ion trajectories when placed in proximity to the ion transit. As dielectric materials are difficult to model, their effect on ion trajectories must be undertaken experimentally, which requires considerable time and energy, and so the practical approach is to avoid the use of dielectrics altogether unless where absolutely necessary such as when isolating electrodes [102]. Many of the problems associated with electrical breakdown can be circumvented through the careful design of drift cell electrode geometries and selection of materials during initial construction of the IMS spectrometer—specific design strategies used in the construction of the drift cell spectrometer described in this dissertation are also aimed at limiting electrical discharge problems and these details are presented in **Section 2-5.6**. Despite how the curves in **Figure 4** are presented, there is a polarity dependence on breakdown, specifically positive polarity voltages are more susceptible to electrical breakdown than are negative polarity voltages [103], and so one approach to maximizing the operational voltage across an IMS cell is to preferentially bias the drift region at a negative potential[8]. Finally, there is also a distinct temperature dependence on electrical breakdown, specifically the electrical breakdown voltage for a dielectric gas is inversely dependant on the gas temperature [106], therefore operating the IMS at low temperature should

[8] The polarity dependence on electrical breakdown is related to the formation of a corona prior to a full propagation of a plasma cascade. While in both polarity cases, a corona forms and ionizes the gas about the electrode, in the positive polarity case the electrons are extracted by the positive electrode surface, leaving positive ions about a positively charged surface and creating a greater localized positive potential which promotes the cathode directed streamer. In the negative polarity case, ions formed in the corona have their electrons repelled away from the electron surface, leaving positive ions about a negatively charged surface, which serves to shield the magnitude of the potential and discourage breakdown. Electron mobility is extremely fast as compared with the ions, so this is a near instantaneous process. The ultimate result is that a negatively charged surface will have a higher breakdown voltage than a positively charged one [104,105].

afford an increase in the maximum voltage that can be applied prior to the onset of a discharge condition, although an exact quantity for voltages gained at low temperature is difficult to arrive at[9].

1-4 Analytical Sensitivity for Hyphenated Ion Mobility Mass Spectrometers

From the discussion thus far, one might conclude that in order to maximize the resolving power and thus the separation ability of IMS instrumentation, all that would be required is to construct a very long drift region incorporating the highest achievable voltages and pressures, operate the experiment at the lowest drift gas temperatures possible, and analyze highly charged ions, but quickly it would become apparent that several technical challenges would limit this design criteria substantially.

1-4.1 Ion Transmission Through the Drift Region and Into the Mass Spectrometer

Among the most compromising factors to consider when designing high resolution IMS instrumentation is analytical sensitivity which is influenced by the transmission efficiency of ions from the ion source to the detector. The problem of sensitivity becomes very apparent when one considers that hyphenated IMS-MS instrumentation equipped with an ambient ionization source requires shuttling ions across 8 to 10 orders of magnitude of gas pressure: atmospheric pressure for the ion

[9] This trend for temperature dependant breakdown is only valid for the same number density of gas. For an ideal gas, as the temperature is lowered, the number density increases for the same pressure and volume, and so the breakdown voltage will actually decrease (become worse) for most low temperature experiments operated under the same pressure conditions as room temperature. While there is a point in the breakdown curve where higher number densities help deter breakdown, for the pressure regime of most IMS experiments, this is not the case.

source (760 torr), low pressure for the ion mobility spectrometer (1-10 torr), and high vacuum for the mass spectrometer (10^{-6} to 10^{-8} torr). In order to maintain these differential pressure regimes, it is necessary to utilize high capacity pumping and pinhole conductance limits, which contributes to high ion losses between each region of pressure. The ionization can also be conducted at reduced pressures, as with laser desorption ionization (LDI) and electron ionization (EI) [107,108], which lessens the pumping requirements and thus ion losses associated with ion transfer from the source to the IMS. Regardless of the ionization methods used, the necessary transfer of ions from the IMS to the MS through a conductance limiting aperture still remains a primary area of ion loss for hyphenated IMS-MS instrumentation. This is due to the fact that within the drift region, ions are constantly experience diffusion both longitudinal to the drift axis, and radially away from the drift axis towards the electrodes of the drift cell. Longitudinal diffusion contributes to band broadening and a decrease in resolving power and radial diffusion contributes to poor ion transmission since radially divergent ions will not pass through a pinhole aperture placed at the back of the IMS drift cell [109]. A practical look at this problem within the last decade has resulted in the discovery of several ion focusing schemes which substantially improved ion transmission through this IMS-MS interface region, specifically based on two strategies i) refocusing radially diffuse ions at the end of the drift cell through the use of decreasing inner diameter RF ion confinement rings (referred to as an ion funnel) [110] and more recently ii) the development of periodically refocusing ion optics integrated within the drift cell geometry that continually directs ions back to the center axis of the drift region during

ion transit through the drift region [111]. Both strategies improve transmission efficiencies in the IMS-MS experiment significantly at a moderate cost to resolving power and have opened the way for development of next generation high resolution IMS instruments. While the radial RF fields employed by the Traveling Wave technology (refer to section 1-1.2) also accomplishes radial compression of the ion beam and thus very high transmission through the drift region, the RF field which is swept across the drift cell complicates measured ion mobility values and results in poor mobility resolving power for the TWIMS device [112].

All of these IMS ion focusing strategies (periodic DC fields, ion funnels and traveling waves) discriminate against low m/z ions due to detrimental collisional scattering experienced as these ions approach the focusing fields [113,114]. For these devices, ions below approximately 200 m/z cannot be efficiently transmitted, and so these ion focusing strategies cannot be used when the study of low mass analytes is desired. This is a general limitation of using strong focusing fields in the presence of gaseous collisions and even uniform field drift cells exhibit some degree of low mass discrimination [115].

1-4.2 The Ion Gate and Associated Ion Losses

Dispersive ion mobility (IMS) is a time-of-flight measurement which requires ions to be introduced into the drift region in discrete packets—their introduction defines the start time of the measurement. For inherently pulsed ionization sources such as laser desorption ionization (LDI), this process is relatively straightforward—each laser pulse

is timed to the data acquisition and in theory all ions generated by LDI are admitted into the drift region and analyzed by the mobility spectrometer [116]. Because the scope of LDI does not ionize the full range of possible analytes and does not generate high charge state ions desirable for high resolving power IMS experiments [117], there remains the need for using continuous ionization sources with IMS, examples being the electron ionization (EI) source used primarily for small organic molecules [118] and the electrospray ionization (ESI) source which, like LDI methods, can generate ions from nonvolatile analytes but unlike LDI can generate ions in high order charge states [119] useful for high resolving power IMS.

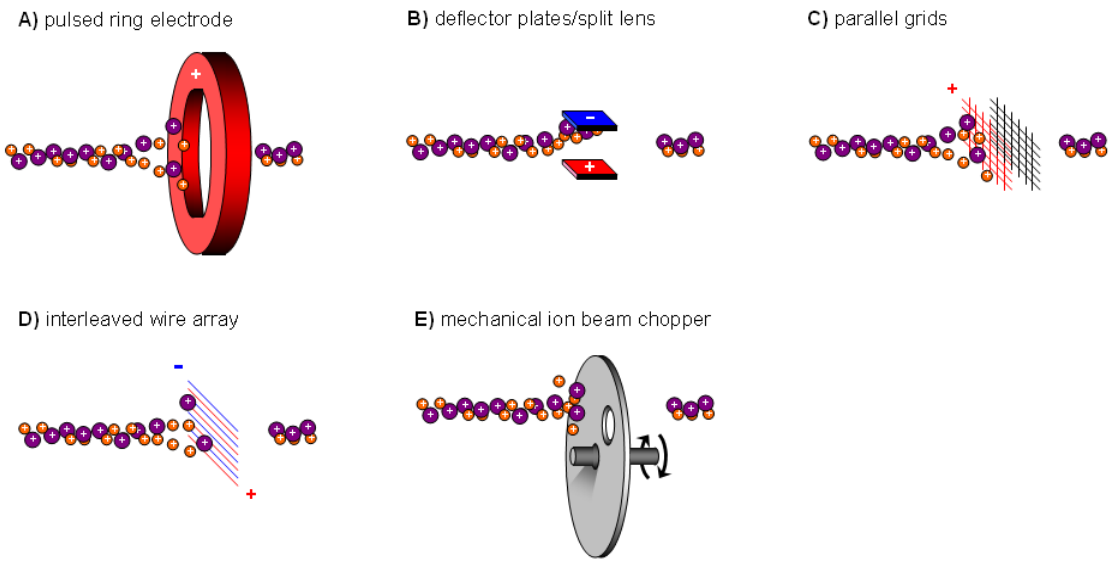

Figure 5 – Various ion gating methods used in ion mobility spectrometry. From left to right these are: **A)** a single element pulsed ring, **B)** deflection style ion gate incorporating two electrode elements **C)** Tyndall ion gates which utilize two grids parallel to one another **D)** Bradbury-Nielsen ion shutter which consists of a single plane of interleaved wires and **E)** a mechanical beam pulsing device. Refer to the text for more discussion and relevant referenced works regarding these methods.

In order to understand how the ion gate can affect IMS instrument performance, it is helpful to have a general overview of ion gates and their operational principles. There are various methods which have been devised for generating a pulse of ions from a continuous ion beam. Conceptual representations of several ion gating methods which have been utilized for IMS are presented in **Figure 5**. Methods for gating ions in ion mobility applications can be as simple as pulsing a single ion lens electrode with a stopping potential (**Figure 5A**) [120,121] or deflecting the beam as it passes through two parallel plates (**Figure 5B**) [122] or a split ion lens [123]. Mechanical choppers (**Figure 5E**) have also been utilized for generating ion pulses in ion mobility, but their use has been limited to proof-of-concept experiments [124] and exotic ionization sources [125]. The vast majority of ion gates used for ion pulse generation in IMS rely on two basic designs first described by Tyndall [126], and jointly by Cravath [127] and van de Graaff [128] which are based on thin wire elements biased at varying potential. The ion gate design utilized by Cravath and van de Graaff was later adopted and extensively used by Bradbury and Nielsen [129] whom it is named for today. For the Tyndall gate (**Figure 5C**), the ion beam passes through two thin wire grids placed parallel to one another; one grid element is pulsed to systematically reject ions from entering the drift region while the second grid shields the resulting ion pulse from the high electric field, reproducing a square wave pulse of ions. The Bradbury-Nielsen (BN) gate (**Figure 5D**) is composed of a series of interleaved wires on a single plane with every other wire connected together, creating a two circuit assembly. During a gate closed event, the wires are biased relative to one another (one set to high potential and the other set to low) to create

a strong, localized electric field that scatters ions and prevents them from entering the drift region. The BN ion gate, sometimes referred to simply as an ion shutter, is the most widely used ion gate for IMS applications, for several reasons i) a strong field can be applied across the wire array, which effectively prevents ions from leaking into the drift region during the gate closed state, ii) the strong field created by the BN gate is localized over a short distance from the array, minimizing problems of perturbing ion trajectories from penetrating fields, iii) the spatially narrow BN gate produces a temporally narrow packet of ions ideal for high resolution IMS, and iv) the rise and fall pulse of the wire array is very sharp due to the above effects and the low impedance nature of the wire electrodes. Because BN gates are difficult to construct, many IMS instruments still utilize the simpler Tyndall gate, especially when narrow ion pulses are not necessary for instrument performance, as in the case of long drift times or low resolution applications. In some applications where high ion survival and transmission is desired over resolution, instrument designers will forego wire ion gates for a two electrode design (split lens) since ion collisions with the wire elements is a mechanism for ion losses. Ion losses at wire grids commonly used in spectrometry instruments are estimated to be ~10% in the best cases for vacuum instrumentation [130,131] and substantially worse in the presence of gas collisions [132], and so constructing a gridless IMS system is an attractive option for high sensitivity applications. Gridless ion gates based on potential energy well trapping and releasing (accumulation) of ions at the front of the drift cell have also been described and some of these designs are discussed in the next section (**Section 1-4.3**).

Introducing the ion gate to the experiment inherently creates a duty cycle condition whereby signal is only acquired for a fraction of the total analysis time. In the conventional IMS ion gating mode of operation, the continuous ion beam is truncated into ion packets which are much smaller in temporal spread as compared to the time between gate events, that is to say, the gate is open for only a short time, less than 1% of the total experimental cycle [32]. This significantly reduces the total number of ions which are transmitted into the IMS cell and adversely affects analytical sensitivity, since most of the sample ions are scattered or neutralized at the ion gate. Data multiplexing strategies incorporating mathematical algorithms to apply digitized potentials to the ion gate, such as Hadamard [133] or Fourier transforms [73], can increase the instrument duty cycle to as high as 50%. These multiplexing strategies rely on the concept of oversampling the ion gate using the algorithm, effectively introducing more than one packet of ions per instrument cycle, and then deconvoluting the data using the same applied algorithm. A continuous, sinusoidal wave potential can also be applied to the ion gate and the resulting data is deconvoluted based on the phase of the recorded signal to achieve the theoretical 50% duty cycle [134]. The limitation of these multiplexing and modulation approaches stem from the accurate reproduction of the mathematical transform onto the ion gate—time-varying distortion in the ion gate waveform results in random baseline noise that can be misinterpreted as signal [135], which complicates the interpretation of the data (what is signal and what is noise?). Applying mathematical transforms to the data also introduces peak distortions (*e.g.,* sidelobes) which require additional data processing (*e.g.*, apodization) to correct [136]. In practical IMS, a low

duty cycle is compensated for by summing more repeat measurements (longer experimental observation time), though this reduces sample throughput and consumes more sample quantity owning to the inherently lower limits-of-detection resulting from low analytical sensitivity.

1-4.3 Ion Losses Between Gating Events and Strategies for Gated Ion Accumulation

Another concern related to the ion gate has been the fate of the ~99% of ions which are not sampled by the IMS spectrometer in the conventional (non multiplexed) ion gate mode. These ions are normally rejected by the ion gate in the "gate off" cycle, scattering from the ion beam and neutralizing on the nearby electrodes. Ion losses originating during the "gate off" cycle do not directly contribute to a low analytical sensitivity since data is not being sampled during this event, however these ion losses will ultimately result in higher sample consumption and thus a reduced limit-of-detection for the instrument, which can become important when low sample volumes are provided and/or analytes of interest exist in very low concentrations in the sample. An approach which has been successfully utilized to minimize ion losses at the ion gate is to accumulate ions during the gate closed event in a trapping potential well and introducing a "higher concentration" of ions into the drift region during the next ion gate event. Such an approach can be accomplished through the use of RF trapping electric fields in an appropriate trapping electrode geometry such as a 2D Paul trap [137,138], a multipole (linear) ion trap [139,140], or a stacked ring trap [141]. The latter linear ion trap and stacked ring trap can be used to overcome space charge accumulation limits common to

2D ion traps [142], and results in higher ion currents being admitted per IMS measurement event, which has the effect of increasing both sensitivity and limits-of-detection. Despite these favorable attributes, ion trapping/accumulation devices have seen very limited applications in ion mobility for very practical reasons—these techniques are substantially more complicated to implement than the more simplistic thin wire/grid ion gates. Additionally, because a high density of ions are accumulated and pulsed from these ion trapping devices, the temporal width of the ion packet generated from ion accumulation will be relatively broad due to space charge effects, and so ion mobility resolving power will be limited when using ion storage devices except in the case when very long drift regions and/or high pressures are utilized in the IMS experiment. With ion accumulation, it is also difficult to reproduce a narrow distribution of ions with a low deviation ion current across the ion swarm (*i.e.*, a square wave pulse), which can further degrade resolving power and lead to anomalous peak distortions such as peak tailing—a common instrument artifact resulting from ions arriving late to the detector. Thus for most practical implementations of ion gating methods in research related IMS instrument platforms, single pulse, electrostatic (lossy) ion gates are more than sufficient.

1-5 The Analytical Advantages of Low Temperature Ion Mobility Spectrometry

So far, we have surveyed the current state of development for ion mobility spectrometry and have identified two defining areas, mobility separation efficiency and instrument sensitivity, which are of analytical interest for ion mobility instrumentation

development, particularly for hyphenated IMS-MS instrumentation. Recall from earlier discussion that resolving power is a useful metric for quantifying instrument separation efficiency and is defined by the quotient term in **Equation 4**, the drift time divided by the temporal spread of the ion swarm (t_d/t_w). From this relationship, one can consider several practical means of increasing the resolving power; several experimental parameters which influence the temporal properties of the ion swarm are presented in **Table 2**.

Table 2 – Experimental parameters which influence the measured resolving power in ion mobility spectrometry. These parameters factor directly into the temporal terms in the resolving power quotient value of **Equation 4**. Most experimental conditions represent a tradeoff between longer drift times and broader peaks, except low temperature which will simultaneously increase ion drift times while counteracting lateral ion pulse broadening (peak width) owing to diffusion. Note that the correspondence between parameters is not one-to-one. For example, increasing the drift voltage will often result in a net increase in resolving power, as the peaks narrow more than the drift times decrease.

Experimental conditions which *increase the drift time* (t_d) of the ion swarm due to greater retention time in the drift region.	Experimental conditions which *decrease the temporal width* (t_w) of the ion swarm due to less diffusion.
Increase the drift region *length*	Decrease the drift region *length*
Increase the neutral gas density (*pressure*)	Decrease the neutral gas density (*pressure*)
Decrease the electric field (*voltage*)	Increase the electric field (*voltage*)
Decrease the number of *charges* on the ion	Increase the number of *charges* on the ion
Decrease the *temperature* of the drift gas	Decrease the *temperature* of the drift gas
Increase ion selectivity towards the *drift gas*	

From a survey of the factors listed in **Table 2**, it is clear that in the IMS experiment, there is a tradeoff for many of the experimental parameters with respect to the two temporal terms, t_d and t_w. For example, increasing the drift length will likewise increase the drift time, but also increase the diffusional broadening of the ion swarm. The same is also true for increasing the pressure, voltage and ion charge. The

relationship between these factors is not 1:1, that is, there is a net gain in resolving power for many of these factors, such as increasing the voltage (or likewise ion charge) will decrease diffusional broadening to a greater extent than decreasing the drift times (refer to **Equation 5**). The exception to this tradeoff between t_d and t_w in the resolving power equation is temperature: at lower temperatures ion drift times will increase due to the increased neutral gas density and temporal peak widths will decrease due to a decrease in diffusional broadening. Drift gas selectivity will also result in a favorable net increase in resolving power except in the case where ion-neutral interactions broaden the distribution of the ion swarm, though recall from earlier discussion that the highest resolving power values are experimentally obtained with the low mass helium drift gas due to less collisional scatter [143]. Numerous technical challenges exist with regards to varying the temperature of the IMS experiment, however if these challenges can be overcome (or sufficiently addressed), then an analytical improvement is expected upon conducting the IMS experiment at low temperature. This improvement is essential across the board in terms of resolving power, though it must be noted that varying the temperature complicates the experiment and thus the resulting interpretation of experimental data. One key example is that at sufficiently low temperature, ion-neutral clustering can occur particularly with gas impurities and this can lead to a broadening of ion distributions in mobility space, resulting in a loss in resolution [144]. This effect is generally not observed for helium drift gas [1].

1-5.1 Temperature Effects on Ion Mobility Resolving Power

Now we will take a closer look at the influence that temperature has on instrument resolving power for IMS. From **Equation 3**, diffusion limited ion mobility resolving power increases as the temperature of the ion and surrounding neutrals is decreased, which can be accomplished experimentally by lowering the drift gas temperature while remaining in the low field limit (*i.e.,* in the absence of ion heating conditions). Conceptually, this can be rationalized by examining the Maxwell-Boltzmann distribution of velocities at various temperatures, which is plotted in **Figure 6** for helium at various temperatures from 300 (room temperature) to 80 Kelvin (the approximate boiling point of liquid nitrogen). The distribution of average speeds narrows as the temperature of the system is decreased, which will result in less broadening of the ion swarm at drift equilibrium with the buffer gas. Additionally, the average velocity of the ion swarm will also decrease, which will serve to increase the overall drift time of the swarm. Ultimately, conducting the IMS experiment at lower temperatures will serve to increase the measured resolving power.

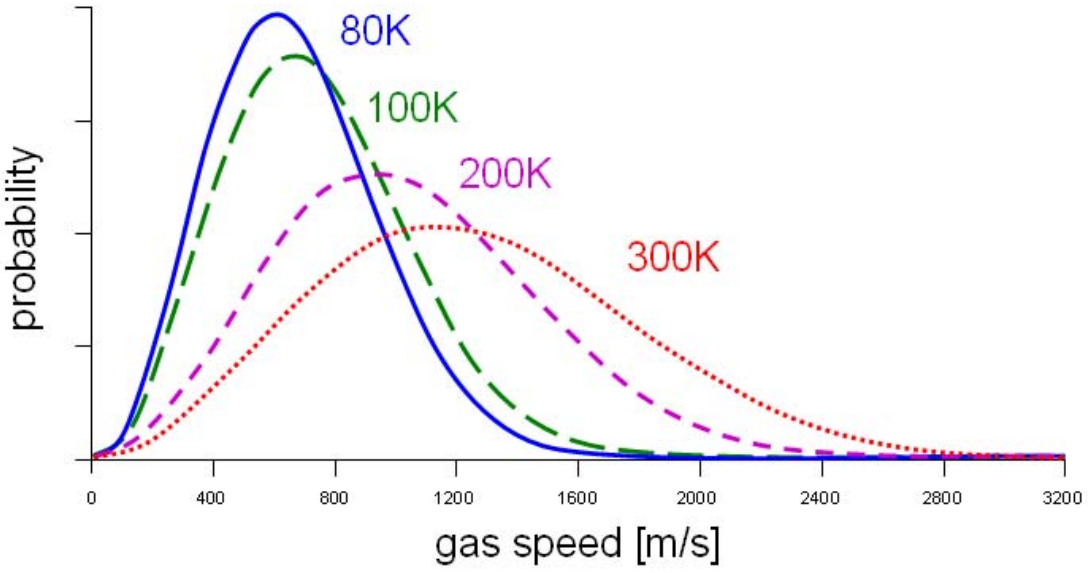

Figure 6 – The Maxwell-Boltzmann distribution of speeds for helium atoms at various temperatures. Temperatures plotted are from room (300 K, dotted red line) to liquid nitrogen temperature (80 K, solid blue line). Speed distributions broaden at higher temperatures and most probable speeds shift to higher velocities. Ions at or near equilibrium with the drift gas will be governed by such a distribution.

The effect of temperature on resolving power in the IMS experiment has been the focus of several studies. In the early ion mobility work, varying the drift gas temperature was utilized primarily as a means of studying the energy dependence on ion mobilities, since previous drift tube work had investigated ion energy effects by varying the electric field or pressure rather than the temperature—these authors concluded that drift gas temperature was the only proper way of studying ion temperature effects on ion mobilities [51]. In these early instruments, a dry ice bath or liquid nitrogen were used to cool the drift gas as these materials were inexpensive, inert and possessed a stable phase change temperature. Temperatures as low as 2 K have been utilized using liquid helium for ion mobility experiments designed to probe ion-molecule interactions at low collision

energies [145]. Neither of these investigations commented or even hinted at the separation efficiency of the IMS technique at low temperature, but rather concerned the ability to probe fundamental ion-neutral interactions at low energies. In more recent work, Hill and coworkers explored the temperature effects on the observed resolution of peaks in the IMS experiment and concluded that there was analytical utility in using low temperature IMS but only if complicating effects such as ion clustering with water could be avoided [65]. One of the earliest practical demonstrations of the analytical power of low temperature ion mobility was undertaken by Kemper and Bowers in the early 1990's where they used low temperature (~150 K) helium to enhance the separation of electronic states (ground and excited) of transition metal ions formed from electron ionization [146]. This work presented clear evidence that a drift cell operated at low temperatures can effectively enhance the resolving ability of the ion mobility technique. Later work by Tabrizchi focused on the temperature dependence on the observed resolution of peaks in the IMS experiment and also demonstrated better resolution for low temperature ion mobility in most cases, though instrument limitations restricted the temperature range which could be evaluated in this study to temperatures higher than ~280 K [144]. In Tabrizchi's work it was also concluded that ion clustering with gas impurities present in their ambient pressure IMS experiment was the primary cause of decreased resolution for specific ions at lower temperatures. While it is clear that low temperature IMS can benefit the separation, careful considerations must be given to the instrument design in order to minimize complicating condensation effects associated with impurities in the drift gas—a point which is developed further in **Section 1-5.4**.

1-5.2 Temperature Effects on Ion Selectivity in the Ion Mobility Experiment

Another figure of merit that is closely related to resolving power is separation selectivity. Selectivity in separation science describes how selective the separation method is to a particular class of analyte[10]. In chromatography, selectivity refers to the physiochemical affinity of the analyte to the stationary phase [71]. In ion mobility, selectivity refers to analyte ion affinity to the drift gas or constituents within the gas. Analogous to changing the stationary phase material in chromatography, different buffer gases or small percent gas mixtures (dopants) have been used to introduce analyte ion selectivity in the IMS experiment [57,58]. Gas impurities such as water or oxygen can also affect ion selectivity, though the effect is unpredictable unless care is taken to control and regulate the percentage of impurities introduced into the experiment [148,149]. A special example of ion selectivity for small molecules (<200 m/z) involves the interaction potential between the ion and the gas. Weak interactions such as ion-neutral dipole "sticking" can be exploited to effectively separate ions which differ very little from one another, such as isomeric ions which differ only in their electronic configuration (**Section 3-3**). These interactions are enhanced as the translational energy between the ion and neutral is reduced, as is accomplished with low field and low temperature. This particular case will be developed further in section three.

[10] Selectivity and specificity have been used interchangeably in separation sciences, though there is a general consensus among the analytical community that selectivity be used in all cases when referring to multi-component separations and the use of specificity should be avoided [147].

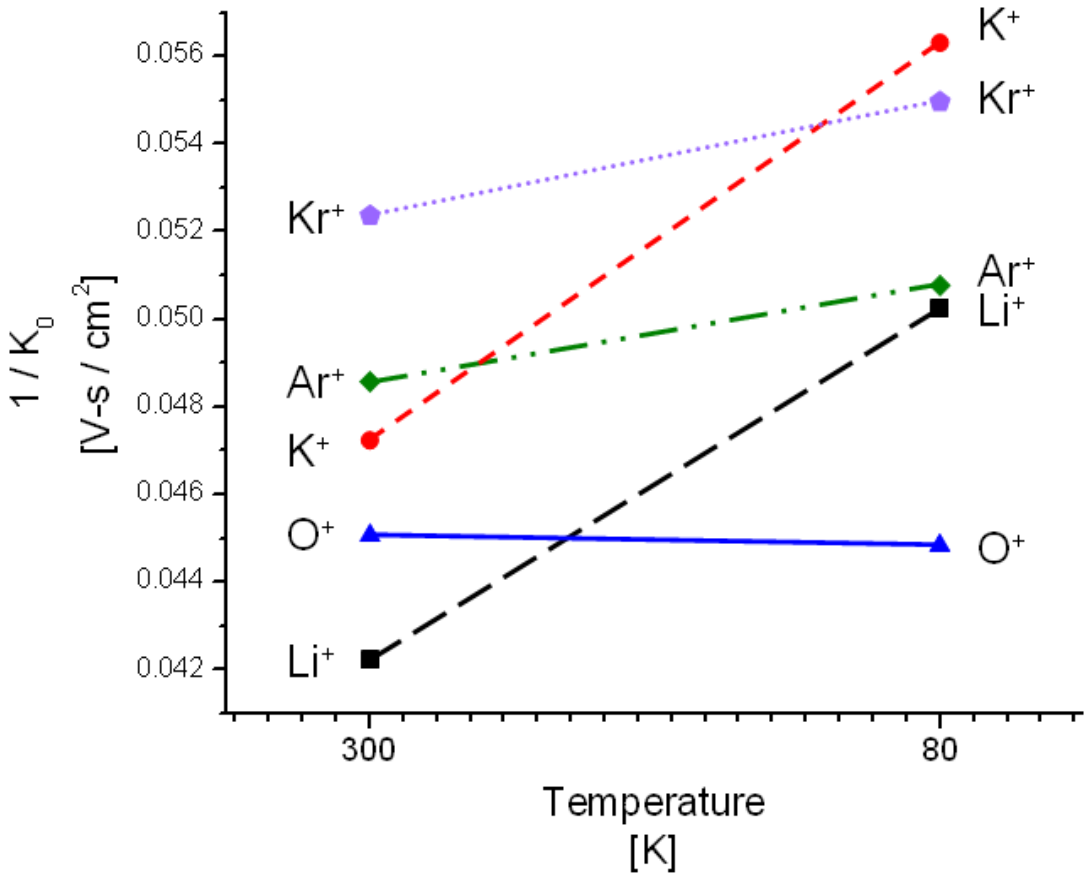

Figure 7 – A plot of the inverse ion mobility of several atomic ions in helium gas at 300 and 80 K. The inverse ion mobility is directly proportional to the observed arrival time of ions in the IMS experiment, thus the ordering of the atomic ions along the y-axis represents the elution order of these ions from the drift region. At low temperature (80 K, right side of plot) the elution orders of the atomic ions change. Data was obtained from references [150-153].

Varying the drift gas temperature can introduce selectivity to the IMS experiment. It has been observed that the measured ion mobility values are temperature dependant and will change as the temperature of the drift gas changes. This percent change is not the same across different analytes of varying chemical classes, and so there exists an optimal temperature range at which any two particular species would separate.

Figure 7 contains a plot of the mobilities of several atomic ions in helium whose gas phase mobilities are known at two different temperatures, 300 and 80 K [150-153]. The y-axis in **Figure 7** represents the inverse ion mobility, *1/K*, which recall from **Equation 1** is proportional to the measured arrival time of ions in the IMS experiment. Thus, the relative ordering of these ionic species along the y-axis of the plot in **Figure 7** is indicative of their elution order in the IMS experiment. The important feature to note in **Figure 7** is that the observed elution orders of ions in IMS change relative to the temperature—this feature can be exploited advantageously in separating ions that would normally not be separated at room temperature and underscores an important analytical advantage of variable temperature IMS experiments. One limitation that is evident from **Figure 7** is that the separation of atomic ions of the same class does not benefit from variable temperature, as can be seen with the relative elution orders of the noble gases (Kr^+, Ar^+) and alkali metals (K^+, Li^+). This effect is not expected to be significant for larger molecular analytes, since the cumulative effects of the heteroatom arrangement of higher molecular weight ions would serve to enhance selectivity differences even for ions of the same chemical class.

A general trend that exists in **Figure 7** is that ion mobility values decrease as the temperature is decreased. This observed decrease in ion mobility at low temperature was first explained by Langevin as a balance between polarization attraction (induced dipole) and hard sphere core repulsion between the ion and the neutral. Langevin predicted that as the collision energy is reduced, the polarization attractive potential would converge to zero and that the dominating ion-neutral interaction at very low

energy would be strictly repulsive [14,154]. This "Langevin polarization limit" has since been observed experimentally for small atomic and molecular ions in low temperature IMS experiments and occurs below ~150 K depending on the electric field [155-157]. The observed decrease in ion mobility as a function of temperature has been qualitatively described as a result of "orbiting" collisions between the ion and the neutral drift gas [158,159], or sometimes explained as a result of ion clustering with the drift gas [160]. It is generally accepted that significant ion-neutral clustering will occur at reduced temperatures for molecular gases such as CO_2 and SF_6 , however there is very little evidence that ion-neutral clustering occurs in a low density of helium gas (<10 torr pressure) even at very low (4.3 K) temperatures in the IMS experiment [161-163]. This conclusion was also made in the early literature where no evidence for ion clustering with helium was found in low pressure IMS experiments [164]. In our own low temperature experiments, we do occasionally observe helium clustering with the transition metal ions, but they occur rarely and only at the lowest temperatures and fields studied (*i.e.*, low effective ion temperatures). This is another reason why helium is a preferred drift gas for low temperature IMS studies. The effective temperature and gas dependence on ion clustering should, however, be considered when designing low temperature and field IMS instrumentation and even when using pure helium gas.

1-5.3 Low Temperature IMS to Improve Instrument Sensitivity

Recall from earlier discussions in **Section 1-3** that in ion mobility instrumentation, as with many other analytical instrumentation, there is a compromise

between resolution and sensitivity—some amount of information must be sacrificed in order to improve the precision of the measurement. High resolution IMS instrumentation inherently suffers from low ion transmission due to the long drift regions and/or high pressures employed [37,38]. While focusing fields can be used within the drift region to improve ion transmission, such strategies cannot be used for low m/z ions due to the detrimental ion scattering effects of high fields and gas collisions on low mass ions.

It is a well-known phenomenon that reducing the gas temperature will likewise reduce the extent of ion diffusion within the gas for the ion mobility experiment [50,165]. This result can be visualized by the Maxwell-Boltzmann distribution for helium, plotted in **Figure 6**, which illustrates the narrowing of speed distributions as the temperature of the gas is lowered. For the IMS-MS experiment, diffusion is strictly a band broadening mechanism that also results in ion losses at the sampling pinhole aperture between the IMS and MS since only those ions at the axis of the drift cell can pass through the aperture. **Figure 8** contains trajectory simulations of ion motion under a weak electric field in a drift cell at two temperatures: 300 and 80 K. For the simulation, individual ion-neutral collisions are modeled using a hard-sphere approximation[11] which factors in the drift gas cross-section, gas temperature and number density to determine the mean free path for ion-neutral collision frequency calculations [166]. As can be seen by the ion trajectory results, there is a noticeable decrease in

[11] Fundamental assumptions of the SIMION trajectory simulation used here and elsewhere are i) elastic collisions with randomized trajectory outcomes ii) energy transfer only a result of collisions and can be ion heating or cooling iii) drift gas velocity Maxwellian, and iv) time steps for the simulation are on the order of each collision—ions are simulated one at a time.

radial ion diffusion when going from room temperature to 80 K (**Figure 8A** and **B**, respectively). This translates into an expected higher ion transmission at lower gas temperatures.

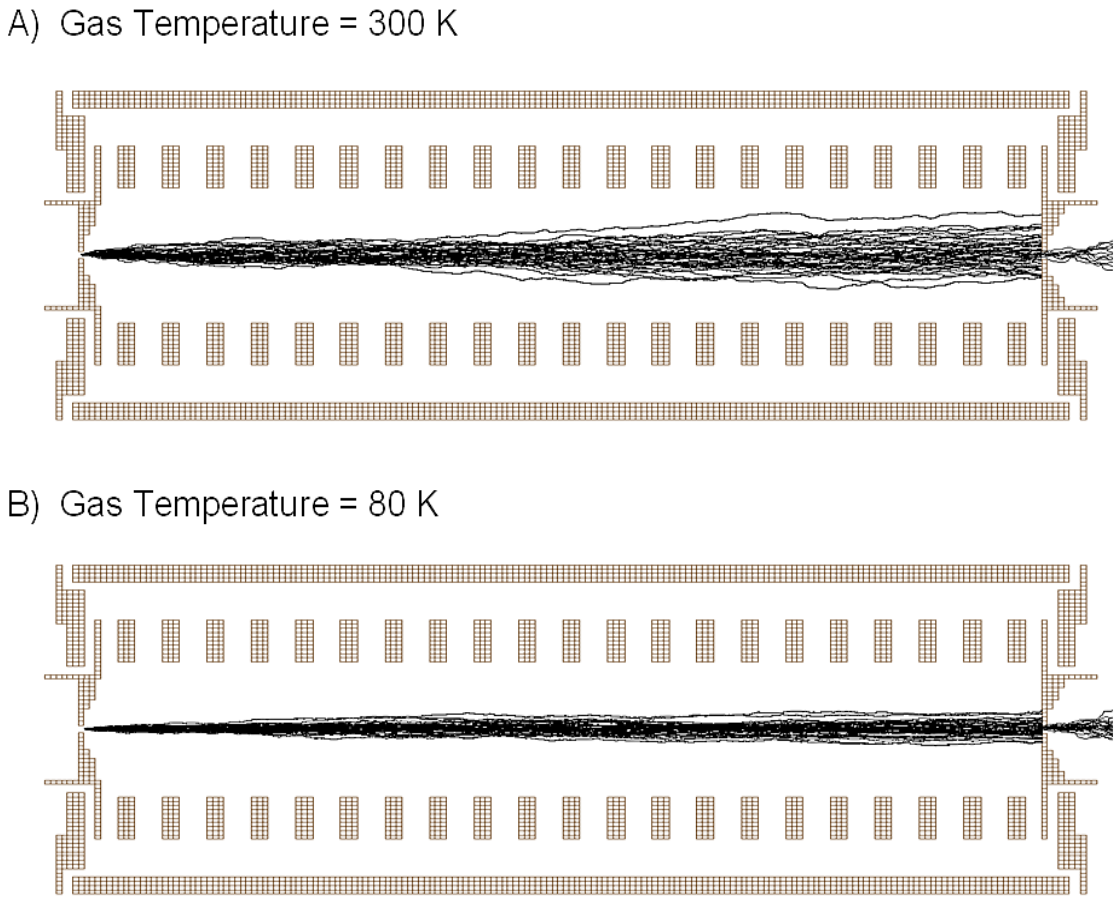

Figure 8 – Ion trajectory simulations of ions traversing a uniform field drift cell in 300 and 80 K helium. Ions travel the gradient of the electric field (not shown) from left to right. **A)** At 300 K, ion motion is characterized by a high degree of radial (away from axis) diffusion. **B)** At 80 K, ion diffusion is substantially decreased, resulting in a higher predicted ion transmission through a pinhole aperture placed at the end of the drift cell. 100 ions of 78 m/z (benzene) were modeled in 1 torr of helium gas at a field strength (E/N) of 10 Td. See accompanying text for descriptions of the statistical model used.

1-5.4 Cryogenic Ion Mobility to Condense Out Drift Gas Impurities

It is a well-known problem in ion mobility experiments that gas impurities present in the drift gas will adversely affect the IMS separation [1,65,167,168]. While in some cases, gas impurities have been purposely introduced in order to enhance ion selectivity in the ion mobility experiment [58,148], generally such impurities are more of a hindrance to the experiment than a benefit, specifically when the amount and identity of the impurity is unknown. There are two primary sources of drift gas contamination in the IMS experiment: i) impurities which make their way into the drift region from the sample ionization region, and ii) impurities carried into the instrument by the drift gas which are either arising from the gas source itself (reservoir tank) or introduced through leaks/contamination in the manifold line. For traditional IMS instrument configurations where the ionization region and the drift region are enclosed in the same volume, an effective strategy for reducing gas contamination into the drift region is to sweep the drift gas from the back of the instrument to the front towards the ion source such that neutrals are effectively blocked from entering the drift region [168]. Decoupling the ionization region from the drift region is the preferred option for minimizing drift gas contamination arising from the introduction of sample to the source; however this is experimentally a more complicated arrangement since the experimenter must also consider how to get ions from the source to the drift region with minimal losses/discrimination. In the properly operated decoupled source/drift cell design, the source operates at a lower pressure than the drift cell, so that neutrals cannot overcome the force of the outflow of gas and thus will not enter the drift region [110]. Carefully

and constructed and tested gas manifold lines can effectively eliminate poisoning of the drift gas through atmospheric leakage into the manifold, or through trapping of impurities prior to introduction into the drift region (see Section 2-5.7).

Impurities arising from the gas source itself can still pose a problem even when high purity gases are used. This issue becomes apparent when one considers the large number of collisions an ion experiences in the IMS experiment. From SIMION trajectory simulations which incorporate a hard sphere approximation for ion-neutral interactions, the number of collisions between a C_{60} ion (760 m/z) in 10 torr helium gas at room temperature is calculated to be about $2x10^6$ collisions across a 30 cm drift region. An impurity present in the drift gas at a 1 ppm concentration will thus collide with the ion about 20 times. If one considers that each ion collision with the impurity can result in ion chemistry which changes the ion identity and thus the subsequent measured mobility, then 1 ppm is not a trivial amount.

Table 3 – Gas purity specifications for helium at several grades of purity. Specifications were compiled from several sources using the lowest concentrations reported for each gas impurity. These specifications and grade designations will differ slightly from one gas supplier to another as no strict standards exist for classifying or quantifying specific gas impurities.

Gas Purity Grade		Assay (% v/v)	Maximum amount of specific impurities (ppm)					
			N_2	H_2O	O_2	H_2	CO + CO_2	Total Hydro-carbons
Research Grade	6.0	99.9999%	0.4	0.2	0.1	0.5	0.1	0.1
Ultra Pure Carrier (UPC) / Chromatography Grade	5.5	99.9995%	2	0.2	1	1	0.5	0.3
Ultra High Purity (UHP)	5.0	99.999%	5	2	1	1	1	0.5
Zero / Laser Grade	4.7	99.997%	5	5	4	1	1	1
High Purity (HP)	4.5	99.995%	--	5	5	--	1	2

But how realistic is the previously mentioned 1 ppm impurity scenario? **Table 3** lists the specifications for impurity levels present in helium gas for several grades of purity surveyed from several high purity gas suppliers[12]. As can be seen from the concentrations in **Table 3**, impurities exist at 1 ppm levels or greater for all but the highest gas grades. For most IMS experiments described in the literature, UHP (5.0) grade purities are used, so impurities can and do pose a real problem to the ion mobility practitioner. Even using the highest grade of purity (6.0), one must pay very careful attention to protecting this purity through gas transfer lines and within the instrument itself.

The ion-neutral collision estimates presented above underscore another important point regarding ion mobility experiments: the operational pressure (gas number density) of the experiment will ultimately determine the likelihood that undesirable reaction chemistry will occur. For example, at ambient pressure (760 torr) where many IMS experiments are conducted, SIMION predicts the average number of ion-neutral collisions across 30 cm to exceed 200 million, which equates to several hundred collisions with a 1 ppm impurity. Under these conditions, if the reaction channel is sufficiently exothermic, then reaction chemistry will almost certainly occur [169,170]. This is one practical reason for conducting the IMS experiment at reduced (1-10 torr) pressures. The phase change temperatures listed in **Table 4** for commonly encountered

[12] Gas grade purity numbers are derived from the purity assay percentage: the first number in the grade represents the number of 9's in the assay percentage while the decimal number is the value of the next subsequent integer measurement in the assay. For example: a 99.995% purity assay contains four 9's and the value of 5 at the highest precision and so would be classified with a purity grade of 4.5. Because the assay percentage value offers no information about the types of impurities present, its use should be general when selecting gases appropriate for analytical usage.

gas impurities illustrates a primary motivation for conducting the ion mobility experiment at cryogenic temperatures. At the boiling point of liquid nitrogen (78 K), one would expect all but nitrogen (and perhaps some carbon monoxide) to condense out of the drift gas onto the chamber walls, eliminating the possibility of ion-neutral interactions with these impurities and thus reducing the occurrence of undesirable reaction chemistry effectively to zero.

Table 4 – Condensed phase transition temperatures for several commonly encountered gas impurities [171,172]. Cooling the helium gas down to liquid nitrogen temperature (far left column in **bold**) will cause all residual impurities except hydrogen (and trace amounts of CO) to condense out of the gas.

Drift gas impurity:	N_2	H_2O	O_2	H_2	CO	CO_2	CH_4	C_2H_6	C_3H_8
Phase Change Temperature (K):	**77.3**	273.2	90.2	20.35	81.6	216.6	111.6	184.5	231.1

1-6 An Overview of the Mass Analysis Methods Used in These Studies

The other critical component of hyphenated IMS instrumentation is the mass analyzer. As with ion mobility spectrometry, there are many variations of mass analyzers each offering their own distinct benefits and limitations to a given experimental design, thus it is of instructional value to summarize these differences. **Table 5** lists the various mass spectrometers which are in common use today alongside several figures of merit which are often considered when utilizing specific mass analyzers in practical instrumentation design.

Table 5 – The various mass analyzers and their defining features.

	Mass Analyzer	Type	Fields Utilized	Upper m/z Range	Resolving Power [a]	Analysis Speed	Ion losses	Press-ure regime	Ref.
Ion Transmission	Quadrupole	scanning / filtering	electrodynamic	<4,000	10,000	10^{-3} to 10^{-1} sec	mod-erate	$<10^{-5}$ torr	[173] [174]
	Magnetic Sector	spatially dispersive[b]	electrostatic & magnetic	<20,000	30,000	10^{-3} to 10^{-1} sec	high	$<10^{-5}$ torr	[175] [176]
	Time-of-Flight	spatially dispersive	electrostatic with dynamic pulsing	<100,000	50,000	10^{-5} to 10^{-4} sec	low	$<10^{-6}$ torr	[177] [178]
Ion Storage	3D Paul Ion Trap	scanning / trapping	electrodynamic	<4,000	10,000	10^{-3} to 10^{-1} sec	low	$<10^{-4}$ torr	[179]
	2D Linear Ion Trap	scanning / trapping	electrodynamic	<4,000	10,000	10^{-3} to 10^{-1} sec	low	$<10^{-4}$ torr	[180]
	Kingdon Ion Trap Orbitrap	scanning / trapping	electrodynamic	<50,000	150,000	10^{-3} to 10^{-1} sec	very low	$<10^{-8}$ torr	[181] [182]
	Ion Cyclotron Resonance Penning Ion Trap	scanning / trapping	electrodynamic & magnetic	<30,000	>500,000	10^{-3} to 10 sec	very low	$<10^{-8}$ torr	[183]

a. Resolving power values reported here are single peak measurements of the ion's mass divided by the full width of the peak at half of its maximum amplitude [64]. These values represent the upper limits experimentally achievable by the technique.
b. Magnetic sectors are fundamentally mass dispersive spectrometers, but due to practical considerations are operate in a scanning mode. Dispersive magnetic sector instruments require multiple detectors and are used in special isotope monitoring applications. A special case has been reported where a sector instrument was used in both scanning and dispersive modes [184].

The scope of this dissertation work will concern two mass spectrometer designs, the *quadrupole* and *time-of-flight* mass analyzers. The basic operational principles of each are discussed in the following sections (**1-6.1** and **1-6.2**, respectively).

1-6.1 The Quadrupole Mass Spectrometer

The quadrupole mass spectrometer is the most widely used mass spectrometer and is commonly encountered in field portable and routine analysis bench top instrumentation. The popularity of the quadrupole mass spectrometer is due to several reasons, the most defining features being the analyzer's relatively low cost, ease of operation, portability and the versatility of the mass analyzer to operate either as a wide

or narrow bandpass m/z ion filter. Exact analytical solutions of ion motion and behavior in a quadrupole device have been developed [173], but these involve complicated differential equations which are not conceptually insightful for the basic principles of the device, and so only a qualitative description of the operational principle of the quadrupole will be provided in this text.

The basic geometry of the quadrupole mass spectrometer is four precision aligned electrodes, ideally of a hyperbolic geometry [185,186], though a reasonably good (quadratic) field can be established using lower cost cylindrical rods, such as those shown in **Figure 9**. The use of cylindrical rods reduces the usable inscribed radius of the device, so is not a preferred option for miniature or large charge capacity applications. The ion beam passes through the center of the four rods as an RF field is applied across opposite rod pairs—in the common operational mode the phase of the RF field is offset by 180 degrees across the rod pairs, creating an oscillating potential well axially between the rods. The frequency and peak amplitude of the RF will govern the stability of low m/z ions, specifically, as the frequency and voltage are increased, the m/z cutoff will also increase to higher m/z values, thus creating a low m/z filter. To discriminate the high m/z ions, a DC voltage is applied across the rod pairs. While low mass ions are influenced strongly by the RF, and thus are periodically repositioned, large mass ions are relatively insensitive to the RF field, and so are influenced more readily by the effect of the DC voltage. The magnitude of this DC offset governs the high m/z cutoff. The combination of RF and DC fields can be tuned in the quadrupole device to create a bandpass filter which effectively transmits only a narrow m/z window of ions, as

depicted conceptually in **Figure 9B**. It is because of this bandpass transmission effect that quadrupoles are commonly referred to as mass filters.

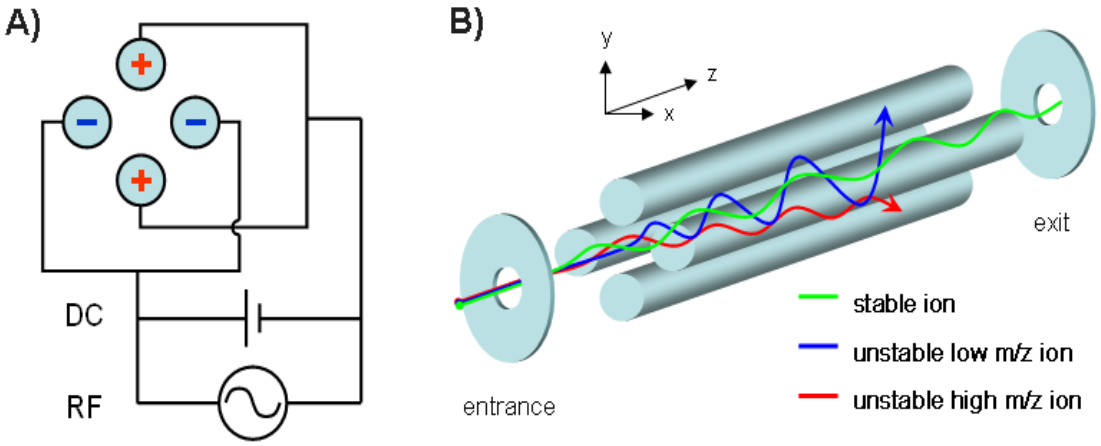

Figure 9 – Operational principle of the quadrupole mass spectrometer. **A)** The quadrupole consists of four aligned rods with RF voltages applied 180 degrees out of phase across opposite rod pairs, shown here with different polarities (+ and -). A DC offset is applied across the rod pairs, creating a potential difference between them. **B)** The trajectory of ions through the quadrupole is m/z dependant. Low m/z ions (blue) are heavily influenced by the RF field and will gain energy as they traverse the device. High m/z ions (red) are relatively unaltered by the RF field, however the applied DC offset across rod pairs will slowly influence their final trajectory. Ions which possess a stable m/z value (green) that is not too high and not too low will be transmitted through the quadrupole.

This mass filtering capability has high analytical utility since an ion beam containing a wide distribution of m/z ions will pass through the quadrupole and come out on the other side with a defined m/z range or single value. As the stability window is narrowed, the overall ion transmission will decrease, and so quadrupoles inherently suffer from low ion transmission when operating in high resolution mode.

The largest contribution to ion losses in a quadrupole device results from the transit of the ions into and out of the electrode assembly. These ion losses are characterized by a necessary crossing of the ion through regions of instable electric

fields, since ions experience a constantly changing RF/DC field as they approach and exit the quadrupole assembly due to the ion's proximity to the electrode surfaces. These fringe fields at the front and back of the quadrupole will ultimately results in significant ion losses since ions are traversing regions of varying RF/DC ratios which define the mass (m/z) stability window [187]. There are two very practical approaches to addressing this problem: i) inject and extract ions from the quadrupole assembly using strong electric fields to minimize the fringe field effects and the temporal residence times of the ions in these undesirable regions [188,189], and ii) spatially separate the RF and DC components of the electric field which combined give rise to ion instability. The use of strong electric fields is undesirable as the presence of neutral collisions will result in ion heating effects that can alter the structure of the ion, initiate ion chemistry and deplete experimentally informative metastable ion configurations (*e.g.*, electronically excited states, proton bound dimers) or even worse induce ions to dissociate. Additionally, strong fields accelerate ions entering the quadrupole such that their velocities through the device are higher, resulting in ions experiencing fewer RF cycles, which ultimately degrades the performance of the device [190]. A common strategy to decreasing the ion's time spent in these undesirable end regions is to assemble the end electrode elements as close to the quadrupole rods as possible (within the limits of promoting electrical breakdown) such that ions quickly enter the rod assembly (**Figure 10B**).

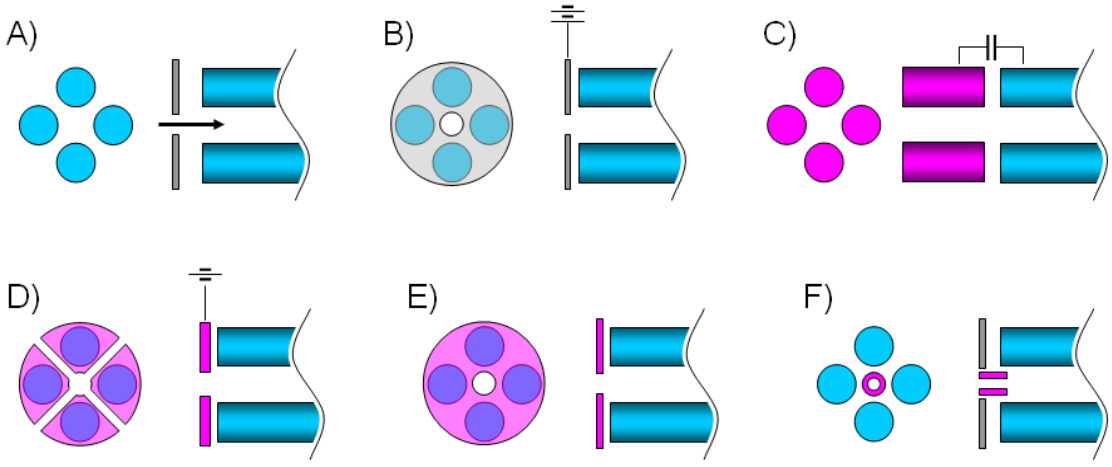

Figure 10 – Ion prefilter devices used for quadrupoles. **A)** No special prefilter used but rather ions are accelerated quickly into the quadrupole device using high electric fields. **B)** The entrance aperture lens is placed in very close proximity to the rods to minimize the fringe field region. **C)** A Brubaker type "delayed DC ramp" prefilter, utilizing a short length of an otherwise geometrically equivalent quadrupole lens in front of the main rod assembly. The rods possess equivalent RF fields (shown here through capacitive coupling) but are absent of the DC component. **D)** Special tab electrodes aligned with the rods possessing opposite magnitude DC potentials that exactly cancel the DC potential of each adjacent rod. **E)** A special "leaky dielectric lens used in place of an entrance aperture plate which is transparent to the RF but not the DC component of the main rod assembly. **F)** A leaky dielectric barrel lens placed at the entrance of the quadrupole and partially inserted into the rod set to more carefully shield the ion beam from the fringing electric fields while retaining the full conductive properties of the entrance ion optic.

Shielding specific components of the electric field is the preferred strategy for addressing the instability issue, and there are several devices which have been successfully implemented as prefilters for quadrupole devices [191]. The first and most utilized means of shielding the undesirable components of the RF/DC fringe field is by using a "delayed DC ramp" implemented with a very short (stubby) quadrupole at the front (and oftentimes back) end of the quadrupole assembly, and possessing a purely RF potential component (**Figure 10C**) [192]. Ions will thus first experience only the RF component of the field before seeing the DC component of the main quadrupole rod set, enabling a gradual transition to the full RF field prior to the introduction of the DC. This

strategy was first devised and implemented by Brubaker in the 1960's and is still commonly referred to as a Brubaker prefilter. While the Brubaker prefilter is the preferred device for transitioning ions through the fringe field region of a quadrupole, the difficulty in aligning and wiring the precision ground rod set against existing instrumentation while maintaining proper capacitive coupling of the RF harmonics has led to more simple alternatives being devised. Among these easier to implement devices is a small 4-sectioned electrode aligned with (but electrically isolated from) each of the four rods of the quadrupole assembly and possessing opposite magnitude DC potentials that exactly cancel the DC field of the rods each electrode element is associated with (**Figure 10D**) [193,194]. The same concept of balancing the rod DC field can be applied to a single DC barrel lens entrance electrode partially inserted into the quadrupole rod set. A two piece concentric barrel lens assembly utilizing this balanced DC design concept has been commercially implemented (*i.e.*, Turner-Kruger entrance lens) and operates by scanning the DC of the inner barrel in proportion to the quadrupole DC scan [195]. A simplistic design for decoupling the RF and DC fields was devised by Fite in the 1970's and consisted of a single barrel lens comprised of a particular class of partially dielectric conductors, referred to as leaky dielectric materials (**Figure 10F**) [196,197]. These materials are characterized by being transparent (leaky) to RF potentials but not DC, and so a barrel lens of this material placed at the entrance of the quadrupole will be sufficient to shield the DC component of the field. Early implementations of the leaky dielectric concept used a piece of roofing slate to improve ion transmission in a quadrupole by over an order of magnitude, however, the variability

in conductivity and undesirable outgassing properties of roofing slate led to the discovery of other suitable alternatives. In Fite's design and the commercial technology which resulting from his work (Extranuclear Laboratories Field Separator (ELFS) ion lens, Extranuclear Laboratories, Pittsburgh, PA), the dielectric material was a proprietary carbon-based coating inside an alumina tube [198]. Later versions of the leaky dielectric prefilter were made from ferromagnetic materials (ferrites) and took the form of an aperture plate in addition to the original barrel shaped design [199]. Subsequent studies confirm that the leaky dielectric prefilter performed as good as other more mechanically complicated designs, though for heavy sample throughput applications, contamination can become an issue [199,200].

For the quadrupole, a mass spectrum is obtained by scanning the bandpass region across an m/z range and recording the resulting ion signal. The speed of analysis will thus depend on the resolution and m/z range desired for the analysis. Quadrupoles can also be operated with RF voltages only, creating a device that effectively transmits a wide m/z range of ions (an RF "ion pipe"). Since the RF field governs the low m/z transmission, the RF voltage can be tuned to remove low m/z ions from the ion beam, which can be useful for eliminating chemical noise resulting from solvent or matrix ions which are present in the sample. RF only operation is particularly useful when mass filtering is not a requirement for the experiment, resulting in high ion transmission across nearly the entire dynamic mass range of the quadrupole itself. This fact is particularly advantageous for transmitting an ion beam through variable pressure regimes. Additionally, the modest pressure requirements (**Table 5**) makes quadrupole

mass filters ideally suited for coupling to high pressure components such as atmospheric ionization inlets and ion mobility spectrometers, as quadrupoles can and oftentimes are operated in pressures as high as 10^{-4} torr [201].

1-6.2 The Time-of-Flight Mass Spectrometer

The principle of m/z dispersion based on time-of-flight (TOF) is one of the earliest known mass separation principles, with foundations in classical mechanics and Newton's second law of motion. TOF principles can be described analytically by the simple kinetic energy relationship:

$$E = \frac{1}{2}mv^2 \tag{8}$$

Where E, m and v can describe an ion's kinetic energy, mass and velocity, respectively. The ion's charge, z, is inclusive in the kinetic energy term while contained within the velocity term are the distance, d, the ion traverses and the time of ion flight, t. If an ion is accelerated to a constant kinetic energy across a constant, known distance, then the ion's measured time-of-flight will be indicative of its mass. The time-of-flight mass separation concept is illustrated in **Figure 11** for a simplified TOF instrument geometry.

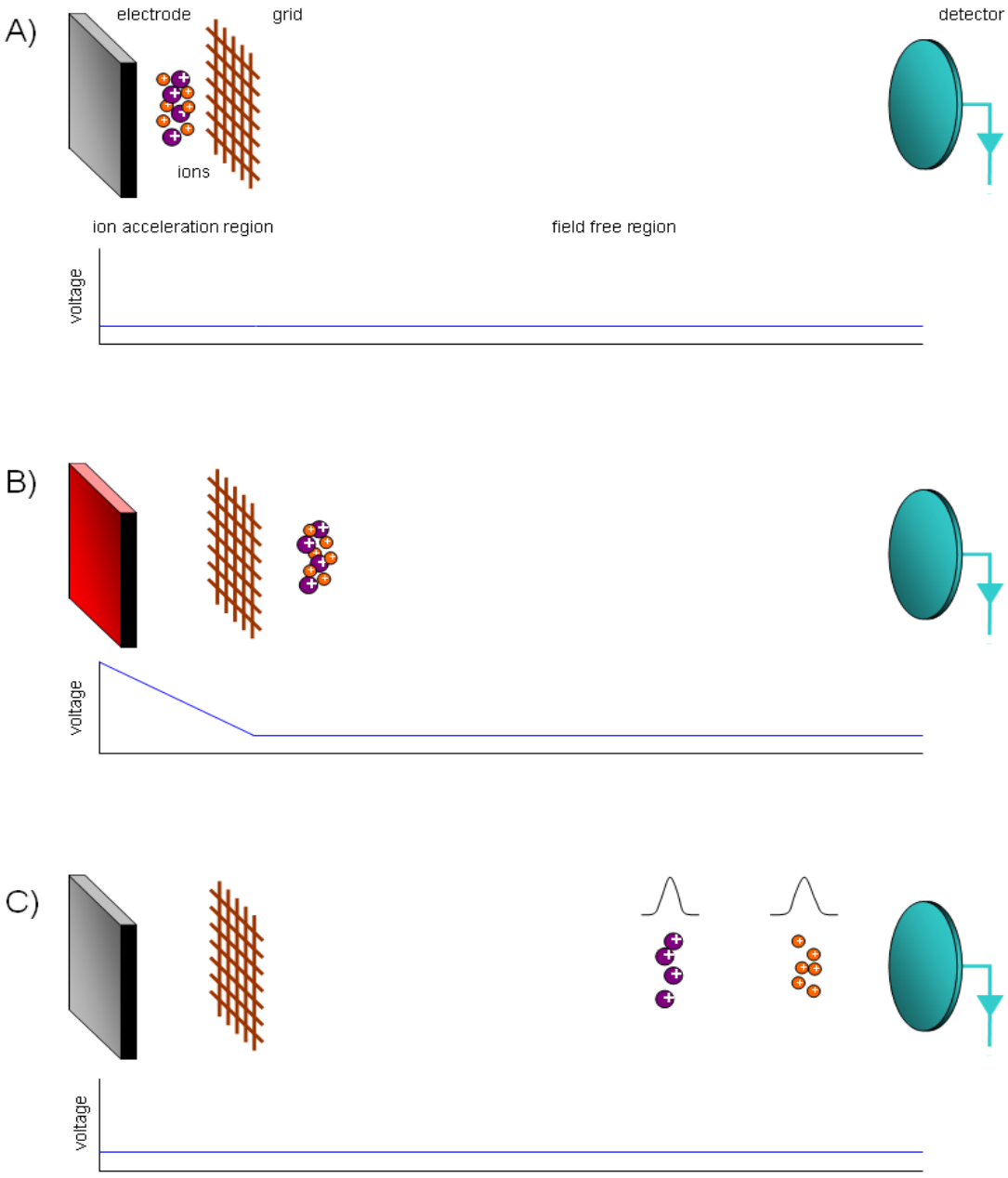

Figure 11 – Operational principle of time-of-flight mass spectrometry. **A)** Ions start (either formed or introduced) between two electrodes: a plate and a grid. **B)** An electrical pulse pushes ions through the grid and accelerates them to a (ideally) constant kinetic energy. Beyond the grid, the ions enter a region of zero field where they neither gain nor lose the kinetic energy imparted to them by the initial electrical pulse. **C)** It is in this field free region that ions of low mass (small spheres) will travel faster than ions of high mass (large spheres) due to their mass dependant differential velocities. Ions arrival times are recorded with an appropriate detector placed at the opposite end of the field free region. Note the recorded signal widths which are indicated above each ion distribution will be indicative of differences in the ions' starting positions and initial kinetic energies. Thus resolving power in time-of-flight is ultimately dependant on the initial pulse width of the ion packet, as it is in drift tube type ion mobility spectrometry.

While the principle of time dispersion of charged particles possessing different masses was known as early as 1897 from J. J. Thompson's famous cathode rays experiments [202], it was William Stephens who proposed what can be regarded as the first true modern implementation of TOF mass spectrometry in a 1946 scientific meeting[13] [203]. The first TOF instrument based on Stephens' description was built by Cameron and Eggers in 1948 and was dubbed the "velocitron" which achieved a resolution of ~5 and a spectral acquisition rate of several hundred spectra per day [204]. Later TOF instruments which were described in the following years operated with mass resolutions between 10 and 20 [205,206]. These early TOF instruments demonstrated that mass information was acquirable through careful arrival time measurements, however technologically these instruments still could not achieve the resolutions of the magnetic sector which was the only practical mass spectrometer at the time [203]. This was due to the fact that the otherwise simple relationship between the ion's mass and measured flight time was complicated by variations in the ion's initial starting position (d) and kinetic energy (E). These variations resulted from the ionization event, which generated ions with a distribution of kinetic energies and spatial locations. In these early experiments, a pulsed electron beam was used for ionization, resulting in ions being

[13] An excerpt from Stephens' original 1946 communication: *"Advances in electronics seem to make practical a type of mass spectrometer in which microsecond pulses of ions are selected every millisecond from an ordinary low-voltage ion source. In traveling down the vacuum tube, ions of different M/e have different velocities and consequently separate into groups spread out in space…This type of mass spectrometer should offer many advantages over present types. The response time should be limited only by the repetition rate (milliseconds)…Magnets and stabilization equipment would be eliminated. Resolution would not be limited by smallness of slits or alignment. Such a mass spectrometer should be well suited for composition control, rapid analysis, and portable use."* This would become a prophetic statement with regards to the current state of time-of-flight mass spectrometry. Many portable TOF instruments are in use today and the magnetic sector has all but disappeared from the commercial mass spectrometry market.

formed across both temporal and spatial dimensions of the electron beam [207]. This kinetic energy variation problem was addressed by the work of Wiley and McLaren in 1955 who introduced a time delay between ion formation and subsequent TOF extraction, which they termed “time-lag focusing” [208]. This small delay gave ions sufficient time to reorder into spatially favorable locations for TOF measurement, as depicted in **Figure 12**. This work led to the commercialization of the TOF mass spectrometer in the 1950’s by the Bendix Corporation, which could achieve a then impressive 500 resolution [209]. Time-lag focusing is implemented in modern laser desorption TOF instruments as delayed extraction, and has proven to be a very useful means of substantially improving the resolution obtainable on these instruments [210,211]. While Wiley and McLaren’s initial implementation of time-lag focusing utilized the potential well formed from an electron beam to reposition the ions during the time delay, delayed extraction is applied to surface generated ions and relies on the ion’s kinetic energy dependant drift away from the surface for energy correction.

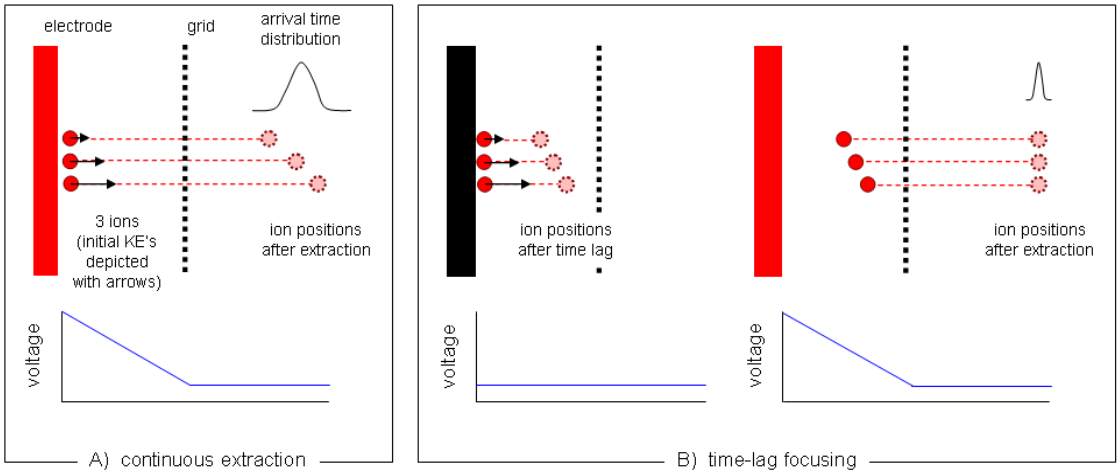

Figure 12 – Principle of time-lag focusing for time-of-flight mass spectrometry. Three ions of the same mass are formed at the electrode surface with varied kinetic energies, shown with arrows. **A)** In continuous extraction, the ion's total kinetic energy will be the energy imparted by the extraction potential plus each ion's initial kinetic energy, resulting in different flight times, and thus different ending positions for ions of the same mass (dotted circles). **B)** By introducing an appropriate time delay, ions will drift to more favorable positions away from the electrode in the absence of the extraction field. Their ending positions during this time delay will be indicative of their initial kinetic energies. When time lag focusing is implemented in surface generated ionization, as depicted here, this technique is more commonly referred to as delayed (ion) extraction.

Time-lag focusing methods can only partially correct for the initial kinetic energy spread of ions, and cannot correct for any kinetic energy deviations introduced after ion extraction, such as those resulting from metastable ion decay or post acceleration fields, and so another significant contribution to the TOF mass spectrometer was made by Mamyrin in the 1970's with the implementation of the electrostatic ion mirror, or more commonly referred to as the reflectron [212-214]. This conceptually simple device introduces a deceleration field in the path of the ion beam, creating a potential hill which ions of the same m/z but different kinetic energies will penetrate at different depths, which has the advantage of spatially correcting the distribution of kinetic energies, as illustrated in **Figure 13**.

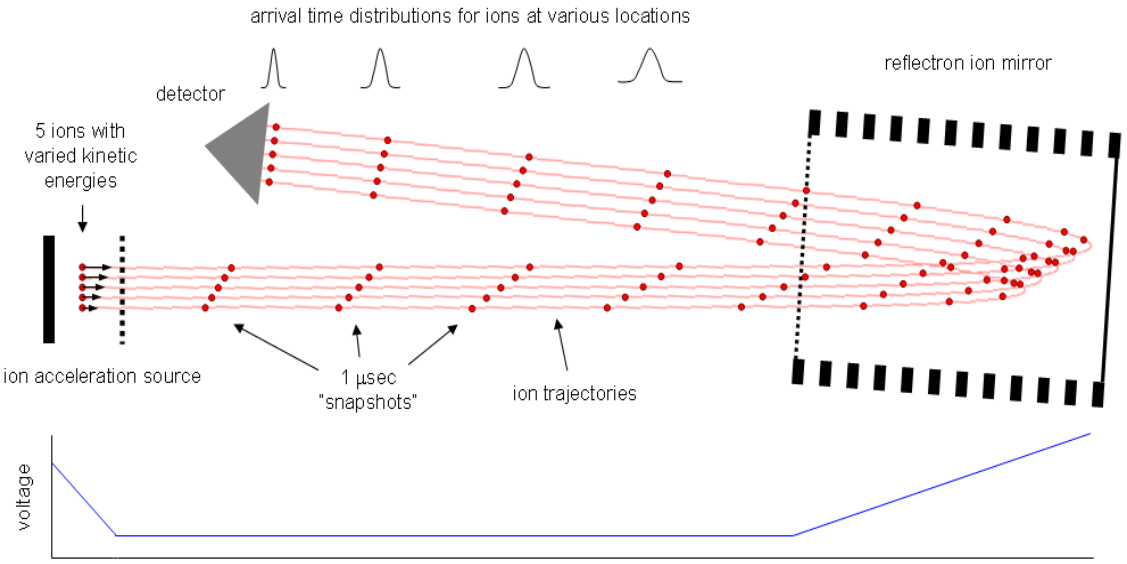

Figure 13 – Principle of kinetic energy correction using a reflectron TOF. Ions are formed in the same position but with different kinetic energies (depicted with arrows) in the ion acceleration source to the left. As a result, ions with more initial kinetic energy will drift further than those with less kinetic energy in the same magnitude acceleration potential. While their spatial locations are disperse entering the reflectron (at right), those ions with more kinetic energy penetrate the uphill potential further, which has the effect of correcting for the initial energy spread, as shown with coincident arrival times to the detector. The same effect can also be observed for ions formed at different spatial positions in the source. Ion trajectories and temporal positions were calculated using SIMION 8.0.

With a reflectron, the achievable mass resolving power of a TOF analyzer can be increased by an order of magnitude or greater [178]. The limitations of reflectron TOF instruments is that ion transmission is substantially lower in this "reflected" mode than in the traditional "linear" mode geometry, with ion losses due to reflectron reported as high as 50%, mostly resulting from the necessary use of wire mesh grids to establish electric field boundaries within the device [215]. While gridless reflectron instruments have been developed that achieve higher ion transmission than their grid bearing counterparts, these instruments require more ion optical elements to align the ion beam precisely, and as such are much more difficult to operate [216,217]. Additionally,

reflectron instruments focus only a narrow range of m/z ions, and so the dynamic range of energy focusing is limited. Multi-stage and nonlinear field reflectrons have been developed to address this issue, which adds further complexity to the overall design [218,219].

Another seminal contribution to the field of TOF mass spectrometry came with the development of the orthogonal acceleration TOF geometry, which introduces the ion beam at a right angle to the TOF analysis trajectory [220]. The orthogonal TOF geometry allows for a continuous or irregularly pulsed ion beam to be sampled by the TOF analyzer, greatly facilitating the coupling of TOF with other stages of analysis. The other inherent advantage of extracting ions orthogonally from an ion beam is that the analyzer dimensions are inverted such that ion spread axially in the beam direction will not contribute to resolution losses in the TOF dimension. This idea can be illustrated metaphorically by considering a drop of oil placed upon a flat surface. As the oil spreads in all directions parallel to the surface, the orthogonal depth of the oil droplet continues to diminish. Thus, high TOF resolutions can be realized from an axially diffuse ion beam, as long as the width of the beam in the TOF dimension is narrow[14]. High resolution orthogonal TOF is achieved with appropriately designed ion optics that can effectively shape and compress the ion beam in the TOF dimension [221,222]. Today TOF instruments can achieve impressive levels of mass accuracy (sub ppm) and

[14] Narrowing of the ion beam in the TOF dimension is facilitated by relaxing the electrostatic confinement of the ions in the orthogonal (or transverse) dimension. In practical TOF instrument design, this is achieved by using two flat, parallel plates with surface areas greatly in excess of the in beam dimension. The closer spacing of these plates facilitates higher spatial confinement in the TOF dimension and thus higher mass resolutions with the usual expense of ion transmission (sensitivity).

resolving power (~50,000)[15], afforded by novel electrode geometries and advancements in precision electronics delivering low voltage ripple power supplies and fast rise time pulse and timing circuits.

1-7 An Overview of the Ionization Methods Used in this Work

A key component required in both mass and mobility spectrometers is the ability to create gas phase ions from samples of various chemical compositions and volatilities. The first mass spectrographs utilized a beam of electrons to ionize gas phase samples. While electron ionization is still the most commonly used ionization method today, many other ionization methods have emerged, each with their own advantages and limitations. **Table 6** lists several of the ionization methods which have been used in mass spectrometry [223]. There are numerous other ionization methods in use today which are derivatives or combinations of the ones listed in **Table 6**. In recent years ionization method development research has focused on ways to generate ions from samples at ambient pressure and desorption methods which can ionize samples directly with little to no sample pretreatment.

The work in this dissertation will concern primarily electron ionization, though two additional sources have been constructed for the cryogenic instrument—one based on laser ionization and another based on a novel electrospray ionization interface design the latter of which holds promise for enhancing the instrument sensitivity and IMS

[15] Performance specification for the "maXis" ultra-high resolution time-of-flight instrument manufactured by Bruker Daltonics, which represents the highest performance TOF instrument on the market in terms of mass resolution. Bruker began installing the first of these latest generation orthogonal TOFs in laboratories starting late 2008.

resolving power through high charge state ion formation. The following sections will introduce the reader to the fundamentals of these three ionization techniques.

Table 6 – Ionization methods used in mass spectrometry and their defining features.

Ionization Method		suitable analytes	mass limit (amu)	Features	Ref.
Glow Discharge	GD	nonvolatile	<200	Produces singly charged atomic ions. Useful for bulk metal analysis.	[224]
Inductively Coupled Plasma	ICP	nonvolatile	<200	Neutral to ion conversion efficiency ~100%. Isotope and elemental analysis.	[225]
Spark Ionization Spark Source Mass Spectrometry	SSMS	volatile or nonvolatile	<500	Useful for elemental/isotopic analysis of solids. Pulsed ionization source.	[226]
Resonant Ionization Resonant Multiphoton Ionization	RIMS REMPI	volatile	<500	Highly selective to the chemical properties of the analyte.	[227]
Photoionization	PI	volatile	<1,000	Selective to the ionization potential of the analyte. Low fragmentation.	[228]
Electron (Impact) Ionization	EI	volatile	<1,000	Extensive fragmentation. These patterns can be used for chemical identification.	[229]
Surface Ionization Thermal Ionization	SI TI	volatile or nonvolatile	<1,000	Low cost, stable ion emission useful for isotopic analysis. High fragmentation.	[230]
Chemical Ionization Atmospheric Pressure CI	CI APCI	volatile	<2.000	Less fragmentation than EI. Can be operated at ambient pressure.	[231]
Field Ionization Field Desorption	FI FD	low volatile and nonvolatile	<2,000	Ionization via a high electric field. Useful for heavy hydrocarbon samples.	[232]
Fast Atom Bombardment	FAB	nonvolatile soluble in matrix	<6,000	Sensitive to preformed ions. Low fragmentation and sample consumption.	[233]
Secondary Ion Mass Spectrometry Liquid SIMS	SIMS	nonvolatile soluble in matrix	<10,000	High spatial resolution on the order of single atoms. Depth profiling possible.	[234]
Plasma Desorption Mass Spectrometry	PDMS	nonvolatile	<15,000	Requires a radioactive fission source. Fission generates a pulsed burst of ions.	[235]
Thermospray	TSP	nonvolatile soluble in solvent	<1,000	Enabled first practical coupling of liquid chromatography to mass spectrometry.	[236]
Sonic Spray Ionization	SSI	nonvolatile soluble in solvent	<2,000	Resulting multiply charged ions are desolvated, improving the mass analysis	[237]
Electrospray Ionization	ESI	nonvolatile soluble in solvent	<200,000	High abundance of intact, multiply charged ions. Enables liquid sampling.	[238]
Laser Ionization Mass Spectrometry	LIMS LDI	nonvolatile	<1,000	Forms a pulse of ions via a high energy laser. Fragmentation at high mass.	[239]
Matrix Assisted Laser Desorption Ionization	MALDI	nonvolatile soluble in matrix	<500,000	Capable of ionizing nonvolatile, high mass analytes. Pulsed ion source.	[240]
Desorption Atmospheric Pressure Photoionization	DAPPI	nonvolatile	<500	Nonvolatile sampling, ambient desorption/ionization variant of PI	[241]
Direct Analysis in Real Time™	DART	volatile and nonvolatile	<1,000	Ambient ionization of samples placed in an energetic, metastable neutral gas jet.	[242]
Desorption Atmospheric Pressure Chemical Ionization	DAPCI	nonvolatile	<1,000	Nonvolatile sampling, ambient desorption/ionization variant of CI	[243]
Desorption Electrospray Ionization	DESI	nonvolatile	<10,000	Ambient desorption/ionization method. Can ionize high mass analytes.	[244]

1-7.1 Electron Ionization

Electron ionization (EI) has had over a century to mature [202], and today EI sources can be found in a variety of MS instruments in common use, including gas chromatographs and residual gas analyzers. The basic principle of EI first involves the formation of a stable beam of electrons which are accelerated to a sufficient kinetic energy through electrostatic or magnetic fields, or a combination thereof [245,246]. An acceleration energy of 70 eV is commonly used, as this value has been experimentally shown to produce the highest flux of ions for organic molecules. As most ionization energies fall 50-60 eV lower than this observed 70 eV maximum, it has been suggested that energy transfer in EI is very inefficient [118]. Estimates are that at most only 0.1% of molecules are ionized in this process. It has also been noted that at 70 eV, the de Broglie wavelength of the electron matches favorably with the average bond lengths encountered in organic molecules (~0.14 nm), which leads to an optimal energy transfer between the electron and molecule at 70 eV [229]. The electron beam is traditionally formed via thermionic emission from a hot filament possessing a low work function, such as tungsten or rhenium. Inorganic crystals such as lanthanum hexaboride have also been used as the hot cathode material, though these refractory ceramic materials are more prone to chemical poisoning by the organic compounds which are commonly analyzed in mass spectrometry [247]. Permanent magnets are often used to collimate and increase the path length of electrons to increase ionization yields and keep the electron beam stable in the presence of the electric fields which are added to extract ions

formed in the EI process [248]. After the electron beam is established, the gas phase neutral analyte is introduced and ionization occurs through the mechanism,

$$M + e^- \rightarrow M^{\bullet+} + 2e^- \quad (9)$$

Where M represents the analyte molecule or atom and $M^{\bullet+}$ is the resulting molecular ion. In addition to the molecular ion, extensive fragmentation is commonly observed in EI due to the high energy of the impending electron. Such fragmentation behavior has been used quite successfully to "fingerprint" the identity of unknown samples as fragmentation patterns are highly reproducible at controlled EI energies [249].

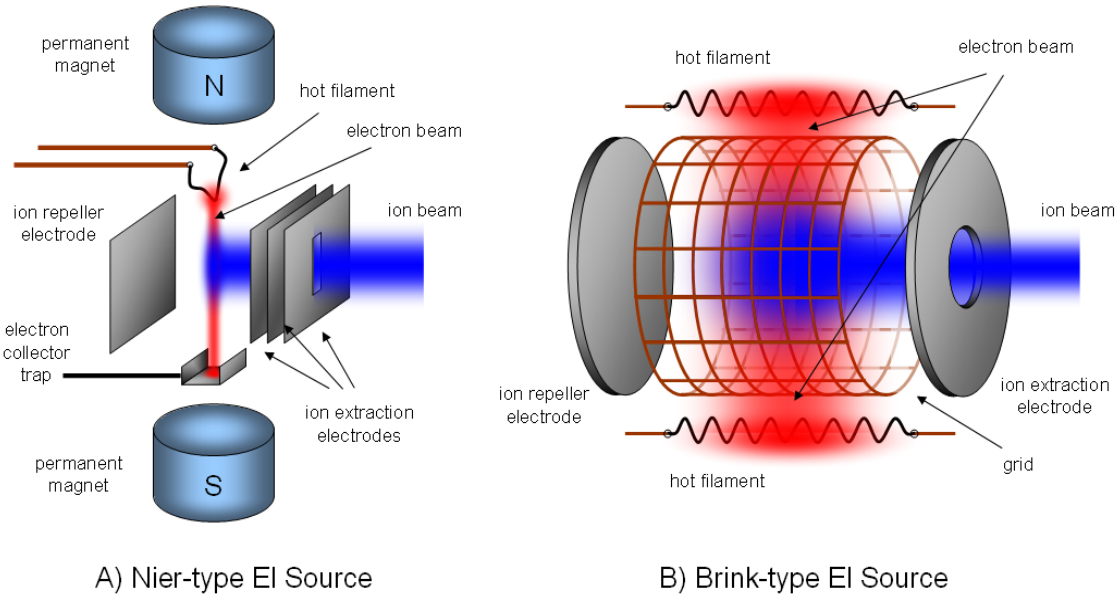

Figure 14 – Two common electron ionization source geometries used in mass spectrometry. **A)** The Nier-type geometry which ionizes samples from a well-defined electron beam orthogonal to the beam axis of the instrument, and **B)** the Brink-type geometry which is a cylindrically symmetric ionization source utilizing a wire cage which can accelerate electrons from all directions towards the instrument beam axis to maximize ion yields from the source.

Once ionization occurs, a means must be established to remove the ions from the electron beam. An effective and widely used method is to extract the ions orthogonally from the electron beam using electrostatic fields formed through ion optical elements. Because the mobility of electrons is much higher than that of ions, the sufficiently accelerated electron beam can pass through a weak ion extraction field relatively unperturbed. This type of EI source geometry is referred to as a Nier EI source, named after Alfred Nier who pioneered its use in mass spectrometry [176]. **Figure 14A** illustrates the Nier-type EI source, reproduced from Nier's original illustrations [250,251]. The Nier electron ionization source uses a hot filament and an electron trap (commonly referred to as an electron collector) to generate an energetically and spatially well-defined electron beam which is very useful for obtaining ion energetics data such as ionization potentials and fragmentation thresholds. Ions formed in the electron beam are extracted with an orthogonally directed electric field created between two electrode elements, commonly referred to as the ion repeller and ion extractor, as shown in **Figure 14A**. In more modern implementations of the Nier-type source, the electron current generated on the electron trap is monitored and readjusts the filament current accordingly to produce a highly stable electron beam which results in the generation of a stable beam of ions. This current regulation is important since electron emission from a hot filament will vary with temperature fluctuations changes in the filament's resistance, which over time will increase as the filament material is sputtered away during normal operation. Nier-type EI sources are still in common use today, as it has been proven to be a high versatile and efficient means of ion production for a variety of applications.

Nier EI sources designed to operate at very high electron energy resolutions are still utilized for the measurement of ionization potentials. Another commonly encountered EI source geometry is the cylindrically symmetric Brink-type EI source (**Figure 14B**), which was first described and used by Gilbert Brink for analyzing molecular beams [252]. In Brink's original design, the ionization region was encased around a cylindrical wire cage outside of which was placed a hot filament electron source. The potential difference between the filament and the cage accelerates electrons through the cage to the center of the source and back to the cage again, causing electrons to pass in and out of the ionization volume several times and enhancing ionization yields. As with the Nier-type source, the electron current can be regulated with appropriate circuitry that monitors the current induced on the cage assembly and feeds this response back to the filament current. Today, the Brink-type EI source has found widespread use in residual gas analyzers as the high ion yields and cylindrical symmetry are convenient for coupling to the quadrupole mass analyzers used in these instruments [253]. Brink-type EI sources come in both open and closed volume designs. Open volume designs allow for the contents of the entire ionization chamber to be sampled by the ion source which is useful for residual gas monitoring. Closed ion source designs are more sensitive to direct sample introduction methods and are preferred where high sensitivity and low sample consumption is desired. Modern variations of these two designs can also incorporate multiple filaments to further enhance ion yields and extend the lifetime of the source operation.

1-7.2 Laser Desorption Ionization

The use of lasers for rapid deposition of high energies in a small, well-defined volume was recognized early on as a useful mechanism for producing gas phase ions for mass spectrometry analysis [254]. One of the most important features of laser ionization was that the rapid energy deposition resulting in the intact ionization of organic molecules with high ion yields, leading to the development of laser ionization mass spectrometry (LIMS) instruments [255,256]. While the formation of organic ions was a significant step for mass spectrometry, the mass range was limited to less than 1,000 mass units in LIMS instruments, and for 20 or so years after its introduction, LIMS technique development focused on the benefits of the laser itself, such as fast and highly sensitive sampling of analytes and the ability to obtain location specific information of samples with high spatial resolution, which collimated into a commercial technique called laser microprobe mass analysis (LAMMA) [257-259]. As features of the laser, such as shorter duration pulse widths and smaller beam diameters, improved, so did the LIMS experiment [260]. Still, reproducibility remained one of the biggest obstacles for laser ionization methods, as the mechanism of laser ionization was poorly understood and many factors were unaccounted for in the experimental setups used, such as laser beam homogeneity and the physiochemical nature of the samples analyzed. The recognition of the two processes of desorption of material from the bulk sample and generating ions of individual analytes led to the more accurate and familiar nomenclature of laser desorption ionization (LDI) [261]. The scope of laser ionization processes broadened to include wavelength resonant and multiphoton energy deposition

methods [262-264], but LDI remained for many years a niche application in mass spectrometry [265,266]. The observation that the presence of laser wavelength resonant chromophores in the sample yielded less fragmentation contributed to the early developments of matrix LDI, and numerous matrices were mixed with various samples and tested, but the low laser fluences necessary to reduced ion fragmentation yielded too few ions to be analytically useful [267,268].

A breakthrough in laser ionization methods occurred in the late 1980's when it was discovered that nanoparticles [269] and organic acids [270] could be added to the sample to greatly increase the ionizable mass range (>100,000 Da) with virtually no fragmentation—a discovery which was recognized with a Nobel Prize in 2002 [271]. Organic acid matrix assisted LDI (MALDI) was an immediate success and remains today the most widely used desorption ionization method for large biomolecules analysis with virtually no upper mass limit restricting what could be ionized [272]. Nanomaterial based LDI methods has regained popularity in recent years as the mass range of these methods is continuing to increase due to technological and methodological improvements in their fabrication. Current nanomaterial LDI methods based on nanoporous silicon substrates and bare transition metals can generate intact ions of masses as high as 6,000 Da without the matrix ion signals and adducts that are present in MALDI [273].

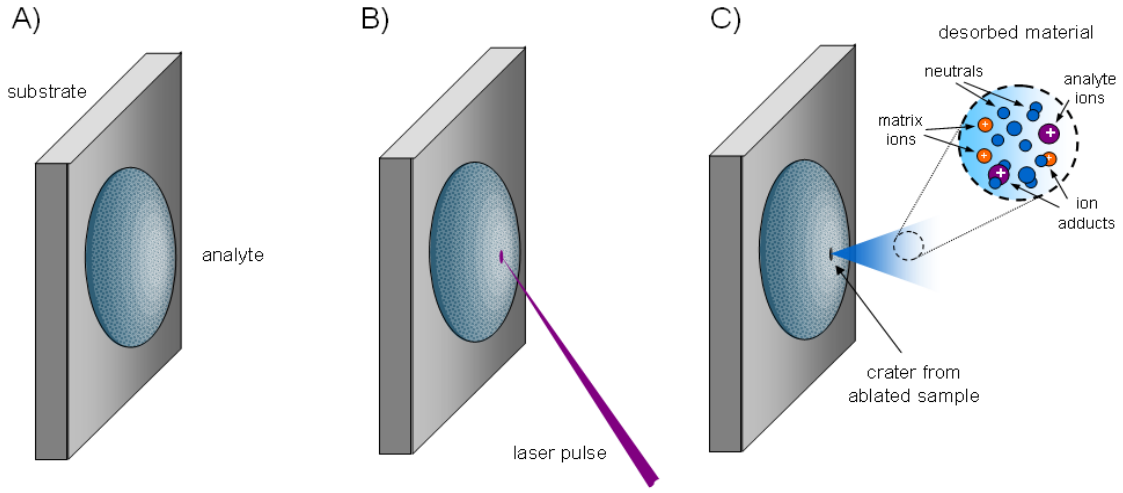

Figure 15 – Operational principle of laser desorption ionization. **A)** Sample is deposited onto a suitable substrate, typically stainless steel. Sample can be deposited as a dried droplet either neat or mixed with an appropriate matrix material. **B)** A laser pulse of appropriate wavelength and power is focused onto a region of the sample, depositing a dense and localized area of energy. **C)** Material desorbs from the surface, which is comprised of mostly neutrals with some ions. Matrix ions and adducts are also shown for the case of matrix assisted LDI. Further ionization can also occur within the ejected plume, increasing ion yields. Ions within the desorbed plume are extracted and directed to the spectrometer for analysis.

The basic principle of LDI is depicted in **Figure 15** and first begins with the deposition of sample (either mixed with or without matrix) onto a suitable substrate which for mass spectrometry is a metal surface upon which an electrical potential can be applied to direct ions from the surface. Several sample spotting methods have been developed for particular analyte analysis and a list of these methods is provided in **Table 7.**

Table 7 – MALDI sample preparation strategies. Variant methods incorporating some of the features of the above techniques have also been described.

Sample Preparation Strategy for LDI	Description	Features	Ref.
Quick & dirty	A drop of analyte is applied to the plate and an equivalent volume of matrix is mixed with the wet droplet and allowed to dry.	Quick and easy. Can be used with on plate digestion. Inhomogeneous matrix-analyte crystallization.	
Dried-droplet	A drop of aqueous matrix compound solution is mixed with analyte solution and the mixture is applied directly onto the plate.	Quick and easy. Works well for many analytes. Inhomogeneous matrix-analyte crystallization, which results in low reproducibility.	[270]
Vacuum-drying	The sample plate and solvated droplets are placed in vacuum, resulting in fast and more homogeneous crystallization.	Creates a thinner sample, improving mass accuracy and resolution; fast sample preparation times. Variable homogeneity in matrix-sample crystallization.	[274]
Crushed-crystal	The dried droplet is crushed (*via*, glass slide, razor), and more sample solution is applied, promoting homogeneous nucleation.	Promotes crystallization in the presence of nonvolatile solvents (*e.g.*, glycerol and dimethyl sulfoxide). Inhomogeneous matrix-analyte crystallization.	[275]
Fast-evaporation	A drop of matrix solution is applied to the plate and allowed to dry. Analyte solution is applied on top of the dry matrix spot.	Matrix and analyte are handled separately. Matrix spotted plate can be prepared ahead of time. Inhomogeneous matrix-analyte crystallization.	[276]
Overlayer (Two-layer)	Same as fast-evaporation (dried drop of matrix only solution) except in the second application, a matrix-analyte solution is applied.	Slightly improved sample homogeneity than fast-evaporation.	[277]
Sandwich	Same as fast-evaporation but with an added layer of matrix only applied to the dried matrix and analyte layers.	Can further improve sample homogeneity over either the fast-evaporation or overlayer methods.	[278]
Spin-coating	The analyte/matrix solution is applied to a spinning sample disk and allowed to spread and crystallize, creating a homogeneous coating.	Homogeneous matrix-analyte crystallization. Can only coat one sample per plate in conventional method. Requires a special sample plate	[279]
Slow-crystallization	Sample preparation is the same as in dried-droplet, except the solution is supersaturated with matrix and evaporated slowly in an incubator.	Promotes crystallization in the presence of nonvolatile solvents (*e.g.*, glycerol and dimethyl sulfoxide) with some improvement over vacuum-drying alone. Crystal quality varies as with vacuum-drying.	[280]
Pneumatic coating	The analyte/matrix solution is sprayed onto the sample plate, forming a homogenous crystal bed.	Homogenous matrix-analyte crystallization. Slower method requiring special equipment. Prone to sprayer clogging.	[281]
Electrospray	The analyte/matrix solution is electrosprayed onto the sample plate, forming a highly homogeneous crystal bed.	Very homogeneous matrix-analyte crystallization. Slower method requiring high voltage equipment;. Increased salt adduction and suppression effects can be observed.	[282]
Matrix-precoated targets	Analyte solution is applied directly to a matrix precoated sample plate.	Fast sample preparation technique; Has many potential applications, including chemically modified surfaces tailored to UV MALDI. Commercial precoated targets can be expensive.	[283]

Following sample deposition and introduction into the spectrometer, a laser is focused onto the sample spot to facilitate desorption and ionization. Most LDI mass spectrometry methods utilize gas discharge (*e.g.,* nitrogen) or solid state (*e.g.,* neodymium doped yttrium-aluminum-garnet crystal) pulsed lasers which emit in the ultraviolet wavelength region (250-400 nm), as this wavelength regime was found to be optimal for generating ions from a variety of analytical samples as they absorb favorably in the UV wavelength regime [272]. The pulsed nature of the LDI method is convenient for coupling to pulsed analysis techniques, such as TOF mass analysis and ion mobility. The important parameter for energy deposition in LDI is fluence (energy per unit area) which can be controlled experimentally by varying the laser spot size (irradiated area) and/or the laser power output (beam attenuation, pulse width) [284]. Whereas higher laser fluences will result in higher ion yields, these ions are often undesirable clusters and/or adducts with matrix molecules, and so it is preferred to operate at slightly above the threshold fluence where ions are formed in abundance, defined by a sharp transition from the absence to the presence of ion signal. LDI inherently forms ions on a timescale much greater than the pulse width of the laser due to two primary ionization mechanisms: one which occurs promptly at the surface, and another which occurs within the plume and extends for several microseconds following the initial laser pulse [285]. Because of this extended timescale for ion formation, consideration must be given in the instrument designs incorporating LDI and for which performance parameters such as the temporal resolution of ion packets are critical, as is the case with linear geometry TOF mass analyzers. Delayed extraction strategies are an effective means of addressing this

long term ion formation mechanism (**Section 1-6.2**). Another strategy is to decouple the temporal dimensions of ion formation and subsequent analysis, as is accomplished through orthogonal extraction methods for TOF analysis (**Section 1-6.2**). For LDI based ion mobility methods, this ion formation time translates into the "ion gate" width of the experiment. As such the same strategies for minimizing ion gate effect in IMS can be employed with LDI IMS, specifically by using extended ion mobility analysis times that render the initial pulse width insignificant as what can be accomplished with long drift regions and/or high neutral gas densities (**Section 1-3.3**).

1-7.3 Electrospray Ionization

Electrospray ionization (ESI) is perhaps the most influential ionization source in modern mass spectrometry, capable of forming ions from very large (>100,000 amu) molecules and readily amendable to accepting a direct liquid sample infusion, which has broad implications for online chemical analysis strategies (*e.g.*, biomedical diagnostics, drug discovery and environmental analysis). It is appropriate that electrospray derives its beginnings from ion mobility experiments, with the first reported description of a charged spray needle device made by John Zeleny in 1914 [286], who coincidentally had previously reported the first known account of the ion mobility phenomenon [287]. Twenty or so years after Zeleny published his observations, Seville Chapman electrosprayed salt solutions and used ion mobility to analyze the resulting ions, demonstrating the analytical value of the technique [288]. In the 1970's, Malcolm Dole pioneered our modern analytical usage of electrospray and realized one of the "holy

grails" of mass spectrometry (there are, of course, many) with the first successful ionization of large biological molecules (lysozyme, mass ~14,300 Da; zein, mass ~50,000 Da), but because the technologies needed to efficiently transfer ions from high pressure to vacuum were not in place at the time, Dole characterized these ions with ion mobility methods rather than mass spectrometry and as a result perhaps sidestepped much of the notoriety he deserved for his discoveries [289,290]. Because Nobel prizes are not awarded posthumously, it was John Fenn's work on electrospray in the 1980's that was recognized with the 2001 Nobel Prize in Chemistry and indeed Fenn advanced our understanding of the ESI technique to a usable method for mass spectrometric analysis [238,271,291].

Today, ESI is the ionization method of choice for a wide range of analytical problems [292]. In additional to experimental convenience of accepting a direct sample effluent from condensed phase separations (*e.g.*, liquid chromatography and capillary electrophoresis), ESI is readily amendable to high resolution (mobility and mass) methods, as the unusual multiply charged nature of the resulting ions serves to enhance the measurement precision and thus resolution (refer to **Equation 5**) [38]. Additionally, the state-the-art technology for mass spectrometers fall in a relatively low m/z range (<4,000) meaning a high mass ion can be formed with a sufficient number of charges to be matched with the optimal performance of the current instrumentation. For spectrometers based on image current detection (*e.g.*, ion cyclotron resonance and the orbitrap), more charges increases the detector response (analytical sensitivity) with no detriment to other figures of merit other than effects at high space charge confinement

[293]. Single ions possessing a large number of charges (~2,000) have been isolated and detected in the ion cyclotron technique due to this enhanced sensitivity [294]. Finally, ion fragmentation techniques (*e.g.*, collisionally activated dissociation) benefit from having an ion with more than a single charge as the highly charged ion is less Coulombically stable and easier to fragment, and the resulting fragments are often charge carriers themselves, enhancing the number of fragments which can be detected for each dissociation event and thus enhancing instrument sensitivity [295,296]. Suffice to say there is much motivation driving the development of ESI based spectrometer methods today.

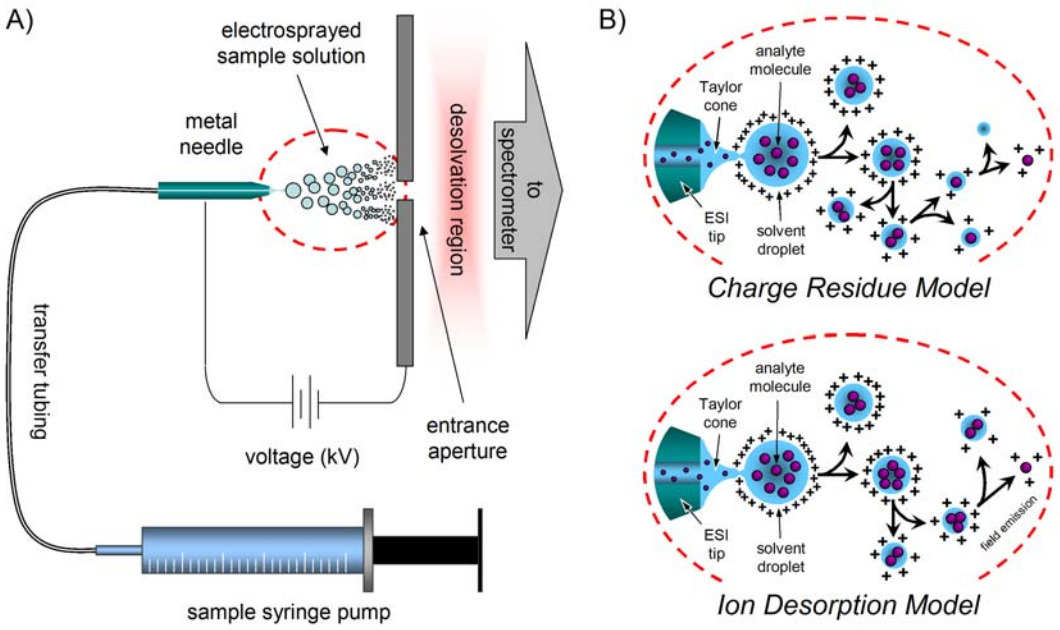

Figure 16 – Operational principle of electrospray ionization. **A)** The basic experimental setup showing the sample introduction line, spray needle and aperture entrance plate leading into the spectrometer. **B)** Two basic models of ion formation in ESI. In the Coulombic fission model, solvent droplets carry several analyte molecules and undergo droplet fission as their surface charge overcomes the surface tension keeping the droplets together. In the ion evaporation model, highly charged solvent droplets containing single analyte molecules evaporate and spontaneously release a charged analyte.

The experimental setup of a typical ESI source is shown in **Figure 16A**. All practical implementations of ESI are conducted at atmospheric pressure conditions. In its most basic form, the electrospray experiment consists of a conductive tube biased to a large potential (2-4 kV) with respect to a metal plate placed a short distance from the tube. The conductive tube is often referred to as a spray needle, since historically these were fabricated from hypodermic needles and can be either completely conductive, or partially conductive, such as the case with coated glass tips and fused silica capillary tubing. The needle potential can be applied either directly, as with the majority of designs, or established through the spray solution itself by inserting a metal wire into the sample stream [297], which is useful when utilizing nonconductive needles. Sample solvent is fed into the electrospray needle from a regenerating source (*i.e.*, a pressurized column or syringe pump) and the large potential difference creates a controlled discharge between the cathode and anode *via* nebulized droplets of the sample. The tip of the spray needle is oftentimes tapered to create the high localized field necessary to initiate the electrospray. The metal plate counter-electrode is almost always the entrance to the spectrometer consisting of a gas conductance limiting aperture or channel.

Ion formation in the ESI process results from a buildup of charge on the surface of the liquid which accumulates on the tip of the spray needle. Due to the pulling force of the counter-electrode, the charged liquid at the needle tip develops a characteristic conical shape as predicted by Geoffrey Taylor and subsequently called the Taylor cone [298]. As the Coulombic forces exceed the surface tension of the liquid, droplets break free from the tip into a stream which migrates towards the counter-electrode. The exact

mechanisms giving rise to charged analyte ions during this charge migration stage is still a matter of some debate. Two mechanisms, the *charge residue model* and the *ion desorption model* (**Figure 16B**) have been proposed to account for the transition of charged droplets into charged analytes. Common to both models are three steps of the ESI process: *i)* formation of the charged droplet, *ii)* subsequent shrinkage of the droplet due to evaporation of neutral solvent molecules, and finally *iii)* Coulombic fission of the droplet once the surface charge exceeds the surface tension holding the droplet together (the Rayleigh instability limit) [299]. In the charge residue model proposed by Dole, droplet fission continues to create smaller and smaller charged droplets until all that remains are charged analytes [300]. While this explanation is elegantly simple and easy to comprehend, it fails a test of logic imposed by Fenn which paraphrases that if a massively charged droplet continues this fission process, it will eventually encounter more analyte ions than charges, resulting in low charge states and analyte adducts—clearly the opposite is observed for electrospray ions [291]. An alternate explanation referred to as the ion desorption model was suggested by Iribarne and Thomson to explain the inconsistencies with Dole's model and in its basic form states that the droplet's increasing surface charge during Coulombic fission can become high enough to spontaneously desorb a charged analyte ion from the droplet prior to reaching further Raleigh instability [301]. This spontaneous field desorption model explains why there is a balance between analyte size (mass) and charge, rather than extremities on either end of the spectrum (*e.g.*, a large analyte with one or two charges or a small analyte with a hundred-fold charges). Spontaneous emission of ions from droplets during ESI has been

observed experimentally [302]. Currently it is believed that both the charge residue and ion desorption mechanisms play a role in the ESI process and the extent of either depends on the analyte—for large, hydrophobic molecules, the charge residue model applies while for small, hydrophilic molecules, ion formation is governed by the ion desorption model [303,304].

Ion formation in the electrospray process can be assisted with the use of a nebulizing gas—a neutral gas which introduces turbulence to the electrosprayed jet that assists in breaking apart charged droplets. The nebulizing gas can be introduced either as a direct stream (inline or counter to the flow) or an inline sheath flow placed around the electrospray tip [305]. Solvent conditions are also important for stabilizing the electrospray and subsequent ion formation, specifically the nature and concentration of organic solvent used which will govern the surface tension of the droplets. Equally important to the outcome of electrospray is the nature of the analyte, and the extent of charging can be controlled through the addition of derivitizing agents which promote the ionization of analytes which are particularly difficult to ionize (*e.g.*, nonpolar and/or hydrophobic molecules) [306].

Following ion formation, ions are introduced into the spectrometer, which in most modern applications is at a reduced pressure to facilitate ion entrainment with the incoming gas. The entry plate is defined by a very small (<1 mm) orifice to maintain the reduced pressure of the spectrometer. The use of a very small electrospray needle with low sample flow volumes enhances the ionization yields and quality of the ions formed (*i.e.*, sufficiently desolvated) as the smaller spray profile better amends itself to the

dimensions of the entrance orifice [307]. A desolvation step is often utilized to remove any excess solvent that remains adducted to the analyte ions following the electrospray process. A listing of some of the more commonly employed desolvation methods in electrospray is provided in **Table 8**.

Table 8 – Desolvation methods utilized in electrospray ionization. Most commercial implementations of ESI desolvation incorporate two or more of the above principles in their design, such as a combination of off-axis needle orientation using a spray stabilizing/desolvating sheath gas into an aperture-skimmer spectrometer inlet, as with the Zspray^{TM} Waters/Micromass ESI source [308,309].

	Desolvation Method	Description	Attributes	Where Implemented	Ref.
Pneumatic / Field Methods	Direct Aperture-Skimmer Inlet	Ions are introduced directly into the spectrometer. Some desolvation occurs at the conductance limit-gas skimmer pumping interface.	Quick and dirty method implemented on the first ESI instruments. Results in high ion transmission, but incomplete ion desolvation if used alone.	Waters/Micromass instruments (with off-axis ESI)	[300]
	Counterflow Gas with Glass Capillary Inlet	Ions migrate under the influence of a potential against a counterflow of dry (N_2) gas towards a glass capillary, where some are entrained into vacuum.	Countercurrent sweeps away solvent, minimizing resolvation during free jet cooling into vacuum. The nonconductive glass interface enables high voltage coupling between source and instrument.	Analytica of Branford ESI sources	[238]
	Cross-flow (Curtain) Gas	Ions travel orthogonal to a cross-flow of gas under the influence of an electric field. The relatively high gas velocity curtain gas facilitates desolvation.	Does not utilize any heating mechanism, so ions are relatively "cool" when formed. Ion losses from the gas flow can be significant.	Applied Biosystems, MDS Sciex instruments	[310]
Thermal Methods	Heated Metal Capillary	Ions travel through a hot (~) metal capillary where collisions with the hot gas and capillary walls facilitates desolvation	Efficient desolvation. The hot gas minimizes resolvation during free jet cooling into vacuum. Does not sweep away solvent, so source contamination is an issue.	Thermo Electron, Agilent, Bruker & Millipore Instruments	[311]
	Heated Desolvation Chamber	Ions travel through several stages of differential pumping. The differential stages are heated and the combined heat and skimmer fields facilitate desolvation.	Simple, rugged and can result in very high ion transmission as no capillary interface is utilized. Contamination of spectrometer components can be an issue.	Vestec Instruments	[312]
	Heated Desolvation Plates/Baffles	Ions travel a nonlinear beam path across a "hot plate" which facilitates desolvation.	Can be gentler than heated capillaries and/or desolvation gas flows, enabling the analysis of fragile ions (*e.g.*, adducts). Ion losses can be higher than line-of-sight methods.	JEOL MicroMass Hitachi instruments	
	Cryogenically Stabilized Electrospray (Cold-ESI)	ESI is conducted using cryogenically cooled nebulizing gases.	A special method for studying ions which easily dissociate in the ESI process, such as noncovalent complexes.	JEOL, Bruker Instruments	[313]

The electrospray process itself is a desolvation method, though not necessarily a complete one. The combined effects of field and gas entrainment all serve some manner of desolvation. In Dole's original ESI design, ions were formed and entrained directly into the vacuum interface of his mobility spectrometer. Desolvation was likely a result of strong electric fields and gas collisions during ion entrainment, and there is some indication that the complications which resulted in his charge state misinterpretations were due to incomplete ion desolvation [300]. Desolvation methods can be broken down into two general categories: *pneumatic methods* which use gas collisions to break apart solvent adducts often assisted by high electric fields, and *thermal methods* which use heat to facilitate solvent evaporation. For pneumatic methods, both counter and cross flow (curtain gas) methods have been used successfully. These pneumatic methods have the added advantage of sweeping away neutral molecules (mostly solvent) before they enter the spectrometer. Since nearly all ESI-spectrometer interfaces are characterized by ions transitioning between high and low pressure regions, there is a significant amount of adiabatic cooling which results from this transition and the presence of neutral solvent molecules in the ion stream can result in ion resolvation as a result of this cooling. The majority of desolvation methods rely on thermally heating a component of the interface, most often a long, metal capillary. The ion path must also be characterized by frequent collisions with hot gas molecules and/or the hot metal component itself, as is the case with the capillary inlets and nonlinear (labyrinthine) ion transfer inlets. Combinations of these methods are common, for example, most ESI sources utilize a sheath and/or counter-flow of gas in addition to a heated inlet to further

aid desolvation. Recently, RF ion focusing devices based on decreasing diameter rings (*i.e.*, ion funnels) have been implemented in the ESI interface of many instruments to help focus ions through the pressure differential region and into the vacuum of the spectrometer. The RF fields in this and other similar RF devices (*e.g.*, multipole lenses) combined with the presence of neutral gas further assists ion desolvation and ultimately the quality of the data acquired [314].

1-8 An Introduction to Charged Particle Detection Methods

The basic components of any spectrometry method are the ability to create, analyze and detect the charged form of the analyte of interest. So far, we have discussed somewhat exhaustively the first two requirements: forming the ion (**Section 1-7**) and analyzing it either through mass or mobility methods (**Sections 1-1** and **1-6**). The final and essential component for a spectrometer is ion detection which is reviewed and summarized in this section. There are two basic categories of ion detection: *current based detectors* and *electron multipliers*. Within each category are numerous detector configurations, most of these configurations are covered in **Table 9**. The purpose of this section is to touch on many of these detector types and frame the motivations behind choosing one particular detector type over another.

Table 9 – Charged particle detection methods used in mass spectrometry and their defining characteristics.

	Detector	Description	Gain	Dynamic Range[a]	Response[b]	Ref.
DC	Faraday Cup/Plate	A single element electrode (typically a cup or barrel) from which a direct current is measured.	none	$>10^5$	>100 ns [c]	[315]
Electron Multiplication	Discrete Dynode Array	An initial ion to electron (conversion) dynode followed by an array of dynodes which propagates an electron cascade.	10^6	$\sim10^5$	<30 ns [d]	[316] [317]
	Continuous Dynode / Channeltron®	A glass or ceramic tube often tapered and coated with an electron emissive material. An ion strike propagates an electron cascade down its length.	10^7	$\sim10^5$	<10 ns	[318]
	Microchannel Plate (MCP)	An array of capillary channels etched on a glass wafer. Each channel acts as a continuous dynode across the wafer's width. MCPs are usually combined to sufficiently increase the gain.	10^4 [e] 10^7 10^8	$\sim10^4$	<100 ps per plate	[319]
Hybrid Designs	Post-Acceleration Detector (PAD) [f]	Any of the electron multipliers combined with a separate conversion dynode element. Especially suited for high m/z ion detection.	varies	adds $\sim10^2$	<50 ns	[320]
	Daly Detector	A conversion dynode first stage and a scintillator and photomultiplier second stage separated by a window. Decoupled design amendable to high voltage separation and increased detector lifetime.	10^4	$\sim10^7$	<40 ns	[321]
	MCP-Photomultiplier / On-Axis Bipolar Detector (MCP-PMT)	Nearly identical to the Daly detector except the first stage also incorporates an electron multiplier, which greatly increases the detector gain. Can operate in both ion polarity modes simultaneously.	10^6	$\sim10^5$	<100 ps	[322]
Position Sensitive Anodes	Discrete Multi-Anode Array Detectors	A conventional MCP detector utilizing a segmented anode to obtain spatial resolution of ion impacts. This also improves sensitivity for ion counting, as coincidental impacts are counted on separate anodes.	--	--	--	[323] [324]
	Delay Line Detector	A conventional MCP detector utilizing two parallel wire arrays as anodes (X and Y direction) which can pinpoint ion impact locations based on circuit response.	--	--	--	[325]
	Resistive Anode / Capacitive Charge Division Detectors	Similar to the delay line technique but utilizing either a resistive anode surface or capacitor anode which senses a differential response in the electron cascade based on spatial location of the ion impact event.	--	--	--	[326] [327]

a. Dynamic range in this case represents the detector's linear response range for pulse counting (digital) mode experiments.
b. Response times in this column represent detector recovery following electron saturation, which is a more useful metric for high speed applications.
c. Faraday cup response times have been reported as low as ~50 ns, but with significant sacrifices to sensitivity.
d. ETP manufactures a discrete dynode detector with a claimed ~3 ns response for time-of-flight applications. Saturation responses are not reported.
e. Gain values for a single, double (chevron) and tripled (Z-stack) stacked MCP configuration, respectively.
f. Strictly speaking, PAD detectors are not limited to conversion dynode arrangements as an on-axis MCP detector can be operated in a PAD configuration by applying an acceleration field in front of the detector *via* a grid.

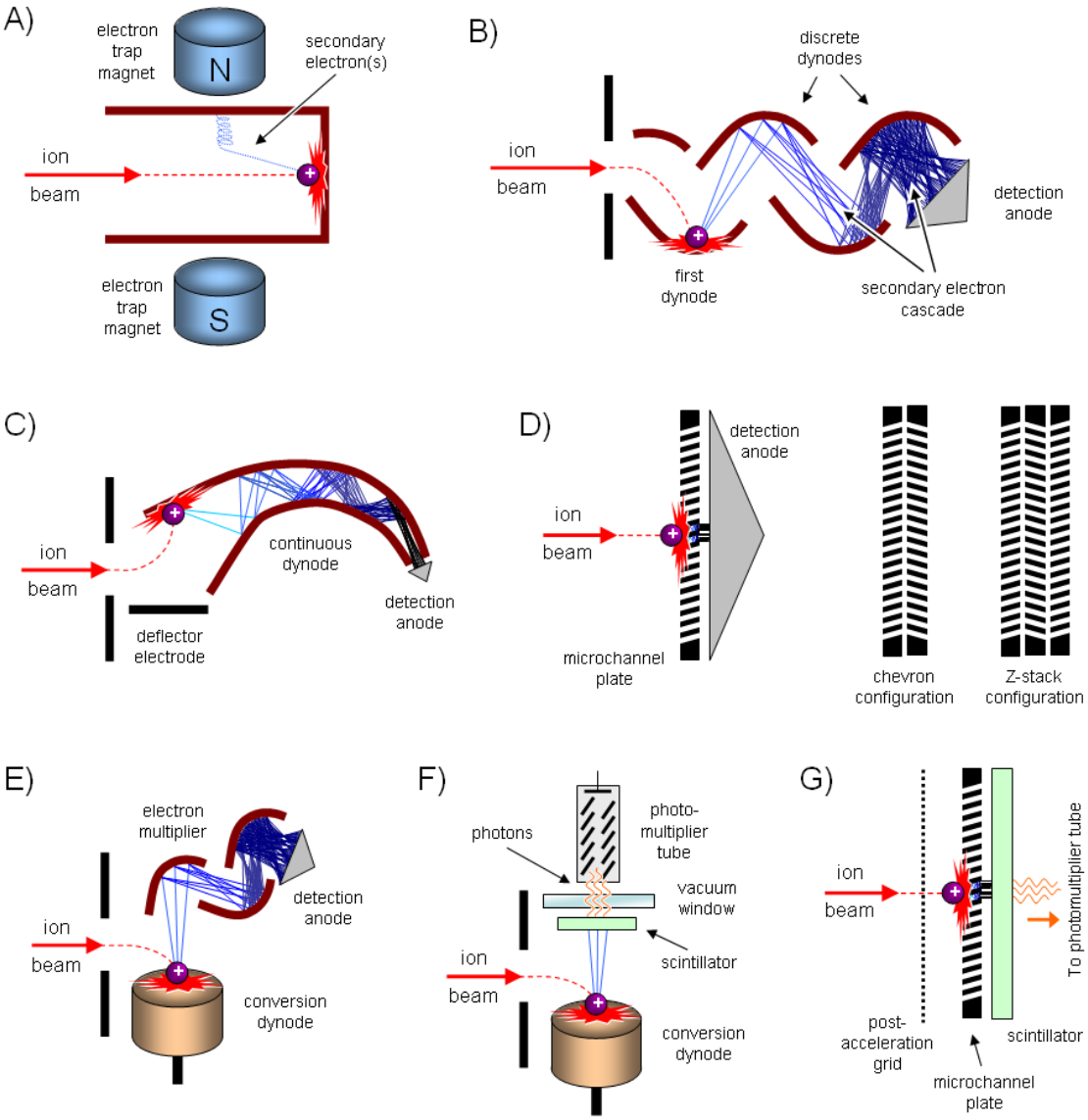

Figure 17 – Charged particle detection methods used in mass spectrometry. **A)** Faraday cup detector utilizing permanent magnets as a secondary electron trap. **B)** Discrete dynode electron multiplier with several individual secondary electron-emissive dynodes. **C)** Continuous dynode electron multiplier detector comprised of a monolithic dynode. **D)** Microchannel plate detector and various plate configurations used to increase detector gain. **E)** Post-acceleration detector configuration utilizing a conversion dynode for more efficient high mass ion detection. **F)** Daly detector utilizing a conversion dynode and a scintillator/photomultiplier arrangement. **G)** Hybrid on-axis microchannel plate-photomultiplier detector with post-acceleration capabilities. Details are provided in the text.

1-8.1 Direct Ion Current Detection: Faraday Detectors

The Faraday cup (**Figure 17A**) represents the simple and most straightforward means of measuring a beam of charged particles. This type of detector consists of a piece of metal of most any shape placed in the path of an ion (or electron) beam. Cup shapes are often preferred for their ability to capture a large spread of charged particles confine resulting secondary electrons, though simple metal plates have found widespread use in research instrument primarily for troubleshooting purposes.

In the Faraday detector, the metal element is electrically isolated within the instrument and, in the simplest form, an electrometer (picoammeter) is used to measure the change in current caused by impending charged particles neutralizing on the surface. Because Faraday detectors directly measure the current induced by a charged particle, they are considered the only absolute means of quantifying the number of charged particles in the beam, as the current reading can be directly related to particle numbers. For ion detection, Faraday detectors do not suffer from a high mass attenuation which occurs in other electron multiplier based detection methods, though since quantitation depends on charge counting, the number of charges on the ion must be known if accurate ion numbers are to be determined from the measurement (*i.e.*, a +6 ion will induce 6x more current than a +1 ion). Additionally, the response of the detector does not depend on the energy of the beam, as with electron multiplier detectors, but only on the charge flux hitting the metal element. Since most applications of Faraday detectors are used to measure relatively high energy ion beams (greater than a few hundred eV), each striking event will release secondary electrons, which if they escape the detector surface, will

register as an additional ion hit. The cup design is an effective geometry for recapturing secondary electrons, and other means such as electrostatic confinement optics and magnets are also routinely used to address the issue of secondary electrons. Specially shaped designs, such as half cylinders, have also been suggested for the purpose of minimizing the escape of free electrons which would otherwise distort the charge measurement [328]. Coating or fabricating the metal detector surface with a high work function material, such as graphite, also minimizes secondary electron emission and graphite in particular is less prone to chemical contamination which increases the usable lifetime of the detector.

Properly matching the impedance of the circuit is important for using Faraday detectors in fast response applications, such as what would be needed for time-of-flight measurements. This is also an important consideration for all charged particle detectors which use a signal anode to measure electron current resulting from an electron multiplier. Impedance is a fundamental (and difficult to quantify) property of electronic circuits related to how readily current will flow (or be impeded by) various components of the circuit. Improper matching of the impedance in the detection signal line will result in slow rise and fall times (*i.e.*, peak fronting and tailing) and in worse cases measurement distortions and noise (*e.g.*, ringing) caused by signal reflections within the circuit. Most coaxial lines are rated for 50 Ω resistance termination, which is one established "standard" for matching impedance of signal lines and components. Ensuring that all components are 50 Ω impedance rated and have the proper resistance termination in place will address the most common problems associated with impedance

mismatch. Fundamentally, there exists an impedance mismatch between the large surface area of the detector (or anode for electron multipliers) and the small area of the signal line—because current is a surface propagation phenomenon, a gross mismatch in surface area results in an impedance mismatch at the junction. Strategies to minimize this mismatch include the use of conical coupling devices which taper to the signal line [329,330] and more simply, restricting the length between the detector and the coaxial line to a few millimeters to force impedance mismatched ringing noise into the GHz range. Since most signal processing electronics have an upper sampling limit of a few hundred MHz, the ringing noise will not be observed [331]. Particularly for fast response applications, it is also desirable to shield the Faraday cup from incoming ions which would induce a charge on the cup prior to the striking event and result in some distortion of the baseline signal [332]. Apertures or grids can be used effectively for this purpose.

While Faraday detectors offer the ability to quantify ion (or electron) numbers, they inherently suffer from low sensitivity. In order to obtain a measurable response, state-of-the art Faraday cups require an ion current of ~10^{-15} A, which represents an ion flux of about 6,000 ions/sec. Most Faraday detectors require a minimum of ~600,000 ions/sec before generating a measurable response which prohibits their use in applications where very few ions are transmitted, such as the injected ion drift tube experiments described in this work [333]. Nevertheless, Faraday current detectors remain one of the few ion detectors capable of operating efficiently at elevated pressures, and enjoys almost exclusive use in standalone IMS devices [334].

1-8.2 Electron Multipliers: Conversion Dynodes and the Discrete Dynode Detector

Secondary electron emission resulting from an ion striking a metal surface was discussed in the previous section as a source of noise and quantitation error for the Faraday detector. This same electron emission principle is fundamental to the operation of the second class of charged particle detectors, the electron multipliers. In its most basic form, the electron multiplier detector is a Faraday detector that detects electron current resulting from an ion striking a metal surface. Early detectors employing this design referred to this first electron emissive element as a *conversion dynode*, due to the way in which it converted a positive ion into many negative electrons. Dynode is a somewhat antiquated term meaning a dynamic electrode and refers to the elements which emit secondary electrons. Inherent to this electron conversion process is charge multiplication with a single dynode element being capable of emitting tens to hundreds of electrons for every ion strike. This charge "gain" will ultimately depend on the velocity of the ion, the applied voltage and the material of the conversion dynode. Potentials applied to the conversion dynode will typically range between 3 and 10 kV, with higher potential being able to accelerate ions to a higher velocity and increasing gain. The voltage limit will depend in the field emissive properties of the dynode surface, so conversion dynodes are polished to remove any "whiskers" or surface pitting that would create electron emission points and introduce detector noise. Since any ion with the same charge number gains the same kinetic energy in the same electric field, the velocity in which they strike the detector will depend on their mass, specifically lower mass ions will be accelerated to a higher velocity than a high mass ion of the same

charge number. Ultimately this means that all electron multiplier based detection schemes have a decreased gain towards higher mass ions since their lower velocity impacts generate less electron emission off the first (conversion) dynode surface. This is fundamentally why mass spectrometry (and IMS) cannot do exact quantitation of sample (though many applications exists which make this very claim). The applied voltage on the detector governs how much stored electrons are available to emit, while the work function of the dynode material will influence the energy and number of electrons emitted. Beryllium-copper (BeCu) alloys are the most commonly used material for dynodes, though silver-manganese (AgMg) and aluminum metals are also used—the latter being a cost effective and more air stable alternative possessing somewhat lower electron emissive properties than the other alloys.

While a single conversion dynode element can be used with a Faraday cup to increase the gain (sensitivity) of the detector, several discrete dynodes placed in a "Venetian-blind" configuration (*i.e.*, staggered and tilted to face on another, **Figure 17B**) can output over 1 billion electrons for every ion strike event. This effect can be readily conceptualized by considering a simple arrangement of 4 discrete dynodes. If each dynode has a modest gain of 4 electrons emitted for every electron (or ion for the first dynode) striking event, then if one ion goes in, 4^4 or 256 electrons come out on the other side! Discrete dynode detectors having as many as 20 dynodes have been reported, with gains up to 10^8 [333]. The discrete dynode detector draws its roots from photomultiplier tube development, where they are still used extensively today.

1-8.3 Electron Multipliers: Continuous Dynode Detectors

As the instrumentation became more technologically advanced, there was a need to compliment their faster scan rates and smaller sizes with an appropriate ion detector. Fundamentally, the discrete dynode detector responds only as fast as it takes electrons to cascade down the length of the dynode array, and while making them smaller and more compact would improve their response times, this strategy imposed several technical challenges. The primary challenge was that in order to maintain the potential drop necessary to accelerate electrons from one dynode to another, the field strength would have to be increased if the distance between dynodes were decreased, otherwise gain would be sacrificed for size. Increasing the field between dynode elements imposed greater restrictions on the vacuum needed to prevent gaseous breakdown, limiting the applications of such miniature detectors. The solution was to develop a different detector geometry based on the same underlying principle of electron multiplication.

A continuous dynode detector (**Figure 17C**), or sometimes referred to by the Channeltron® trade name, is a continuous length of lead silicate glass tubing which possesses electron emission properties due to the metal inclusions in the silicate structure. A resistive coating is added to maintain a linear potential drop across the length of the tube and many of these proprietary coatings also serve to enhance the electron emissive properties of the glass. The basic principle of a continuous dynode's operation relies on an ion striking the inside surface of the tube, preferably close to the front, and generating a subsequent cascade of electrons down the length of the tube. An anode placed at the other end measures the resulting electron propagation current. Gain

is directly related to how far in the front of the tube the ion strikes, so the majority of continuous dynodes are bent into a horn shape to prevent an ion from striking deep within the tube, which also otherwise increases detector noise. These horn-shaped tubes are also tapered to ensure the electron cascade propagates down to the anode surface efficiently. Because there is variability between the detector response and the location of ion impact, additional ion optics are often used with continuous dynode detectors to steer and focus the ions to a specific location on the dynode surface. Continuous dynode detectors utilizing such ion optics are oftentimes placed off-axis to the incoming ion beam in order to minimize noise due to neutral impacts and reduce contamination of the detector. This also protects the detector from plasma streaming events which can occur particularly in IMS applications. In addition to the common horn-shape, straight and spiral shaped (Spiraltron^{TM}) continuous dynodes have also been developed for specialty applications. The average geometry continuous dynode has less overall gain than a discrete dynode, but possesses faster response characteristics. Unlike discrete dynodes which are prone to atmospheric poisoning of the dynode surface, particularly with BeCu and AgMg alloys, continuous dynodes are incredibly rugged, withstanding repeated vacuum to air cycles with no changes in their performance characteristics. As a result, continuous dynode detectors are still the workhorse ion detection method for many small form factor and routine analysis mass spectrometers on the market today.

1-8.4 Electron Multipliers: Post-Acceleration Detection

Because the momentum of the initial ion strike affects the response of the detector, there is inherent high mass ion discrimination in electron multiplier detectors, as mentioned previously. To help address this issue, an electron multiplier detector can be fitted with an initial conversion dynode at the entrance which can post-accelerate the ion to more efficiently generate electrons at the conversion dynode and thus improve the detector's response to high mass ions. This forms the basis of the so-called post acceleration detector (**Figure 17E**), which is tailored towards analyzing high mass ions. Post acceleration detectors are also more amendable to ion measurement in negative mode, since only the conversion dynode polarity needs to be switched to effectuate electron emission from the dynode surface [335]. It should be noted that the high mass discrimination can also be somewhat addressed by analyzing multiply charged ions since the charge number affects the ion's velocity in a fixed electric field. Electrospray ionization is thus ideally suited for the study of higher mass (but consequently lower m/z) samples. Conversion dynode technology is commonly marketed in existing electron multiplier detectors as a high energy dynode (HED) accessory.

1-8.5 Electron Multipliers: Microchannel Plate Detectors

As instrument technologies continue to improve, the size and response time of the continuous dynode eventually becomes a limiting factor in spectrometer performance. An increasing need to make detectors smaller and faster but without compromising the gain led to the concept of fabricating an array of small, continuous

dynodes on a single substrate [318]. Such a detector is called a microchannel plate (MCP) detector and consists of several hundred micron sized channels etched across a thin (~2 mm) glass wafer (**Figure 17D**). Because the electron propagation occurs across the width of the MCP, response times are extremely fast, with state-of-the art MCP detectors responding at picosecond speeds per ion striking event, as compared with 1-10 ns for the best continuous and discrete dynodes on the market. The microchannels are angled ~8° within the wafers for most electron multiplier applications to ensure that the charged particles do not penetrate into the channels before striking the surface. The gain for a single MCP is low compared with other electron multipliers, but multiple MCP plates can be stacked together to increase the gain as high as 10^8. Two MCP's stacked together are often stacked in a "chevron" configuration, representing the angled channels rotated 180° relative to one another (/\). A three MCP configuration is often placed in a Z-stack, whereby the angle of channels is staggered with respect to one another (/\/). This maximizes gain and retains memory of the ion strike location to the anode, which is important for positive sensitive detection schemes. Staggering the angled holes also breaks the line of sight for the detector assembly, which helps suppress gas ionization propagation effects within the channels—the primary cause of MCP detector "saturation". When assembling MCP detectors by hand, one must pay attention to this configuration in order to optimize the detector gain. It is also important to combine MCP sets in matched resistances so that an equal amount of current flows across each plate during operation. An insufficiently matched set of MCPs will hasten the degradation of the lowest resistance plate, which endures the highest current flow during

operation. MCPs are sold from the vendor in matched sets with resistive coating tabs along the rims marking the angled direction of the channels to facilitate ease of assembly. A potential drop of ~1000 volts is required for each plate to activate the surface for electron emission, with two plates requiring doubled this potential. The polarity of this detector potential is critical to ensure ions are directed towards the first MCP and that subsequent secondary electrons propagate towards the anode. Because such a high potential is applied across a relatively short distance (~5 mm), there is a greater chance of electrical discharge occurring with MCP detectors than with discrete or continuous dynode detectors. While the latter detectors can survive a direct electrical discharge, an MCP assembly will likely be destroyed during a discharge event, and so special precautions are often taken to ensure a path to ground is not favorable. Usually the nearest path to ground is between the MCP and the anode, which is placed ~2-5 mm from the back of the MCP assembly and so isolating the anode with a capacitor is an effective strategy for preventing discharge issues. This also protects detector electronics which will certainly be damaged without a capacitor in the signal line. A resistance of high value leading to ground (or a suitable current sink) can also be added on the detector side of the circuit to ensure excess charge caused by the electron cascade is dissipated from the circuit which will otherwise degrade the response of the detector due to lengthy capacitor discharge times. Finally, special requirements must be ensured when storing MCPs as the highly porous surface is highly hydroscopic. As water adsorbs onto the MCP, the wafer expands and oftentimes cracks under the excess force. This is particularly problematic for the standard “rimmed” design which utilizes a solid

rim about the porous surface to ensure adequate electrical contact with the detector assembly. Rimless MCPs are offered using small resistive tabs on the edges to ensure electrical contact is made. While rimless MCPs have less stringent storage requirements, the microchannels which are present along the edges can contribute to excess electron noise leaking from the detector to the anode, so special shielding is often required for their use. Otherwise, MCPs must always be stored either under inert gas atmospheres, or more preferably within a vacuum chamber to minimize the adsorption of water. Thus, while MCPs offer attractive incentives in terms of detection response and compact form factor, they are delicate to handle and require more care to maintain, and as a result their benefits in many cases are not worth the added grief. Still, a well cared for MCP detector will last for many years with good sensitivity.

Recall from **Table 9** that MCP's have one or two orders of magnitude lower gain than most other electron multiplier detectors. This situation is often referred to as MCP detector *saturation*, and results from gas molecules ionizing in the microchannels and creating an ion feedback current that opposes the avalanche of electrons. This is a consequence of the direct line of sight of the microchannels which creates an efficient path length for the ions to propagate. This is also the reason why the electron path length in most other electron multipliers is nonlinear, such as in the case of the horn-shaped continuous dynode. One solution to this problem of MCP charge saturation is to make the microchannels curved rather than straight. The curved channels will greatly increase the chances that ions formed in the channels will hit the walls and neutralize rather than propagate down the channel length, improving the gain of a single MCP by

one to two orders of magnitude [336]. Curved channel MCPs are available from the major ion detector vendors, though they are decisively more costly due to the greater difficulty involved in their fabrication. Operating an MCP within a magnetic field also helps suppress ion feedback due to the Lorentzian forces acting on the ions which increases the likelihood that they will collide with the channel walls rather than propagate [337]. Another approach which has gained some recent attention is the use of microspheres rather than microchannels to reduce ion feedback effects. Microsphere plates operate in the same manner as an MCP though electron cascades occur within the volume between closely spaced spheres, which creates a nonlinear path for the avalanche. In addition to being easier to fabricate, and thus less costly, microsphere plates possess the advantageous characteristic of being able to operate at low vacuum ($\sim 10^{-3}$ torr), which makes them particularly attractive in specialized applications. This ability results directly from the volume formed from packed spheres creating a path length for the electrons which will not exceed the mean free path of the gas at these high pressures, discouraging any breakdown that might occur [338].

1-8.6 Hybrid Electron-Photon Multiplier Detectors: Daly and MCP-PMT Detectors

An alternative to the purely electron multiplying detector is a hybrid design which offers some amount of ion to electron conversion and supplants the remainder with a combined scintillator (phosphor screen) and photomultiplier tube (PMT) stage. Such a detector relies on an electron-induced luminescence of a phosphor substrate

which is detected by a PMT. A prerequisite of such a detector is an initial ion to electron conversion step, either through a conversion dynode or an electron multiplier.

The first detector described in this manner was developed by Norman Daly for molecular beam applications [321]. The Daly detector (**Figure 17F**) consists of a conversion dynode (often referred to as the Daly "doorknob") followed by the scintillator/photomultiplier stage. In this configuration, the Daly detector is a post-acceleration detector, and is thus sensitive to high mass ions. The conversion dynode is necessary to generate secondary electrons for the scintillator. Electrons are directed towards the scintillator surface and a stream of photons is ejected on the back end which is amplified by a photomultiplier and detected with the conventional detector electronics. The primary advantage of the Daly detector is that the conversion dynode/scintillator can be completely isolated from the photomultiplier through a quartz vacuum window, such that the photomultiplier is operated outside of the vacuum system. This simplifies restraints on the detector being at vacuum during high voltage operation and allows for the photomultiplier to be serviced without breaking vacuum. Thus, a catastrophic venting of the vacuum system during high voltage operation of the detector is much less likely to result in damage to the detector. In Daly's original design, the conversion dynode and scintillator assembly are orthogonal to the ion beam, which also reduces the detector noise resulting from neutrals and photons originating coaxial to the beam. The other advantage of the Daly detector is bipolar operation, meaning that both negative and positive ions can be readily detected from the molecular beam simply by switching the

polarity of the conversion dynode. All hybrid detectors incorporating a photon multiplication stage is technically a bipolar detector.

Photomultiplier ion detectors based on a microchannel plate first stage (**Figure 17G**) have been commercially developed for fast response applications. These microchannel plate-photomultiplier tube (MCP-PMT) detectors are marketed as on-axis, bipolar detectors, due to the placement of the MCP in the line-of-sight of the ion beam and the ability of these detectors to detect positive and negative charged particles by changing the voltage polarity of the MCP first stage. The on-axis design facilitates a faster response by the detector as compared with orthogonal ion beam conversion methods (*i.e.*, an off-axis conversion dynode). Post-acceleration can be achieved in an on-axis design by decoupling the field drop to the MCP surface *via* a grid. The advantages of such a detector include fast response times approaching those of MCP detectors with a somewhat extended lifetime of operation as compared with MCP detectors alone. The added benefits of high mass ion sensitivity (*via* post-acceleration) and bipolar operation makes this one of the most versatile detector configurations available, at a cost of more complicated operational requirements as each component of the detector requires a separate voltage offset (*i.e.*, post-acceleration, MCP activation, scintillator acceleration and PMT operation).

1-8.7 Nondestructive Ion Detection Based on Image Current Sensing

Though not a mature technique for beam spectrometer applications, image current detection is widely used in Fourier transform mass spectrometers and the newly

developed orbitrap spectrometer. Such methods rely on the residual charge built up on an electrode as an ion passes across its surface, and as such are not inherently sensitive. Their success in ion trap spectrometers rely on several thousand transits across an image current sensing electrode, and thus are practical for such applications. In order to differentiate different m/z ions, the ion trap must be able to selectively promote specific m/z ions to transit in proximity to the detection electrode(s). This is accomplished in FTMS through the application of a coherent RF potential which pumps energy into ions that cyclotron at the same frequency. A similar coherent RF potential is applied for image current detection in 3D ion traps, though very few 3D traps implement this kind of ion detection. For orbitraps, ions oscillate parallel to the axial electrode with a frequency that is m/z dependant and can be detected directly through the use of two hemispherical electrodes which surround the axial electrode [182]. The obvious advantage of image current detection is that ions are not destroyed during the detection process, and so can be analyzed continuously, within the vacuum limit of neutral collisions. This is one of the primary reasons why FTMS instruments perform with the highest mass resolutions, mass accuracies, and overall sensitivities over any other mass analysis method [339].

2. INSTRUMENTATION DEVELOPMENT AND DESIGN CONSIDERATIONS

2-1 The Design Rationale for the Cryogenic IMS-MS Instrument

In this section, the cryogenic IMS-MS instrument is presented alongside the rationale for the choice of each instrument component. Performance test data will also be provided with relevant discussion. A conceptual experimental scheme of the instrument configuration is provided in **Figure 18**. The configuration of the instrument is comprised of i) the ionization source where sample is introduced to the instrument and converted into gas phase ions ii) the forward mass spectrometer which serves as both an ion transfer device through differential pressure regions and an ion m/z selector for ion mass specific studies iii) the cryogenic drift cell spectrometer where ions are separated in mobility space at varying temperatures from ambient (298 K) to cryogenic (78 K) iv) and the back end mass spectrometer which mass analyzes the ions which elute from the IMS cell. Various ion optical components occupy the regions in between components and will be discussed within the next few sections dealing with each component of the instrument in more detail.

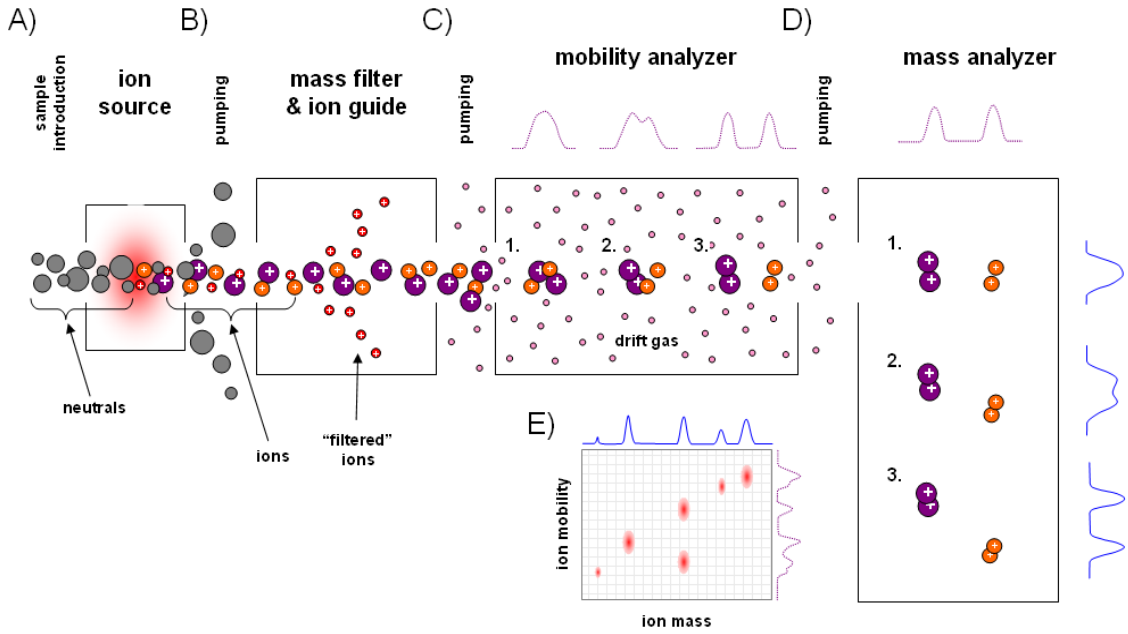

Figure 18 – Experimental scheme of the cryogenic MS-IMS-MS instrument. From left to right: **A)** the sample is introduced as neutral molecules into the ionization source where a small percentage is converted into ions. **B)** Excess sample neutrals are pumped away as ion optics direct a beam of ions into a mass filter where undesired ions can be removed from the ion beam. **C)** Ions are gated into the drift region of a mobility analyzer, where they are dispersed based on their interaction with the drift gas. **D)** Mobility separated ions are transferred to a mass analyzer where they are dispersed based on their mass-to-charge values. Mass data can be generated from each peak which elutes from the mobility analyzer. **E)** A 2D plot of the mobility dispersion and mass dispersion data can be generated and analyzed for information.

2-2 The Instrument Vacuum System and Infrastructure

The instrument was designed from the ground up using ion trajectory simulation and computer aided design (CAD) software. A representative schematic of the instrument is contained in **Figure 19A**, which provides an overview of the component details. A cutaway CAD schematic of the instrumentation is provided in **Figure 19B** which shows accurately scaled details of the vacuum housing and ion optical components.

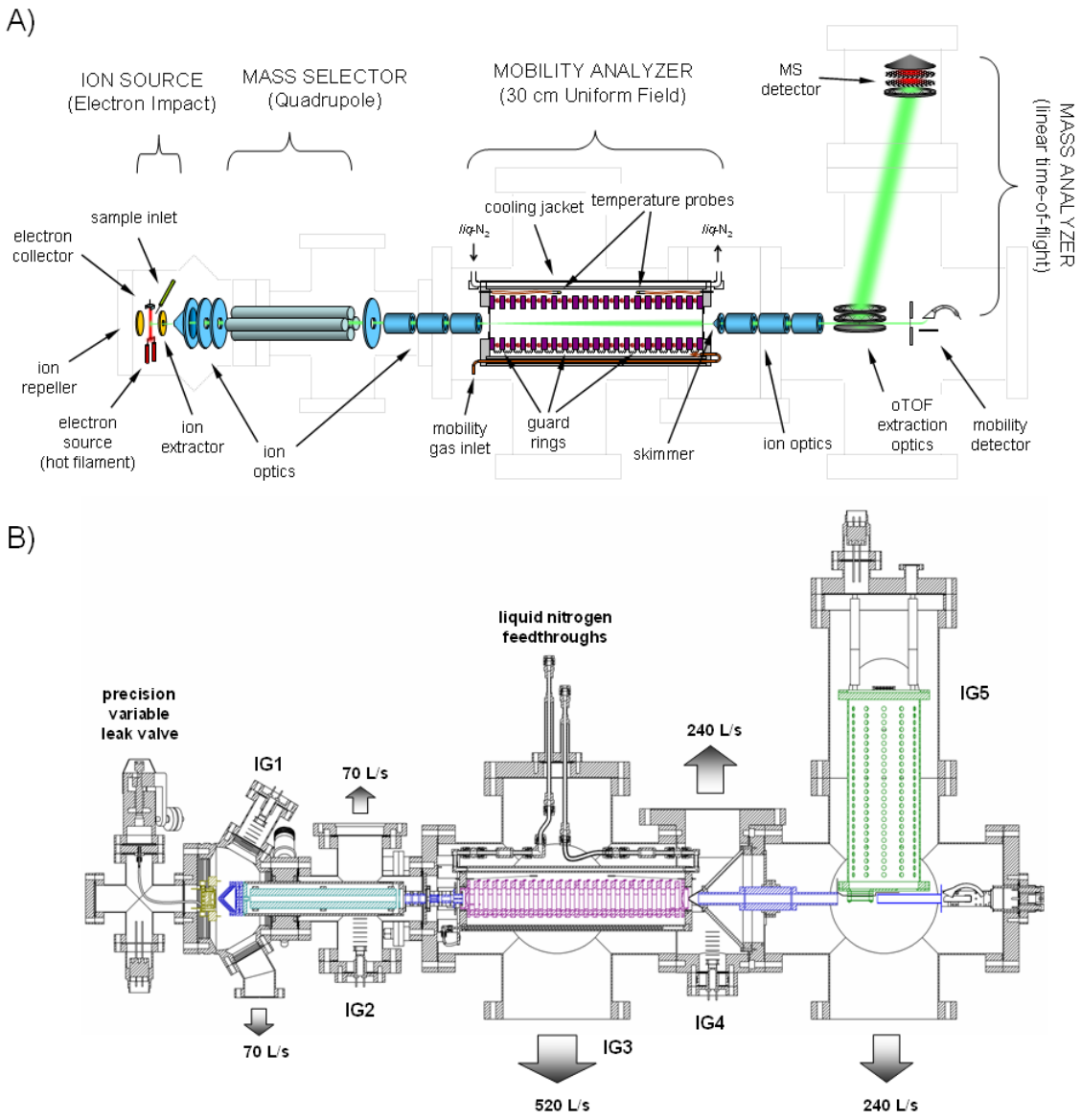

Figure 19 – Schematics of the cryogenic MS-IMS-MS instrument. **A)** Conceptual schematic with relevant component detail. From left to right, the instrument is comprised of the ionization source, mass selector, mobility and mass analyzers. **B)** A CAD generated schematic with scaled details regarding the vacuum housing. Arrows depict the locations and pumping speeds of the various turbo molecular pumps used to achieve high vacuum. Components labeled "IG" are ionization gauges used to measure the pressure of each of the chamber sections. Schematics are color coded by components: gold for the ion source, cyan for the forward quadrupole, magenta for the ion mobility spectrometer, green for the time-of-flight mass spectrometer and blue for ion optical components.

2-2.1 Vacuum Hardware and Design Considerations

Because all mass spectrometry and the majority of ionization methods necessitate the use of high vacuum (free molecular flow regime), an appropriate vacuum system was designed around the individual instrument components. Time-of-flight methods in particular are sensitive to ion-neutral collisions with background atmosphere, and so ultrahigh vacuum materials and assembly strategies were chosen for the vacuum system and all components housed within. The housing of the instrument is fabricated from stainless steel (austenitic alloys 304 and 316) and assembled using compressed metal (copper) gasket junctions (Conflat® vacuum standard, Varian, Inc., Palo Alto, CA) [340]. Silver plated, 12-point head bolts are used at each flange junction to achieve the required compression (16-20 N·m of torque per bolt) on the metal gasket. The silver plating acts as a zero outgassing lubricant and reduces thread galling commonly associated with heterometal junctions (*e.g.,* stainless steel bolts threaded into tapped stainless steel flanges). 12-point head bolts are fully compatible with closed (box) ended wrenches and offers higher torque per tool contact area compared with more commonly used socket head and hex head bolt styles which greatly reduces the chance of tool slippage that can damage the vacuum system during fabrication and disassembly. The silver plating also reduces friction on the fastener, replacing the typical use of lubricants, such as molybdenum disulfide ("moly lube") and graphite powder which can otherwise contaminate the vacuum system [341].

2-2.2 Vacuum Pumps and Pressure Measurement

High vacuum is obtained through the use of turbo molecular pumps. Turbo molecular pumps, or turbo pumps for short, operate on the principle of statistical pumping of gas molecules which have chance encounters with a series of appropriately shaped turbines that direct their motion away from the vacuum chamber. As gas molecules gather and concentrate on the back end of these turbines, the gas density increases such that the gas transitions to the viscous flow regime where a suitable "rough" backing pump can be used to pull these gas molecules out of the system [342]. Pumping in the instrument is achieved by six turbo pumps of varying pumping capacities placed in locations where the pumping speed is necessitated (arrows in **Figure 19B**). Two 70 L/s turbo pumps (Turbo-V70D, Varian, Inc., Palo Alto, CA) are placed at the source and mass filter chambers, generating a base vacuum of $<10^{-9}$ torr when no gas is present in the ion mobility spectrometer. A high gas capacity, 520 L/s turbo pump (TMU 521YP, Pfeiffer Vacuum GmbH) evacuates the ion mobility spectrometer chamber, which reaches a base pressure of $<10^{-8}$ with no drift gas present. Two additional 240 L/s turbo pumps (TPH 240, Pfeiffer Vacuum GmbH) evacuates the IMS-MS interface region and the MS spectrometer chamber, both of which reaches a base pressure of $<10^{-8}$ torr with no drift gas present in the system. With 1-4 torr of helium present in the IMS drift cell, the base pressures of the instrument are as follows: $\sim10^{-6}$ torr in the source and mass filter (quadrupole) region, 10^{-5} to 10^{-4} torr in the outer IMS chamber, 10^{-4} in the IMS-MS interface region, and 10^{-7} torr in the TOF chamber. These

pressures are sufficient for efficient ion transfer and mass analysis[16]. The turbo pumps are backed by a series of oil-seated, rotary vane pumps capable of pumping viscous gases, each with pumping speeds of approximately 3.3 L/sec (Pascal 2010 SD, Alcatel Vacuum Technology, Hingham, MA; Edwards RV8, BOC Edwards Vacuum, Tewksbury, MA). A narrow-cut-fraction distillate hydrocarbon oil (TKO-19 Ultra, Kurt J. Lesker, Co., Clairton, PA) is used for all mechanical pumps. Molecular sieve traps (0.45 kg capacity containing zeolite 13X, 3.2 mm diameter sieves) are placed between the turbo and backing pumps and prevents excessive backstreaming of hydrocarbon oils into the vacuum system. Sieve traps also protect the vacuum system by taking on the majority of the oil load that backstreams into the instrument as a result of power failure. This oil backflow situation arises when power is shutoff from the backing pumps, creating a higher vacuum in the instrument chamber than the pump can generate (an automated up-to-air valve is another means of addressing this issue). All rough vacuum lines are assembled using the ISO standard quick release fittings, referred to as the *klein flansche*[17] (KF) system [340]. The vacuum chamber pressures are measured using Bayard-Alpert style (hot filament) ionization gauges (IG) placed at each vacuum chamber section (IG1-IG5 in **Figure 19B**). Dual filament designs are utilized for the ionization gauges to minimize instrument downtime due to filament burnout. Low

[16] The mean free path between collisions at $5x10^{-6}$ torr is ~3 meters which exceeds the total ion traversal distance from source to detector across the entire instrument. In the interface region into and out of the ion mobility cell, pressures can reach as high as $1x10^{-4}$ torr, which corresponds to a mean free path of ~14 cm—a distance which is still much longer than the ion traversal distance in these regions (the longest traversal distance is from the quadrupole into the IMS chamber, corresponding to a distance of ~7 cm).

[17] *Klein flansche* is german for "small flange" and describes the compact size of these particular class of fittings, the largest of which is under 76 mm (3 inches) in diameter.

vacuum is measured using thermocouple gauges placed on the rough vacuum manifold. Thermocouple pressure gauges operate on the principle of measuring the gas density-specific resistance changes in a bimetallic junction. Thermocouple pressure sensors are robust and inexpensive, but the subsequent pressure reading is gas species dependant and not as accurate as other gauge types which measure in the same pressure regime (*e.g.*, capacitance manometers, piezoelectric gauges) [343]. Accurate pressure measurements are not necessary for the operation of the vacuum manifold, and so thermocouple gauges are sufficient for use in this application. An appropriate vacuum gauge controller (Granville-Phillips® 307 Controller, Brooks Automation, Austin, TX) is used to convert the temperature reading from the thermocouple gauge and the ion current from the ion gauge into usable pressure values. Because different gases have different ionization efficiencies, the response of the ionization gauge is gas species dependant. Ion gauge controllers are factory calibrated from nitrogen gas readings and so an appropriate correction factor must be used to derive an accurate measure of the pressure when gases other than nitrogen are present in the vacuum chamber in significant amounts. Ionization gauge correction factors for common gases can be found in the literature [344,345]. For helium gas, a correction factor of 0.18 is used—this correction is divided directly into the IG reading to obtain the corrected pressure.

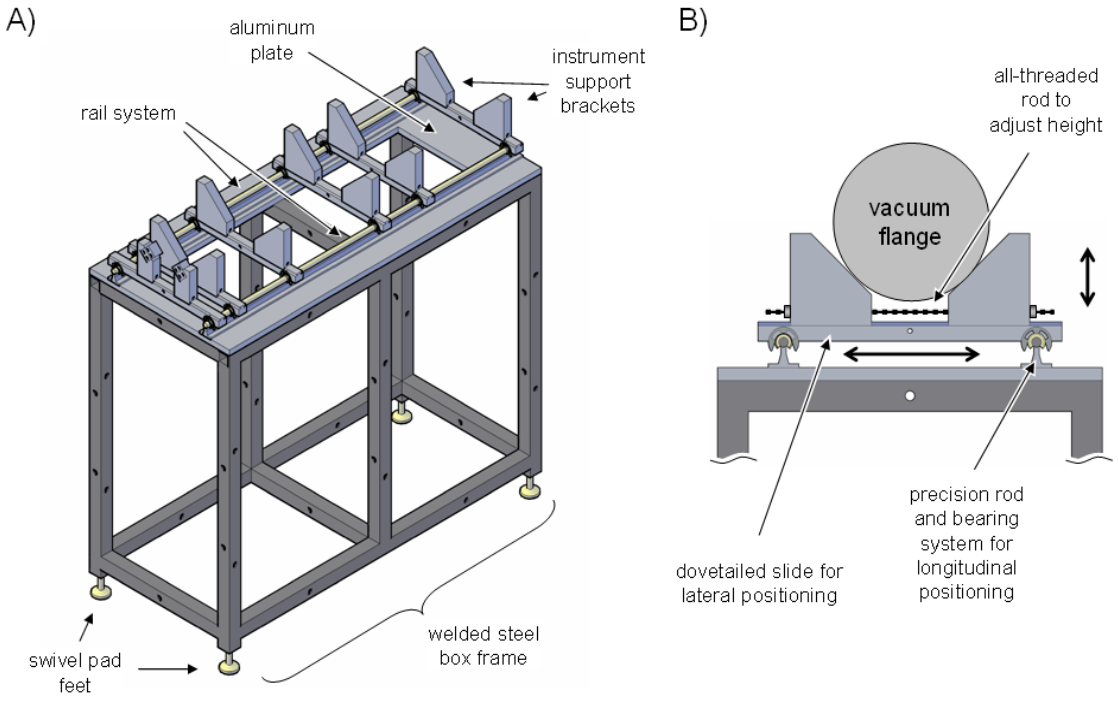

Figure 20 – The instrument support table and alignment hardware. The box frame is spaced to accommodate standard rack mountable modules. A set of custom brackets (not shown) is used to secure rack-mount hardware to the instrument table.

2-2.3 The Instrument Support Table and Alignment Brackets

A custom built support table and alignment system was developed for this project. The details of this system are contained in **Figure 20**. The instrument is mounted on a stainless steel welded box frame and measures approximately 216 cm long, 56 cm wide and 88 cm tall. Adjustable padded feet are used to dampen room vibrations to the instrument and add ~7 cm to the height of the table, bringing the instrument to a total height of ~118 cm from ground to instrument center axis. Supporting bars are spaced to accept the width of a standard full-sized rack mountable module. A set of rack mounting bars are fastened to the inside frame. L-brackets are

fastened in other locations and fitted with a 1 cm thick aluminum plate to provide shelving for non-rack mountable instrument hardware (*e.g.*, turbo pump controllers, temperature sensors, *etc*.). The box frame is topped with a 1.6 cm thick aluminum plate. A 25 cm wide opening is milled down the center length of the plates, allowing for the turbo pumps and other accessory vacuum hardware to drop into the frame. This opening is bracketed with a precision grounded rail system (case hardened 1556 steel shaft with support rail, McMaster-Carr, Aurora, OH). A series of cross width aluminum bars are fastened with split sleeve bearings (fixed alignment, 440C stainless steel, McMaster-Carr) and free glide along this rail system, providing longitudinal positioning of the instrument and components. Each cross support is dovetailed along the top to accept a pair of triangular support blocks which support and distribute the instrument load across the rail system (**Figure 20B**). A length of all-thread stainless steel is passed through the brackets and can be adjusted to lift or lower the vacuum system. Full XY and Z motion of the instrument can be achieved using a combination of the blocks supports and rails. The instrument components are designed in a modular fashion to facilitate maintenance on individual components—each component is made to slide out from the vacuum chamber along the rail system for user access. Individual components attach to a single flange for ease of removal. These specific components and their design are described in the following sections.

2-3 Sample Introduction, Ionization Source and Associated Ion Optics

Electron ionization (EI) was chosen as the ionization method for these studies. This ionization method is well-suited for generating ions from small mass analytes. EI is considered a "hard" ionization source, meaning that significant energy is used in the ionization process which leads to molecular dissociation (fragmentation). Oftentimes complete fragmentation of the primary analyte ion (the molecular ion) occurs. As EI is one of the oldest and still most widely used ionization methods for mass spectrometry, considerable work is represented in the literature for characterizing and understanding the ions which originate from electron processes. As such, there are over 15,000 reference mass spectra generated from EI which are freely available from the National Institute of Standards and Technology (NIST) online database and can be used to "benchmark" the data obtained on the instrument [346]. Additionally, EI is inherently a very "bright" ion source, generating a large and stable flux of ions which allows for a more straightforward characterization of the instrumentation. A measurement of the ion current on an electrode ~30 cm downstream from the EI source indicates an ion flux of over 600 billion ions per second! Refer to **Section 2-3.2** for more details of this measurement.

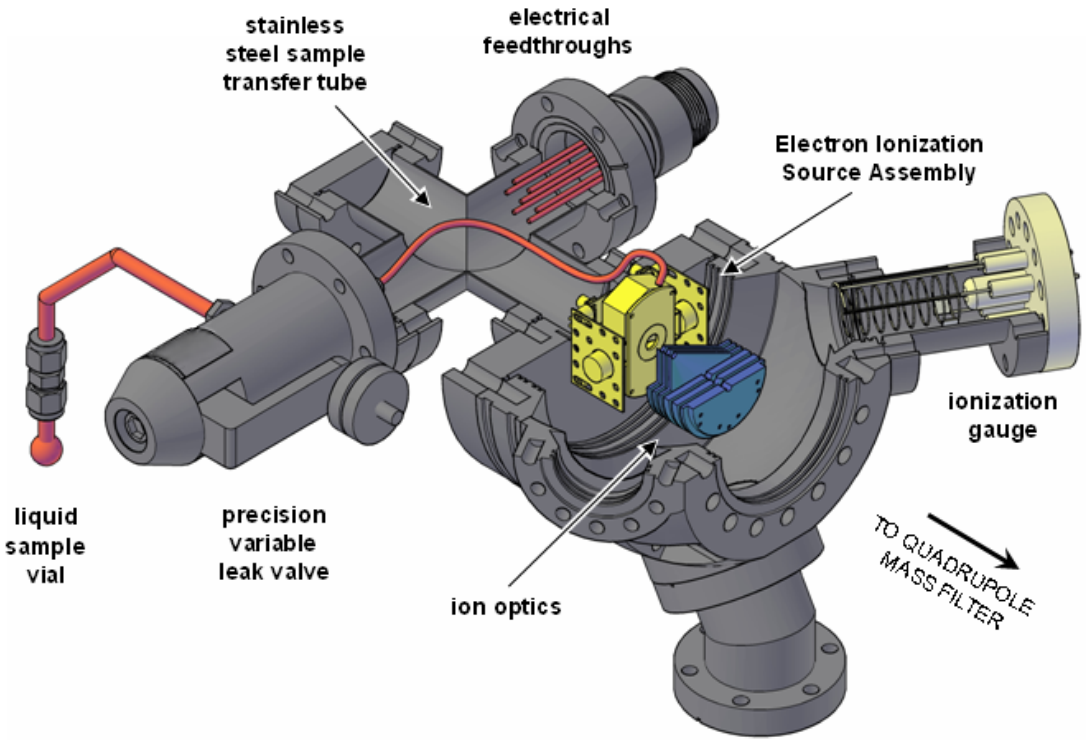

Figure 21 – Schematic of the sample introduction manifold and ionization source. Sample is introduced either as a liquid or gas through stainless steel tubing, shown in red to the left. For liquid samples, a reservoir vial is used (shown at left) which can be passively heated to assist volatilizing the sample. A sapphire seated precision leak valve facilitates a controlled leak of sample into the system. Gas phase sample is directly infused into the ionization region *via* stainless steel tubing. Ions formed in the source (highlighted in gold) are extracted through appropriately shaped ion optics, shown here in blue. Background source pressure is monitored with an ionization gauge.

2-3.1 The Sample Introduction Manifold

Figure 21 contains a CAD generated schematic of the sample introduction manifold, electron ionization source, and ion optical elements. Sample is introduced to the vacuum instrument through a stainless steel tube coupling. Gaseous samples are connected directly to the manifold after the manifold volume is evacuated to millitorr pressures in order to remove undesirable background gases. A 5 L/sec oil seated direct drive pump (Alcatel 2012A, Alcatel Vacuum Products, Hingham, MA) is used for

evacuating the sample manifold line and is fitted with a foreline oil trap to minimize oil backstream contamination of the manifold. Liquid samples are introduced into a vial reservoir either through direct pipetting or injecting through an injection port inlet. The injection port is fabricated by replacing the o-ring of an Ultra-Torr® fitting with a septum and is useful for atmospheric sensitive samples. The resulting liquid or sublimation of sample in the vial evaporates into the headspace of the manifold and establishes a vapor pressure which can be directly sampled into the spectrometer. The quartz reservoir vial (Scientific Instrument Services, Ringoes, NJ) is attached to the manifold using a fluoroelastomer (Viton®, DuPont Performance Elastomers L.L.C., Wilmington, DE) compression o-ring coupling (1/4" Ultra-Torr® fitting, Swagelok Co., Solon, OH). All other manifold junctions are made using compressed metal-to metal-junctions (Swagelok® tube fitting system, Swagelok Co.) which ensure a leak-tight joining of components. For low volatile liquids and some solids, the reservoir and tubing which comprise the headspace volume can be heated to a controlled temperature up to ~425 K to maintain a continuous and stable pressure of sample in the manifold. Volatile impurities which are dissolved in the liquid sample are removed through several freeze-pump-thaw cycles whereby the sample vial contents are frozen (either through liquid nitrogen or dry ice/acetone slurry immersion, depending on the freezing temperature of the analyte) and the headspace volume is evacuated to remove unfrozen gaseous impurities. During the sample thawing process, impurities will evaporate first and bubble out of the liquid sample once it thaws and can be removed from the headspace through additional freeze-pump-thaw cycles. This process effectively removes those

gases which possess a lower freezing point than the sample—for organic samples this is inclusive of nearly all atmospheric gases (refer to **Table 4** for phase change temperatures of some common atmospheric gases alongside several hydrocarbon species). After impurities are removed and a sufficient pressure of the gas phase sample is built up in the manifold, controlled amounts of the sample are leaked directly into the ionization region through a precision variable leak valve (MDC Vacuum Products, Hayward, CA). The variable leak valve utilizes an optically flat sapphire pressed against a copper seat to form an adjustable seal that can deliver stable leaks into the vacuum chamber as low as $1x10^{-10}$ torr-liter/sec. As a result, the amount of sample introduced into the ionization region can be precisely controlled and monitored through an ionization gauge placed within the source chamber, as shown in **Figure 21**, to the right. Additional valves (chemical/temperature resistant polychlorotrifluoroethylene seated, Nupro® bellows valves, Swagelok, Co.) are used to isolate the headspace manifold from the sample and vacuum pump line and can be toggled to initiate analyte sampling or evacuation. All materials of the source manifold assembly are bakeable and compatible with ultrahigh vacuum. The manifold line is wrapped with resistively heated tape (468 watt heavy fiberglass braided, HTS/Amptek®, Co., Stafford, TX) with voltage controlled through a variable AC (Variac) transformer unit (3PN1010, Staco Energy Products, Dayton, OH). Temperatures are monitored at several locations with thermocouple sensors (K-type, Omega Engineering, Inc.). The ultimate bakeout temperature of the sample manifold is ~425 K which is limited by the temperature tolerances of the fluoroelastomer seal used in liquid sampling. Higher temperatures can be achieved by using silicone or

perfluoroelastomer (Kalrez® ~525 K max) o-rings, by cooling the seal fitting (*e.g.,* water circulation or air circulation over an appropriate heat sink), or replacing the elastomer seals with metal junction components (*e.g.*, copper stems and ferrules), however an overnight bakeout of the source and sample manifold at ~375 K under vacuum is sufficient to remove any residual sample that may be left in the source assembly following routine operation, therefore these higher temperatures are not necessary.

2-3.2 The Electron Ionization Source

The ionization source used in this work was modified from a closed volume Nier-type electron ionization source (AEI MS9/50, Kratos Analytical, Manchester, England) shown conceptually in **Figure 22A**. The original configuration of the source was designed for generating a thin sheet of ions compatible with high resolution magnetic sector mass spectrometry. This performance was accomplished by shaping the electron beam into a thin sheet and limiting the ionization region to a very thin (~3 mm) space, which improves the spatial resolution at a cost of reduced ion yields. Ion formation across a spatially thin volume also improves the accuracy of ion energy measurements as ions are created in a well defined potential region. In this source configuration, the resulting ions were extracted through a narrow (~1 mm) slit which further defined the ion beam for high resolution sector analysis, but resulting in significant ion losses at the source (the slit area transparent to ions constituted less than 1/3 of the estimated ionization area in the source). Because high spatial resolution of ion formation is not necessary for the beam experiments conducted with the MS-IMS-MS

instrument configuration, the EI source underwent several modifications in order to increase ion formation yields and the efficiency of ion extraction from the source.

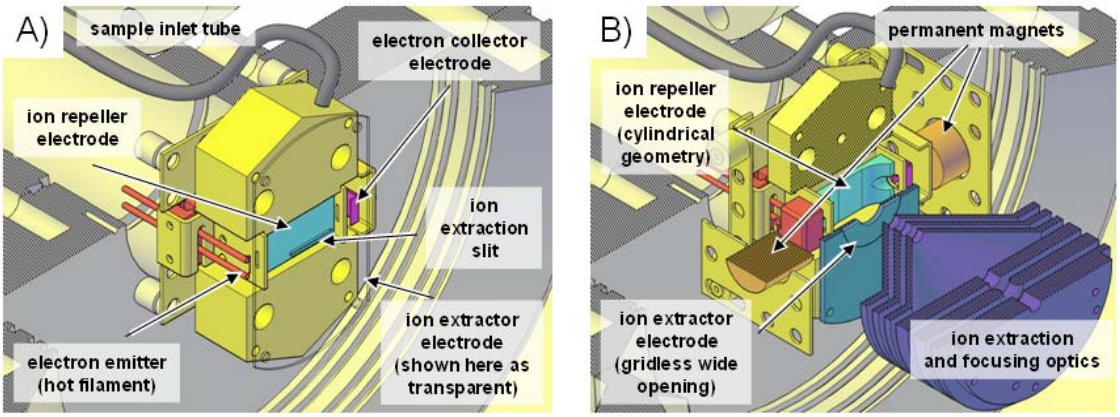

Figure 22 – Details of the electron ionization source assembly. **A)** The original configuration of the MS9 source used a planar repeller electrode (cyan) and slits for defining the electron beam as a thin sheet. The ion extractor electrode (shown transparent) also defined the ion beam as a thin sheet orthogonal to the electron beam to facilitate high resolution sector instrumentation. Neutral sample is delivered directly to the ionization volume from a metal tube, at top. **B)** The modifications made to the EI source to improve ionization yields for the studies outlined in this dissertation. Permanent magnets (orange) were added to help define the electron beam and increase the electron-neutral interaction cross-section. The flat repeller was replaced with a cylindrical geometry (cyan) to draw ions from the source volume. The ion extractor electrode slit was bored out to a large diameter (~6 mm) (dark cyan) to further increase ion extraction efficiencies. Electron slits were bored out to larger diameter (3.2 mm) holes and a filament with a wider emission area (ribbon) was added (behind red shield, not visible). Conical ion optical elements (dark magenta) create a stronger extraction field than the conventionally used plate electrodes and facilitate more efficient ion recovery from the source.

Details of the source modifications used in this work are depicted in the CAD schematic in **Figure 22B**. The EI source modifications can be classified into two major categories: i) modifications made to improve *ion formation yields* and ii) modifications made to increase *ion extraction yields*. For improving the *ion formation yields*, the electron beam volume was increased by boring out the electron beam shaping slits into larger holes of 3.2 mm diameter. The ionization volume was also increased accordingly by spacing the repeller and extractor electrodes further apart from ~3 mm to ~6.4 mm.

The repeller and extractor elements are spaced such that their electrode surfaces are equidistant from the center line of the electron beam, optimizing the volume occupied by both the electron beam and subsequent ions formed. The thin wire tungsten filament (0.5 mm diameter) used in the original EI source design was replaced with a thoriated[18] tungsten ribbon (1 mm wide x 0.025 mm thick, 1% thorium, Scientific Instrument Services, Ringoes, NJ) to increase the electron yields. Materials such as thorium and yttrium are often added to filament material (*e.g.,* tungsten, iridium or rhenium) to lower the material's work function and enhance their electron emission properties [347-349]. In operation, the thin wire filament requires between 3 and 4 amperes of current to glow white and thermionically emit electrons. In contrast, the ribbon filament requires an excess of 7 amperes for comparable electron emission due to the decreased filament resistance, which requires more current in order to generate sufficient heating of the filament to initiate thermionic emission of electrons. An additional step to increase electron emission is to create a "kink" at the center of the filament material such that the localized heating in that region increases and subsequently boils off more electrons. This can be accomplished by depressing a shallow channel into a soft metal such as copper and indenting the bend into the filament by sandwiching it between this metal channel and a thin, blunt tool such as a jeweler's screwdriver with the sharp corners buffed down. This procedure was used in a few of the studies conducted, however the

[18] Recent concerns regarding the radioactivity and toxicity of thorium has limited the availability of purchasing off the shelf thoriated filament materials. Zirconiated and yttria filament materials are becoming more readily available and are suitable alternatives to thorium. In addition to improving the electron emission properties of hot cathode materials, these additives improve the robustness and subsequently the lifetime of the filament under constant heating and cooling stress from routine operation.

shorter lifetime of the "kinked" filaments does not make them suitable for the long term, and eventually a straight filament was settled upon in routine experiments. Finally, two permanent alnico magnets salvaged from a separate EI source (VG-70S, VG Analytical Instruments, Manchester, UK) were mounted, poles aligned, on the outside of the electron filament and electron collector, creating a magnetic field parallel to the electron beam. The magnets help to collimate the electron beam as well as direct their motion into a cyclotron path which increases the electron-neutral interaction cross-section [350]. The remaining modifications to the EI source were aimed at improving *ion extraction yields* from the ionization volume. First, the planar geometry ion repeller electrode was replaced with a cylindrically shaped repeller designed to direct ions to the center opening of the extraction electrode. This strategy was utilized by Park and Ahn in a similar EI source design in order to enhance the number of ions pulled from the source and is reproduced in nearly the same manner in this work [351]. Ion trajectory simulations were conducted to compare the performance of the EI source between a planar repeller geometry with no penetrating extraction fields (gridded extraction electrode, **Figure 23A**) and a geometry utilizing a cylindrical repeller and extraction fields which penetrate from a conical ion lens assembly into the source (**Figure 23B**). Simulation results predict a net gain in ion transmission for using the modified source geometry, at a cost of decreased energy and spatial resolution for ion formation, which are parameters that do not influence the performance of this particular instrument configuration. In previous experiments using the original unmodified EI source configuration, the ion current measured by an electrometer (610C Analog Solid State Electrometer, Keithley

Instruments, Cleveland, OH) on an electrode element several inches downstream the source was in the sub-nanoampere range. Following the modifications described here, the measured ion current on the electrode is routinely in excess of 100 nanoamperes[19] under similar conditions, which constitutes a net gain of over two orders of magnitude for ion generation and recovery with this new source. The potential difference between the filament and the average potential at the center of the ionization source (determined as the average potential between the source housing, repeller and extractor elements) defines the ionization energy of the EI source, which for most experiments was maintained between 35 and 70 eV. The repeller electrode voltage defines the upper potential of the ion beam, which was around 110 V. A thin wire platinum resistive temperature device (RTD, PT-100 ceramic encased, Omega Engineering, Inc., Stamford, CT) was inserted into the main EI block assembly to monitor the temperature of the block, which gives a very good indication of both the sample volatility and thermionic emission characteristics of the filament source. Inherent to all electron ionization sources is the need to "warm up" the filament and block assembly before optimum and stable emissions are observed. Finally, two ceramic heater rods were inserted into the EI block to help regulate block heating and facilitate volatility of low vapor pressure sample. The heater rods were fabricated by passing nichrome wire back and forth longitudinally within the channels of a 4-channel alumina rod. This back and forth

[19] 100 nA corresponds to approximately 600 billion ions striking the electrode per second (ion current divided by elementary charge). At these ion fluxes, the sources supplying the DC to the ion optical electrodes must be able to regulate (source) this many ions striking the electrode surface. These high ion yields are necessary in the experiments described here, as very few ions enter and make it through the drift cell (less than 5 ions per second are recorded exiting the drift cell under ideal experimental conditions).

design also helps cancel out magnetic fields created by the high current flow in the wire, which might otherwise distort ion and electron trajectories.

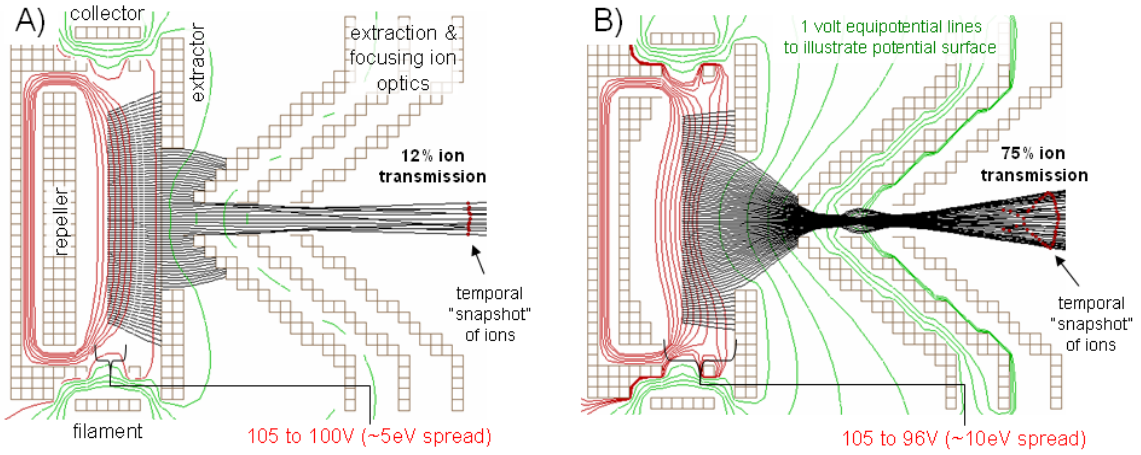

Figure 23 – Ion trajectory simulations of the electron ionization source and associated ion optics. **A)** Source geometry using the planar repeller and gridded extraction electrode. Ions are formed in a narrow distribution of energies (5 eV, shown with red equipotential lines) and temporal positions, shown with red dots representing each ion's position at the same time interval. While space and energy resolutions are quite high for this source configuration, ion transmission remains low, with an estimated 12% of the ions formed across a range of electron beam positions being transmitted into an ion beam. **B)** Source geometry with the modified cylindrical repeller and gridless extraction element, allowing the extraction field of the conical ion lens assembly to protrude into the ionization region (shown with green equipotential lines). Ion transmission is substantially increased (75%), but ions are less energetically and spatially defined, as indicated with the widespread position of ions (red dots) in the same time interval. Since high spatial and energy resolutions from the EI source does not affect instrument performance in the MS-IMS-MS configuration, these figures of merit can be sacrificed to improve the overall ion yields of the source.

2-3.3 Post Ionization Source Ion Optics

Post EI source ion optics consists of three stacked conical geometry electrodes and three plate electrodes all of 3.2 mm inner diameter which serves to collimate the ion beam into a tightly focused diameter for efficient transfer into the quadrupole assembly. Operational voltages vary from one experiment to the other, but approximately work in the same manner as two *einzel* lens arrays in which every three elements form a radially

focusing lens whereby ions do not gain energy as it traverses the array[20] [352,353]. This net zero gain in ion beam energy works by operating the first and last electrode of the three element array at the same potential while varying the middle element, such that ions enter and exit the array at the same potential, *i.e.*, the energy at object and image space is the same. Ion trajectory simulations illustrating the operational principle of a 3-element ion optical lens are contained in **Figure 24A**, while simulations of the two-stage lens system used in the post EI source assembly is contained in **Figure 24B**.

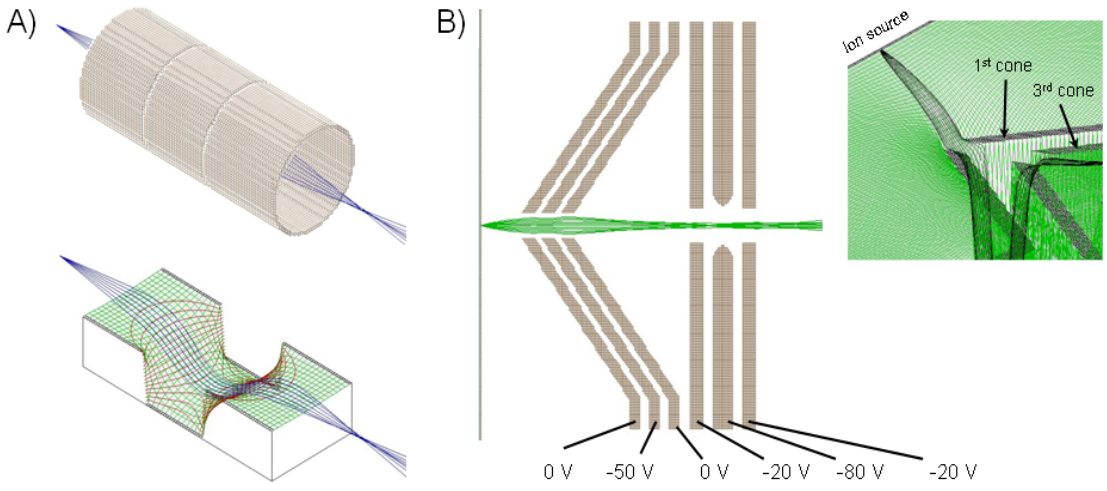

Figure 24 – Ion trajectory simulations of the source ion optics. **A)** The basic focusing concept of a 3-element *einzel* lens. A diverging ensemble of ions is forced to a convergence (focal) point as they pass through the lens array. At bottom, a potential energy diagram shows that ions enter and exit the array at the same energy. **B)** Simulations of the ion lens used with the EI source. Two sets of 3-element lenses gradually correct the position of a diverging ion ensemble into a collimated beam. The ion extraction potential well formed by the conical shape of the lens is contained in the inset to the right. The center electrode of the second set of 3-element lenses is hyperbolic to minimize the defocusing field effects (abberated beam trajectory) as ions traverse in close proximity to this electrode.

[20] The true *einzel* lens consists of three electrodes with the outer two at ground potential, such that the lens operates with a single potential adjustment. *Einzel* lenses were used extensively in electron optics, such as in cathode ray tubes. *Einzel* is German meaning "single" or "individual" and describes the single voltage operation of these lenses.

The potentials on all source ion optical elements are controlled with two 6-channel power supplies (Model 10096, Analytica of Branford, Branford, CT). Each channel was modified with a two-way switch to bypass the onboard, 10-turn potentiometer and relay the variable resistance value to a computer controlled card (16-bit PCI-6704, National Instruments, Austin, TX) to allow for remote operation of all voltages *via* the LabVIEW instrument control software package ("Laboratory Virtual Instrumentation Engineering Workbench", National Instruments, Austin, TX). A high current power supply (HY3005, Precision Mastech Enterprises, Co., Kowloon, China) provided the necessary current to heat the filament. Floatable inputs on the power supply allowed for an external negative voltage (relative to the EI source) to be superimposed on top of the filament circuit to provide a sufficient negative potential on top of the filament necessary to push electrons away from the filament surface and into the ionization region. Computer control of the EI source and ion optics voltages were accomplished using a custom written LabVIEW soft front panel interface, which integrates complete computer control of all voltages on the instrument. Control voltages from the LabVIEW interface are supplied through shielded, twisted-pair cables to maintain stability. All electrical connections were made to the instrument through hermetically sealed ceramic-metal junction electrical feedthroughs (4 and 7-pin power feedthroughs, Insulator Seal, Inc., Sarasota, FL) rated above the maximum voltages and currents used.

2-4 The Quadrupole Mass Filter and Associated Ion Optics

A transmission type, filtering quadrupole mass spectrometer was chosen for the forward stage of the instrument, as it was deemed important to be able to unambiguously characterize the mass-to-charge (m/z) value of ions which originate directly from the EI source. In particular, a quadrupole mass spectrometer offers the unparalleled ability to operate both as a broadband ion transmission device or a tunable bandpass m/z filter. Additionally, quadrupoles remain operational even at vacuum pressures as high as 10^{-4} torr [173], which is anticipated for ion mobility instrumentation, and actually increase in performance in the presence of some background of cooling ion-neutral collisions [354]. Quadrupoles commonly come in lengths between 10 to 20 cm, depending on rod geometry and application, which also makes them suitable as efficient ion transfer devices for transporting ions across variable pressure regimes where conventional electrostatic ion lenses operating at comparable electric fields would perform with significant ion losses due to collisional scatter losses [355,356]. Additionally, electrostatic ion optics have optimal focusing properties that are pressure dependant, while RF ion guide devices are relatively insensitive to pressure changes between 10^{-6} to 10^{-4} torr.

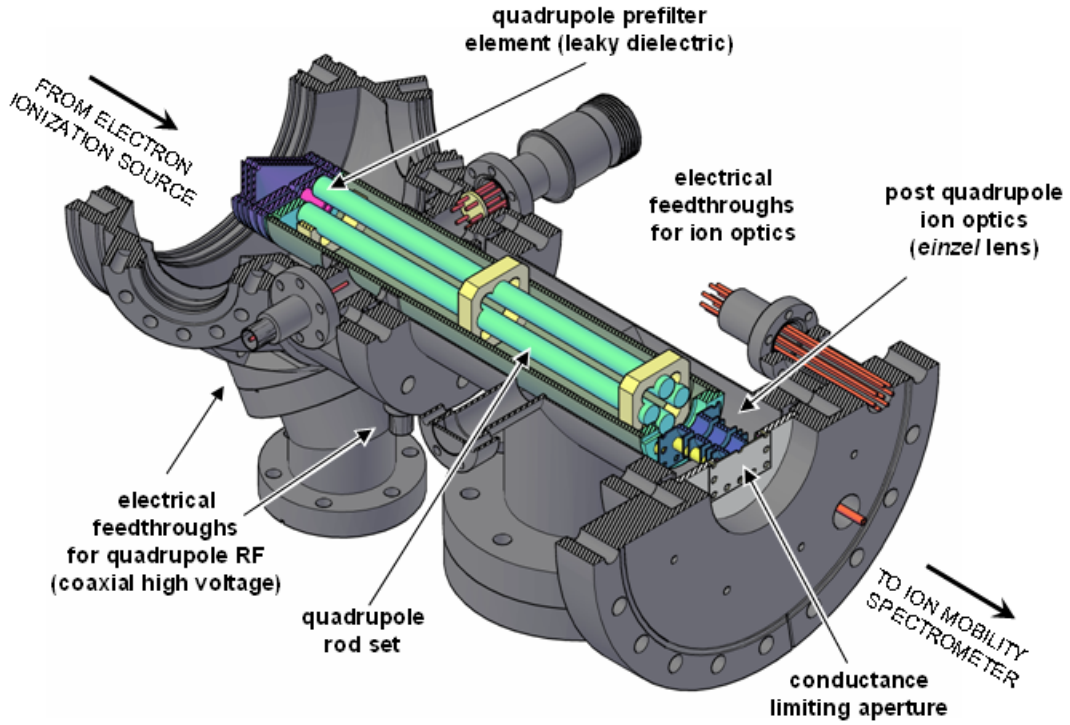

Figure 25 – Schematic of the quadrupole and ion optics. Ions extracted from the EI source are collimated into a narrow beam by the forward ion optics (dark magenta). The ion beam passes through a short (6.4 mm) prefilter barrel lens (magenta) which helps transition the ion beam into the RF field. Ions pass down the center of the quadrupole rod assembly (cyan), where most are transmitted (RF potentials only) or select m/z ions are chosen through a combination of fields (RF and DC potentials). As the ions exit the quadrupole, a series of ion optical elements (dark blue) recapture and collimate the ions back into an ion beam. A narrow conductance limiting aperture (6.4 mm, shown in light grey) helps maintain the pressure difference between the two spectrometer regions, as well as minimize source contamination of the drift cell. Pressure in the chamber is monitored by an ionization gauge placed directly above the rod assembly (not shown).

A CAD generated schematic of the quadrupole assembly, associated ion optics and vacuum chamber is contained in **Figure 25**. Ions extracted from the EI source are collimated into a narrow (<3.2 mm) ion beam through two sets of 3-element lenses, as described in **Section 2-3.3**. This narrow diameter focusing is important for matching the ion beam with the acceptance angle of the quadrupole, as a wide angle distribution of

injection will degrade the performance of the quadrupole mass filter [357]. After beam collimation, the ions are directed down the center of the four rods which comprise the quadrupole assembly.

2-4.1 The Quadrupole Assembly

A leaky dielectric lens is used as a prefilter for the quadrupole used in this work (refer to **Section 1-6.1**). The lens is a graphite coated ceramic barrel mounted onto the entrance lens aperture and inserted partially into the rod set. Trajectory simulations approximating the prefilter as a perfect conducting lens suggest that a barrel lens mounted in this manner helps shield the undesirable fringe fields and translate into higher ion transfer efficiencies (**Figure 26A** and **B**). Experimental observations with and without this dielectric lens show a slight (less than 10%) decrease in ion transmission when using the dielectric lens in broadband ion transmission mode (RF only) but significant improvements in ion transmission for mass selective (RF-DC) modes, sometimes orders of magnitude in ion counting, depending on ion m/z. The slight loss in ion transmission in broadband mode is possibly due to some amount of surface charging (pooling) of the graphite coating on the dielectric, but could also be attributed to a narrowing of the acceptance angle for the entrance to the quadrupole when using a barrel lens geometry as opposed to a thin aperture entrance plate. The dielectric lens and quadrupole rod assembly were recovered from a commercial instrument (ELQ-400 triple stage quadrupole, Extrel, Co., Pittsburgh, PA) and mounted onto a custom flange and electrical feedthrough network. The quadrupole consists of

four precision ground stainless steel rods (9.5 mm diameter) aligned with ceramic yokes press fitted within a vented stainless steel tube housing, which gives a total length of the assembly at 200 mm with an inscribed diameter on the rod set (distance between opposite rods) of 8.3 mm. An RF/DC power supply (150-QC, Extrel) capable of ±800 V DC and ~7,200 V_{p-p} RF is used to drive the quadrupole. This supply utilizes a harmonic crystal to achieve the precise RF frequency required for high stability. Oscillator modules which resonate at 880 kHz (<4,000 amu), 1.2 MHz (<2,000 amu) and 2.1 MHz (<500 amu) are interchangeable and can be used to adjust the optimal mass range for experiments. The higher frequency oscillator achieves more RF cycles for ions of the same transit time and thus can achieve higher resolution and sensitivity than their lower frequency counterparts, but the greater number of RF cycles cannot handle high mass ions as efficiently. Unless otherwise noted, the 2.1 MHz oscillator is used for all experiments conducted with the quadrupole. The RF/DC power supply is controlled through a series of digital inputs (±5 V and TTL). Parameters such as the RF, DC, and pole bias voltages and scan line offsets (slope and intercept) are driven through a custom LabVIEW soft front panel. The quadrupole is operated in a static settings mode and parameters are manually adjusted to transmit fixed m/z ranges. Most experiments utilize the quadrupole in a broadband ion transmission (RF only) mode, since RF/DC mass resolving experiments can reduce total ion signals at least to about 80%, while for high mass ions (>1,000 amu) observed ion signal in RF/DC mode can be degraded to less than 1% of what is observed in a purely RF only operational mode [358]. To improve the mass filtering performance of the quadrupole, it is desirable to perform the

quadrupole analysis on ions possessing a low (10-20 eV) kinetic energy such that they experience a suitable number of RF cycles. Low ion energies can be achieved experimentally by biasing the rod assembly such that the potential defining the ion injection energy (as defined by the EI repeller potential minus the entrance lens potential) and quadrupole remains low [359]. In the experiments described here, the ion energy is tuned to ~20 eV when conducting the mass selective experiments using the quadrupole.

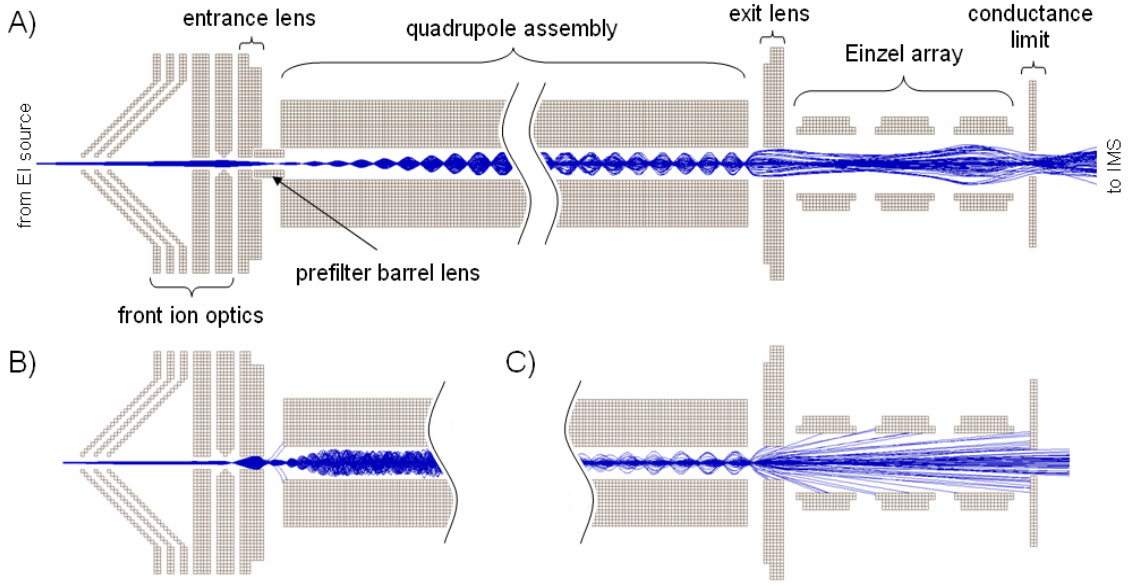

Figure 26 – Ion trajectory simulations of the quadrupole and ion optics. **A)** With a barrel lens prefilter and properly selected potentials, ions effectively transit into, through and out of the quadrupole device. The barrel lens brings ions into the stable region of the RF field. **B)** Without a barrel lens placed at the entrance of the quadrupole there is significant perturbation of ion trajectories resulting from the RF fringing field. **C)** Ions exiting the quadrupole are ejected at a wide distribution of angles relative to the beam axis, which is dependant on the RF phase in which the ions leave the device. Without focusing and collimating fields, these ions are lost from the ion beam. Trajectory simulations were conducted with SIMION 8.0 using a modified dynamic fields user program (quad.prg).

2-4.2 Post Quadrupole Ion Optics

No special filtering strategy is utilized the back end of the quadrupole. Instead, a wide (8.3 mm) exit aperture is utilized in combination with a large inner diameter (9.5 mm) *einzel* lens array to recapture ions exiting the quadrupole device. Trajectory simulations suggest this approach is efficient enough to recapture nearly all of the ions which exit the quadrupole (**Figure 26C**). Since the fringe field at the end regions of any quadrupole can be characterized as an ion rejection field, ions depart the quadrupole much more readily than they approach it, which can be used advantageously to recollect ions which exit the field of an RF device. The *einzel* lens effectively captures and point focuses ions through a conductance limiting aperture (6.4 mm) which helps define the pressure differential between the quadrupole and ion mobility chambers. Voltages are supplied by a 6-channel power supply (Analytica of Branford, Branford, CT) interfaced to LabVIEW control.

2-5 The Cryogenic Drift Cell, Drift Gas Manifold, Ion Gate and Associated Ion Optics

The primary component of this instrument is the cryogenic ion mobility spectrometer, which consists of the drift gas manifold, drift cell, cryogenic dewar, ion gate, ion optics and vacuum housing. A cutaway CAD schematic of the cryogenic ion mobility spectrometer and all associated hardware is contained in **Figure 27**.

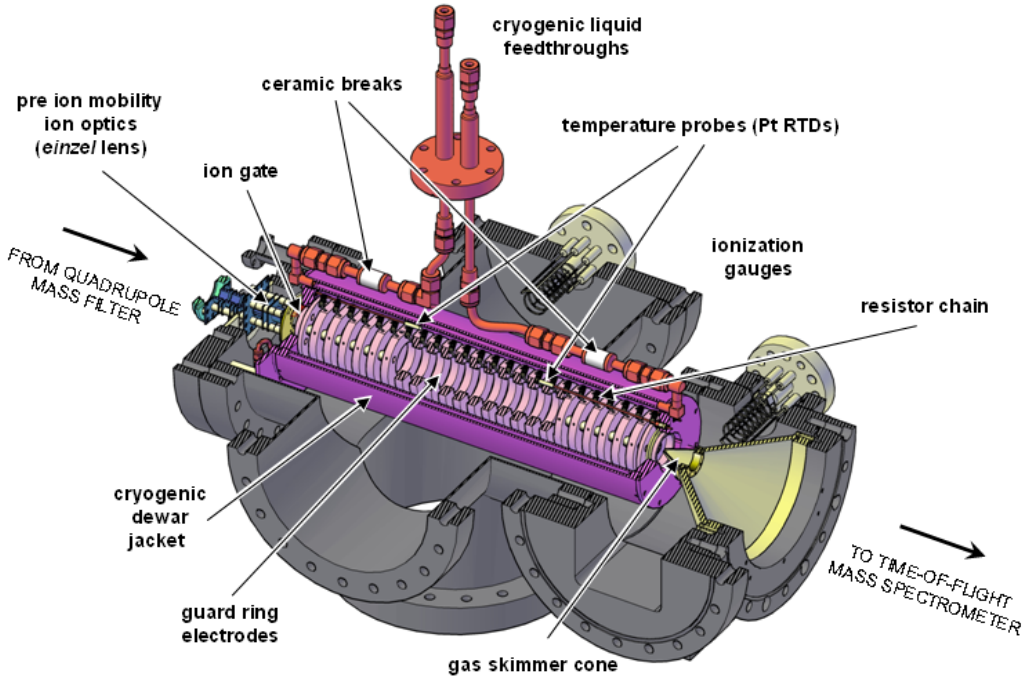

Figure 27 – Schematic of the cryogenic drift tube spectrometer. Ions collected from the quadrupole are collimated by two stages of focusing, separated by a conductance limiting aperture. The second lens stage simultaneously focuses, steers and truncates the ion beam into discrete packets which are directed through a 600 μm aperture at the entrance of the drift cell. The drift cell consists of a stacked ring network encased in a stainless steel dewar jacket. Liquid nitrogen is introduced into the jacket to facilitate cooling of the drift gas. Temperature is measured by two RTD probes. Ions pass through the drift region where they are separated by their ion mobilities and some exit the other end through a 800 μm aperture. A skimmer cone refocuses ions while directing away stray buffer gas. Ions then continue through additional ion optics (not shown) to a mass spectrometer for mass analysis. Pressure in the drift cell and interface regions are monitored by ionization gauges.

2-5.1 Ion Mobility Entrance Ion Optics and Beam Steering Element

The ion optics between the quadrupole and the ion mobility spectrometer are custom fabricated from stainless steel and mounted onto a commercially available charged optics assembly system (eV Parts® component system, Kimball Physics, Inc., Wilton, NH). Ions which are collected from the exit of the quadrupole and passed through a conductance limiting aperture are further collimated by a second 3-element

lens stage, shown with more detail in **Figure 28A** and **B**. This second 3-element lens system differs from the post quadrupole lens array in several ways. The second 3-element lens system is in a region of higher (~10^{-5} torr) pressure, and so electrodes are fabricated with a high gas conductance design to help facilitate efficient evacuation of gases which may otherwise interfere with the ion beam. This "multipole" design (labeled "high conductance ion optics" in **Figure 28A**), helps create an effective ion focusing potential at their center axis while remaining relatively transparent to gas molecules to allow efficient pumping in this region. Both sets of 3-element lenses (post quadrupole and pre ion mobility) effectively collimate, focus and decelerate the ions to condition them for injection into the gas filled drift region, as can be seen by the ion trajectory simulations in **Figure 29A**. This lens system is similar in scope to a multi-element lens described by Schlunegger *et al*. for decelerating a high energy ion beam (from 3 keV to 30 eV) for introduction into a quadrupole mass analyzer [360]. Both Schlunegger's lens and the one described here are analogous in operation to a Heddle configuration lens in which the exit focal point of the first lens array coincides with the entry focal point of the second [361]. In this particular case, the focal point of the first lens also coincides with the conductance limiting aperture, as shown in **Figure 29A**.

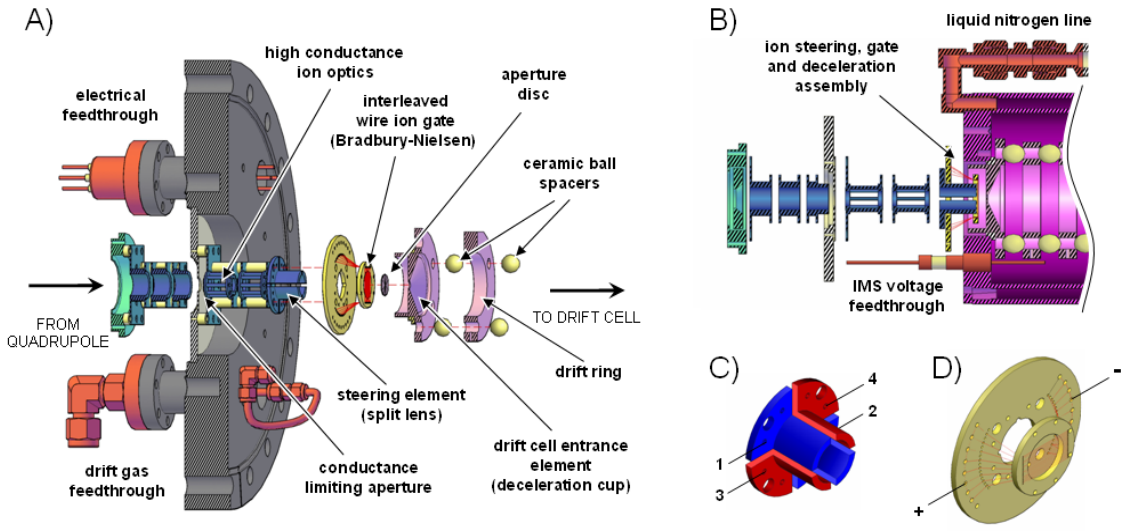

Figure 28 – Details of the ion optics at the entrance to the IMS. **A)** A cutaway schematic of the lens system from the quadrupole exit to the drift cell. The ion gate, aperture, and front ion mobility electrodes are offset for clarity. **B)** Side view of the front ion optics, showing the correct placement of the steering element, ion gate, and front "cup" lens of the ion mobility entrance electrode. **C)** Details of the steering optic, which is a barrel lens divided into quadrants. Opposite elements form one set of steering electrodes (1-2 and 3-4). **D)** Details of the ion gate, showing the PEEK support assembly and wire network. The wires break out into two circuits, labeled + and – in the schematic.

Because the ion optics are mounted on a separate mounting system as the drift cell, alignment between the ion optics and this pinhole aperture is not exact, requiring that the ion beam be repositioned with appropriate ion optical elements in order to ensure ion transmission into the drift cell. The last element in the second 3-element ion lens array is an ion beam steering lens, which consists of a barrel lens truncated into four sections (**Figure 28C**). Each of the four segments of this lens element can be independently biased to a voltage to fine tune the position of the ion beam. Fine voltage adjustment is achieved with a floatable 2 channel DC power supply (6234A, Hewlett-Packard, Co., Palo Alto, CA) whereby each channel is split into two additional channels controlled with a variable resistor to shim the potential on each output. What results are

four total outputs, variable by ±20 V from the main floating bias, which gives all "potential" possibilities for positioning of the ion beam.

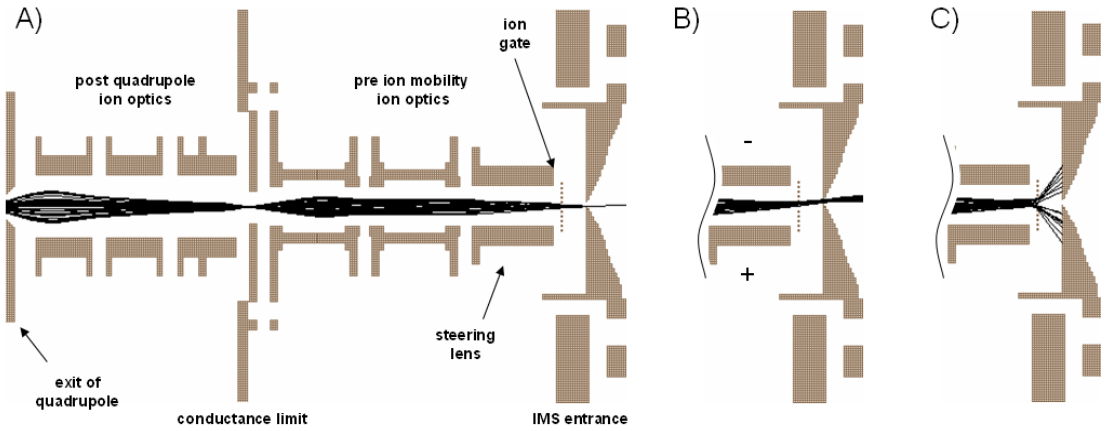

Figure 29 – Ion trajectory simulations of the ion optics between the quadrupole and ion mobility spectrometer. **A)** Ion optics collimate and focus ions from the quadrupole through a conductance limit into a second stage of optics, where the ion beam is point focused onto the entrance aperture of the drift region. The optics are purposely misaligned in these simulations by ~2 mm with respect to the entrance aperture, which results in significant ion losses at the drift cell entrance. **B)** The potentials on the truncated steering lens can be adjusted to properly correct the position of the ion beam, resulting in all ions passing into the drift region. **C)** The ion gate can be pulsed to selectively reject ions from entering the drift region. The cup shaped electrode comprising the front of the drift cell effectively decelerates the ion beam by about 90% of its initial kinetic energy, such that ion injection occurs at ~15 eV or less.

2-5.2 The Interleaved Wire Ion Gate

The ion beam is truncated into narrow ion pulses through the use of an interleaved wire ion gate (Bradbury-Nielsen type, **Figure 28D**). The ion gate is built up with two discs of polyetheretherketone (PEEK, Boedeker Plastics, Inc., Shiner, TX), which is an excellent temperature stable thermoplastic possessing high dielectric and tensile strengths and very low outgassing properties [362,363]. A larger disc is drilled with an array of tapped holes (0-80 UNF) to anchor the tension on each wire, while spreading the array for ease of assembly the ion gate circuit. The larger disc also serves

as the support substrate for the truncated steering lens (**Figure 28C**). A smaller PEEK disc is drilled with two rows of closely spaced holes (0.34 mm diameter, 0.5 mm spacing) straddling a larger inner diameter for the center beam axis. High density wire spacing is achieved by staggering the hole pattern on each of the two rows. The wires are spaced ~0.5 mm apart in the array, with every other wire connected to a common circuit, creating a two circuit design. Thin tungsten wire (0.01 mm diameter, Lamp Metals, Ltd, Wembley, Middlesex, UK) is used for the ion gate as tungsten possesses excellent conductor properties and a high modulus of elasticity (400 GPa) which is advantageous for use in high tension applications where voltages are applied. The dielectric support disc substrates are mounted such that they are shielded from the ion beam by the steering ion optic. This is particularly important when dielectrics are used in low energy ion beam applications where surface charging effects would perturb the ion beam's intended trajectory [364]. The ion gate circuit is controlled with a bipolar, high voltage pulser (Dual HV Pulser, Ionwerks, Inc., Houston, TX) with independent magnitude control of each channel. Pulse widths are scaled with the input trigger width supplied by a computer controlled card which is driven with a custom LabVIEW soft front panel as described previously. Trajectory simulations suggest efficient blocking of the ion beam with this ion gate operated at a wire-to-wire potential difference of ~10 V (**Figure 29C**). In practice, a voltage of ~50 V is necessary to prevent ion leakage into the drift region. This required higher bias is presumably due to the elevated pressures present under experimental conditions which collisionally cool ions and dampen the

effect of the ion gate. A similar decrease in efficiency for electrostatic grids operated at elevated pressures has also been suggested by recent computational studies [132].

2-5.3 The Drift Cell Entrance Electrode and Considerations for Ion Injection

The entrance to the ion mobility cell can be considered an extension of the ion optical system described above. Its purpose in the setup described here is to define the final potential of the ion beam before the beam's translational energy is quenched through ion-neutral collisions in the drift region. The total injection energy of the beam into the ion mobility is defined as the difference between the EI source repeller potential (the top of the potential hill) and that of the entrance electrode into the mobility drift cell. In order to prevent ion activation resulting from high energy ion-neutral collisions, the ion injection energy must be kept low. Jarrold investigated the rate of association between silicon cluster ions and a small percentage of ethylene admitted into a drift cell and found no contribution to the ion injection energy under ~20 eV [365]. Kemper and Bowers also investigated the injection energies in a hybrid MS-IMS-MS configuration, particular with regards to drift cell penetration of ions before thermalization. In their work, the drift times of a pulse of ions were measured as a function of injection energy for a small length (4 cm) drift cell. It was concluded that injection energies of <5 eV were needed to ensure insignificant ion penetration into their particular drift region [366]. For the longer drift region used in this work (30 cm), a higher injection energy could be tolerated with regards to perturbing drift time measurements. In our own laboratory, we have investigated the extent of reaction for charge transfer chemistry

between various ions with water present in the drift cell and concluded there was no net increase in the abundance of water ion products (H_2O^+ and H_3O^+) for injection energies below ~20 eV. At injection energies above 20 eV, the product ion abundance of H_2O^+ began to increase, suggesting activating collisions were taking place at the source. For all experiments described in this work, injection energies of <20 eV were utilized to observe adequate ion signal while minimize collisional activation effects. The potential on the entrance of the drift cell is operated at ~100 V, creating a deceleration field which drops the ion beam kinetic energy to less than 15 eV. In this deceleration region, the presence of dielectric materials is minimized to help alleviate issues related to surface charge potentials perturbing the low energy ion beam. The "cup" shape of the entrance lens is important for shielding the ion beam from fringing fields and for creating an effective deceleration potential that directs the ion beam axially into the drift region. Shielding is particularly important for protecting the ion beam when its translational energy is low.

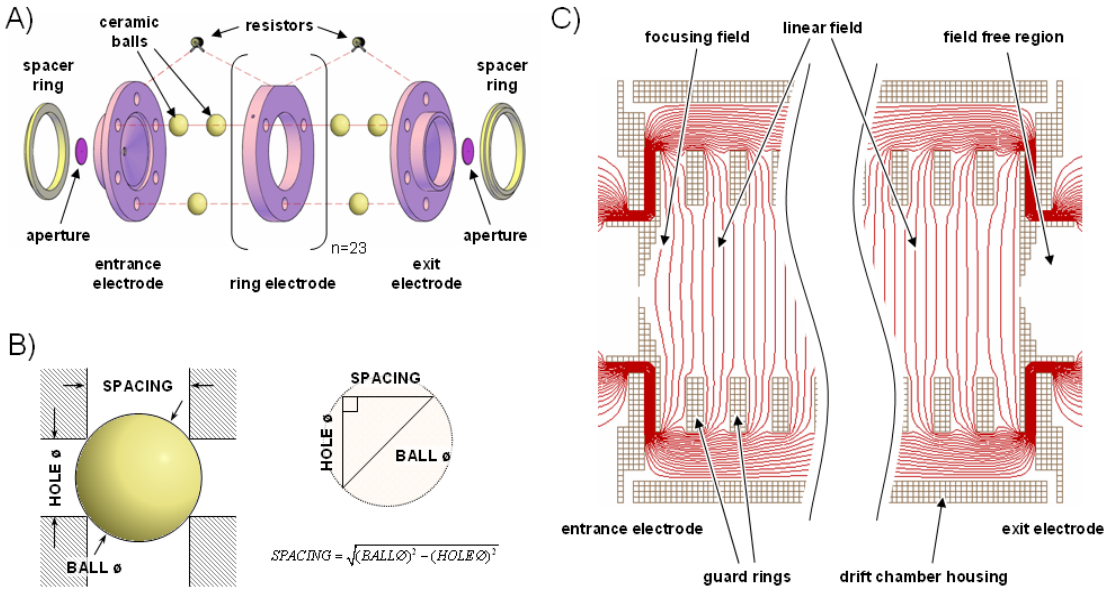

Figure 30 – **A)** Assembly details of the stacked ring drift cell design. The isolation spacer, aperture disk, front, back and center drift electrodes are shown. **B)** Method for determining the spacing between electrodes using the sphere spacer design. **C)** Equipotential lines (10 V) at the entrance and exit of the drift cell, showing the shielding effect of the cup design as well as the nature of the potentials at the center of the drift region and in proximity to the endcap electrodes.

2-5.4 The Drift Cell Electrode Assembly

The ion optical components of the cryogenic drift cell is built up using a stacked ring system of electrodes aligned and spaced with bearing grade ceramic balls (~8 mm diameter, grade 25 high alumina nonporous ceramic, McMaster-Carr, Aurora, OH). A kinematically stable design is ensured by using 3 uniformly spaced balls between every two lens element compressed with uniform force across each element. The ceramic balls are captured between every ring electrode (28.6 mm inner diameter, 6.4 mm thick) through two precision bored holes (~4.8 mm diameter, vented), ensuring an exact spacing from one electrode to another (**Figure 30A** & **B**) [102]. Two electrodes placed at either end of the stacked ring assembly support the conductance limiting apertures and

are designed with appropriate geometries to shield fringing fields present at the entrance and exit of the drift cell (**Figure 30C**). The pinhole apertures placed at either end of the drift cell are commercially available laser drilled discs (stainless steel, Small Parts, Inc., Miramar, FL) which can be interchanged to achieve the appropriate balance between pressure and ion transmission. An aperture diameter of 600 μm is used at the entrance to the drift region, while a slightly larger, 800 μm aperture is used at the exit where diffusion radially broadens the ion packets. The apertures are epoxied (H2OE Epo-Tek® Conductive Silver Epoxy, Ted Pella, Inc., Redding, CA) into an equivalent thickness (0.5 mm) machined groove on the end electrodes to minimize distortions in the field lines which contribute to ion losses. Aperture discs are thin to ensure minimal ion losses during transfer. The electrode surfaces behind the apertured diverge away from the beam axis to help create a radially focusing field and allow ions room for radial expansion as they traverse the tight focus of the apertures (**Figure 30C**). In this configuration, ions are focused through the first aperture into the drift region, traverse the drift region through the force of a weak electric field established by the guard rings, partition into populations governed by their ionic mobilities, and a fraction of these ions exit the second aperture on the other end of the drift region where they go on for further mass analysis and detection.

2-5.5 The Drift Cell Cryogenic Jacket

The drift region is enclosed in a cryogenic jacket. The jacket is formed in the annular region of two concentric tubes, welded together at either end with appropriate

ring flanges. Two endcap pieces enclose the drift region and apply the compression necessary for keeping the guard ring assembly assembled. A thin ring of temperature stable polyimide (Vespel® SP-1, DuPont, Wilmington, DE) is compressed between the dewar assembly and the end electrodes to shim the length and ensure electrical isolation between the drift ring electrodes and the dewar. Vacuum seals are achieved through compression of silver wire alloy (Safety-Silv® 35 brazing alloy, J. W. Harries, Mason, OH) between rigid right angle joints. All materials which comprise the cryogenic dewar are stainless steel welded together using same alloy, tungsten inert gas (heliarc) joining which uses an inert shielding gas to prevent atmospheric gas contamination of the weld. While stainless steel is a poor heat conductor, its rigidity and shape retention at cryogenic temperatures is superior to that of other, more conductive alloys (*e.g.*, copper and brass), making stainless steel a preferred choice for uses where compressive forces are present and temperature variation can otherwise weaken the assembly. Additionally, the poor heat conductive properties of stainless steel are used advantageously in these experiments to maintain a stable temperature during data acquisition. Because ion mobility is inherently a statistical counting experiment, a greater number of counts will facilitate more accurate statistics and increased signal-to-noise, however the time allotted for experimental counting is ultimately governed by the stability of experimental conditions which will affect the results, such as temperature in this case. Two stainless steel fittings (right angle Micro-Fit® weld fittings, Swagelok Co.) are welded directly onto both end rings of the dewar at the top to allow cryogens (liquid nitrogen) into the jacket region and relieve boiloff pressure. The level of liquid nitrogen admitted into the

dewar determines the temperature of the drift gas inside with the liquid level being controllable by the flow from the main reservoir dewar (160 liters, LS-160, Union Carbide, Co., Houston, TX). When completely filled with liquid nitrogen, the temperature of the drift gas is ~80K. Temperature is monitored by two redundant platinum resistive temperature detectors (RTD, PT-100 ceramic encased, Omega Engineering, Inc., Stamford, CT) which are suspended directly in the drift gas at approximately 1/3 the total length of the drift region from front and from back. Resistive temperature measurements have the widest range of any other temperature measurement method and are more accurate than more commonly used thermocouple devices [367]. The two redundant RTD's track within 1 degree of one another during rapid cooldown cycles (ΔT of >5 degrees/minute) when using helium, nitrogen or argon bath gases, indicating that thermal equilibrium in the drift region is quickly established from drift gas collisions with the chamber walls. The entire dewar assembly is mounted onto the vacuum flange using ceramic standoffs (glazed steatite) and all gas/liquid feedthroughs (drift gas and cryogens) are isolated *via* ceramic breaks, facilitating electrical and thermal isolation of the dewar jacket. Mounting the dewar jacking within a vacuum chamber eliminates problems associated with ice buildup and in this vacuum-enclosed design the dewar also functions as a cryopumping surface for the vacuum system. Additionally, vacuum is an ideal insulator which promotes temperature stability. Since the liquid nitrogen can remain in the dewar for days following a fill, a flow of room temperature nitrogen can be used to facilitate boiloff of the residual liquid nitrogen and return the drift cell to ambient temperature within ~30 minutes. If

otherwise desired, cold ion mobility experiments can be conducted for days following an initial cryogen fill. Following a series of cold temperature experiments, an excess concentration of impurities will be present in the drift chamber, as indicated by comparing room temperature drift spectra before and after a cooldown. A bakeout of the drift cell can hasten the evacuation of these impurities—typically one full day of bakeout at ~50°C will be sufficient to remove these impurities (higher temperatures will improve pumping even further). A small amount of water is always observed in the IMS spectra (m/z 18 and 19, the latter being protonated water) at temperatures >0°C and quadrupole selection experiments verify that this water originates through charge exchange reactions with ions in the drift chamber rather than from the ionization source.

2-5.6 Voltage Limitations in the Drift Cell Design

Gaseous electrical discharge within the dewar chamber is an phenomenon that can limit the maximum obtainable voltage for the drift cell spectrometer. Recall from earlier discussion that Paschen curves predict optimal discharge conditions in helium gas at ~1-2 torr pressure (**Section 1-3.3**), which describes the experimental conditions in this work. Because ion mobility methods necessitate the use of a continuously decreasing potential hill for ions to traverse the gas region, the potentials at the front and back of the drift cell represents the greatest potential difference in the enclosed metal chamber IMS described here. To minimize the occurrence of gaseous discharge, the dewar jacket chamber is electrically biased to a potential that lies in between the first and last electrode of the drift cell—this has the effect of minimizing the voltage difference

between any two conductors which in this particular drift cell represents the end electrodes and the chamber housing. Utilizing this chamber bias method, the maximum obtainable potential drop between the front and back of the drift cell is ~500 V at 1 torr of helium, which is ~17 $V \cdot cm^{-1} \cdot torr^{-1}$, or ~52 Td at room temperature. Mixtures or other pure bath gases allow for higher drift cell voltage operation, however voltages of this magnitude are not necessary except in the case of conducting high field ion selectivity experiments. All experiments described in this work involve small mass ions (<100 amu), and so the field strength is maintained well below ~10 $V \cdot cm^{-1} \cdot torr^{-1}$ (<30 Td at room temperature). For some of the electronic state studies described in section three, the field strength is <2 Td.

2-5.7 The Drift Gas Manifold

The manifold which transfers and monitors the gas supplied to the drift region is assembled from stainless steel tubes and metal-to-metal fittings (6.4 mm diameter tubing joined with Swagelok® fittings). A reservoir tank of gas is regulated down to a pressure of ~200 kPa and controlled amounts of gas are admitted into the drift cell through a fine leak needle valve (203 valve, Granville-Phillips®, Longmont, CO). Impurities present in the gas are filtered through combined stages of moisture trapping (750 cc molecular sieve 5A trap, Supelco, Bellefonte, PA) and a cryogenic trap consisting of a coil of 6.4 mm diameter tubing (20 turns) immersed in a liquid nitrogen bath. The cryogenic trap is utilized when noticeable impurities appear in the mobility spectrum. A 10 torr ranged capacitance manometer (SKY® CDG045, Inficon, Syracuse, NY) monitors the absolute

pressure of gas within the manifold. The manometer is placed just prior to the gas feedthrough into the instrument vacuum system. Ultra high purity (UHP) grade gases (helium & argon, Matheson Tri-Gas, Houston, TX; neon, Praxair Distribution, Bryan, TX) are used for all mobility experiments. Upon entering the vacuum system, the drift gas line is passed through the bottom region of the drift cell dewar jacket, where liquid nitrogen pools during a cooling experiment. The tubing line makes several passes before the drift gas is admitted into the drift cell. This ensures a final stage of cryotrapping occurs prior to admitting the gas into the drift cell, which eliminates virtually all impurities for the low temperature experiments (refer to **Section 3-2.2**). All drift gas lines within vacuum are 3.2 mm I.D. stainless steel tubing and utilize vacuum welds and swaged metal fittings to ensure a leak tight fit. The drift gas line is thermally and electrically isolated from the main chamber through a ceramic break (temperature stable alumina ceramic and stainless steel, 3.2 mm tube diameter, Insulator Seal, Inc.).

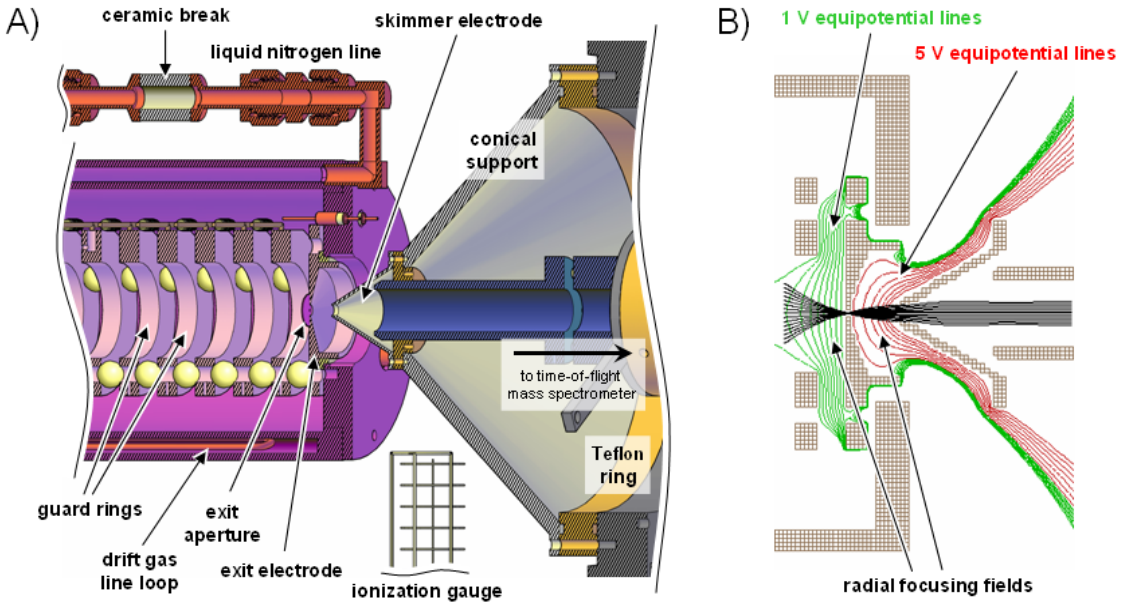

Figure 31 – Details of the ion optics at the exit of the drift cell. **A)** Schematic of the ion optics and support hardware, showing scaled placement of all components. **B)** SIMION generated potential energy contour lines showing the focusing effect of the drift cell exit electrode and skimmer. A distribution of ions is also modeled, showing radial focusing and transfer of the ions through the drift cell exit region. Ion energies were assumed to be near thermal and gas collisions were not simulated in the model. Gas collisions empirically exist in this region and will dampen the effect of any electrostatic focusing optics such that the trajectory predictions in **B)** represent an optimistic case.

2-5.8 Ion Mobility Exit Ion Optics

At the exit of the drift cell is placed a custom machined stainless steel nozzle skimmer cone (30^{o} total included angle). This skimmer is mounted on a larger conical support (45^{o} total included angle), creating a large conical assembly that is 3.2 mm at the orifice entrance and 146 mm at its base (**Figure 31A**). The entire assembly is mounted on a teflon ring machined with appropriate o-ring retaining grooves, allowing the conical assembly to be floated to a desired potential while maintaining the necessary high vacuum of the back end mass spectrometer. High ion transmission is accomplished by establishing a focusing field at the tip of the conical electrode which draws in a large

number of the near thermal ions that elute from the drift region exit (**Figure 31B**). At the same time, many of the escaping neutrals expand into vacuum and are pushed away by the geometry of the skimmer assembly, where a turbo pump removes them from vacuum. The tip of the skimmer cone electrode is placed 9.3 mm from the exit aperture of the ion mobility cell to allow sufficient room for neutral gas expansion and pumping. A potential drop of ~30 V is applied between the drift cell exit aperture and the skimmer electrode.

2-6 The Time-of-Flight Mass Spectrometer, Ion Detectors, and Associated Ion Optics

Mass analysis based on time-of-flight (TOF) measurements offers a very fast and sensitive means of obtain m/z specific information of ions. With orthogonal geometry ion extraction (see **Section 1-6.2**), TOF mass analysis is readily coupled to ion beam instruments, adding the ability to analyze ions from the beam across a wide dynamic range of masses. Because TOF is a dispersive (in time) type of mass analysis method, each ion extraction event generates a complete mass spectrum, so successive ion extractions provide a continual overlaying of mass spectra, improving signal-to-noise. With appropriate hardware, the speed of a TOF analyzer is limited only by the dispersion time of ions. For the small ions investigated in this work (<500 amu), the TOF is capable of running in excess of 100 kHz (100,000 spectra/sec), representing ion dispersal times of ~5 μsec. While each ion extraction may only yield 1-2 ion counts due to low ion transmission through the drift region, the power of the technique lies in its

speed: at 100 kHz and 1 ion per extraction, over 100,000 ions can be counted and summed together each second into a final mass spectrum.

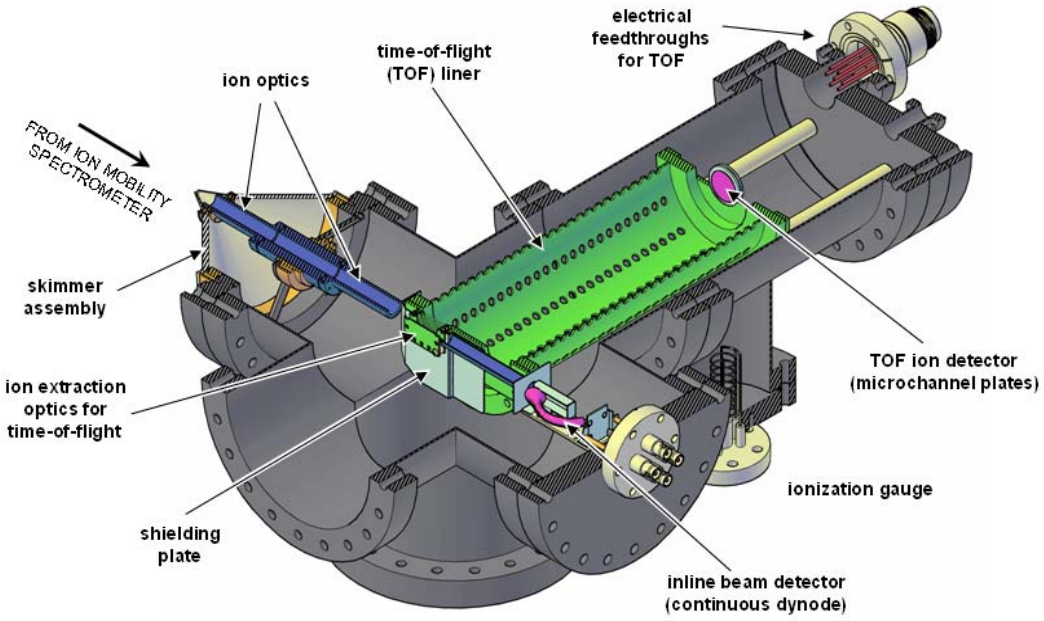

Figure 32 – Schematic of the orthogonal time-of-flight mass spectrometer. The ion detectors and associated ion optical components are also shown. A beam skimmer and series of ion optics steer and focus ions towards the extraction region of the TOF, where discrete slices of the ion beam are sampled for mass analysis. A continuous dynode detector is placed inline with the ion beam (bottom right) for monitoring the ions exiting the drift cell region. The TOF is fitted with a fast response microchannel plate assembly with ion counting capabilities.

2-6.1 Ion Beam Optics for Ions Entering the Time-of-Flight Extraction Region

Details of the TOF system designed and constructed for the cryogenic IMS is contained in **Figure 32**. Ions exiting the drift region are extracted and focused into an ion beam using a series of axially symmetric ion optical elements. The ion optics effectively focus the ion beam into the ion extraction region of the TOF, as illustrated in

Figure 33B. The extraction region consists of two parallel plates (3.5 cm wide "Series C" square plates, eV Parts®, Kimball Physics, Inc., Wilton, NH), with the plate defining the entrance to the TOF consisting of a gridded opening (2.5 cm diameter) to allow ions to traverse. Grid materials used here and elsewhere in the TOF ion optics are 70 lines per inch (lpi) electroformed nickel mesh (Precision Eforming LLC, Cortland, NY) possessing ~90% optical transmission. Ions not extracted in this region (either between extraction events or when the TOF is not operating) pass through the parallel plate region and into a single element barrel lens which is connected to an electron multiplier detector (Channeltron® model 4770, Burle Technologies, Inc., Lancaster, PA). This barrel lens is used primarily to shield the ion beam from the high voltage of the TOF (equipotential lines in **Figure 33A** and **B**), which must be floated negative to ground due to the necessary potential drop of the IMS[21]. The beam axis detector consists of a deflector plate and a horn-shaped continuous dynode (refer to **Section 1-8.3**). The deflector plate steers ions off the beam axis into the monolithic dynode and can be tuned to optimize detector gain by directing ions to the front most part of the dynode structure, where a greater degree of electron amplification will occur. This off-axis configuration is also useful for reducing detector noise resulting from neutrals colliding with the dynode surface, as would be continuously leaking from an on-axis IMS drift cell.

[21] Alternately, the front end before the IMS can be floated to a positive potential and the TOF operated relative to ground (zero) potential, however recall from discussion in **Section 1-3.3** that gaseous electrical discharge is more probable for a positive potential than a negative. Floating the back end mass analyzer to a negative bias and isolating it within a vacuum chamber represents the most acceptable means of addressing the biasing issues associated with hyphenated IMS-MS instrumentation. This also alleviates issues associated with floating the sample introduction region, where the user interfaces the instrument, to a high voltage.

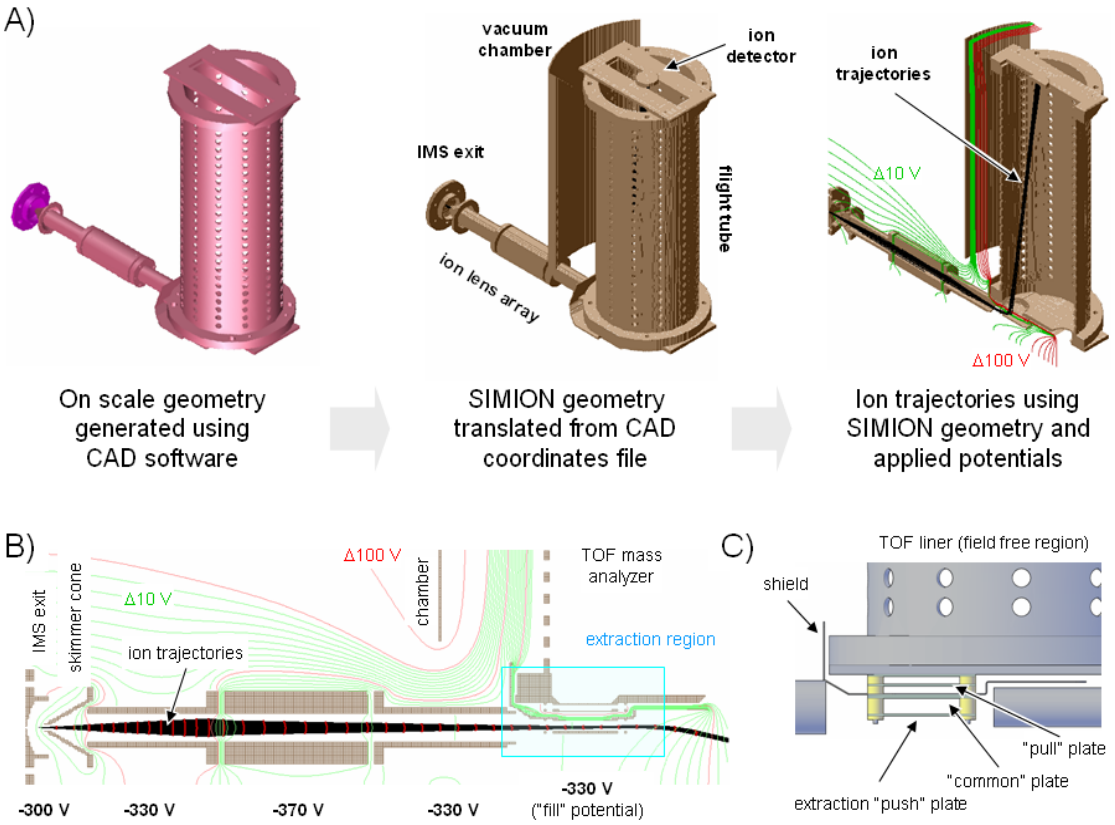

Figure 33 – **A)** The procedure for modeling ion trajectories and evaluating optimal instrument geometries for the TOF. A scale model is drawn using computer assisted design (CAD, **left**), then translated into SIMION readable coordinates to generate the boundary conditions for the trajectory calculations (**center**). Electrode potentials are assigned to the surfaces and ions are "flown" to determine their likely trajectories in the electric fields (**right**). **B)** Trajectories of ions traversing the beam ion optics to the TOF. Optics effectively collimate the beam through the extraction region (boxed in blue). **C)** Mechanical details of the TOF ion extraction region, showing the three plate design, TOF liner, and shielding necessary to block the high liner field from the ion beam.

The ion optics are supplied with the appropriate potentials via a 4-channel, 0-1 kV power supply (Ortec® model 710 Quad Bias Supply, Advanced Measurement Technology, Inc., Oak Ridge, TN). This supply module is built for the Nuclear Instrumentation Module (NIM) standard platform [368] and is appropriately stable for TOF applications, with <2 mV peak-to-peak ripple at full load. The first and last element is maintained at the same potential such that negligible kinetic energy is

imparted to the ions during focusing. Ions exiting the pressurized drift region are assumed to be near thermal (<1 eV of kinetic energy) and so the ion beam kinetic energy is defined as the difference between the exit of the drift cell and the back ion optical element. **Section 2-6.4** describes optimal beam kinetic energies for the experiment.

2-6.2 The Time-of-Flight Ion Extraction Optics

In the simplest case, a TOF mass spectrometer consists of an ion acceleration region (source) and a field free region (flight tube) where ions spatially partition into their respective m/z values (as depicted previously in **Figure 11**). The acceleration region is defined typically by two electrodes: a solid plate where the acceleration field is applied and a transparent (*via* a grid or aperture) plate which defines the entrance to the field free region and is kept at the same potential as the flight tube. Recall from earlier discussion that ions extracted from the TOF source region can be at any location between these two plates (**Section 1-6.2**). This results in ions which are closer to the acceleration plate receiving more kinetic energy than those further away. The consequence is that an extracted ensemble of ions at the same m/z will represent a distribution of velocities[22]. Ultimately, this limits mass resolution since the width of arriving peaks of the same m/z is governed by this velocity spread, however the resolution limit can be minimized by taking into account the *spatial refocusing* of ions which occurs as a consequence of their differential velocities [369]. In other words,

[22] The same result is also caused by ions having a distribution of kinetic energies, as with ions formed in the source by laser ionization methods. The means of addressing both space and energy distributions of ions in the source is the same.

since ions in the source start at different positions and are given different kinetic energies in the field, there is some distance from the source at which all ions will be at the same position, called the *space focus plane*—this is the most desirable location to place an ion detector. The space-focus plane for this simple, two plate source geometry will be the distance when ions spend an equal amount of time in the source and field free region [178]. As a consequence, this space focusing distance from the acceleration region will be very short, since ions spend a short amount of time in the actual acceleration region. Placing a detector very close to the extraction source is not desirable, since ions will not have spent sufficient time in the field free region to disperse *via* their m/z values. This problem limited the technological implementation of time-of-flight mass analysis, until Wiley and McLaren demonstrated that by introducing a two field extraction source, the location of the space focus plane can be made independent of the first field source geometry (to first order), governed rather by the magnitude of a second electric field region placed immediately after the first [208]. Two-stage ion extraction sources form the basis of all commercial TOF spectrometers, linear and orthogonal geometries, and is utilized in the TOF ion optics described here.

The two-stage extraction source of the orthogonal TOF is built up with a three plate design, as illustrated in **Figure 33C**. The stainless steel plates used are commercially available components designed for building up ion optical assemblies (eV Parts®, Kimball Physics, Inc., Wilton, NH). A flat plate is used as the acceleration plate, called here and elsewhere the PUSH plate. A second plate possessing a gridded opening (2.5 cm diameter opening, 70 lpi nickel grid) defines the end of the extraction field and

the start of the second stage acceleration field and is referred to here and elsewhere as the PULL plate. An additional plate with the same dimensions is used to define the field boundaries for the entrance of the TOF field free region, referred to here and elsewhere as LINER [370].

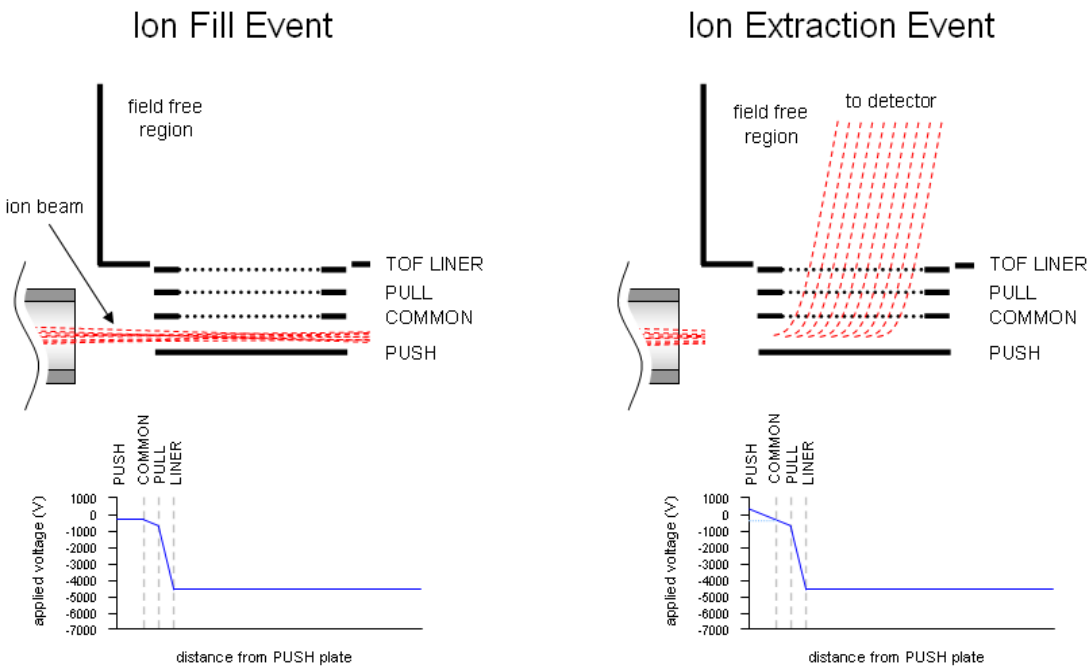

Figure 34 – Principle of operation of the orthogonal TOF ion source. At left, the electrical potentials on the PUSH and COMMON elements are kept the same to allow ions to enter this region. At right, an acceleration pulse is applied to extract ions from the source and into the second stage between the PULL and LINER elements. Ions accelerated in this manner will partition by m/z in the field free region while spatially refocusing to some far distance from the source to allow for adequate mass separation. Note that the fields depicted here are the same immediately before and after the COMMON element, creating the ideal two-field source which satisfies second order focusing requirements. In practice, this is not always the case as the potential slope before and after COMMON are in many experimental cases, not the same.

In orthogonal TOF methods, ion analysis proceeds *via* two distinct steps: an "ion fill" step whereby the source region is populated with ions from the beam, and an ion

extraction step, whereby an accelerating field is applied to push ions from the source and accelerate them for TOF mass analysis [220]. Illustrative details of this two stage process are presented in **Figure 34**. During the "ion fill" step, it is necessary to maintain the source region at zero field with respect to the TOF axis so ions will enter this region. The most straightforward means of accomplishing this is to introduce a third element which partitions the first source stage into two. This COMMON electrostatic element is maintained at the potential reference of the ion beam while the PUSH element pulses from this common potential to the acceleration potential, such that between ion pulses the field in this region is zero. Introducing this COMMON electrode also facilitates a narrowing of the ion fill region, which further enhances mass resolution capabilities. In most cases, it is also preferable to use a series of two pulses rather than one to simultaneously lift the PUSH and lower the COMMON (in which case it is no longer common). This will minimize the magnitude of the field which protrudes away from the ion source which perturbs the trajectories of those ions present in the beam but not extracted in the pulse. This two pulse strategy is not used in this particular source design, as the modest gain in sensitivity was not justified by the experimental complexity of the setup. Finally it should be noted that a second pulse opposite in polarity direction to the PUSH pulse can also be applied to the PULL element to create a blocking potential during the ion fill event so ions will not "leak" into the TOF region. No ion leakage was observed with the PULL bias on, so this two pulse strategy was not utilized in these experiments.

The dimensions comprising the space between ion optical elements are as follows: 6.4 mm from PUSH to COMMON, 4.1 mm from COMMON to PULL, and 3.2 mm from PULL to the entrance of the TOF liner. The relevant source dimensions are thus: 10.4 mm for the first stage and 3.2 mm for the second stage of the extraction. These dimensions incorporate the finite thickness of plate elements and are measured from grid surfaces. All electrode plates are all 0.6 mm thick. The unconventionally large dimension for the first extraction source region allows for a greater "ion fill" volume which serves to increase the experimental sensitivity, but at a cost of mass resolution. The longer first stage also lengthens the ion residence time in the source region, which has the beneficial consequence of allowing a longer drift path length and/or higher TOF acceleration voltages to be used in the second stage for the same space focusing which both serve to improve mass resolution, though it is unclear if these gains outweigh the detriments associated with the wide spatial distribution of ions in the source.

Voltages on the static ion extraction electrodes (COMMON and PULL) are supplied by two channels of a 4-channel, 0-1 kV power supply (Ortec® model 710 Quad Bias Supply, Advanced Measurement Technology, Inc., Oak Ridge, TN). The PUSH pulse is supplied with a fast pulser specifically designed for TOF applications (Dual HV Pulser, Ionwerks, Inc., Houston, TX). Because this pulser supply cannot be biased to a high potential (<15 V limited), an AC coupled circuit was assembled to superimpose the high voltage pulse to the biased PULL electrode. The simple circuit is a capacitor (1.9 nF 6 kV Cera-Mite, Vishay Intertechnology, Inc., Malvern, PA) which connects the

pulser to the DC circuit of the PULL electrode. An additional resistor (20 MΩ, 3W Geka® wire-wound, Vishay Intertechnology, Inc.) is placed in series between the DC supply and the PULL electrode to buffer the DC supply from the pulse as well as serving as a current limiting component in the event of a discharge [371]. One limitation to this approach is that when the capacitive pulsed circuit is applied, a percentage of the DC bias is dropped from the main circuit, such that the actual potential on the electrode is lower than the potential being supplied by the DC power supply. This is a well known phenomenon in AC coupled circuits and must be accounted for in this TOF ion extraction design to ensure that the PUSH and COMMON electrodes are maintained at the same (or close to the same) potential so that ions will preferentially populate the region in between. To correct for this DC offset, a separate power supply is used for the PUSH plate (rather than conveniently stringing the COMMON power supply to this input) and the DC offset correction is applied to this separate supply. The required DC offset correction will depend on the pulse frequency and amplitude, but constitutes about 1-10 V for the range of possible pulser settings. The effect of the DC offset can be directly observed and experimentally corrected for by monitoring the resulting mass resolution. For most all experiments described here, the offset is optimal between 2-5 V negative, supplied to the PUSH element. Finally, the short flight times of the low mass ions studied in this work allow for the TOF to extract at a much higher frequency than conventional for hybrid IMS-MS instruments of this design. The TOF sampling frequency is routinely operated between 70-80 kHz, which represents the upper limit of frequency that will still allow ion dispersal and recovery of electronics and the detector.

More details regarding the timing and operation of the data acquisition system is providing in **Section 2-7**.

2-6.3 The Time-of-Flight Field Free Region and Ion Detector

As a result of the necessary potential hill required to convey ions through the pressurized drift region, either the front or the back of an IMS instrument must be referenced to a potential other than ground potential. As mentioned in **Section 1-3.3**, it is more desirable to float the back end MS of a hybrid mobility-mass spectrometer negative in order to maintain the ion source at a safe, ground potential and minimize discharge probabilities in the back end region where sensitive ion detectors are placed. As a result, the entire back end of the instrument, including ion optics and the TOF, is referenced to the back of the drift cell, which for all experiments described here is between 100-400 volts negative. Since ions are further accelerated in a high field for mass analysis, the field free region of the TOF must be further biased in excess of ~4000 volts negative (for positive ion analysis). Therefore, an appropriate field free liner must be used in order to maintain ions at this low potential.

The TOF liner consists of a stainless steel tube, perforated with 0.6 cm holes to allow for pumping and closed on both ends with stainless steel caps appropriately machined to support the ion extraction optics at the source end and the ion detector at the detection end. The liner was originally designed to incorporate a reflectron ion mirror device, and thus has a larger endcap opening at the detector end and an additional mounting opening for a second detector on the ion source endcap. For the linear TOF

design, these openings were closed using stainless steel shim stock material. The TOF liner measures 27.25 cm from end to end. The total ion path length from surface center of the PUSH element to the surface center of the detector is 29.3 cm. The location of the detector center is offset by 3.3 cm with respect to the center of the PULL electrode to facilitate efficient ion coincidence due to beam axis kinetic energy [372]. The ion detector consists of two, 25 mm diameter MCPs assembled into a chevron configuration (refer to **Section 1-8.5**). A 25 mm stainless steel disk is mounted ~5 mm behind the MCP assembly and serves as the signal anode. A capacitor (10 pF 6 kV Cera-Mite, Vishay Intertechnology, Inc., Malvern, PA) is placed in series with the signal anode wire to break the conducting path, which discourages electrical discharge through the MCP assembly. This capacitor also protects the detection electronics in the event of a discharge and prevents anything connected to the signal end downstream from the detector to damage the detector in the event of a electrical malfunction. To sink electron current which is generated on the anode, a 10 MΩ resistor (MG series, Caddock Electronics, Inc., Roseburg, OR) connects the anode end to instrument ground. This resistance is sufficiently high to prevent sinking the current prior to charging the capacitor in which the signal is read through.

The TOF liner voltage is supplied with a 0-10 kV supply which also biases a 0-3.5 kV detector supply (HP and HF series, Applied Kilovolts Ltd., West Sussex, UK). This floatable module is convenient for operating the MCP detector on a floated system, and greatly reduces the chances of applying too much voltage to the MCP assembly. Additionally, these supplies possess low ripple (50-75 mV peak-to-peak at full load)

which translates into higher TOF resolutions. These latter two modules are integrated into a home built chassis fitted for manual voltage control and monitoring and incorporates shutdown interlocks which trip in the event of a power outage. Such an interlock system is necessary for protecting the MCP detector from catastrophic electrical discharge in the event of losing high vacuum ($<10^{-4}$). Refer to **Section 1-8.5** for a more in depth description of this discharge problem as it relates to MCP detectors.

2-6.4 Optimal Time-of-Flight Settings for Mass Resolution and Sensitivity

Observed mass resolution for the IMS orthogonal TOF arrangement will be governed by several parameters, including the mechanical alignment and tolerances of electrodes and stability of the power supplies used. These latter issues should be addressed in the design and construction process—once the instrument is assembled there are basically two key factors which govern the performance of the linear TOF mass spectrometer: the spatial spread of ions which populate the ion extraction region and the location of the space focus plane with respect to the detector. Both parameters can be controlled with the proper potentials, and an adequate estimate of what potentials to apply can be drawn from ion trajectory modeling using accurately scaled geometries in SIMION (this procedure is outlined in **Figure 33A**). The ion beam can be collimated into a relatively narrow dimension with respect to the TOF axis, as illustrated by the trajectory modeling in **Figure 33B**. The importance of the ion spatial distribution for mass resolution is illustrated in the trajectory simulations in **Figure 35A** which model an accurate statistical weight of Xe^+ isotopes and sums resulting arrival time values. As the

TOF axis distribution of ions in the extraction source is narrowed, the mass resolution increases. Some beam aberrations and the relatively large spacing of the "ion fill" region will limit the practical mass resolution at the benefit of ion transmission, however a resolution ~100 can be achieved for this linear TOF which is more than adequate for the small molecules studied herein.

The location of the space focus plane for a given set of TOF dimensions and potentials can be calculated from equations derived for second order TOF focusing (found in reference [178]). However, this calculation tends to underestimate the focal distance found empirically in this instrument due to the fact that the addition of the COMMON electrode complicates the simple two-field source unless special care is taken to ensure the electric field between PUSH and COMMON is the same as the field between COMMON and PULL. In other words, the actual source configuration used in this work incorporates three separate fields, such that the theory currently established for second-order focusing does not fully apply here.

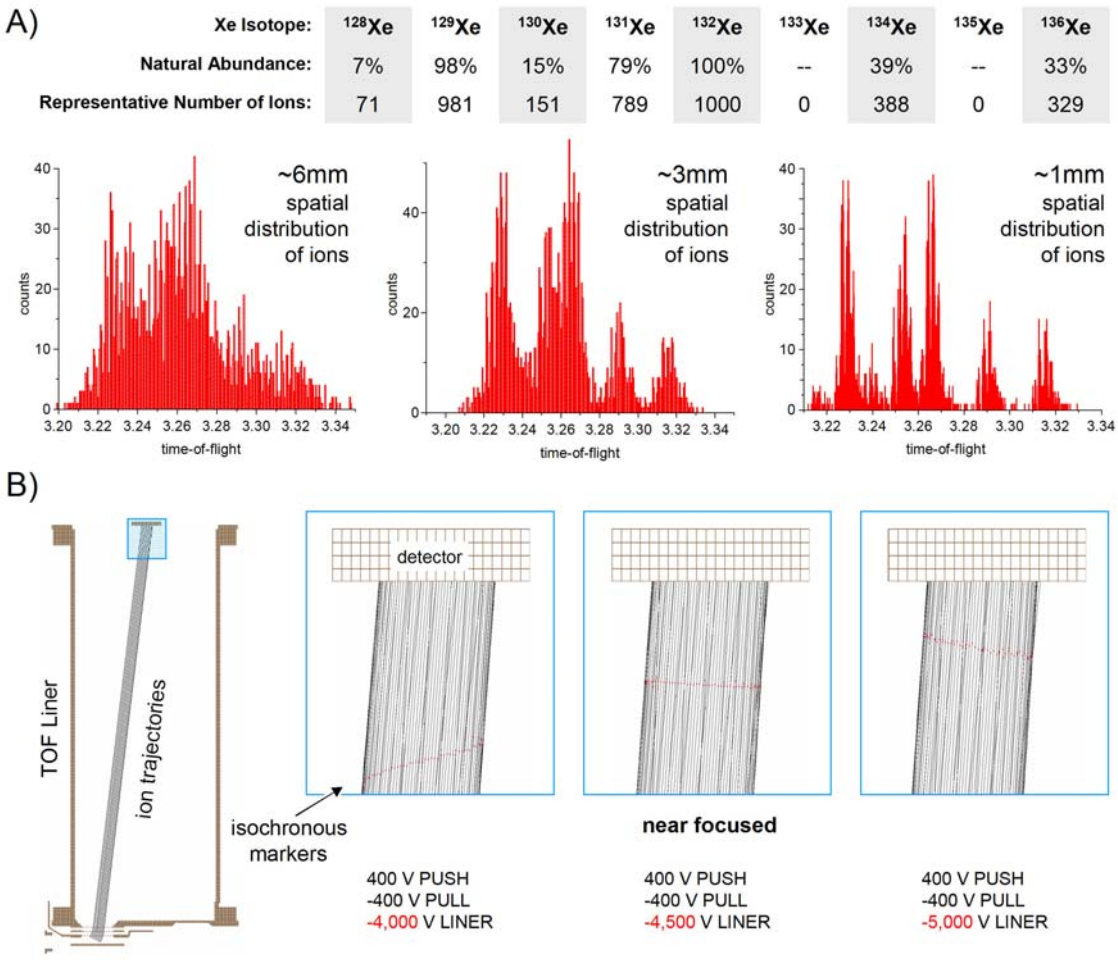

Figure 35 – Ion trajectory simulations evaluating the TOF mass resolution. The results illustrate the factors which influence the observed mass resolution of the orthogonal TOF configuration used in this work. **A)** Histogram plots of simulated arrival time data for xenon ions which are made to populate various spatial distributions in the TOF ion extraction source. Ion numbers are statistically weighed with respect to the natural isotopic abundances of xenon. 6 mm (left histogram) represents the full width of the extraction region, and thus a "worst case" resolution. **B)** Simulated ion trajectories at various TOF potentials. Time markers (insets, in red) indicate the location of ions at a specific time interval. The space focus plane is the location when ions arrive at the same plane parallel to the source/detector—the center ion trajectory inset represents settings which give a close to ideal arrival time for ions, *i.e.*, at the surface of the detector.

A satisfactory solution has been to rely on ion trajectory models to estimate the conditions for space focal plane detector coincidence. Trajectory simulation results of this procedure are contained in **Figure 35B**. In practice, these calculated values are

close to what is found through experimental tuning, however they can deviate by as much as 10%. Nevertheless, such calculations are invaluable as a starting point for empirical tuning of the instrument, particularly when no prior knowledge exists as to where to begin, as is the case with instrumentation components built from the ground up. Experimentally, the PUSH potentials is optimal between 200-400 V positive, the PULL between 300-600 V negative and the TOF LINER between 4000-5000 V negative. All potentials are with respect to ground rather than what is outputted by the power supplies on top of additional DC biases.

Finally there are additional considerations which must be taken into account for ensuring ions which are extracted from the TOF source will coincide with the detector. The orthogonal TOF configuration represents a two vector system whereby the beam axis momentum of ions is retained during TOF extraction due to the kinetic energy of the ion beam. This kinetic energy must be properly tuned to the extraction potentials of the TOF (or vice versa) to maximize the number of ions that reach the detector. SIMION modeling of ion trajectories suggest that a range between 20-50 eV of kinetic energy for the ion beam is optimal for ions to coincide with the detector during TOF extraction when using ion extraction potentials that optimize mass resolution. Experimentally, it is observed that higher kinetic energies (>30 eV) result in greater ion counts at the detector, while lower kinetic energies (<30 eV) result in higher observed mass resolutions, presumably due to a narrower ion distribution in the ion extraction source region. For all experiments, the ion beam kinetic energy is maintained between 30-40 eV to balance

high resolution with adequate sensitivity. This value is consistent with results obtained on other IMS instruments in our laboratory.

2-7 Data Acquisition and Visualization Methods

Critical to the success of this instrument is the ability to quickly and efficiently acquire and correlate multidimensional data sets. Speed is particularly important for the cryogenic IMS instrument since low ion recovery through the drift cell is a consequence of high resolution, low field experiments. The data acquisition methods described here represent a refinement of several generations of previous ion mobility work made possible through a longstanding collaborative relationship between our laboratory at Texas A&M and scientists at Ionwerks of Houston. The resulting hardware and software make it possible to simultaneous acquire, correlate and visualize the two dimensions of data in such a straightforward way that it is somewhat difficult to see the underlying principles which govern how the methods work.

2-7.1 Interleaving of Mobility Arrival Time Data with Mass Data

While it may seem rather simple to consider how one might correlate the signal from two detectors together into a single, two dimensional data plot, it is somewhat less intuitive to rationalize if there is only one detector in the experiment. Acquiring two sets of data simultaneously on a single detector in the IMS-MS experiment is made possible through a clever time correlation method known as *data interleaving*.

Recall that there are two duty cycles in the IMS-MS experiment: one for the mobility (the ion gate event) and one for the TOF mass analyzer (the ion extraction event). Consider that after ion mobility separation, the ions which exit the drift region are partitioned into mobility-specific ion populations dispersed in time. As these ion packets pass through the extraction region of the orthogonal TOF, the extraction potential can be timed such that it only extracts and mass analyzes ions corresponding to only one of these ion populations. This is made possible by setting a specific delay time between the start of the IMS analysis and the start of the TOF analysis and repeating this same delay time over and over to obtain sufficient ion counts. Now by scanning the delay time across the full time in which the mobility separated ions are dispersed, a complete mass spectrum can be obtained for every ion population. This is essentially how data interleaving works, except for reasons of maximizing the acquisition efficiency, the time is offset for each new ion mobility pulse such that scanning is done in an interleaved fashion. In this way, there is a minimum number of offsets (interleaves) which must be acquired before a complete mobility spectrum is represented.

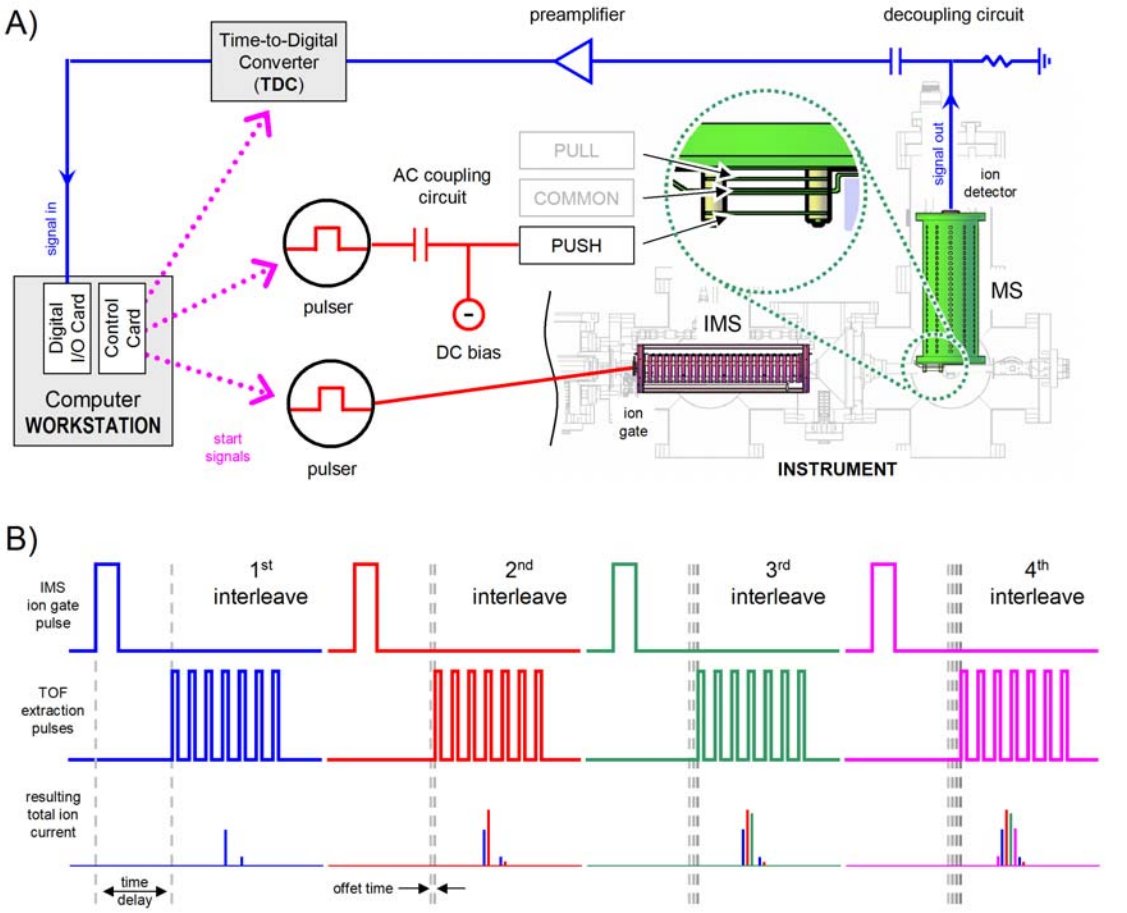

Figure 36 – Data acquisition setup and principle of mobility data interleaving. **A)** Experimental details of the data acquisition setup. Software driven timing initiates a series of control card outputs that triggers the ion gate and time-of-flight pulses, respectively. This timing sequence is fed into the TDC and used to correlate ion extraction events with mobility arrival times. **B)** The data interleaving strategy used to deconvolute mobility arrival times from the TOF data. TOF acquisition proceeds through several interleave events, each differing by a specified offset time (2^{nd} panel). Each mass spectral signal is correlated to a specified extraction pulse and through a series of interleave events (shown here with four), the mobility arrival time profile is generated for each mass spectral bin (4^{th} panel).

In **Figure 36B**, the principle data interleaving is illustrated for four hypothetical interleave events. A time delay is introduced between the IMS and MS modes, since it takes a finite amount of time before ions begin to reach the TOF. Because the TOF operates at a much higher frequency than the IMS, several TOF acquisitions can be

initiated for each IMS pulse, increasing the efficiency of the data acquisition. As can be seen in the far right panel, after the fourth interleave, a complete mobility peak is represented. Repeating this process multiple times serves to enhance the ion counting statistics and thus the accuracy of reproducing the actual ion population distribution. The number of interleave events determines how many data points are taken across each peak profile and should be optimized for each system investigated.

2-7.2 Experimental Setup of the Data Acquisition System

An experimental overview of the data acquisition setup is contained in **Figure 36A**. Depicted to the left is a computer workstation, which manages both the timing of the experiment and the storage of the resulting data. The experiment is driven by acquisition software developed specifically for IMS coupled to orthogonal TOF spectrometers. The software contains several user adjustable parameters, including *i)* timing controls for the ion mobility pulse width and frequency, *ii)* TOF extraction number, pulse width, frequency and duration, *iii)* desired number of interleaved events, and *iv)* delay times between experimental sequences. The software takes the user defined number of TOF extractions and calculates the ion mobility acquisition window. The interleave event number is used to calculate the ion mobility bin (digital channel) size. Using these set of parameters, the entire acquisition of 2D data can be adjusted to suit the system under study. For example, small molecular ions have very fast drift times and marginally low mobility separation efficiencies and so it would be desirable to tune TOF acquisition for many short, quick bursts shortly after the start of the IMS. For

larger ions, the TOF acquisition can be delayed for a much greater duration and can utilize fewer TOF extractions across a larger time window in order to analyze a larger dynamic mobility and mass range. Lower frequencies and wider pulse widths would also be desirable for the latter case to account for the slower flight time of these larger ions.

The software communicates with the instrument via two computer cards: a control card (32-bit, x8 TTL lines at 80 MHz, model PCI-6602, National Instruments Co., Austin, TX) for outputting the control voltages to various modules and a digitizer card (Fastlink for TDCx8, Ionwerks) for reading the time-dependant digitized data sets directly from an 8-channel time-to-digital converter module (TDCx8, Ionwerks). The 8 TDC channels are not utilized in this experiment. An additional module (TTL to NIM, Ionwerks) is used to convert the TTL control voltages to the NIM standard for communication with the TDCx8. Instrument control voltages (TTL hi) initiate the two pulsers (Dual HV Pulser, Ionwerks) which drive the IMS ion gate and TOF extraction pulse. The latter is AC-coupled to the DC biased circuit of the PULL electrode, which is necessary to float the back end of the instrument at a negative potential. As mentioned previously, the resulting potential drop in the DC circuit must be corrected for so that the PUSH to COMMON field remains near or at zero for efficient ion filling.

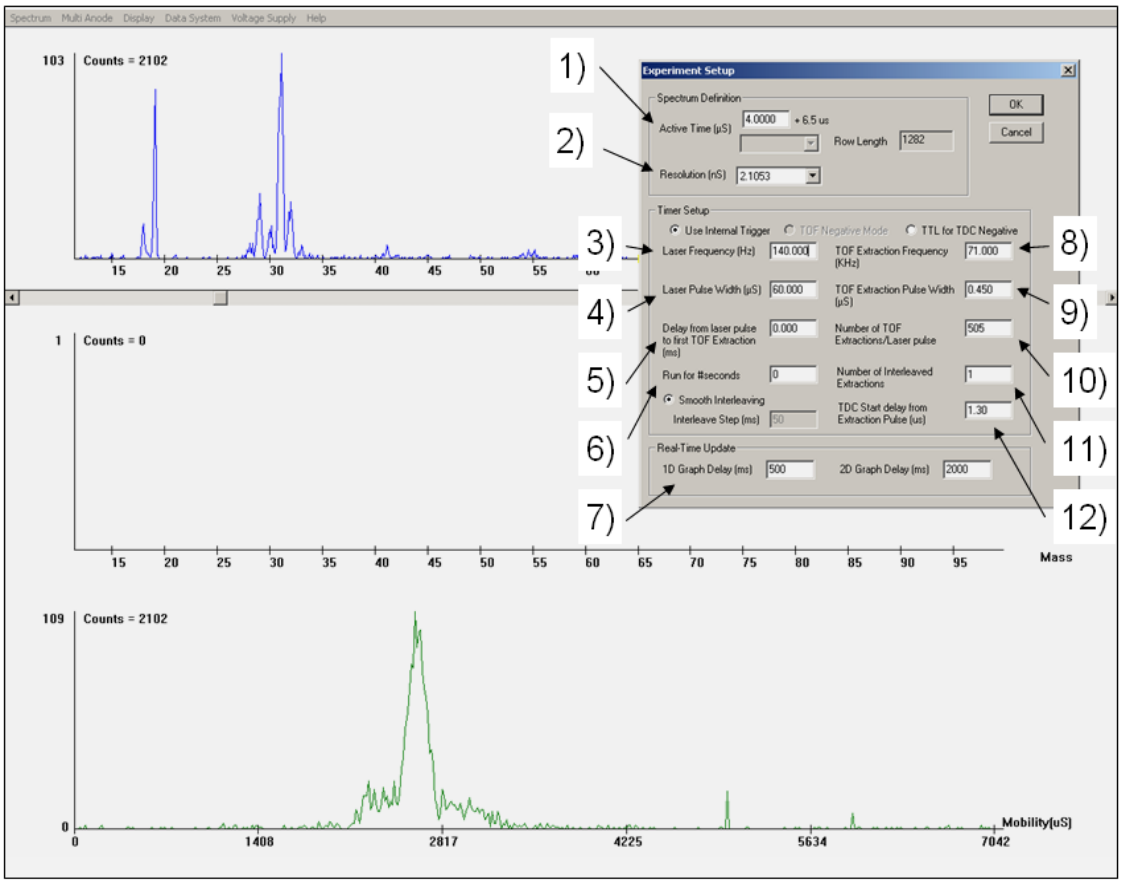

Figure 37 – Front panel interface of the data acquisition software. The top panel is the integrated mass spectrum; the bottom panel is the integrated mobility spectrum. The middle panel displays the real time acquisition of data. Windows of mass can be selected and the resulting mobility traces integrated across the window in the bottom panel. The "Experimental Setup" popup interface is shown which has the following controls: **1)** TOF time window, **2)** TOF time resolution, **3)** ion gate frequency, **4)** ion gate width, **5)** time delay before TOF begins acquisition, **6)** optional acquisition timer, **7)** refresh rate of the middle data panel, **8)** TOF frequency, **9)** TOF pulse width, **10)** number of TOF ion extractions, **11)** number of interleave offset events, **12)** time delay before TDC acquires TOF data (useful for circumventing noise resulting from the initial pulse). The data displayed is the 70 eV electron ionization of methanol with argon as the drift gas.

The detector output signal is decoupled through a capacitor to regulate current flow and protect both the detector and the electronics from path-to-ground initiated discharging. In this configuration, the detector anode is maintained at ground potential, so a resistor to ground can be used to sink excess electron current from the line (**Figure**

36A). The ion signal from the TOF is fed first through a preamplifier (200x amplification, <1 ns rise time, Ortec® model FTA820A fast timing amplifier, Advanced Measurement Technology, Inc., Oak Ridge, TN) and then digitized and time correlated through the TDCx8. The resulting digitized signal is sent to the digitizer card of the computer workstation. The acquisition software deconvolutes the ion mobility traces with the method described in **Figure 36B** and generates two sets of spectra corresponding to mobility and mass space data. The acquisition software interface is shown in **Figure 37**.

2-7.3 Data Format, Visualization and Post Acquisition Workup

The 2D data is saved in a single data file format. The data files are stored in a matrix format retaining the spatial locations of each data bin as it pertains to the 2D mobility-mass space. The numerical data in each XY location corresponds to the ion counts at that particular bin. Thus a full integration across either X or Y results in the total mass and mobility spectra of the experiment, respectively. This matrix data can be viewed in a 2D contour map format using custom mobility visualization software (Ionwerks) produced with the IDL development language (ITT Visual Information Solutions, Boulder, CO). This software projects mass data on the x-axis and mobility data on the y-axis, which is a logical arrangement given that the dependant variable in these experiments is the mobility data rather than the mass data. A convention stemming from LC-MS stipulates that the mass data be projected on the y-axis and thus this type of projection (mobility on the x-axis) is also seen in some IMS-MS data, specifically in the

commercial Synapt^{TM} traveling wave IMS instrument (Waters Co., Milford, MA). Projection of the data in this manner draws parallels to IMS as a chromatographic separation. The variability in projecting 2D mobility-mass data should be considered when comparing 2D ion mobility-mass data from various sources. The 2D trace is a simple contour map with user definable color mapping. The threshold for the contour map can be adjusted, representing a line scan across the mobility and mass data. Because the contour map represents a linear scan across the data, the resulting 2D projected data is not scaled by half heights and as such cannot be compared for relative broadening. Inherently this line scan method discriminates across low and high abundance signals—a fact which should be considered when visualizing the data with this software. Some degree of data interpolation occurs during post data processing as digital data inherently lacks information between points. The software allows for user selectable smoothing which attempts to curve fit between data points. With no smoothing, the software processes the data *via* linear interpolation (*i.e.*, "connect the dots"). Fewer data points are often taken in order to address low levels of ion abundances present in some of the more challenging experiments, such as the low field, low temperature experiments in **Section 3-2**. In these cases, the data appears "choppy" with simple linear interpolation and so a low level of smoothing is applied to the mobility data to assist in visualization. This fact should be considered when interpreting some of the more subtle spectral features in mobility trace data, such as peak "shoulders" or non-Gaussian broadening.

3. EXPERIMENTAL RESULTS AND INTERPRETATIONS

3-1 Instrument Performance Benchmarks and Calibration Data

Performance data on the various instrument components was obtained during each of the several iterations of the instrument's development. Documentation of the more pertinent experimental results is given in the next few sections.

3-1.1 Mass Selective Capabilities of the Quadrupole and Observed Ion Chemistry in the Drift Cell

The addition of the quadrupole prefilter is an important experimental capability for the cryogenic IMS. The ability to unambiguously determine the m/z value of ions which are admitted into the drift region can lend significant credibility to data interpretation, particularly with regards to the origin of specific ions which appear following the IMS experiment. In most all cases, the IMS experiment is marked with a certain amount of ion chemistry, resulting from the ion's interaction with trace level impurities in the drift gas. In fact, this favorable ion chemistry forms the basis of chemical detection technologies which employ IMS, such as explosives detectors at airports which monitor the appearance of a product ion rather than the chemical precursor. To illustrate the importance of mass selection capabilities, consider three ions which are formed in the source and introduced into the drift region. Each of these three hypothetical ions are capable of efficient ion chemistry in the drift cell and give rise to several product ions in addition to their precursor ion signature. The resulting mobility-

mass spectrum will thus be a composite spectrum of precursors and product ions and our three ion situation quickly becomes one marked with six or more ions. With ion selection capabilities, each of our three ions can be selected one at a time, and the resulting mobility-mass data can be compared to determine the origins of the superfluous ion signals.

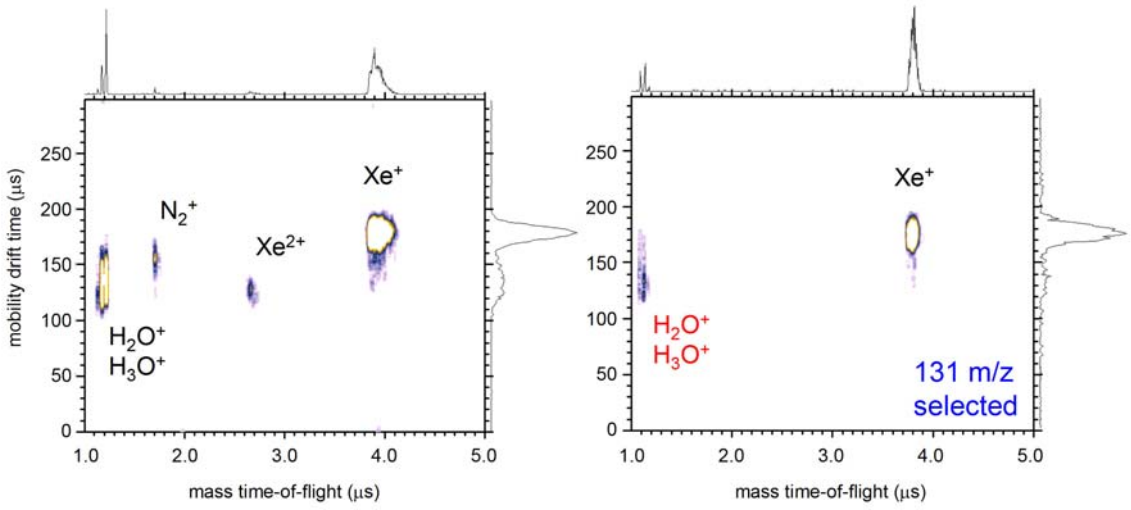

Figure 38 – Spectra of Xe^+ identifying water impurities in the drift gas. Left, resulting spectrum with the quadrupole set to total ion transmission (broadband). Several peaks are observed. Right, resulting spectrum with the quadrupole set to transmit m/z 131. Xe^+ and the two signatures for water (18 and 19 m/z) are present, indicating that neutral water impurities are present in the drift gas and initiate ion chemistry with Xe^+. The 2D plot also reveals signal "smearing" which is characteristic of an ion that has undergone conversion during its transit through the drift region, most notable here in the right spectrum as fronting on the Xe^+ peak and tailing on the water ion signatures. Note that the mass axes are displayed as the uncalibrated flight times. Experimental conditions for both spectra are: 70 eV electron ionization, 0.9 torr helium drift gas, 10 μs ion gate and ~8.5 $V \cdot cm^{-1}$ drift field.

Figure 38 illustrates the utility of mass selection using a simple example of xenon. The electron ionization of pure xenon will give only two ion signals: Xe^+ and Xe^{2+}, with more of the latter for higher EI energies (reference spectrum from NIST, not

shown). The mobility-mass data contains ion signals for both singly and doubly charged xenon atoms, as well as ion signatures representing H_2O^+ and H_3O^+ (water and hydronium ion, respectively) and N_2^+. The water ions could result from the source manifold, being introduced along with the xenon gas. Atmospheric contamination of the sample is suggestive of the presence of the N_2^+ ion and water is also a common contaminant, especially in the high humidity environment where these experiments are conducted (College Station, Texas). By selecting only the Xe^+ ion (131 m/z) to be transmitted through the quadrupole, any other ions formed at the ion source will be rejected from entering the drift region. The selection of xenon (m/z 131) using a wide mass window results in both the Xe^+ ion and the two water signature ions appearing in the 2D spectrum (**Figure 38**, right). This indicates that water is present in the drift gas. The formation of the hydronium and water ions in ion mobility methods is a well known, fast reaction process and the hydronium ions is often used as a precursor ion for the detection of specific chemical species [1,148]. For this particular case, the reaction is a charge exchange (electron transfer) between Xe^+ and neutral water, which has been documented in previous reports to be a favorable reaction for noble gas cations [373].

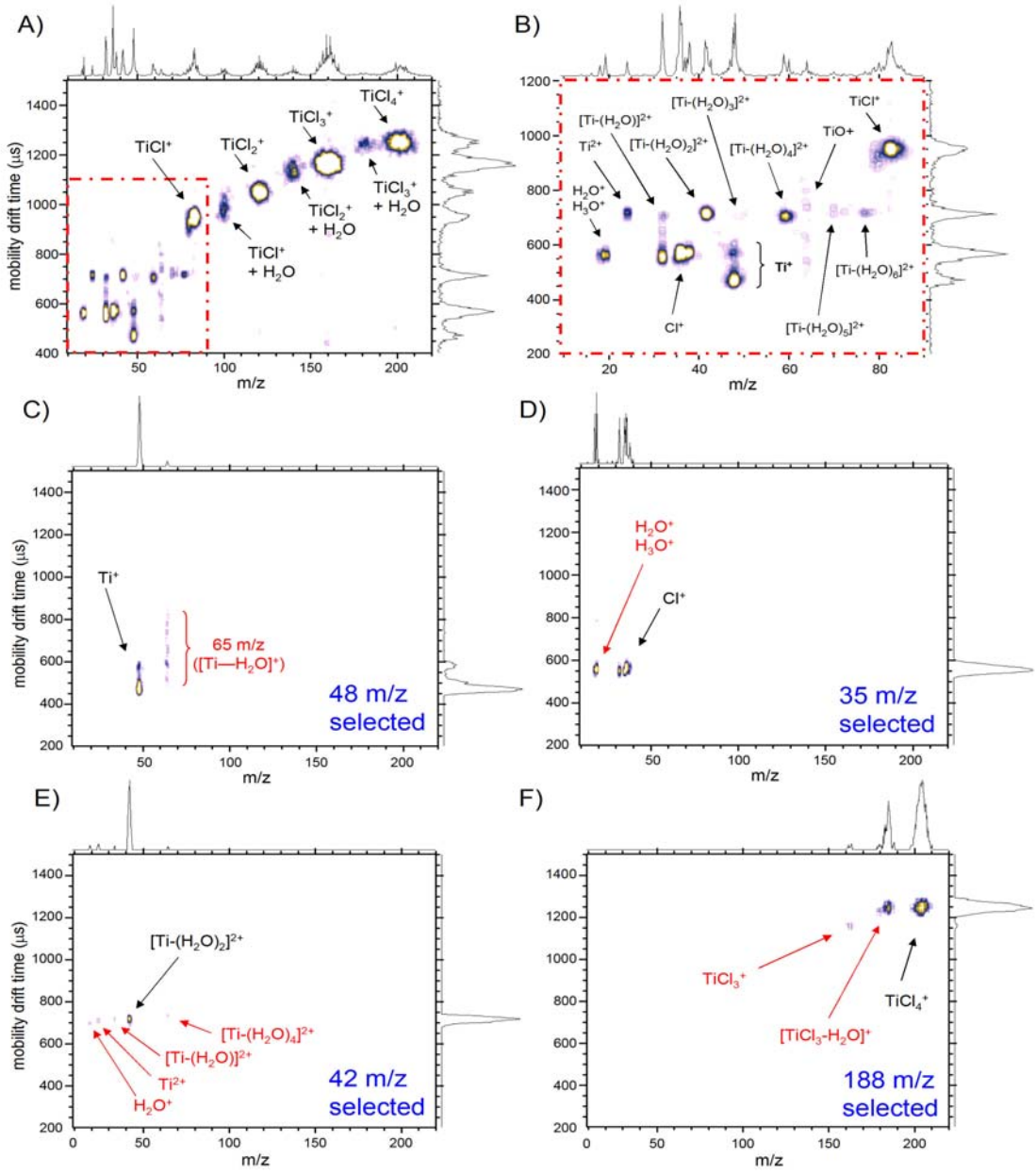

Figure 39 – Spectra of $TiCl_4$ demonstrating mass selective experiment utility. **A)** The total ion transmission spectrum containing various $TiCl_4$ fragment and hydrated clusters. **B)** The low mass region which contains numerous ion signatures, many of which cannot be identified using the m/z information alone. **C)** Mass selective transmission of the Ti^+ ion only into the drift region reveals the origin of the "smearing" at m/z 64 (TiO formation) and confirms the bimodal distribution of Ti^+ results from the ionization event rather than through ion chemistry in the IMS. **D)** Selection of the Cl^+ ions (33-35 m/z) reveals that the charge exchange products water and hydronium ions (18 and 19 m/z) originate primarily from this ion. **E)** Selection of one of the prominent ions for the hydrated doubly charged titanium indicates that other hydrated ions originate through this reaction channel. **F)** The same result is found for selection of one of the hydrated $TiCl_x$ clusters. Experimental conditions are as follows: ionization with 70 eV electrons and 3.1 $V \cdot cm^{-1} \cdot torr^{-1}$ drift region conditions in 298K helium gas. Titanium results are discussed in more detail in **Section 3-3.2**.

A more powerful demonstration of the utility of mass selection is contained in **Figure 39** for the study of electron ionized $TiCl_4$ (**Section 3-3.2**). **Figure 39A** contains the full 2D mobility-mass spectrum of $TiCl_4$ at 70 eV of EI energy with the quadrupole set to transmit all ions. The spectrum contains numerous ion signals, many of which can be identified using m/z data. Several low m/z ions indicated with the dotted box cannot be definitively assigned by their m/z values alone. This region is expanded in **Figure 39B**. Many of these ions do not fall on an expected mobility-mass correlation trendline, but rather their horizontal alignment across isobaric mobility values imply that these ions originate from slow ion chemistry within the drift region. Consider that an ion which undergoes a conversion sometime during its transit within the drift cell will have a composite drift time comprised of reactant and product ionic mobility. Ions which rapidly convert to products at the entrance of the drift region will be measured primarily as the product ion and have it's indicative mobility arrival time. The third situation contained in **Figure 39B** is for ions which convert or dissociate at the end of their mobility transit time, either in or outside the drift region. These ions will have been measured as their precursor mobilities and so will line up across a horizontal line which leads to the precursor ion mass. The line deviates slightly, indicative of a situation where one or more of these scenarios have occurred. Another indication that ion chemistry is occurring can be seen in several of the peaks which tail across the mobility dimension—the characteristic "smearing" which was also observed in the xenon data, though to a lesser extent than what is seen here. In order to determine some of the origins of these ion signals, a series of mass selective experiments can be conducted.

This is contained in **Figure 39 C-F** which corresponds to the selection of several prominent ions in the spectra. As these spectra illustrate, several product ions can originate from a single precursor, creating a complicated ensemble of chemical reactions which cannot easily be teased out of the data. Using the mass selective information, the correct ion assignments can be made, as is done in **Figure 39B**. As it were, the complicated series of ion reactions which characterize the spectra in **Figure 39A** and **B** result primarily from the presence of water in the drift gas. Water was present in the system in high concentrations immediately following a venting to atmosphere of the main chamber for routine maintenance. Most of the hydrated ions were absent from the spectra following a flushing of the drift gas and overnight bakeout of the instrument and gas manifolds. Water is a ubiquitous and highly invasive reactant species which can be addressed particularly effectively through low temperature condensation, as can be done using the cryogenic IMS instrument described here (refer to **Section 3-2.2**).

3-1.2 Performance of the IMS Ion Gate: A Simple 2-Wire vs. an Interleaved 9-Wire Arrangement

Two ion gate designs were tested during the development of the instrument. The first was a simple, 2-wire "deflection" based ion gate, which was technically easier to construct and operate. The basic premise of a 2-element ion gate is to deflect the ion beam from entering the drift cell between IMS measurement events, thus the ion beam is passed between the two wires. Since the entrance to the mobility cell is defined by a small aperture, only a minor deflection of a focused ion beam is necessary to prevent

transmission into the IMS, and so it follows that the 2-wire ion gate should be more than sufficient.

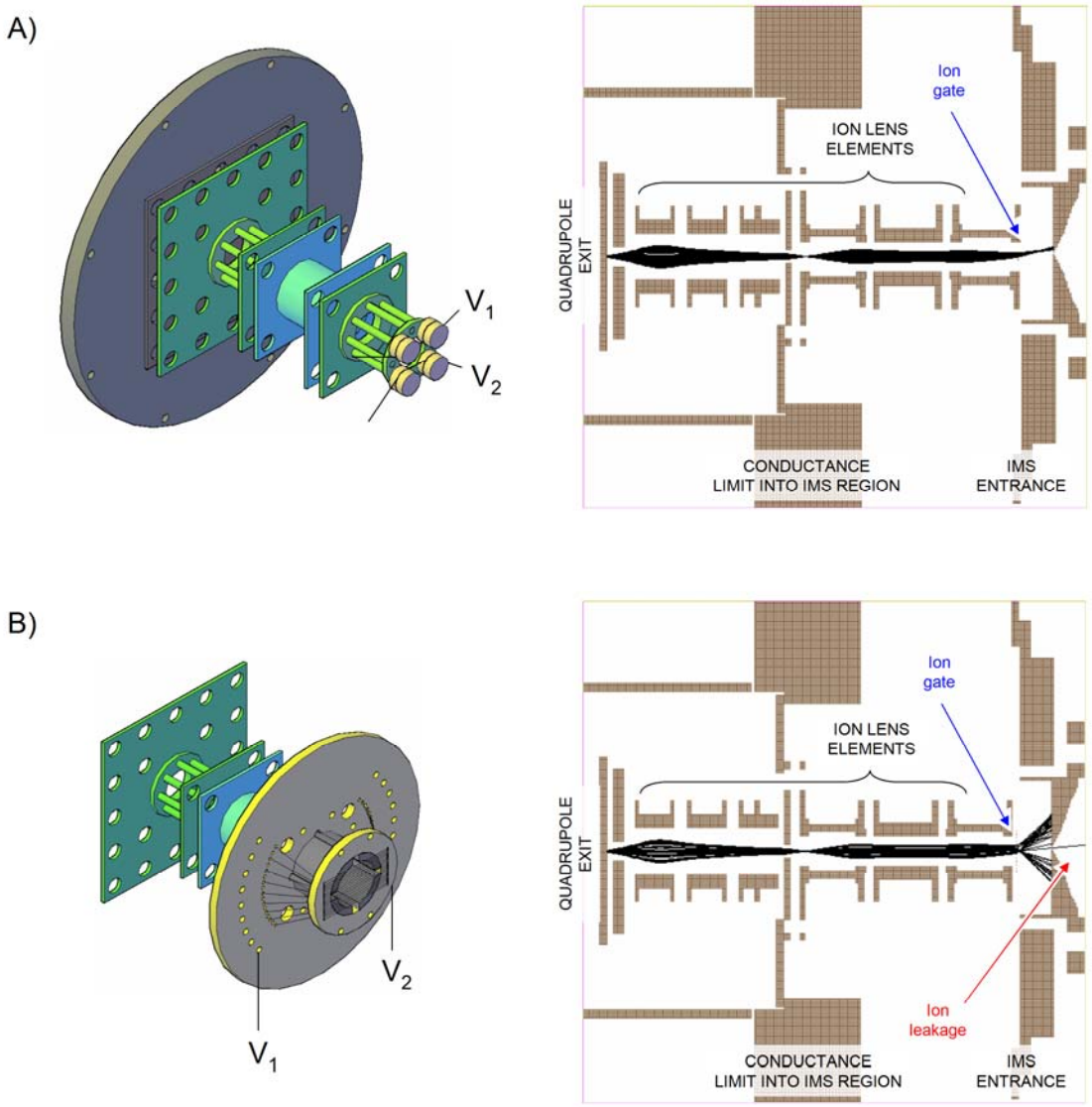

Figure 40 – Schematic and simulations of the two ion gates developed. **A)** The 2-wire ion gate design effectively deflected the ion beam from entering the drift region aperture in the simulations. The potential difference across the wires is simulated here with 20 V. **B)** The 9-wire design required somewhat higher potentials to effectively block ions from entering the drift region, here simulated with 40 V wire to wire difference. The interleaved gate also displayed some amount of ion leakage due to the multiple deflected ion trajectories at each wire pair. Simulation results suggest that the 2-wire design will gate ions more efficiently.

Figure 40 contains CAD generated illustrations and ion trajectory simulation results for the two ion gates developed for the cryogenic IMS instrument. Ion trajectory simulations were conducted with SIMION 8.0 utilizing a properly scaled potential surface geometry imported directly from the CAD coordinate file. Simulation results favor the 2-wire over the 9-wire design with respect to how efficiently ions are blocked from entering the drift region defined by a small aperture (600 μm actual, 1 mm simulated). In the 2-wire simulations, a potential difference of 20 V across the wires effectively diverted a 20 eV beam of ions. The simulation (**Figure 40A**, right) maintained one (bottom) wire at ground (ion beam reference) potential while biasing the bottom (top) wire to +20 V. For the 9-wire simulations, a potential difference of 40 V was necessary to minimize the number of ions which entered the drift region *via* the aperture. In this simulation (**Figure 40B**, right), one set of wires was maintained at ground while the other was biased to +40 V. Some ion leakage into the drift region was still observed for the 9-wire design, even at this higher blocking potential. This results from having a series of deflector electrodes which results in a distribution of ion trajectories that "fan" across the entrance aperture, increasing the simulation probability that one or more ions will be transmitted through.

Both ion gate designs were constructed and tested with experiments. While both ion gates effectively blocked ions at relatively low (<60 V) potential differences across the wire elements, the interleaved ion gate (9-wire) performed substantially better in terms of ion transmission characteristics and ion pulse generation. Results from measuring ion arrival times pulses in vacuum using these two ion gates are contained in

Figure 41. The 2-wire gate was characterized as generating ion pulses which had a longer rise and fall time and significant tailing of ion signal (**Figure 41A**) which is suggestive of ion leakage during the gate off event, presumably due to space charge initiated penetration of ions as they bunch at the front of the gate [374]. In contrast, the 9-wire ion gate generated much sharper ion pulses that were closer to the ideal (square pulse) shape (**Figure 41B** and **C**). Ultimately this improved ion pulse shape will allow for a higher repetition rate on the ion gate and translate into better resulting ion peak shapes in the IMS experiment. The reasons why the interleaved ion gate performed better experimentally than predicted by simulations may be a result of the experimental ion gate operating in the presence of gas collisions (at the IMS entrance), which would serve to dampen deflected ion trajectories. The observed performance differences could also be a result of the 2-wire gate performing worse than designed, owing to the use of ceramic wire supports which are in proximity to the ion beam. Ceramic is known to be prone to surface charging effects when subjected to charged particles, and at least some characteristic "charge buildup" effects were observed during the operation of the 2-wire gate, most notable an unstable ion signal subject to rising and falling responses on the detector. In either case, the interleaved ion gate was utilized for all experiments described in this dissertation.

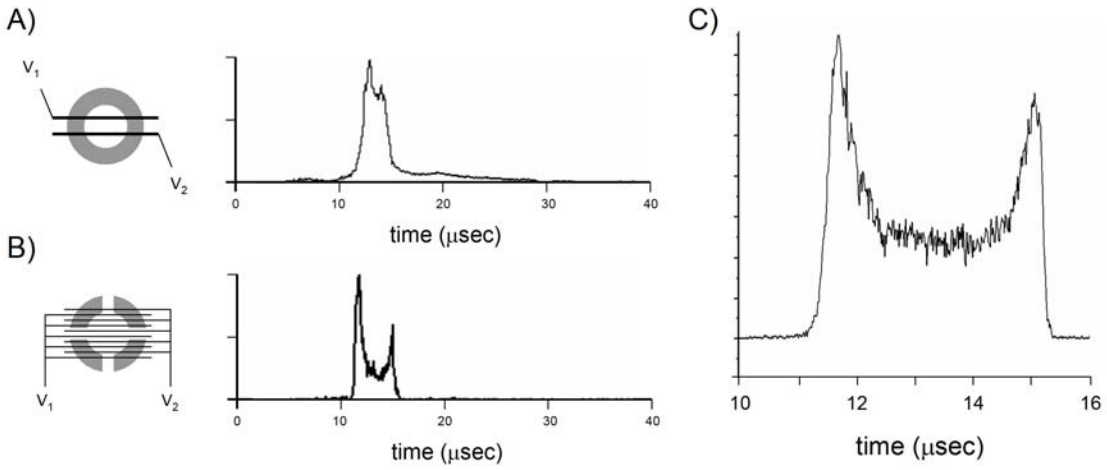

Figure 41 – Performance data for the 2- and 9-wire ion gates. **A)** The 2-wire ion gate configuration and resulting arrival time pulse of a packet of ions. The pulse is characterized with relatively slow (>500 ns) rise and fall times and tailing due to ion leakage. **B)** The interleaved 9-wire ion gate configuration and resulting ion pulse shape. Here, rise and fall times are much more succinct and a definitive bimodal distribution is observed in the ion distributions. **C)** A scaled time axis for a typical arrival time distribution generated with the interleaved wire ion gate, showing clearly the bimodal ion distributions and sharp rising and falling edges. Ion distributions remain constant at the center of the pulse. Both pulses were obtained in current monitoring mode over a series of ion gate pulses (~100 or more). Refer to text for an explanation of the pulse shape.

An interesting feature of the ion gate generated peak shapes in **Figure 41** is the high signal amplitudes at the front and back of the peak. This is a reproducible phenomenon and it is suggested that this is an experimental artifact resulting from ion bunching during the rise and fall pulse of the ion gate. The reason why a greater distribution of ion signal appears at the start of the pulse may be a result of the greater penetration of the stop potential towards the front (ion source) end of the gate rather than the back (ion mobility) end. Field penetration is expected to be dampened at the exit of the ion gate due to the entrance aperture of the IMS, while at the front of the ion gate, ions see the retarding field at a further distance and thus have a "temporal head start" in terms of bunching. This is to say, ion bunching is more prevalent for ions approaching

the ion gate than leaving it when the stop potentials are applied. Such observations provide insight into ion optical designs which rely on ion bunching or chopping, such as accumulation ion optics.

3-1.3 Ion Injection Energy into the IMS: Considerations for Ion Activation and Drift Region Penetration

The MS-IMS-MS instrument configuration utilizes two small apertures at the entrance and exit of the IMS to define the elevated pressure of the drift region while maintaining the vacuum in the bracketing MS components. As a consequence, the two apertures serve as gas leaks for the IMS drift chamber, characterized by a jet of gas leaking from both the entrance and exit of the drift cell. In order to transfer ions into the entrance aperture, the electric field must exert a force on the ions that is in excess of the force experienced by the ion-neutral collisions. This type of injection ion drift cell configuration has been utilized in previous work and it was recognized early on that a balance must be struck between high injection energies for ion transmission and low injection energies for minimizing ion activation processes (*e.g.*, ion dissociation and exothermic reaction chemistry) [375]. For example, flow tube experiments have recognized that ion injection energies below ~30 eV are necessary to prevent activating ion reaction channels which would otherwise deplete the ion of interest [376]. Kemper and Bowers noted that deactivation of electronically excited metal ions occurred if the injection energies were above ~5 eV. In their injected ion MS-IMS-MS experiment, the first stage MS was a double focusing sector instrument, requiring several thousand eV of

kinetic energy for the beam which had to be decelerated to 2-3 eV while maintaining spatial focus, which by all accounts is impressive [146]. Clemmer and coworkers have purposely utilized high injection energies (80-200 eV) in an injected ion drift tube IMS configuration for ion dissociation and structural reordering experiments [377].

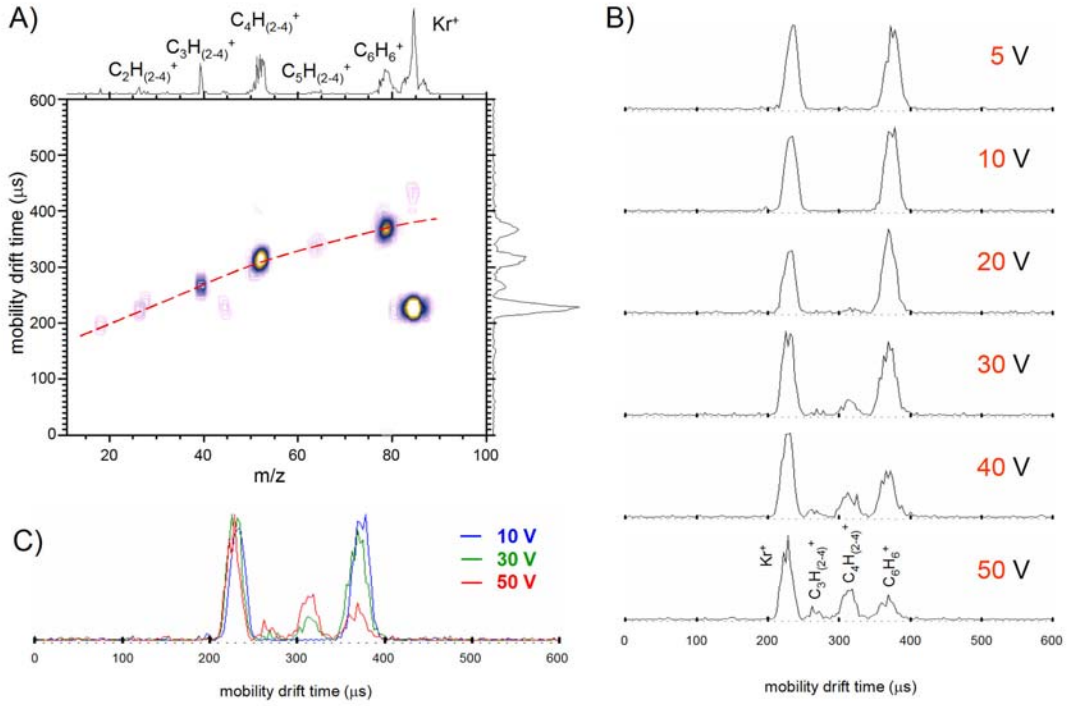

Figure 42 – Spectra of a benzene/krypton sample mixture demonstrating energy limitations for ion injection. The quadrupole is set to inject only ions of these two masses into the IMS **A)** 2D mobility-mass plot with an ion injection energy of 50 eV. The spectrum is characterized by a series of fragment ions resulting from the collisional activation of the benzene cation. A line illustrating the hydrocarbon trendline is drawn to help guide the eye. **B)** Mobility arrival time traces of the same krypton/benzene sample taken at various ion injection energies from 5 to 50 eV. Fragment ions appear above 20 eV. **C)** Overlaid mobility traces at 10, 30 and 50 eV injection energies. A small but measurable shift in arrival time is observed as the injection energy is increased resulting from ion penetration into the drift region. Higher injection energy represents a shift of ~5 μs at 50 eV as compared to 10 eV. Experimental conditions for above spectra are as follows: 34 eV electron ionization, 10 μs ion gate, 7.5 $V \cdot cm^{-1}$ drift field in ~1.5 torr helium gas at 298 K.

Figure 42 contains experimental data for a mixture of benzene and krypton, which are two chemically different ions with similar masses (nominal masses of 78 and 81 m/z, respectively). In these experiments, only the two parent ion masses are injected into the IMS, achieved by tuning the quadrupole to a wide mass window about m/z 80. Of immediate note is the markedly different ionic mobilities of these two ions in the 2D contour plot (**Figure 42A**). The red dotted line represents a hydrocarbon trendline and can be used to aid in differentiating chemically dissimilar ions in the 2D analysis. Several fragment ions also appear in this spectrum resulting from collisional activation of benzene which occurs at this high injection energy of 50 eV. The effect of increasing ion injection energy on collisional activation is apparent when comparing the one dimensional mobility traces of data taken at various injection energies (**Figure 42B**). At 20 eV the fragment ions begin to appear in the spectra and increase in abundance as the injection energy is increased. **Figure 42C** contains three overlaid mobility traces taken at 10, 30 and 50 eV of ion injection energy. The center of the arrival time distributions in the 50 eV spectrum is offset by ~5 μs sooner as compared to the 10 eV spectrum. This situation occurs when high translational energy ions penetrate into the drift region before thermalization. The result is that ions start at some distance into the drift region, effectively shortening the drift distance and leading to faster arrival times than what would be measured at the ideally low injection energy situation. Bowers noted that ion penetration reduced their drift cell length by ~3% for the worst experimental cases with their short length (4 cm) drift cell [366]. While ion penetration considerations are not important for qualitative comparisons of mobility data, this effect must be accounted for

if quantitative information (*e.g.*, reduced mobilities and collision cross sections) are desired from the measurement.

3-1.4 Calibration of the Manometer Pressure Reading for the IMS Drift Cell

Inherent to nearly all ion mobility instruments is a discrepancy between the measured drift region pressure and the actual pressure of this region. This comes about because most often the pressure gauge is measuring a volume restricted by a conductance limiting tube that connects to the main drift chamber, creating a two vessel system. Only if the temperature and pressure in both volumes (the gauge volume and the drift region) are at equilibrium will the pressure measured by the gauge be accurate. Temperature variations between the drift cell and the pressure gauge introduce thermal transpiration effects whereby a pressure differential is established between two unchanging volumes of different temperature (*i.e.*, Gay-Lussac's Law). This results in an increasing discrepancy between the gauge reading and the actual pressure as the temperature of the drift cell is decreased, necessitating a pressure calibration methodology that spans across a wide range of temperatures.

The design of a correctly configured pressure monitoring system can greatly facilitate accuracy in the measurement results. A pressure gauge which is capable of measuring an accurate pressure independent of the type of gas is also a requirement. Mechanical pressure gauges such as the bourdon and capacitance manometer are appropriate gas-independent devices. The preferred drift cell design suspends the

pressure gauge directly into the drift cell volume or at least prevents choking the gas conductance between the pressure measurement volume and the drift cell volume.

Neither preferred design was possible in the cryogenic drift cell constructed for this dissertation work due to the necessary enclosure of the drift cell within a dewar jacket. To facilitate pressure measurement, a capacitance manometer gauge was fitted to the drift gas inlet line outside of the vacuum system, representing a two volume system whereby the conductance is choked by the 6 mm diameter transfer line. Despite this unfavorable configuration, an accurate pressure can still be gained from the experiment if an appropriate calibration curve is plotted for pressure. The method is outlined below.

Calibrating the pressure in an ion mobility experiment requires that all other variables be known in the mobility relationships given in **Equations 1** and **2**, which are the mobility proportionality constant and the reduced mobility equation, respectively. By substituting **Equation 1** into **Equation 2**, expanding out terms and solving for pressure, we get the following expression:

$$P = 760 \cdot \frac{K_0 \cdot E}{v_d} \cdot \frac{T}{273.15} \tag{7}$$

Temperature (T) and electric field (E) can be measured directly. Drift velocity, v_d, can be calculated from the measured arrival time, corrected against the flight time outside of the drift region (see **Section 3-1.5**). The calibration ion's reduced mobility, K_0, is obtained from the literature for the (approximate) conditions of the experiment. Because exact experimental conditions are not known, specifically the pressure, it is desirable to choose a calibration ion with a reduced mobility that changes very little over

a wide range of *E/N*. The noble gases are an excellent choice; the reduced mobilities are relatively constant over a range of both *E/N* and temperature and these gases are appropriately volatile to facilitate sample introduction and pumping away of unionized neutrals. **Table 10** lists some reduced mobilities of select noble gas ions in helium at various fields and temperatures.

Table 10 – Reduced mobility values (K_0) for several noble gases at 300 and 80 K. Data is in helium drift gas for various field strengths. Data for two temperatures are shown. The highest field strength in the table (30 Td) represents an inflection point for most all atomic ions regarding their mobility values and is generally considered the limiting value for low field conditions. Data is taken from the ion mobility data published in the *Atomic Data and Nuclear Data Tables* [150-153].

E/N	Ne^+		Ar^+		Kr^+		Xe^+	
[Td]	300 K	82 K	300 K	82 K	300 K	80 K	295 K	82 K
3	20.3	--	--	--	--	--	16.5	17.5
4	20.3	--	--	--	--	17.7	16.5	17.6
5	20.3	19.0	20.8	18.8	18.6	17.8	16.5	17.7
6	20.3	--	--	--	18.6	17.9	16.5	17.8
8	20.4	--	--	--	18.6	18.0	16.6	18.0
10	20.5	19.0	21.3	19.1	18.6	18.2	16.7	18.2
12	20.7	--	--	--	18.6	18.4	16.7	18.4
15	20.9	19.1	21.5	20.0	18.6	18.8	16.8	18.6
20	20.9	19.5	21.6	21.2	18.6	19.6	16.8	18.8
25	20.9	20.1	21.4	--	18.6	20.4	16.6	18.9
30	20.8	20.6	21.2	23.5	18.6	20.7	16.2	18.8

As can be seen from **Table 10**, all noble gas ion reduced mobilities below about 30 Td are relatively constant values, which is the defining characteristic of low field ion mobility conditions. Low field conditions in the experiment can be verified by measuring the arrival time at various electric fields (drift voltages) and determining which field gives rise to nonlinear behavior in the arrival times. This is the threshold for

high field for that particular ion. Prior to knowing the experimental pressure, a relative electric field axis of *E/N* (where *N* is arbitrary) can be used and the resulting plot compared directly against a plot of the reduced mobilities *vs.* field. Lining up the inflection points in each graph will reveal the actual field of the experiment, then a simple matter of back calculating the pressure from the number density using the ideal gas relationship. This is the first procedure which should be used to obtain a reasonable estimate for the actual pressure. Using this result, one can obtain a fairly accurate value for the reduced mobility and then use **Equation 7** to determine the pressure. Both pressure results should be near consistent, with the method utilizing **Equation 7** to be considered the more proper value.

The resulting plot from the pressure calibration method using **Equation 7** is contained in **Figure 43** for ambient and liquid nitrogen temperature data. While this particular correction is specific to the instrument used in these studies, the method is general. The trends depicted in **Figure 43** are also general—for a two volume system separated by a conductance limit the downstream pressure will not follow linearly with the upstream pressure, as gas equilibrium is weighted in favor of the larger downstream volume.

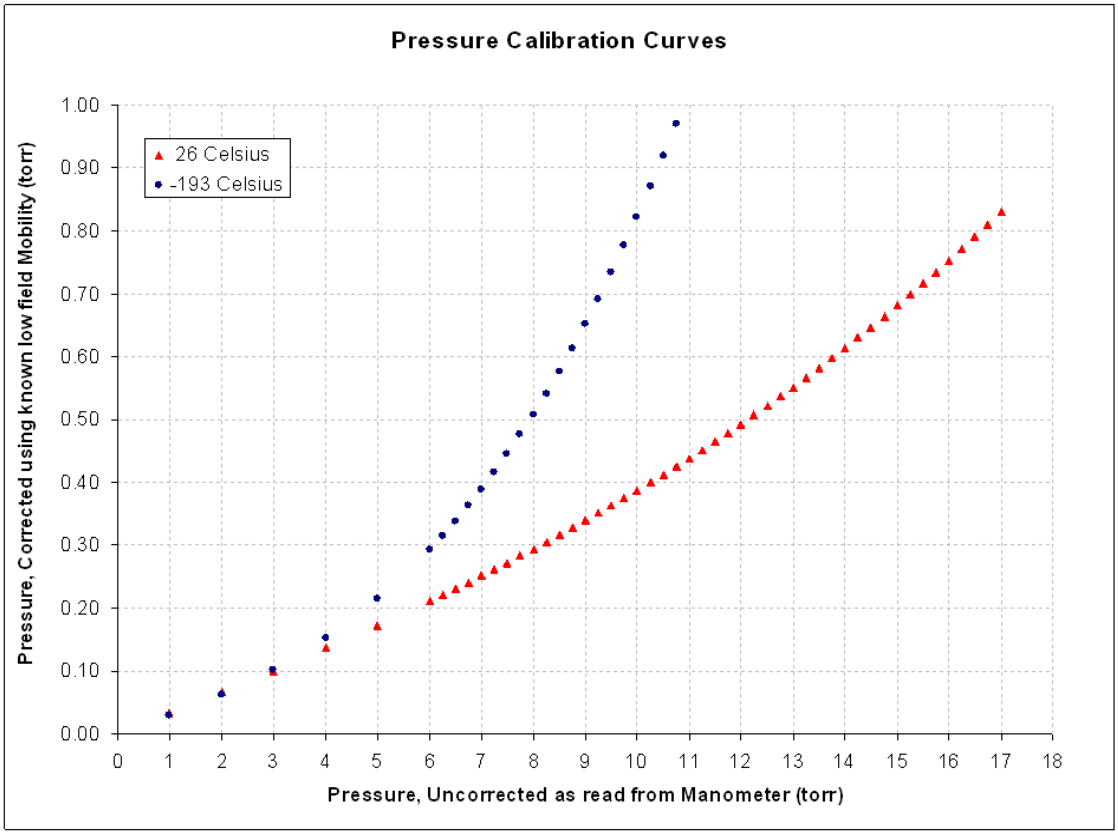

Figure 43 – Pressure calibration plot for 300 and 80 K manometer readings. Data trends for two temperatures (ambient and liquid nitrogen) are shown. Pressures at temperatures in between these two values can be directly extrapolated from the plot as pressure and temperature follow an ideal gas relationship. The plot was generated using the method described in the text.

3-1.5 Drift Time Correction for Ion Flight Time Outside of the Drift Region

In the ion mobility experiment described in this dissertation, a continuous ion beam is truncated into discrete packets of ions immediately prior to entering the drift region. This defines the start time of the experiment. Through the data interleaving process, the mobility arrival times are deconvoluted from the mass arrival times (refer to **Section 2-7.1**). This gives the arrival time distributions of ions from the start of the drift region to the ion extraction region of the TOF mass analyzer, which includes residence

time in the drift cell and flight time through the ion optics between the exit of the cell and the TOF. What is desired is the actual time that ions spend in the drift region[23]. While this time correction is not necessary for qualitative comparisons of drift spectra, accurate ion mobility constants (*K*) cannot be obtained without knowing the true drift time of ions. The preferred approach to obtaining the actual drift time is to use a two gate experiment, where one gate is at the front of the drift region and the other is at the back. By pulsing these gates in sequence and controlling the offset of this pulse, only ions which possess the same drift time as the offset time will be transmitted, and so the true drift time can be empirically measured. Alternately, the second gate at the drift region exit can be pulsed by itself to determine the flight time of ions once they leave the drift cell. Another common approach that has been used extensively in recent ion mobility research is to measure the arrival time of an ion at various voltages and plot the inverse voltage (*1/V*) as a function of the drift time. At low field, this will yield a straight line (refer to **Section 1-3.3**). The y-intercept of the fit will represent the time when the voltage is approaching a very large value, *i.e.*, when the ion's flight time through the drift region is dominated by the field and thus approaching zero. Consequently, extrapolation to the y-intercept will give the time ions do not spend in the drift region. Because the ion's flight time will have a mass dependence associated with it, this correction must be plotted for a series of ions and this non-IMS flight time correlated to ion mass to generate a correction plot. Fitting this plot to an exponential

[23] This is also an issue with IMS instruments incorporating an ion gate a distance away from the drift region entrance, such as LDI based IMS instruments which use the laser pulse for gating. In such instruments, the non-drift flight times must be accounted for at the front and back of the IMS region. This is commonly referred to as "end effects" [378].

will generate the proper flight time correction equation. Note that this mass-dependant flight time is inherent to any time correction and must be accounted for by measuring ions of various masses.

The voltage plotting method works reasonably well for larger ions in which a wide range of voltages can be sampled without introducing nonideal ion drift behavior (high field conditions), and is appropriate for IMS instruments where the non-IMS flight times are a significant fraction of the drift time, such as with higher voltage and/or shorter length drift cells.

Ideally, it would be desirable to construct and operate an IMS instrument where the non-IMS flight times are only a small fraction of the total measured time, such that the error in the experimentally measured mobility drift time is very small. The instrument in this work incorporates a long drift cell and examines ions using a very small electric field (<10 $V \cdot cm^{-1}$), resulting in measured drift times on the order of several hundred microseconds, and so the drift time errors are expected to be minor in the instrument used in this work. In some of the low temperature, low field experiments, ion drift times greater than 3 ms have been observed. However, to validate this presumption, a time correction method was developed.

A second gate was not built at the exit of the IMS described here, so the preferred two-gate method of determining drift times cannot be easily implemented. The approach taken here is to estimate the flight times of ions outside of the drift region using ion trajectory models. This was a preferred approach since an accurate geometric model of the instrument existed due to CAD development, and the previous modeling of ion drift

times had yielded reasonably accurate values as compared with experiment. An additional consideration was that such calculations could be conducted across a large data set of ion masses, yielding a time correction equation that could be utilized for all experiments conducted.

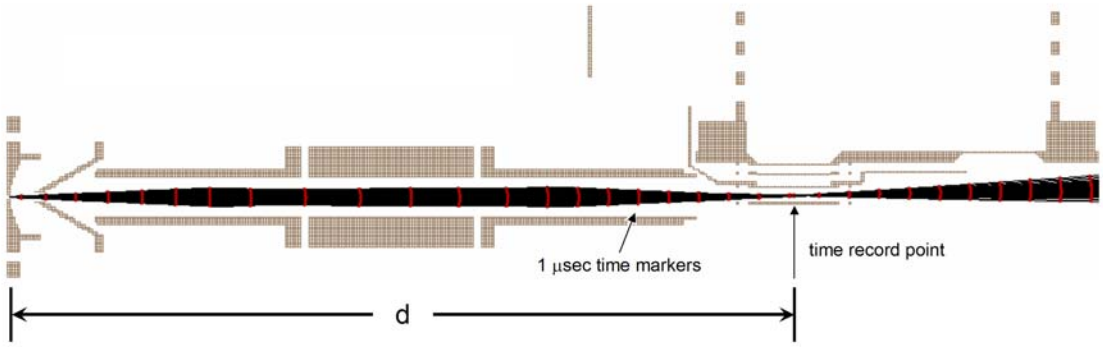

ion mass [amu]	flight time [μsec]	ion mass [amu]	flight time [μsec]
12.00	10.64	50.94	21.92
18.01	13.03	58.10	23.40
20.18	13.80	62.07	24.18
28.01	16.27	78.11	27.13
32.00	17.38	83.80	28.12
39.95	19.42	131.29	35.20
44.01	20.39		
47.87	21.27		

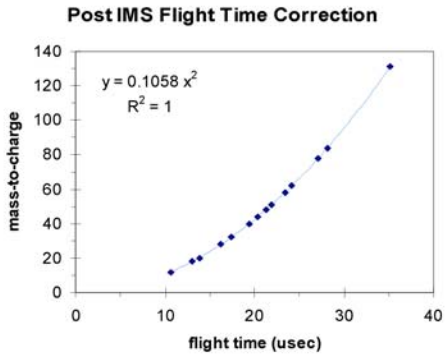

Figure 44 – Method used for determining the flight time of ions outside of the drift region. Ion trajectories were simulated using ideal potentials which are close to those used experimentally (at top). 100 ions of various m/z values were modeled and their flight times recorded and averaged between the distance from the drift cell exit to the center of the TOF ion extraction region. The tabulated flight times (bottom left) were plotted and fit with an exponential (bottom right) which gives a correction equation that can be applied to any ion mass of interest.

Details of the time correction trajectory modeling methods are contained in **Figure 44**. An ensemble (100) of ions were started at a point representing the exit of the

mobility cell and given an initial kinetic energy of >1 eV. A potential drop of 35 V accelerated ions through the first ion optic and focused the ions to a point representing the center of the ion extraction region of the TOF. The front and back ion lens element was kept at the same potential, so the beam kinetic energy was defined as 35 eV laboratory frame. Optimal focusing potentials were used in the model. The ion flight times of each ion was recorded between the start and the center point of the extraction region. Each set of 100 ions were averaged into a mean flight time. This procedure was repeated for a series of ion masses, tabulated in **Figure 44, bottom right**. This tabulated data was then plotted and the modeling results fitted to an exponential which represents the correction. The perfect fit of the trendline (R^2=1) is indicative of the relationship between mass and time-of-flight. This correction equation is convenient as it can be used for any ion mass being studied.

Limitations in this approach are primarily in the potentials modeled and any collisional dampening that ions may experiments in the region immediately following the drift cell. A negligible propagating error is also present in this method. Changes in the lens potentials will alter flight times, however under the ideal focusing conditions as depicted in **Figure 44**, the ratio of these potentials should be nearly the same across a range of absolute voltage values, that is, the focusing of an ion lens will scale with the energy of the ion beam, which is kept the same in all experiments. The second source of error, ion-gas collisions, is not expected to be significant. The experimentally measured pressure in the region immediately following the drift cell is in the mid 10^{-4} torr range at

~2 torr in the drift region, which represents a mean free path of ~30 mm[24], less than the distance ions transit as they leave the drift cell and enter the focusing ion optical region of the TOF (beyond the skimmer cone assembly). Although the ion gauge pressure measurement is taken several centimeters from the IMS exit, it is reasonable to assume that ions experience very few collisions as they are traversing this interfacing region.

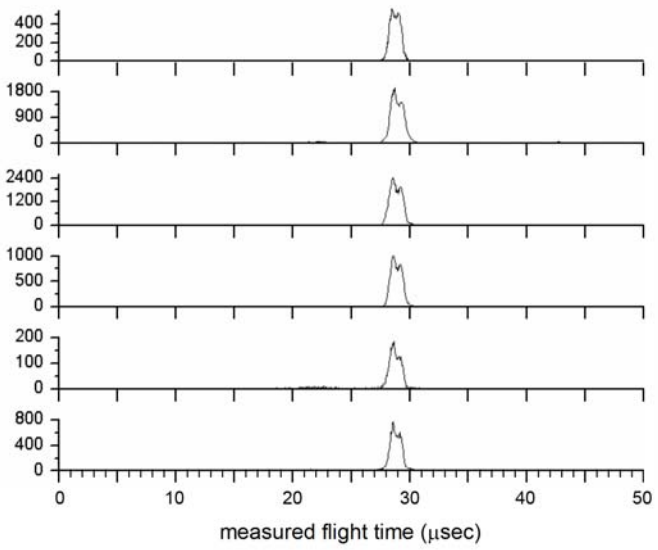

$$t_{corrected} = \frac{d_{post-IMS}}{d_{total}} \cdot t_{measured}$$

measured flight time [μsec]	correction factor (d_{IMS}/d_{total})	post-IMS corrected flight time [μsec]
28.03		15.25
28.02		15.24
28.04	X 5.44×10^{-1} (54.4%)	15.25
28.02		15.24
28.03		15.25
28.01		15.24

Figure 45 – Empirical method for estimating the flight time of ions outside of the drift region. Left, five arrival time distributions of argon ions from the ion gate to the on-axis detector. The bimodal characteristics of the peaks are a reproducible ion bunching artifact of the ion gate on either side of the distribution. Right, the equation used to weigh the measured arrival times against the time spent only in the post-IMS region, using a distance ratio, which assumes a constant ion velocity in both regions. The tabulated results are at bottom, yielding an average non-IMS flight time for argon of ~15 μsec. Distances used in the correction factor are: $d_{post\text{-}IMS} = 36.78$ cm, and $d_{total} = 67.61$ cm.

A relatively simple test to validate these results is to evacuate the drift region and measure the flight times of ions in vacuum from the ion gate to a detector (or TOF

[24] Mean free path calculation utilizes an argon-helium collision diameter at room temperature. The mean free path decreases ~1 cm for every 100 degree drop in temperature due to the increased gas density at constant pressure conditions.

extraction region). Such a test will give the total vacuum flight time of an ion, which will approximate the flight time outside of the drift region if the average kinetic energy of the ion beam is maintained to that of the gas filled drift cell experiment. This flight time can be further refined by weighing it against the ratio of the distance representing the post IMS length over the total flight length. Assuming constant velocity, which is valid under these experimental conditions, the resulting product will be indicative of the post IMS flight time only. Results from this kind of vacuum flight time treatment of the drift time correction is contained in **Figure 45**. Argon ions were injected through the drift region at vacuum and resulting arrival time distributions recorded on the on-axis detector. An average of five consecutive experiments weighed against the residence time of ions in the post-IMS region yields a post-IMS flight time of ~15 μsec. This value is lower than what was predicted by ion trajectory simulations for argon (m/z 39.95) by ~5 μsec, however this estimate is close enough that we can assume our trajectory modeling method is reasonable. Additional data points at different m/z values can be taken to lend more statistical weight to this correction, but since quantitative information is not sought out in the experiments conducted herein, such an experiment was not undertaken.

3-1.6 Time-of-Flight Mass Resolution and Sensitivity Tuning Strategies

While it is desirable to operate the mass spectrometer in terms of the highest mass resolution performance and the greatest ion sensitivity, most always optima for each performance metric do not overlap, and so a compromise must be made in one or

the other, or both to achieve an acceptable level of performance for the spectrometer. Mass resolution is our primary concern, since if ions cannot be mass resolved, then they cannot be mass identified. Numerous experimental parameters will influence the observed mass resolution, however it is preferable to narrow down which parameters will affect the performance the most, and begin with tuning these. The mass resolution depends primarily on achieving optimal space-focus plane coincidence of ion distributions to the detector during the TOF measurement event. Recall from Section 2-6.4 that the space focus plane can be adjusted by varying the field in either of the two regions of a two-stage TOF. For this and most TOF instruments, adjusting of the field in each stage can be achieved by adjusting the applied voltage to the PUSH and PULL electrodes. Since we are utilizing a biased TOF, we can also adjust the LINER voltage to tune the second stage region. It is also important to account for the DC offset when using an AC-coupled circuit for pulsing a biased electrode. With this in mind, one way to tune the TOF mass resolution is to select a set of reasonable values and create a tuning grid of the data. This approach is contained in **Figure 46**. An appropriate analyte is chosen for the tuning experiment, conveniently the analyte being studied, but also a suitable calibrant can be used which possesses an appropriate mass to be resolved. In **Figure 46**, krypton is chosen as it has a mass which is close to the mass resolving limit of the TOF (~100). Krypton and the other noble gases are also useful for such experiments, as they can be readily introduced into the ion source at a stable pressure and do not contaminate components of the vacuum system.

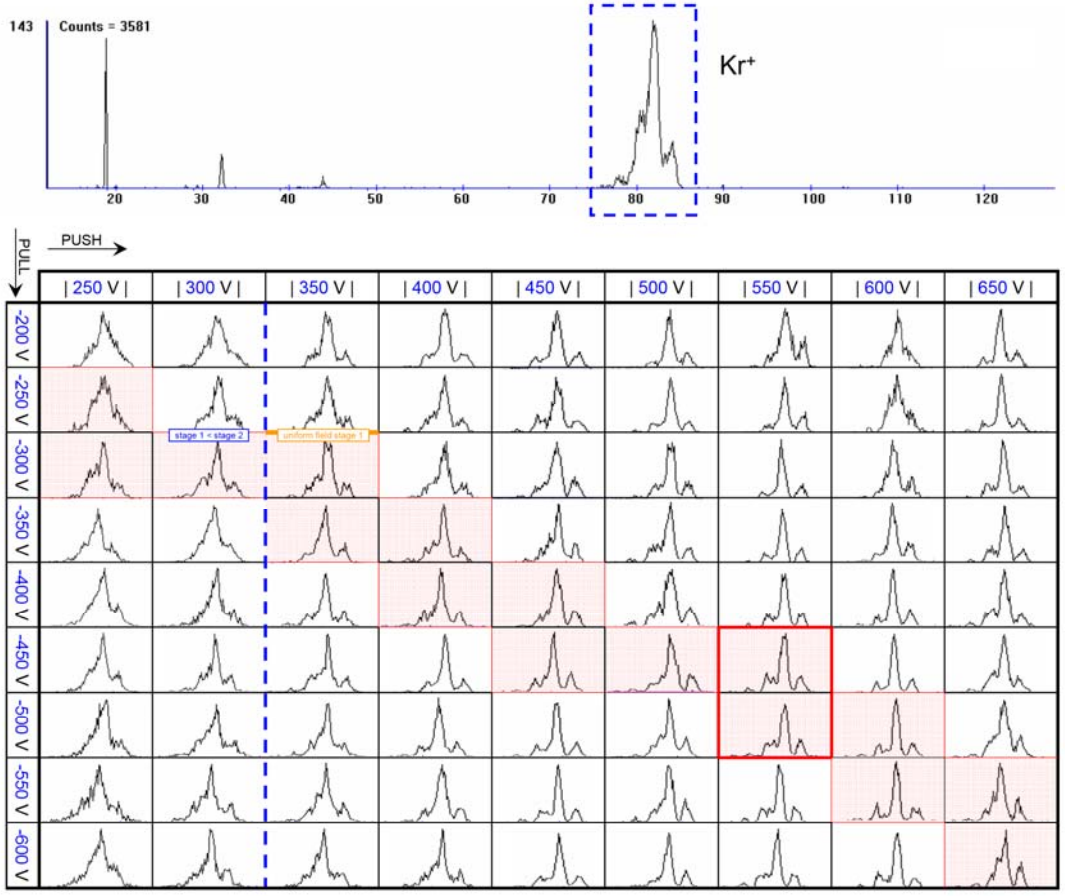

Figure 46 – Method for optimizing mass resolution using a tuning matrix. At top, the mass spectrum of krypton using a "best guess" as to the tuning parameters. Bottom, a matrix representing the results of varying the two most influential tuning parameters for mass resolution, the first and second stage fields of the ion extraction region. The PUSH plate potential is along the x-coordinate and the PULL electrode potential is on the y-coordinate. The red shaded boxes represent the voltages which represent an equal electric field slope for the first region, which recall is truncated by the COMMON electrode. These potentials are also where the highest mass resolutions are observed. Data to the left of the blue dotted line represents the unfavorable situation where the stage 1 field is less than the stage 2 field which results in ions traversing an uphill potential and equates to poor mass resolution. Data representing the optimal mass resolution settings found in this particular example are outlined in red. Other matrices can then be constructed by starting with these optimal settings and choosing two more parameters, until the desired mass resolution is obtained.

As can be seen, this approach generates a large amount of data sets, but can be used as a comparative tool for determining in which direction to tune electrode potentials. Once a series of these grids are constructed, it is relatively straightforward to predict a set of parameters which will give a decent first approximation as to the optimal

mass resolution. There is, however, another method of approximating a reasonable first guess for tuning potentials settings.

In **Section 2-6.4**, we discussed how to use ion trajectory modeling to estimate the optimal focusing conditions and such methods give a good approximation to the potentials needed for high resolution, but in most cases tuning the instrument to these modeling result values will not yield the acceptable instrument performance. A practical tuning approach is to start with the ion modeling results and then tune in an iterative fashion, optimizing the value for one parameter at a time. While this method greatly limits the amount of time spent tuning the instrument, only a small number of the possible voltage settings are surveyed. Other more preferable voltage setting combinations are likely to be missed in this iterative strategy, however for the pragmatist, this is not a concern.

So far we only discussed the procedure for optimizing mass resolution. Optimizing for instrument sensitivity is much more straightforward. Once the range of settings that give acceptable mass resolutions are found, a semi-quantitative experiment can be conducted whereby spectra are obtained in a set amount of time for each experiment. After several experiments involving the adjustment of a single variable at a time, the ion counting statistics can be compared with one another to determine which settings result in the highest transmission of ions to the detector. Limitations in this approach stem from the stability of the static experiment parameters, and considerations for optimizing ion counts to a certain ion signal should be properly considered as relative abundances will shift somewhat on the extremities of settings for TOF analysis (*i.e.*, the

TOF experiment will discriminate m/z values to some degree). If a set acquisition time is established during the mass resolution tuning experiments, then one can use ion counting statistics along with the spectral features to simultaneous compare instrument resolution and sensitivity. This is a revealing experiment in that nearly always the highest resolutions are characterized by the lowest ion counting values, requiring a compromise to be made in one or the other area. This is why it is preferable to choose which figure-of-merit (resolution or sensitivity) to prioritize first.

It is instructive here to reiterate the hierarchy of settings which influence mass resolution as well as provide a list of optimal settings for this particular instrument. From experimental investigations the order is as follows from most influential to least: PUSH, PULL, LINER, DC offset correction, ion beam kinetic energy, TOF pulse width, TOF pulse frequency, ion beam optics leading to the TOF, and MCP detector gain. Optimal settings change with respect to the system under investigation, but current values are as follows: +520 V on pulser coupled to PULL, -800 V on PULL, -4500 V on LINER, +4 V offset on PUSH, 35 V beam kinetic energy, 0.45 μsec width, 70 kHz frequency, and 2000 V across the MCP assembly, respectively. The pulse is AC-coupled to the PUSH bias which is at ~100 V negative (same as the *einzel* lens float), giving a total PUSH potential of around 400 V. It is found that these settings work for a wide array of ion systems investigated. Biasing the DC offset on the PUSH slightly positive with respect to COMMON will increase ion transmission to the TOF and by the same respect decrease the mass resolution (too much however and ion leakage into the TOF will occur, evident by noncorrelated ion signal). Offsetting the DC in this manner

is a useful strategy if the mass resolution is more than sufficient and can be sacrificed for some gains in sensitivity.

3-1.7 Procedure for Initiating Ion Entrainment into the IMS Entrance Aperture

In the course of testing the parameters and limitations of instrument tuning, the author has developed a method of effectuating ion injection into the pressure filled drift region at low (<10 eV) ion injection energies. Low injection energies are crucial to minimizing ion heating effects which leads to accessing reaction chemistry and quenching of sensitive ion configurations such as metastable excited electronic states. This method is documented here with no phenomenological explanation other than speculative.

In the course of tuning the ion beam to efficiently inject into the narrow entrance aperture of the drift chamber, ion signal will drop substantially as the injection energy is lowered to the limit of 10 eV. This is a natural consequence of scatter losses due to ion-neutral collisions with the gas jet as ions approach upon the entrance aperture. Oftentimes, complete loss of ion signal is observed as the injection energy is lowered to 10 eV. The procedure which has been tried and tested for recovering ion signal involves initiating current-controlled gaseous breakdown within the drift chamber, localized at the entrance electrode. This can be accomplished by biasing the dewar chamber potential negative with respect to the positive entrance lens potential and monitoring the current on either supply until it begins to rise (in most experiments, between 10-15 μA of current during plasma formation). This will often accompany an increase in the number

of ion counts to the coaxial detector created as a result of charged species in the plasma. Incidentally, this same procedure can be used with the ion source off to determine the identity of impurities in the drift gas—mass analyzing (*via* the TOF) these ions formed from the discharge plasma in the drift region will reveal what species are inherently present in the chamber (see, for example, **Section 3-2.2**). The favorable result of this plasma formation at the drift cell entrance is a systematic increase in the ion counts to the coaxial detector, starting slow and gradually increasing as the plasma is maintained at constant voltage. This represents ions which now find their way into the drift region and can be successfully used to regain ion signal initially lost at the IMS entrance.

Two plausible explanations as to why ions find their way into the drift region during this plasma formation are presented as follows. It is possible that the plasma ionizes gas molecules at the entrance, which is immediately quenched by the neighboring electrodes, lowering the localized pressure at the front of the drift region. This would create a weak Venturi effect at the entrance aperture whereby the exiting gas jet is disrupted, and the force of electrostatics redirects ions into this "void" region. Once ions entrain into this void, the beam current stabilizes. The second possibility is that the localized ionized gas creates a negative potential with respect to the retarding potential of the lenses and entrance cup. This negative potential directs ions into the drift region and stabilizes the beam current. No experimental investigations were undertaken to validate either of these two hypotheses. They are documented here in hopes that future investigators might find such information practically useful.

3-2 Demonstrations of the Analytical Utility of the Cryogenic Mobility-Mass Spectrometer

Presented in this section are the proof-of-concept experimental data that demonstrates some of the analytical advantages of the cryogenic MS-IMS-MS instrument configuration.

3-2.1 Trendline Partitioning of Small Molecular Ions in the 2D IMS-MS Analysis

Low temperature aside, there is high utility in developing an ion mobility-mass spectrometer capable of direct (online) 2-dimensional analysis of small molecular ions. To date, there are few examples of a dispersive (TOF) IMS-MS instrument being developed for small ions. Two known exceptions include an ambient pressure IMS-TOF developed for drug and pesticide analysis [379] and an earlier cryogenic IMS-TOF constructed in our own laboratory for studying electronic isomers of small organic ions [61]. Nearly all IMS-MS systems which have been used to analyze small ions incorporated a quadrupole as the mass analyzer, as they readily couple to the back end of an IMS and can operate at elevated (10^4 torr) pressures. All modern dispersive IMS-TOF instruments are designed to investigate large, biologically relevant molecules and as such many do not possess the capabilities for small mass studies. For example, most all modern IMS instruments employ the use of focusing fields (*i.e.*, periodic focusing or RF ion funnels) to redirect ions which would otherwise be lost due to diffusion in the drift region. Such focusing fields are sufficiently strong to redirect ions possessing high moments of inertia, but inherently have a low mass discrimination effect, often as high

as 500 m/z and certainly discriminate ions <100 m/z [380]. Additionally, these modern IMS-MS instruments are not equipped with the proper ion source for such studies (*e.g.*, electron or chemical ionization). The trend away from fundamental ion studies is understandable: Small ions have been the focus of ion mobility research for well over 80 years, though only recently has technological advances made the use of fast time-of-flight analyses possible.

In the early literature, several reports focused on the ability (or lack thereof) to obtain mass information from ion mobility measurements [381,382]. Many manuscripts attempted to draw correlations between gas phase ion mobility and ion mass, but were only marginally successful, resulting in published mobility-mass (linear) trendlines that had a standard error as high as 20% [383]. This and the erroneous comparisons of IMS with chromatography and time-of-flight spectrometry eventually led to an unfavorable opinion of the IMS technique in regards to its analytical utility. This explains why for a period of almost 20 years (late 1970's to early 1990's), very little groundbreaking ion mobility research can be found in the literature. The failings of obtaining accurate mobility-mass trend correlations were a result of a poor understanding of the IMS technique and the nature of the data obtained, which was chemical specific. We now know several key pieces of information regarding the mobility-mass correlation i) mobility does not scale linearly with mass but rather is semi-logarithmic to account for enhanced gas-phase packing efficiency at higher mass, and ii) the mobility-mass correlation is similar for ions of similar chemical composition (*e.g.*, hydrocarbons, halides, proteins, lipids, etc.). On a narrow mass scale, the mobility-mass correlation can

be linearly approximated [98] and such trendlines have been used to differentiate large ion classes, such as lipids, proteins and glycans [21,42]. The author is unaware of a similar type of trendline correlation analysis being conducted for small ions, as few instruments exist to acquire data in the necessary 2-dimensional mode.

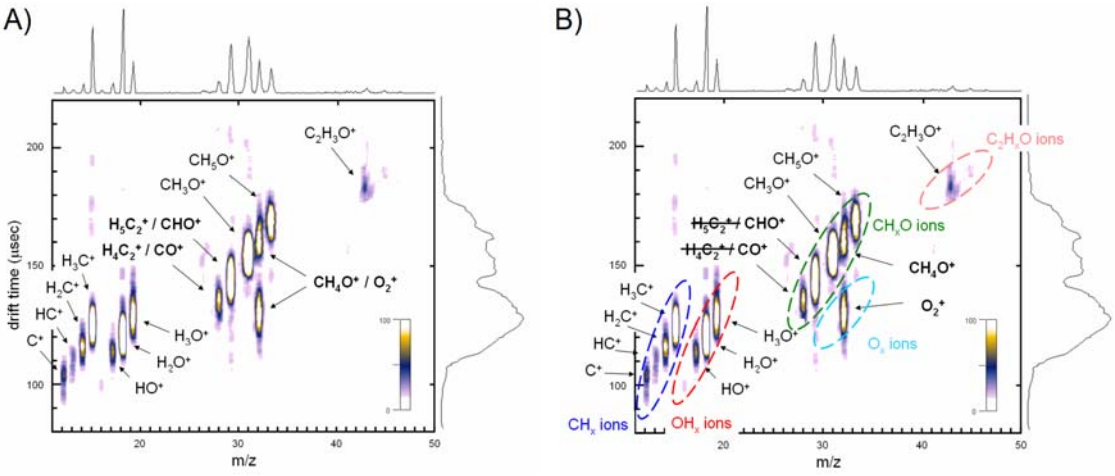

Figure 47 – Spectra of ethylene glycol demonstrating chemical specific trendline partitioning for small mass ions. **A)** 2D plot with ion assignments made based solely on the mass data. Several ion assignments (in **bold**) are ambiguous, with more than one chemical composition representing the ion masses. **B)** Ion assignments made using a trendline analysis of the data. Ions partition into trends based on their chemical composition, thus correct assignments can be made based on a combination of mass and trend information. Experimental conditions are: 70 eV electron ionization using a 10 µs ion gate, 10.5 $V \cdot cm^{-1} \cdot torr^{-1}$ in helium gas at 318 K for the mobility analysis.

Figure 47 contains a 2D mobility-mass spectrum of ethylene glycol taken at elevated (318 K) temperature. Higher temperature was used to generate a high vapor pressure of the sample and also demonstrates the high temperature capabilities of the drift cell design, which is not explored extensively in this dissertation. In **Figure 47A**, the ion assignments are made based solely on the mass data and using logical

combinations of the atoms C, H, O and N, the latter of which is not present in the sample but is considered for ions originating *via* atmospheric contamination. Using this method, most ion identities can be assigned, however there are at least three ion signals in the spectrum which can have more than one possible ion assignment (highlighted in bold in **Figure 47A**). An identification of linear mobility-mass correlations between ions of the same chemical classes greatly facilitates ion identification, as demonstrated in **Figure 47B** with the now unambiguous determination of all ions in the spectrum. It is interesting to point out that this trendline information is present in the data even for a relatively simple series of ions consisting of combinations of only three atoms (C, H, and O).

3-2.2 Condensation of Drift Gas Impurities Using Low Temperature IMS

Inherent in all small molecule ion mobility experiments is an ion-neutral interaction between ions and impurities present in the drift gas. Such interactions can be either long-term (sticky) or reacting. As discussed in **Section 1-3.2**, nonselective ion-neutral interactions give rise to broadening of IMS arrival time profiles and ambiguous product ions which can complicate experimental interpretation. Reducing or eliminating the effect of gas impurities is the primary motivation for mass selective ion injection experiments (**Section 3-1.1**) and low pressure IMS. While such strategies can be effective for understanding or minimizing experimental results which are characterized by ion chemistry, the most desirable strategy is to eliminate the gas impurities from the drift cell altogether. This can be accomplished by conducting the IMS experiment at a

drift gas temperature that is below the condensation temperature of the most invasive impurities, which in most all cases is moisture. **Figure 48** contains a 2D mobility-mass spectrum of ambient air, which is provided here to illustrate some of the common gas impurities encountered as a result of atmospheric contamination.

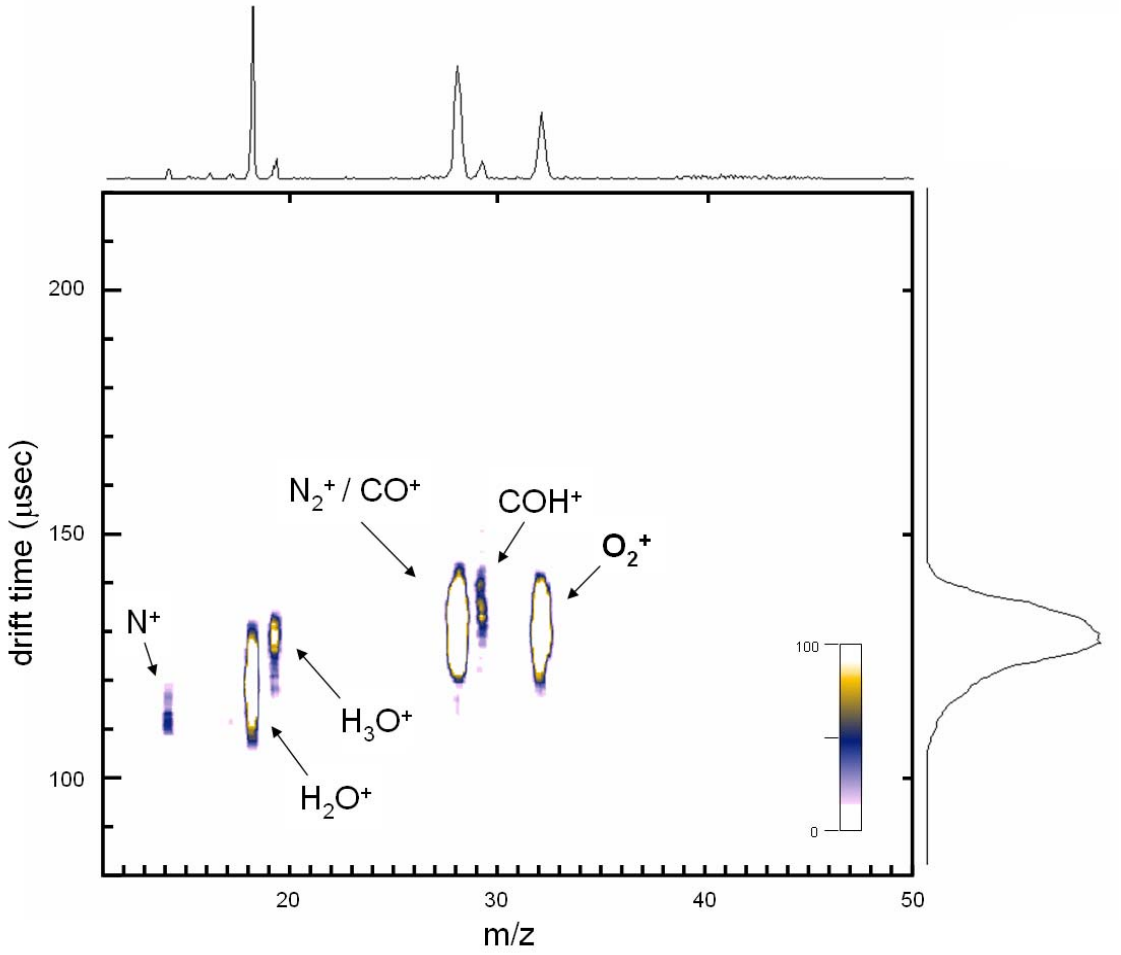

Figure 48 – Spectra of ambient air in helium drift gas. N_2, CO, H_2O and O_2 all are common gas impurities which can be introduced to the drift gas by atmospheric contamination. The rather poor mobility resolutions observed for this particular sample is likely a result of ion chemistry between these ions and other impurities in the drift gas.

A more direct means of determining the identity of impurities present in the drift gas is to initiate a sustained electrical breakdown in the drift tube and sample the afterglow of ions extracted from the plasma with the time-of-flight mass analyzer. Results from such an experiment are contained in **Figure 49** for ambient and low temperature drift gas. The ion source is turned off in these experiments and the ion gate is set to transmit all ions, resulting in no correlation information in the mobility dimension. Notable in the low temperature spectrum is the absence of water.

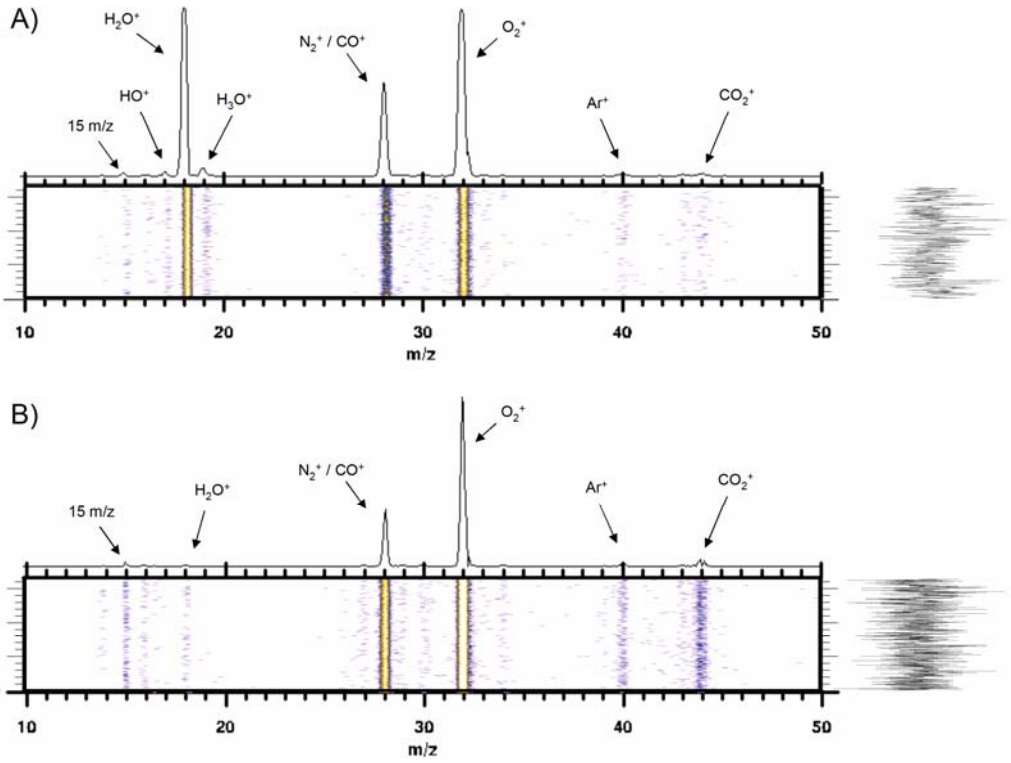

Figure 49 – Mass analysis of the ions formed from initiating gaseous helium breakdown in the drift cell at 298 and 185 K. The ion gate was left open resulting in no mobility correlation data. **A)** At room temperature, several atmospheric derived impurities are observed, including water, nitrogen, oxygen and carbon dioxide. **B)** At 185 K, water is virtually absent from the spectrum, causing other ions to appear more prominently, such as carbon dioxide. Variations exist between the spectra as they were taken on different days. Argon appears prominently as it was used immediately prior to acquiring these spectra. 15 m/z is likely CH_3^+ ionized from residual hydrocarbon sample in the gas.

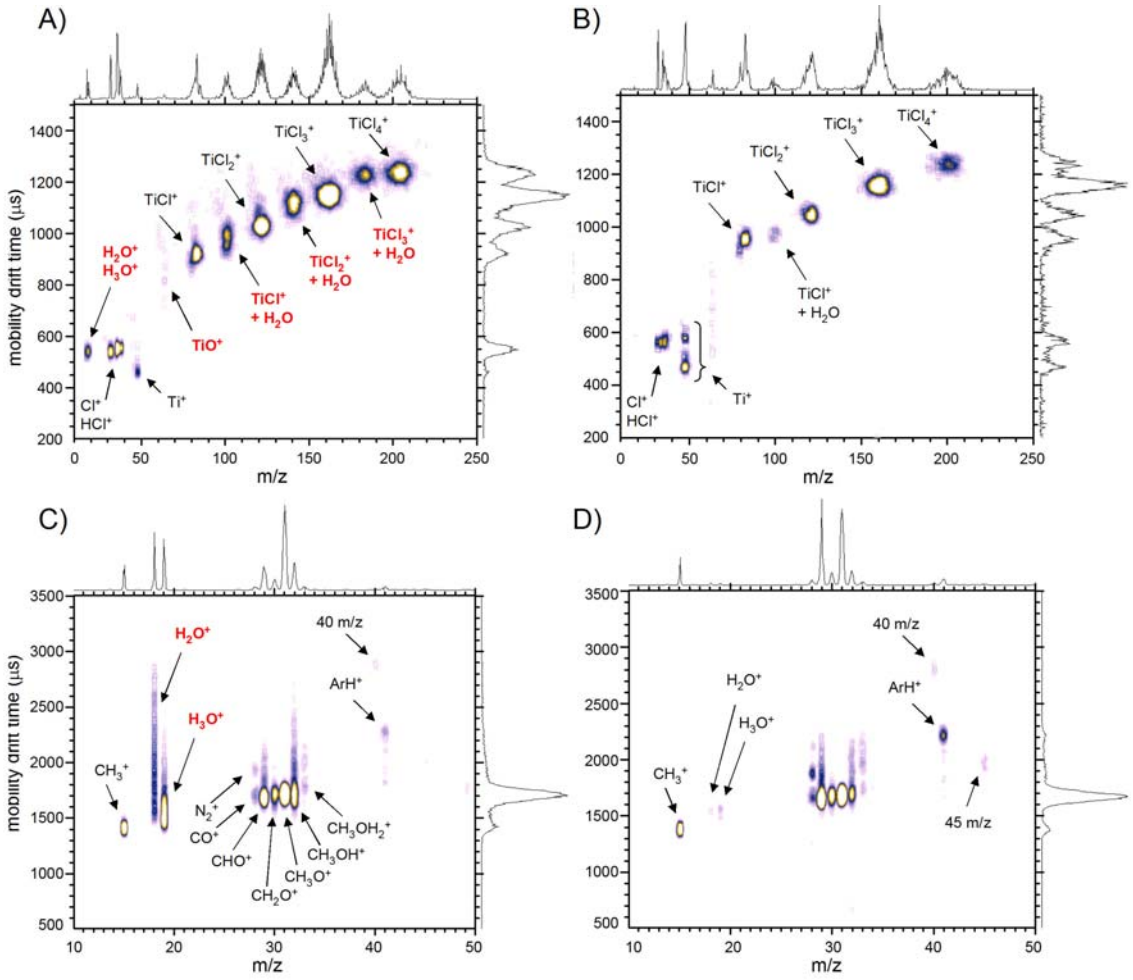

Figure 50 – Spectra of $TiCl_4$ and methanol demonstrating the utility of low temperature for removing drift gas impurities. **A)** The room temperature spectrum of electron ionized (60 eV) titanium chloride exhibits a series of ions derived from reaction chemistry with water impurities (highlighted in **red**) which are present in the helium drift gas. **B)** Reducing the drift gas temperature to ~270 K condenses water out of the drift cell and results in a less congested spectrum. In this case, removing water results in fewer ion channels and allows the bimodal distribution of Ti^+ to be clearly seen. **C)** The room temperature spectrum of methanol in argon drift gas shows a distinct smearing of the two peaks representing the water and hydronium cation, highlighted in **red**. **D)** At 270 K, water is condensed from the drift cell and these product ions are not present in the spectrum, resulting in several peaks appearing more prominently in the 2D plot.

Figure 50 illustrates two examples where ion chemistry with water can lead to complicated experimental results. For the case of titanium tetrachloride (**Figure 50A**), the room temperature spectrum is characterized by an abundance of water adducts with

the chloride clusters. This is a fast reaction process, evident by the fact that all water derived product ions appear on a mobility correlation with the chloride clusters. The water and hydronium ion both appear in the room temperature spectrum, which are common marker ions for the presence of moisture in the drift gas. By reducing the drift gas temperature to below the freezing point of water, in this case to 270 K (**Figure 50B**), water is condensed from the drift gas and virtually all product ions which were derived from water impurities is absent. The result is a less congested spectrum and reduced ion signal suppression, which in this example allows the bimodal distribution of the titanium cation to be clearly discerned. A similar case where water impurities cause spectral congestion is contained in **Figure 50C** for electron ionized methanol. Argon was used as the drift gas in this example. Here, the hydronium and water ions appear as a broad peak across the active window of mobility, indicating that the ion chemistry occurs across the entire drift cell. At 270 K (**Figure 50D**), water is no longer present and as a result, these product ion signals are absent, resulting in an easier to interpret spectrum whereby several ion signals are enhanced, notably signals for N_2^+, CO^+ and ArH^+. This is a general observation that ion signals are oftentimes enhanced at lower temperatures, presumably due to progressive condensing of various impurities as the temperature is decreased.

3-2.3 Ion Selectivity at Variable Temperatures

Recall from our introductory discussions that measured ionic mobilities are both field and temperature dependant (**Section 1-2.2**) and can vary quite substantially from

one chemical species to another. Thus, by varying the temperature, it is possible to optimize the peak separation of a given sample mixture.

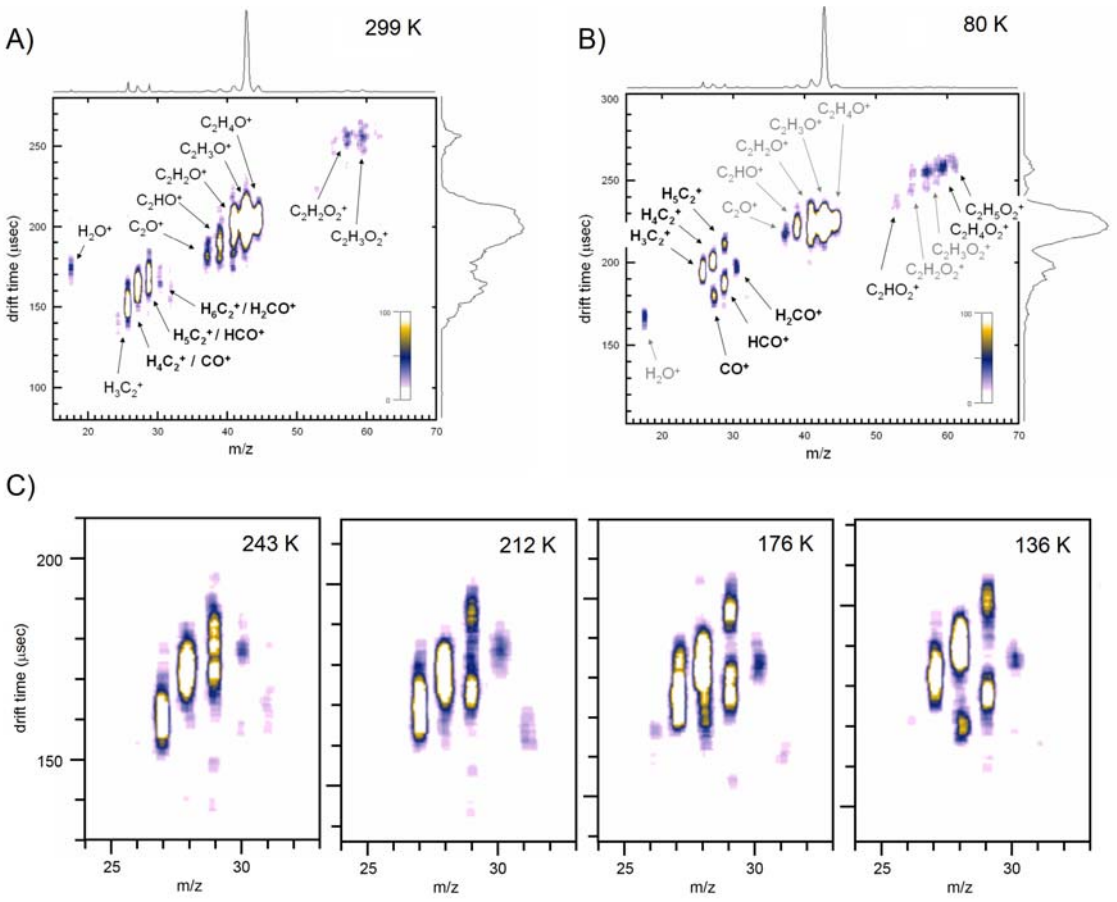

Figure 51 – Spectra of acetone demonstrating temperature dependant ion mobility selectivity. **A)** At ambient temperature, mass assignments can be made based solely on the predicted fragment masses, however some ion signals can represent more than one possible ion (highlighted in **bold**). **B)** At cryogenic temperature (80 K), ion signals become resolved due to differential ion selectivity at this temperature and ion assignments are easily made based on a trendline analysis. Additional ions also appear due to an enhancement of ion signal at low temperature as noted previously. **C)** Evolution of the resolution of the ion signals between 27 and 30 m/z as the temperature is lowered from 243 to 136 K.

An example of temperature selectivity is contained in the spectra in **Figure 51** for electron ionized acetone. At room temperature (**Figure 51A**), various ion signals are

observed which represent the fragment ions formed during ionization. Ion assignments can be made based solely on predicted fragment masses, however there is more than one possible fragment mass which exists for the ions at m/z 28 to m/z 30 (highlighted in **bold** in **Figure 51A**). As the temperature is lowered, the ambiguously assigned ion signals between m/z 28 and m/z 30 begin to resolve into distinct ion signatures, which can be seen in the spectra in **Figure 51C**. At the lowest temperature utilized in these studies (80 K, **Figure 51B**), two distinct ion trendlines appear in the low mass region and ion assignments can now be made with the aid of the trendline analysis method (**Section 3-2.1**). Additional ion signatures also appear at higher m/z and are labeled in **Figure 51B**. The appearance of additional ion signals at low temperature is a general result of condensing the drift gas impurities and eliminating possible reaction channels whereby these ions are either depleted or suppressed (**Section 3-2.2**). While in the acetone example the lowest temperature resulted in the highest resolution, this will not always be the case since ionic mobilities of two chemically different ions do not always diverge as the temperature is decreased.

3-2.4 Low Temperature Enhancement of IMS Resolving Power

Perhaps the most significant motivation of conducting low temperature IMS experiments is the gain in resolving power. Resolving power is a direct result of peak widths, which are governed in ion mobility by diffusional broadening. As developed in **Section 1-5.1**, at low field, the ion swarm equilibrates and diffuses along with the drift gas. Lowering the drift gas temperature has the direct consequence of narrowing the

Maxwell-Boltzmann distribution of gas velocities (**Figure 6**), resulting in less diffusional broadening of the ions over the same experimental time scale. Narrower arrival time profiles translate directly into a higher peak capacity in the mobility dimension.

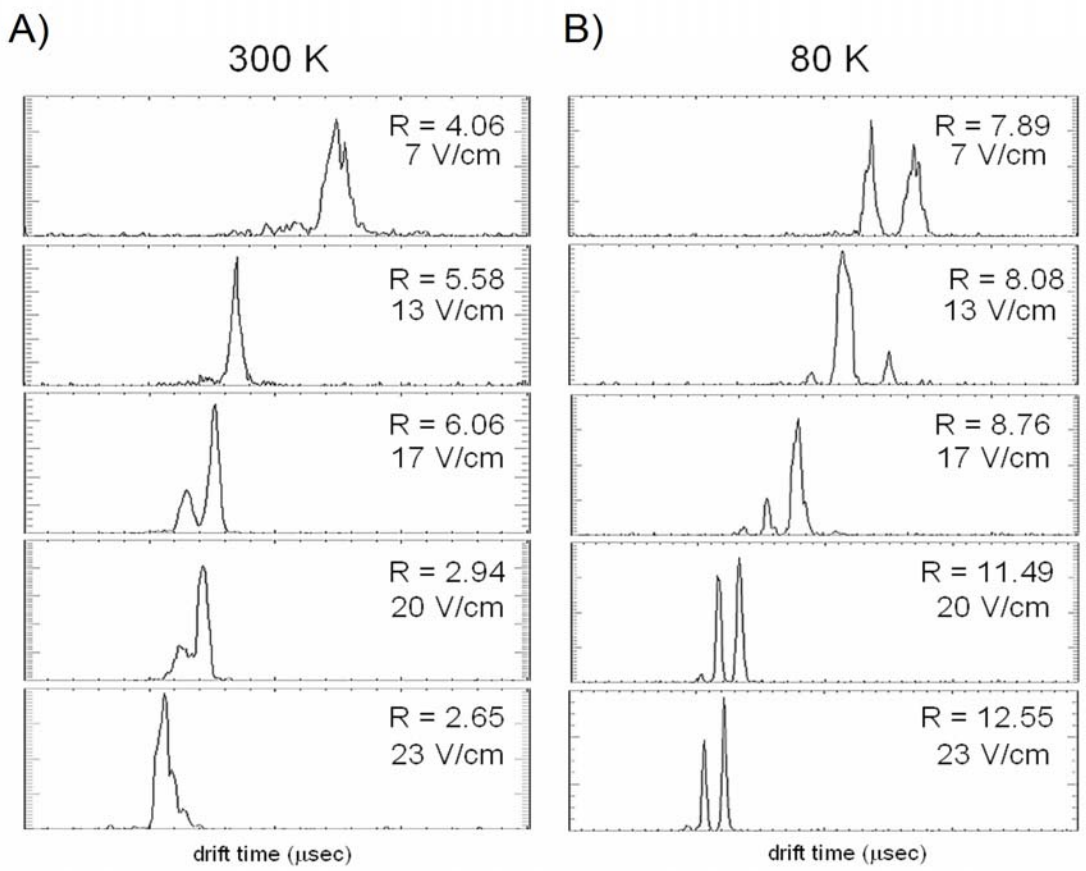

Figure 52 – Ion mobility spectra of benzene demonstrating enhancement of ion mobility resolving power at low temperature. **A)** A field experiment at room temperature whereby the field is increased (from top to bottom). Theory predicts that resolving power will improve as the drift cell voltage is increased, to the limit of low field conditions. Resolution of the fragment peaks is optimal at around 17 $V \cdot cm^{-1}$. **B)** The same field experiment conducted at cryogenic (80 K) temperature. Resolving power for even the low field case (top) is higher than the best case resolving power at room temperature, with two clearly resolving fragment ion peaks. As the field increases (top to bottom) the resolving power and resolution continue to increase and remains high even for the highest field utilized (23 $V \cdot cm^{-1}$). Mobility traces were acquired directly with the on-axis detector and as such does not have complimentary mass data. The drift gas is helium and the pressure is approximately 1 torr. This data represents the first low temperature data obtained on the cryogenic instrument.

An example of the resolving power improvement of low temperature IMS is provided in **Figure 52** for electron ionized (~120 eV) benzene and its fragments. In the left column of data (**Figure 52A**), the mobility traces from top to bottom represent an experiment whereby the electric field is increased. Theory predicts that the resolving power will continue to increase as the voltage across the drift cell increases as a result of less diffusional broadening, that is, less resident time of ions in the drift region. In the data, this trend is experimentally observed, as the single peak at the lower field (7 $V \cdot cm^{-1}$) is resolved into two distinct ion populations at a field strength of 17 $V \cdot cm^{-1}$. However, above 17 $V \cdot cm^{-1}$, the resolution becomes worse, signifying a change in ion elution profiles characteristic of higher field conditions. This is the opposite result of the ion selectivity example demonstrated in the previous section (**Section 3-2.3**). Conducting the same electric field scanning experiment at cryogenic (80 K) temperature (**Figure 52B**) results in a clear separation of two ion populations at the lowest field examined (7 $V \cdot cm^{-1}$) and increasing this field continues to improve the resolution up to the highest field examined (23 $V \cdot cm^{-1}$) which in this case also represents the highest resolution of these particular ions. The third peak which is resolved at around 13 $V \cdot cm^{-1}$ in the 80 K spectra is partially discernible in the room temperature data, however as pointed out previously (**Section 3-2.2**), the lower temperature operation of the drift cell often enhances low abundance ion signals as is seen in **Figure 52B**.

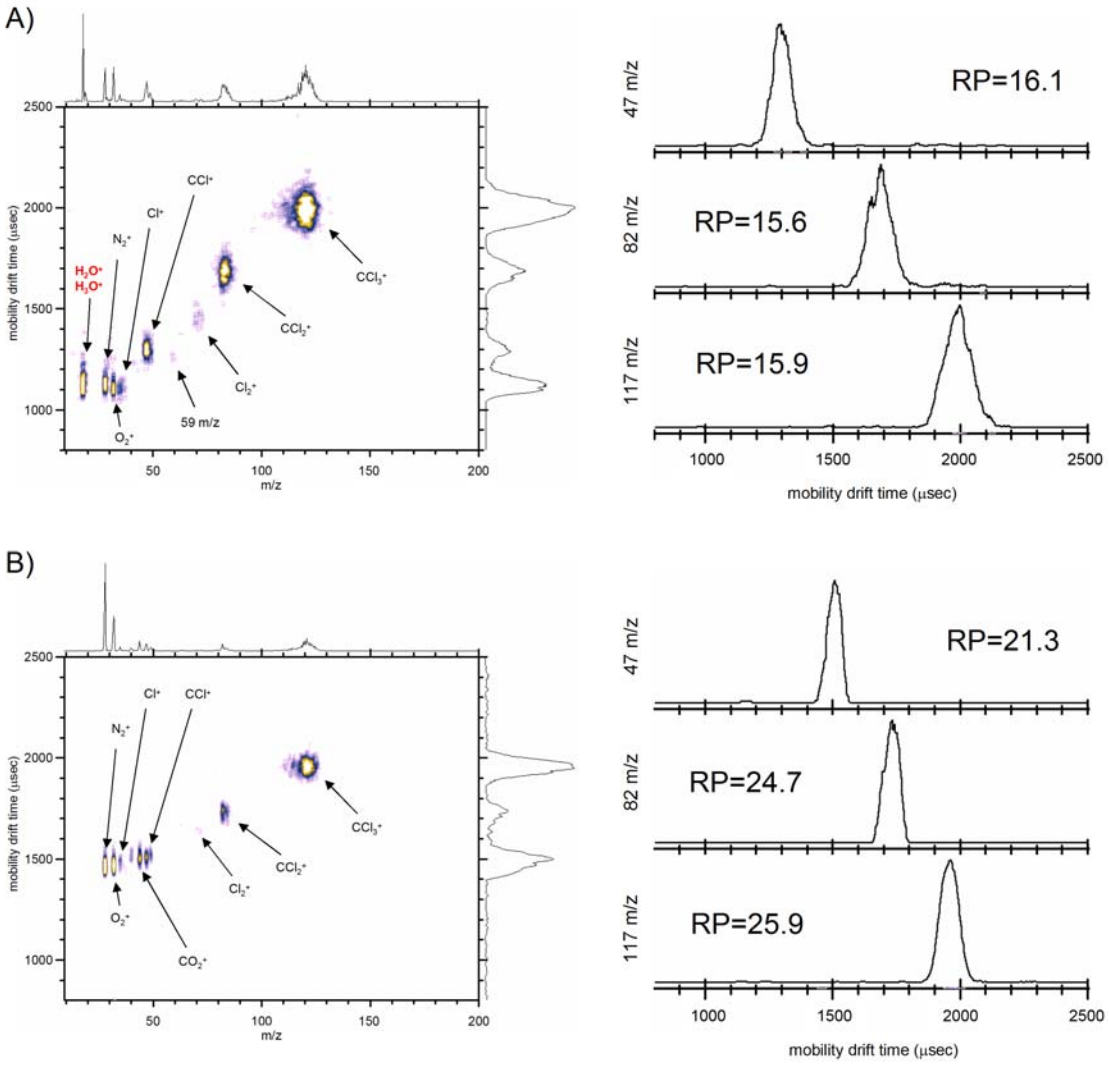

Figure 53 – Spectra of carbon tetrachloride demonstrating enhancement of ion mobility resolving power at low temperature. **A)** Data obtained with elevated temperature (314 K) helium drift gas and 1D mobility traces for three sample derived ions (right). Resolving power values are indicated next to each peak profile. **B)** Data obtained at low temperature (103 K). 1D mobility traces represent the same 3 ion masses selected previously. A marked improvement in resolving power is observed at lower temperature. Air derived ions (N_2^+, O_2^+ and CO_2^+) are present in the sample, which was not purified (freeze-pump-thaw) prior to introduction to the instrument. The drift cell was operated at 10 $V \cdot cm^{-1}$ with ~1.2 torr helium, and utilized a 20 μsec ion gate for both experiments.

A typical example of improved resolving power at low temperature is provided in **Figure 53** with electron ionized (60 eV) carbon tetrachloride. At elevated

temperatures (314 K, **Figure 53A**) the resulting 2D spectrum is defined by the expected appearance of the chlorine ion series (CCl_x) and various contaminant ions which are present in the sample. These atmospheric contaminants were purposely introduced for diagnostic purposes by foregoing the routine freeze-pump-thaw sample cleanup protocol (refer to **Section 2-3.1**). The 1D mobility arrival time traces were generated for three prominent ions in the spectrum (**Figure 53A, right**). Resolving power values are provided next to each ion distribution and indicate that the average resolving power at this temperature is ~16, which is typical. In contrast, 1D mobility traces for the same three ions taken at low temperature (103 K) show significant improvement in resolving power, with the average value being ~23. This improvement in resolving powers is always observed for low temperature experiments, barring effects due to ion chemistry and contributions by multiple ion populations (*e.g.*, mass isomers, *vide infra*).

3-3 Scaling IMS Plateaus: Separation of Mass Isomers

We conclude this chapter by surveying the frontier of ion mobility-mass spectrometry research with applications in the separation of isomeric electronic states. For ion mobility to be regarded as a chemical analysis technique that is complimentary to mass spectrometry, it must offer something that mass spectrometry cannot, namely additional information regarding ions which are isomeric in mass. *Mass isomer* is a broadly encompassing category, as there are numerous ways in which two ions of the same mass can differ. It is instructive here to define the term mass isomer and discuss the role that ion mobility has played and will play in this realm of analysis.

3-3.1 Separation of Nominal Mass Isomers by Ion Mobility

From a broad standpoint, two chemically different ions with the same nominal mass can be regarded as isomeric in mass, particularly if the mass analysis technique employed cannot differentiate the ions by mass measurement alone. A classic example of *nominal mass isomers* is N_2^+ and CO^+, which differ in mass by only 0.011 amu, requiring a minimum mass resolution of *ca.* 2500 to be partially resolved. Ion mobility methods can readily resolve chemically different ions of the same nominal mass [384,385], and the separation of N_2^+ and CO^+ is demonstrated in the ion mobility spectrum in **Figure 50C**. Other examples of ion mobility separation of nominal mass isomers can be found throughout this dissertation and are summarized in **Table 11**.

Table 11 – Examples of nominal mass isomers which are separated using the cryogenic ion mobility-mass spectrometer. Figure numbers of specific spectral examples are provided for reference.

Ion	Exact Mass* (amu)	Mass Difference	Required MS Resolution	IMS Separation Example
N_2^+ CO^+	28.006148 27.994915	0.011233	2492.203	**Figure 50C**
$C_2H_4^+$ CO^+	28.0313 27.994915	0.036385	769.408	**Figure 51B**
$C_2H_5^+$ CHO^+	29.039125 29.00274	0.036385	797.107	**Figure 51B**
$C_2H_6^+$ CH_2O^+	30.04695 30.010565	0.036385	879.204	**Figure 51B**
CH_4O^+ O_2^+	32.026215 31.98983	0.036385	824.806	**Figure 47**

* masses were calculated using the *Exact Mass Calculator* provided by Scientific Instrument Services, Inc. [386].

A more stringent definition of a mass isomer is an ion which contains the same type and numbers of atoms but differ by the placement of these ions to some degree or another. These are regarded as true isomeric ions: *structural and positional isomers* which ion mobility has been able to differentiate, though these applications have not been explored in this dissertation work. Some examples from the literature include the separation of positional [387], conformational [41], and even enantiomeric ions [58].

Further still are ions which are exactly the same in terms of chemical composition and mass but differ in some way by their electronic configurations. There are two broadly defined categories of electronic isomers which are investigated in this dissertation: *electronic excited states* in which an electron is promoted to a higher energy orbital, and *electronic positional isomers* where the electron is stable in two different locations in the same ion. A well-known example of the latter is keto-enol tautomerism whereby a proton and bonding electron shift in position relative to one another. The separation of electronic conformations by ion mobility methods has been documented in a few but impressive cases for C^+ [388], O^+ [389,390], first row transition metal ions [146], and more recently, the methanol radical cation [61]. Ions drifting through their parent gas also partition based on electronic configuration (spin-orbit splitting) and has been observed for most of the noble gases (Ne^+, Ar^+ [391], Kr^+ [61]and Xe^+ [392]).

In the following sections, we revisit a few electronic isomers previously observed by ion mobility and present the highest resolutions obtained so far on these electronic states using the cryogenic IMS-MS instrument.

3-3.2 Separation of Chromium Ground and Excited Electronic States by Ion Mobility

Early investigations of the reactivity of chromium cations with small organics resulted in the observation that the chromium ion population was only partially depleted in the presence of a reactive species [393]. The extent of chromium ion depletion was both ionization energy and transition metal identity dependant and rate constant measurements showed clear indications of a two-part reactant system, leading to the conclusion that the electron ionized chromium cations populated long-lived excited states that had drastically different reactivities than their ground state counterparts [394,395]. While it was further discovered that essentially all of the transition metal ions exhibited some fraction of excited state reactivity, chromium remained among the most reactive, presumably due to an increased production of a long-lived excited state population. At around the same time, ion mobility measurements of atomic ions in the helium flow tube reactor experiment demonstrated differences in ion mobilities for ground and excited state populations by as much as 20%, specifically for O^+ [389] and C^+ [388], demonstrating that helium was sensitive to the electronic state of atomic ions (this is despite the fact that helium is very weakly polarizable). Shortly thereafter, Kemper and Bowers published their pioneering work on the separation of electronically excited first row transition metals resolved from their ground states by low field ion mobility methods [146]. Integral to their ability to resolve out these electronic states was the lowering of the helium gas temperature, which lowered the effective ion temperature in the experiment and resulted in an increased interaction between the metal cation and neutral helium gas. Their work also confirmed a previous observation that as much as

60% of the chromium ion population exists as a long-lived excited state, among the highest of all the transition metals cations formed from electron ionization methods [395]. Also inferred in this work was the existence of an additional third excited state population which appeared as a low abundance shoulder on the peak identified as the second excited state of Cr^+ (^4D). While chromium was investigated at least two additional times using ion mobility-mass spectrometry methods, resulting arrival time distributions were bimodal and did not hint at this additional excited state population, though it should be noted that the ion mobility resolutions observed in these latter studies were significantly lower than what was observed in Kemper and Bower's original work [396,397].

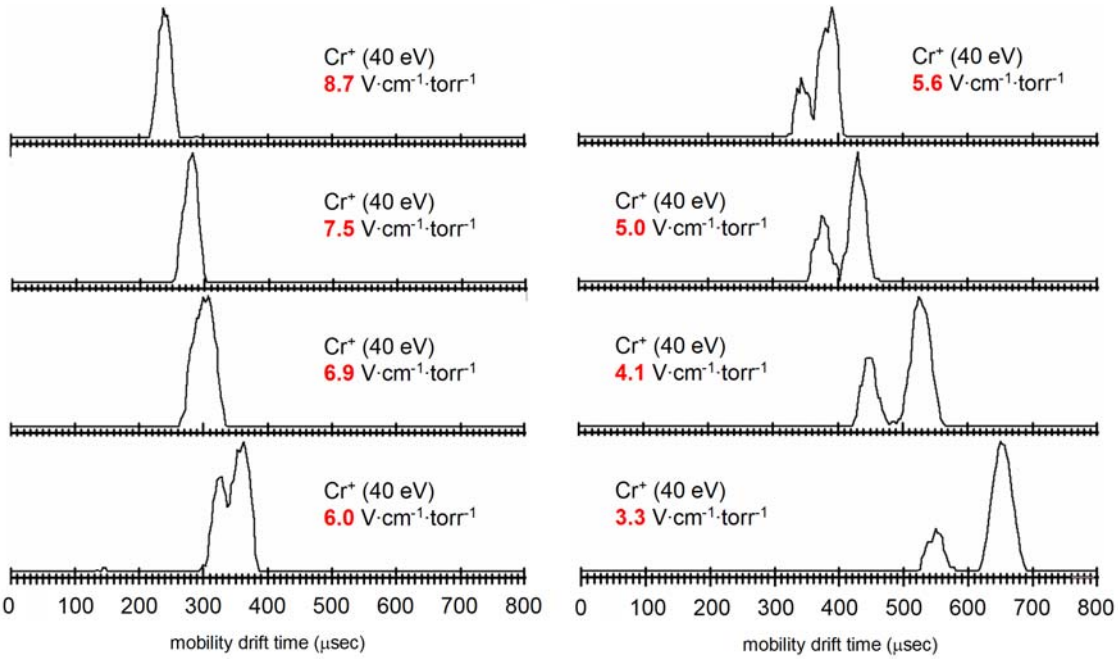

Figure 54 – Ion mobility spectra of Cr^+ at various electric fields. As the field is lowered, the peak profile splits into two distributions. Resolution of these two ion populations continue to increase to the lowest field investigated (3.3 $V \cdot cm^{-1} \cdot torr^{-1}$). Cr^+ was formed from chromyl chloride (CrO_2Cl_2).

Initial ion mobility experiments failed to measure more than a single arrival time for the chromium cation. After some experimental investigation, it was apparent that the electronic state separation was highly dependant on drift field conditions and further experiments confirmed that at sufficiently high electric fields, the resolution degraded to the extent that only one ion population is measurable (**Figure 54**). This is somewhat contrary to the conventional thinking set forth by **Equation 5**, whereby ion mobility resolving power is improved at higher voltages. It turns out that the distinction between resolution and resolving power is very specific in the case of electronic isomer studies, specifically, while resolving power may improve at higher field, the resolution of two electronic isomers will not. Indeed, the peak width at the highest field in **Figure 54** (8.7 $V \cdot cm^{-1} \cdot torr^{-1}$) is narrower than the peak width at the lowest field (3.3 $V \cdot cm^{-1} \cdot torr^{-1}$), but nothing is resolved at the highest resolving power. Resolution is actually highest at the lowest resolving power settings (3.3 $V \cdot cm^{-1} \cdot torr^{-1}$). Suffice to say that the field limits of such studies were established, and electronic state investigations could resume.

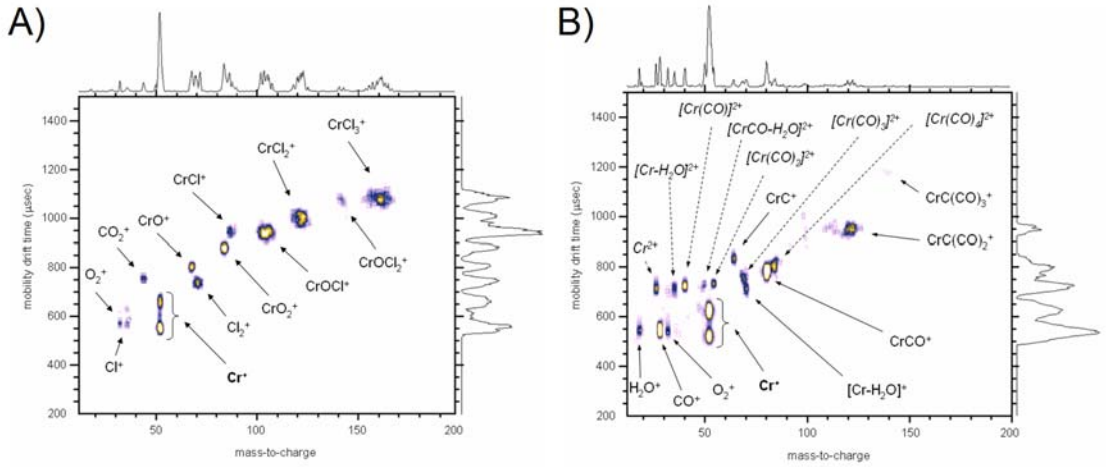

Figure 55 – Spectra of chromyl chloride (CrO_2Cl_2) and chromium hexacarbonyl ($Cr(CO)_6$) at 60.2 eV electron ionization. **A)** 2-dimensional ion mobility-mass spectrometry plot of the ions formed from 60.2 eV electron ionization of CrO_2Cl_2. Ion mobility conditions were 2.1 torr helium, 3.3 $V \cdot cm^{-1} \cdot torr^{-1}$ (10.2 Td) and 298 K. **B)** 2-D plot of the ions formed from 60.2 eV electron ionization of $Cr(CO)_6$. Ion mobility conditions were 2.1 torr helium, 3.4 $V \cdot cm^{-1} \cdot torr^{-1}$ (10.3 Td) and 300 K. In both cases, the Cr^+ ion exhibits a clearly resolved bimodal distribution in the mobility dimension.

Figure 55A contains the 2-dimensional plot of the ions formed from 60.2 eV electron ionization of chromyl chloride (CrO_2Cl_2). The spectrum was obtained in 2.1 torr of helium at room temperature (298 K). The ions observed in this spectrum are as expected, with ions corresponding to the systematic losses of individual atomic ligands distributed across the mass spectrum. An interesting observation is that the Cl^+ ion exhibits some degree of bimodality in mobility space which is reproducible with sufficient ion counts. This could be indicative of a long lived chemical species measured in the ion mobility experiment as another ion but dissociating prior to final mass analysis, however this determination is difficult to make with the current data as no ion signature remains in the 2D plot which is isobaric in mobility to this signal that could be identified as a precursor ion. A more intriguing possibility is that the two mobility peaks

of Cl^+ originate from an excited electronic state of Cl^+, however this is presented merely as speculation.

Of immediate interest in the CrO_2Cl_2 2D spectrum is the chromium cation, which exhibits a bimodal distribution in mobility space. **Figure 55B** contains the 2D plot for the 60.2 eV electron ionization of chromium hexacarbonyl ($Cr(CO)_6$) taken in 2.1 torr helium at near room temperature (300 K). Both spectra in **Figure 55** are scaled to the same mobility and mass and there are obvious differences in the way each chemical compound behaves under the same electron ionization conditions. For example, far less high mass ions are observed for chromium hexacarbonyl and there is a greater extent of doubly charged ions (indicated by dotted arrows in **Figure 55B**). No doubly charged ions are present in the chromyl chloride spectrum. The formation of Cr^{2+} from electron ionization of the hexacarbonyl is confirmed in a 70 eV standard reference spectrum (not shown) [398]. The remaining doubly charged ions are characterized by neutral losses from a parent Cr^{2+} ion which likely occurs at the exit of the drift cell. The slight shift in mobility times for these doubly charged ions also suggests that some mass-dependant time of flight has occurred after the mobility analysis, linking the dissociation event to the exit of the drift cell rather than at the ion extraction event of the time-of-flight analyzer.

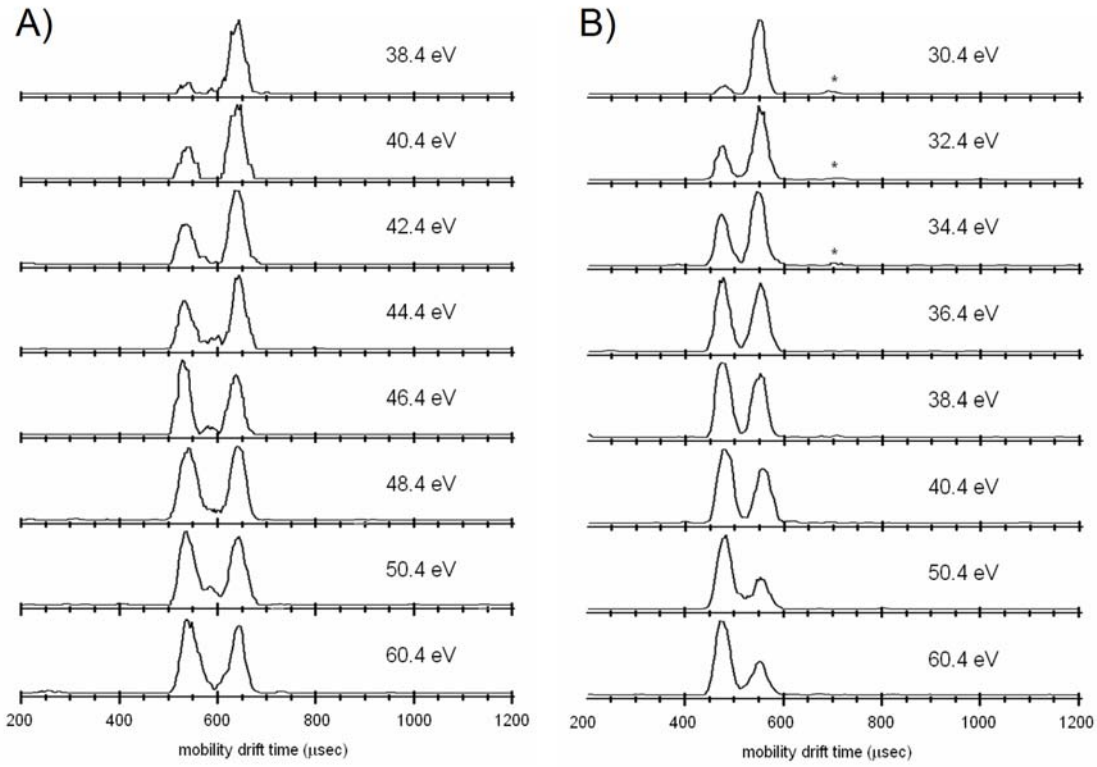

Figure 56 – Mobility spectra of Cr^+ at various electron ionization energies. Cr^+ is formed from **A)** chromyl chloride (2.1 torr helium, 301K) and **B)** chromium hexacarbonyl (2.0 torr helium, 322 K). Mobility traces are generated by integrating ion signal across a narrow mass window (in these cases 51-53 m/z). In both compounds, the earlier arriving ion population corresponds to a higher ionization energy and provides evidence that it contains the electronically excited state or states. The formation of this excited state population reaches a steady state between 50-60 eV for both compounds. The small signal marked with an asterisk at ~650 μsec in the hexacarbonyl spectra lies isobaric in mass with the chromium cation and is reproducible at low electron energies.

In order to determine the identity of the excited state in the mobility arrival time data, an appearance energy experiment is conducted whereby the electron energy is raised and the resulting ion mobility populations of the Cr^+ ion are observed. **Figure 56** illustrates this experiment for ion formed from both chromyl chloride (**Figure 56A**) and chromium hexacarbonyl (**Figure 56B**). As the electron energy is increased for both compounds, the faster arriving ion population grows in and reaches a steady state with

the slower arriving ion signal between 50-60 eV. This suggests that the high mobility ion population contains the electronically excited state or states of the chromium cation. It is also evident that the carbonyl forms considerably more of the excited state of chromium than does the chloride, by about 50% more based on peak height comparisons. This conclusion was also made by Elkind and Armentrout based on their measurements of the chromium cation's reactivity with H_2 and its deuterated analogues, though we observe more excited state resulting from the chloride, about ~50% as compared to the previously reported ~20% [395]. The appearance of the doubly charged chromium species in the hexacarbonyl spectrum (**Figure 55A**) suggests than the ionization process for this compound is a much higher energy process than forming the same cation from the chloride (**Figure 55B**).

For some of the mobility spectra of chromyl chloride, there also appears to be a third peak partially resolved between the existing two peaks. The possible existence of a third peak in the ion mobility arrival time spectrum was reported previously for the chromium cation formed from $Cr_2O_2Cl_2$. In this previous report, the third ion signal manifests itself as a low abundance tailing on the mobility distribution representing the excited state population [146]. Because of the limited mobility resolution and poor reproducibility, the possibility of this third peak cannot be made strictly from the data in **Figure 55A**. Since the electronic state separations observed in the ion mobility experiment are a result of an extended ion-helium interaction potential (extended for the ground state in the case of Cr^+), then it follows that one can increase the ion mobility resolution by enhancing this ion-helium interaction, either by lowing the energy of

interaction or by increasing the total number of interaction events. Higher neutral gas densities and longer drift regions accomplish the latter, but at a cost of increased diffusional broadening of ion populations resulting in diminishing returns with regards to the observed resolution. Lowering the temperature of the drift gas, on the other hand, serves to both lower the collision energy of the ion with the neutral and decrease diffusional broadening such that a net gain in resolution is expected.

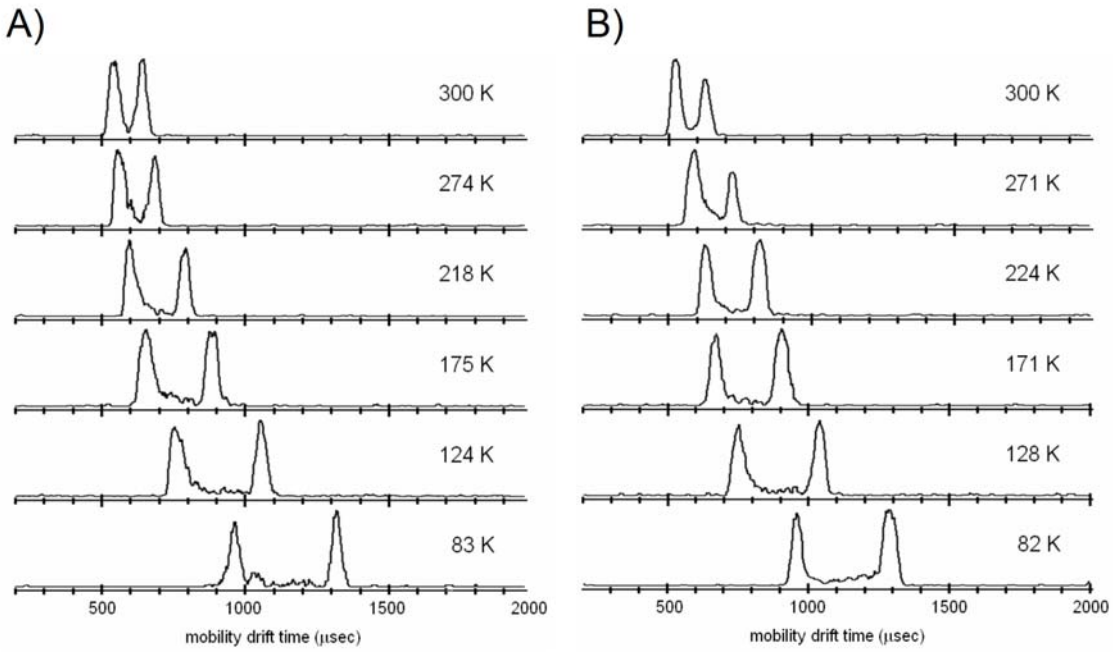

Figure 57 – Mobility spectra of Cr^+ at various temperatures. The chromium cation is formed from **A)** chromyl chloride (CrO_2Cl_2) and **B)** chromium hexacarbonyl ($Cr(CO)_6$). Both sets of spectra were obtained in ~2.1 torr helium and ~3.3 V cm torr, with field strengths varying from 10.2 Td down to 2.8 Td at the lowest temperatures investigated. Both sets of spectra are very similar and exhibit bridging between the ion populations, particularly at lower temperatures.

Such a low temperature experiment is contained in **Figure 57** for the chromium cation formed from both chemical compounds. Both sets of data in **Figure 57** resulting

from the two different compounds are remarkably similar. Arrival times shift to longer times due to the increase in helium number density as the pressure and volume are kept constant in the experiment. Of interest is the nature of the supposed third peak which appears as a small but distinctive tailing on the first arrival time population in nearly all of the mobility spectra. Even at low temperatures, a better resolution of this peak is not obtained and in some cases it is not observed at all, particularly below about 150 K. This suggests one of two possibilities: i) the excited state population comprising this third distribution is not formed in significant abundance to be differentiated in cases of low signal-to-noise ii) the tailing is not a result of a third excited state distribution but rather a result of constant radiative/collisional decay of the primary excited state population to the ground state, manifesting as a the observed tailing. Evidence for the latter can be seen as bridging between the two ion populations, most prominently at the lowest temperatures investigated. Bridging in the ion mobility experiment is indicative of an ion which changes mobility during its transit through the drift cell such that its measured mobility lies between that of the two bridged ion populations. Intriguing is the fact that the amount of bridging seems to increase as the temperature of the drift gas is decreased.

An additional experiment was conducted at ~80 K whereby the drift field is lowered in order to enhance the resolution further. The results of this experiment are contained in **Figure 58**. Two observations are immediately obvious. First, the amount of bridging continues to increase as the drift field is lowered. Second, at the lowest drift fields investigated (1.4 $V \cdot cm^{-1} \cdot torr^{-1}$, 1.2 Td), the ion population representing the excited

state is near completely depleted. The depletion of the excited state at low temperature and low field likely results from reactive/collisional quenching through interaction with a trace impurity within the drift gas. The number of collisions with a small amount of impurity will increase as the drift gas temperature is lowered, since experiments are conducted under same pressure conditions, that is, at the same pressure and volume, lowering the temperature will raise the gas number density. There are very few candidate impurities which would remain in the drift gas at temperatures approaching 80 K. Carbon monoxide and oxygen (condensation temperatures of 81 and 90 K, respectively) are two possible candidates which are known to exist as impurities in the drift gas used, and both CO and O_2 are known to be reactive to the excited states of transition metal ions [395,399]. While the temperature can be reduced below the condensation point of both gases, it is possible these impurities remain within the drift gas much like moisture remains in ambient air below its boiling point. Such trace impurities are also expected to increase in concentration in this particular drift cell design where pumping is through two narrow apertures. Under such diffusion limiting gas transport, enrichment of the higher mass gases is a likely possibility, particularly over extended experimental timeframes at reduced temperatures.

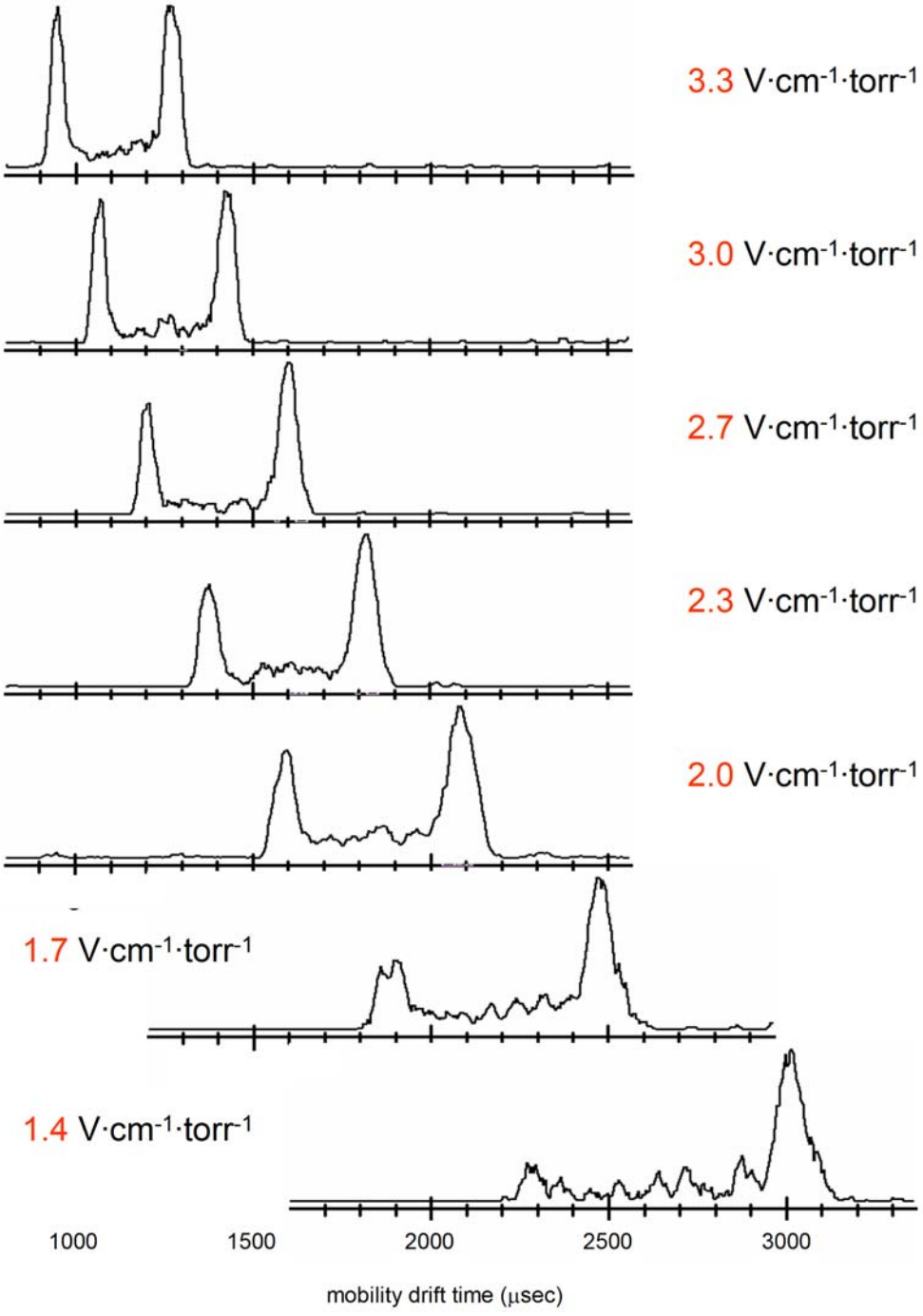

Figure 58 – Cryogenic (80 K) mobility spectra of Cr^+ at various electric fields. Cr^+ is formed from chromium hexacarbonyl. Helium pressure was maintained at ~2.1 torr. The first ion population representing the excited state(s) is depleted at the lowest field utilized. Bridging between the two ion population is also observed. The bottom two spectra are taken with low ion counting statistics and the periodic appearance of the signal between the two peaks is a result of insufficient ion counts to interpolate data points.

3-3.3 Separation of Titanium Ground and Excited Electronic States by Ion Mobility

The electronically excited states of titanium represent an interesting isomeric system to study for two reasons. One is that previously electronic state chromatography experiments identified as many as three stable electronic structures measurable by ion mobility. The second motivation to revisit this system is that titanium possesses excited state populations which have lower ionic mobilities than the ground state, opposite of what is observed for chromium [146].

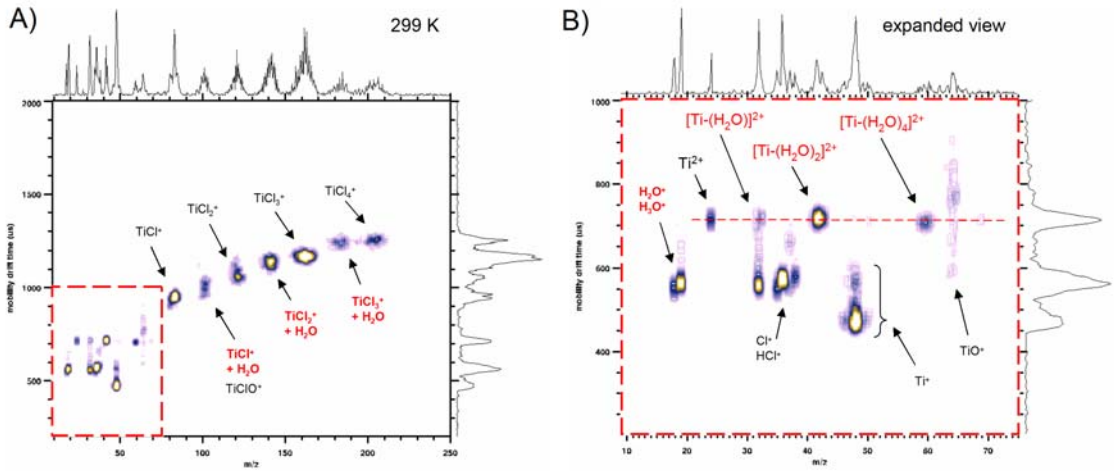

Figure 59 – Room temperature spectra of $TiCl_4$ at 70 eV electron ionization. **A)** The full 2D mobility-mass spectrum of titanium chloride at 299K. The spectrum contains the entire series of metal chloride ions as well as corresponding hydration product ions (highlighted in red). **B)** An expanded view of the low mass range (10-75 m/z) contains several ions of note, including a series of doubly charged hydrated ions which likely originate from Ti^{2+}. These ions are formed in the drift cell and can be differentiated by the mobility correlation along a horizontal line (red dotted line) representing the mobility of their precursor ion. A small amount of TiO^+ is also present with a long mobility profile characteristic of mid-drift ion conversion chemistry. Ti^+ appears as a bimodal distribution, with a greater abundance of the higher mobility species. The spectrum was taken with a 20 msec ion gate using helium drift gas at a field strength of 3.3 $V \cdot cm^{-1} \cdot torr^{-1}$.

The 2D mobility-mass spectrum for 70 eV ionized titanium chloride is contained in **Figure 59A**. An expanded view of the low mass region is also provided (**Figure 59B**) which contains additional hydrated ions. These ions do not originate from the ion source since they do not fall along an expected mobility-mass trendline, but rather line up isometric in mobility along a horizontal trend. This behavior is indicative of measuring the mobility of one ion that subsequently dissociates into another prior to mass analysis [372]. The precursor ion in this situation is likely a highly hydrated cluster ion, possibly $[Ti\text{-}(H_2O)_5]^{2+}$ which has a small but measurable ion signal in the expanded spectrum (not labeled). A broad mobility profile at 64 m/z is also observed (**Figure 59B**) and corresponds to the mass of TiO^+.

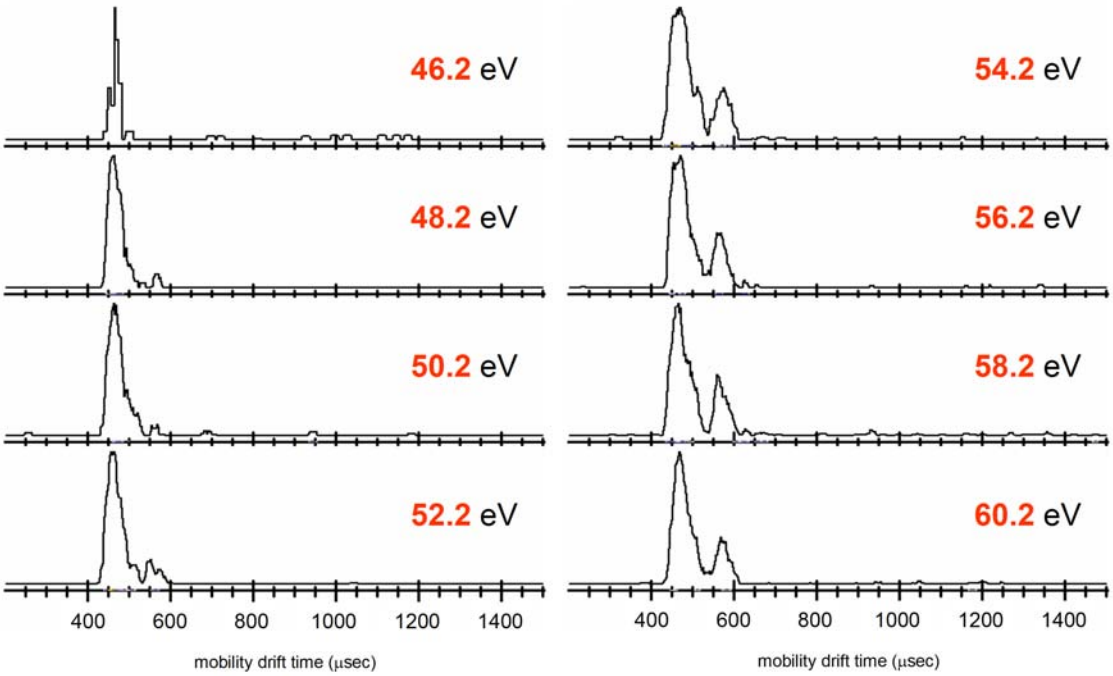

Figure 60 – Mobility spectra of Ti^+ at various electron ionization energies. The lower mobility arrival time distribution appears at higher ionization energies, revealing it as the excited state. The abundances of the ground and excited states plateau at around 55 eV EI energy.

The previous Ti^+ ion mobility experiments reported by Kemper and Bowers had failed to baseline resolve the ground and electronically excited states of Ti^+ at room temperature [146]. Examination of the Ti^+ mobility profile in **Figure 59** reveals a bimodal distribution that is baseline resolved at 299 K. The identity of the electronically excited state ion population can be probed with the same appearance energy experiment utilized in the chromium study. The results of this appearance energy experiment are contained in the mobility spectra in **Figure 60**. As the electron ionization energy is raised, the lower mobility arrival time distribution (second to elute) appears, identifying it as the excited state. This confirms previous reports of the higher mobility of the ground state of Ti^+ and is the opposite elution order observed for chromium, where the ground state of Cr^+ had a lower mobility than the corresponding excited state (**Section 3-2.1**). The plateau effect of the formation of the excited state past ~55 eV was also reported previously and confirmed here.

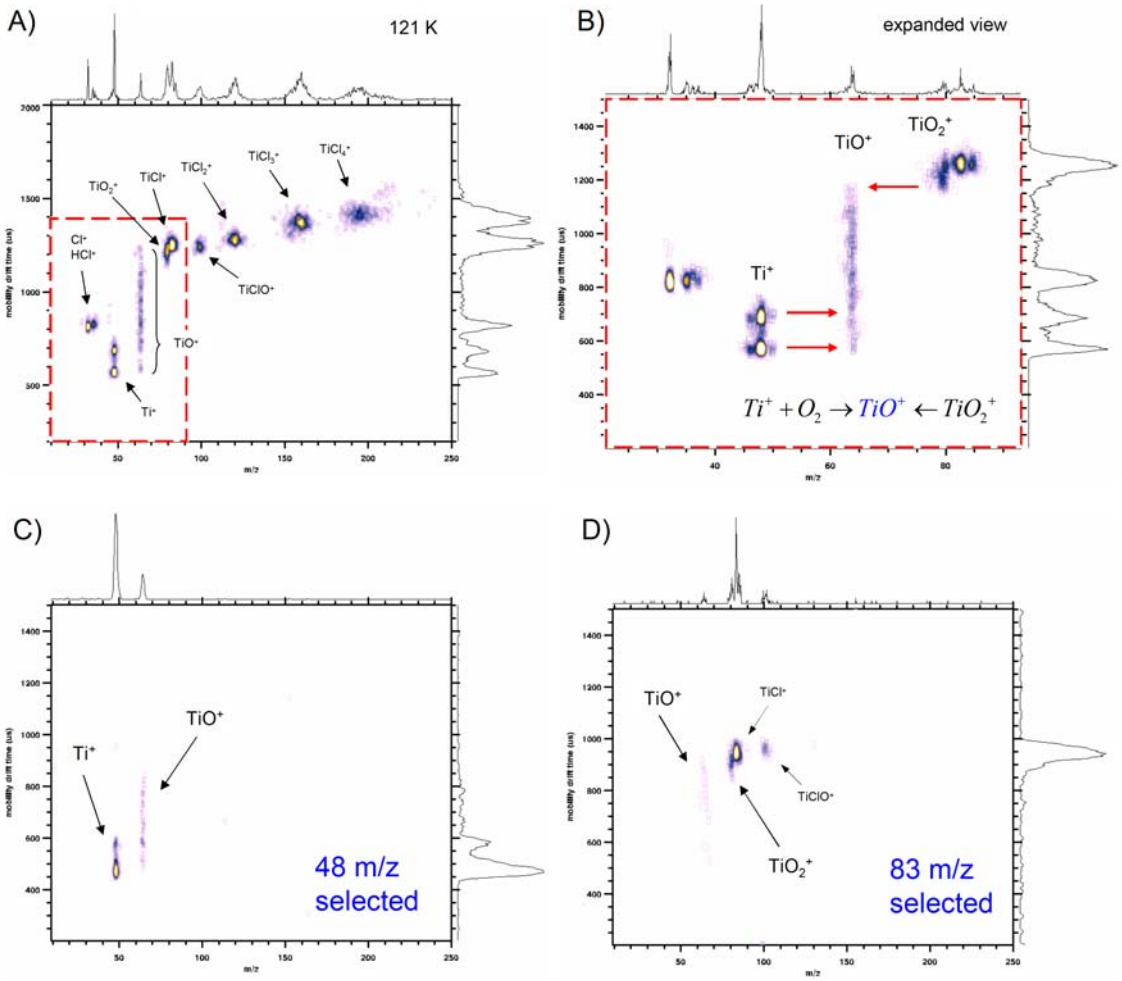

Figure 61 – **A)** Spectra of $TiCl_4$ at 121 K and 70 eV electron ionization. Compared with the room temperature spectrum, the low temperature data is absent of hydrated ions, resulting in an enhancement of the remaining ion signals. **B)** In the expanded spectrum of the low mass region, the origin of the TiO^+ ion is revealed to be bracketed in mobility between the ion signals for Ti^+ and TiO_2^+ (indicated by red arrows), suggested these as precursor ions for the formation of TiO^+. Mass selection of **C)** 48 m/z and **D)** 83 m/z also reveal some amount of TiO^+ in the spectra. Ion mobility conditions were the same here as the room temperature data shown previously.

Low temperature experiments were also conducted on the $TiCl_4$ system. **Figure 61A** contains a 2D spectrum at 121 K. In comparison to the 299 K spectrum (**Figure 59A**), the low temperature data is absent of the various hydrated ion species due to the

removal of water from the drift gas. An expanded spectrum of the low mass region (**Figure 61B**) also shows a prominent "smearing" the TiO^+ ion noted previously. This broad mobility profile indicates that TiO^+ was formed across the length of the drift region and is measured as a composite of ionic mobilities of one or more precursor ions. A proposed formation scheme for TiO^+ is provided in **Figure 61B** based on the bracketing of TiO^+'s mobility profile between Ti^+ and TiO_2^+. This scheme is supported by two mass selective experiments where **C)** Ti^+ (48 m/z) and **D)** a closely neighboring ion to TiO_2^+ ($TiCl^+$, 83 m/z) are selectively injected into the IMS. Both spectra reveal small amounts of TiO^+, suggesting it is formed from precursor ions present in these mass selected windows. Oxygen has a condensation temperature of ~90 K and is expected to be present as a drift gas impurity for nearly the entire tunable range of temperatures in these experiments. The formation of TiO^+ from Ti^+ is a very facile reaction [400] that is readily catalyzed with drift fields in excess of a few volts [401].

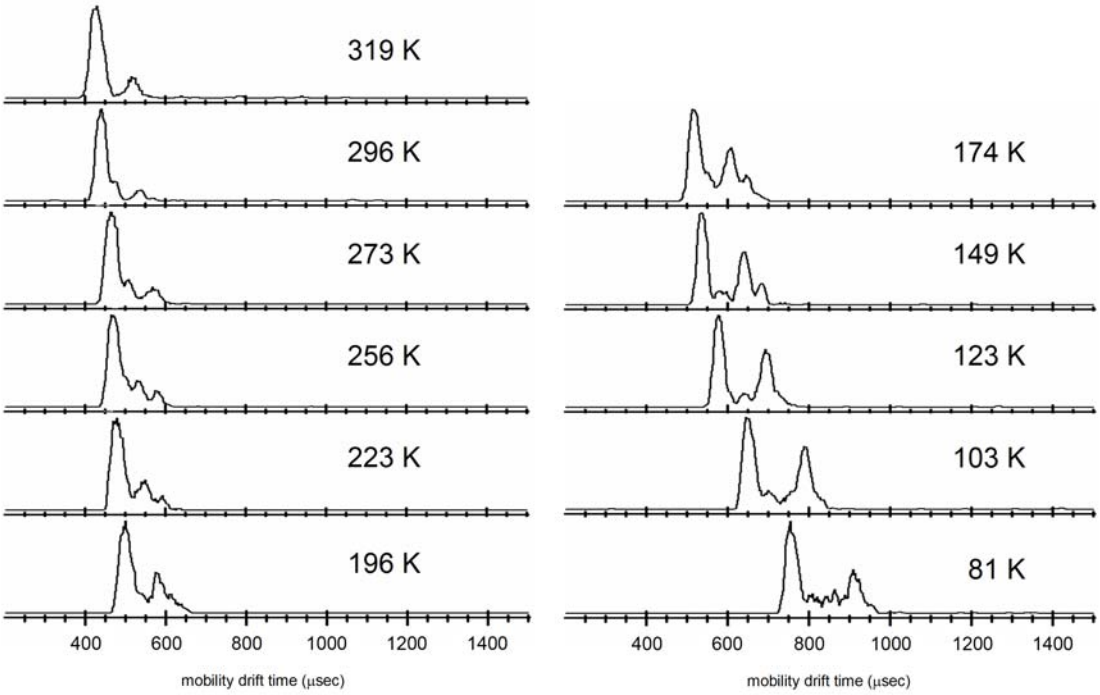

Figure 62 – Mobility spectra for Ti^+ at various temperatures from 319 to 81 K. The temperature data is marked by various degrees of resolution, with 3 resolved peaks at 256 K and again at 174 K, and a fourth peak appearing at 149 K down to 123 K. At temperatures at and below 103 K, the system returns to a bimodal distribution. This behavior suggests that excited states possess differential ionic mobilities that deviate in a nonlinear fashion as a function of temperature. In all experiments, EI energies are 70 eV, ion gates are 20 μsec and drift fields are 3.3 $V \cdot cm^{-1} \cdot torr^{-1}$ in helium drift gas.

The primary motivation of the low temperature experiments here is to obtain higher resolution on the electronic states of Ti^+. **Figure 62** contains mobility traces for Ti^+ at various drift gas temperatures from above ambient (319 K) down to cryogenic (81 K). Immediately evident from surveying the data is that the Ti^+ system is comprised of several electronic states which shift in and out of resolution as the temperature is changed. At room temperature (296 K) two mobility profiles are measured with a third, partially resolved profile appearing beneath the high mobility ion distribution previously identified as the ground state. Decreasing the temperature, these three ion distributions

become fully resolved at 256 K. Further still, the two lower mobility excited electronic state distributions coalesce into a single peak at 196 K. This behavior is also evident by the increase in signal amplitude. At 149 K, these two low mobility profiles are once again resolved, and a fourth profile appears in the valley region. Below 149 K, the low mobility excited state ion distributions again coalesce into a single distribution and the system becomes bimodal once again. At 81 K, depletion of the excited state profile is observed as was the case with Cr^+. A similar mechanism is occurring here as was seen with chromium with regards to the low temperature ion depletion of the excited state. This may not necessarily be a temperature phenomenon but a residence time phenomenon whereby the excited state ions are collisionally or radiatively relaxing back down to the ground state. A third body (collision mediated) catalytic mechanism may also be attributing to this observed behavior, which is enhanced at low temperature and/or longer interaction times within the buffer gas.

Kemper and Bowers previously reported this complex ionic mobility behavior for Ti^+, observing in their experiment two excited state profiles that became less resolved at 137 K than they were at 300 K. Their results also confirm that the excited states continued to separate further from the ground state distribution as the temperature was lowered [146]. No other ion mobility study has been conducted on this system.

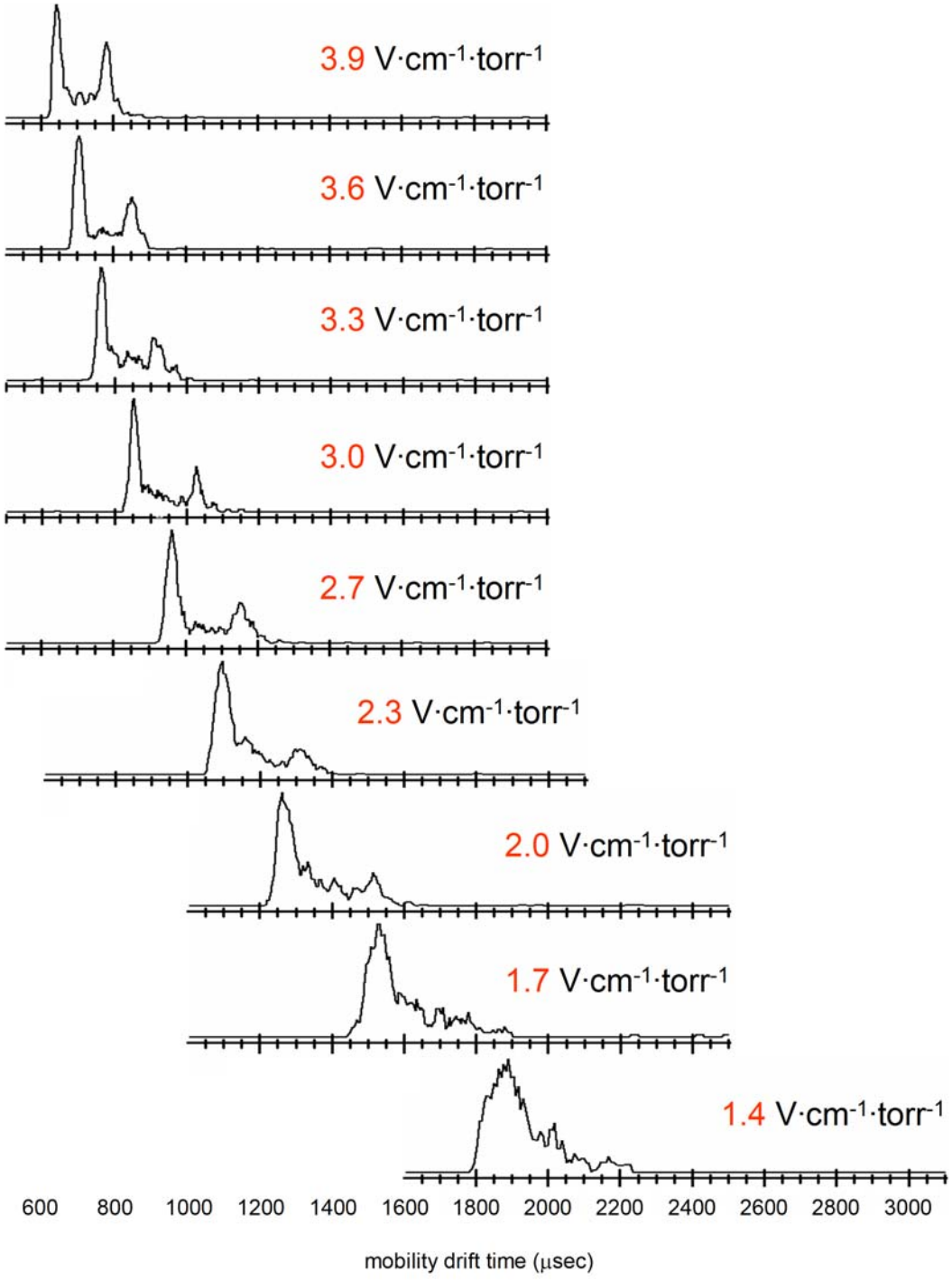

Figure 63 – Cryogenic (80 K) ion mobility data for Ti^+ at various fields. The lower mobility ion population representing the ensemble of excited states is depleted at the lowest field utilized (1.4 $V \cdot cm^{-1} \cdot torr^{-1}$). Bridging between the two ion populations observed here is also observed for the Cr^+ system taken at low temperature and low field.

As a final attempt to improve the resolution of the Ti^+ electronic states, the drift field was lowered at cryogenic temperatures to increase the number of ion-neutral interactions, as was done in the Cr^+ study. The results from this low temperature, low field experiment is contained in **Figure 63**. As was seen with the Cr+ system, bridging between the ion populations is observed at low temperature and becomes more prominent as the field is lowered. The excited state population is also depleted here as it was for Cr^+, though in this case, it is the lower mobility ion distribution that represents the excited ion state rather than the higher mobility distribution for Cr^+. This observation supports the claim that the excited states are undergoing relaxation back to the ground state, either through collisional or radiative means.

3-3.4 Ion Mobility Investigations of the Conventional and Distonic Electronic Isomers of the Methanol Radical Cation

In the 1980's, a series of papers were published detailing the discovery of two stable electronic isomers of ionized methanol: the *conventional ion* ($CH_3OH^{\bullet+}$) and the *distonic ion* form ($^{\bullet}CH_2OH_2^+$) whereby the charge and radical sites are formally separated within the molecule. Theory had predicted that the methanol distonic ion was a stable ion-dipole complex, lying in a potential energy well that was 45 $kJ \cdot mol^{-1}$ lower than that of the conventional ion form [402]. The intermolecular conversion of the conventional and distonic ion forms of methanol was predicted to be separated by a large energy barrier which suggested that either isomeric form would be stable if an appropriate method was found to form them. Radom and coworkers proposed using

ethylene glycol as a progenitor ion which could initiate an internal hydrogen shift *via* a McLafferty rearrangement mechanism [403] to form the distonic ion of methanol. This scheme is depicted in **Equation 8** for ethylene glycol.

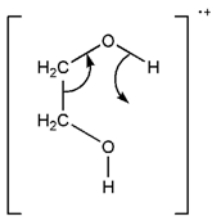

$$\longrightarrow \quad CH_2{=}O \quad + \quad CH_2OH_2^{\bullet +} \qquad (8)$$

Because these ion-dipole complexes are characterized by an ion-neutral association, collisional dissociation of the ion should preferentially result in charge retention on the ion species within the complex and loss of the neutral counterpart. Subsequent mass selected collisional activation of the EI generated m/z 32 ion from ethylene glycol confirmed the absence of the CH_3^+ fragment ion which suggested that the precursor ion was the distonic $^{\bullet}CH_2OH_2^+$ rather than conventional $CH_3OH^{\bullet +}$. This results from the expected favorable loss of the neutral dipole counterpart upon collisional activation. Further collisional activation experiments on deuterated methanol (CD_3OH) and ethylene glycol ($HOCD_2CD_2OH$) confirmed that no deuterium scrambling product ions were formed in either case (*e.g.*, CH^+, CHD^+, and CHD_2^+), suggesting that facile loss of the CH_x group was the fragmentation pathway governed in both collisional activation experiments [404]. Closely following this publication was another by Holmes and coworkers reporting the formation of the methanol distonic ion from glycoaldehyde ($HOCH_2CHO$) and hydroxyacetic acid ($HOCH_2COOH$) electron ionization

fragmentation. Mass selected collisional spectra confirmed the formation of the distonic ion through both the absence of CH_3^+ fragment ion and the formation of a doubly charged mass 32 ion (16 m/z), which indicates that mass 32 is a strongly bound species not prone to fragmenting during the ionization process [405]. The latter result is supported by the consideration that the distonic ion ($^{\bullet}CH_2$-OH_2^+) is a particularly stable class of ions characterized by a strong association between a radical species ($CH_2^{\bullet+}$) and a neutral molecule (H_2O), *i.e.*, a transient methanol ion-water complex [404]. Both the Radom and Holmes reports represent the first experimental observation of the methanol distonic ion. Other gas phase distonic ions have since been discovered, most of which originate through secondary formation pathways, such as hydrogen rearrangement and ring opening processes [406].

Previous work with transition metal and noble gas ions has firmly established the selectivity of the ion mobility technique towards the electronic structures of atomic ions [146,392,396,407]. In our laboratory, first evidence of the separation of the conventional and distonic methanol ions was observed in the ion mobility experiment for electron ionized methanol in argon drift gas [61]. Parnis and coworkers theoretically investigated rare gas (xenon, krypton and argon) catalyzed interconversion between the distonic and conventional forms of methanol using density functional theory and their results suggest that the more massive drift gases corresponding to higher gas phase basicities are expected to lower the barrier of isomerization between the conventional and distonic forms and promote interconversion (and thus degraded ion mobility resolution) [408]. By this rationale, neon and helium drift gases should result in even

higher observed resolution of the two isomeric forms as opposed to using argon. Argon was the sole drift gas used in our original investigation of the methanol isomer system. Finally, questions remains as to the nature of formation of the distonic form from direct ionization of methanol. Based on the work of Radom and coworkers [404], it is not expected that the distonic methanol ion would be formed directly from methanol, but rather through a rearrangement from a suitable precursor ion such as what was suggested in **Equation 8**. Our previous experimental results suggest that distonic methanol can be formed *directly* from methanol neutral [61]. These unanswered questions have motivated us to revisit the methanol electron isomer system with the recently developed cryogenic IMS system. The new cryogenic instrument which is the focus of this dissertation incorporates a drift cell that is over twice the length of the former drift cell used in our previous cryogenic IMS experiments, which is expected to improve mobility resolution, specifically by a factor of ~1.4 [88]. In addition, mass selected ion injection afford new experimental possibilities for identifying ion species, specifically through mass selective collisional dissociation experiments, which will be described in further detail, *vide infra*.

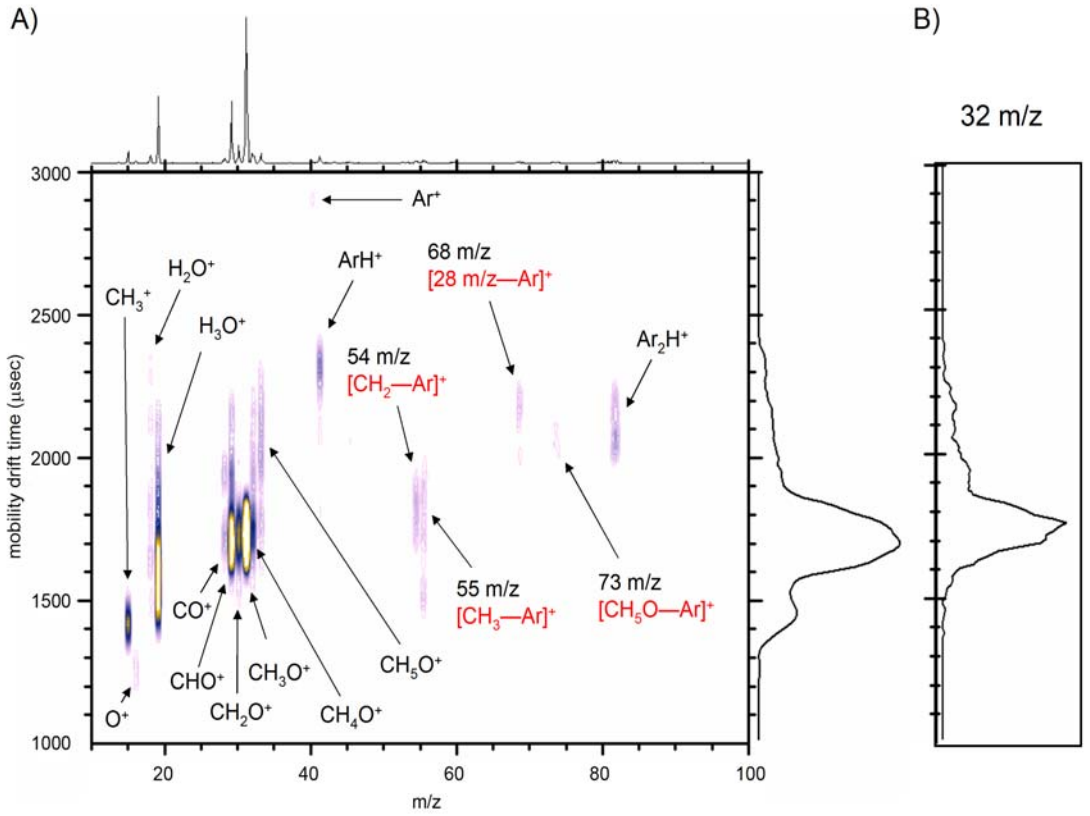

Figure 64 – Spectra of methanol in argon drift gas at 302 K. Electron ionization energy is 70 eV. **A)** 2D spectrum which contains the methanol molecular ion (32 m/z) as well as several fragment ions resulting from the EI event. Most ion signals are characterized by significant tailing in the mobility arrival times, which is most likely resulting from ion chemistry with argon. Several of the higher mass ion signals can be assigned as species resulting from clustering with argon (highlighted in red). **B)** The integrated mobility spectrum for 32 m/z exhibits significant tailing. The existence of additional ion distributions at 32 m/z is inconclusive from this data. Data was obtained at a field strength of 6.5 $V \cdot cm^{-1}$ in 0.75 torr argon drift gas.

The mobility spectrum of electron ionized anhydrous methanol using argon as the drift gas was reinvestigated. **Figure 64A** contains the 2D spectrum of methanol with room temperature (302 K) argon in the drift chamber. The spectrum is characterized by the expected EI generated ions (15, 28-32 m/z) as well as several ions which likely originate through reaction chemistry, as evident by the long mobility profiles (fronting and tailing) which suggests ion formation occurring throughout the drift region. The

appearance of the ArH^+ ion likely results from a hydrogen transfer reaction to Ar^+ formed in the ion source [409]. **Table 12** contains proton affinities for several chemical species encountered in this work. The proton affinity of argon is much lower than that of any other neutral encountered in this experiment and so direct argon protonation in the drift cell is not likely.

Table 12 – Proton affinities (PA) for several atomic and molecular species. Proton transfer is not favorable for any constituents which have proton affinities lower than that of the corresponding proton donor neutral. For example, the only constituent which can protonate argon in this table would be protonated helium. Data was obtained from reference [410].

	He	Ar	O_2	N_2	CO_2	CO	H_2O	CH_3OH
PA [kJ/mol]	178	369	421	493	541	594	691	754

Figure 64B contains the integrated mobility arrival time distribution for 32 m/z which corresponds to the molecular ion of methanol. The mobility spectrum is characterized by a narrow distribution at high ionic mobility and a broad tailing component which extends to lower mobility. This is suggestive of an ion conversion process occurring for 32 m/z. Indeed there is some evidence for ion clustering with argon, specifically for 28 and 33 m/z. This is a plausible cause of the observed peak tailing for ions at 28-32 m/z.

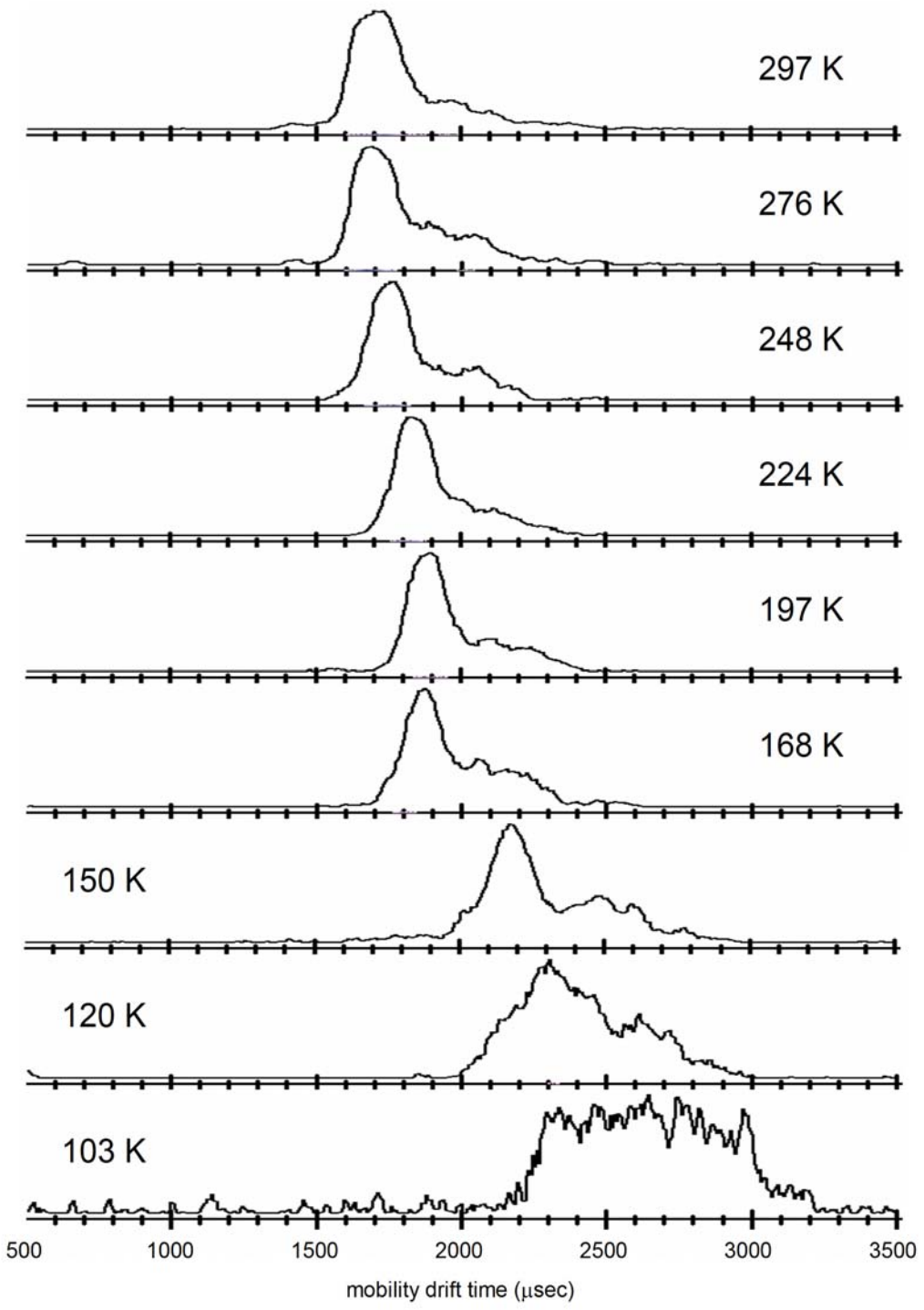

Figure 65 – Mobility spectra of anhydrous methanol in argon drift gas from 297 to 103 K. The distribution is characterized by a broad tailing of the peak. At 120 K and below, mobility resolution quickly degrades. IMS field strengths were ~6.5 $V \cdot cm^{-1}$ and argon gas pressure was ~0.75 torr for all experiments.

A series of low temperature spectra were acquired for methanol in argon drift gas in an attempt to improve the mobility resolution. The resulting mobility spectra are contained in **Figure 65**. At temperatures below 150 K, mobility resolution abruptly degrades, presumably due to condensation processes with argon. Immediately obvious in the spectra is that the peak tailing of 32 m/z continues throughout the entire range of sampled temperatures. The mobility peak profile never resolves into more than a single distinct distribution, despite the improvements in resolving power, which is evident by the narrowing of the primary ion distribution at lower temperatures. As suggested earlier, the reason for the peak tailing is likely a result of ion conversion processes occurring as the ion drifts through the gas filled cell. The 2D mobility-mass plot of methanol at 150 K (**Figure 66**) shows evidence of increased ion clustering with argon, which results in distortion of the mobility distributions due to this process. Post IMS declustering is observed and is characteristically identified by isobaric mobility correlations with other ions in the spectrum, as indicated with the red dotted lines in **Figure 66**. Numerous other product ions appear in the low temperature spectra, many of which have not been confidently identified (*e.g.*, 54-57 m/z).

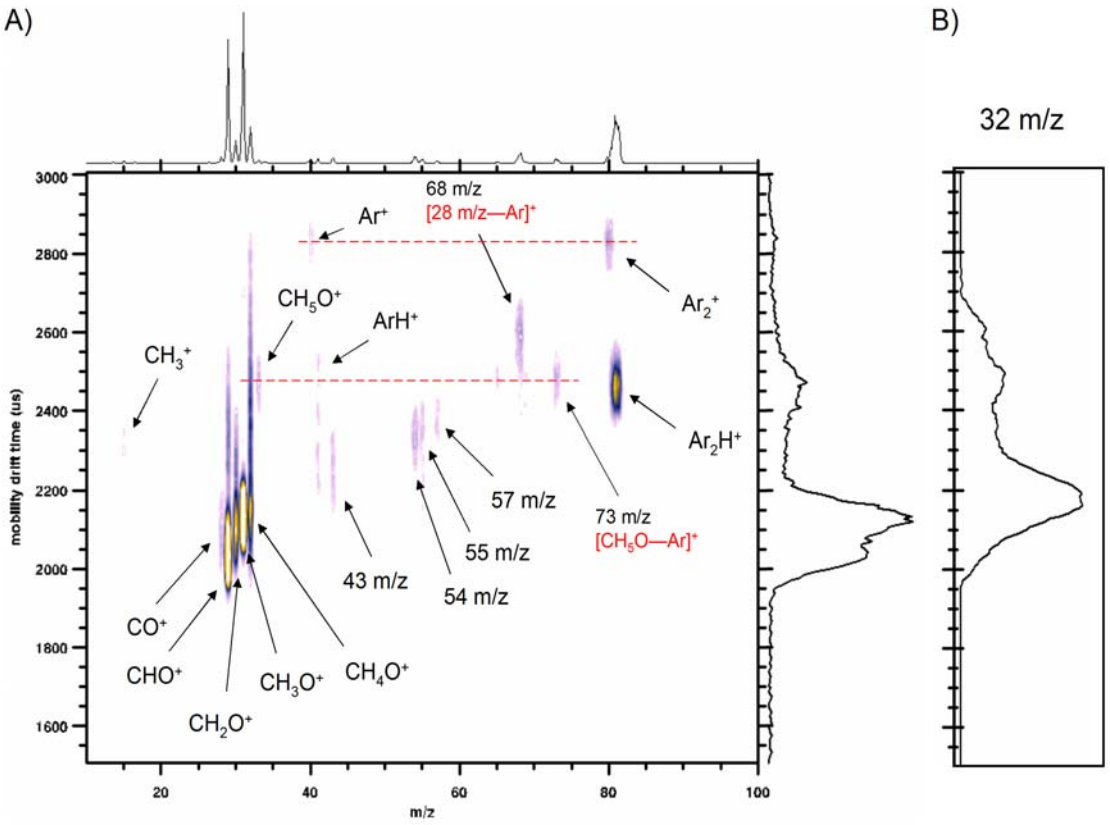

Figure 66 – Spectra of methanol in argon drift gas at 150 K. Electron ionization energy is 70 eV. **A)** 2D spectrum containing the ions derived from the EI process as well as several originating from ion chemistry within the drift cell. Isobaric mobility correlations (red dotted lines) are indicative of ions which are measured as one ion species in the IMS but dissociate prior to mass analysis. The two ions indicated are derived from argon clustering which is a relatively weak interaction. **B)** The integrated mobility spectrum for 32 m/z exhibits significant tailing as was seen at 302 K. This tailing is a mobility measurement distortion likely resulting from ion chemistry processes in the drift cell. Data was obtained at a field strength of 6.5 $V \cdot cm^{-1}$ in 0.75 torr argon drift gas.

While low temperature experiments of methanol in argon drift gas fail to provide improved resolution of the peak distribution of the molecular ion, the results offer insight as to the complex chemistry which occurs when using argon gas. A general hypothesis inferred from the mobility distributions for 32 m/z is that the distribution is comprised of multiple ion populations which are poorly resolved due to ion conversion processes. Parnis and coworkers had predicted that argon can be sufficiently basic as to

lower the barrier of isomerization for the conventional and distonic forms of methanol [408]. This may be the cause of the observed peak distortions for 32 m/z. Another possibility which cannot be ruled out is that some amount of O_2^+ is present at 32 m/z and contributing to the measured ion mobility distributions seen here. The linear time-of-flight mass analyzer utilized in this instrument cannot differentiate O_2^+ and CH_4O^+ by mass, which requires a mass resolution of >800.

Published reduced mobility data can predict, *a priori*, the placement of O_2^+ if the reduced mobility of another peak in the spectrum (a suitable point of reference) is known. The basis for this method is the relationship in **Equation 1**, whereby the gas phase ionic mobility, K, is inversely proportional to the measured drift time, t_d. With the assumption that the same experimental conditions of field strength and temperature are utilized, identical ion species measured with the same method using two different instruments will have the same fixed ratio of t_d. Methanol molecular ion reduced mobility is not published, however CH_3^+ has been reported and can be used to predict the relative arrival time of O_2^+ in argon drift gases. Thus $K_{O2}:K_{CH3}$ will be equivalent to the measured drift times $t_{CH3}:t_{O2}$, that is, an inverse relationship with regards to K. The ratio $K_{O2}:K_{CH3}$ is ~0.76 for the reported argon reduced mobility values (K_{CH3}=3.4 and K_{O2}=2.57) [150]. The measured drift time of CH_3^+ in the argon spectrum (**Figure 66**) is t_{CH3}=1.42 msec, and using the reduced mobility ratio 0.76, this predicts an arrival time of 1.88 msec for O_2^+. For the argon spectrum, 1.88 msec corresponds to the observed peak tailing of the 32 m/z ion distribution (t_{32}=1.73 msec), which suggests that if O_2^+ is present in the argon spectrum, then it is likely contributing to the observed low

resolution of the mobility profile. The accuracy of this time prediction method is limited by the choice of the reference ion and the experimental deviation of the two measurements with respect to one another. While this method can be further refined to incorporate temperature and pressure corrections, the approximation used here is more than sufficient for gauging the relative placement of an ion of interest independent of the experiment measurement.

Briefly, the methanol system was also investigated using neon drift gas as it possesses a lower gas phase basicity than argon and thus is expected to promote less interconversion of the conventional and distonic ion forms. The resulting mobility spectra are contained in **Figure 67**. While there appears to be a second ion distribution at 32 m/z, the quality of the spectra is not sufficient to make a confident determination. This low quality mobility spectra seems to be an experimental characteristic of using neon drift gas as opposed to argon or helium. We have also observed similar reductions in separation ability for other analyte systems when using neon as the drift gas.

Based on the theoretical work of Parnis *et al.*, helium is not expected to possess a gas-phase basicity sufficient enough to catalyze the interconversion of the conventional and distonic forms of methanol. The ion mobility spectrum of methanol was investigated in helium drift gas. **Figure 68** contains the 2D mobility-mass spectrum of methanol in helium drift gas at room temperature (298 K). The lack of ion-drift gas clustering results in a less congested spectrum as opposed to what was observed for argon (**Figures 64** and **66**) and neon (data not shown). Also characteristic of helium drift gas is the improved mobility resolution.

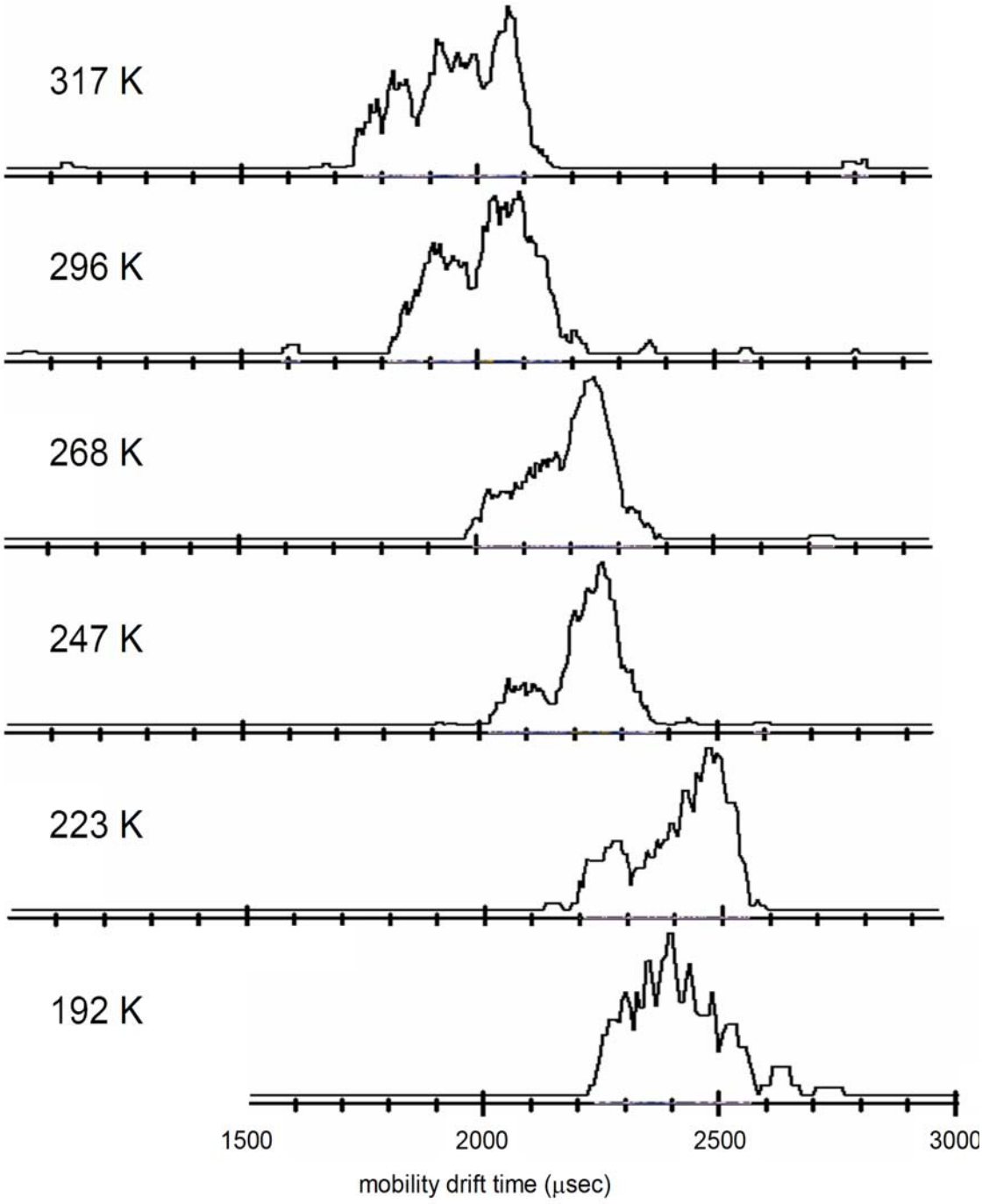

Figure 67 – Mobility spectra of methanol in neon from 317 to 192 K. Spectral reproducibility and ion counting statistics are not sufficient to make a determination as to the presence of multiple ion distributions at 32 m/z. Data was obtained at a field strength of 7.0 $V \cdot cm^{-1}$ in ~2.1 torr of neon drift gas.

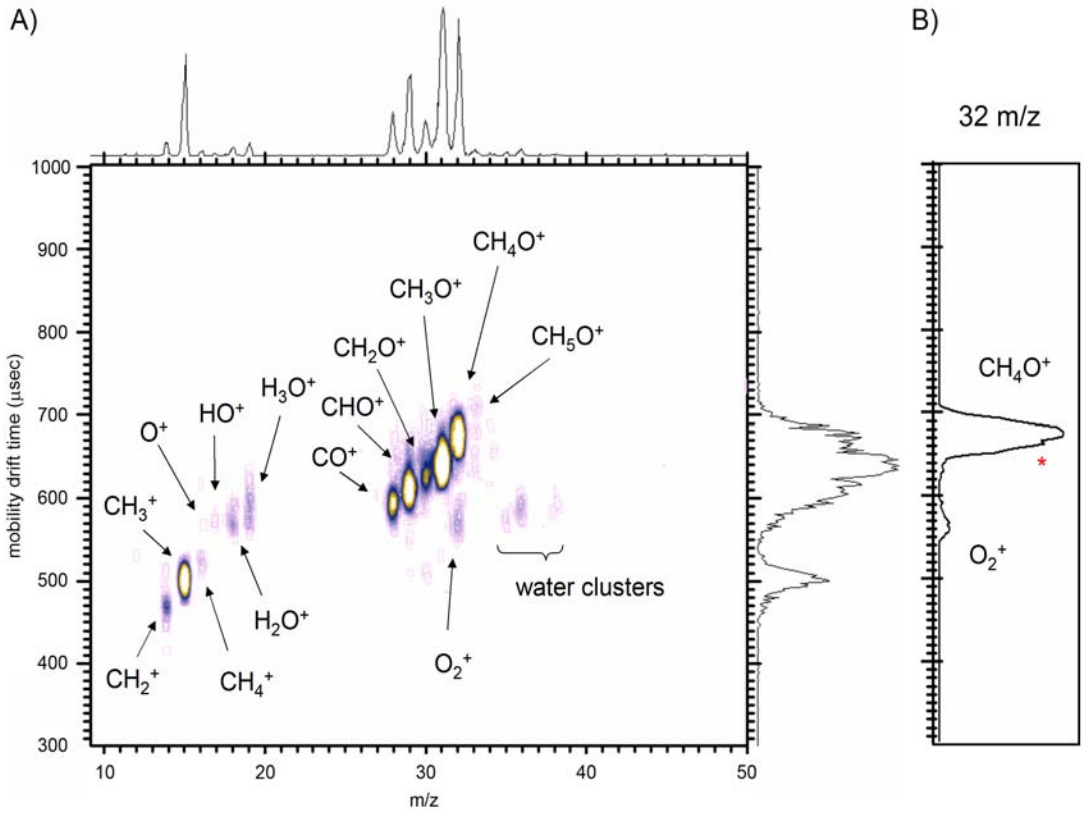

Figure 68 – Spectrum of methanol in helium at room temperature. **A)** The 2D mobility-mass plot contains the expected ions from EI and the previously observed water derived ions at 17-19 m/z. **B)** The mobility spectrum of 32 m/z is bimodal in helium. The higher mobility distribution is assigned as O_2^+ (see text). A small, reproducible shoulder feature on the primary ion distribution is indicated with an asterisk. Data was obtained at a field strength of 7.0 V·cm^{-1} in ~2.1 torr helium at 298 K.

Immediately obvious in the mobility spectrum of 32 m/z are two distributions. Comparisons with the mobility spectrum in ambient air (**Figure 48**) under the same conditions confirm that the higher mobility distribution is O_2^+. This assignment is also supported by the predicted arrival time of O_2^+ based on the published reduced mobility values for O_2^+ and CH_3^+ in helium (K_0=21.9 and 26.0, respectively at 10 Td, 300 K). In this case K_{O2}:K_{CH3} is ~0.84 and the measured arrival time of CH_3^+ is 502 μsec, predicting an arrival time of 595 μsec for O_2^+, which is relatively close to the peak

assignment for the ion distribution at 571. Interesting to note here is that this time prediction places O_2^+ with a lower ionic mobility in argon but a higher ion mobility in helium as compared with the methanol molecular ion. In both cases, the experimental data supports this prediction. The observed presence of O_2^+ in the helium drift gas spectrum is significant in that it is likely also present in the argon drift gas experiments which used the same anhydrous methanol sample.

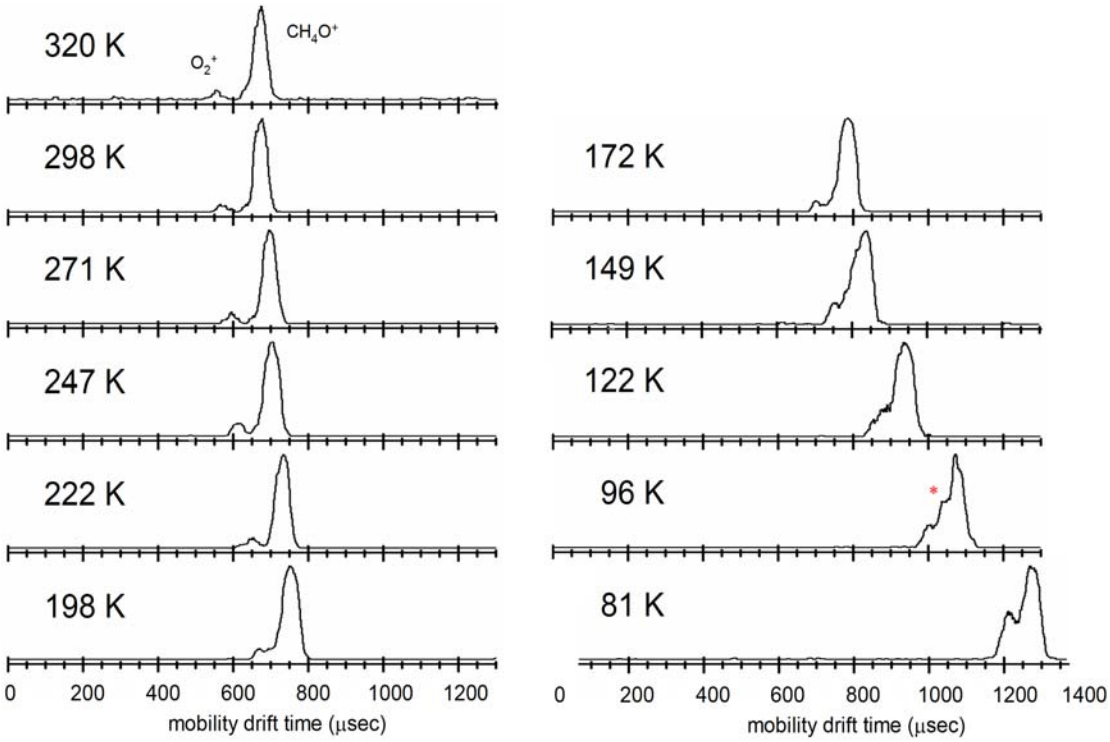

Figure 69 – Mobility spectra of methanol in helium from 320 to 81 K. Two mobility distributions at 32 m/z are resolved at room temperature with the higher mobility distribution assigned as O_2^+ (see text). As the temperature decreases, the arrival time of O_2^+ migrates towards the primary ion distribution. The primary ion distribution begins to resolve into two peaks, indicated with a red asterisk. At 81 K, two distribution are observed, with the higher mobility peak comprised of O_2^+ and another ion distribution, as suggested by the higher ion abundance compared with the O_2^+ distributions at higher temperatures.

Low temperature mobility experiments were also conducted for the methanol in helium drift gas study in order to facilitate higher resolution mobility separations. The resulting mobility spectra of 32 m/z are contained in **Figure 69** for the temperature range of 320 to 81 K. Lower temperatures will not affect the abundance of O_2^+ since it is formed in the ion source and so the O_2^+ ion distribution remains throughout the temperature ranges investigated. At lower temperatures, the O_2^+ peak migrates towards the lower mobility distribution until both distributions are nearly completely isobaric at 81 K. This complicates the experimental separation. However, in the 96 K spectrum, there is a distinct peak emerging from the primary ion distribution, labeled in **Figure 69** with the red asterisk. In most of the higher temperature spectra, this distribution is partially observed as a shoulder on the main mobility peak. It appears that at 81 K, this ion distribution and the distribution for O_2^+ merge, as suggested by the increase in ion abundance which cannot be accounted for by O_2^+ alone. This partial separation offers a tantalizing glimpse as to the existence of two ion distributions comprising the molecular ion mobility of methanol, but does not provide conclusive evidence.

The near isobaric mobility of the nominal mass isomer O_2^+ with the molecular ion of methanol complicates the interpretation of the mobility spectra. In order to address this issue, deuterated methanol (methanol-D4, CD_3OD, Cambridge Isotope Laboratories, Andover, MA) was investigated using the same experimental procedure outlined above. The resulting mobility spectrum of 36 m/z (CD_3OD^+) from methanol-D4 is contained in **Figure 70** for temperatures between 298 and 81 K. There is no evidence of a second distribution present in this spectrum. This lends evidence against

the presence of two electronic configurations resulting from the direct ionization of methanol.

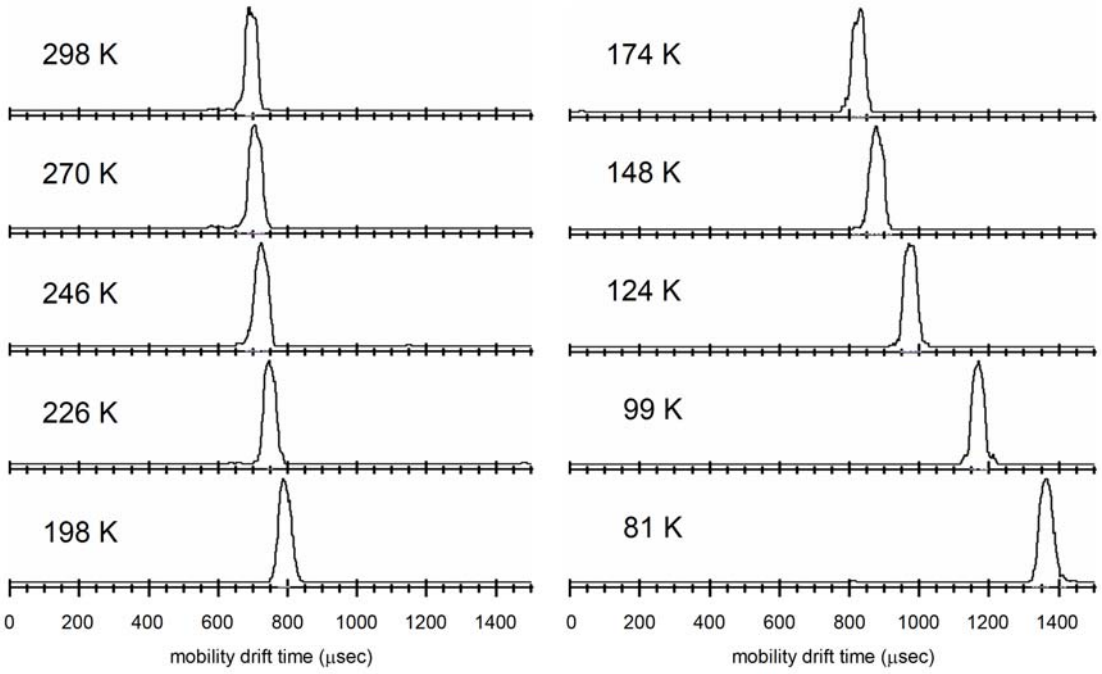

Figure 70 – Mobility spectrum of 36 m/z from electron ionized methanol-D4 at temperatures from 298 to 81 K. This m/z represents the deuterated analogue of the methanol molecular ion. The absence of a second distribution at this m/z suggests either that a second electronic configuration is not formed from direct EI of methanol-D4, or that the ion mobility methods employed cannot differentiate the two configurations. Spectra were acquired with a field strength of 6.6 $V \cdot cm^{-1}$ in 2.1 torr helium.

In order to investigate the assertion by Holmes *et al.* regarding the inability to form the distonic ion from direct electron ionization of methanol, methyl formate was evaluated as a suitable precursor ion that may go on to form the distonic ion through electron fragment rearrangement [405]. The same methodology employed for methanol was also used in the experimental evaluation of methyl formate, namely the use of varied drift gases, fields and temperatures.

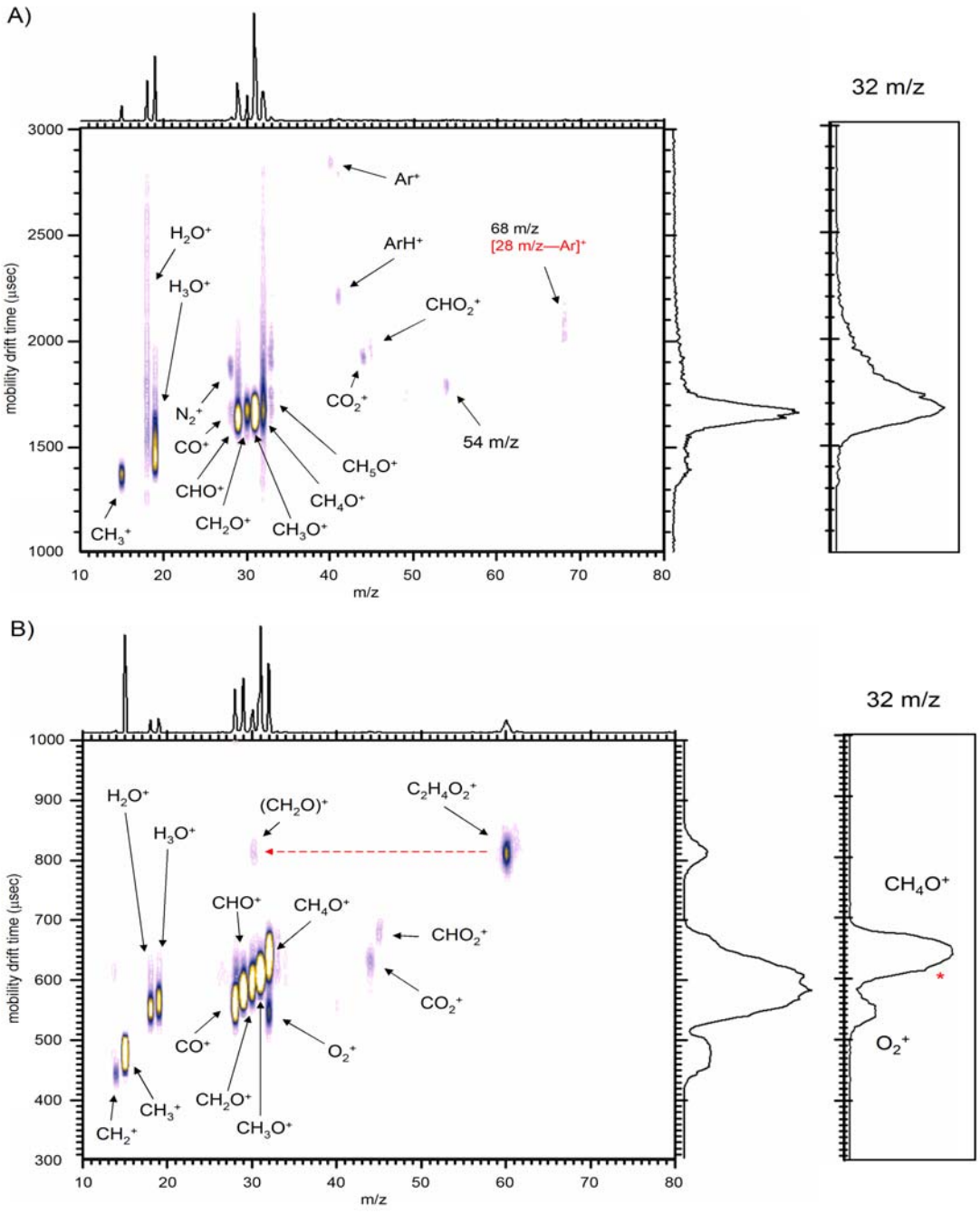

Figure 71 – Spectra of methyl formate in argon and helium at room temperature. **A)** Methyl formate in argon drift gas exhibits lower resolution and the characteristic "smearing" of ion signals resulting from argon ion chemistry. A peak at 30 m/z correlates to the molecular ion of formate (dotted red arrow), and can be assigned as the fragment ion shown, or could perhaps be a doubly charged molecular ion. The 32 m/z mobility profile exhibits tailing as was seen for methanol. **B)** Methyl formate in helium is at a noticeably higher resolution. The 32 m/z mobility spectrum contains the O_2^+ and a broadened primary ion distribution which also has a reproducible shoulder feature. Data was obtained at a field strength of ~6.7 $V \cdot cm^{-1}$ for both experiments with an argon pressure of 0.75 torr and a helium pressure of 2.1 torr.

Figure 71 contains the 2D mobility-mass spectra of methyl formate in argon and helium gas a room temperature. Characteristic of the argon spectrum is the presence of peak tailing on most ions. The mobility trace corresponding to 32 m/z exhibits a significant amount of tailing. This arrival time is near identical to what was observed for the 32 m/z mobility spectrum for methanol (**Figure 69**) and was previously attributed to the isobaric mobility of O_2^+ with CH_4O^+ in argon. The methyl formate spectrum in helium (**Figure 71B**) is also remarkably similar to the methanol spectrum in helium. A reproducible shoulder feature on the main 32 m/z mobility peak is also observed for this system. Low temperature experiments for methyl formate (**Figure 72**) also bear a remarkable resemblance to those obtained on methanol in both drift gases. In argon (**Figure 72A**), tailing of the 32 m/z mobility peak distribution continues throughout the temperature range and only hints at being resolved into multiple peaks in some instances. In helium (**Figure 72B**), two mobility peaks are observed at 32 m/z and as seen with methanol, the O_2^+ peak migrates towards the main ion distribution as the temperature is lowered. Also observed here somewhat more prominently is partial resolution of a shoulder feature on the main 32 m/z mobility distribution, most prominent at 199 and 174 K (marked with red asterisks in **Figure 72B**). The higher resolution at these two temperatures is indicative of less temperature deviation during the signal summing acquisition. Considerably more temperatures can be sampled using helium drift gas, owing to both the increased ion transmission in helium (resulting from less collisional scatter) and the lower ultimate temperature, which for helium is down to the boiling point of liquid nitrogen.

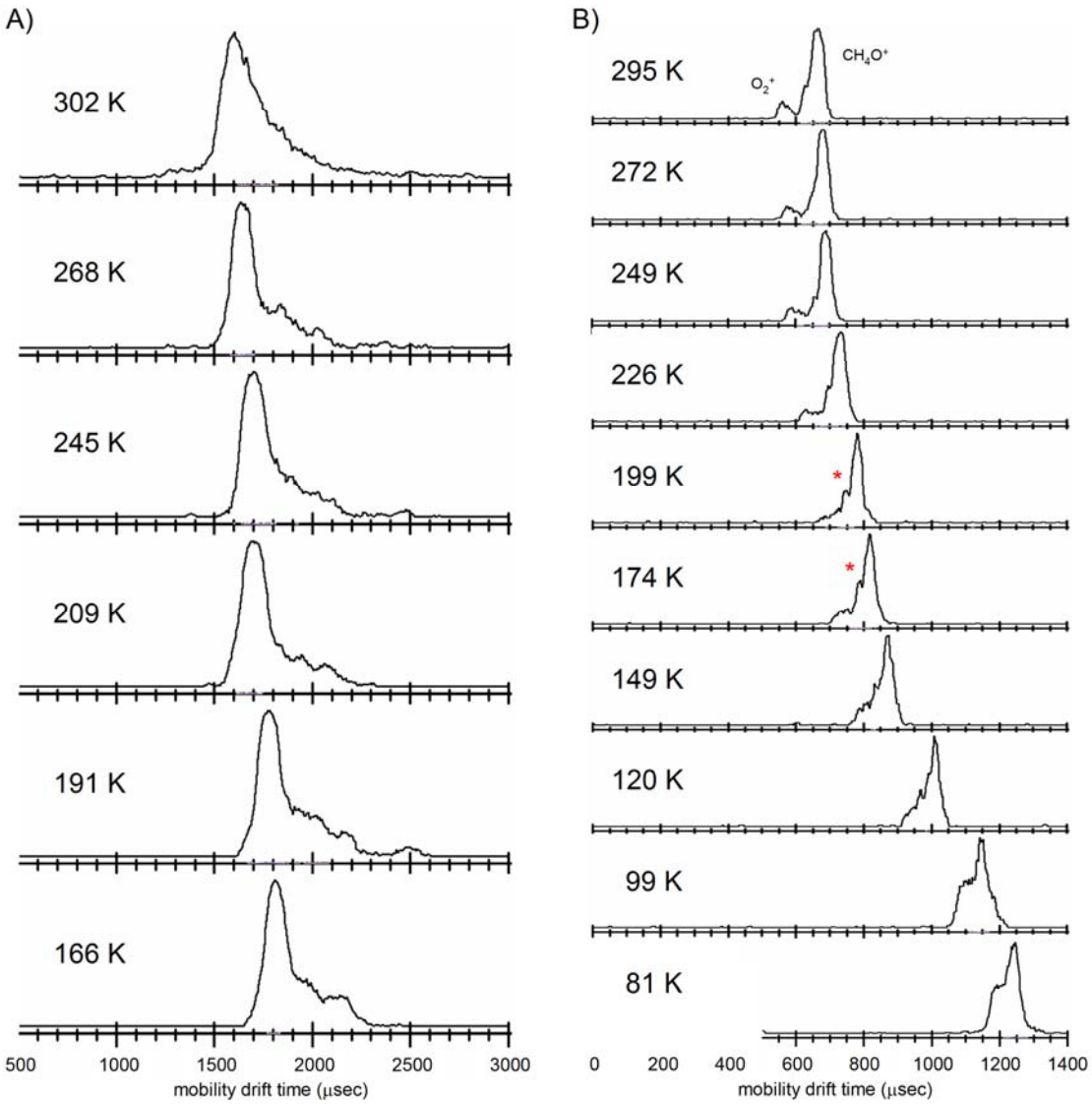

Figure 72 – Mobility spectra of 32 m/z from electron ionized methyl formate for argon and helium drift gas from 302 to 81 K. **A)** Argon drift gas data from 302 to 166 K. Peak tailing is observed across all temperatures sampled. While it appears that multiple ion distributions exist beneath the tailing feature, the resolution is poor. **B)** Helium drift gas data from 295 to 81 K. Two ion distributions are observed at room temperature, one corresponding to O_2^+ and the other CH4O+. An additional shoulder feature is observed for some of the spectra, marked with a red asterisk. Both sets of data bear a remarkable resemblance to the corresponding methanol spectra for argon and helium. Field strengths were ~6.7 $V \cdot cm^{-1}$ in 0.75 torr argon and 2.1 torr helium.

4. NOVEL IMPROVEMENTS FOR THE CRYOGENIC ION MOBILITY INSTRUMENT

4-1 Ionization Source Designs for High Mass Ion Studies on the Cryogenic IMS

The analysis of biologically relevant ions is the focus of most modern ion mobility-mass spectrometry research. Indeed, it was only within the last 20 years that two ionization methods changed the direction of mass spectrometry research, namely the discovery of matrix-assisted laser desorption ionization (MALDI) and electrospray ionization (ESI), which still enjoy nearly exclusive access to modern biological ion mobility and mass spectrometry research. These two very different ionization methods compliment one another in terms of what each can offer analytical ion mobility-mass spectrometry (refer to **Sections 1-7.2** and **1-7.3**).

It is clear that biological ion mobility-mass spectrometry research would benefit from low temperature ion mobility capabilities. The work of Martin Jarrold demonstrates the utility of variable temperature for elucidating higher order peptide and protein gas-phase structure [123,411] and the thermodynamics of these structural transition processes [412,413]. No clear study has been undertaken to explore the resolution gains that low temperature may afford for these high mass ion studies. Indications are clear that biological ions undergo structural transitions at high effective ion temperatures which is often the case at room temperature. If the ion is changing structurally during the ion mobility measurement, then it is certainly being measured at a low resolution defined as a composite of the conformational space the ion samples. Low

temperature can thus be used as a means of stabilizing ion conformations, resulting in higher resolution measurement. There is also motivation for conducting injected ion experiments with large ions. The higher momentum resulting from the increase in ion mass will likewise decrease ion losses due to scatter during ion injection. Though not developed previously, there is also a mass and temperature dependence on injected ion losses. Ion trajectory simulations are contained in **Figure 73** for three ion masses (15, 50 and 200 m/z) injected into a gradient of helium drift gas (increasing pressure from left to right) at two temperatures (300 and 80 K). High mass ions (<500 m/z) would not be subject to the collisional losses observed in **Figure 73** due to the increased momentum.

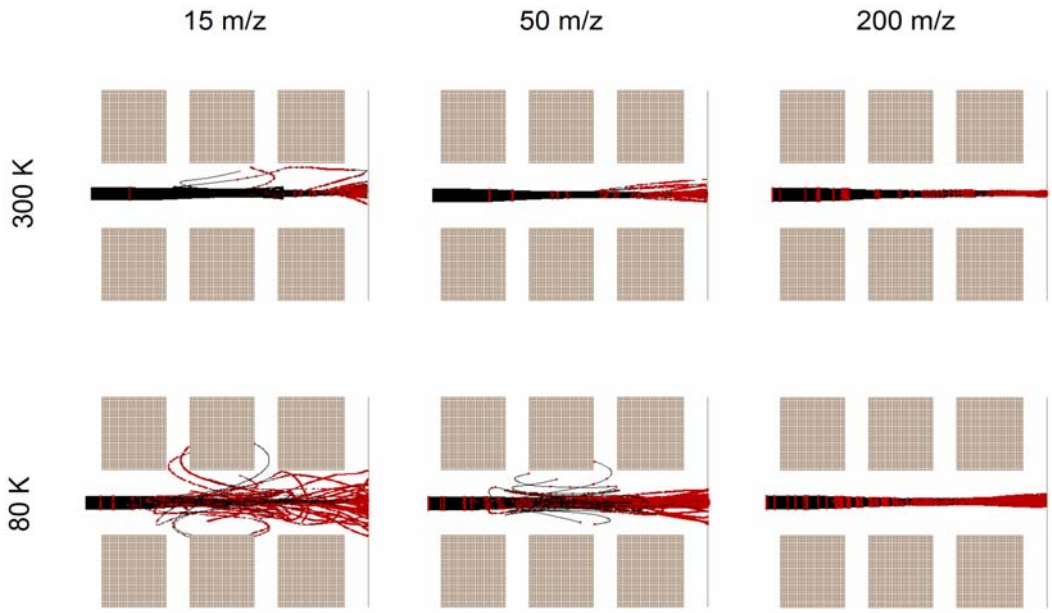

Figure 73 – Ion trajectory simulations for three ion masses at 300 and 80 K. Ion masses of 15, 50, and 200 m/z are simulated for ion injection into a density gradient of helium drift gas (increasing from left to right) which simulations ion injection conditions in the experiments described in this dissertation. Scatter losses are most severe for the case of small mass ions at liquid nitrogen temperature (**lower left**) and transmission is the highest for heavy ions at room temperature (**upper right**). High mass ions >500 m/z are not expected to be subject to significant scatter losses within the range of 1-10 torr in helium at 80 K.

In additional to increased ion transmission into the drift cell, high mass ions possess greater degrees of freedom and as such have a higher energy threshold for activation, which means greater ion injection energies can be utilized, further increasing ion transmission. Higher mass ions are also less subject to losses due to field effects, as with focusing fields in the presence of gaseous collisions. The uniform field drift cell design presented here is certainly capable of transmitting higher masses and the ion optics utilized are standard for all spectrometer platforms, so it follows that if high mass ions can be formed, then the instrument will be capable of analyzing them. Thus there is much motivation for developing high mass ionization methods for the cryogenic MS-IMS-MS instrument.

4-1.1 Design of a MALDI Ionization Source

A laser ionization source was developed by the author during the preliminary stages of instrument design as a means of diagnosing certain instrument components such as the quadrupole and charged particle detectors. A pulsed ionization source is also convenient for diagnosing the IMS, as the ion gate need not be operated to obtain ion mobility spectra. This laser ionization source is readily amendable to MALDI studies and can be directly fitted to existing ion optics in the source with no additional instrument modifications (this was the motivation for tapering the first three ion optical elements following the ion source).

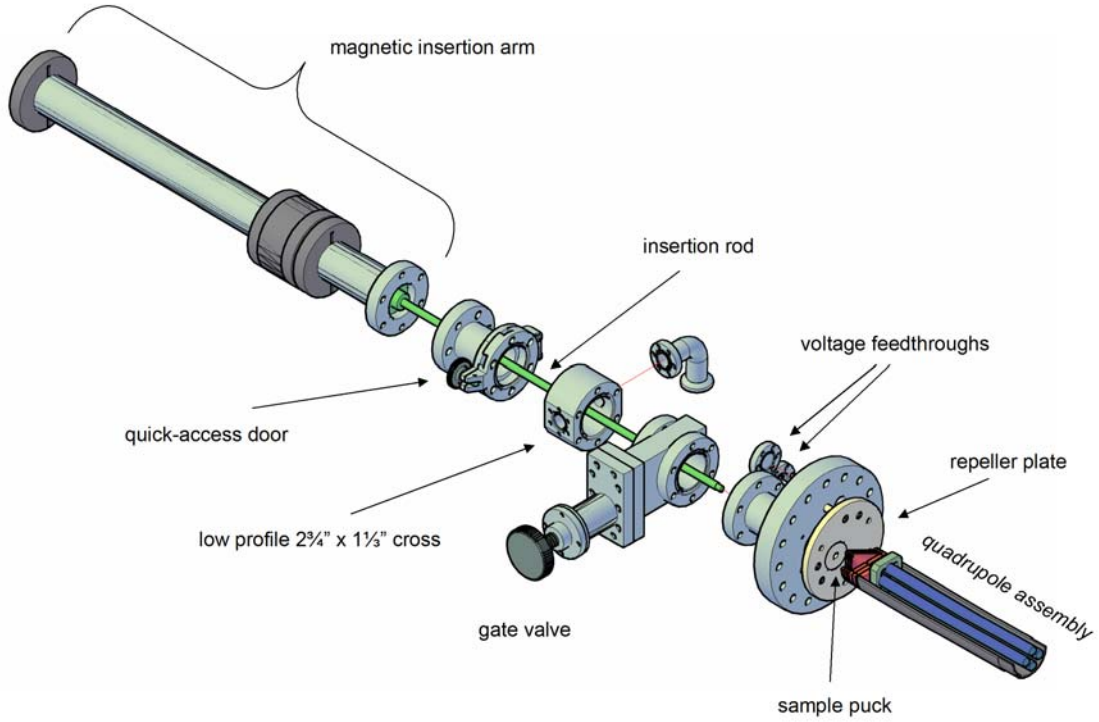

Figure 74 – The MALDI ionization source developed for the cryogenic ion mobility instrument.

A CAD generated schematic of the MALDI source is contained in **Figure 74**. The source is based on a rotating sample puck design whereby several samples can be spotted on the outer rim of the puck and rotated into alignment with the ionization laser and beam extraction axis. This facilitates the analysis of numerous samples without the need to withdraw and vent the probe assembly, then reinsert, pump and realign. The sample puck inserts flush with a large planar electrode, creating a uniform field surface for directing ion extraction forward. The existing conical ion optics create a moderate ion focusing field for efficient ion extraction and can be placed within 1-2 mm of the sample surface for high ion transmission. The sample loading system is based on an annular chamber isolation design whereby the sample puck is withdrawn to the chamber

and isolated from the vacuum system *via* a gate valve (2¾" Conflat®, MDC Vacuum Products, Hayward, CA) prior to accessing through a quick access door (Viton® sealed, MDC). This greatly minimizes the risk of atmospheric contamination of the main vacuum system. Furthermore, the insertion probe is a magnetically coupled design (5 lb. axial force insertion arm, Huntington Mechanical Laboratories, Inc., Mountain View, CA) whereby the linear motion is facilitated by a magnetic coupling through a vacuum isolated tube. The ionization laser (337 nm N_2 discharge, Spectra-Physics, Mountain View, CA) is secured onto a triple axis alignment stage and a neutral density filter (variable reflective, OptoSigma Corporation, Santa Ana, CA) combined with an optical lens (BK7 plano convex, 6" focal length, OptoSigma) is used to attenuate and focus the ionization laser. A rotatable linear motion stage (LFM-1, Newport Corporation, Irvine, CA) can fine adjust the optical focal length ±2.5 mm with 1 μm resolution.

4-1.2 Design of an ESI-Ion Funnel Interface Ionization Source

An electrospray ionization source was also developed by the author specifically for ion mobility instrumentation. Drift tube ion mobility instruments require special consideration for high voltage since either the front or the back side of the IMS will be at a biased potential. While the instrument described in this work utilizes back end (TOF) biasing, the electrospray source was developed with the option for floating up to 8,000 V in order to allow it to be coupled to commercial instrumentation which operates at ground potential at the source. Also incorporated into the ESI design is the use of an electrodynamic ion funnel, which has been shown in recent literature to provide

significant improvements in ion transmission as compared to more traditional skimmer inlet designs [314]. Current capabilities of the Laboratory for Biological Mass Spectrometry at Texas A&M University do not include ESI ion mobility, which offers a distinct advantage in terms of ion mobility accessible mass range and ultimate resolving power [38]. This combined with the ability for direct sample infusion are strong motivators for developing an ESI for our current generation of ion mobility instruments, including the cryogenic IMS.

A schematic of the ESI source developed for ion mobility is contained in **Figure 75**. The electrospray needle is of the conventional design and utilizes a multi-axis (XYZ and rotation, OptoSigma Corporation, Santa Ana, CA) positioning system to fine tune the location of the spray. A stainless steel disk defines the spray cathode. A 500 μm heated metal capillary (cartridge type, Thermo Electron Corporation, Waltham, MA) facilitates desolvation of the ions before admission into the ion funnel. This capillary also serves as the conductance limit, defining a base pressure in the source block between 1-10 torr. The capillary is mounted on a flange which is coupled to the main chamber body through a flexible stainless steel bellows. This allows the capillary to be canted up to ~30^{o} left and right to bring ions into the funnel off-axis. Off-axis operation in this manner greatly reduces the potential for main chamber contamination by direction most of the neutral solvent away from the inlet. Off-axis motion is controlled through a custom pivot support system with the pivot axis set to a point just inside the funnel such that the heated capillary can rotate with a static position at the funnel entrance.

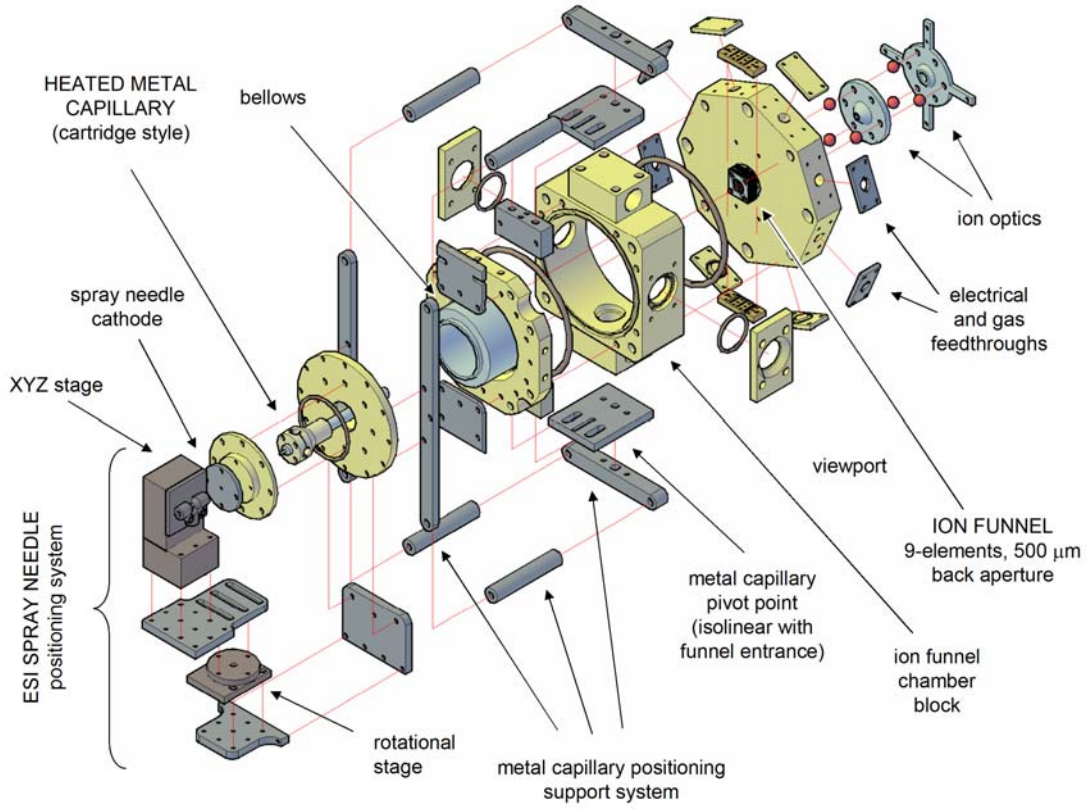

Figure 75 – Schematic of the ESI-ion funnel source developed for ion mobility. Source incorporates a spray needle (conventional or nanospray), a heated metal capillary, a 9-element electrodynamic ion funnel, and back ring ion optics for recollecting and focusing ions which exit the funnel device. Pale yellow components are made of insulating thermoplastic material. Source can be biased to several thousand volts.

The 9-element electrodynamic ion funnel is built up from an off-the-shelf ion optical component system (modified eV Parts®, Kimball Physics, Wilton, NH) which greatly reduces the cost and time for fabrication. The operation of the funnel requires two RF inputs on every other electrode plate, 180^{O} out of phase for collisional-assisted radial focusing. The ion funnel is driven with a custom designed RF power supply (Ardara Technologies LP, North Huntingdon, PA) capacitively decoupled to the funnel electrodes through high temperature stability capacitors (1,000 pF C0G ceramic

capacitors, KEMET Electronics Corporation, Greenville, SC). A DC drop across the length of the funnel maintains forward ion motion. The DC drop is created with a resistive network (1 MΩ) defined by two voltages at the front and back of the assembly. The last plate is fitted with a 300 μm aperture disk (Small Parts Inc., Miramar, FL) and is decoupled from the ion funnel circuit and driven with an independent DC voltage. This independent DC drop is necessary to draw ions through the last few RF electrodes, which otherwise create a "pinching" stop potential during the high end RF. Behind the aperture are two ring electrodes which are spaced in the periodic focusing design (1:1 inner diameter to spacing [111]) for recapturing and focusing the ions which exit the funnel. The main body of the heated capillary and ion funnel chamber is fabricated from polyacetal (natural Delrin®, McMaster-Carr, Aurora, OH) to allow the capillary, funnel and electrodes to be floated to a high potential. All other vacuum chamber components are stainless steel. The capillary pivoting support system is fabricated from aluminum. O-ring seals (high temperature silicone) are utilized in the design to maintain vacuum.

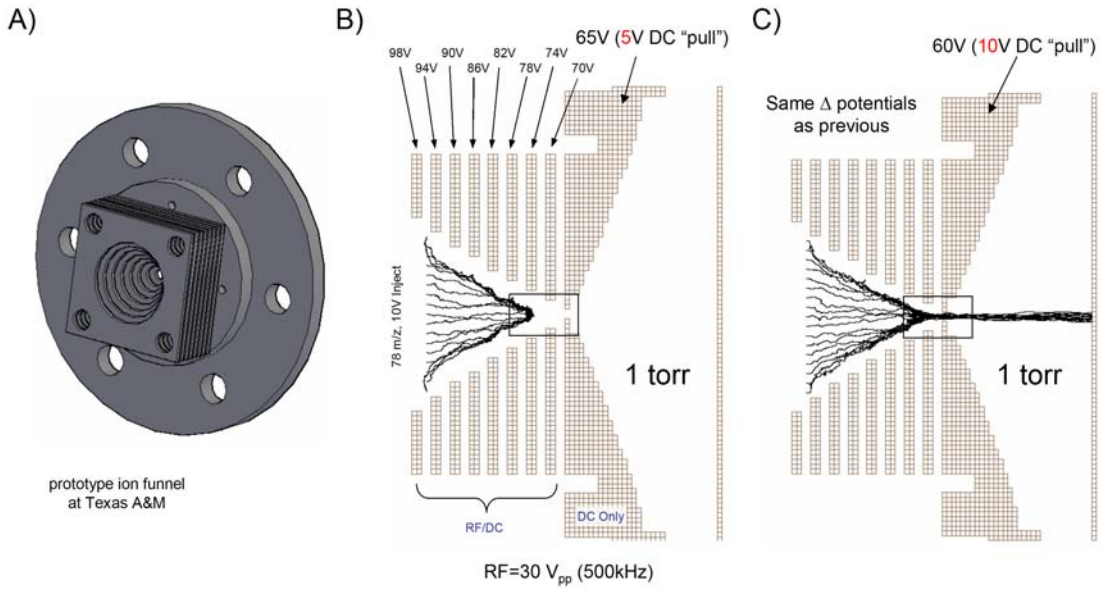

Figure 76 – Ion trajectory simulations of the ion funnel developed for ESI ion mobility. **A)** CAD generated rendering of the ion funnel. **B)** Ion trajectories showing ion trapping for a DC extraction voltage (funnel to aperture) of 5 V. **C)** Raising the DC extraction voltage to 10 V pulls all ions from the trapping well. This principle forms the basis of operating the ion funnel as a gated ion accumulation device for IMS experiments. Space charge effects were not considered in the model. Ions traverse the model left to right.

Ion trajectory simulations were conducted both to guide initial design of the ESI-ion funnel source and to determine optimal conditions for its operation. The simulations utilized SIMION 8.0 and the hard sphere collisional model described elsewhere [166]. **Figure 76** contains simulation results for determining the required DC drop between the funnel and the aperture plate necessary for pulling ions from the device. A relatively small (5 V) potential difference constitutes the difference between ion *trapping* and ion *transmission.* Incidentally, this forms the basis for operating the ion funnel as an ion gating and accumulation device which is necessary for ESI IMS experiments. The model does not incorporate a space charge theory and so it is expected that the duration

for IMS ion trapping is critical for minimizing Coulombic leakage of ions into the drift cell. Space charge limits will be reached very quickly in a device such as this.

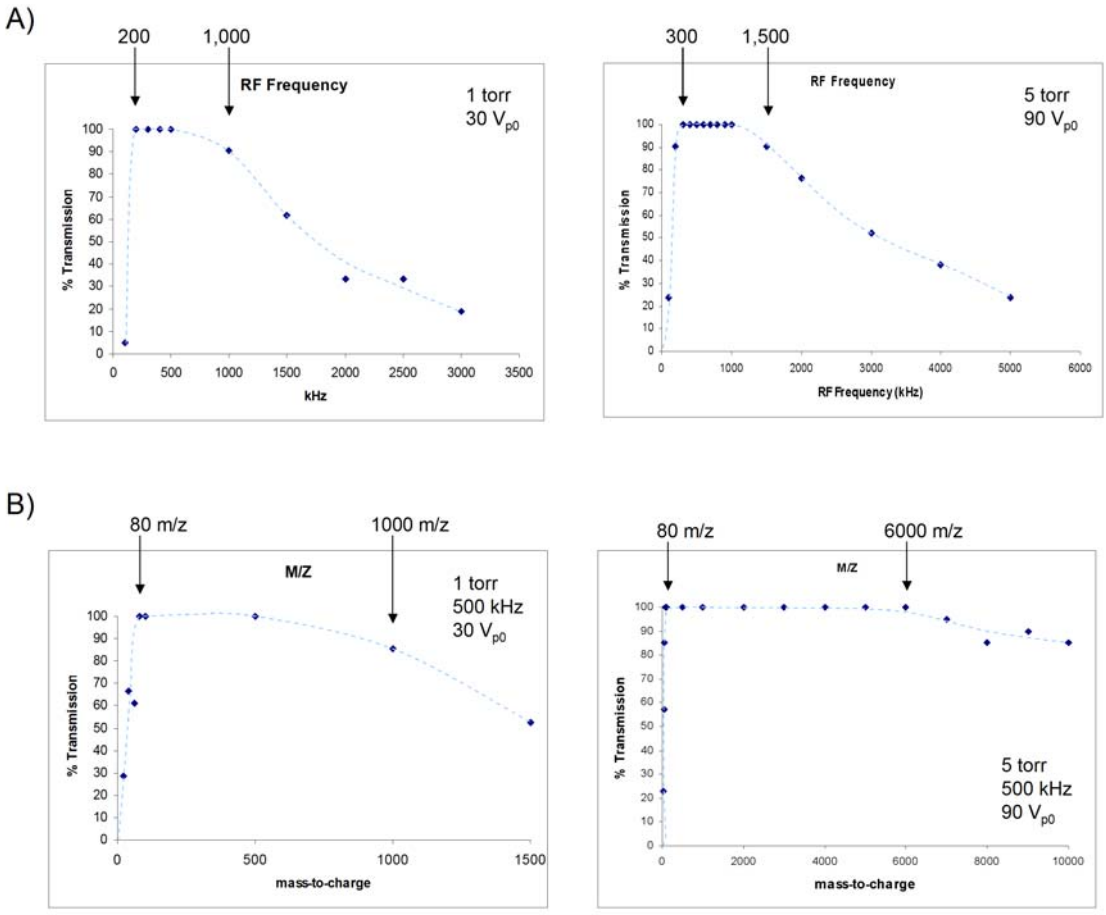

Figure 77 – Performance plots of the ion funnel generated from ion trajectory simulation results. **A)** Increasing the RF frequency as the pressure of the funnel is increased is necessary to maintain ion transmission performance. Simulation is for a 100 m/z ion. **B)** The m/z transmission window at 1 and 5 torr is markedly different, with a higher mass more efficiently transmitted at higher pressure. This is a result of more dampening collisions being necessary for higher mass ions. The m/z cutoff remains the same.

Figure 77 contains some results of the ion trajectory data, plotted relative to percent ion transmission through the ion funnel. As the pressure is increased (**Figure 77A**, left to right), the frequency must also be increased to afford the same approximate

ion transmission. The mass transmission window will increase at higher pressures (**Figure 77B**), due to improved collisional focusing of higher momentum ions, however the focusing of low m/z ions will ultimately be limited by the RF frequency as with quadrupole devices (**Section 1-6.1**). This inherent low m/z cutoff limits the application of ion funnels to large m/z ion studies, which is the reason this technology was not implemented in the cryogenic work described in this dissertation.

Experimental conditions are also technically limited, for example, by the ability of the RF source to drive the ion funnel to full power and the pumping system's ability to achieve low base pressures. The small electrode ion funnel described here is novel in that the low surface area of the electrodes creates a minimal amount of capacitance between the two RF channels (measured < 150 pF before capacitor placement). This low capacitance ultimately allows for higher frequency operation of the funnel, which in turn allows it to focus ions at higher base pressures, reportedly up to ~30 torr [414]. The small, 9-electrode ion funnel described here has the lowest capacitance ever reported for ion funnel devices, as compared for example with the 100 plate, 1.6 nF described in the high-pressure, high frequency report. This should allow high frequency operation of the ion funnel and improve the ion transmission performance substantially. Experiments are currently underway with the ESI source, and as such empirical performance results cannot be provided at this time.

4-2 Drift Cell Improvements for High Sensitivity IMS

The drift cell design presented and utilized here is effective but by no means optimal with regards to ion transmission. This is purposeful in that nearly all strategies utilized to focus ions in the presence of gas collisions introduces ion heating and low mass ion losses, both of which are undesirable in these experiments which seek to optimize the IMS analysis of small molecules. For high mass ion studies, however, focusing fields can be utilized.

4-1.3 An Electrostatic Analogue of the RF Ion Funnel for High Sensitivity Ion Mobility Applications

The RF ion funnel is a relatively new technology originally developed for ion sources [314], but is now being utilized as a back-end refocusing device for uniform field ion mobility drift tubes in order to improve the ion transmission properties of the mobility spectrometer [110]. The device works by altering the trajectory of an ion as it approaches a radially symmetric (ring) electrode with an electrodynamic potential applied to it. A strong RF potential redirects the ion's trajectory axially and the presence of gas collisions corrects the translational energy of the ion to a vector direction that is opposite of the RF field. The gas number density is critically tied to the focusing properties of the RF ion funnel, since the RF energy must be imparted to the ion between gas collisions, otherwise focusing becomes dampened by thermalizing collisions. Thus for a given range of pressure, there is an optimal frequency and amplitude of the RF necessary for optimal focusing to the axis. Because the ion funnel geometry only

corrects trajectories axially, a declining potential must also be provided longitudinally to maintain forward ion motion. This requires a series of ring electrodes with decreasing inner diameters and an overall drop in the DC potential from front to back, which effectively describes the entire RF ion funnel device. One consequence of using strong focusing fields is that ions with too little momentum will be overcorrected and lost in the device. This creates an inherent low mass cutoff for the RF ion funnel and as such it is unsuitable for small molecule studies. For large molecules, however, the RF ion funnel can recapture ions at near 100% efficiency.

A temporally dynamic RF potential is analogous to a spatially dynamic DC potential with the frequency in the latter supplanted by the velocity of the ion in the longitudinal dimension [221,415]. Thus it is possible to axially refocus ions using purely DC only potentials if the ion's position is temporally dynamic. This forms the basis for the DC only periodic field focusing ion mobility spectrometer, which was developed in our own laboratory for high transmission IMS [78]. Conceptually, a series of small inner diameter rings replace the conventional large diameter guard ring assembly of a drift tube, which has the effect of confining ions in a narrow axial corridor. Refocusing towards the spectrometer axis occurs within every ring and this focusing is relaxed in the space between the rings, effectively creating an oscillating field condition. The optimal geometry of such a periodic stacked ring configuration is 1:1:1 of inner diameter, ring spacing and spacing between the ring, respectively [111]. This effectively creates the ideal sinusoidal field necessary for efficient ion refocusing.

While the transmission through a periodic field ion mobility spectrometer approaches 100%, transmitting these focused ions through the exit conductance limit (necessary for differential pressure operation) results in ion losses. This is an unavoidable outcome of the necessarily small requirement of the exit aperture for maintaining the high vacuum requirements of a back end mass spectrometer. While it is possible to match the dimensions of the periodic focusing electrodes to that of the exit aperture, the required inner diameters (~1 mm) of the ring electrodes would impose space charge limits on the spectrometer such that scattering losses would increase and space charge initiated band broadening would degrade mobility resolution. An inner diameter of ~5 mm or so offers an ideal balance between focusing and space charge confinement. One possible solution to this mismatch between the periodic and exit aperture geometries is to decline the electrode inner diameter at the last few rings to transition ions through the exit aperture. If the optimal periodic ratio of 1:1:1 is maintained, ion refocusing should remain high as the ions traverse the decreasing inner diameter electrodes until the exit the aperture. This forms the basis for the electrostatic ion funnel.

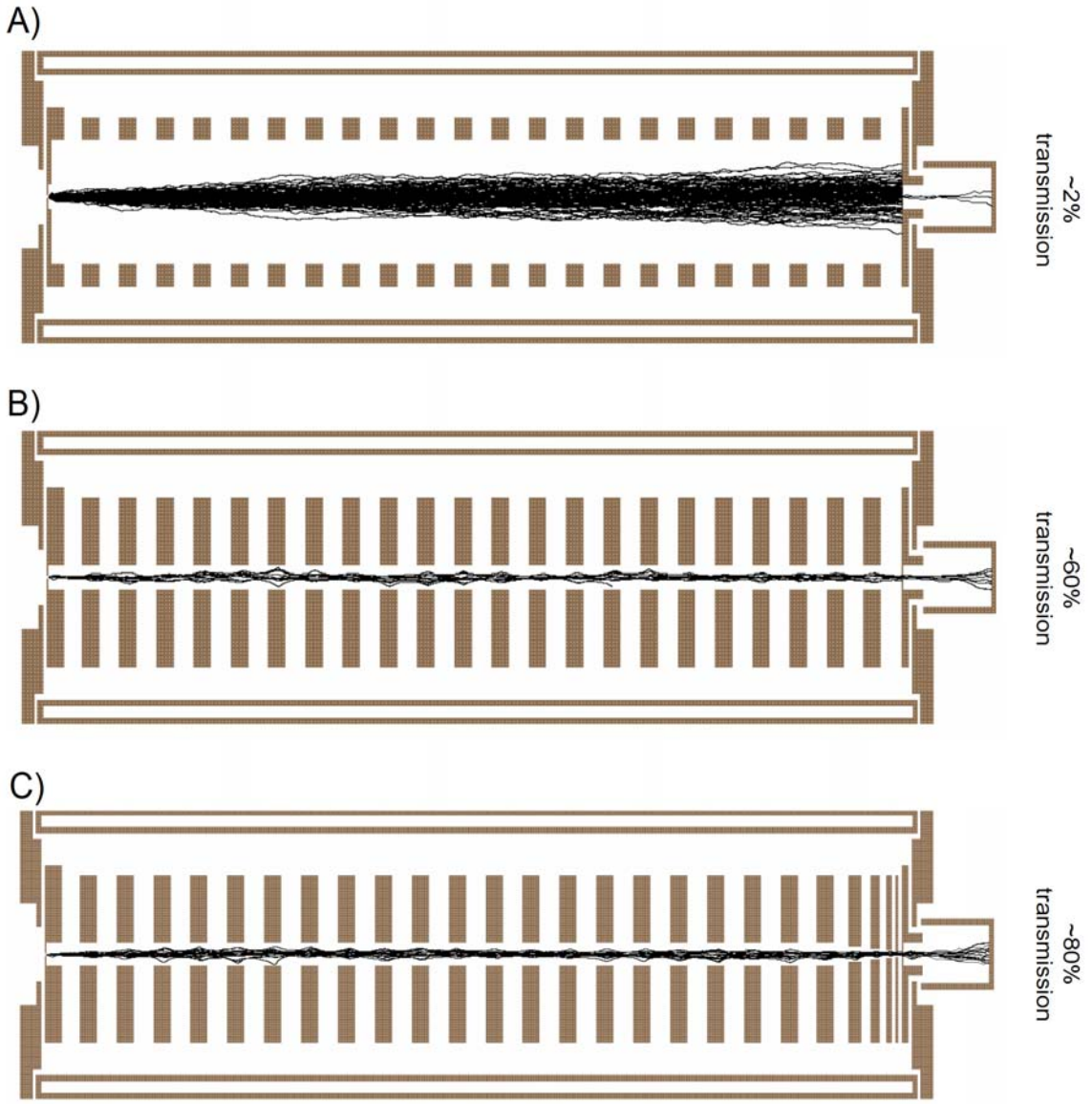

Figure 78 – Ion trajectory simulations of three DC field ion mobility drift cell geometries: uniform, periodic and periodic with a DC-only ion funnel. A) A conventional uniform field design incorporating conductance limits results in very high ion losses, here about 2% of the ions are transmitted. B) In a periodic field design (6.3 mm), nearly all ions traverse the device, but the necessarily small exit aperture (here ~1 mm) results in significant ion losses. About 60% of the ions are transmitted through the exit aperture in this simulation. C) If an electrostatic ion funnel geometry is incorporated into the periodic design, transmission increases to about 80%. The simulation is for 78 m/z ions utilizing a fixed number density collision program (1 torr helium) at room temperature.

Ion trajectory simulations for three ion mobility electrostatic geometries (uniform field, periodic field, periodic field incorporating an electrostatic ion funnel) are contained in **Figure 78**. These simulations clearly indicate the gain in ion transmission with the periodic field design (**Figure 78A**, ~60%) as compared with the uniform field (**Figure 78B**, ~2%). Ion transmission to the back plate in both geometries is 100%, indicating that this is the location where ion losses occur. When a series of declining inner diameter electrodes are added as the last few ring elements (**Figure 78C**), ion transmission through the exit aperture improves, here to ~80%.

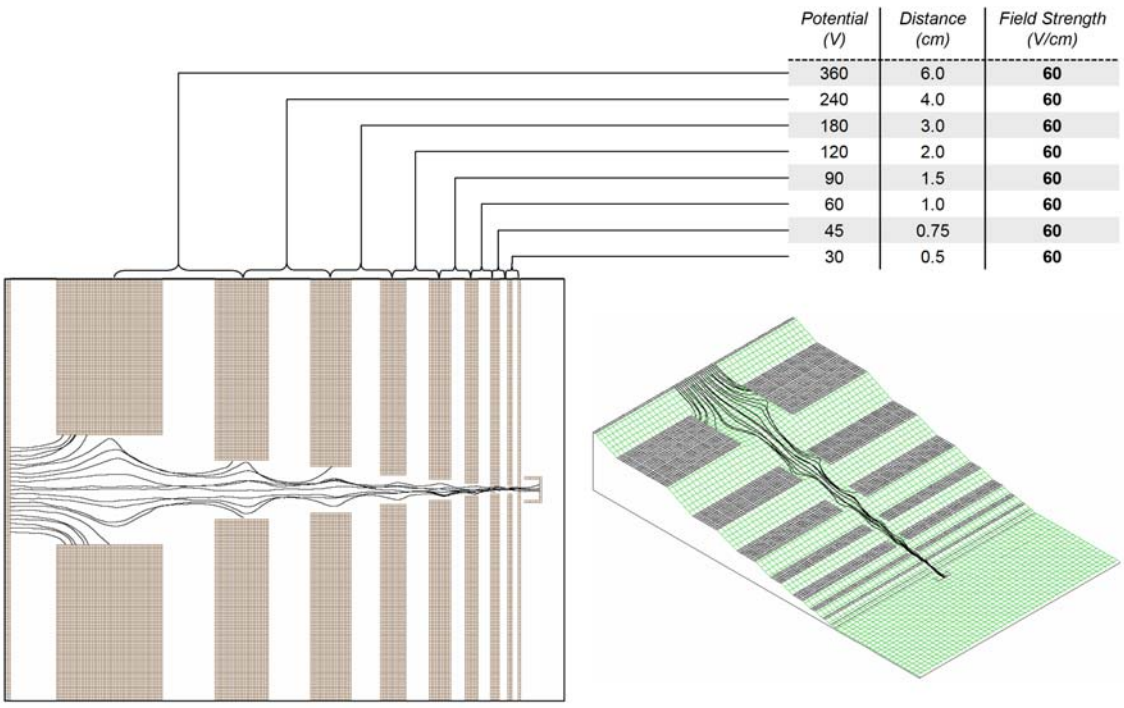

Figure 79 – Details of the electrostatic ion funnel. Ion trajectory modeling indicates that the greatest ion losses occur at the first few decreasing inner diameter electrodes. In this particular simulation, ions are started across a distribution in the y-dimension and do not reflect the actual distribution of ions exiting a periodic drift ring geometry. Most ion losses thus occur for ions too far off axis for the lens to refocus. The field strength in this design is constant, which couples favorably to a DC field IMS. Ions are 78 m/z in 1 torr helium at room temperature. No space charge model is utilized.

Figure 79 contains details of the ion simulation for the electrostatic ion funnel, which indicates that most ion losses are occurring at the first decreasing inner diameter ring electrode. Important to note here also is that the average electric field between any two electrodes in the electrostatic funnel is kept the same, here at 60 $V \cdot cm^{-1}$. Certainly higher fields can be utilized to improve ion focusing, but at a cost of significant ion heating which can have deleterious effects on the ion structure. This particular geometry is by no means optimal, but it effectively illustrates the concept of an electrostatic ion funnel for ion mobility applications.

5. SUMMARY AND CONCLUSIONS OF WORK

5-1 Summary of the Motivations for Low Temperature Ion Mobility

A general overview of the ion mobility spectrometry-mass spectrometry analytical technique was provided in the first section. It was noted that while ion mobility fails to achieve the high resolutions and information content observed in chromatographic methods (*e.g.*, gas and liquid chromatography) the technique excels in its separation speeds and the specific nature of the information obtained, *i.e.*, the chemical class-specific mobility-mass correlation trendlines and gas-phase cross section. Thus, there remains much motivation to improve the ion mobility-mass spectrometry technique, specifically in regards to separation and resolving abilities of ion mobility. Several alternatives to the traditional "drift tube" ion mobility technique have been developed and were surveyed in **Section 1-1.2**. In terms of the information content and overall analytical throughput, the drift tube ion mobility is still preferred, since for every analysis cycle, a complete ion mobility spectrum can be obtained (a characteristic of all dispersive types of analysis).

Further technical details underlying the drift tube ion mobility technique was discussed, specifically the influence of various instrument parameters on the separation efficiency. Resolving power remains the most popular and convenient means of characterizing the separation abilities of various ion mobility spectrometers and resolving power is defined by the drift time of a single peak divided by its temporal width at half of its maximum. From this definition, high separation abilities are

achieved when ions spend a long time in the drift tube, but remain temporally narrow, which is somewhat contradictory considering that the band broadening mechanism in ion mobility is ion diffusion, which scales with the residence time of ions in the drift gas. Thus, there is a balance which must be struck between adjusting the various instrument parameters that influence the ion residence time, such as the gas pressure, drift region length and the magnitude of the voltage driving ions across the drift region. However, for the drift gas temperature, lower temperatures will serve to both increase the ion residence times in the drift region and decrease the temporal width of ion distributions, the latter made possible by decreased Brownian motion at reduced gas temperature. Thus it follows at least on a qualitatively theoretical basis that lower temperatures should always improve the resolving power for drift tube ion mobility separations. This forms the primary motivation for pursuing the cryogenic ion mobility work.

Because the ionic mobility of different chemical species in the gas phase changes with respect to temperature, varying the temperature in the IMS experiment also introduces a degree of selectivity to the ion mobility analysis. Specifically, the separation of ionic mixtures can be improved by changing the drift gas temperature. Optimal temperatures cannot be predicted a priori since ionic mobility is a complicated phenomenon related to the interaction potential of the ion-neutral collision events.

Instrument sensitivity should improve at lower temperatures since ion losses are directly related to the amount of ion diffusional broadening. These ion losses are specific to hyphenated ion mobility-mass spectrometry instrumentation utilizing conductance limiting apertures to define various pressure regimes in the experiment.

Finally it was noted that low temperature, and specifically cryogenic, ion mobility offers the added advantage of condensing out trace impurities from the drift gas, which otherwise serves to broaden ion mobility peak profiles due to reaction chemistry. An attempt was made to define the concentrations of various drift gas impurities which would be considered significant for distorting ion mobility peak profiles. The general prediction was made that part-per-million concentrations would be a significant impurity given that each ion-gas collision resulting in a long-term interaction.

5-2 Summary of the Instrumentation Design Rationales

In section two, the instrumentation developed to explore the temperature effects on the ion mobility separation efficiency was described. Specific instrument component designs were rationalized. Electron ionization was chosen as the ionization method for this work primarily as a means of convenience for comparing experimental results to the large body of published data generated from these ion sources. An appropriate ion gate was developed to generation ion pulses from this continuous ion source. A quadrupole mass prefilter was utilized as an additional experimental stage prior to the ion mobility-mass analysis. Mass filtering abilities provides added experimental flexibility that helps to alleviate ambiguity in the interpretation of data. The quadrupole was chosen for its m/z dependant ion filtering abilities and convenience operational principle of turning this ability off or on (*i.e.*, a broadband or narrow bandpass ion filter). A drift tube ion mobility spectrometer was developed for the reasons described in the first section. A

time-of-flight mass analyzer was utilized as the mass spectrometer as this is a dispersive method which affords all the advantages previously outlined for the drift tube IMS technique. Finally, special considerations for coupling the various instrument components were discussed and an overview of the data acquisition and visualization methods was provided.

5-3 Summary and Conclusions of Benchmarking Experiments

Several experiments were described in the first part of section three which serve to benchmark the analytical performance of the instrument. Various instrument components were individually tested. The quadrupole test results show that it effectively mass selects ions in a relatively narrow window (2-3 amu), however in mass selective mode, ion signal is reduced by over 50 %. This is a general consequence of all quadrupole mass filters. Mass selective experiments on Xe^+ identified reaction chemistry with water that served to broaden ion mobility peak profiles (**Section 3-1.1**).

The performance of two ion gate designs was evaluated (**Section 3-1.2**). The more complicated, 9-wire interleaved ion gate created a more favorably defined ion pulse than did a simpler, 2-wire ion gate design and was used for all subsequent experiments. The poor performance of the 2-wire ion gate design was contributed to a combined result of ineffective ion stopping/deflecting during gate off events as well as surface charging of dielectric elements (alumina ceramic spacers) used in the design. No dielectrics were used in significant proximity to the ion beam in the 9-wire design, which likely contributed to the improved performance.

The effect of the ion injection energy into the drift tube was evaluated (**Section 3-1.3**) and it was concluded that less than ~10 eV of kinetic energy must be used for the small mass ions studied if complicating ion activation and reaction chemistry is to be avoided. High energy ion injection was shown to cause depletion of ion signal of ions derived from benzene either as a result of fragmentation and/or reaction chemistry. A krypton dopant was added to the benzene sample in these experiments to serve as a marker for the relative abundance. This is effective since atomic species cannot fragment.

The capacitance manometer pressure gauge was identified as providing a false reading when not sampling the direct pressure of the drift region. This problem is compounded when temperature variable experiments are conducted due to thermal transpiration effects. A method for calibrating the manometer using the known ionic mobility of the argon cation at 300 and 80 K was developed (**Section 3-1.4**). Argon ion mobilities at various temperatures and electric fields have been published by several previous research groups and are considered accurate enough to use for this particular application.

It was noted that ion drift time outside of the drift region contributes to an erroneous measured mobility drift time and must be accounted for (**Section 3-1.5**). For the instrument configuration utilized in this dissertation work, the ion gate is directly prior to the drift region entrance and so only the drift time between the drift tube exit and the detector (in these experiments, the entrance to the mass analyzer) need be taken into account. A method for determining the non-drift region ion flight time was developed

using ion trajectory modeling. This method was compared with empirical experiments measuring ion flight times in vacuum and was determined to be accurate enough for qualitative comparison. It was concluded for this drift time correction that the method developed was appropriate enough for obtaining qualitatively useful information, however a more accurate method need be employed if quantitative information such as reduced mobility values is to be sought.

Various tuning strategies for both the ion mobility and time-of-flight spectrometers were surveyed in **Sections 3-1.6** and **3-1.7**, respectively. Nominal voltage settings for the TOF was provided as a starting point for tuning, with the *caveat* that optimal performance is only achieved by custom tuning to the system under investigation. A practical method of promoting ion transmission into the drift tube was described involving initiating gaseous breakdown at the front of the drift tube. This method is most effective at low (<10 eV) ion injection energies, where ion losses are very high.

5-4 Summary and Conclusions of Proof-of-Concept Experiments

A series of proof-of-concept experiments was described in the latter part of section two. The analytical utility of the 2-dimensional mobility-mass analysis method was demonstrated for small mass ions. Specifically, it was shown that ions partition into chemical class specific trendlines which can be used to guide the data analysis and provides additional information regarding the sample. This was demonstrated with the ethylene glycol system (**Section 3-2.1**), which exhibits no less than 5 distinct ion

trendlies in the mobility-mass spectrum owing to the chemical diversity of ion fragments generated from the electron ionization of this sample.

The analytical utility of condensing drift gas impurities using low temperature drift gas was demonstrated with several systems. First, it was established that chemical impurities existed in the drift gas by mass analyzing the afterglow formed from gaseous discharge in the mobility spectrometer. In these experiments the ion source was not operating, thus all ions detected in the mass analysis could only have come from the discharge itself. Atmospheric contaminants such as water, nitrogen, and oxygen were identified as being in the drift gas. At low temperature (185 K), water was virtually eliminated from the spectrum. Two samples, TiCl4 and methanol, were evaluated at room and reduced drift gas temperatures. It was observed that water derived ions was eliminated at low temperature, and peak broadening due to reaction chemistry was significantly reduced.

The concept of varying the drift gas temperature to effect the elution of ions was evaluated with acetone (**Section 3-2.3**). It was observed that several nominal mass isomers were resolved only at low temperature, presumably due to enhanced ion selectivity of one ion species over the other. It was also observed that additional ion signals are observed at lower temperatures, resulting from the attenuation of chemical noise caused by water and related reaction chemistries.

Enhanced resolving power was observed at lower temperatures for ions resulting from the electron ionization of benzene and carbon tetrachloride (**Section 3-2.4**). Across the board, the resolving power values increased as the temperature was lowered and was

always greatest at the lowest temperatures investigated. This is attributed to the decrased diffusion at low temperature and is one of the primary benefits of conducting the ion mobility experiment at cryogenic temperatures.

5-5 Summary and Conclusions of Discovery Driven Experimental Investigations

A series of experiments were conducted strictly for the sake of curiosity. These experiments provide insight as to the power of this technology for conducting discovery driven experimental research, *i.e.*, experiments which are conducted "just for the hell of it". It was first established that one of the more dramatic applications of ion mobility lies in its ability to differentiate mass isomers, that is, ions which cannot be separated with the mass spectrometry alone. Several examples of the separation of mass isomers was provided throughout the text and summarized in **Table 11**.

Two special systems were revisited which involve the ion mobility separation of true mass isomers, *i.e.*, ground and electronically excited states of metal cations. Chromium cation exhibited a bimodal peak profile in the mobility spectrum at room temperature and sufficiently low field conditions ($< 6\ V \cdot cm^{-1} \cdot torr^{-1}$). Appearance energy experiments were conducted to determine which profile represented higher energy ionization conditions, *i.e.*, the electronically excited state. It was determined that the electronically excited state or states fell beneath the first arriving ion population, that is, the higher mobility distribution. A third distribution can be observed in some of the spectra, falling between these two primary distributions, however its existence was not concluded as definite due to poor reproducibility. Low temperature ion mobility down

to 80 K improved the resolution of the two electronic state populations. Depletion of the electronically excited state distribution was observed at low temperature and low field conditions (<2 $V \cdot cm^{-1} \cdot torr^{-1}$ at 80 K). This was attributed to a depletion mechanism involving a trace impurity in the drift gas. Previous experiments had identified the presence of impurities and collisional/reactive depletion of these excited states by reactive neutrals is well documented, so this is a plausible conclusion. These results are consistent with three previous ion mobility investigations of the Cr^+ system, with the mobility spectra shown in this work representing the highest ion mobility resolutions observed to date for chromium cation electronic states.

The electronic states of the titanium cation were also investigated. A bimodal mobility distribution was observed at room temperature and appearance energy experiments identified the lower mobility distribution as representing the electronically excited state or states. Significant reaction chemistry of Ti^+ with water was also observed in the 2-dimensional mobility-mass spectra. At lower drift gas temperatures, additional ion mobility distributions were observed, as many as five, though no single temperature allowed all five to be separated at once. Optimal temperatures for resolution varied with the different electronic states observed. In the only previous ion mobility study conducted on the titanium system, three electronic states were observed for Ti^+, so this work represents the most electronic states observed by ion mobility to date.

If low temperature ion mobility is sensitive enough to differentiate electronic states of ions, then it is possible that cryogenic ion mobility could differentiate electronic

configurations of ions, that is, mass isomers which differ only in the location of an electron. One well documented electronic isomer is methanol, specifically the conventional and distonic ion forms. Several experiments were conducted in order to explore whether or not ion mobility could separate these isomers. The methanol molecular ion (32 m/z) was measured using argon, neon and helium drift gases. It was rationalized that the stronger polarizability of argon and neon might result in an enhanced selectivity towards one of the isomeric forms. The resulting mobility spectrum in argon of 32 m/z displayed a broad peak with significant tailing to higher mobility. Resolution did not improve at lower temperatures. In neon, a partial bimodal mobility profile was observed which did not improve in resolution at low temperature. It was inconclusive whether the two peaks observed were a result of isomeric ions or methanol ion and residual oxygen ion, which also has a m/z of 32. In helium, the presence of O_2^+ was distinctive in the mobility spectrum as a high mobility ion distribution. The methanol molecular ion was represented by a high abundance peak at lower mobility. At lower temperatures, the spectrum was complicated by the fact that O_2^+ moved towards the methanol ion distribution. A partial, third distribution was observed at 96 K. Completely deuterated methanol (methanol-D4) was also investigated to eliminate the interference of the O_2^+ ion, but failed to demonstrate more than a single ion distribution in the ion mobility spectrum of the methanol-D4 molecular ion. Results were inconclusive, but can be interpreted as i) the isomeric forms do not exist in the sample or ii) ion mobility cannot differentiate the two forms.

It was hypothesized that the distonic ion is not favorably formed from direct ionization of methanol and so methyl formate was investigated which when electron ionized will generate a strong ion signal at m/z 32. Very similar mobility spectra were observe in both argon and helium for the 32 m/z ion of methyl formate as compared with the 32 m/z ion formed from methanol. Low temperature partially resolved a third peak at 199 and 174 K, though no direct conclusions could be made as to the nature of this third distribution.

REFERENCES

[1] G.A. Eiceman, Z. Karpas, Ion Mobility Spectrometry, CRC Press, Boca Raton, FL, 1994.

[2] M.J. Cohen, F.W. Karasek, J. Chromatogr. Sci. 8 (1970) 330.

[3] R.G. Ewing, D.A. Atkinson, G.A. Eiceman, G.J. Ewing, Talanta 54 (2001) 515.

[4] H. Tammet, J. Aerosol Sci. 26 (1995) 459.

[5] B.C. Bohrer, S.I. Merenbloom, S.L. Koeniger, A.E. Hilderbrand, D.E. Clemmer, Annu. Rev. Anal. Chem. 1 (2008) 293.

[6] C. Becker, K. Qian, D.H. Russell, Anal. Chem. 80(22) (2008) 8592.

[7] G.A. Eiceman, J.A. Stone, Anal. Chem. 76 (2004) 390A.

[8] G.A. Eiceman, Analyst 129 (2004) 488.

[9] J.A. McLean, D.H. Russell, J. Proteome Res. 2 (2003) 427.

[10] K. Cottingham, Anal. Chem. 75 (2003) 435A.

[11] H.H. Hill, Jr., G. Simpson, Field Anal. Chem. Technol. 1 (1997) 119.

[12] G.A. Eiceman, Trends Anal. Chem. 21 (2002) 259.

[13] P. Langevin, Ann. Chim. Phys. 28 (1903) 289.

[14] P. Langevin, Ann. Chim. Phys. (1905) 245.

[15] A.B. Kanu, P. Dwivedi, M. Tam, L. Matz, H.H. Hill, Jr., J. Mass Spectrom. 43 (2008) 1.

[16] D.J. Rose, G.J. Opiteck, Anal. Chem. 66 (1994) 2529.

[17] L. Schweikhard, G.M. Alber, A.G. Marshall, Phys. Scr. 46 (1992) 598.

[18] B.T. Ruotolo, K.J. Gillig, E.G. Stone, D.H. Russell, J. Chromatogr. B 782 (2002) 385.

[19] Y.-F. Cheng, Z. Lu, U. Neue, Rapid Commun. Mass Spectrom. 15 (2001) 141.

[20] M.M. van Deursen, J. Beens, H.G. Janssen, P.A. Leclercq, C.A. Cramers, J. Chromatogr. A 878 (2000) 205.

[21] J.A. McLean, B.T. Ruotolo, K.J. Gillig, D.H. Russell, Int. J. Mass Spectrom. 240 (2005) 301.

[22] M.J. Cohen, F.W. Karasek, J. Chromatogr. Sci. 8 (1970) 330.

[23] K. Giles, S.D. Pringle, K.R. Worthington, D. Little, W.J. L., R.H. Bateman, Rapid Commun. Mass Spectrom. 18 (2004) 2401.

[24] R. Kurulugama, F.M. Nachtigall, S. Lee, S.J. Valentine, D.E. Clemmer, J. Am. Soc. Mass Spectrom. 20 (2009) 729.

[25] S.I. Merenbloom, R.S. Glaskin, Z. B. Hensen, D.E. Clemmer, Anal. Chem. 81(4) (2008) 1482.

[26] J.F. de la Mora, L. de Juan, T. Eichler, J. Rosell, Trends Anal. Chem. 17 (1998) 328.

[27] R. Guevremont, Can. J. Anal. Sci. Spectrosc. 49 (2004) 105.

[28] A.A. Shvartsburg, Differential Mobility Spectrometry: Nonlinear Ion Transport and Fundamentals of FAIMS, CRC Press, Boca Raton, FL, 2009.

[29] S.D. Pringle, K. Giles, J.L. Wildgoose, J.P. Williams, S.E. Slade, K. Thalassinos, R.H. Bateman, M.T. Bowers, J.H. Scrivens, Int. J. Mass Spectrom. 261 (2007) 1.

[30] M. Labowsky, J.F. de la Mora, J. Aerosol Sci. 37 (2006) 340.

[31] B.M. Kolakowski, Z. Mester, Analyst 132 (2007) 842.

[32] B.H. Clowers, W.F. Siems, H.H. Hill, Jr., S.M. Massick, Anal. Chem. 78 (2006) 44.

[33] S.J. Valentine, S.T. Stokes, R. Kurulugama, F.M. Nachtigall, D.E. Clemmer, J. Am. Soc. Mass Spectrom. 20 (2008) 738.

[34] N. Agbonkonkon, Ph.D. Dissertation, Brigham Young University, Provo, UT, 2007.

[35] A. Loboda, J. Am. Soc. Mass Spectrom. 17 (2006) 691.

[36] V.V. Laiko, J. Am. Soc. Mass Spectrom. 17 (2006) 500.

[37] P. Dugourd, R.R. Hudgins, D.E. Clemmer, M.F. Jarrold, Rev. Sci. Instrum. 68 (1997) 1122.

[38] C. Wu, W.F. Siems, G. Reid Asbury, H.H. Hill, Jr., Anal. Chem. 70 (1998) 4929.

[39] C.A. Srebalus, J. Li, W.S. Marshall, D.E. Clemmer, Anal. Chem. 71 (1999) 3918.

[40] A.A. Shvartsburg, R.R. Hudgins, P. Dugourd, M.F. Jarrold, Chem. Soc. Rev. 30 (2001) 26.

[41] T. Wyttenbach, M.T. Bowers, Top. Curr. Chem. 225 (2003) 207.

[42] L.S. Fenn, J.A. McLean, Anal. Bioanal. Chem. 391 (2008) 905.

[43] M.E. Belov, B.H. Clowers, D.C. Prior, W.F. Danielson III, A.V. Liyu, B.O. Petritis, R.D. Smith, Anal. Chem. 80 (2008) 5873.

[44] E.W. McDaniel, L.A. Viehland, Phys. Rep. 110 (1984) 333.

[45] H.-S. Hahn, E.A. Mason, Phys. Rev. A 6 (1972) 1573.

[46] H.E. Revercomb, E.A. Mason, Anal. Chem. 47 (1975) 970.

[47] R.W. Purves, R. Guevremont, S. Day, C.W. Pipich, M.S. Matyjaszczyk, Rev. Sci. Instrum. 69 (1998) 4094.

[48] E.V. Krylov, E.G. Nazarov, R.A. Miller, Int. J. Mass Spectrom. 266 (2007) 76.

[49] B.T. Ruotolo, J.A. McLean, K.J. Gillig, D.H. Russell, J. Am. Soc. Mass Spectrom. 16 (2005) 158.

[50] E.A. Mason, E.W. McDaniel, The Mobility and Diffusion of Ions in Gases, Wiley, New York, 1973.

[51] L.M. Chanin, M.A. Biondi, Phys. Rev. 106 (1957) 473.

[52] M.D. Wessel, J.M. Sutter, P.C. Jurs, Anal. Chem. 68 (1996) 4237.

[53] N. Agbonkonkon, H.D. Tolley, M.C. Asplund, E.D. Lee, M.L. Lee, Anal. Chem. 76 (2004) 5223.

[54] E.A. Mason, H.W. Schamp, Ann. Phys. 4 (1958) 233.

[55] M.F. Jarrold, Annu. Rev. Phys. Chem. 51 (2000) 179.

[56] M.F. Mesleh, J.M. Hunter, A.A. Shvartsburg, G.C. Schatz, M.F. Jarrold, J. Phys. Chem. 100 (1996) 16082.

[57] G. Reid Asbury, H.H. Hill, Jr., Anal. Chem. 72 (2000) 580.

[58] P. Dwivedi, C. Wu, L. Matz, B.H. Clowers, W.F. Siems, H.H. Hill, Jr., Anal. Chem. 78 (2006) 8200.

[59] M. Rusyniak, Y. Ibrahim, E. Alsharaeh, M. Meot-Ner, M.S. El-Shall, J. Phys. Chem. A 107 (2003) 7656.

[60] Z. Karpas, R.M. Stimac, Z. Rappoport, Int. J. Mass Spectrom. Ion Processes 83 (1988) 163.

[61] G.F. Verbeck, K.J. Gillig, D.H. Russell, Eur. J. Mass Spectrom. 9 (2003) 579.

[62] H. Haken, H.C. Wolf, The Physics of Atoms and Quanta: Introduction to Experiments and Theory, Springer Berlin Heidelberg, New York, 2005.

[63] D.H. Russell, R.D. Edmondson, J. Mass Spectrom. 32 (1997) 263.

[64] A.G. Marshall, C.L. Hendrickson, S.D.-H. Shi, Anal. Chem. 74 (2002) 252A.

[65] S. Rokushika, H. Hatano, M.A. Baim, H.H. Hill, Jr., Anal. Chem. 57 (1985) 1902.

[66] W.F. Siems, C. Wu, E.E. Tarver, H.H. Hill, Jr., P.R. Larsen, D.G. McMinn, Anal. Chem. 66 (1994) 4195.

[67] P. Price, J. Am. Soc. Mass Spectrom. 2 (1991) 336.

[68] C.S. Harden, D.B. Shoff, R.G. Ewing, 6th International Workshop on Ion Mobility Spectrometry, Bastei, Germany, 1997.

[69] G.A. Eiceman, E.G. Nazarov, J.A. Stone, Anal. Chim. Acta 493 (2003) 185.

[70] J. Viidanoja, A. Sysoev, A. Adamov, T. Kotiaho, Rapid Commun. Mass Spectrom. 19 (2005) 3051.

[71] B.L. Karger, L.R. Snyder, C. Horvath, An Introduction to Separation Science, John Wiley & Sons, New York, 1973.

[72] G. Reid Asbury, H.H. Hill, Jr., J. Microcolumn Sep. 12 (2000) 172.

[73] E.E. Tarver, Sensors, and Command, Control, Communications, and Intelligence (C3I) Technologies for Homeland Security and Homeland Defense III, Orlando, FL, 2004.

[74] J. Xu, W.B. Whitten, J.M. Ramsey, Anal. Chem. 72 (2000) 5787.

[75] M. Tabrizchi, E. Khezri, Int. J. Ion Mobility Spectrom. 10.1007/s12127-008-0002-9 (2007).

[76] Y.-F. Wang, MS Thesis, New Mexico State University, Las Cruces, NM, 1999.

[77] J. Xu, W.B. Whitten, Int. J. Ion Mobility Spectrom. doi: 10.1007/s12127-008-0001-x (2008).

[78] K.J. Gillig, D.H. Russell, Texas A&M University, US Patent 6639213, 2003.

[79] G.E. Spangler, Int. J. Mass Spectrom. 220 (2002) 399.

[80] G.E. Spangler, Anal. Chem. 64 (1992) 1312.

[81] E.W. McDaniel, Collision Phenomena in Ionized Gases, Wiley, New York, 1964.

[82] M. van Gorkom, R.E. Glick, Int. J. Mass Spectrom. Ion Phys. 4 (1970) 203.

[83] M. van Gorkom, D.P. Beggs, R.E. Glick, Int. J. Mass Spectrom. Ion Phys. 4 (1970) 441.

[84] P. Watts, A. Wilders, Int. J. Mass Spectrom. Ion Processes 112 (1992) 179.

[85] E.J. Davis, P. Dwivedi, M. Tam, W.F. Siems, H.H. Hill, Anal. Chem. 81(9) (2009) 3270.

[86] E.W. McDaniel, J.T. Moseley, Phys. Rev. A 3 (1971) 1040.

[87] L.G.H. Huxley, R.W. Crompton, M.T. Elford, Br. J. Appl. Phys. 17 (1966) 1237.

[88] G.F. Verbeck, B.T. Ruotolo, K.J. Gillig, D.H. Russell, J. Am. Soc. Mass Spectrom. 15 (2004) 1320.

[89] S.J. Valentine, A.E. Counterman, D.E. Clemmer, J. Am. Soc. Mass Spectrom. 10 (1999) 1188.

[90] W.E. Steiner, B.H. Clowers, K. Fuhrer, M. Gonin, L.M. Matz, W.F. Siems, J.A. Schultz, H.H. Hill, Jr., Rapid Commun. Mass Spectrom. 15 (2001) 2221.

[91] J.D. Cobine, Gaseous Conductors: Theory and Engineering Applications, Dover Publications, Inc. , New York, 1958.

[92] K.T.A.L. Burm, Contrib. Plasma Phys. 47 (2007) 177.

[93] M.A. Hassouba, F.F. Elakshar, A.A. Garamoon, Fiz. A 11 (2002) 81.

[94] G.G. Raju, Dielectrics in Electric Fields, Marcel Dekker, Inc., New York, 2003.

[95] G.G. Raju, Gaseous Electronics: Theory and Practice, CRC Press, Boca Raton, FL, 2006.

[96] P. Osmokrovic, M. Vujisic, K. Stankovic, A. Vasic, B. Loncar, Plasma Sources Sci. Technol. 16 (2007) 643.

[97] P. Hartmann, Z. Donko, G. Bano, L. Szalai, K. Rozsa, Plasma Sources Sci. Technol. 9 (2000) 183.

[98] B.T. Ruotolo, J.A. McLean, K.J. Gillig, D.H. Russell, J. Mass Spectrom. 39 (2004) 361.

[99] L.G. Christophorou, J.K. Olthoff, Gaseous Dielectrics IX, Kluwer Academic Publishers, New York, 2002.

[100] S.N. Ketkar, S. Dheandhanoo, Anal. Chem. 73 (2001) 2554.

[101] C. Biloiu, I.A. Biloiu, Y. Sakai, Y. Suda, M. Nakajima, Jpn. J. Appl. Phys. 42 (2003) L201.

[102] J.H. Moore, C.C. Davis, M.A. Coplan, S. Greer, Chapter V of Building Scientific Apparatus: A Practical Guide to Design and Construction, Westview Press, Boulder, CO, 2003.

[103] V.Y. Ushakov, V.A. Usakov, Insulation of High-Voltage Equipment, Springer, New York 2004.

[104] J.J. Mankowski, Ph.D. Dissertation, Texas Tech University, Lubbock, TX, 1997.

[105] M.S. Naidu, V. Kamaraju, Chapter II of High Voltage Engineering, McGraw-Hill Publishing, Oxford, New York, 2000.

[106] H.S. Uhm, S.J. Jung, H.S. Kim, J. Korean Phys. Soc. 42 (2003) 989.

[107] K.J. Gillig, B.T. Ruotolo, E.G. Stone, D.H. Russell, K. Fuhrer, M. Gonin, J.A. Schultz, Anal. Chem. 72 (2000) 3965.

[108] N. Mirsaleh-Kohan, W.D. Robertson, R.N. Compton, Mass Spectrom. Rev. 27 (2008) 237.

[109] D.E. Hunka, D.E. Austin, Technical Report SAND2005-6908, Ion mobility spectrometer / mass spectrometer (IMS-MS), Sandia National Laboratories, Albuquerque, NM, 2005.

[110] K. Tang, A.A. Shvartsburg, H.N. Lee, D.C. Prior, M.A. Buschbach, F. Li, A.V. Tolmachev, G.A. Anderson, R.D. Smith, Anal. Chem. 77 (2005) 3330.

[111] K.J. Gillig, B.T. Ruotolo, E.G. Stone, D.H. Russell, Int. J. Mass Spectrom. 239 (2004) 43.

[112] A.A. Shvartsburg, R.D. Smith, Anal. Chem. 80 (2008) 9689.

[113] E.C. Lynn, M.-C. Chung, C.-C. Han, Rapid Commun. Mass Spectrom. 14 (2000) 2129.

[114] K.J. Gillig, J.C. May, R.C. Blase, D.H. Russell, 55th Annual American Society for Mass Spectrometry Conference on Mass Spectrometry and Allied Topics, Indianapolis, IN, 2007.

[115] H.B. Milloy, M.T. Elford, Int. J. Mass Spectrom. Ion Phys. 18 (1975) 21.

[116] J.A. McLean, D.H. Russell, Int. J. Ion Mobility Spectrom. 8 (2005) 66.

[117] F. Hillenkamp, J. Peter-Katalinic (Eds.), MALDI MS: A Practical Guide to Instrumentation, Methods and Applications, Wiley-VCH Verlag GmbH & Co, Berlin, 2007.

[118] E. de Hoffmann, V. Stroobant, Mass Spectrometry: Principles and Applications, John Wiley & Sons Ltd., West Sussex, England, 2002.

[119] R.B. Cole (Ed.) Electrospray Ionization Mass Spectrometry: Fundamentals, Instrumentation and Applications, John Wiley & Sons, Inc., New York, 1997.

[120] R.R. Hudgins, J. Woenckhaus, M.F. Jarrold, Int. J. Mass Spectrom. Ion Processes 165-166 (1997) 497.

[121] R. Fromherz, G. Ganteför, A.A. Shvartsburg, Phys. Rev. Lett. 89 (2002) 083001.

[122] G.E. Yefchak, G.A. Schultz, J. Allison, C.G. Enke, J.F. Holland, J. Am. Soc. Mass Spectrom. 1 (1990) 440.

[123] B.S. Kinnear, D.T. Kaleta, M. Kohtani, R.R. Hudgins, M.F. Jarrold, J. Am. Chem. Soc. 122 (2000) 9243.

[124] L. Zhou, D.C. Collins, E.D. Lee, M.L. Lee, Anal. Bioanal. Chem. 388 (2007) 189.

[125] V. Katta, A.L. Rockwood, M.L. Vestal, Int. J. Mass Spectrom. Ion Processes 103 (1991) 129.

[126] A.M. Tyndall, The Mobility of Positive Ions in Gases, Cambridge University Press, Cambridge, U.K., 1938.

[127] A.M. Cravath, Phys. Rev. 33 (1929) 605.

[128] R.J. van de Graaff, Nature 124 (1929) 10.

[129] N.E. Bradbury, R.A. Nielsen, Phys. Rev. 49 (1936) 388.

[130] J. Zhang, B.D. Gardner, C.G. Enke, J. Am. Soc. Mass Spectrom. 11 (2000) 765.

[131] C.-C. Chen, C.-S. Su, Int. J. Mass Spectrom. Ion Processes 124 (1992) 37.

[132] D.A. Dahl, T.R. McJunkin, J.R. Scott, Int. J. Mass Spectrom. 266 (2007) 156.

[133] R.N. Zare, F.M. Fernández, J.R. Kimmel, Angew. Chem. Int. Ed. 42 (2003) 30.

[134] A.W. Szumlas, G.M. Hieftje, Anal. Chim. Acta 566 (2006) 45.

[135] J.R. Kimmel, Ph.D. Dissertation, Stanford University, Palo Alto, CA, 2004.

[136] S.-F. Fan, X.-C. Xu, Mikrochim. Acta 94 (1988) 239.

[137] C.S. Hoaglund, S.J. Valentine, D.E. Clemmer, Anal. Chem. 69 (1997) 4156.

[138] C.S. Creaser, M. Benyezzar, J.R. Griffiths, J.W. Stygall, Anal. Chem. 72 (2000) 2724.

[139] I.M. Taban, L.A. McDonnell, A. Römpp, I. Cerjak, R.M.A. Heeren, Int. J. Mass Spectrom. 244 (2005) 135.

[140] S.V. Prada, D.K. Bohme, V.I. Baranov, Int. J. Mass Spectrom. 261 (2007) 45.

[141] A.A. Shvartsburg, K. Tang, R.D. Smith, Battelle Memorial Institute, US Patent 6818890, 2004.

[142] R.C. Thompson, Meas. Sci. Technol. 1 (1990) 93.

[143] A. Sharma, F. Sauli, IEEE Trans. Nucl. Sci. 41 (1994) 826.

[144] M. Tabrizchi, Talanta 62 (2004) 65.

[145] H. Tanuma, M. Sakamoto, H. Fujimatsu, N. Kobayashi, Rev. Sci. Instrum. 71 (2000) 2019.

[146] P.R. Kemper, M.T. Bowers, J. Phys. Chem. 95 (1991) 5134.

[147] J. Vessman, R. Stefan, J.F. Van Staden, K. Danzer, W. Lindner, D.T. Burns, A. Fajgelj, H. Muller, Pure App. Chem. 73 (2001) 1381.

[148] J. Puton, M. Nousiainen, M. Sillanpää, Talanta 76 (2008) 978.

[149] M.A. Baim, H.H. Hill, Jr., J. High Resolut. Chromatogr. 6 (1983) 4.

[150] H.W. Ellis, R.Y. Pai, E.W. McDaniel, E.A. Mason, L.A. Viehland, At. Data Nucl. Data Tables 17 (1976) 177.

[151] H.W. Ellis, E.W. McDaniel, D.L. Albritton, L.A. Viehland, S.L. Lin, E.A. Mason, At. Data Nucl. Data Tables 22 (1978) 179.

[152] H.W. Ellis, M.G. Thackston, E.W. McDaniel, E.A. Mason, At. Data Nucl. Data Tables 31 (1984) 113.

[153] L.A. Viehland, E.A. Mason, At. Data Nucl. Data Tables 60 (1995) 37.

[154] D.R. Bates, J. Phys. B: At. Mol. Opt. Phys. 15 (1982) L259.

[155] J. Sanderson, H. Tanuma, N. Kobayashi, Y. Kaneko, J. Phys. B: At. Mol. Opt. Phys. 26 (1993) L465.

[156] H. Hidaka, S. Jinno, H. Tanuma, N. Kobayashi, J. Phys. B: At. Mol. Opt. Phys. 36 (2003) 1515.

[157] T. Koizumi, N. Kobayashi, Y. Kaneko, J. Phys. Soc. Jpn. 47 (1979) 1031.

[158] T. Su, M.T. Bowers, J. Chem. Phys. 60 (1974) 4897.

[159] W.W. Smith, O.P. Makarov, J. Lin, J. Mod. Opt. 52 (2005) 2253.

[160] A.K. Viitanen, T. Mattila, J.M. Mäkelä, M. Marjamäki, O. Anttalainen, J. Keskinen, Atmos. Res.90 (2008) 115.

[161] H. Hidaka, S. Jinno, H. Tanuma, N. Kobayashi, J. Phys. B: At. Mol. Opt. Phys. 36 (2003) 1515.

[162] Z. Berant, Z. Karpas, O. Shahal, J. Phys. Chem. 93 (1989) 7529.

[163] Z. Karpas, Z. Berant, O. Shahal, J. Am. Chem. Soc. 111 (1989) 6015

[164] A.M. Arthurs, A. Dalgarno, Proc. R. Soc. London, Sect. A 256 (1960) 552.

[165] G.H. Wannier, Bell System Technical Journal 32 (1953) 170.

[166] SIMION 8.0.4 incorporating the "Collision Model HS1" user program, Scientific Instrument Services, Inc., 2008.

[167] M.A. Baim, H.H. Hill, Jr., J. Chromatogr. 299 (1984) 309.

[168] M.A. Baim, H.H. Hill, Jr., Anal. Chem. 54 (1982) 38.

[169] Y. Kaneko, L.R. Megill, J.B. Hasted, J. Chem. Phys. 45 (1966) 3741.

[170] W.L. Fite, Can. J. Chem. 47 (1969) 1797.

[171] D.R. Lide (Ed.) CRC Handbook of Chemistry and Physics, 88th Edition; Taylor and Francis: Boca Raton, FL, 2008.

[172] Y. Ogawara, A. Bruneau, T. Kimura, Anal. Chem. 66 (1994) 4354.

[173] P.H. Dawson, Quadrupole Mass Spectrometry and Its Applications, Elsevier, NY, 1976.

[174] P.H. Dawson, Mass Spectrom. Rev. 5 (1986) 1.

[175] J.R. Chapman, R.T. Gallagher, E.C. Barton, J.M. Curtis, Peter J. Derrick, Org. Mass Spectrom. 27 (1992) 195.

[176] J. De Laeter, M.D. Kurz, J. Mass Spectrom. 41 (2006) 847.

[177] P. Håkansson, Braz. J. Phys. 29 (1999) 422.

[178] R.J. Cotter, Time-of-Flight Mass Spectrometry: Instrumentation and Applications in Biological Research, American Chemical Society, DC, 1997.

[179] R.E. March, R.J. Hughes, Quadrupole Storage Mass Spectrometry, John Wiley and Sons, New York, 1989.

[180] D.J. Douglas, A.J. Frank, D. Mao, Mass Spectrom. Rev. 24 (2005) 1.

[181] K.H. Kingdon, Phys. Rev. 21 (1923) 408.

[182] R.H. Perry, R.G. Cooks, R.J. Noll, Mass Spectrom. Rev. 27 (2008) 661.

[183] A.G. Marshall, C.L. Hendrickson, G.L. Jackson, Mass Spectrom. Rev. 17 (1998) 1.

[184] C.G. Enke, J.T. Stults, J.F. Holland, J.D. Pinkston, J. Allison, J.T. Watson, Int. J. Mass Spectrom. Ion Phys. 46 (1983) 229.

[185] W.M. Brubaker, 16th Annual American Society for Mass Spectrometry Conference on Mass Spectrometry and Allied Topics, Pittsburgh, PA, 1968.

[186] W.M. Brubaker, NASA Tech. Rep. NASW (1969) 1.

[187] P.H. Dawson, Int. J. Mass Spectrom. Ion Phys. 6 (1971) 33.

[188] P. Marmet, J. Vac. Sci. Technol. 8 (1971) 262.

[189] R.A. Yost, C.G. Enke, J. Am. Chem. Soc. 100 (1978) 2274.

[190] A.E. Holme, W.J. Tatcher, J.H. Leck, J. Phys. E: Sci. Instrum. 5 (1972) 429.

[191] C. Trajber, M. Simon, M. Csatlos, Meas. Sci. Technol. 2 (1991) 785.

[192] W.M. Brubaker, "An Improved Quadrupole Mass Analyzer" in Volume 4 of Advances in Mass Spectrometry, Elsevier, Amsterdam, 1968.

[193] W.M. Brubaker, J. Vac. Sci. Technol. 10 (1973) 291.

[194] W.M. Brubaker, Jpn. J. Appl. Phys. 2 (1974) 179.

[195] E.F. Barnett, W.S.W. Tandler, W.R. Turner, U.S. Patent 3560734, 1971.

[196] P. Clauzon, L. Krähenbühl, A. Nicolas, IEEE Trans. Magn. 35 (1999) 1223.

[197] J.S. Seybold, Chapter II of Introduction to RF Propagation, John WIley & Sons, Inc., Hoboken, NJ, 2005.

[198] W.L. Fite, Rev. Sci. Instrum. 47 (1976) 326.

[199] S.N. Ketkar, W.L. Fite, Rev. Sci. Instrum. 59 (1988) 987.

[200] H.F. Dylla, J.A. Jarrell, Rev. Sci. Instrum. 47 (1976) 331.

[201] J. Visser, J. Vac. Sci. Technol. 10 (1973) 464.

[202] J.J. Thompson, Philos. Mag. 44 (1897) 293.

[203] W.E. Stephens, Bull. Am. Phys. Soc. 21 (1946) 22.

[204] A.E. Cameron, J.D.F. Eggers, Rev. Sci. Instrum. 19 (1948) 605.

[205] M.M. Wolff, W.E. Stephens, Rev. Sci. Instrum. 24 (1953) 616.

[206] R. Keller, Helv. Phys. Acta 22 (1949) 382.

[207] W.E. Stephens, Phys. Rev. 69 (1946) 691.

[208] W.C. Wiley, I.H. McLaren, Rev. Sci. Instrum. 26 (1955) 1150.

[209] W.C. Wiley, Science 124 (1956) 817.

[210] R.S. Brown, J.J. Lennon, Anal. Chem. 67 (1995) 1998.

[211] M.L. Vestal, P. Juhasz, S. A. Martin, Rapid Commun. Mass Spectrom. 9 (1995) 1044.

[212] B.A. Mamyrin, Soviet Union Patent 198,034, 1966.

[213] I. Karataev, B.A. Mamyrin, D.V. Schmikk, J. Tech. Phys. 16 (1971) 1498.

[214] B.A. Mamyrin, V.I. Karataev, D.V. Schmikk, V.A. Zagulin, Sov. Phys. JETP 37 (1973) 45.

[215] E.V. Moskovets, Appl. Phys. B: Lasers Opt. 57 (1993) 397.

[216] H. Wollnik, U. Grüner, G. Li, Ann. Phys. 503 (1991) 215.

[217] R.P. Schmid, C. Weickhardt, Int. J. Mass Spectrom. 206 (2001) 181.

[218] B.A. Mamyrin, Int. J. Mass Spectrom. Ion Processes 131 (1994) 1.

[219] T.J. Cornish, Robert J. Cotter, Rapid Commun. Mass Spectrom. 7 (1993) 1037.

[220] M. Guilhaus, D. Selby, V. Mlynski, Mass Spectrom. Rev. 19 (2000) 65.

[221] J.H. Barnes, G.D. Schilling, M.B. Denton, D.W. Koppenaal, G.M. Hieftje, J. Anal. At. Spectrom. 18 (2003) 1015.

[222] V.D. Berkout, V.M. Doroshenko, J. Am. Soc. Mass Spectrom. 17 (2006) 335.

[223] M.L. Gross, R. Caprioli, Volume 6 of The Encyclopedia of Mass Spectrometry, Elsevier Science and Technology, St. Louis, MO, 2006.

[224] F.L. King, W.W. Harrison, Mass Spectrom. Rev. 9 (1990) 285.

[225] N.P. Vela, L.K. Olson, J.A. Caruso, Anal. Chem. 65 (1993) 585A.

[226] H.E. Beske, A. Hurrle, K.P. Jochum, Fresnius J. Anal. Chem. 309 (1981) 258.

[227] J.P. Young, R.W. Shaw, D.H. Smith, Anal. Chem. 61 (1989) 1271A.

[228] M.D. Evans, J.A. Syage, Spectrosc. 16 (2001) 14.

[229] T.D. Märk, Electron Impact Ionization, Springer-Verlag, Vienna, 1985.

[230] R. Stoll, F.W. Röllgen, J. Chem. Soc., Chem. Commun. (1980) 789.

[231] M.S.B. Munson, F.H. Field, J. Am. Chem. Soc. 88 (1966) 2621.

[232] R. Gomer, Field Emission and Field Ionization, Springer, New York, 1995.

[233] H.R. Morris, M. Panico, M. Barber, R.S. Bordoli, R.D. Sedgwick, A. Tyler, Biochem. Biophys. Res. Commun. 101 (1981) 623.

[234] R.F.K. Herzog, F. Viehboeck, Phys. Rev. 76 (1949) 855.

[235] R.D. Macfarlane, D.F. Torgerson, Science 191 (1976) 920.

[236] C.R. Blakley, J.J. Carmody, M.L. Vestal, Anal. Chem. 52 (1980) 1636.

[237] A. Hirabayashi, M. Sakairi, H. Koizumi, Anal. Chem. 67 (1995) 2878.

[238] J. Fenn, M. Mann, C. Meng, S. Wong, C. Whitehouse, Science 246 (1989) 64.

[239] K.L. Busch, R.G. Cooks, Science 218 (1982) 247.

[240] M. Karas, F. Hillenkamp, Anal. Chem. 60 (1988) 2299.

[241] M. Haapala, J. Pol, V. Saarela, V. Arvola, T. Kotiaho, R.A. Ketola, S. Franssila, T.J. Kauppila, R. Kostiainen, Anal. Chem. 79 (2007) 7867.

[242] R.B. Cody, J.A. Laramée, H.D. Durst, Anal. Chem. 77 (2005) 2297.

[243] C.N. McEwen, R.G. McKay, B.S. Larsen, Anal. Chem. 77 (2005) 7826.

[244] Z. Takáts, J.M. Wiseman, R.G. Cooks, J. Mass Spectrom. 40 (2005) 1261.

[245] K.L. Busch, Spectrosc. 19 (2004) 35.

[246] K.L. Busch, Spectrosc. 21 (2006) 14.

[247] L. Kelner, H.M. Fales, S.P. Markey, C.K. Crawford, Int. J. Mass Spectrom. Ion Phys. 43 (1982) 249.

[248] W. Bleakney, Phys. Rev. 34 (1929) 157.

[249] F.W. McLafferty, F. Tureček, Interpretation of Mass Spectra, University Science Books, Sausalito, CA, 1993.

[250] A.O. Nier, Rev. Sci. Instrum. 11 (1940) 212.

[251] A.O. Nier, Rev. Sci. Instrum. 18 (1947) 398.

[252] G.O. Brink, Rev. Sci. Instrum. 37 (1966) 857.

[253] J.H. Batey, Vacuum 37 (1987) 659.

[254] R.E. Honig, J.R. Woolston, Appl. Phys. Lett. 2 (1963) 138.

[255] F.J. Vastola, R.O. Mumma, A. J. Pirone, Org. Mass Spectrom. 3 (1970) 101.

[256] F.J. Vastola, A.J. Pirone, Volume 4 of Advances in Mass Spectrometry, Adlard and Sons, NY, 1968.

[257] F. Hillenkamp, E. UnsoLd, R. Kaufmann, R. Nitsche, Nature 256 (1975) 119.

[258] A.H. Verbueken, F.J. Bruynseels, R.E.V. Grieken, Biol. Mass Spectrom. 12 (1985) 438.

[259] L. Van Vaeck, H. Struyf, W. Van Roy, F. Adams, Mass Spectrom. Rev. 13 (1994) 189.

[260] R.J. Conzemius, J.M. Capellen, Int. J. Mass Spectrom. Ion Phys. 34 (1980) 197.

[261] L.D. Detter, O.W. Hand, R.G. Cooks, R.A. Walton, Mass Spectrom. Rev. 7 (1988) 465.

[262] D.M. Lubman, Mass Spectrom. Rev. 7 (1988) 535.

[263] D.M. Lubman, Mass Spectrom. Rev. 7 (1988) 559.

[264] D.H. Smith, J.P. Young, R.W. Shaw, Mass Spectrom. Rev. 8 (1989) 345.

[265] J.S. Becker, H.J. Dietze, Fresnius J. Anal. Chem. 344 (1992) 69.

[266] D. Schuetzle, T.L. Riley, J.E.d. Vries, T.J. Prater, Mass Spectrom. Rev. 3 (1984) 527.

[267] B. Spengler, M. Karas, U. Bahr, F. Hillenkamp, J. Phys. Chem. 91 (1987) 6502.

[268] M. Karas, D. Bachmann, F. Hillenkamp, Anal. Chem. 57 (1985) 2935.

[269] T. Yoshida, K. Tanaka, Y. Ido, S. Akita, Y. Yoshida, Mass Spectrosc. Jpn. 36 (1988) 59.

[270] M. Karas, D. Bachmann, U. Bahr, F. Hillenkamp, Int. J. Mass Spectrom. Ion Processes 78 (1987) 53.

[271] K.D. Cook, J. Am. Soc. Mass Spectrom. 13 (2002) 1359.

[272] M. Karas, U. Bahr, U. Gießmann, Mass Spectrom. Rev. 10 (1991) 335.

[273] A. Vertes, Soft Laser Desorption Ionization — MALDI, DIOS and Nanostructures, Springer, Berlin / Heidelberg, 2007.

[274] S.R. Weinberger, K.O. Boernsen, J.W. Finchy, V. Robertson, B.D. Musselman, 41st Annual American Society for Mass Spectrometry Conference on Mass Spectrometry and Allied Topics, San Francisco, CA, May 31−June 4 1993.

[275] F. Xiang, R.C. Beavis, W. Ens, Rapid Commun. Mass Spectrom. 8 (1994) 199.

[276] O. Vorm, P. Roepstorff, M. Mann, Anal. Chem. 66 (1994) 3281.

[277] Y. Dai, R.M. Whittal, L. Li, Anal. Chem. 68 (1996) 2494.

[278] L. Li, R.E. Golding, R.M. Whittal, J. Am. Chem. Soc. 118 (1996) 11662.

[279] I.K. Perera, J. Perkins, S. Kantartzoglou, Rapid Commun. Mass Spectrom. 9 (1995) 180.

[280] F. Xiang, R.C. Beavis, Org. Mass Spectrom. 28 (1993) 1424.

[281] J. Yao, J.R. Scott, M.K. Young, C.L. Wilkins, J. Am. Soc. Mass Spectrom. 9 (1998) 805.

[282] R.R. Hensel, R. King, K.G. Owens. in 43rd Annual American Society for Mass Spectrometry Conference on Mass Spectrometry and Allied Topics: Atlanta, GA, 1995.

[283] H.J. Köchling, K. Biemann, 43rd Annual American Society for Mass Spectrometry Conference on Mass Spectrometry and Allied Topics, Atlanta, GA, 1995.

[284] K. Dreisewerd, M. Schürenberg, M. Karas, F. Hillenkamp, Int. J. Mass Spectrom. Ion Processes 141 (1995) 127.

[285] R. Knochenmuss, Analyst 131 (2006) 966.

[286] J. Zeleny, Phys. Rev. 3 (1914) 69.

[287] J. Zeleny, Philos. Mag. 46 (1898) 120.

[288] S. Chapman, Phys. Rev. 52 (1937) 184.

[289] M. Dole, R.L. Hines, L.L. Mack, R.C. Mobley, L.D. Ferguson, M.B. Alice, Macromol. 1 (1968) 96.

[290] J. Gieniec, L.L. Mack, K. Nakamae, C. Gupta, V. Kumar, M. Dole, Biol. Mass Spectrom. 11 (1984) 259.

[291] M. Yamashita, J.B. Fenn, J. Phys. Chem. 88 (1984) 4451.

[292] R.D. Smith, J.A. Loo, R.R.O. Loo, M. Busman, H.R. Udseth, Mass Spectrom. Rev. 10 (1991) 359.

[293] C.L. Hendrickson, M.R. Emmett, Annu. Rev. Phys. Chem. 50 (1999) 517.

[294] R.D. Smith, X. Cheng, J.E. Brace, S.A. Hofstadler, G.A. Anderson, Nature 369 (1994) 137.

[295] J.A. Loo, H.R. Udseth, R.D. Smith, J.H. Futrell, Rapid Commun. Mass Spectrom. 2 (1988) 207.

[296] K. Vékey, Mass Spectrom. Rev. 14 (1995) 195.

[297] N.L. Kelleher, M.W. Senko, M.M. Siegel, F.W. McLafferty, J. Am. Soc. Mass Spectrom. 8 (1997) 380.

[298] G. Taylor, Proc. R. Soc. London, Ser. A Math. Phys. Sci. 280 (1964) 383.

[299] L. Rayleigh, Proc. London Math. Soc. s1-10 (1878) 4.

[300] M. Dole, L.L. Mack, R.L. Hines, R.C. Mobley, L.D. Ferguson, M.B. Alice, J. Chem. Phys. 49 (1968) 2240.

[301] J.V. Iribarne, B.A. Thomson, J. Chem. Phys. 64 (1976) 2287.

[302] K. Tang, A. Gomez, Phys. Fluids 6 (1994) 2317.

[303] C. Dass, Chapter II of Fundamentals of Contemporary Mass Spectrometry, Wiley-Interscience, New York, 2007.

[304] C.J. Hogan, J.A. Carroll, H.W. Rohrs, P. Biswas, M.L. Gross, Anal. Chem. 81 (2009) 369.

[305] A.P. Bruins, T.R. Covey, J.D. Henion, Anal. Chem. 59 (1987) 2642.

[306] N.B. Cech, C.G. Enke, Mass Spectrom. Rev. 20 (2001) 362.

[307] D.C. Gale, R.D. Smith, Rapid Commun. Mass Spectrom. 7 (1993) 1017.

[308] I. Manisali, D.D.Y. Chen, B.B. Schneider, Trends Anal. Chem. 25 (2006) 243.

[309] A.P. Bruins, Electrospray Ionization Mass Spectrometry: Fundamentals, Instrumentation, and Applications, John Wiley & Sons, Inc., NY, 1997.

[310] T.R. Covey, E.D. Lee, J.D. Henion, Anal. Chem. 58 (1986) 2453.

[311] S.K. Chowdhury, V. Katta, B.T. Chait, Rapid Commun. Mass Spectrom. 4 (1990) 81.

[312] M.H. Allen, M.L. Vestal, J. Am. Soc. Mass Spectrom. 3 (1992) 18.

[313] K. Saito, Y. Sei, S. Miki, K. Yamaguchi, Toxicon 51 (2008) 1496.

[314] S.A. Shaffer, D.C. Prior, G.A. Anderson, H.R. Udseth, R.D. Smith, Anal. Chem. 70 (1998) 4111.

[315] J.D. Thomas, G.S. Hodges, D.G. Seely, N.A. Moroz, T.J. Kvale, Nucl. Inst. Methods Phys. Res., Sect. A 536 (2005) 11.

[316] J.S. Allen, Phys. Rev. 55 (1939) 966.

[317] L.G. Smith, Rev. Sci. Instrum. 22 (1951) 166.

[318] G.W. Goodrich, W.C. Wiley, Rev. Sci. Instrum. 33 (1962) 761.

[319] J. Ladislas Wiza, Nucl. Inst. Methods 162 (1979) 587.

[320] P.G. Friedman, K.J. Bertsche, M.C. Michel, D.E. Morris, R.A. Muller, P.P. Tans, Rev. Sci. Instrum. 59 (1988) 98.

[321] N.R. Daly, Rev. Sci. Instrum. 31 (1960) 264.

[322] C. Field, T. Hadig, M. Jain, D.W.G.S. Leith, G. Mazaheri, B.N. Ratcliff, J. Schwiening, J. Va'vra, Nucl. Inst. Methods Phys. Res., Sect. A 518 (2004) 565.

[323] J.G. Timothy, R.L. Bybee, Appl. Opt. 14 (1975) 1632.

[324] D.C. Barbacci, D.H. Russell, J.A. Schultz, J. Holocek, S. Ulrich, W. Burton, M. Van Stipdonk, J. Am. Soc. Mass Spectrom. 9 (1998) 1328.

[325] G.R. Riegler, K.A. More, IEEE Trans. Nucl. Sci. 20 (1973) 102.

[326] W. Parkes, K.D. Evans, E. Mathieson, Nucl. Inst. Methods 121 (1974) 151.

[327] J.P. Carrico, M.C. Johnson, T.A. Somer, Int. J. Mass Spectrom. Ion Phys. 11 (1973) 409.

[328] A. Kashefian Naieni, F. Bahrami, N. Yasrebi, B. Rashidian, Vacuum 83(8) (2009) 1095.

[329] G. Beck, Rev. Sci. Instrum. 47 (1976) 849.

[330] P. Wurz, L. Gubler, Rev. Sci. Instrum. 65 (1994) 871.

[331] H. Wollnik, Int. J. Mass Spectrom. Ion Processes 131 (1994) 387.

[332] R. Janmohamed, G. Redman, T. Ying Yin, IEEE Trans. Plasma Sci. 34 (2006) 455.

[333] S. Evans, A.M. James, in: Chapter III of Methods in Enzymology, Academic Press, NY, 1990.

[334] D.C. Collins, M.L. Lee, Anal. Bioanal. Chem. 372 (2002) 66.

[335] J.R. Chapman, Chapter I of Practical Organic Mass Spectrometry: A Guide for Chemical and Biochemical Analysis, John Wiley & Sons, Inc., NY, 1995.

[336] J.G. Timothy, Rev. Sci. Instrum. 52 (1981) 1131.

[337] J. Va'vra, T. Sumiyoshi, Nuclear Science Symposium Conference Record, 2004 IEEE, 2004.

[338] R. Naaman, Z. Vager, Rev. Sci. Instrum. 67 (1996) 3332.

[339] A.G. Marshall, Int. J. Mass Spectrom. 200 (2000) 331.

[340] J.H. Moore, C.C. Davis, M.A. Coplan, S. Greer, in: Chapter III of Building Scientific Apparatus: A Practical Guide to Design and Construction, Westview Press, Boulder, CO, 2003.

[341] W. Harkins. "Public Lessons Learned Entry: 0675" published online at www.nasa.gov/offices/oce/llis/0675.html: Jet Propulsion Laboratory, National Aeronautics and Space Administration, 1999.

[342] J.F. O'Hanlon, A User's Guide to Vacuum Technology, John Wiley & Sons, Inc., Hoboken, NJ, 2003.

[343] R.E. Ellefson, A.P. Miiller, J. Vac. Sci. Technol., A 18 (2000) 2568.

[344] J.E. Bartmess, R.M. Georgiadis, Vacuum 33 (1983).

[345] F. Nakao, Vacuum 25 (1975).

[346] H.Y. Afeefy, J.F. Liebman, S.E. Stein (Eds.), "Mass Spectra" by NIST Mass Spec Data Center, S.E. Stein, director, National Institute of Standards and Technology, Gaithersburg MD, http://webbook.nist.gov, (retrieved December 2 2008).

[347] W.H. Brattain, J.A. Becker, Phys. Rev. 43 (1933) 428.

[348] W.B. Nottingham, Phys. Rev. 49 (1936) 78.

[349] I. Langmuir, Phys. Rev. 22 (1923) 357.

[350] S. Magari, H. Kokichi, Mass Spectrom. 23 (1963) 94.

[351] C.J. Park, J.R. Ahn, Rev. Sci. Instrum. 76 (2005) 044101.

[352] G. Liebmann, Proc. Phys. Soc. London, Sect. B 62 (1949) 213.

[353] F.H. Read, J. Phys. E: Sci. Instrum. 2 (1969) 679.

[354] A.N. Krutchinsky, I.V. Chernushevich, V.L. Spicer, W. Ens, K.G. Standing, J. Am. Soc. Mass Spectrom. 9 (1998) 569.

[355] A. Dodonov, V. Kozlovsky, A. Loboda, V. Raznikov, I. Sulimenkov, A. Tolmachev, A. Kraft, H. Wollnik, Rapid Commun. Mass Spectrom. 11 (1997) 1649.

[356] A.V. Tolmachev, I.V. Chernushevich, A.F. Dodonov, K.G. Standing, Nucl. Instrum. Methods Phys. Res., Sect. B 124 (1997) 112.

[357] P.H. Dawson, Int. J. Mass Spectrom. Ion Processes 83 (1988) 295.

[358] R.E. Pedder, R.A. Shaeffer, 43rd Annual American Society for Mass Spectrometry Conference on Mass Spectrometry and Allied Topics, Atlanta, GA, 1995.

[359] S.S. Medley, Rev. Sci. Instrum. 49 (1978) 698.

[360] M.J.-F. Suter, R.M. Stepnowski, U.P. Schlunegger, Rapid Commun. Mass Spectrom. 3 (1989) 417.

[361] D.W.O. Heddle, J. Phys. E: Sci. Instrum. 4 (1971) 981.

[362] S.M. Walley, J.E. Field, M. Greengrass, Wear 114 (1987) 59.

[363] J.C. Salamone, in: Volume 8 of Polymeric Materials Encyclopedia, CRC Press, Boca Raton, FL, 1996.

[364] S. Yogev, J. Levin, M. Molotskii, A. Schwarzman, O. Avayu, Y. Rosenwaks, J. Appl. Phys. 103 (2008) 064107.

[365] M.F. Jarrold, J.E. Bower, K. Creegan, J. Chem. Phys. 90 (1989) 3615.

[366] P.R. Kemper, M.T. Bowers, J. Am. Soc. Mass Spectrom. 1 (1990) 197.

[367] L. Michalski, K. Eckersdorf, J. Kucharski, J. McGhee, Temperature Measurement, John Wiley & Sons, West Sussex, UK, 2002.

[368] U.S. Committee on NIM Standard, "Standard NIM Instrumentation System": National Technical Information Service, Springfield, VA, 1990.

[369] M. Yildirim, O. Sise, R. Aydin, U. Akin, M. Ulu, M. Dogan, H.S. Kilic, 6th International Conference of the Balkan Physical Union, Istanbul, Turkey, 2007.

[370] D.S. Selby, V. Mlynski, M. Guilhaus, Int. J. Mass Spectrom. 210-211 (2001) 89.

[371] P. Horowitz, W. Hill, Chapter I of The Art of Electronics, Cambridge University Press, Cambridge, UK, 1989.

[372] W. Sun, J.C. May, K.J. Gillig, D.H. Russell, Int. J. Mass Spectrom. In Press, Corrected Proof (2009) doi:10.1016/j.ijms.2008.11.011.

[373] N. Einolf, B. Munson, International Journal or Mass Spectrometry and Ion Physics 9 (1972) 141.

[374] J. Puton, A. Knapa, B. Siodłowski, Sens. Actuators, B 135(1) (2008) 116.

[375] E.A. Mason, E.W. McDaniel, Section 2-5 of Transport Properties of Ions in Gases, John Wiley & Sons, NY, 1988.

[376] N.G. Adams, D. Smith, Int. J. Mass Spectrom. Ion Phys. 21 (1976) 349.

[377] C.S. Hoaglund, S.J. Valentine, C.R. Sporleder, J.P. Reilly, D.E. Clemmer, Anal. Chem. 70 (1998) 2236.

[378] E.A. Mason, E.W. McDaniel, Section 2-2 of Transport Properties of Ions in Gases, John Wiley & Sons, NY, 1988.

[379] D.C. Collins, M.L. Lee, Fresnius J. Anal. Chem. 369 (2001) 225.

[380] J.S. Page, A.V. Tolmachev, K. Tang, R.D. Smith, J. Mass Spectrom. 40 (2005) 1215.

[381] F.W. Karasek, D.W. Denney, Anal. Lett. 6 (1973) 993.

[382] F.W. Karasek, W.D. Kilpatrick, M.J. Cohen, Anal. Chem. 43 (1971) 1441.

[383] G.W. Griffin, I. Dzidic, D.I. Carroll, R.N. Stillwell, E.C. Horning, Anal. Chem. 45 (1973) 1204.

[384] S.H. Kim, G.E. Spangler, Anal. Chem. 57 (1985) 567.

[385] P.W. Harland, B.J. McIntosh, R.W. Simpson, N.R. Thomas, J. Chem. Soc., Faraday Trans. 2 82 (1986) 2039.

[386] "Exact Mass Calculator, Single Isotope Version", Scientific Instrument Services, Inc.: Ringoes, NJ, http://www.sisweb.com/referenc/tools/exactmass.htm, (accessed May 2009).

[387] J.P. Williams, T. Bugarcic, A. Habtemariam, K. Giles, I. Campuzano, P.M. Rodger, P.J. Sadler, J. Am. Soc. Mass Spectrom. 20(6) (2009) 1119.

[388] N.D. Twiddy, A. Mohebati, M. Tichý, Int. J. Mass Spectrom. Ion Processes 74 (1986) 251.

[389] B.R. Rowe, D.W. Fahey, F.C. Fehsenfeld, D.L. Albritton, J. Chem. Phys. 73 (1980) 194.

[390] R.W. Simpson, R.G.A.R. Maclagan, P.W. Harland, J. Chem. Phys. 87 (1987) 5419.

[391] H. Helm, M.T. Elford, J. Phys. B: At. Mol. Phys. 11 (1978) 3939.

[392] H. Helm, J. Phys. B: At. Mol. Phys. 9 (1976) 2931.

[393] R.B. Freas, D.P. Ridge, J. Am. Chem. Soc. 102 (1980) 7129.

[394] L.F. Halle, P.B. Armentrout, J.L. Beauchamp, J. Am. Chem. Soc. 103 (1981) 963.

[395] J.L. Elkind, P.B. Armentrout, J. Chem. Phys. 86 (1987) 1868.

[396] C. Iceman, C. Rue, R.M. Moision, B.K. Chatterjee, P.B. Armentrout, J. Am. Soc. Mass Spectrom. 18 (2007) 1196.

[397] Y. Ibrahim, E. Alsharaeh, R. Mabrouki, P. Momoh, E. Xie, M.S. El-Shall, J. Phys. Chem. A 112 (2008) 1112.

[398] H.Y. Afeefy, J.F. Liebman, S.E. Stein (Eds.), "Mass Spectra" by NIST Mass Spec Data Center, S.E. Stein, director, National Institute of Standards and Technology, Gaithersburg MD, http://webbook.nist.gov, (retrieved March 16 2009).

[399] P.B. Armentrout, Annu. Rev. Phys. Chem. 41 (1990) 313.

[400] J. Herman, J.D. Foutch, G.E. Davico, J. Phys. Chem. A 111 (2007) 2461.

[401] B.C. Guo, K.P. Kerns, A.W. Castleman, Int. J. Mass Spectrom. Ion Processes 117 (1992) 129.

[402] W.J. Bouma, R.H. Nobes, L. Radom, J. Am. Chem. Soc. 104 (1982) 2929.

[403] F.W. McLafferty, Anal. Chem. 31 (1959) 82.

[404] W.J. Bouma, J.K. MacLeod, L. Radom, J. Am. Chem. Soc. 104 (1982) 2930.

[405] J.L. Holmes, F.P. Lossing, J.K. Terlouw, P.C. Burgers, J. Am. Chem. Soc. 104 (1982) 2931.

[406] S. Hammerum, J. Henriksen, T. Henriksen, T.I. Solling, Int. J. Mass Spectrom. 195/196 (2000) 459.

[407] K. Okuno, T. Koizumi, Y. Kaneko, Phys. Rev. Lett. 40 (1978) 1708.

[408] T.D. Fridgen, J.M. Parnis, Int. J. Mass Spectrom. 190-191 (1999) 181.

[409] B. Hoegger, P. Bommer, International Journal or Mass Spectrometry and Ion Physics 13 (1974) 35.

[410] E.P.L. Hunter, S.G. Lias, Journal of Physical and Chemical Reference Data 27 (1998) 413.

[411] R. Sudha, M. Kohtani, M.F. Jarrold, J. Phys. Chem. B 109 (2005) 6442.

[412] G.A. Breaux, M.F. Jarrold, J. Am. Chem. Soc. 125 (2003) 10740.

[413] D.T. Kaleta, M.F. Jarrold, J. Phys. Chem. B 107 (2003) 14529.

[414] Y. Ibrahim, K. Tang, A.V. Tolmachev, A.A. Shvartsburg, R.D. Smith, J. Am. Soc. Mass Spectrom. 17 (2006) 1299.

[415] Y. Takada, M. Sakairi, Y. Ose, Rev. Sci. Instrum. 67 (1996) 2139.

APPENDIX A

DIGITAL IMAGES OF THE CRYOGENIC MS-IMS-MS INSTRUMENT:

A PICTURE IS WORTH 10^3 WORDS

Instrument Development Overview

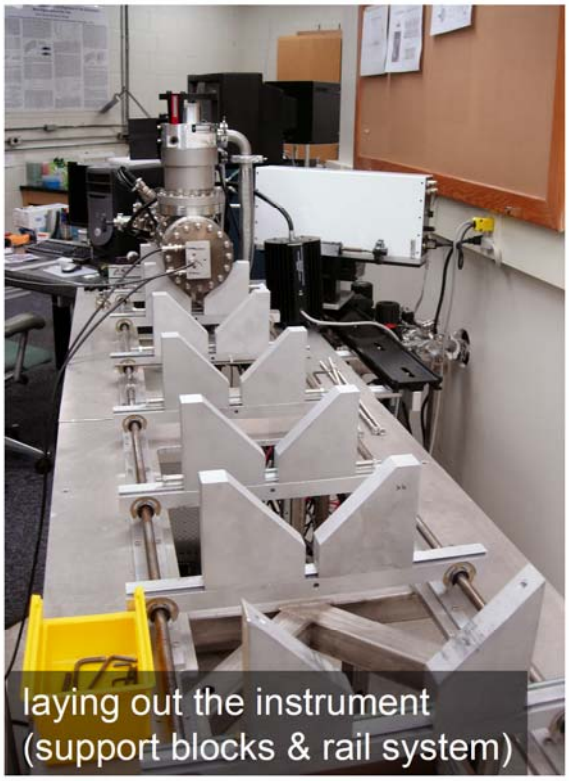

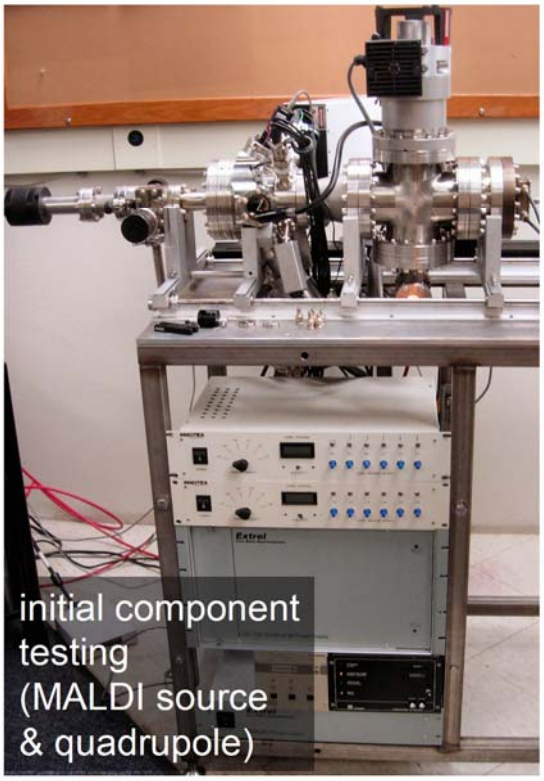

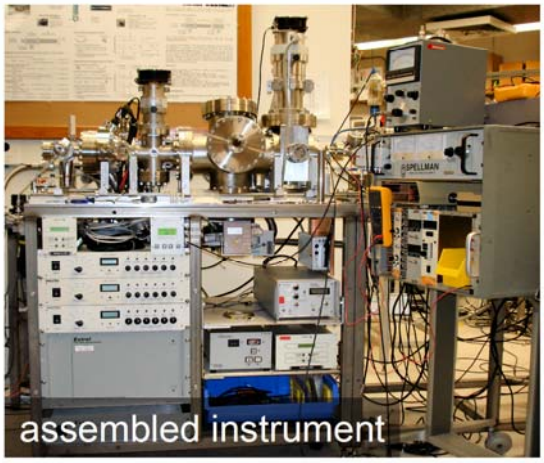

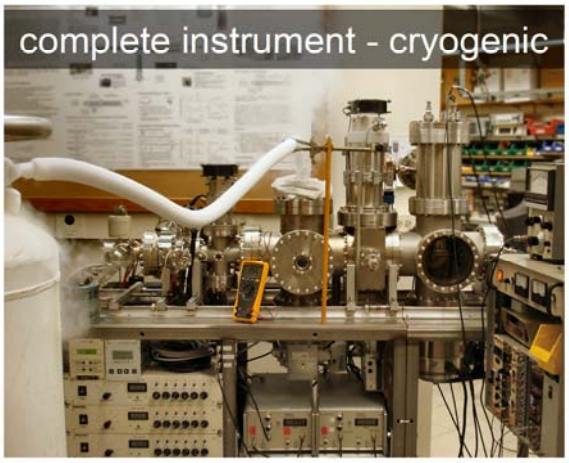

Electron Ionization Source

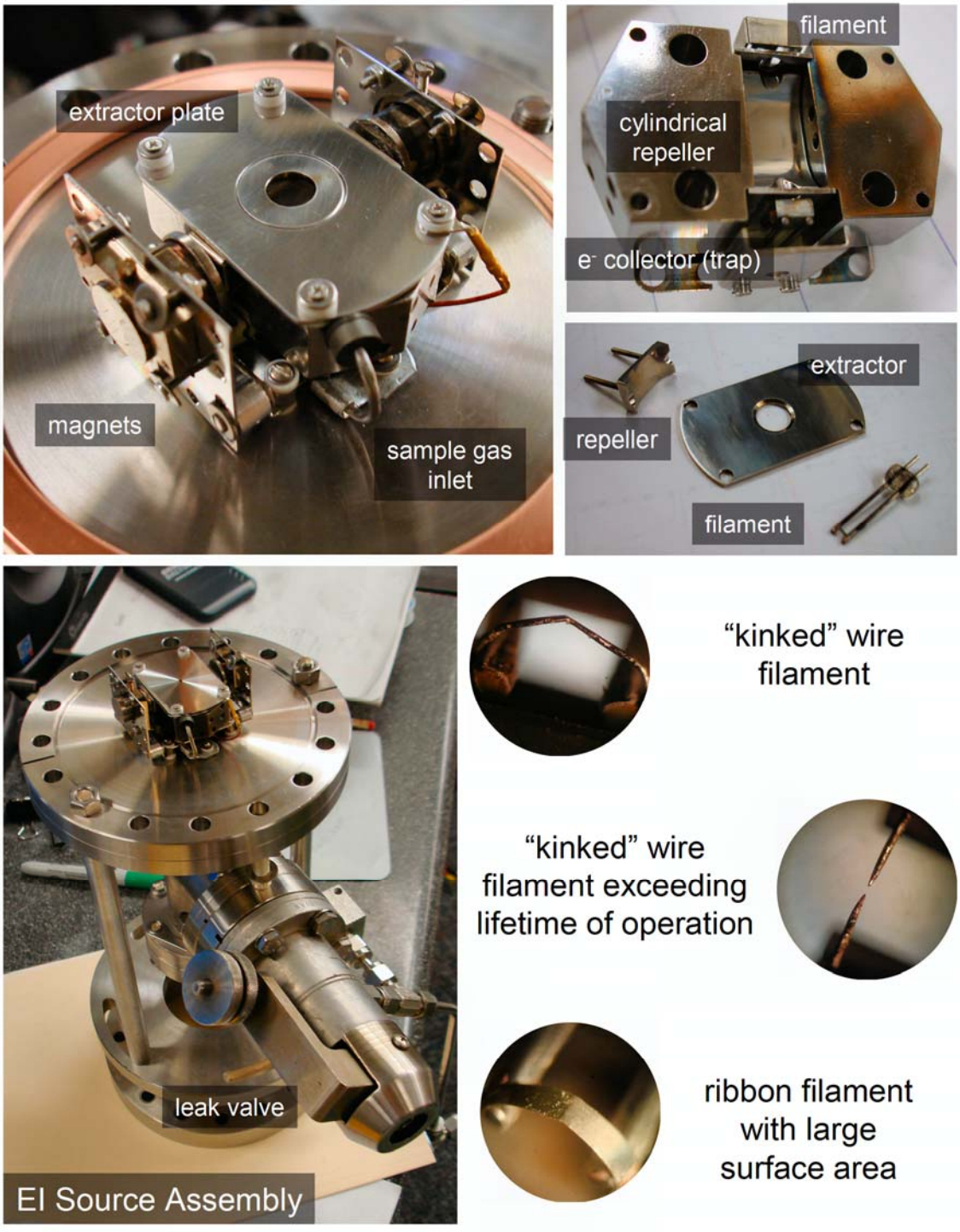

Quadrupole Mass Filter

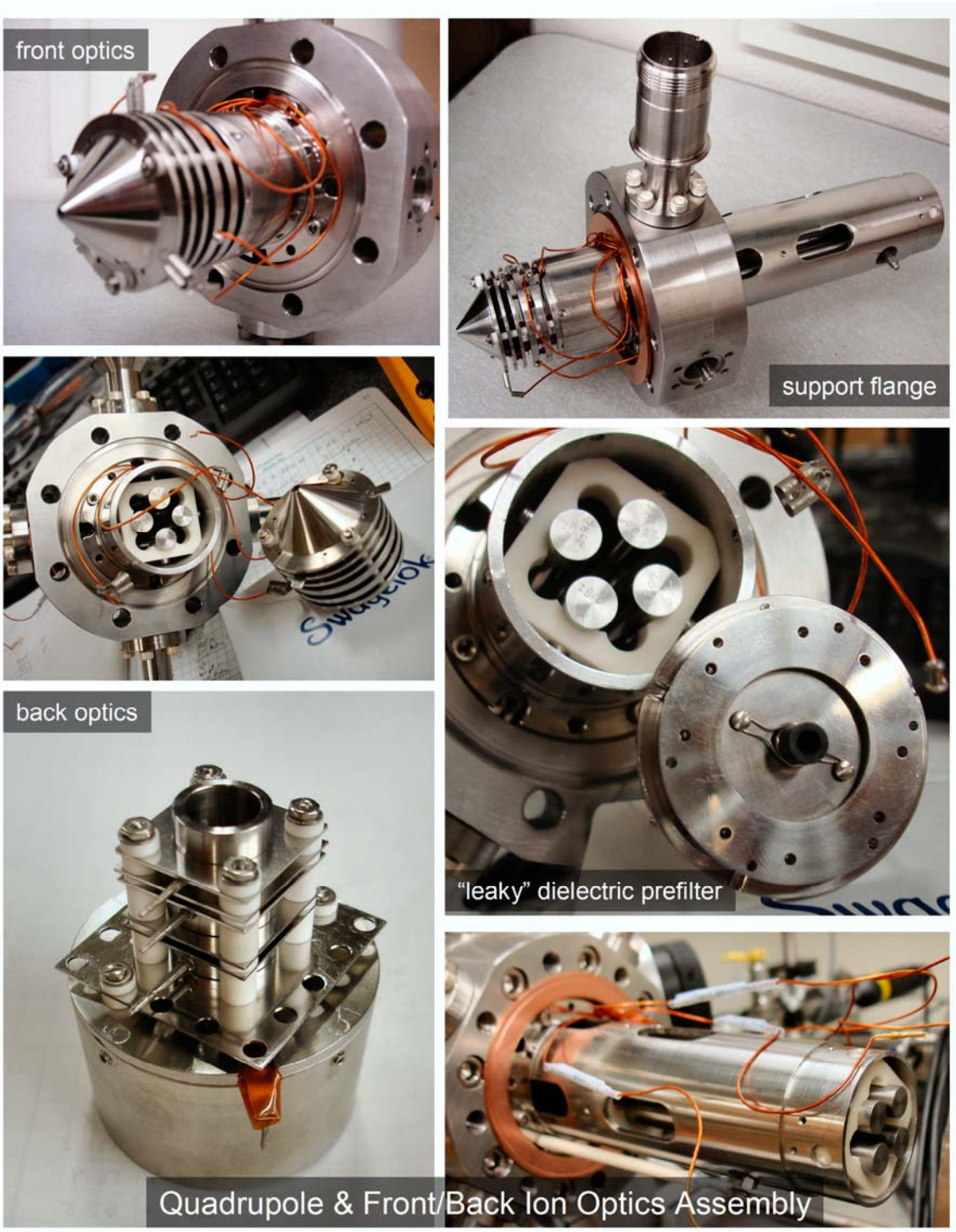

IMS Entrance Ion Optics

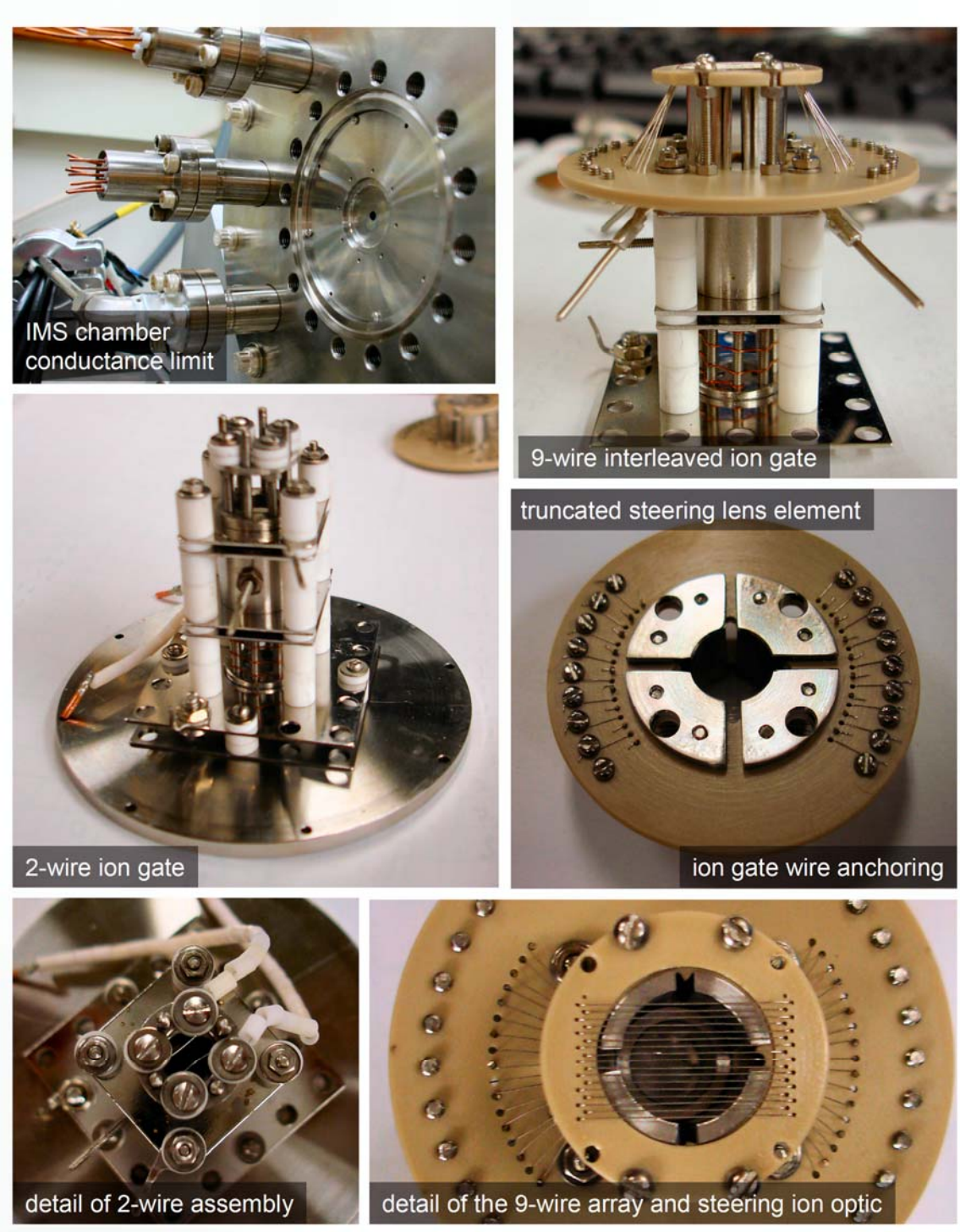

IMS Drift Cell

IMS Exit Ion Optics

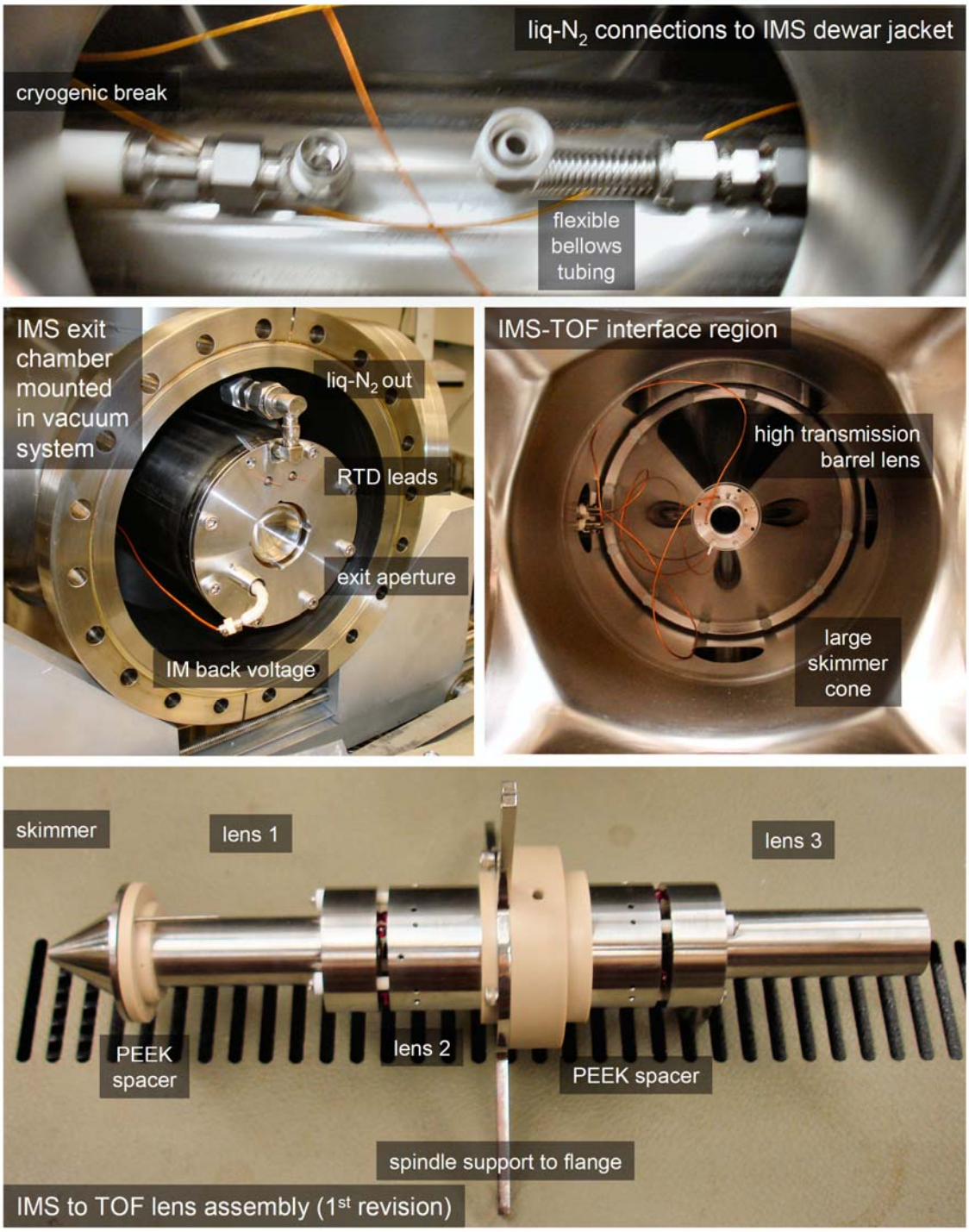

TOF Mass Spectrometer

Instrument Operating in Cryogenic IMS Mode

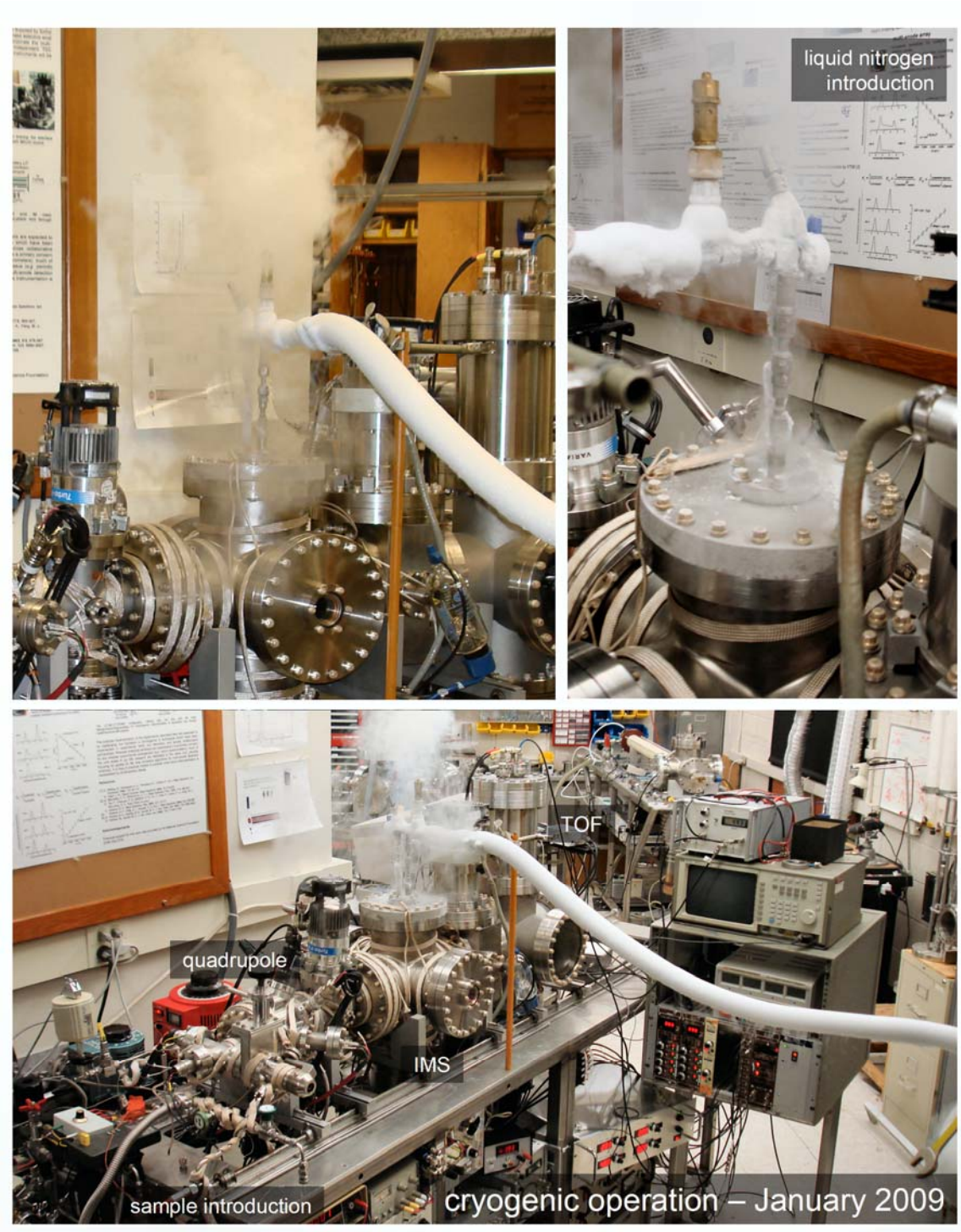

MALDI Ion Source

ESI Ion Source with Ion Funnel Interface

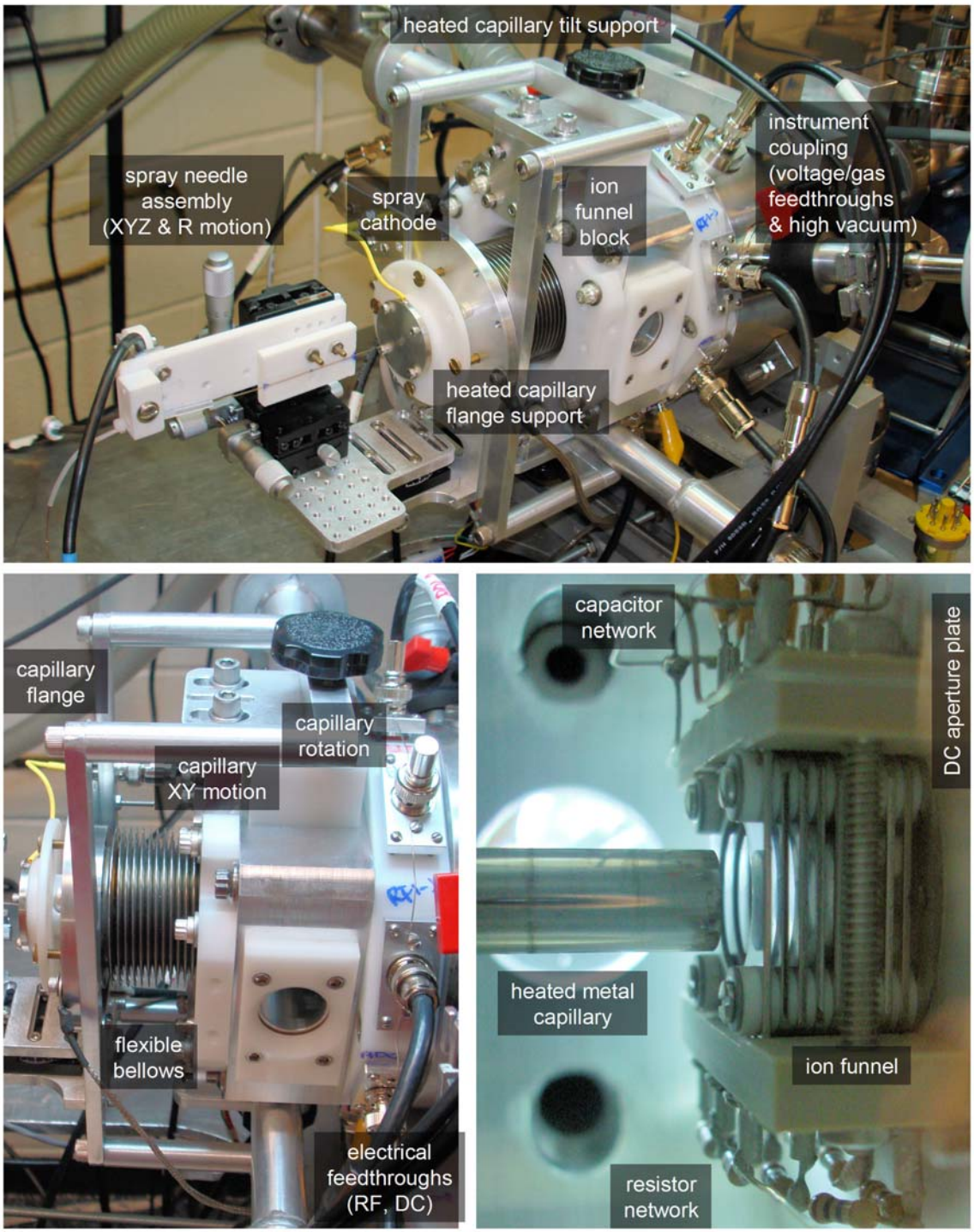

APPENDIX B

MECHANICAL DRAWINGS OF THE CRYOGENIC ION MOBILITY SPECTROMETER

NOT TO SCALE

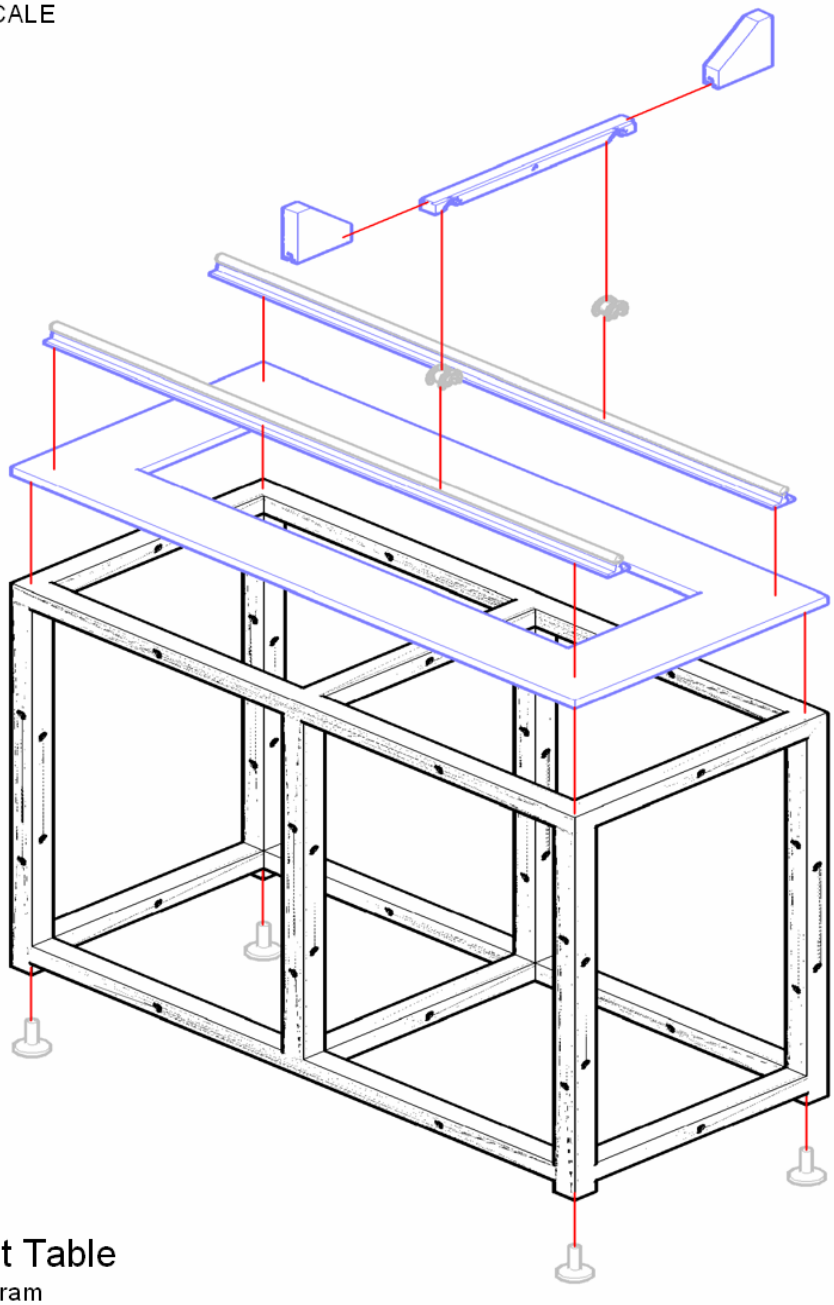

Instrument Table
Assembly Diagram

Chamber Support Bracket System

Dovetailed Crossbar and Flange Brackets

aluminum

NOT TO SCALE

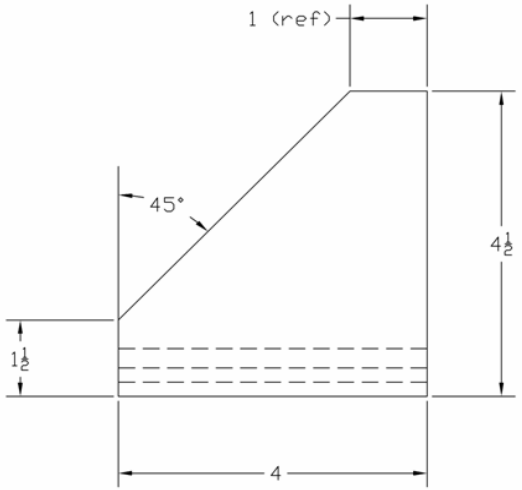

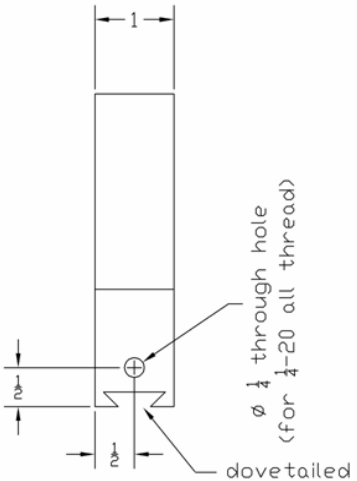

4-10" Conflat Flange Bracket

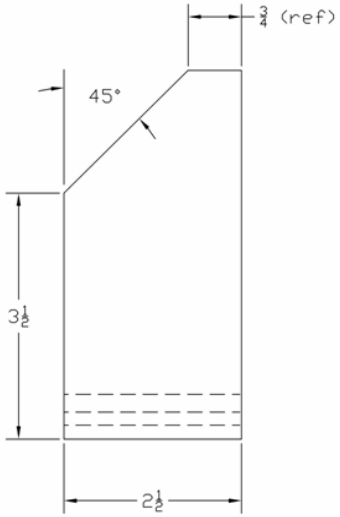

2 3/4" Conflat Flange Bracket

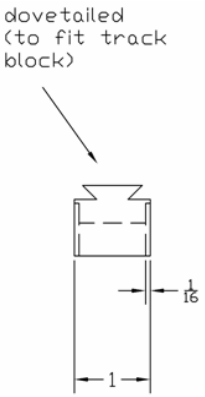

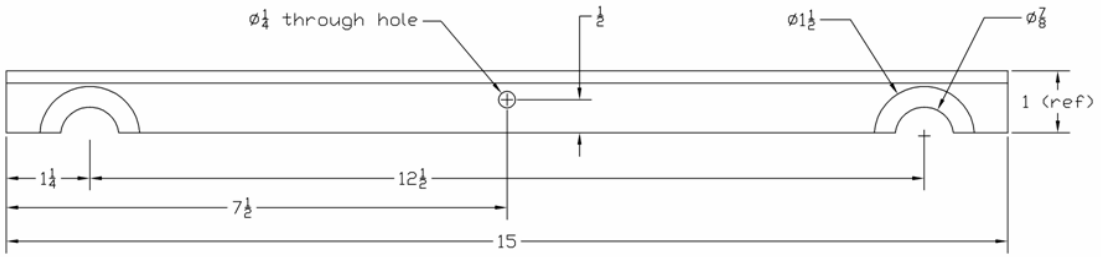

Electrical Socket Feedthrough Plates

Banana Style Chassis Mount Sockets - 1.33" conflat mounted "L" plate

aluminum

NOT TO SCALE

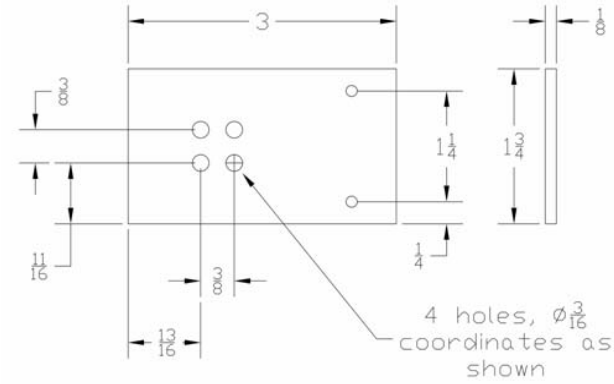

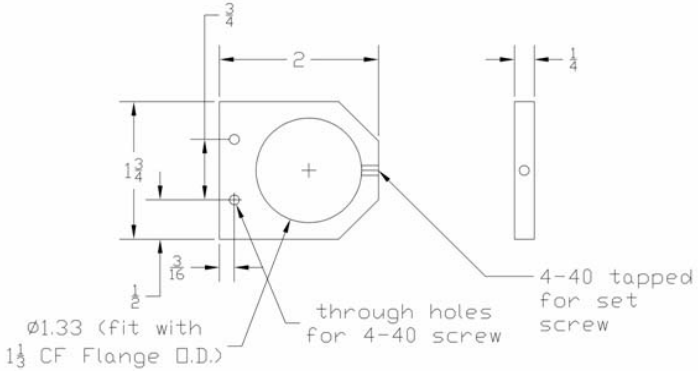

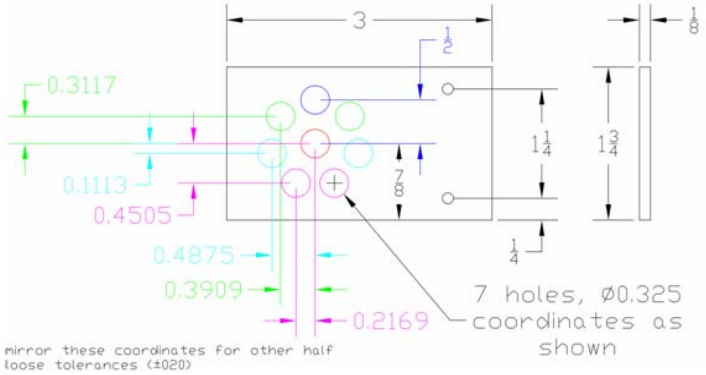

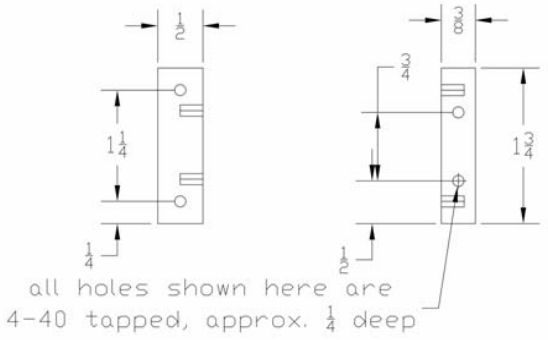

Miscellaneous Infrastructure Components

Channel Strut Rack Mounting Brackets, Turbopump Fan Brackets, CCD Camera Brackets

NOT TO SCALE

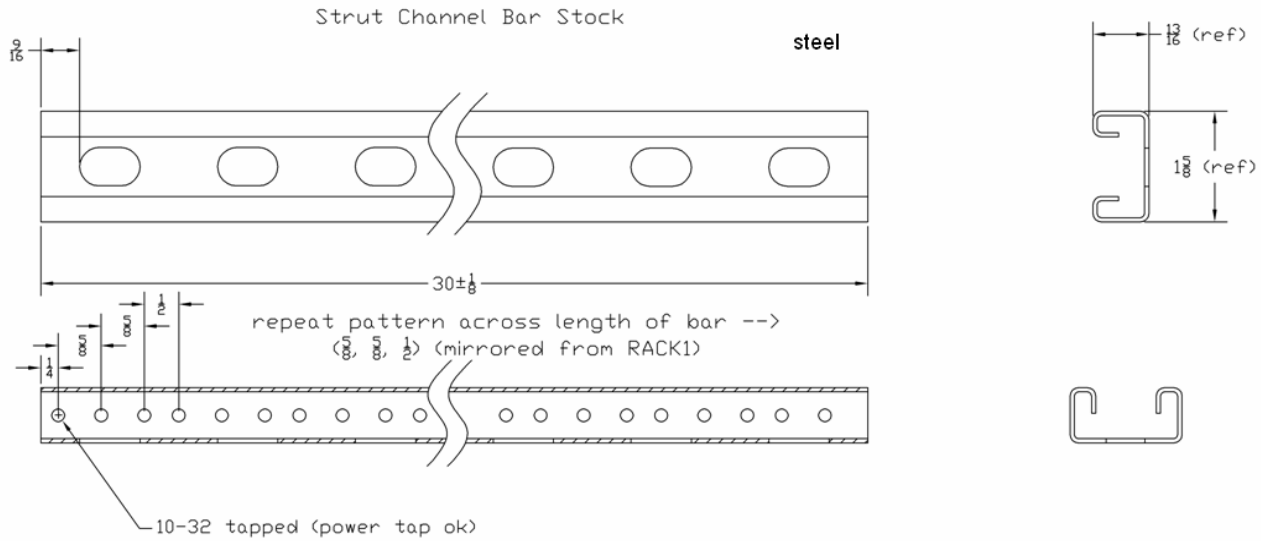

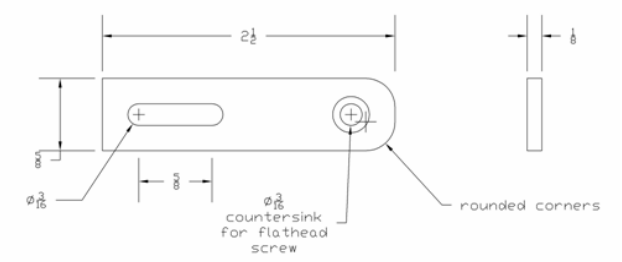

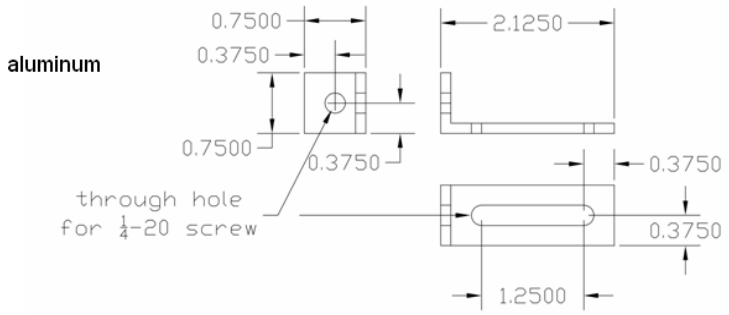

Zero Length Adapter Flanges – ISO to CF

4 ½" CF to ISO NW63 & 2 ¾" CF to ISO NW63 – Zero Length Improves Base Vacuum

stainless steel

NOT TO SCALE

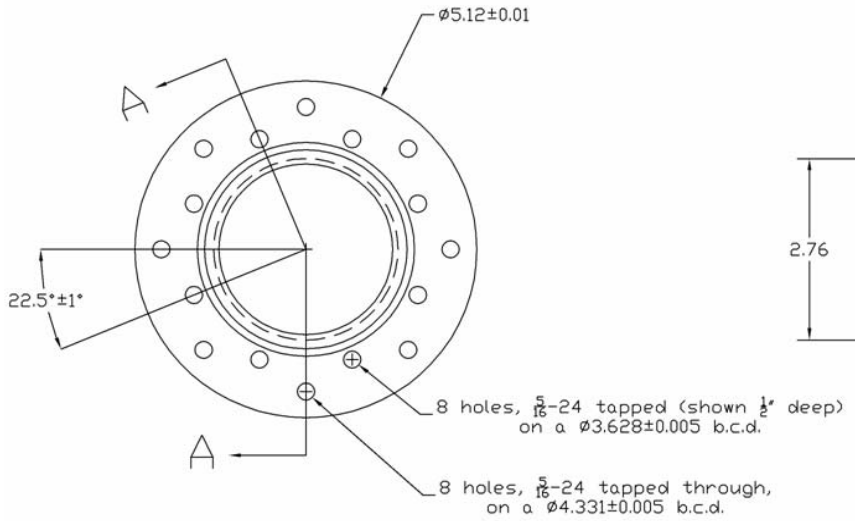

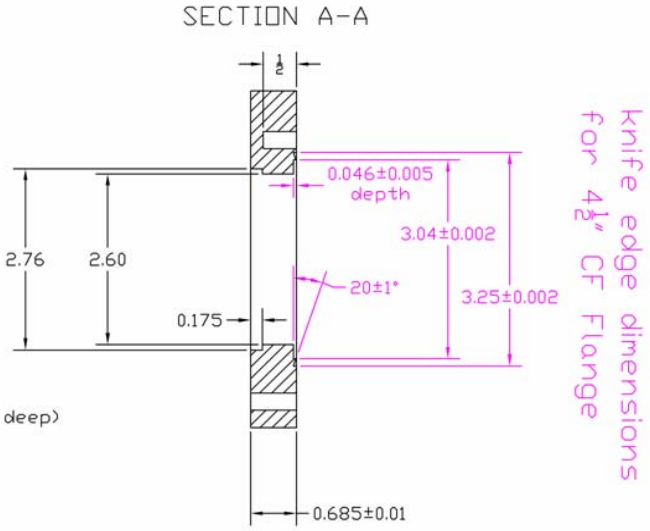

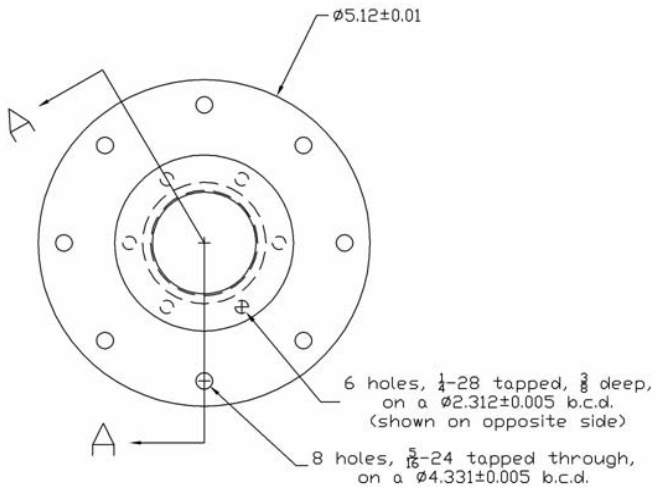

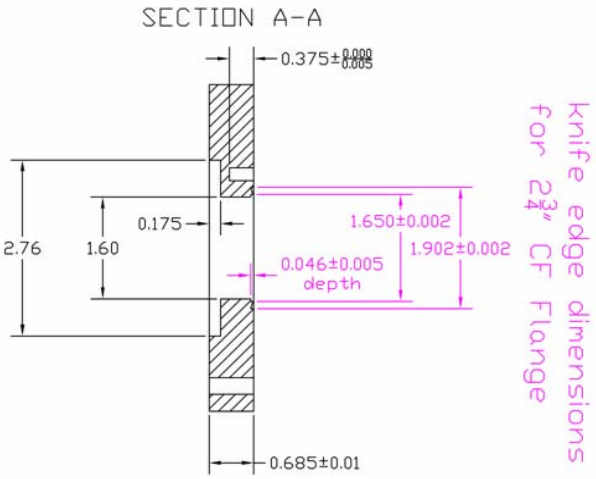

Volatile Sample Inlet

Metal Capillary Delivery Fitting Flange

stainless steel

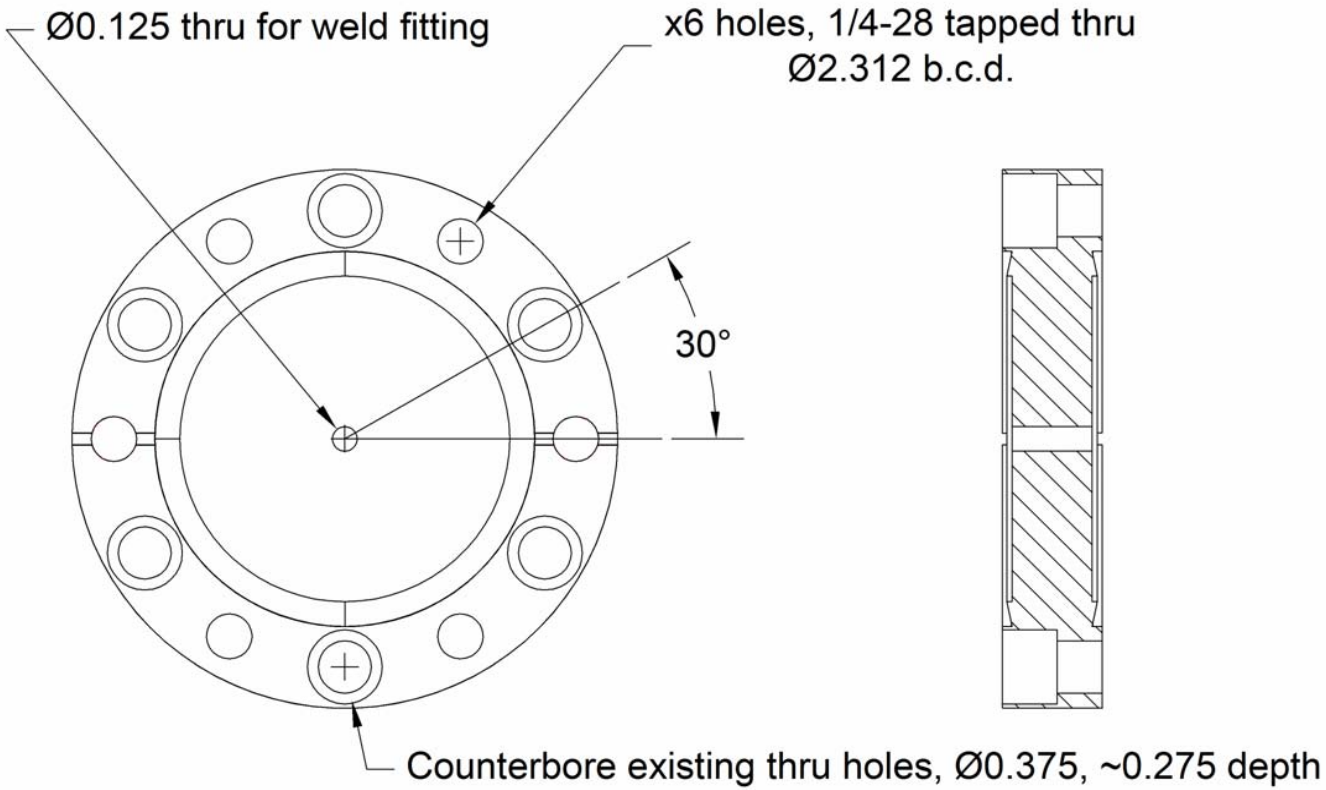

Electron Ionization Source

Assembly Diagram

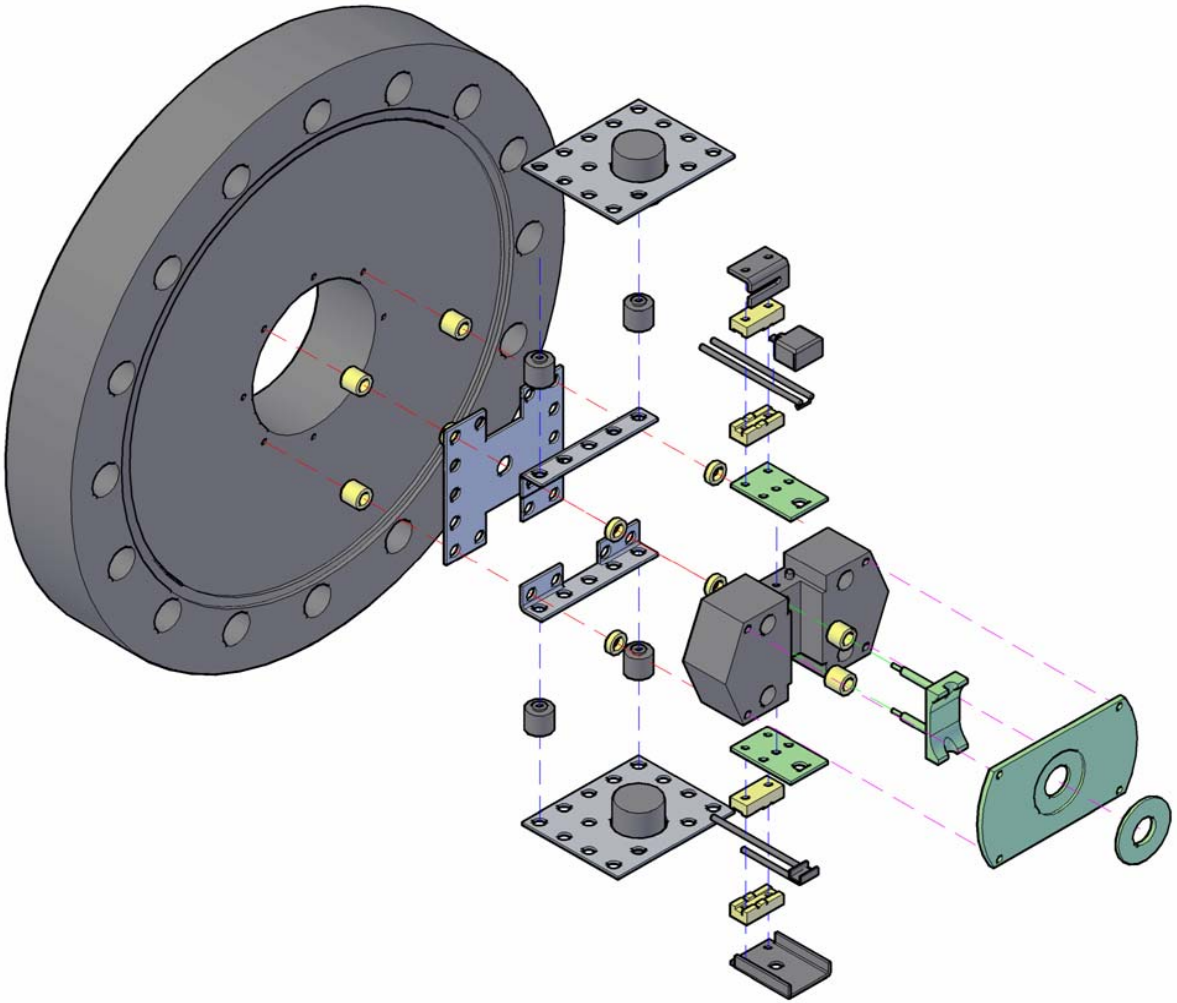

Electron Ionization Source

Mounting Flange (fabricated from Conflat 6" to 2 ¾" zero length reducing flange)

stainless steel

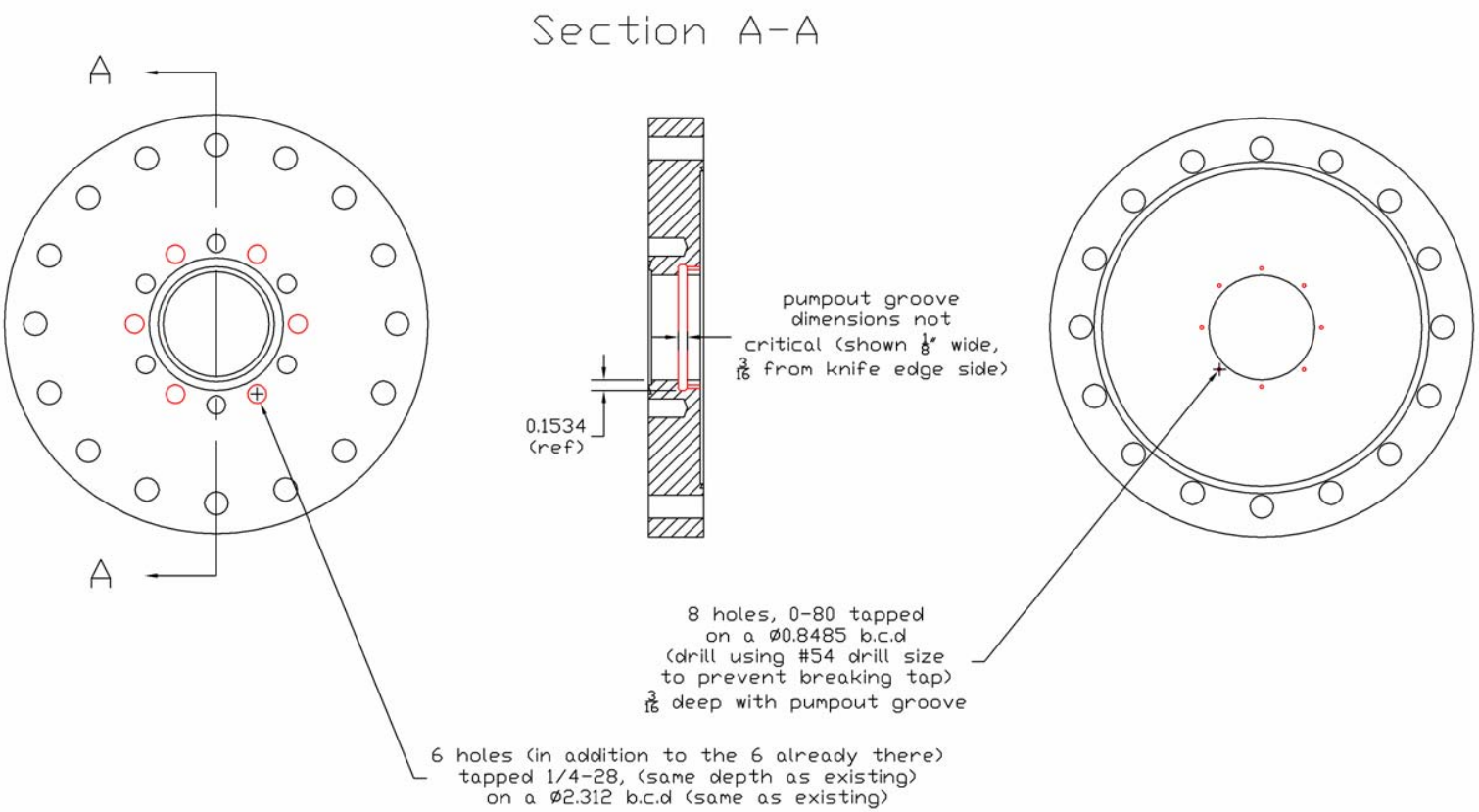

Electron Ionization Source

Cylindrical Repeller, Ion Extraction Optic & Optional Grid Support, Magnet Mounting Parts (fabricated from eV Parts)

stainless steel NOT TO SCALE

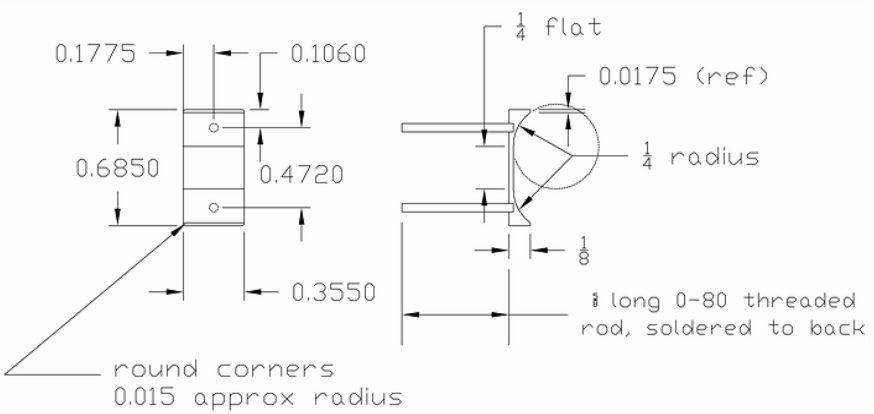

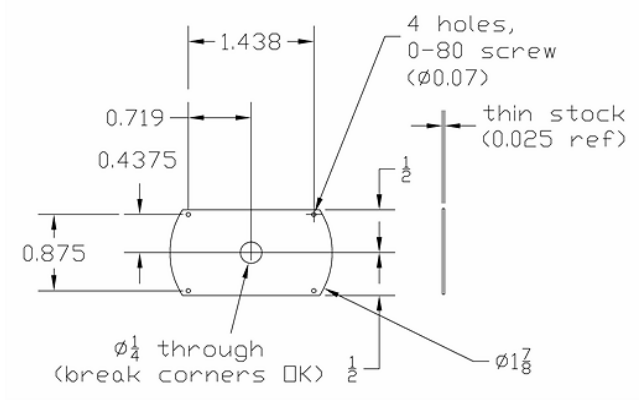

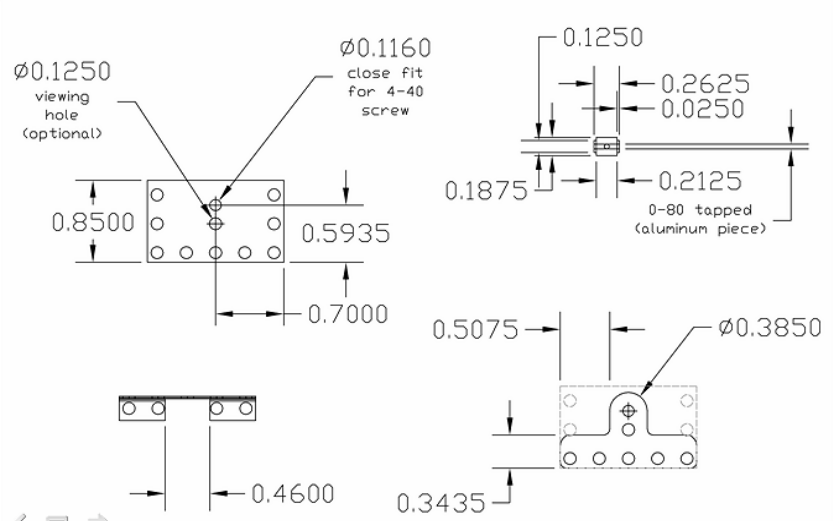

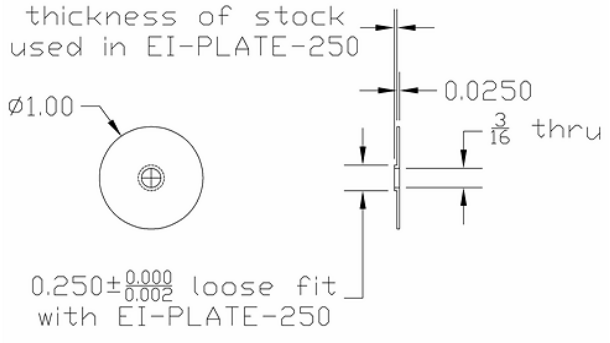

Source Chamber Accessory Parts

Custom 5-way Cross, Tapped Viewport for CCD Camera Mount

30° High Conductance Elbow for Turbopump

stainless steel

NOT TO SCALE

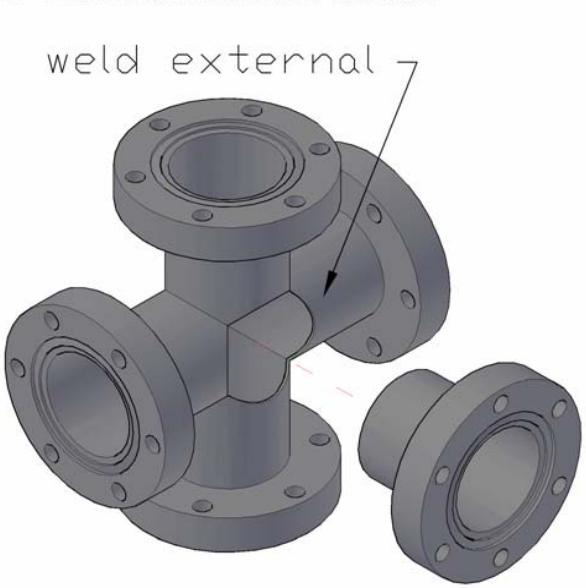

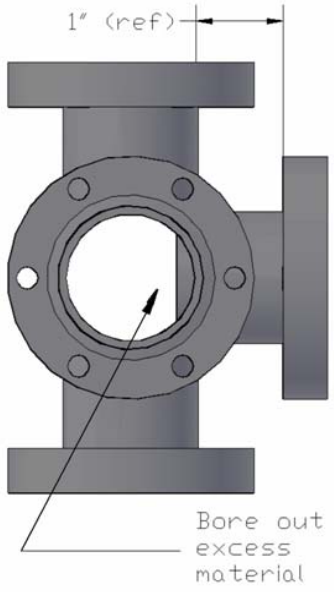

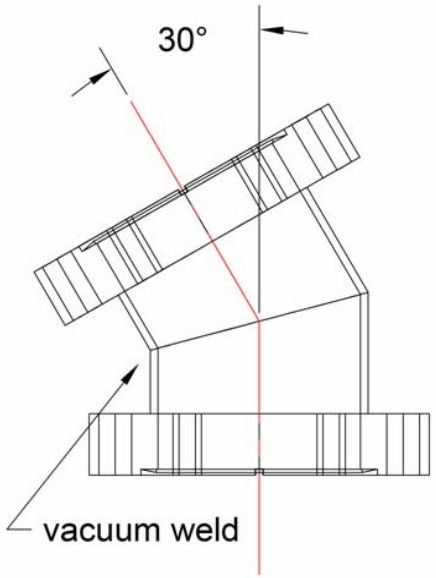

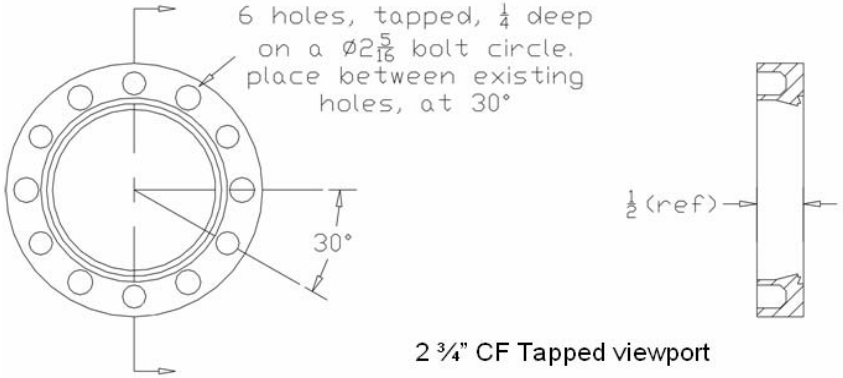

2 ¾" CF Tapped viewport

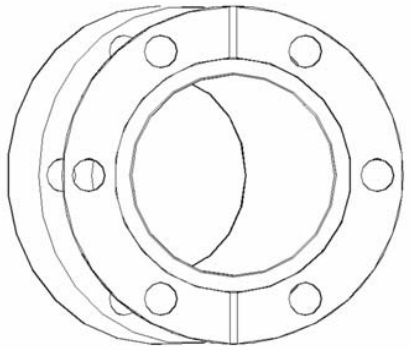

2 ¾" CF 30° Elbow

Source Chamber Ion Optical Components – EI Source

Assembly Diagram of EI Source & Ion Optics to Quadrupole

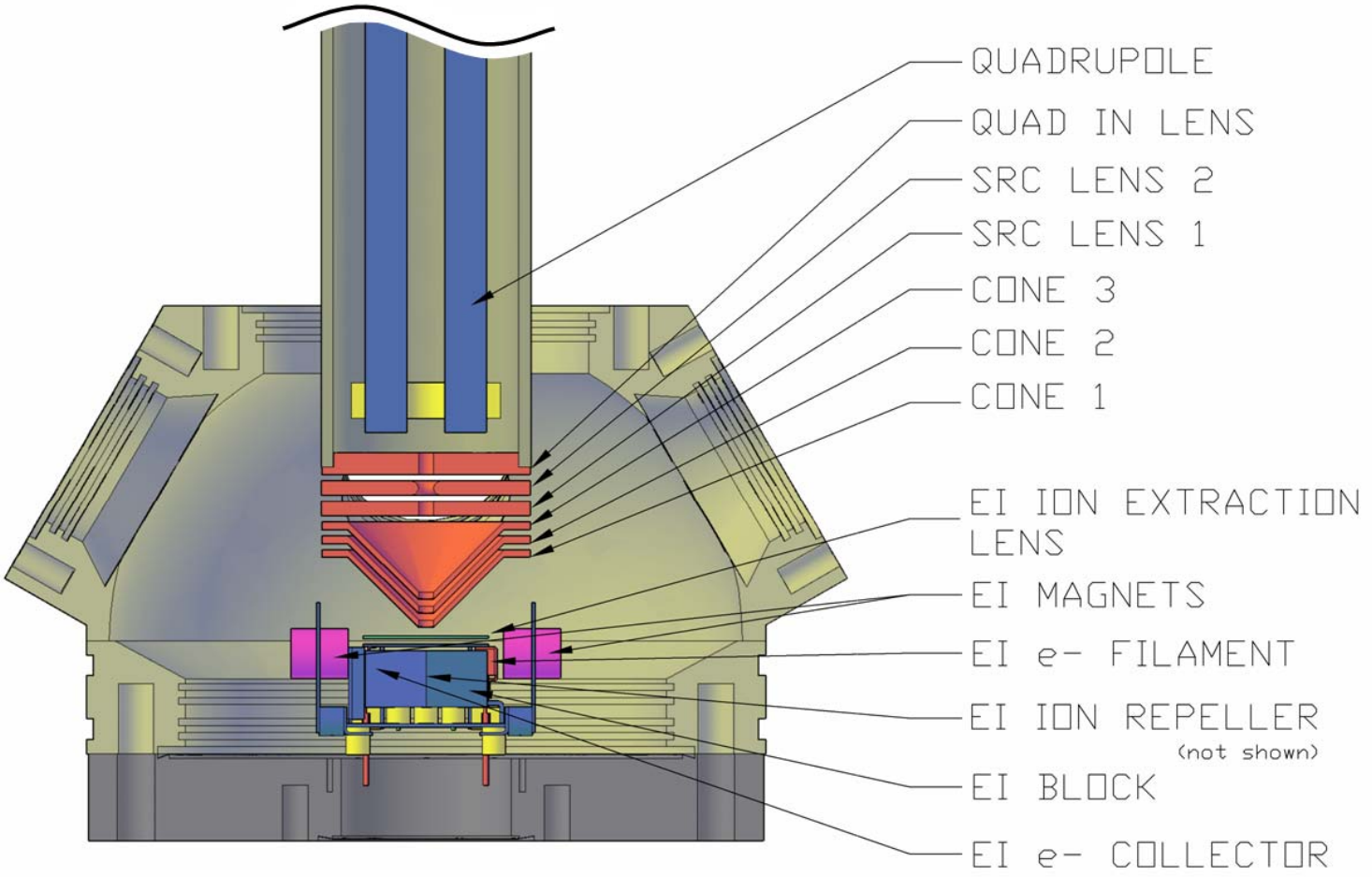

Source Ion Optics

Extraction Cone Lens

stainless steel

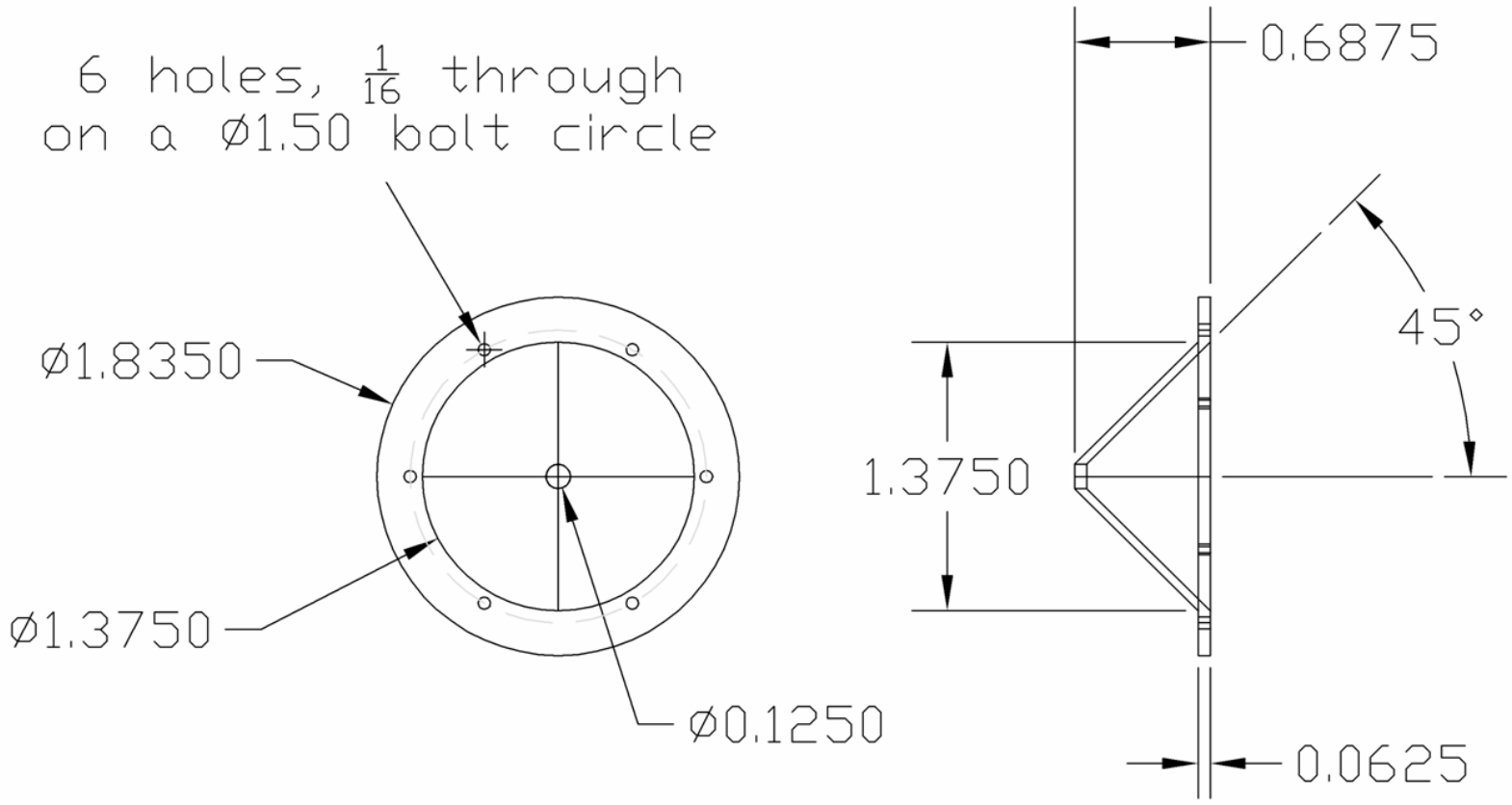

Source Ion Optics

Collimating Lens - Outer

stainless steel

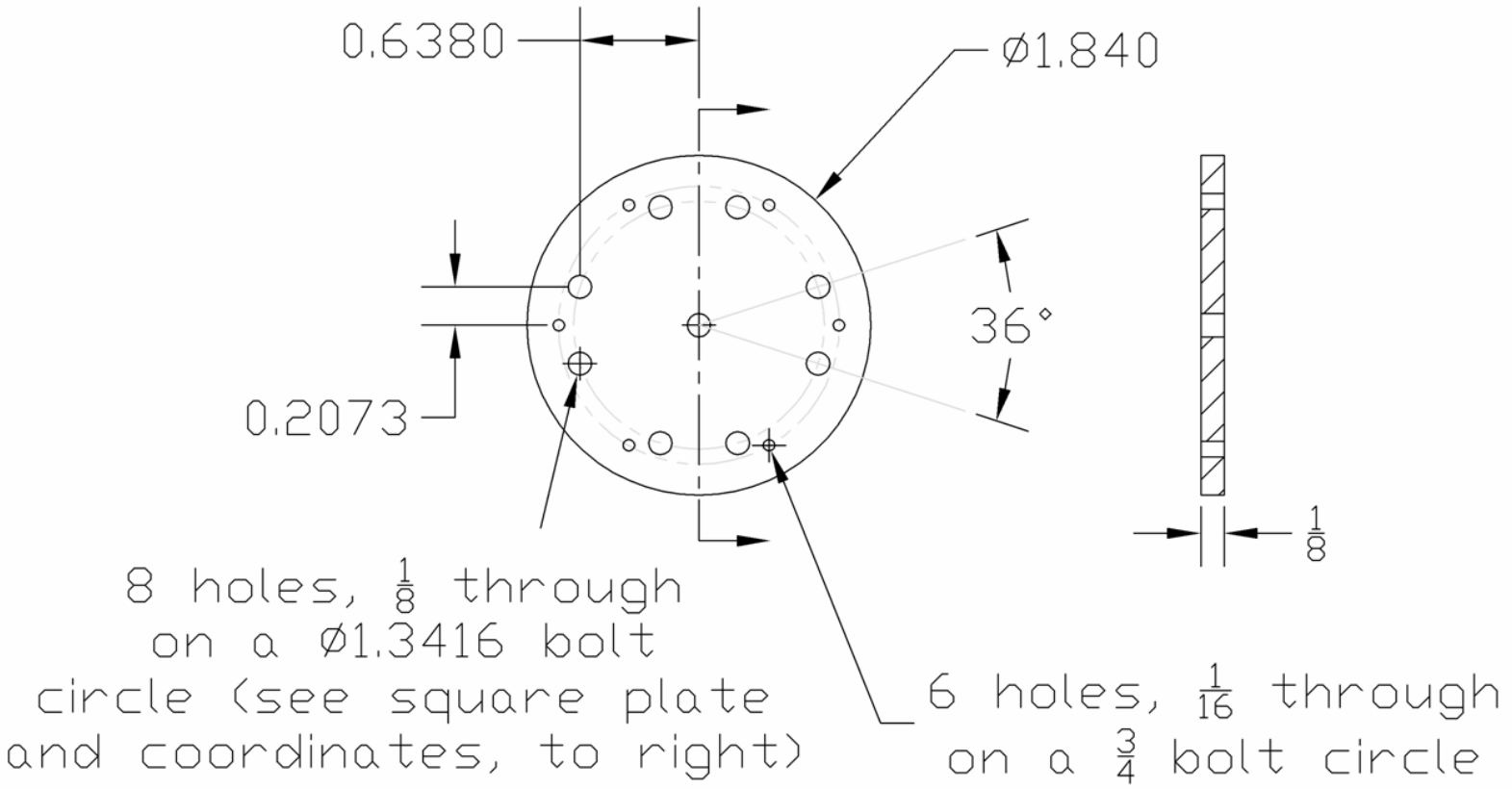

Source Ion Optics

Collimating Lens – Inner (Hyperbolic)

stainless steel

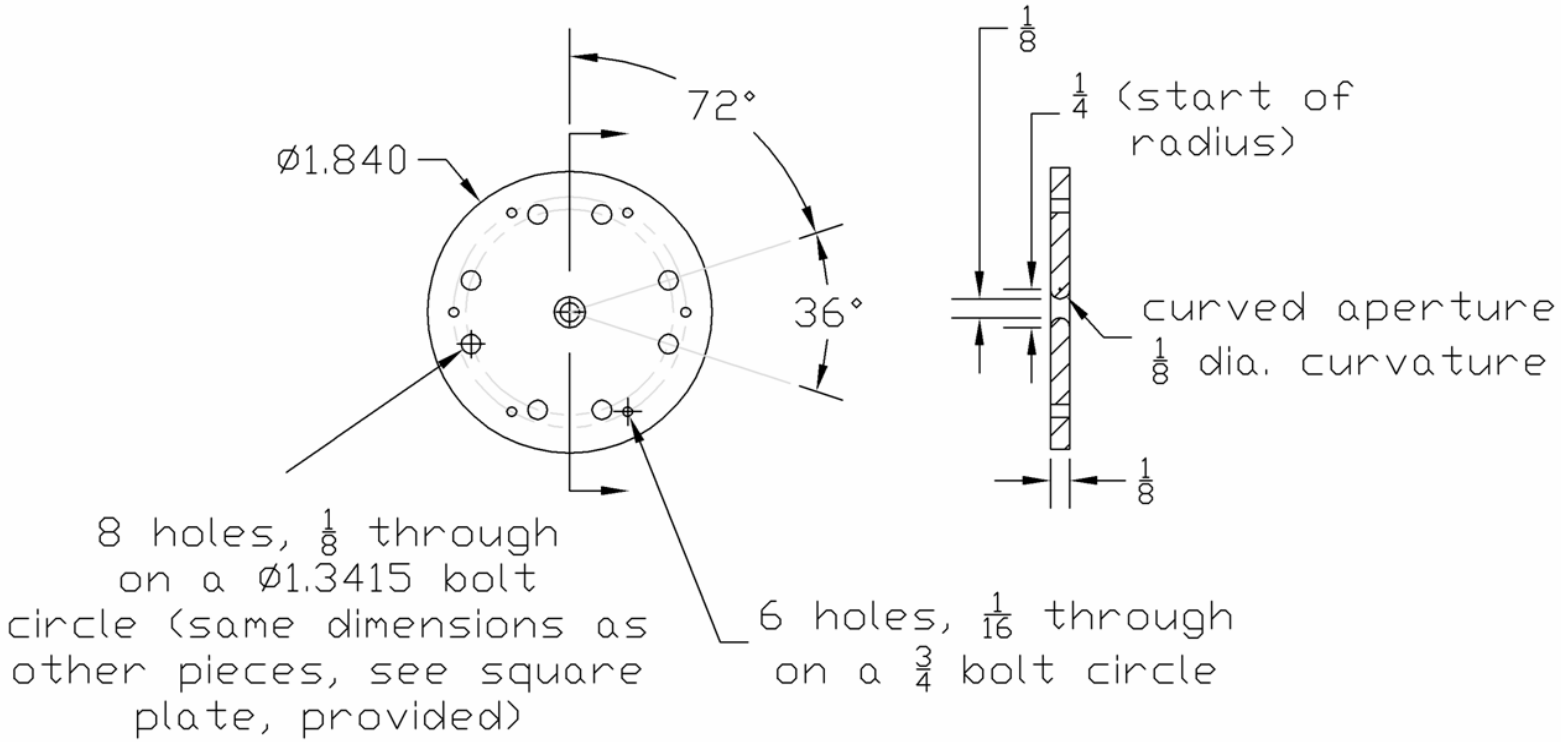

Quadrupole

Assembly Diagram

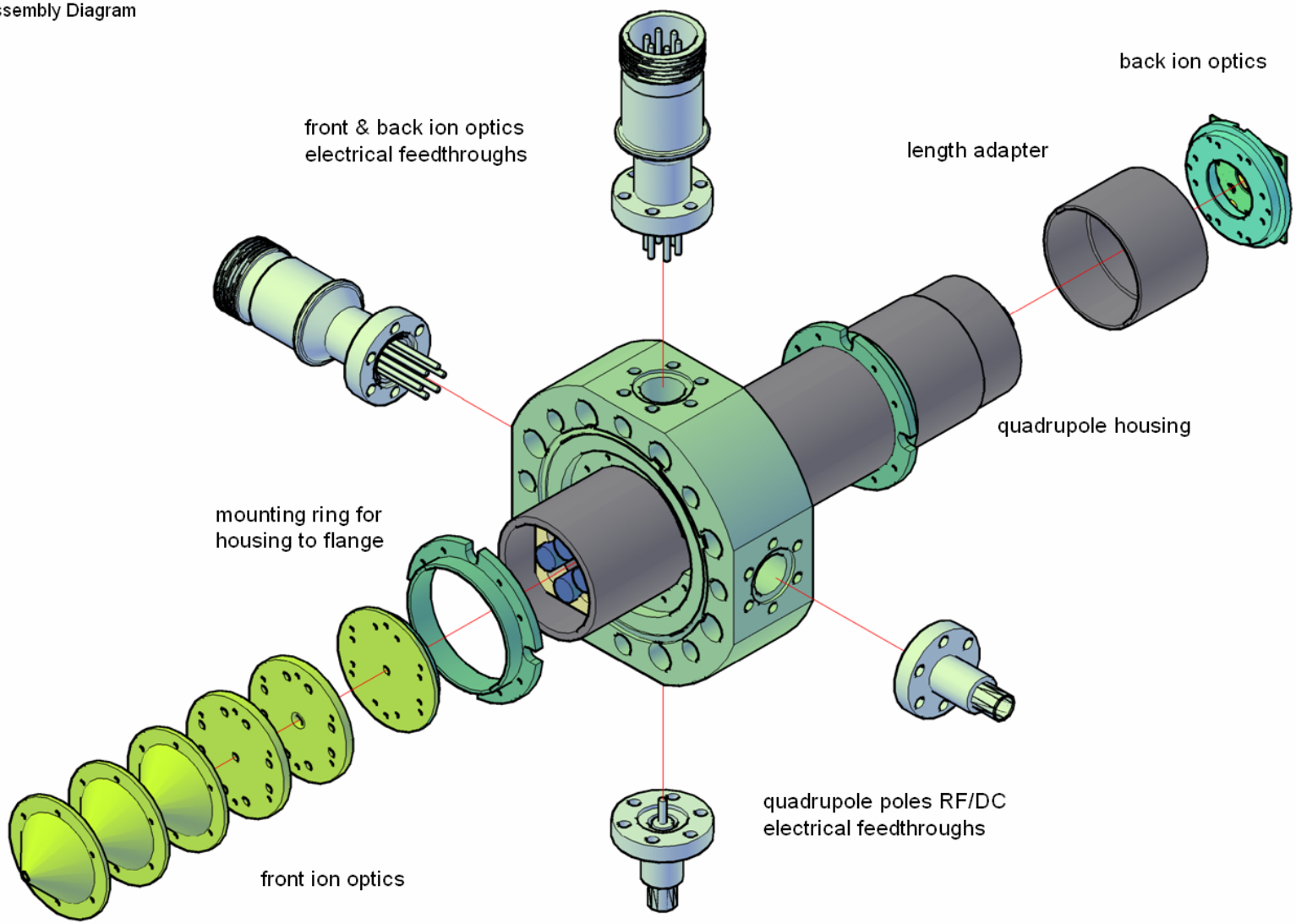

Quadrupole Vacuum Chamber

Modified 4 ½" Conflat 4-way Cross – weld additional 1 1/3" Conflat Half Nipple

stainless steel

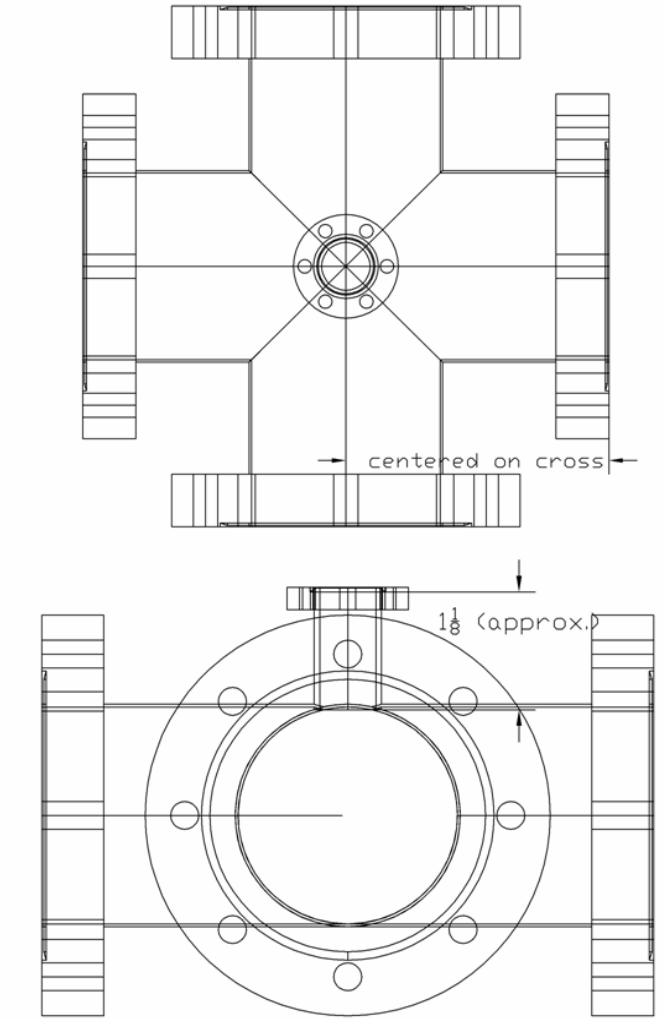

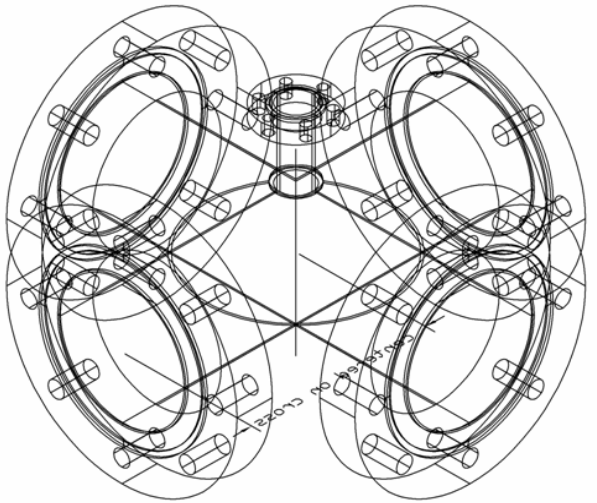

Quadrupole – Optional Leak Valve Adapter Flange

Modified 2 ¾" to 1 1/3" Zero Length Conflat Flange

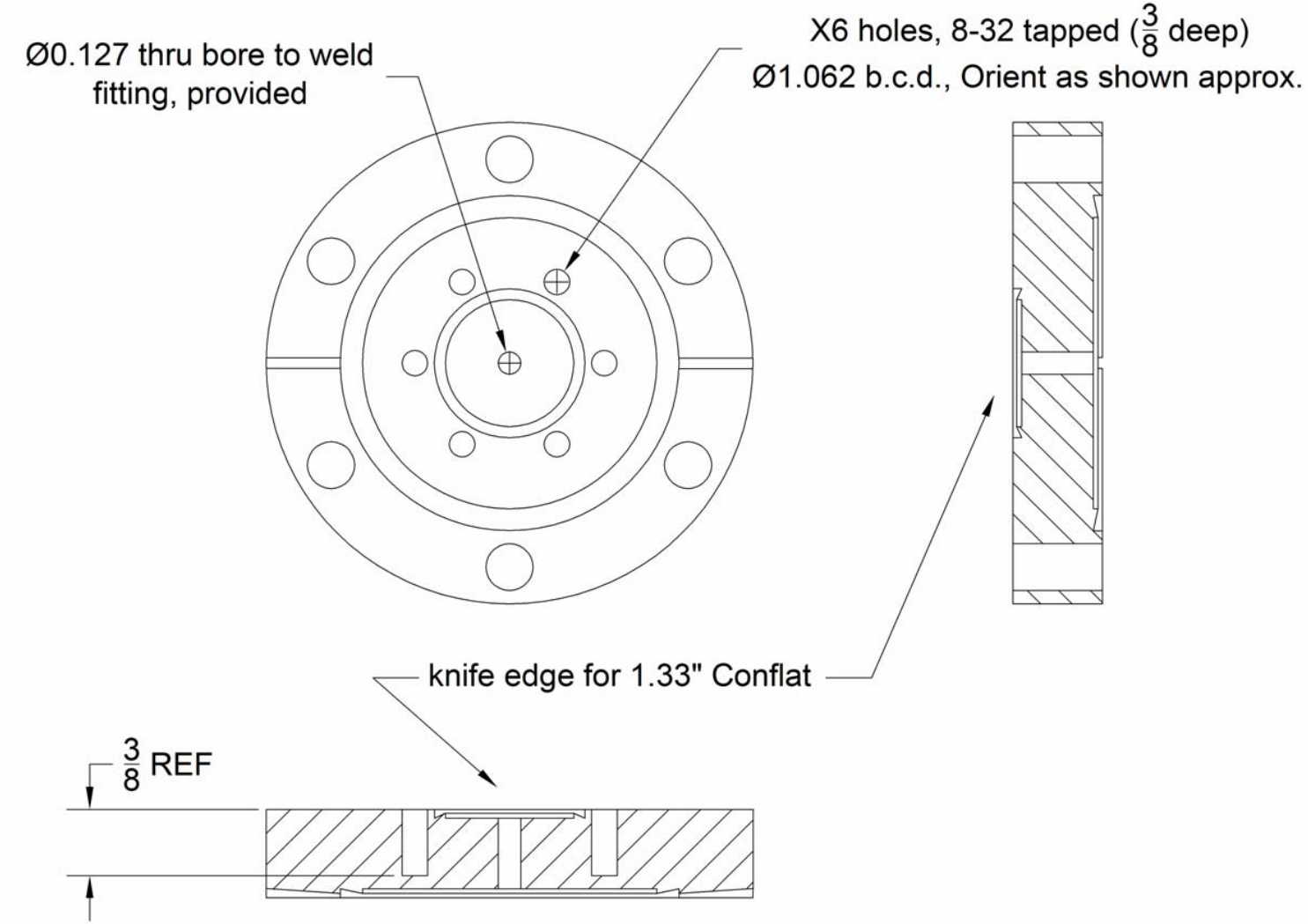

Quadrupole Mounting Flange

Custom Double Sided 4 ½" Conflat with x4 1 1/3" Conflat Ports for Electrical Feedthroughs stainless steel

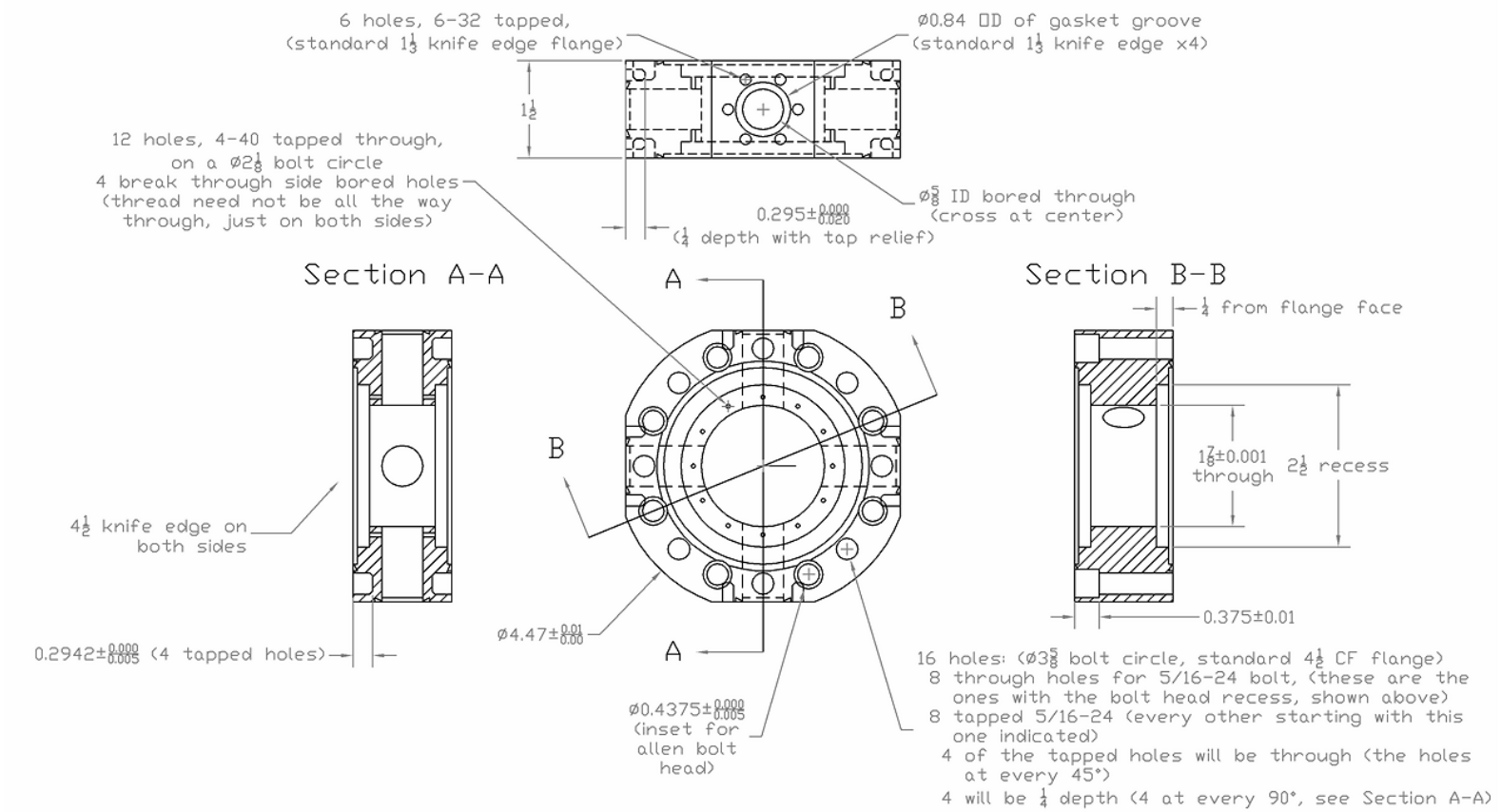

Quadrupole Mounting Ring

Housing to Flange Mounting Ring

stainless steel

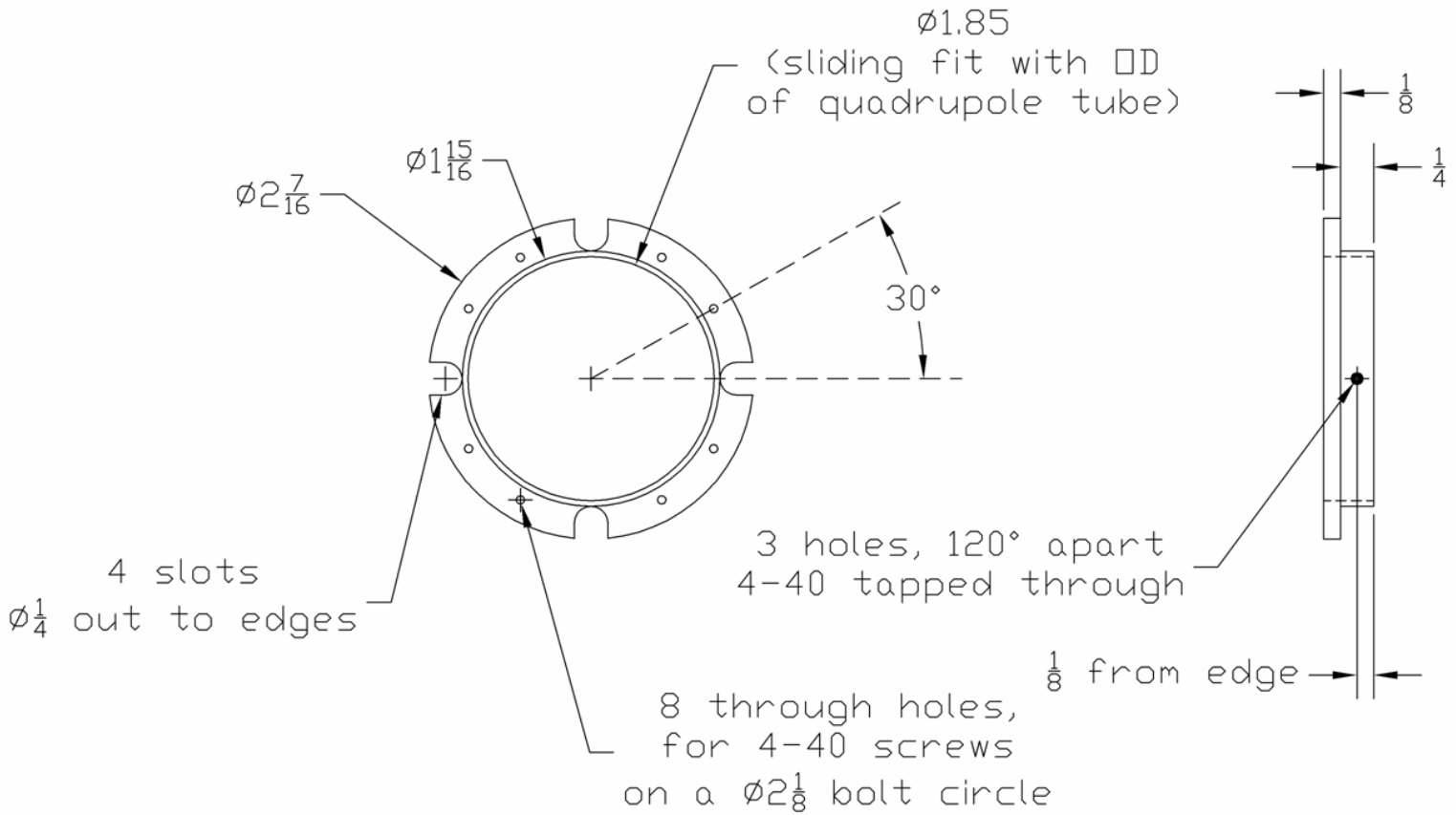

Quadrupole Back Adapter

Adapter Piece to Mount Exit Ion Optics & Correct for Length

stainless steel

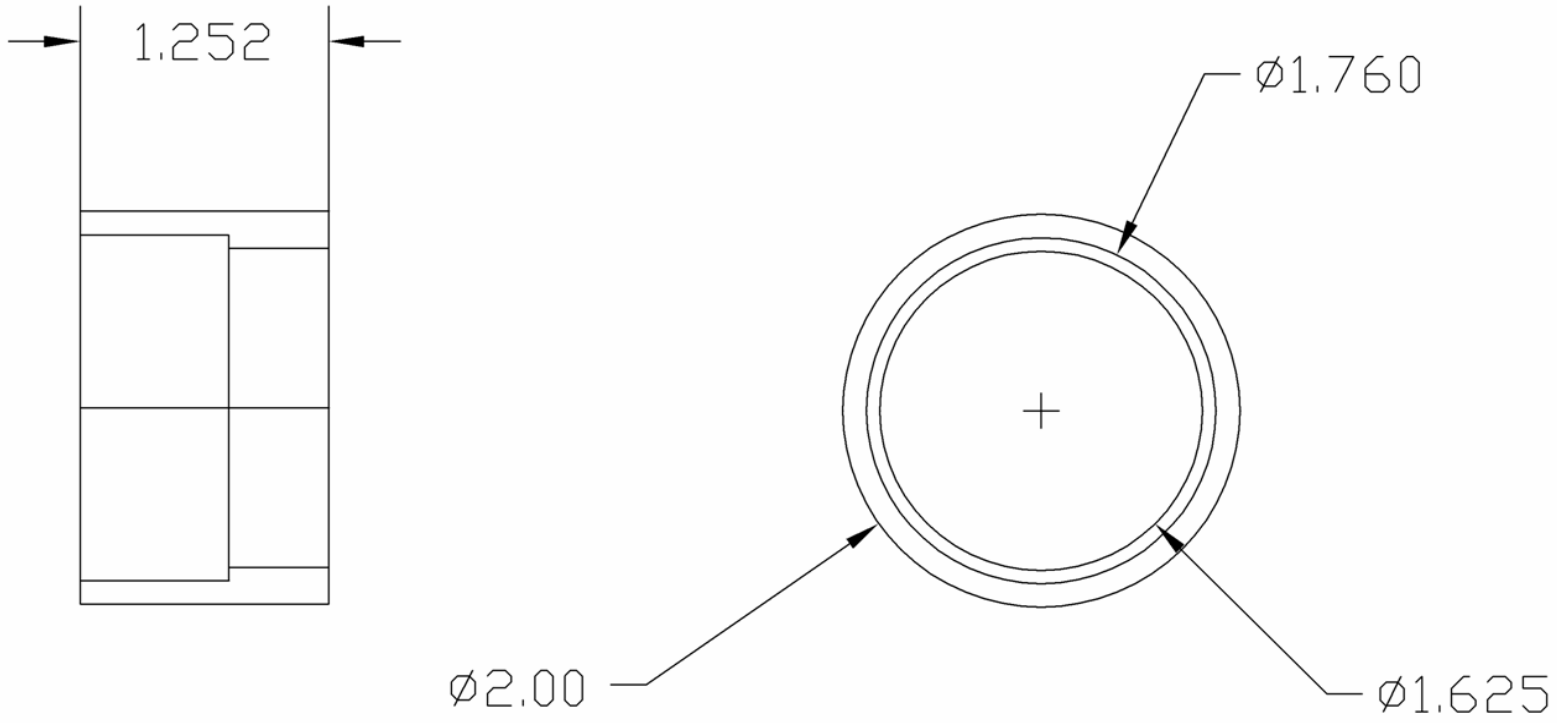

Quadrupole Front and Back Ring Caps

Encap Rings for Mounting Entrance & Exit Ion Lenses

stainless steel

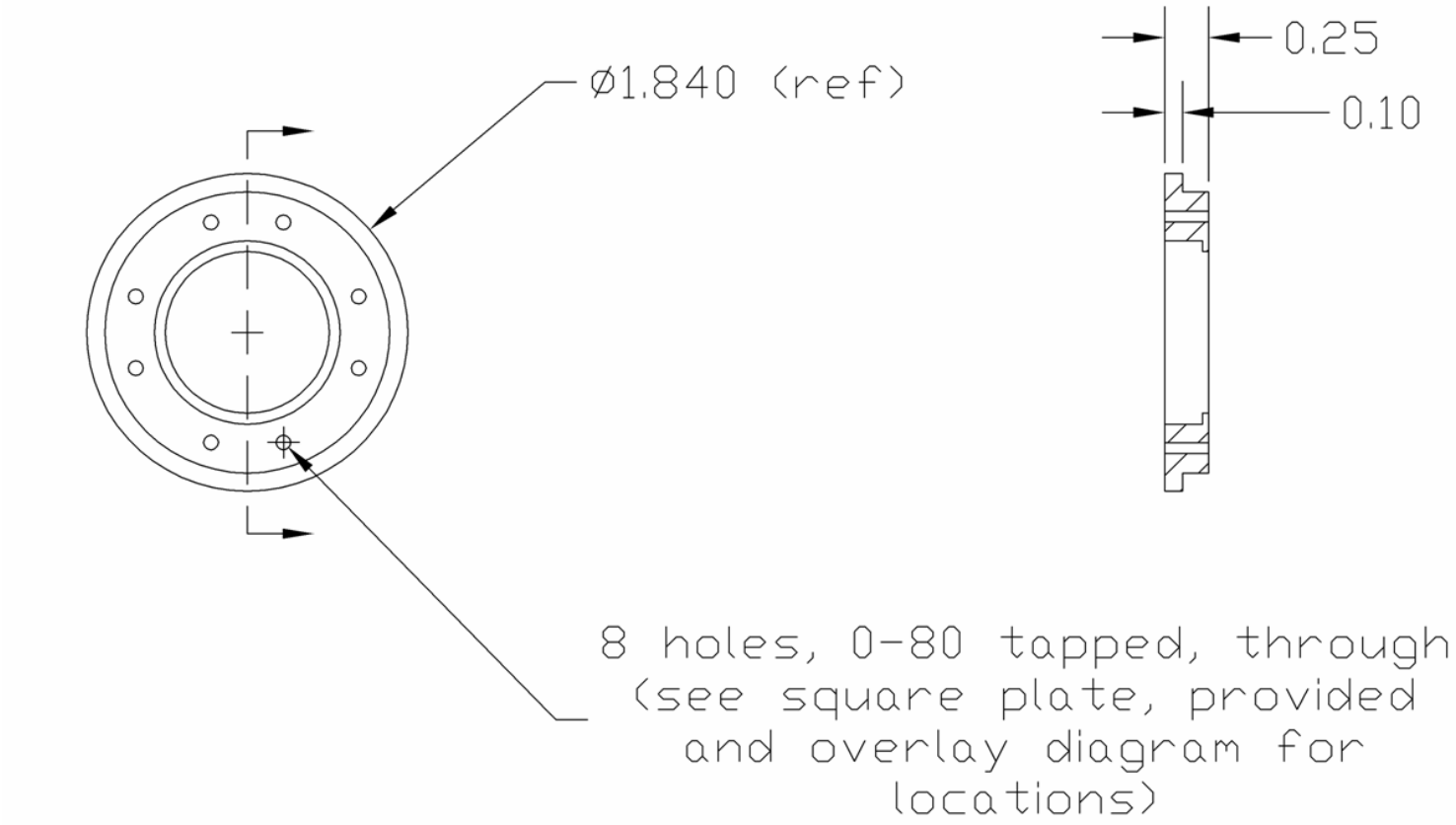

Quadrupole Exit Lens

Assembly Diagram

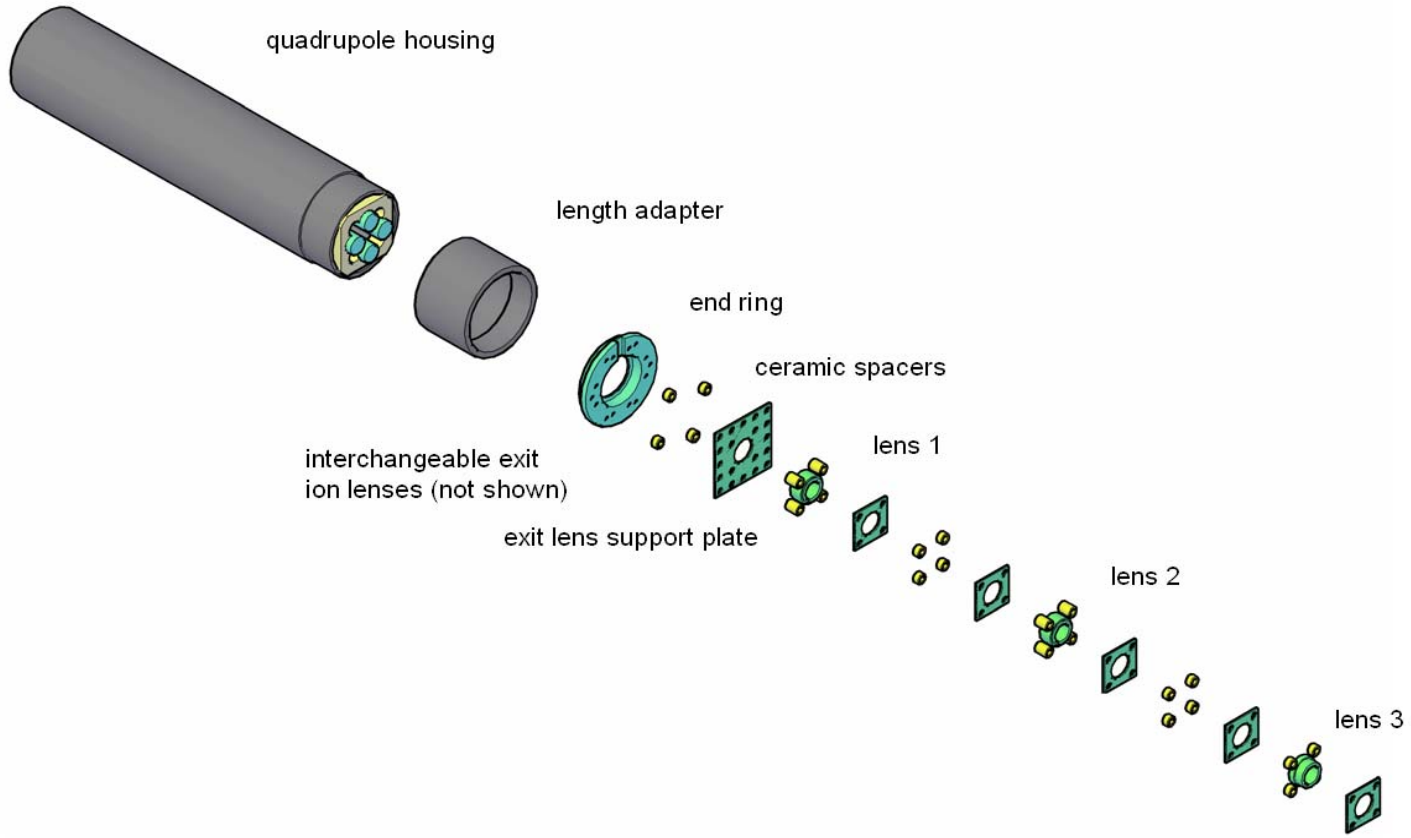

Quadrupole Exit Lens Elements

Barrel Lenses Built up from Component eV Parts®

stainless steel

NOT TO SCALE

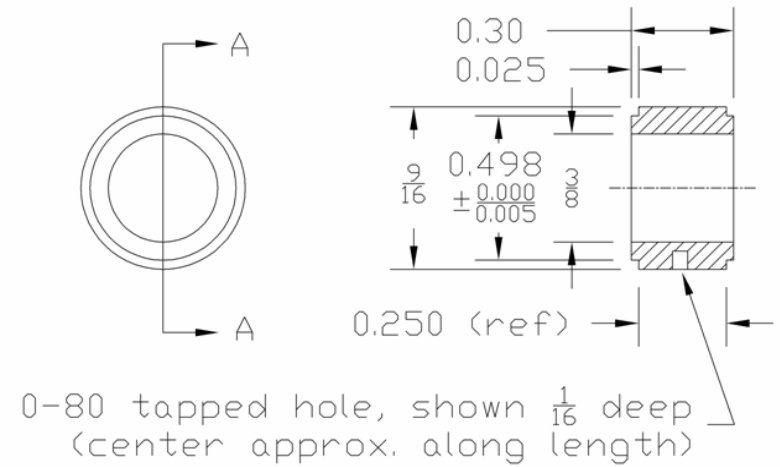

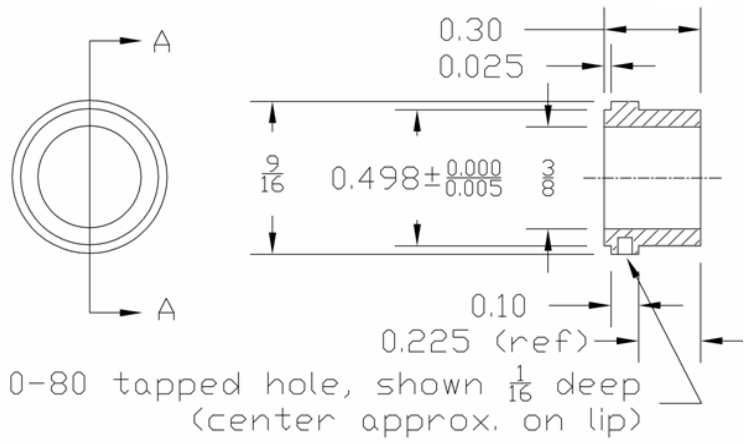

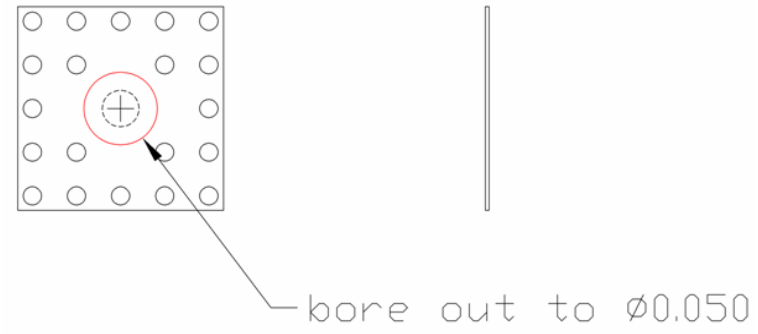

Ion Mobility Spectrometer (IMS) Entrance Lens & Ion Gate

Assembly Diagram

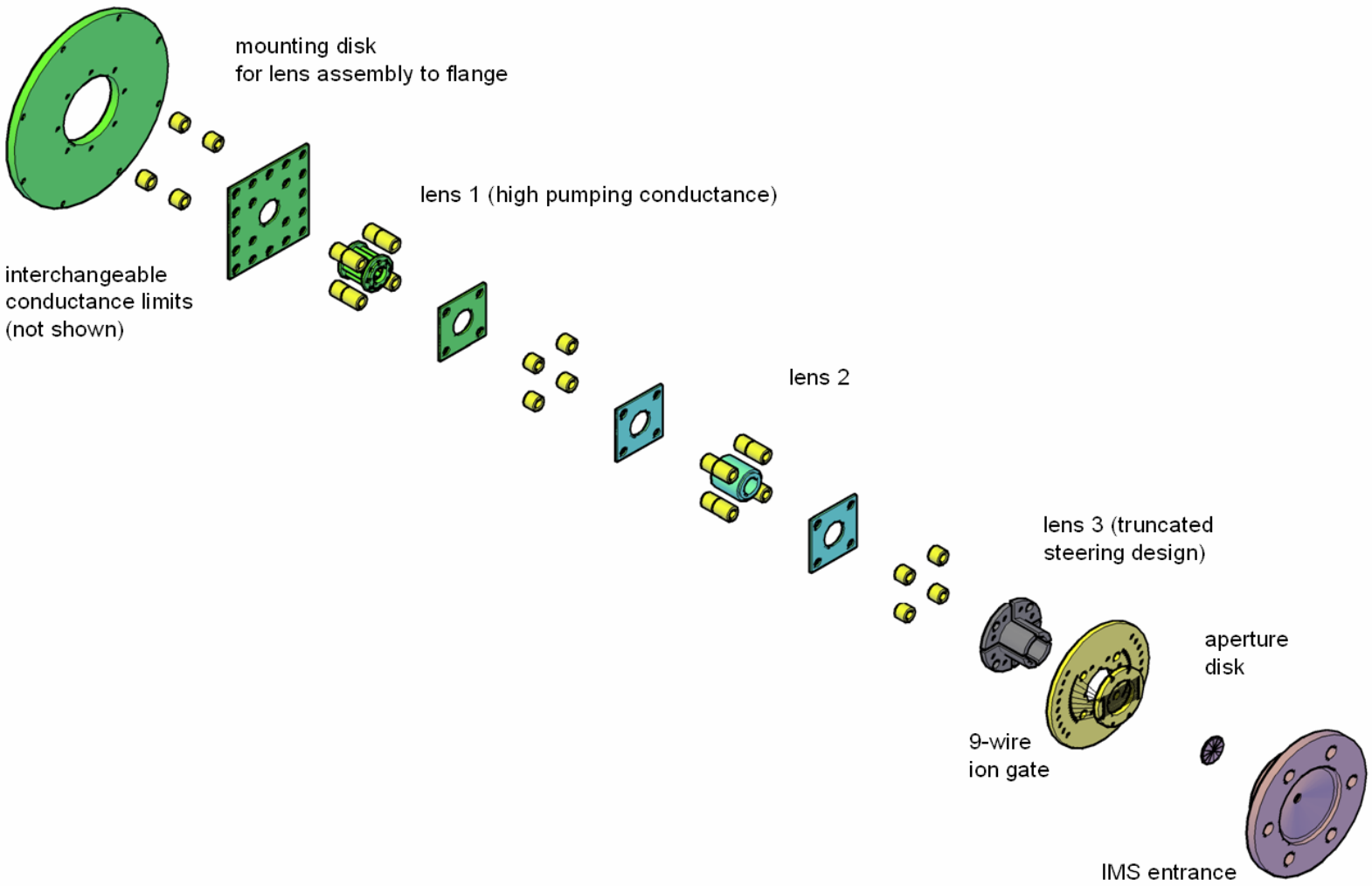

IMS Support Flange for Cryogenic Chamber & Front Ion Optics

Modified 6" to 4 ½" Zero Length Conflat Flange

stainless steel

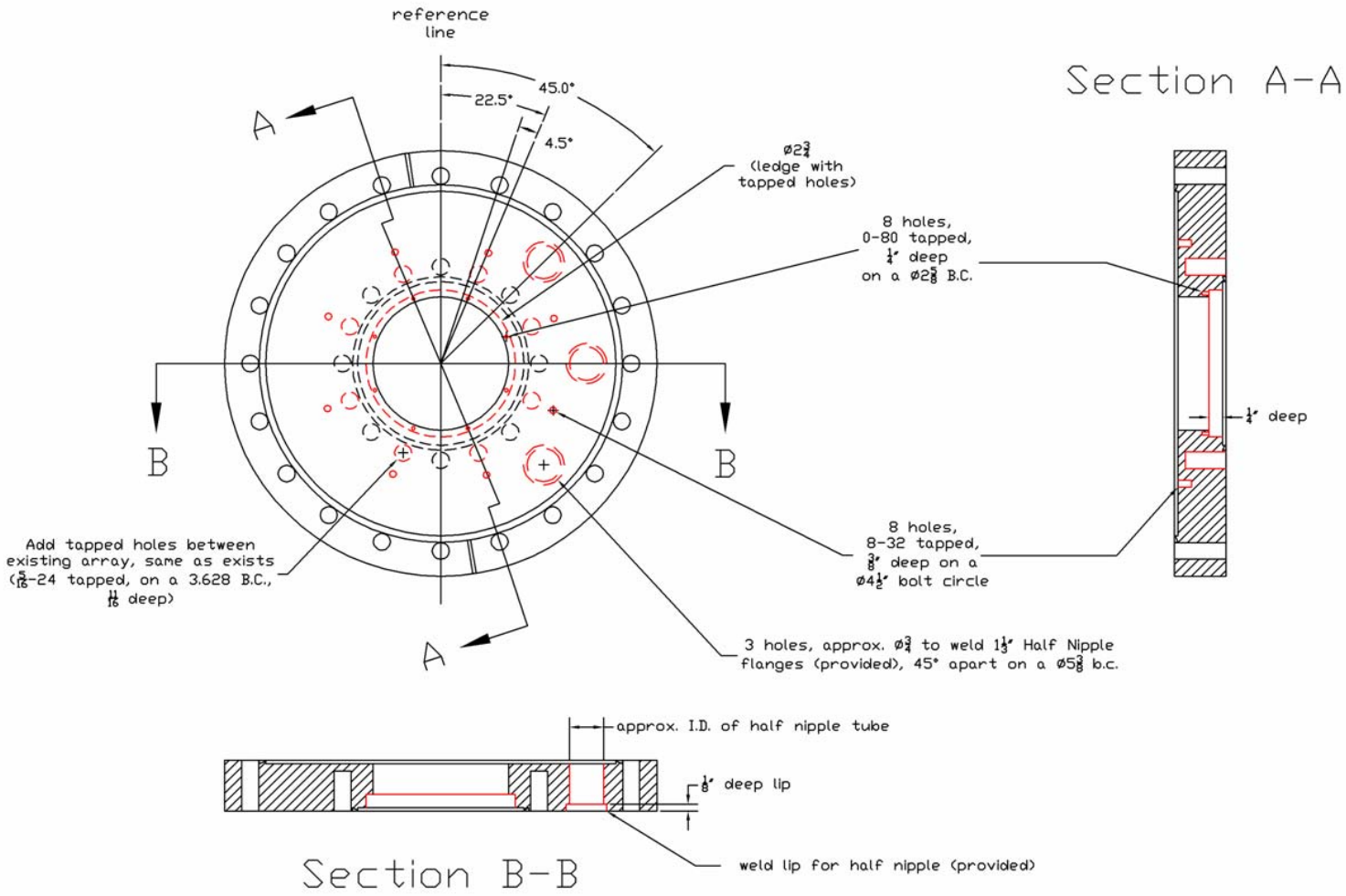

IMS Entrance Lens & 1st Conductance Limit Mounting Disk

Adapted to Component eV Parts®

stainless steel

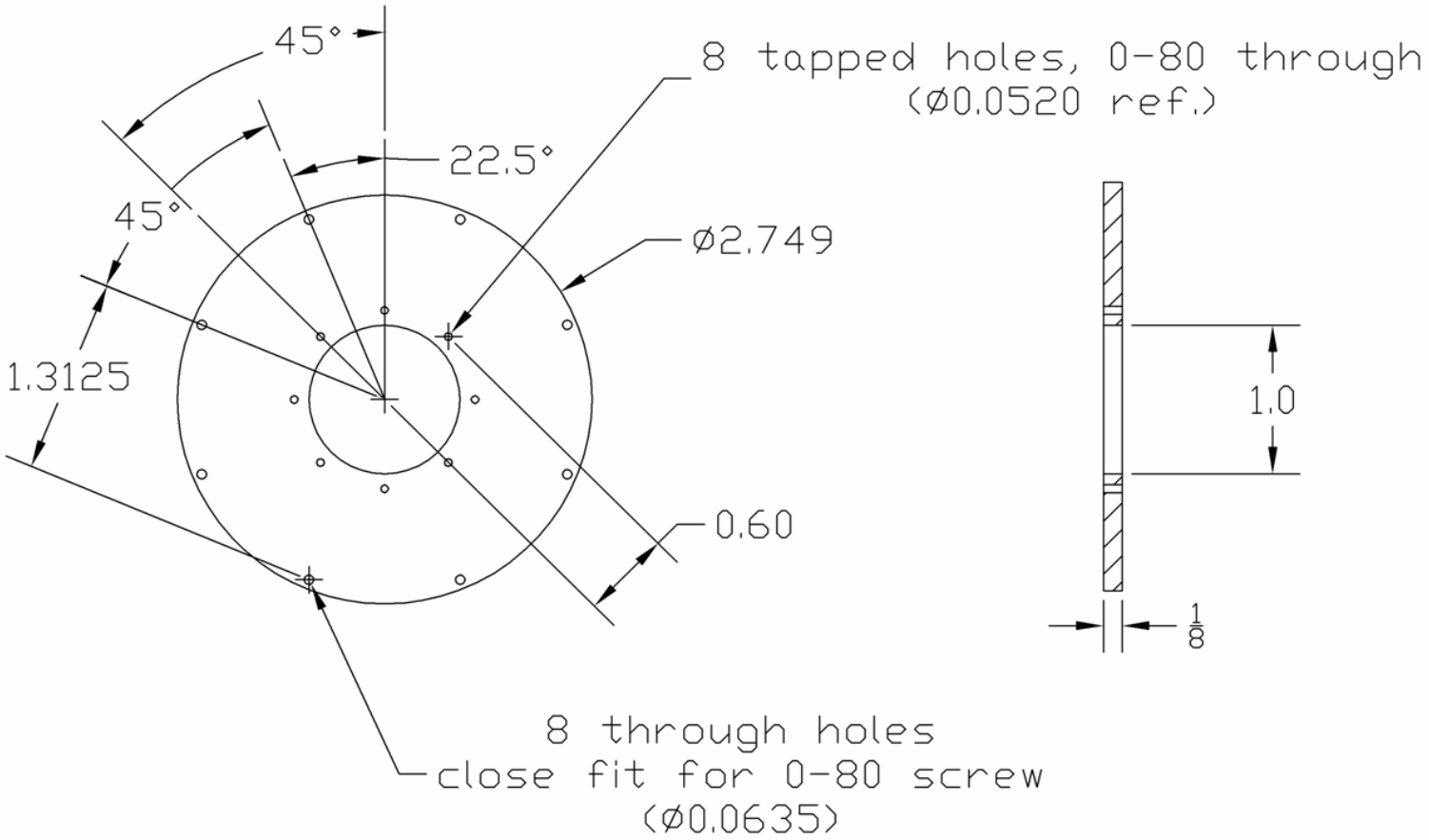

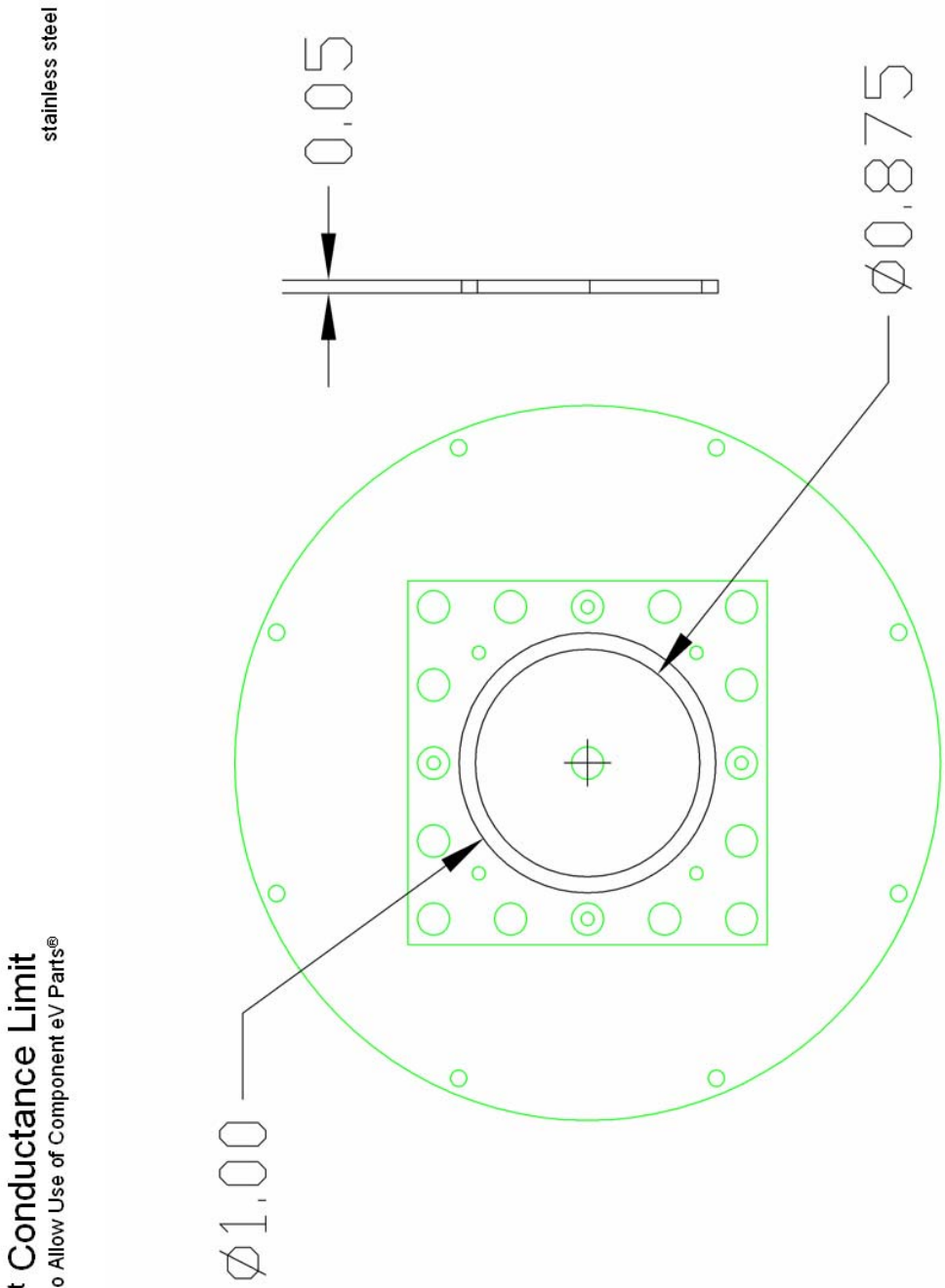
IMS 1st Conductance Limit
Ring Piece to Allow Use of Component eV Parts®
stainless steel
0.05
Ø0.875
Ø1.00

IMS Entrance Lens Pieces

Lenses Built up from Component eV Parts®

stainless steel

NOT TO SCALE

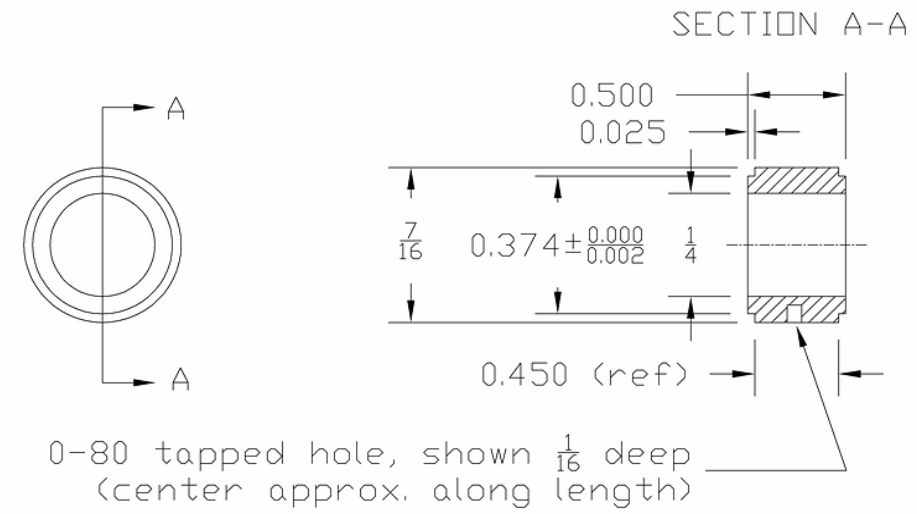

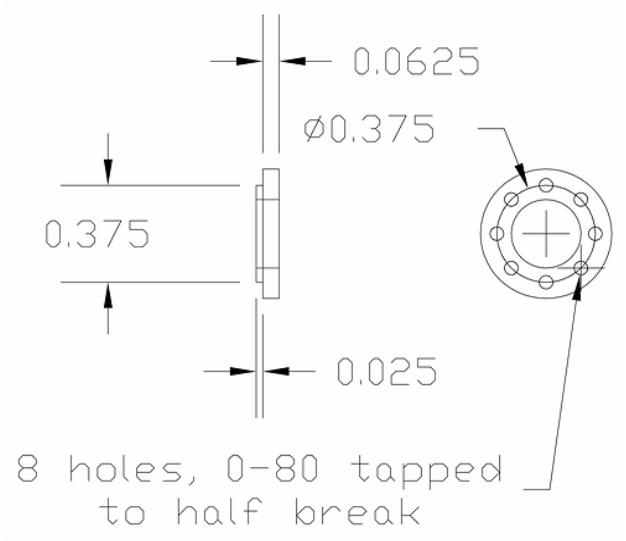

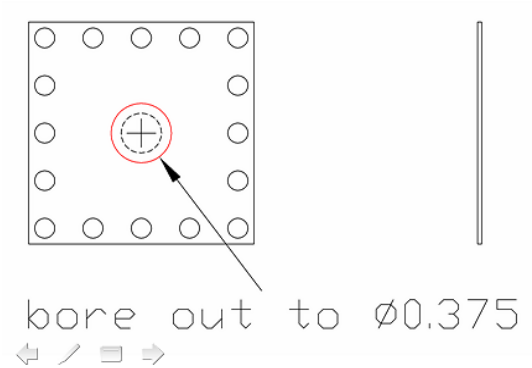

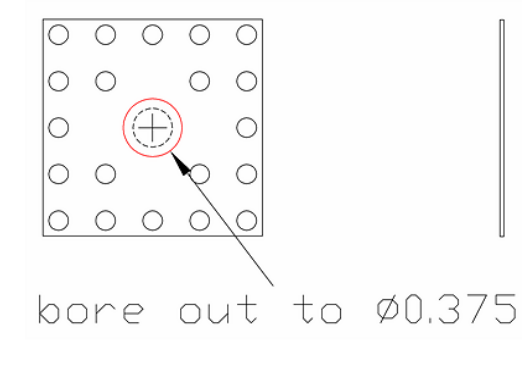

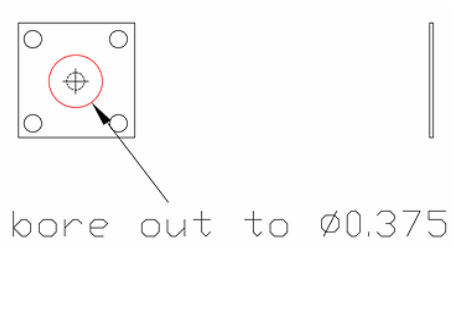

IMS Entrance 3rd Lens – Truncated Steering Electrodes

Attaches to Lens Assembly & Supports the Ion Gate

stainless steel

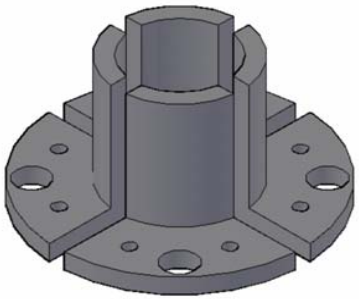

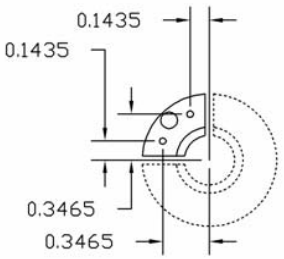

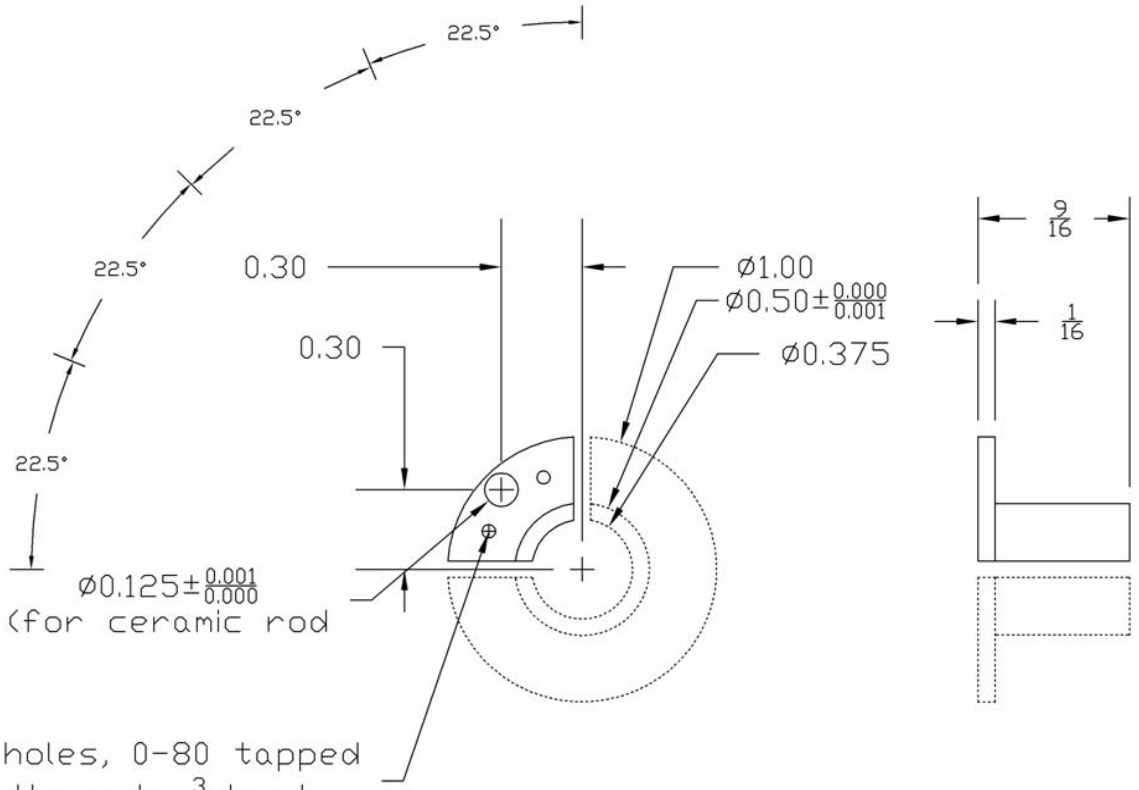

IMS Interleaved Wire Ion Gate Tension Disk

Anchors Tension to the Tungsten Wires

polyetheretherketone (PEEK)

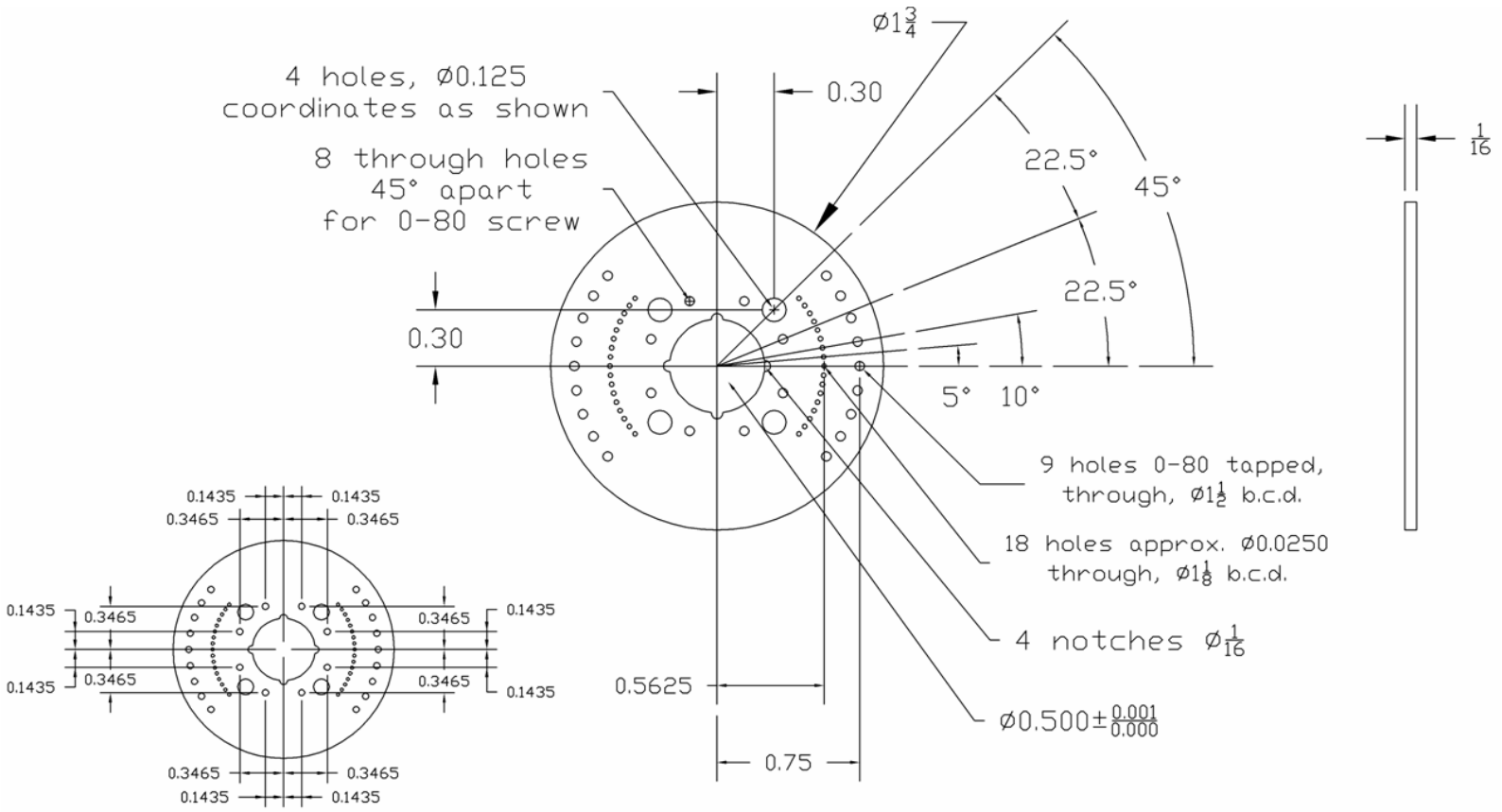

IMS Interleaved Wire Ion Gate Primary Support Disk

Weaves the Tungsten Wire Potential Gating Grid

polyetheretherketone (PEEK)

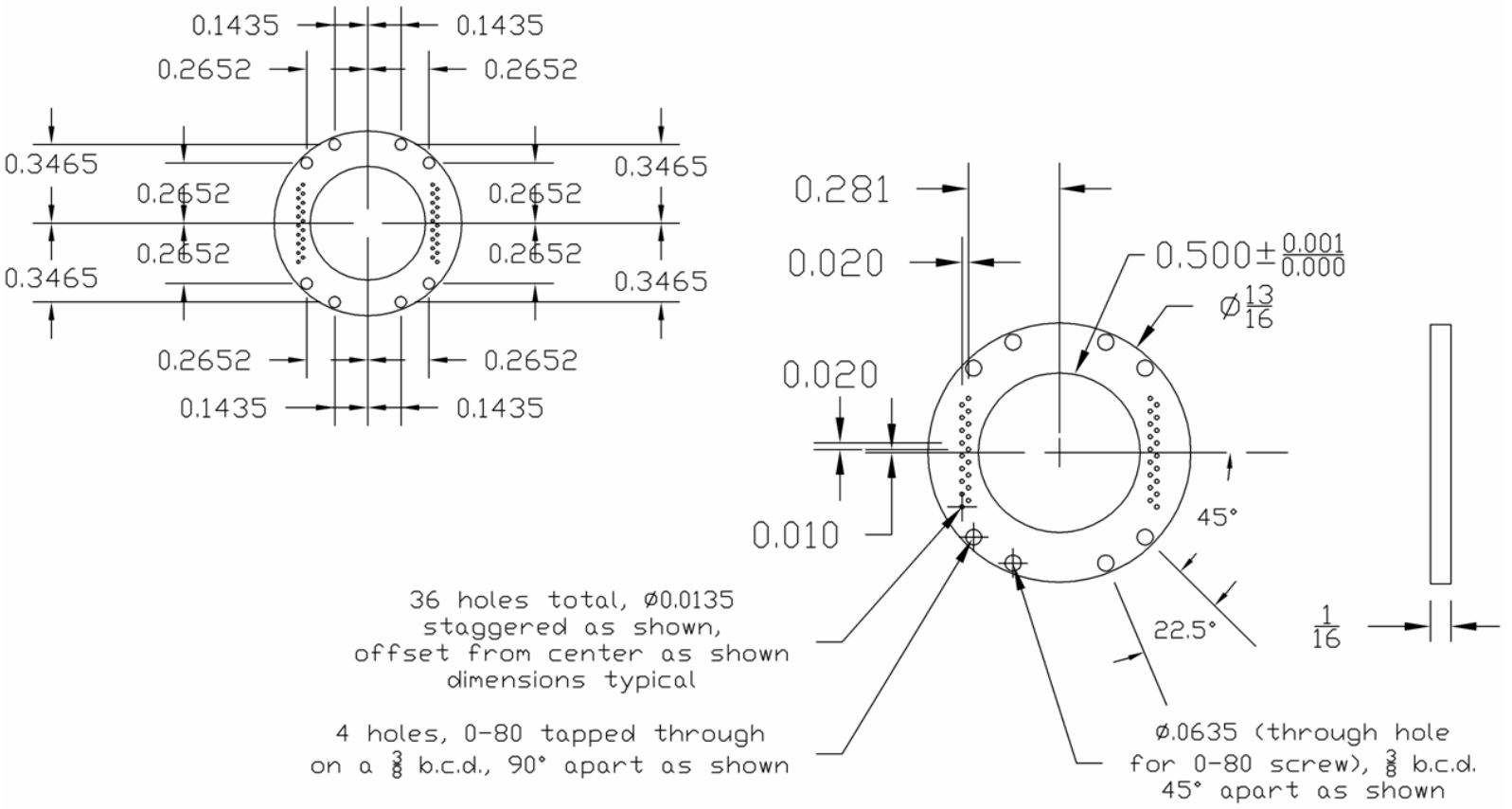

IMS Cryogenic Dewar System

Assembly Diagram

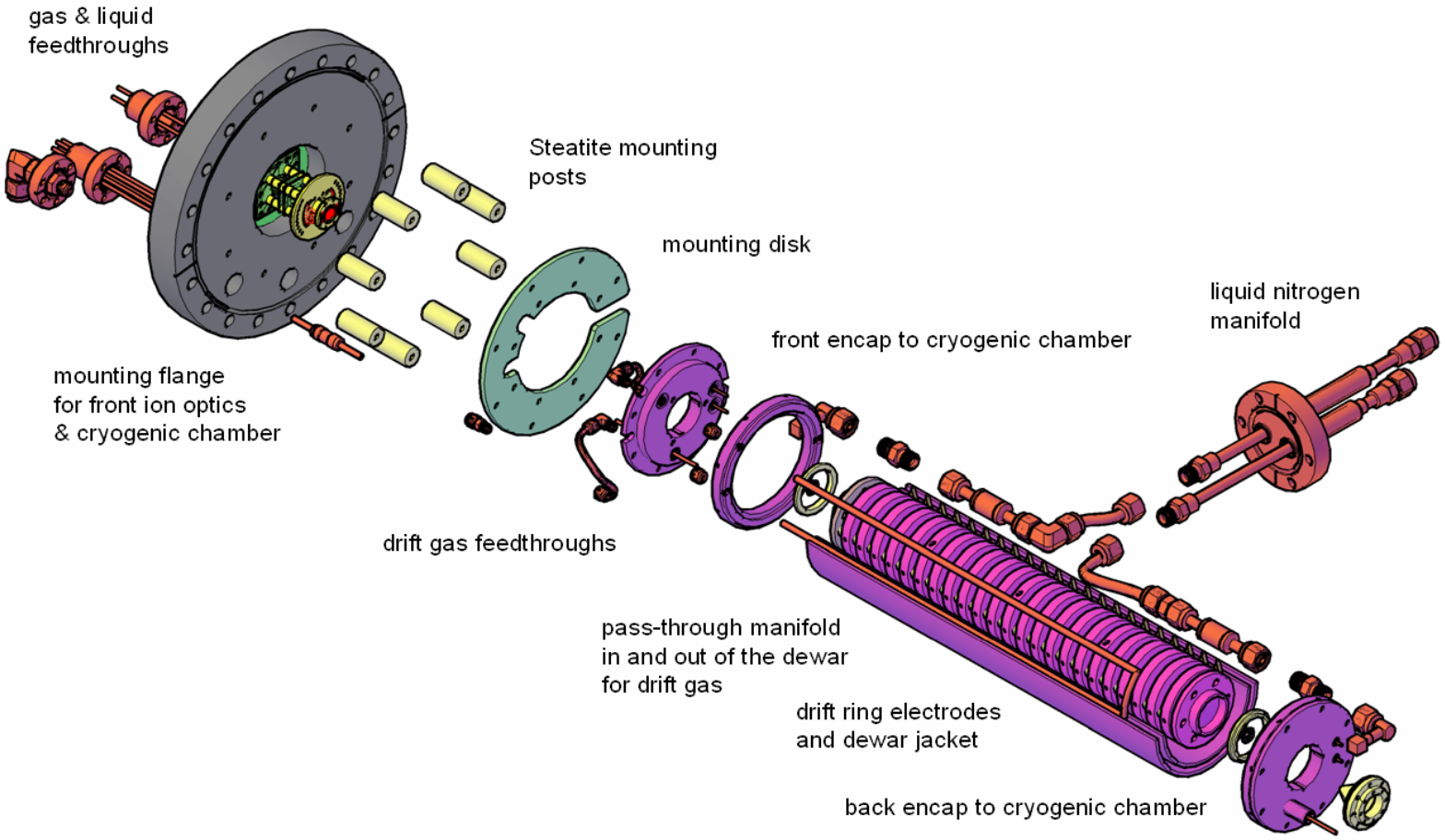

IMS Drift Gas Feedthrough

Welded Components

stainless steel

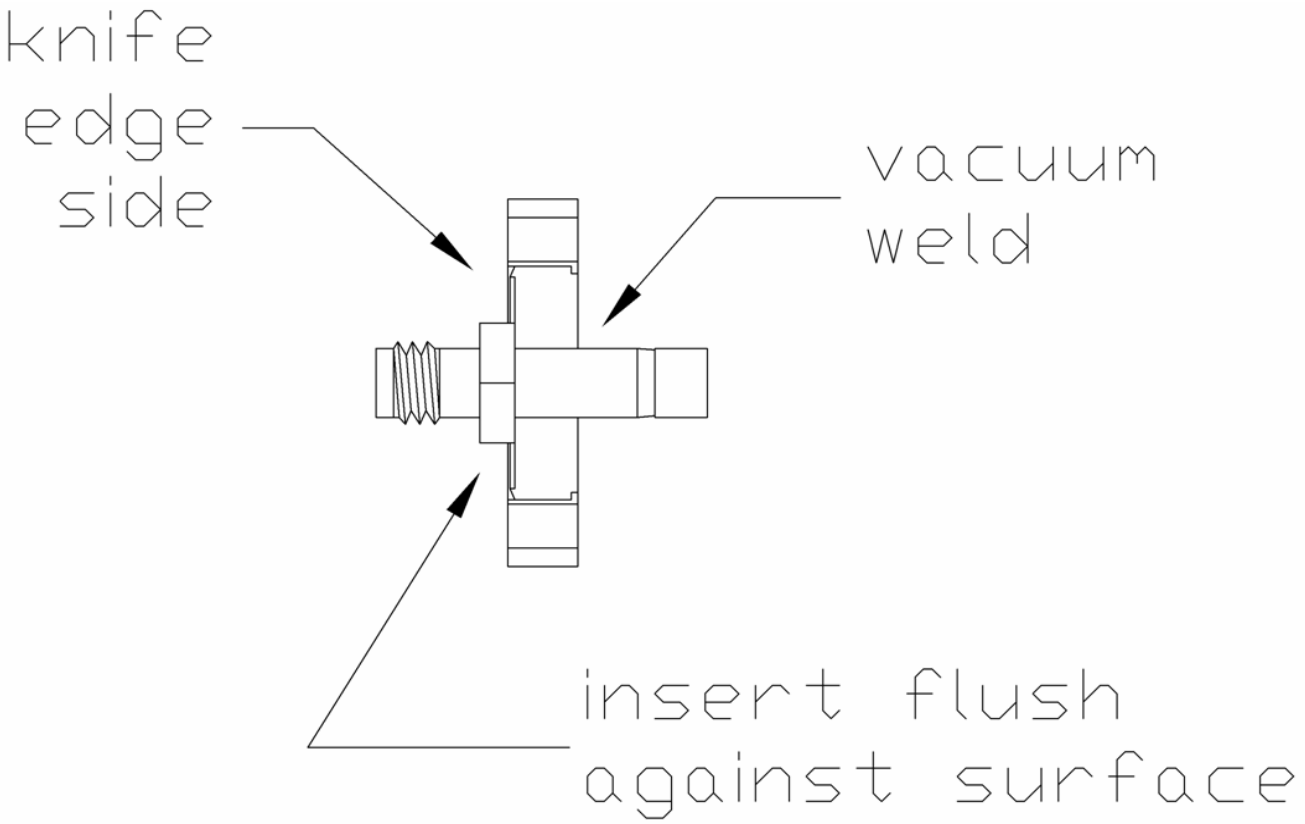

IMS Cryogenic Chamber Mounting Ring

Slotted to Accommodate Gas and Liquid Feedthroughs

stainless steel

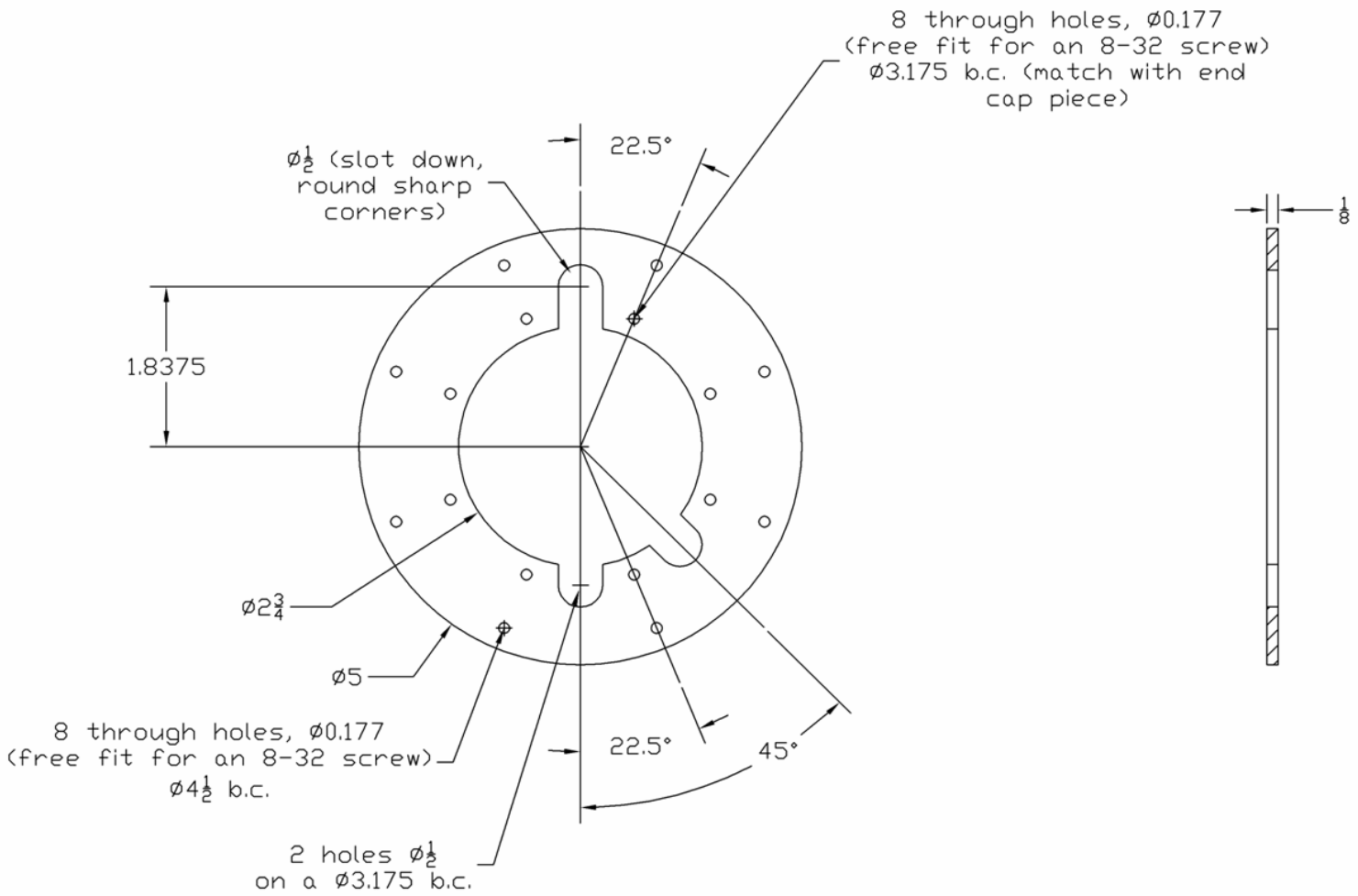

IMS Entrance Electrode

Deceleration Cup & Aperture Support

stainless steel

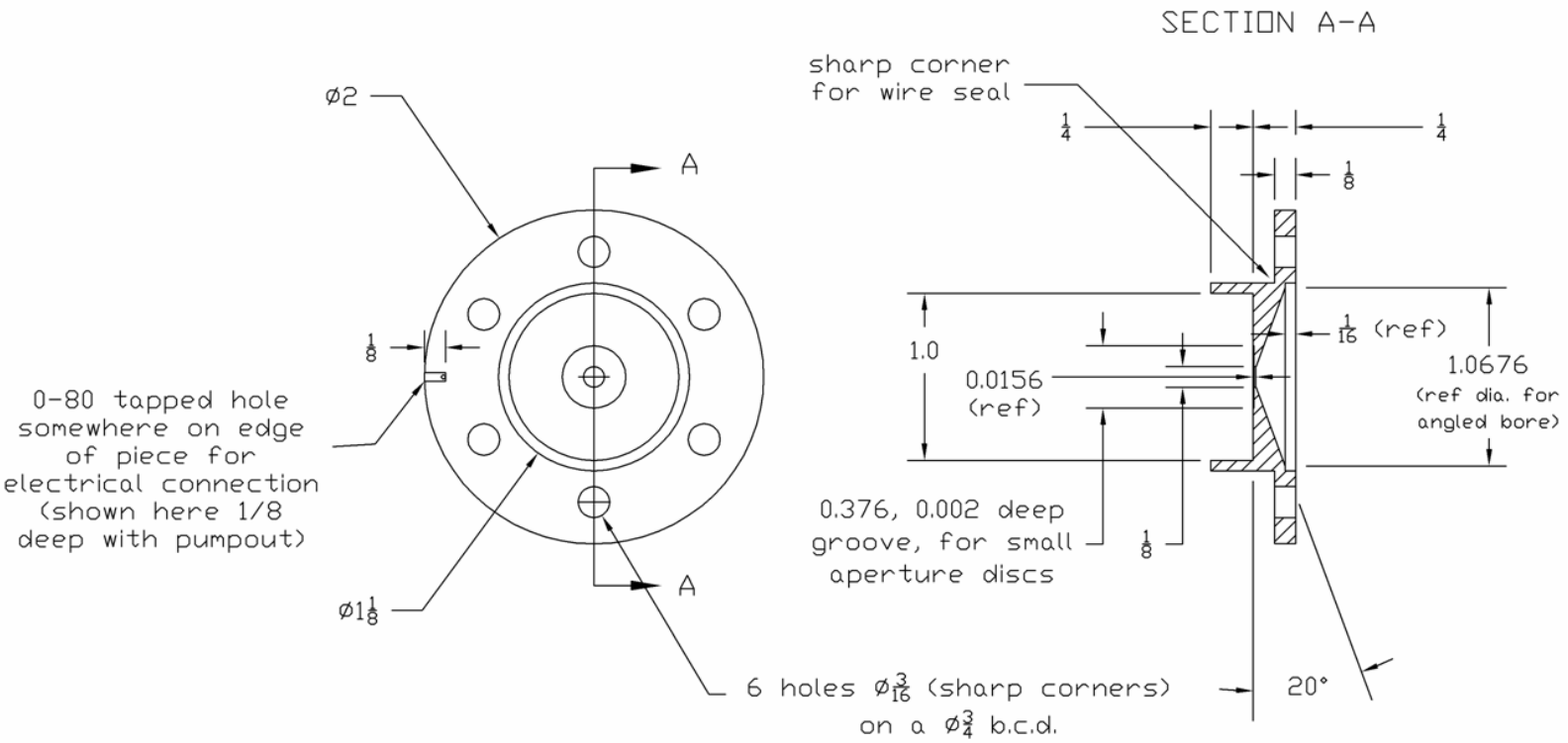

IMS End Electrode Seal & Isolation Ring

Rigid Dielectric Ring to Sandwich Wire Seal and Enables Voltage and Thermal Isolation

polyimide (Vespel®)

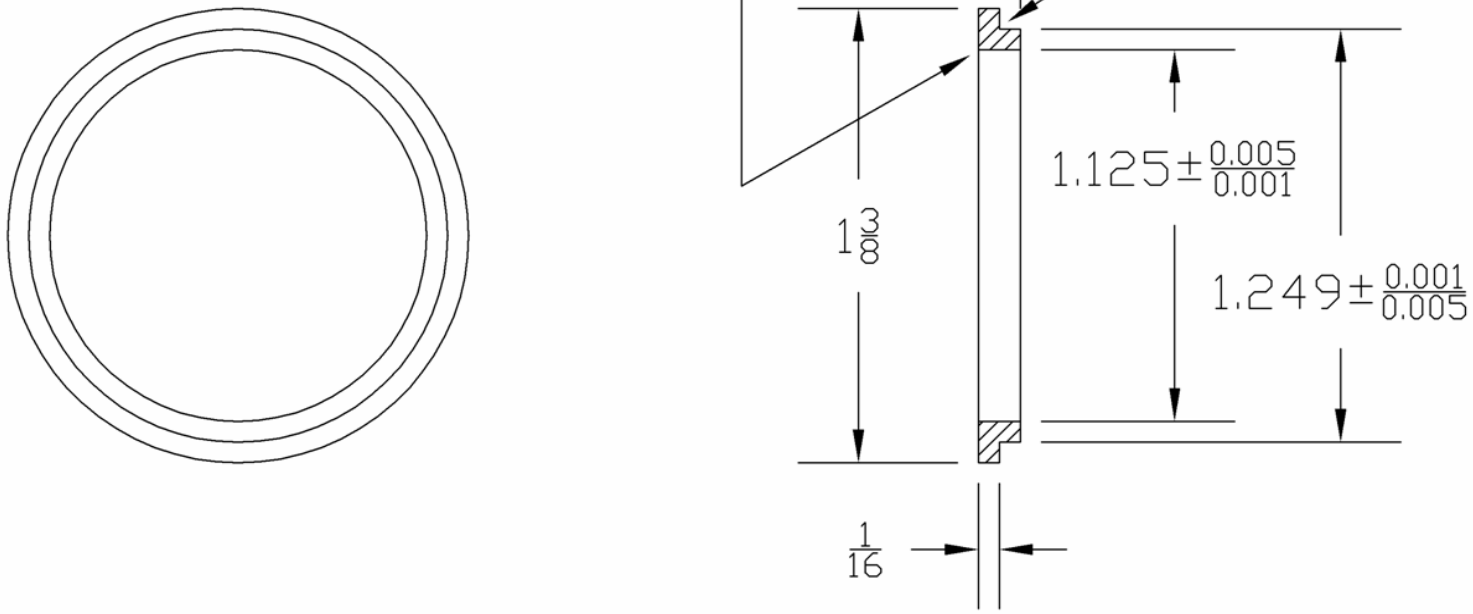

IMS Drift Ring – Uniform Field Design

Insulating Ball Spacer Stacked Ring Design – Large ID For Uniform Field

stainless steel

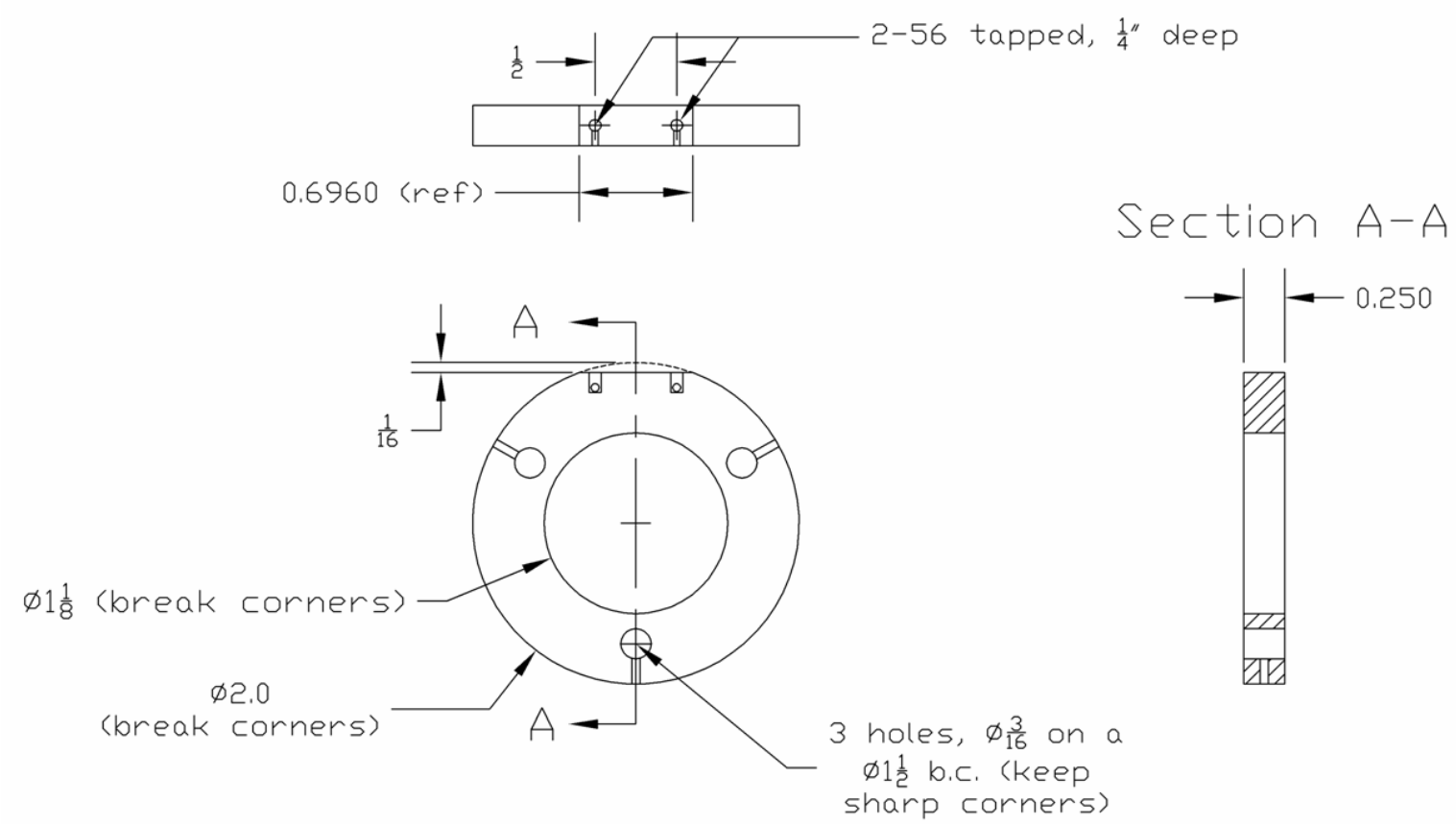

IMS Drift Ring – Double Density Spacer Design

Extra Spacer Seating Holes to Stagger Force Exerted on Stacked Ring Assembly

stainless steel

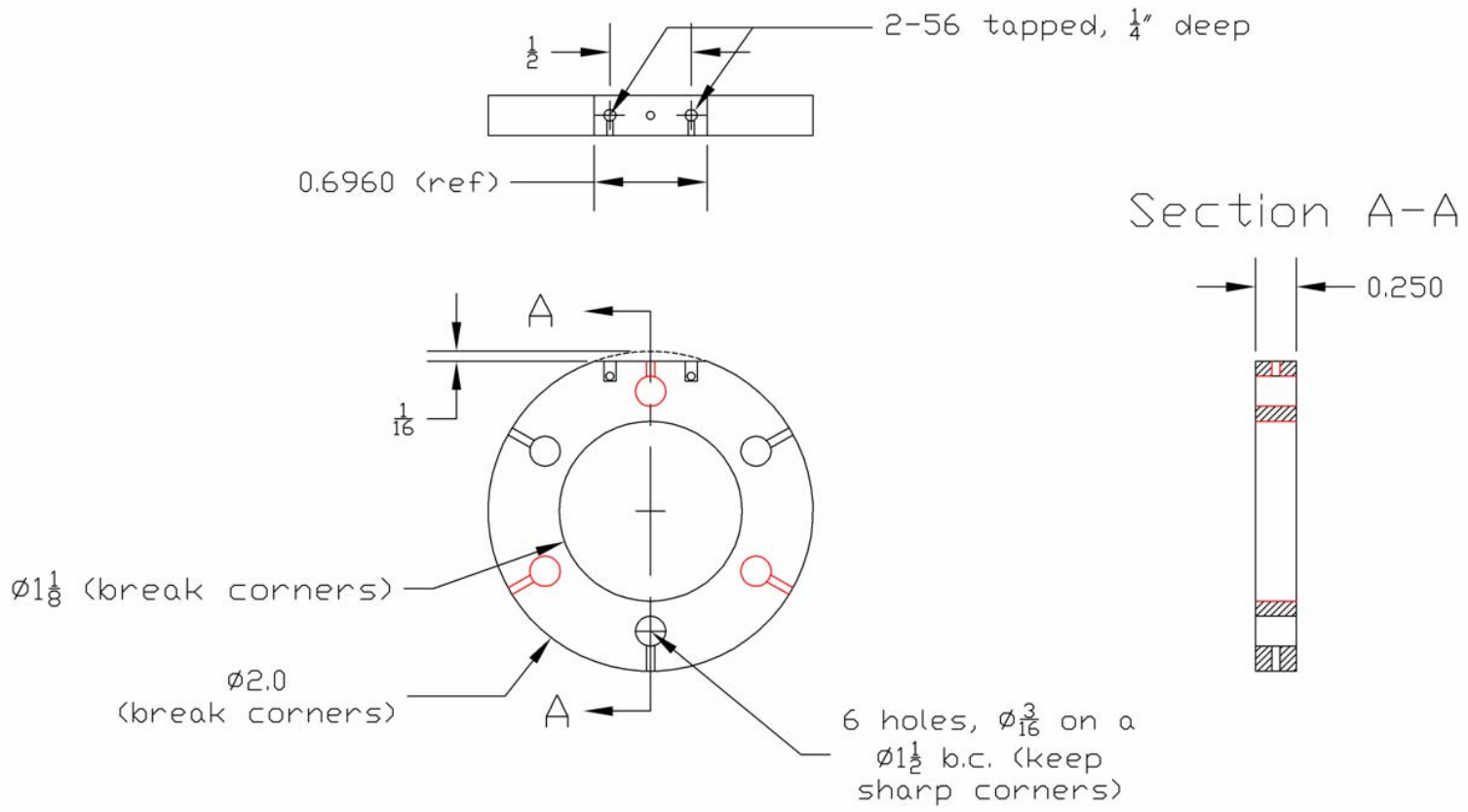

IMS Drift Ring – Radial Support Design

Radial Supports to Minimize "Sagging" Of Drift Cell After Numerous Temperature Cycling

stainless steel

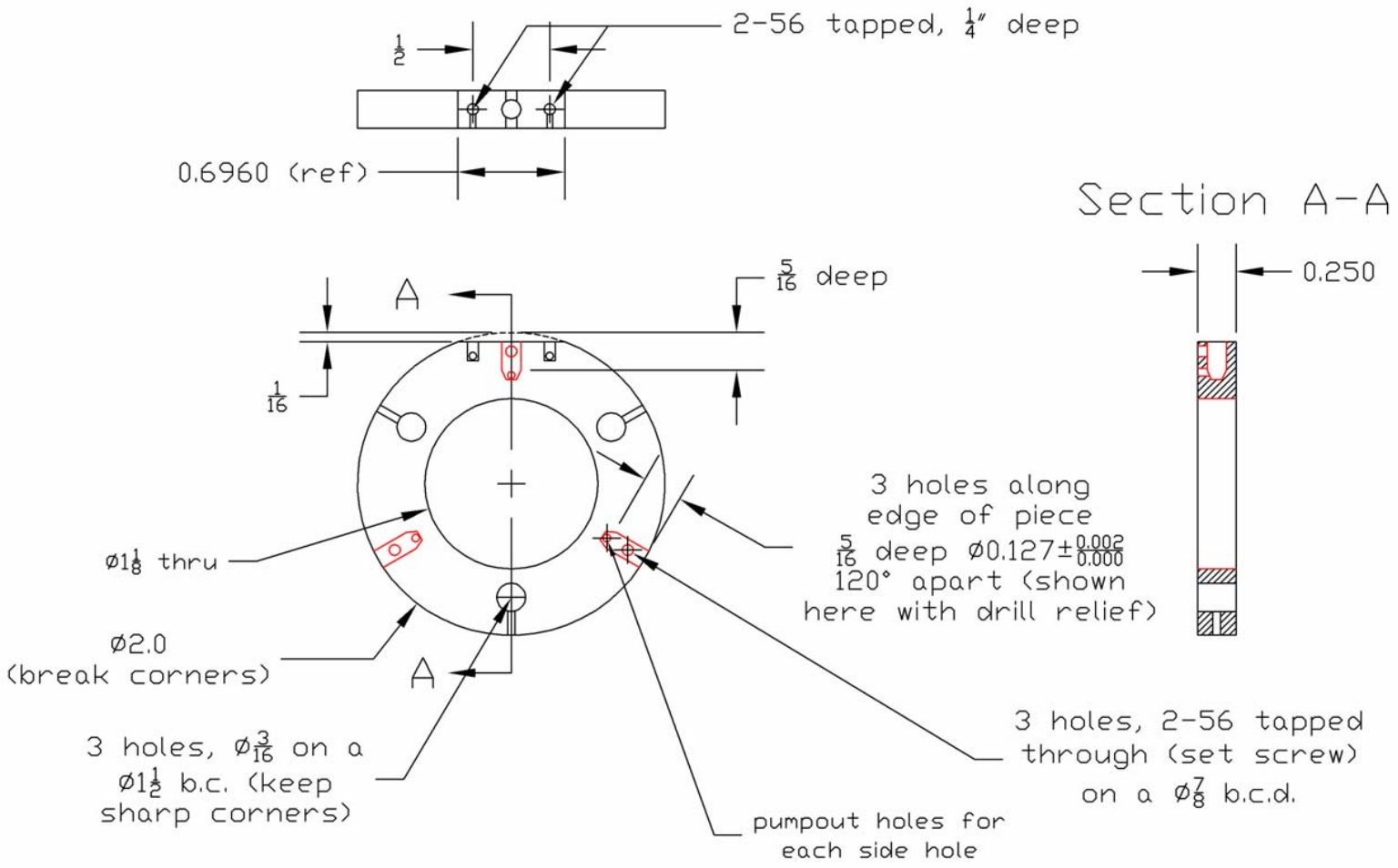

IMS Exit Electrode

Beam Shielding & Aperture Support

stainless steel

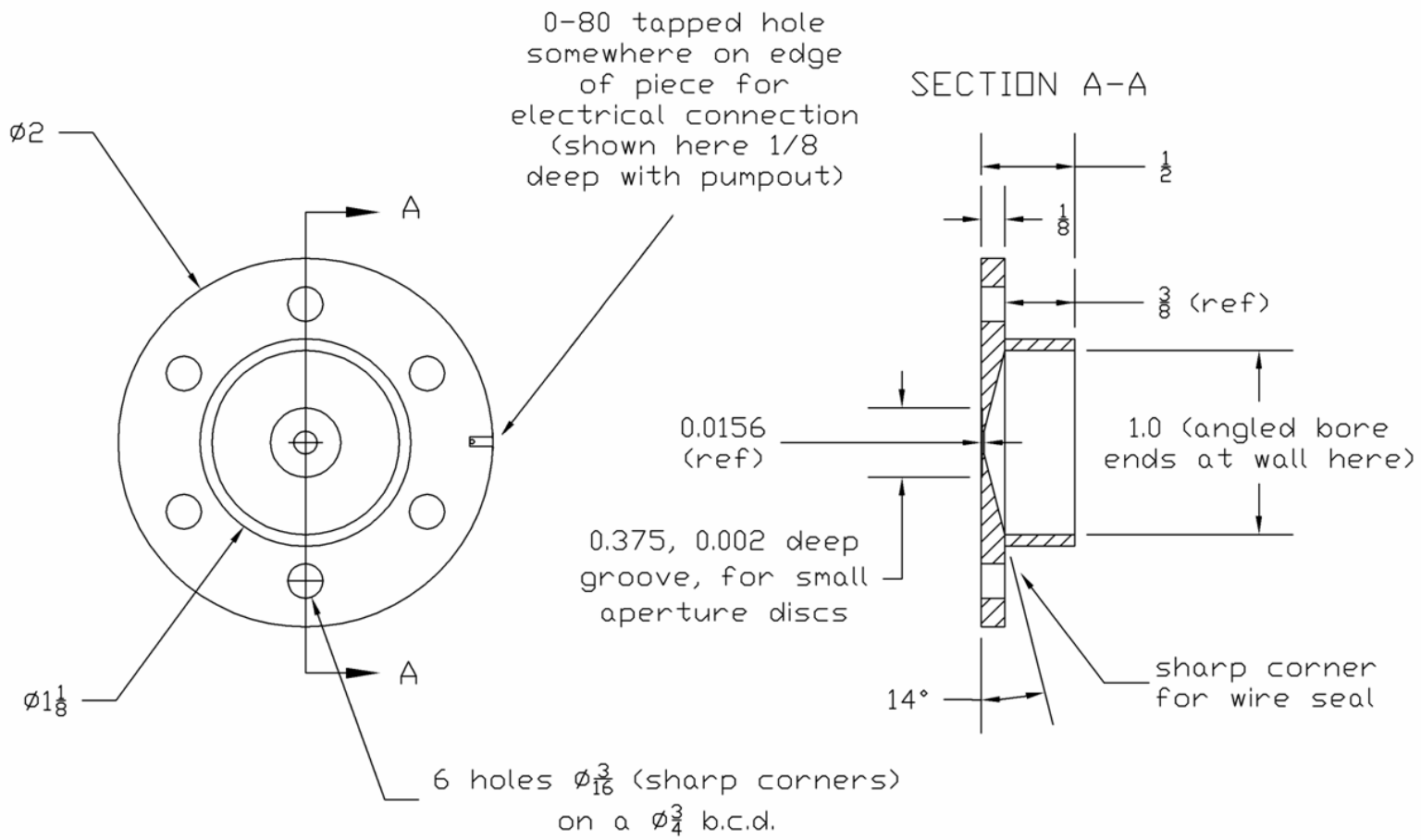

IMS Cryogenic Chamber Front Endcap

Revision Prior to Bore Through Modification

stainless steel

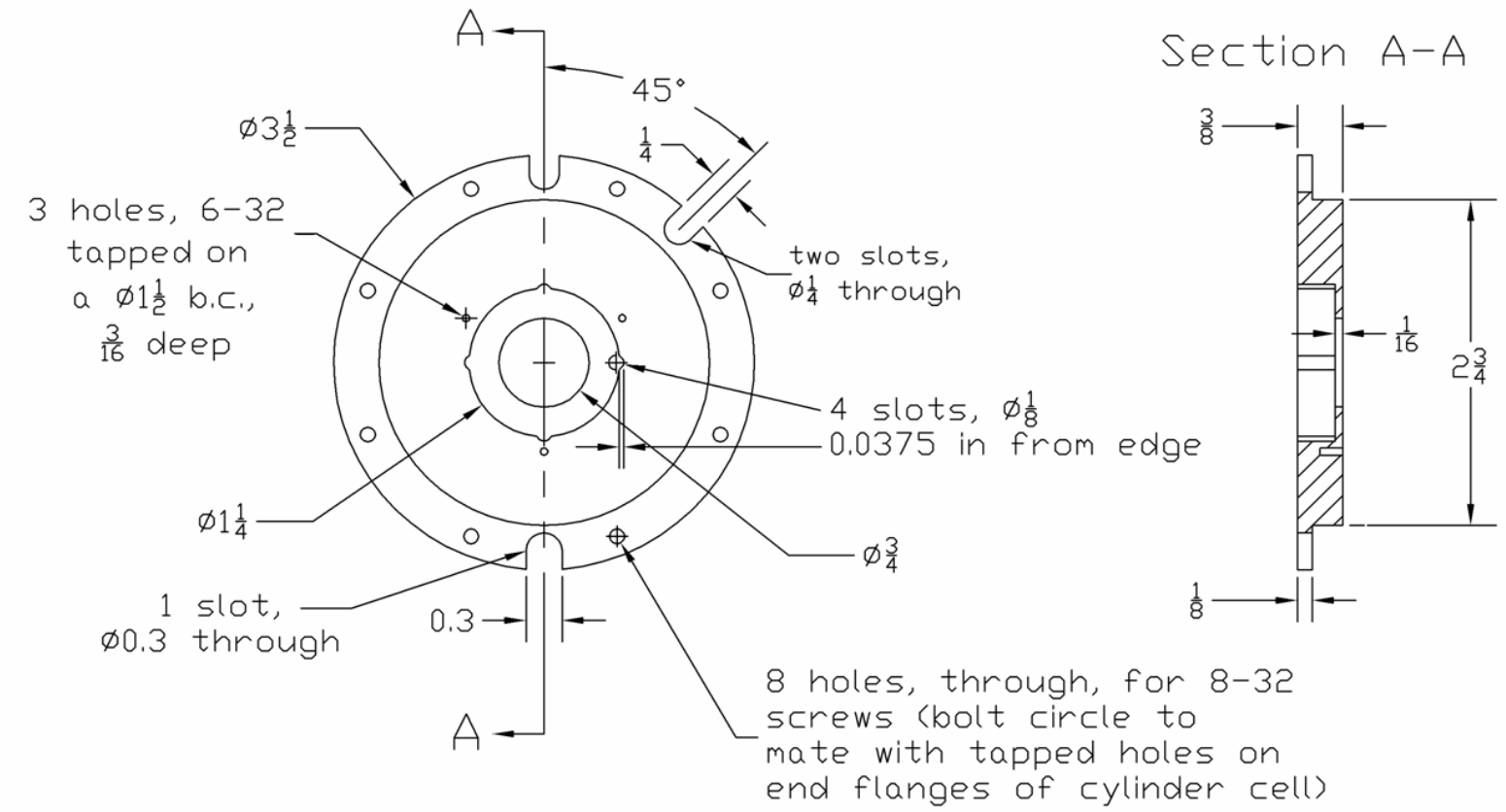

IMS Cryogenic Chamber Back Endcap

Revision Prior to Bore Through Modification

stainless steel

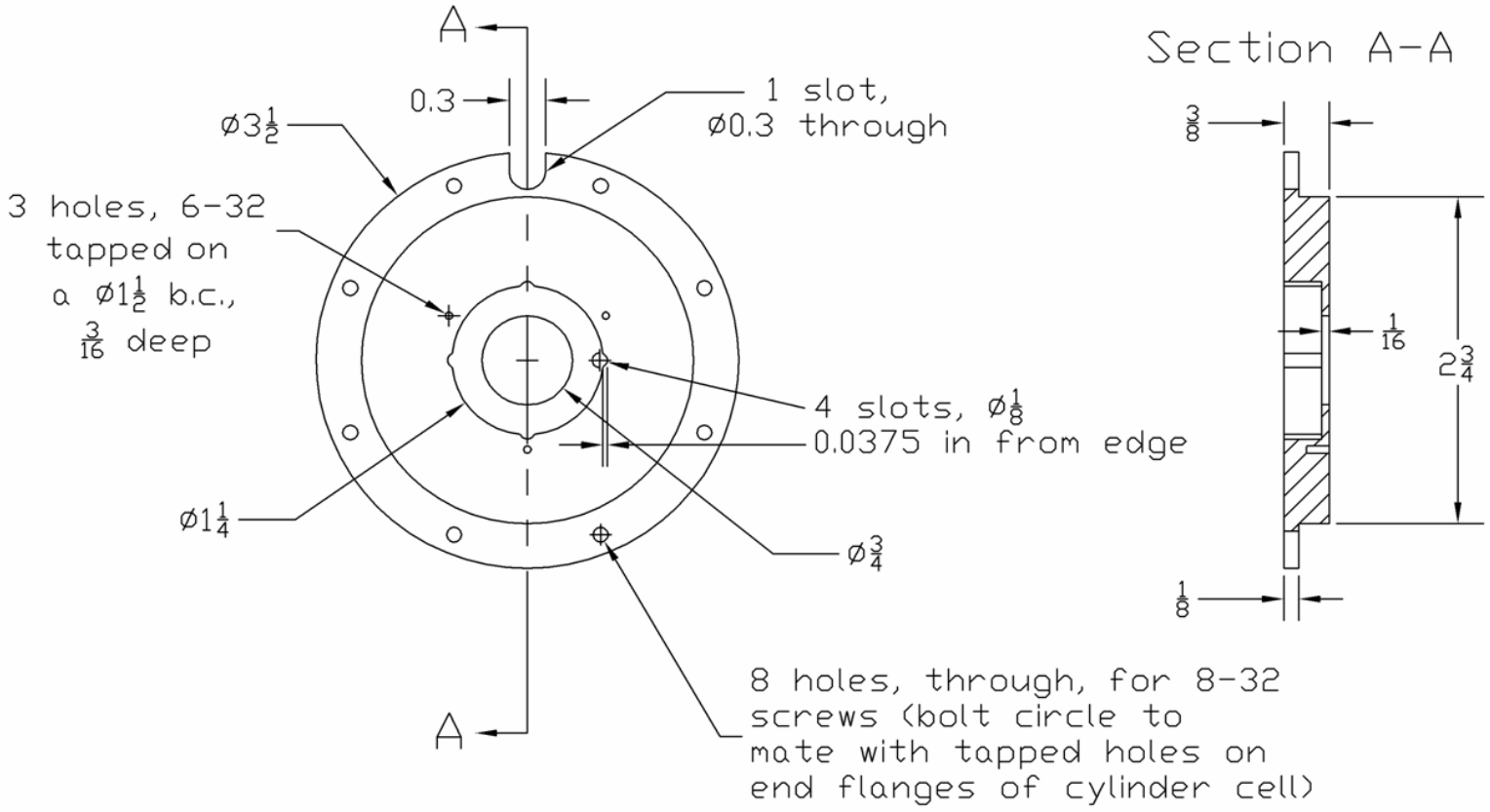

IMS Cryogenic Chamber Front Endcap

Feedthrough Details

stainless steel

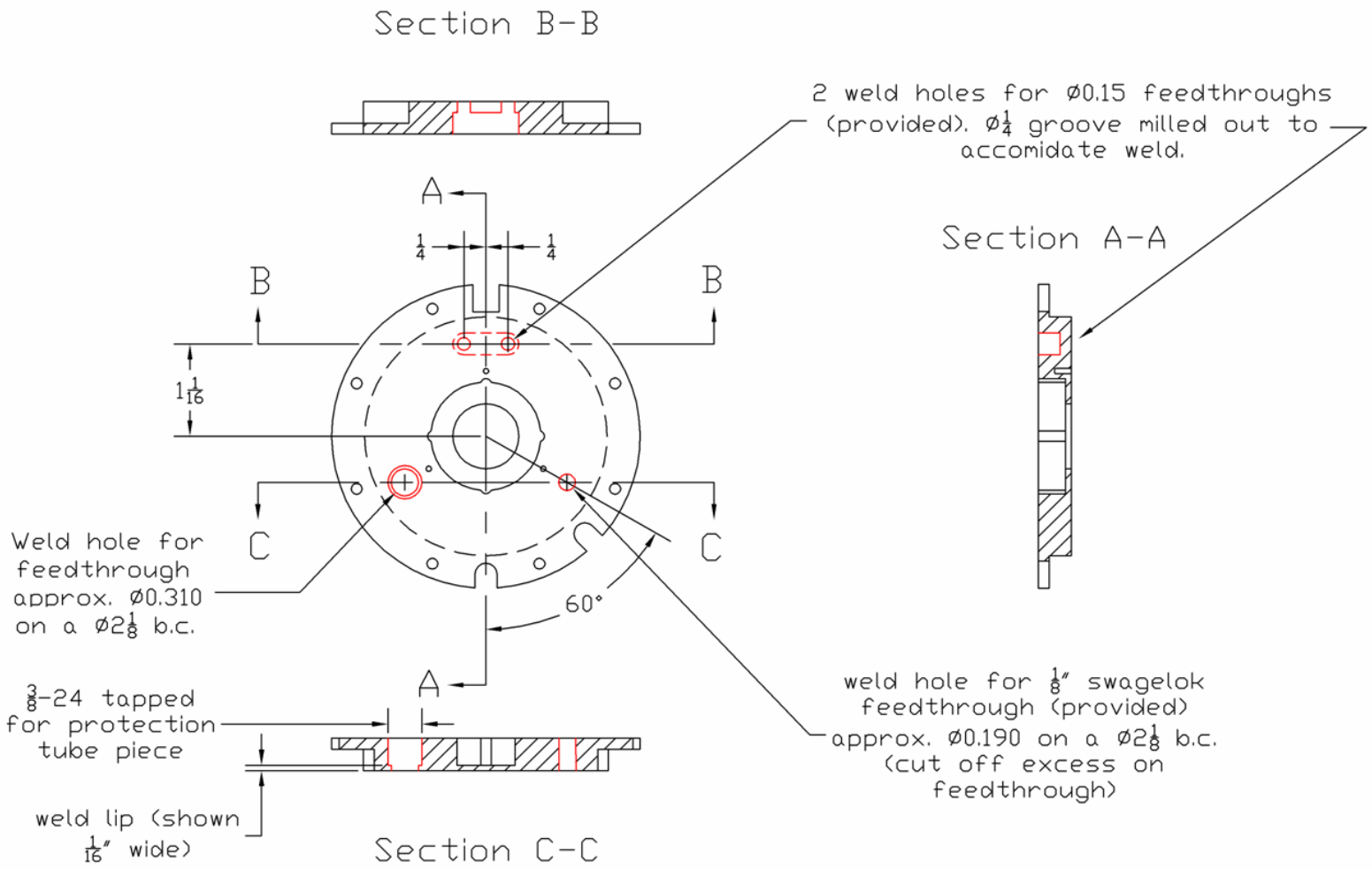

IMS Cryogenic Chamber Back Endcap

Feedthrough Details

stainless steel

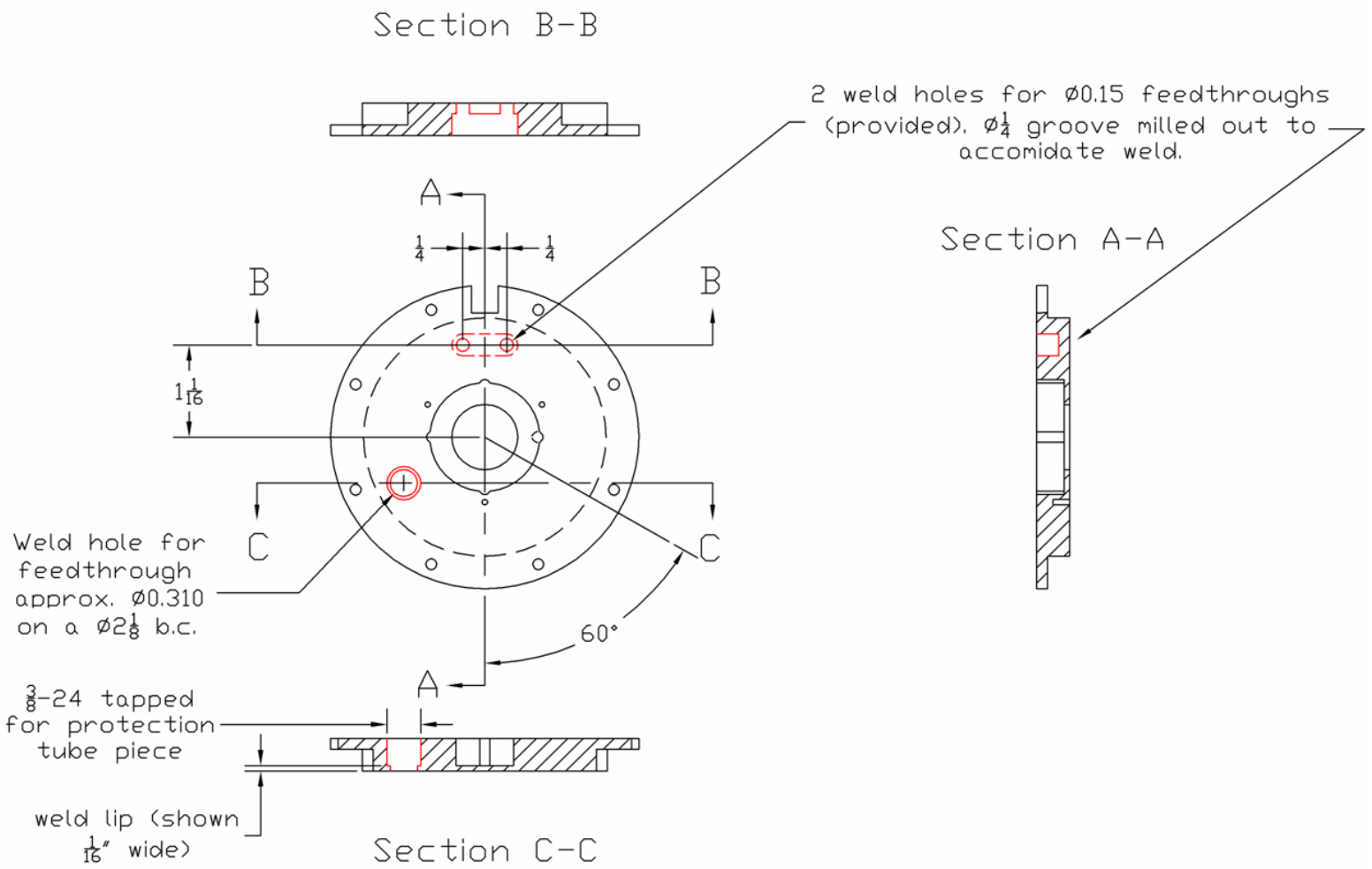

IMS Cryogenic Chamber Front & Back Endcap
Bore Through Modification

stainless steel

Wider Bore to Accommodate Entrance/Exit Electrode Shielding Cup Design

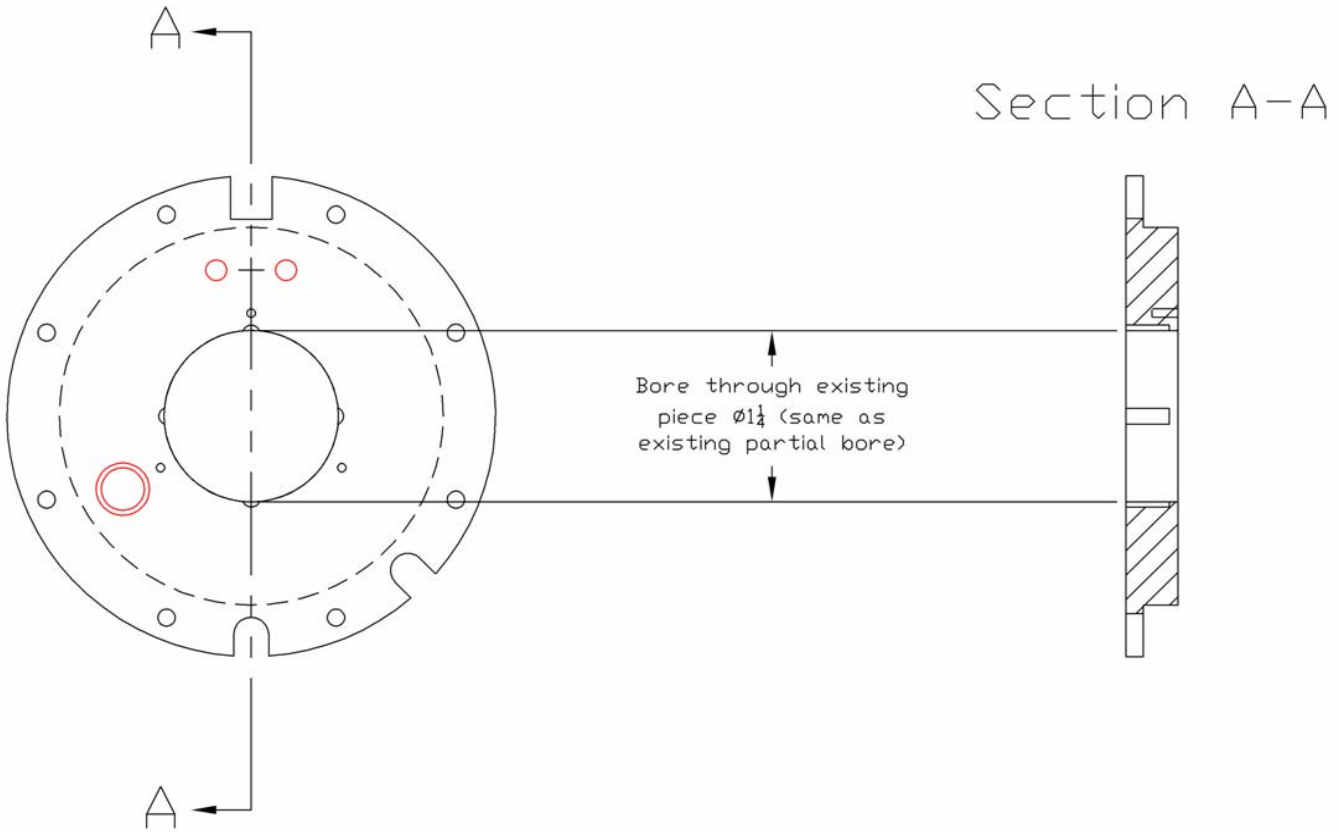

NOTE: modification is same for both endcaps

IMS Cryogenic Chamber Feedthrough Assembly

Welded Components

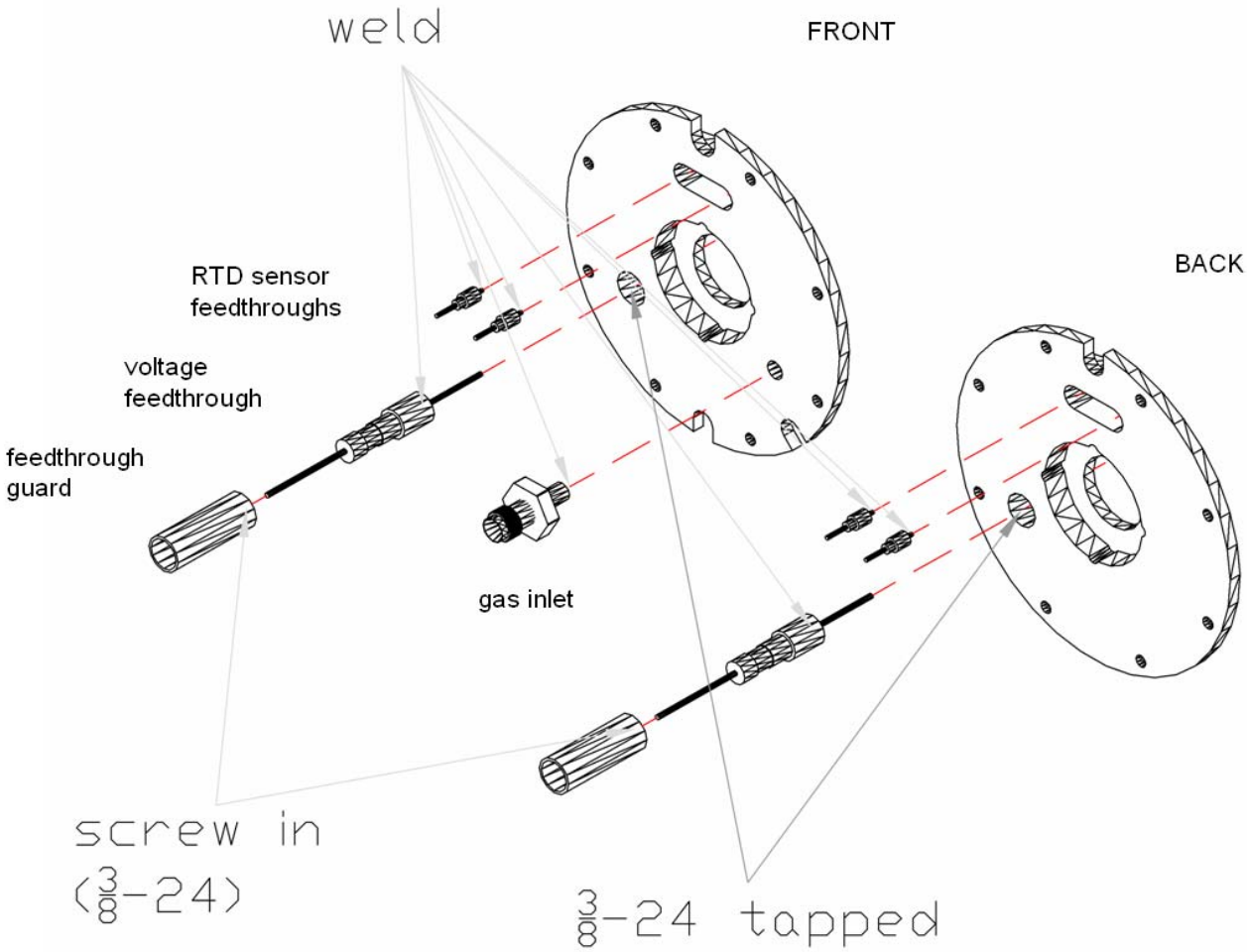

IMS Cryogenic Chamber – Inner and Outer Jacket Tube

Dimensions Selected from Common Stainless Steel Stock

stainless steel

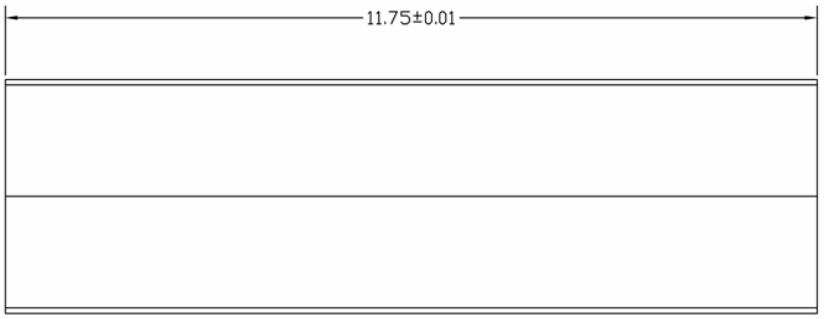

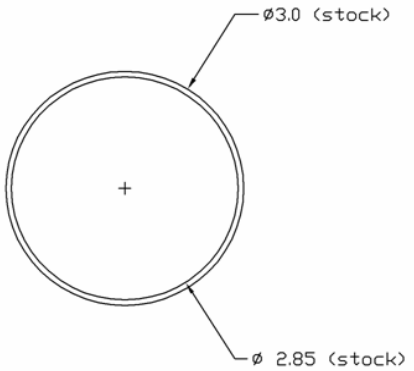

From SST Stock. Use the straightest section with minimal warping in walls.

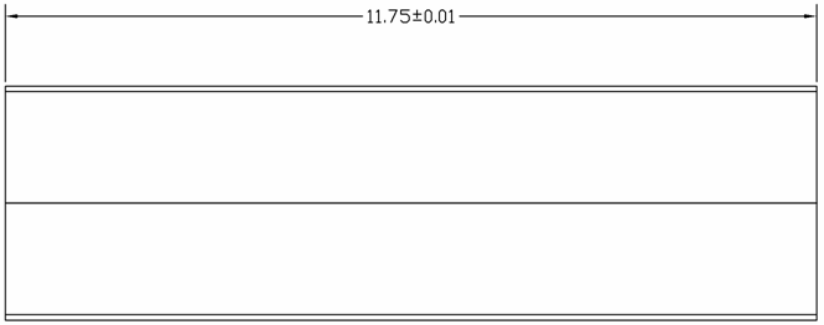

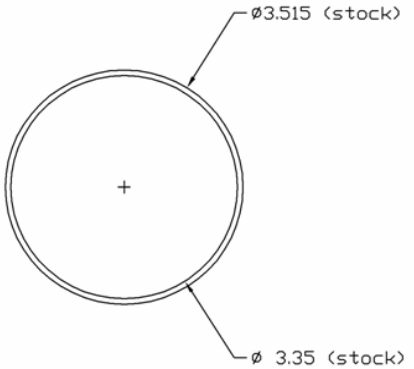

From SST Stock. Use the straightest section with minimal warping in walls.

IMS Cryogenic Chamber – Front Endring

TIG Welded to Dewar Jacket Assembly

stainless steel

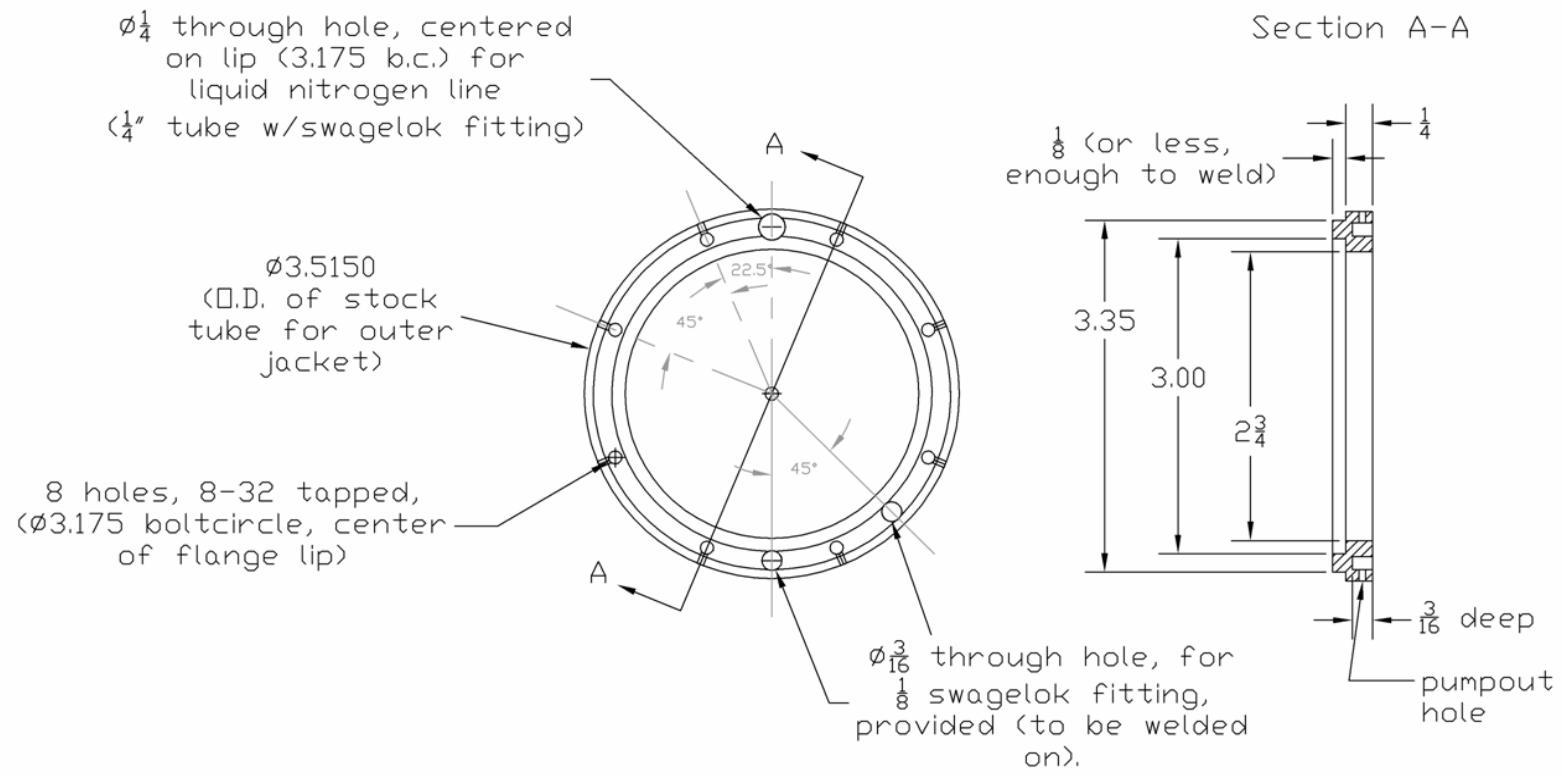

IMS Cryogenic Chamber – Back Endring

TIG Welded to Dewar Jacket Assembly

stainless steel

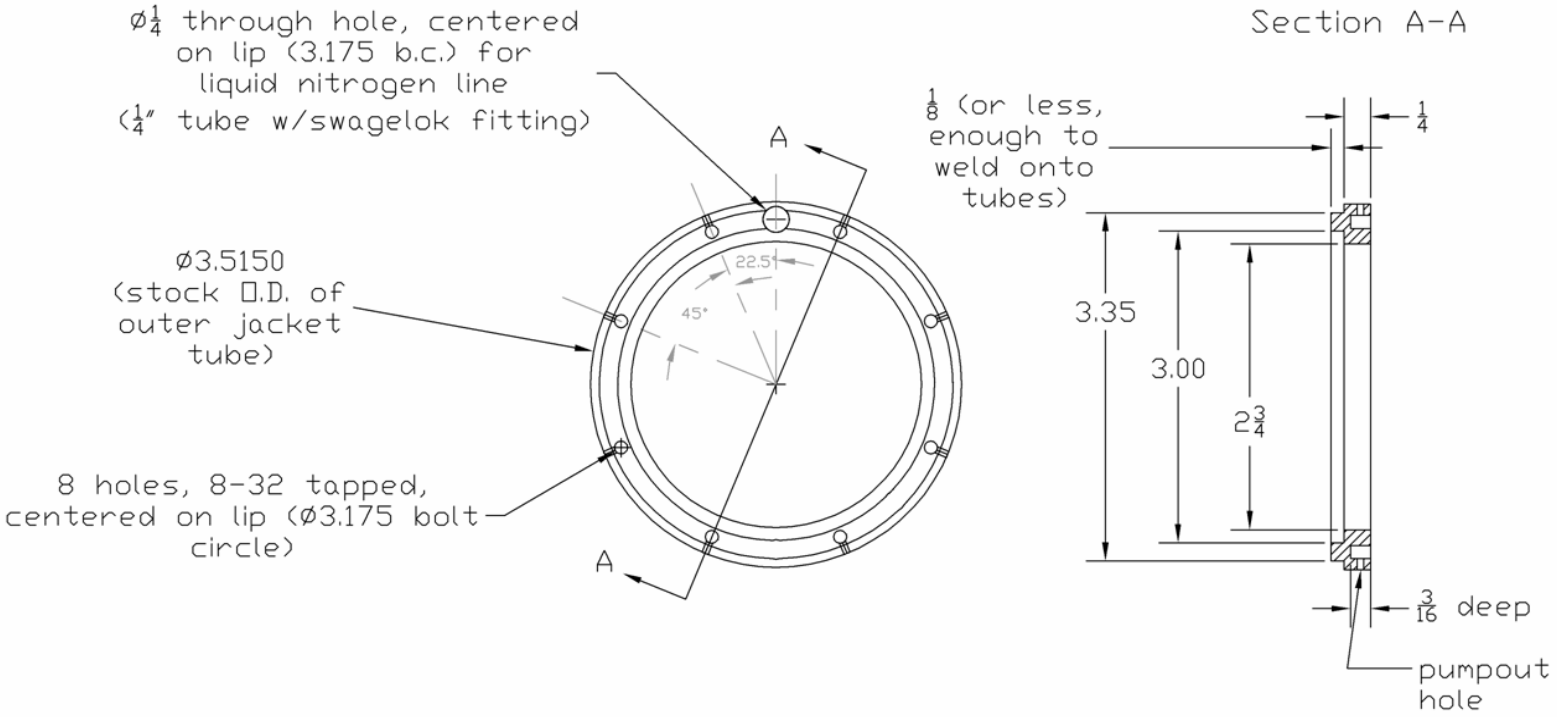

IMS Cryogenic Chamber – Liquid Nitrogen Weld Fittings

TIG Welded to Dewar Jacket Assembly – Routes IN_2 Up and Away from Ion Optical Assembly Front & Back

stainless steel NOT TO SCALE

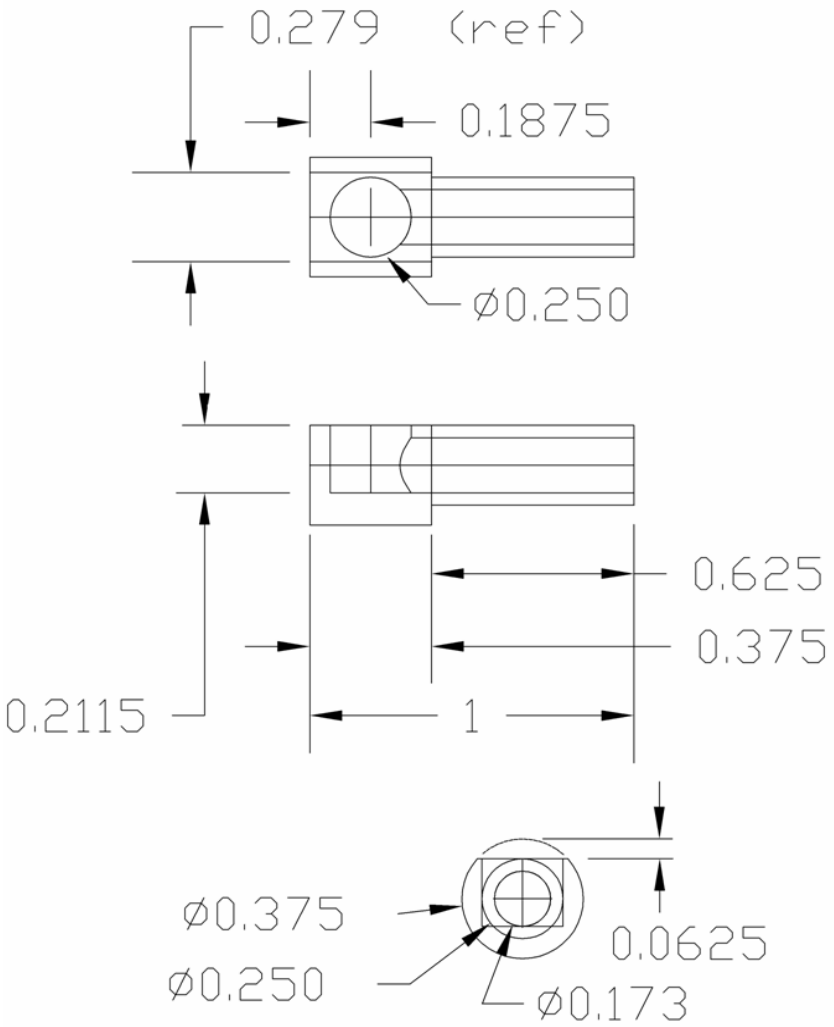

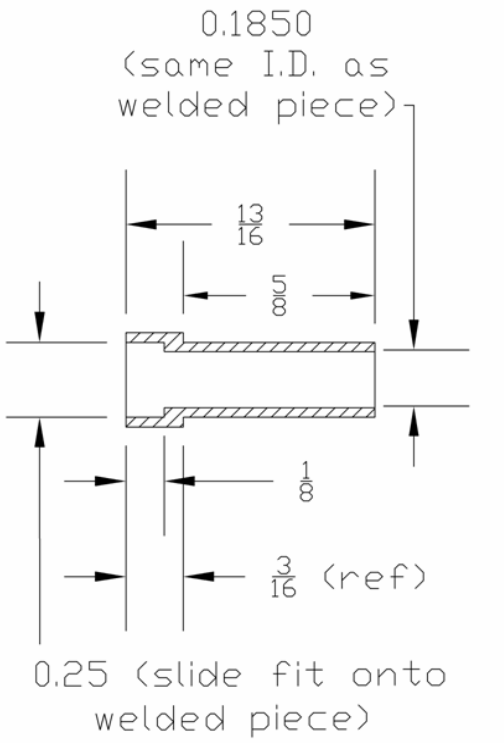

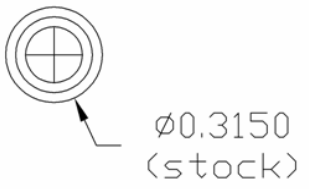

IMS-TOF Interface – Lens Stack (Original Design)

Assembly Diagram

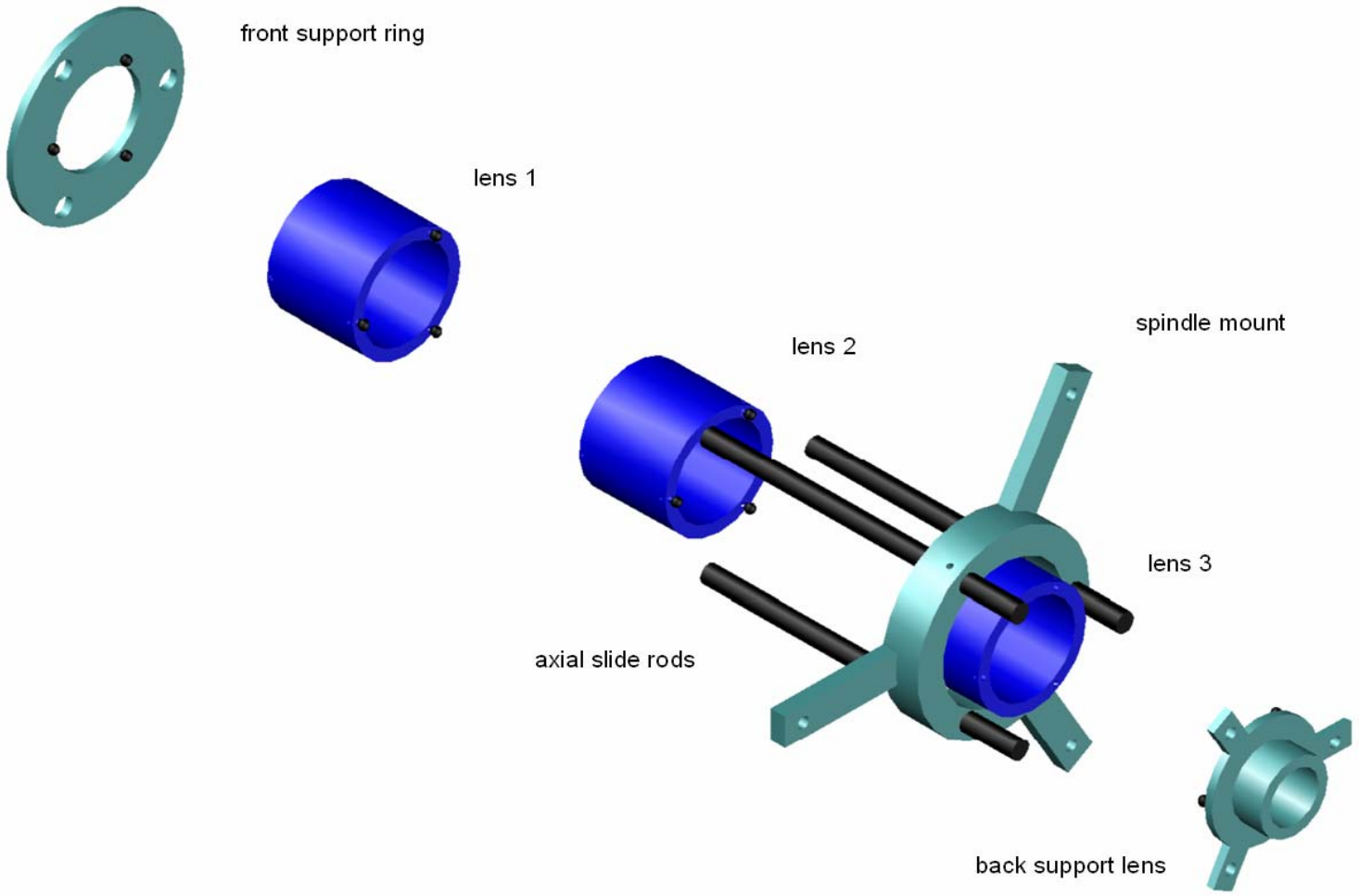

IMS-TOF Interface – Barrel Lens (Original Design)

Barrel Lens Assembly Built Up with Component eV Parts®

stainless steel

NOT TO SCALE

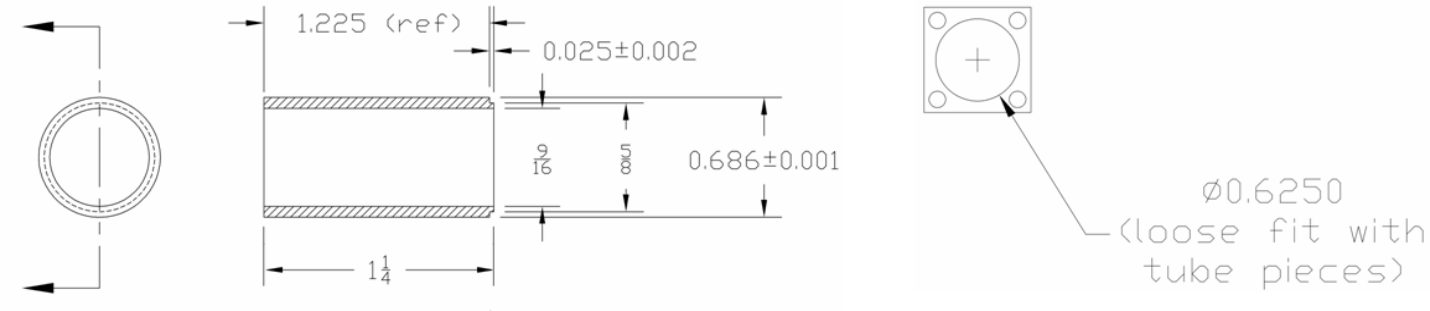

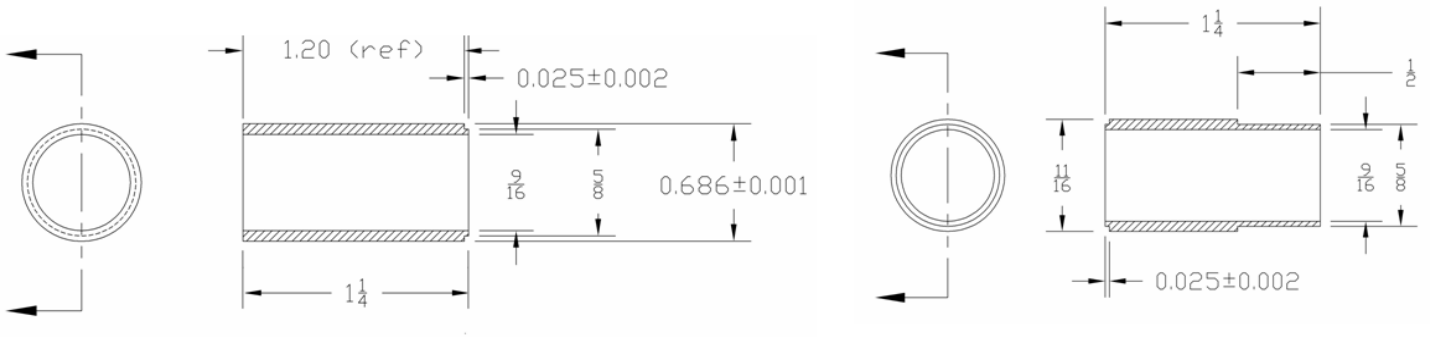

IMS-TOF Interface (1st Revision Assembly)

Assembly Diagram

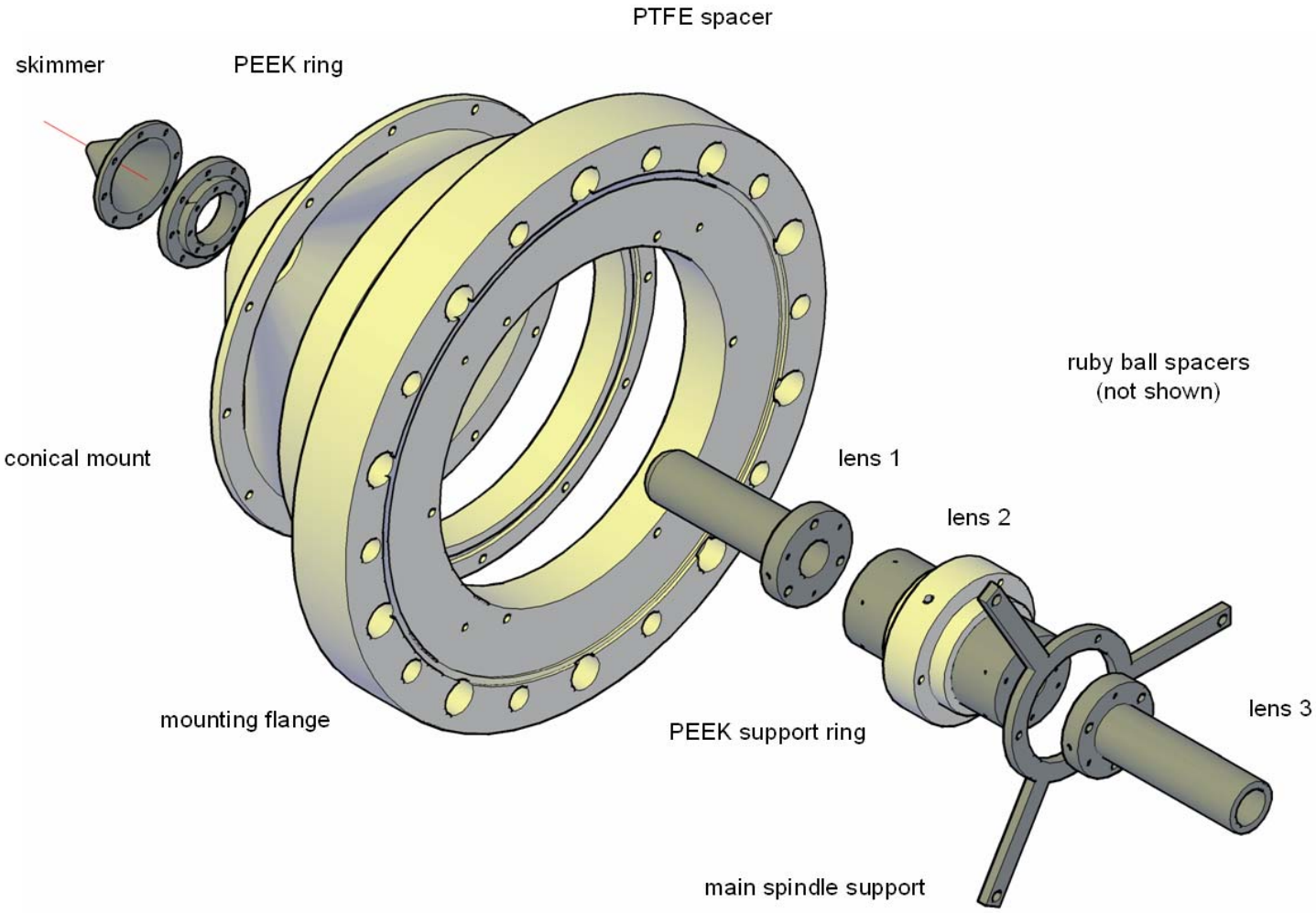

IMS-TOF Interface – Support Flange

Supports Skimmer Assembly on One Side, IMS-TOF Ion Optics on the Other

stainless steel

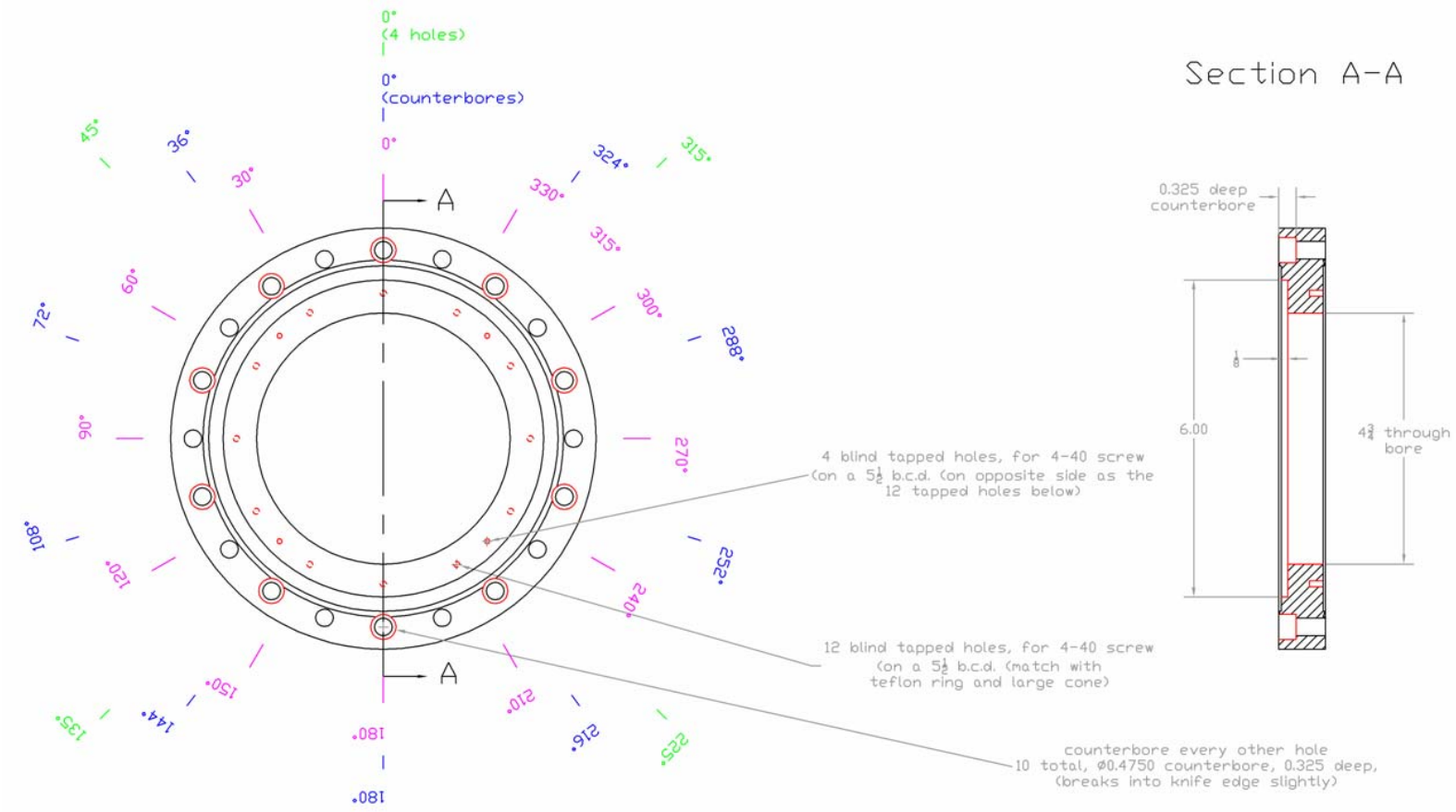

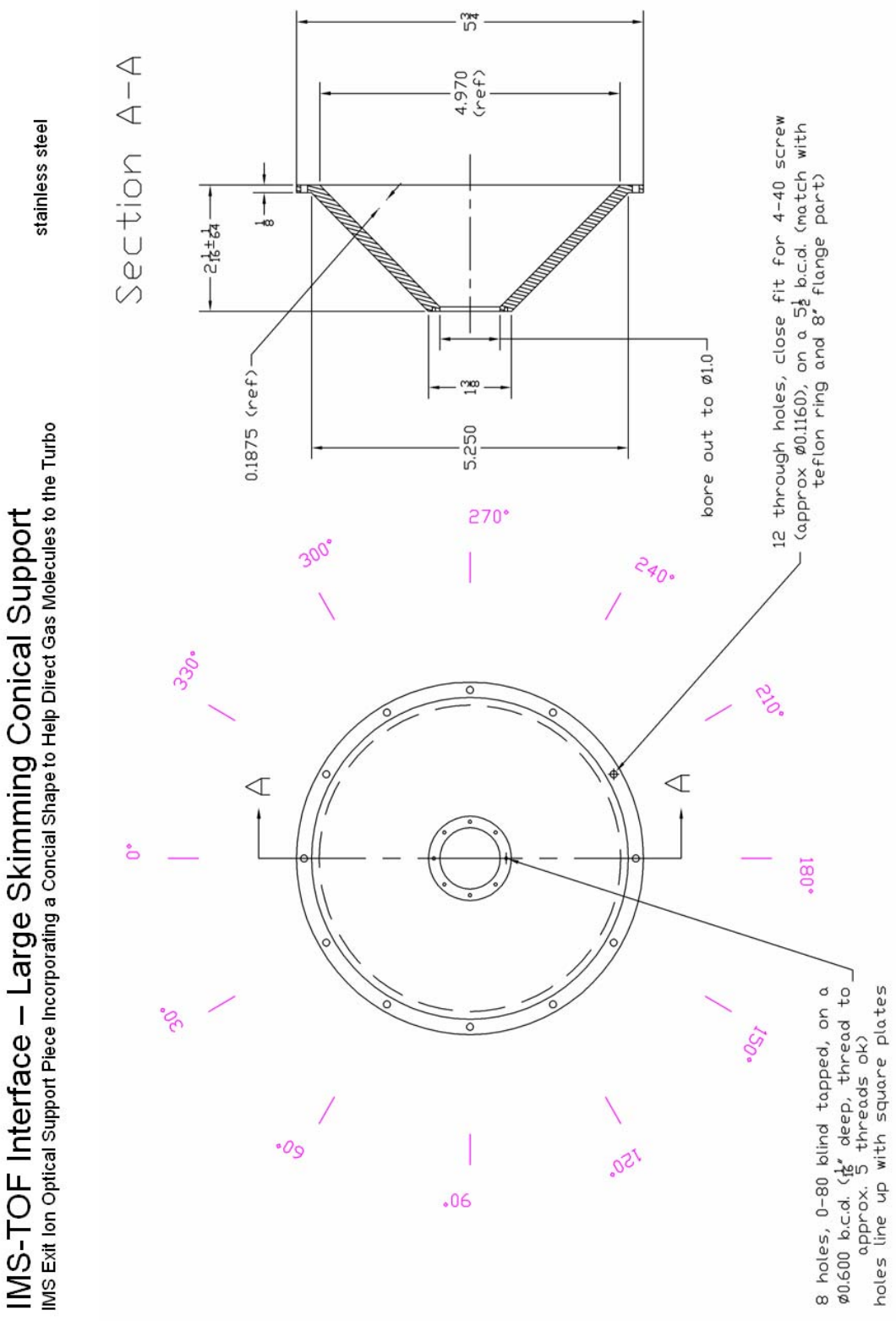
IMS-TOF Interface – Large Skimming Conical Support
IMS Exit Ion Optical Support Piece Incorporating a Concial Shape to Help Direct Gas Molecules to the Turbo
stainless steel
Section A-A
0.1875 (ref)
5.250
4.970 (ref)
bore out to ø1.0
12 through holes, close fit for 4-40 screw (approx ø0.1160), on a 5 1/2 b.c.d. (match with teflon ring and 8" flange part)
8 holes, 0-80 blind tapped, on a ø0.600 b.c.d. (1/4" deep, thread to approx. 5 threads ok) holes line up with square plates
0°
30°
60°
90°
120°
150°
180°
210°
240°
270°
300°
330°
A
A

IMS-TOF Interface – Insulating Support for Large Cone

Electrically Isolates Large Cone to Allow it to be Biased. Also Supports O-rings to Seal Chamber

polytetrafluoroethylene (PTFE Teflon®)

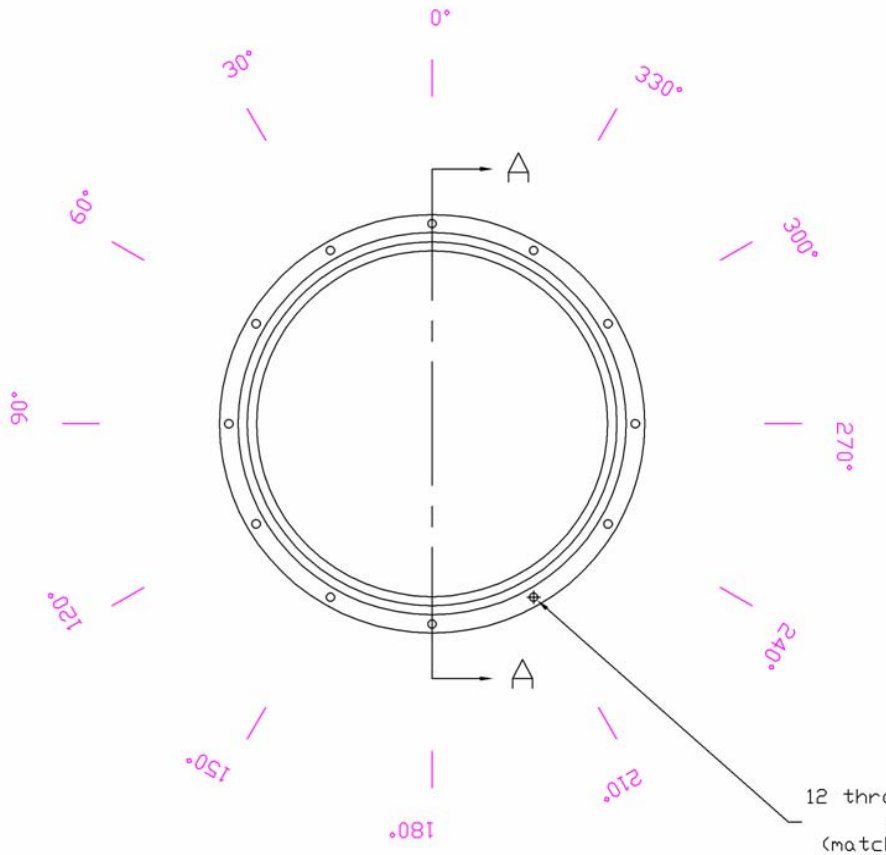

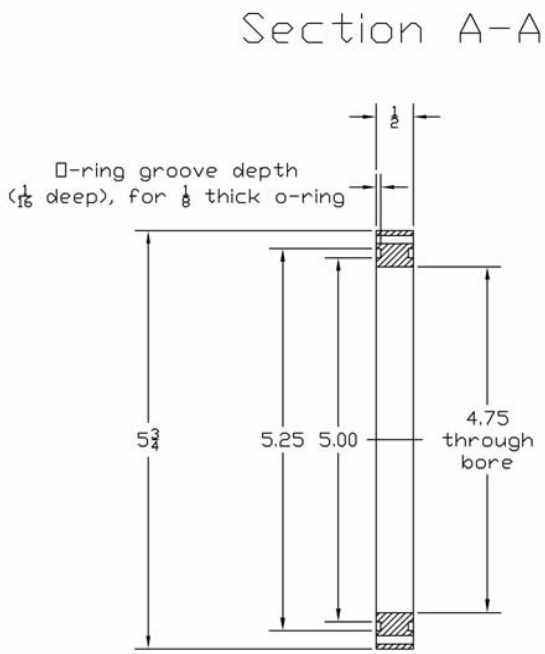

12 through holes, close fit for 4-40 screw
(approx ø0.1160), on a 5 1/2 b.c.d.
(match with large cone & 8" flange piece

IMS-TOF Interface – Barrel Lens Support Ring

Metal Ring Support for High Conductance Barrel Lens – High Transmission Alternate to the Skimmer Design
When TOF Vacuum is Not an Issue

stainless steel

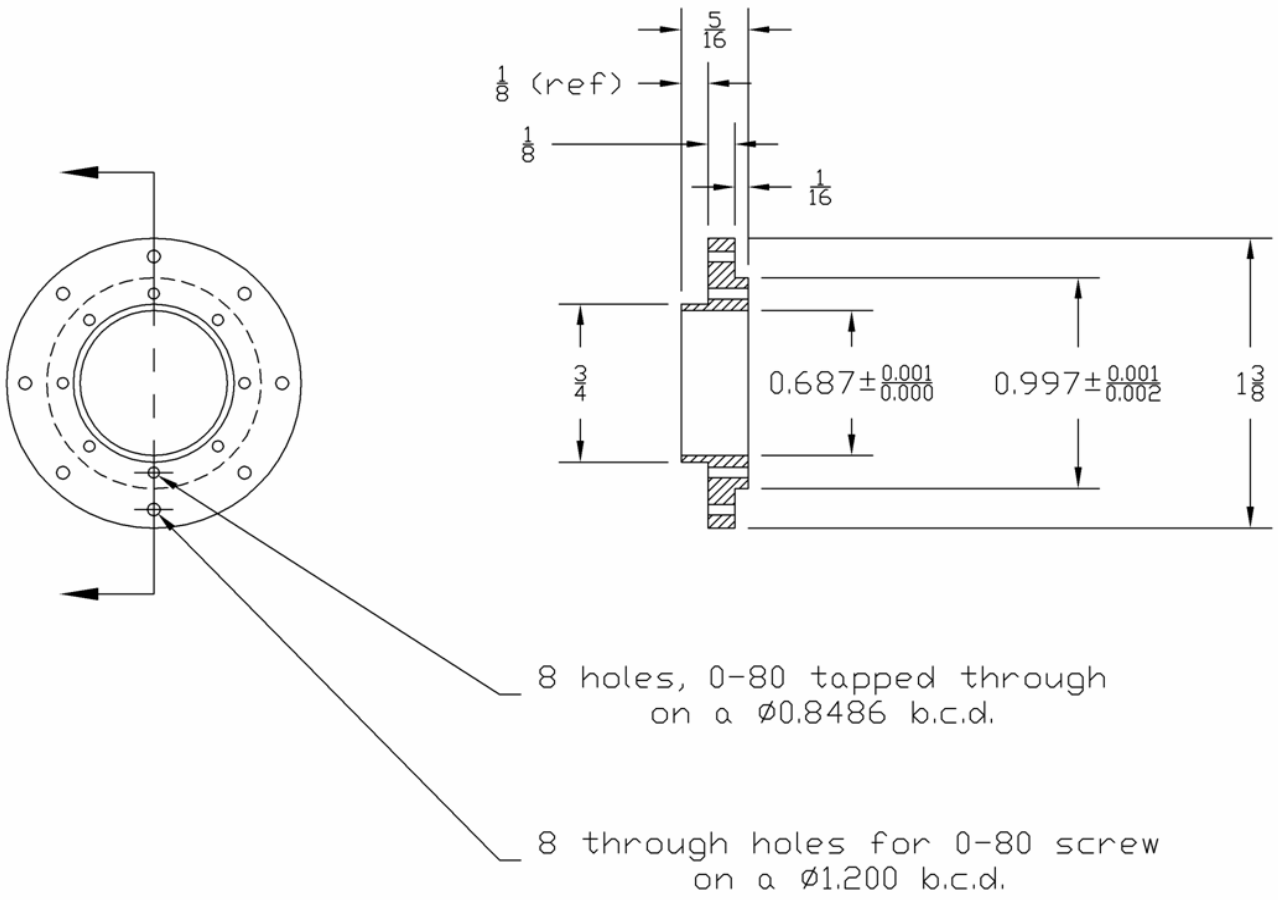

IMS-TOF Interface – 30° Skimmer (1st Revision Assembly)

Gas Skimmer and Extraction Ion Optic for Ions Exiting the IMS

stainless steel

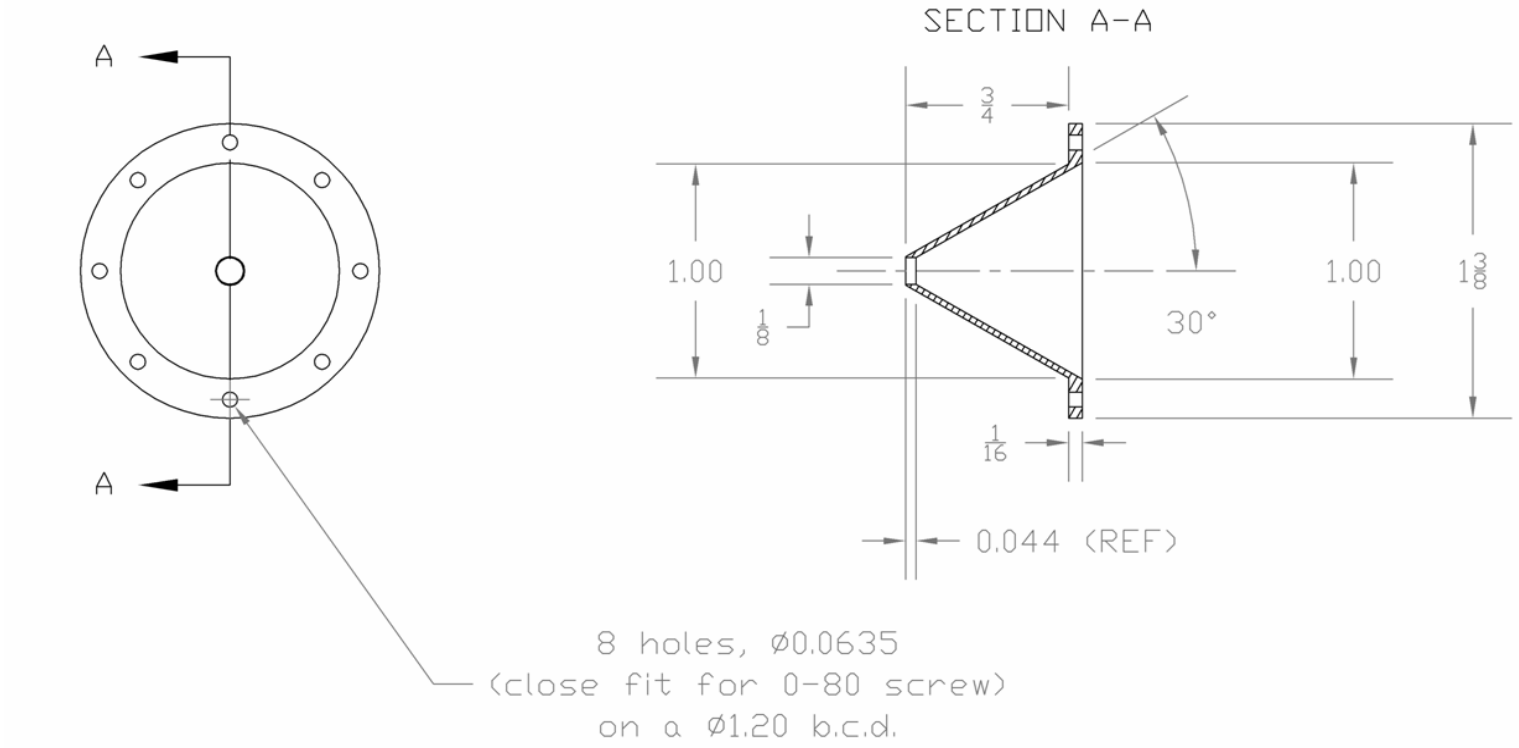

IMS-TOF Interface – Skimmer Adapter Ring
(1st Revision Assembly)

polyetheretherketone (PEEK)

Barrel Lens Design PEEK Spacer for Isolation Between 1st Lens and Skimmer

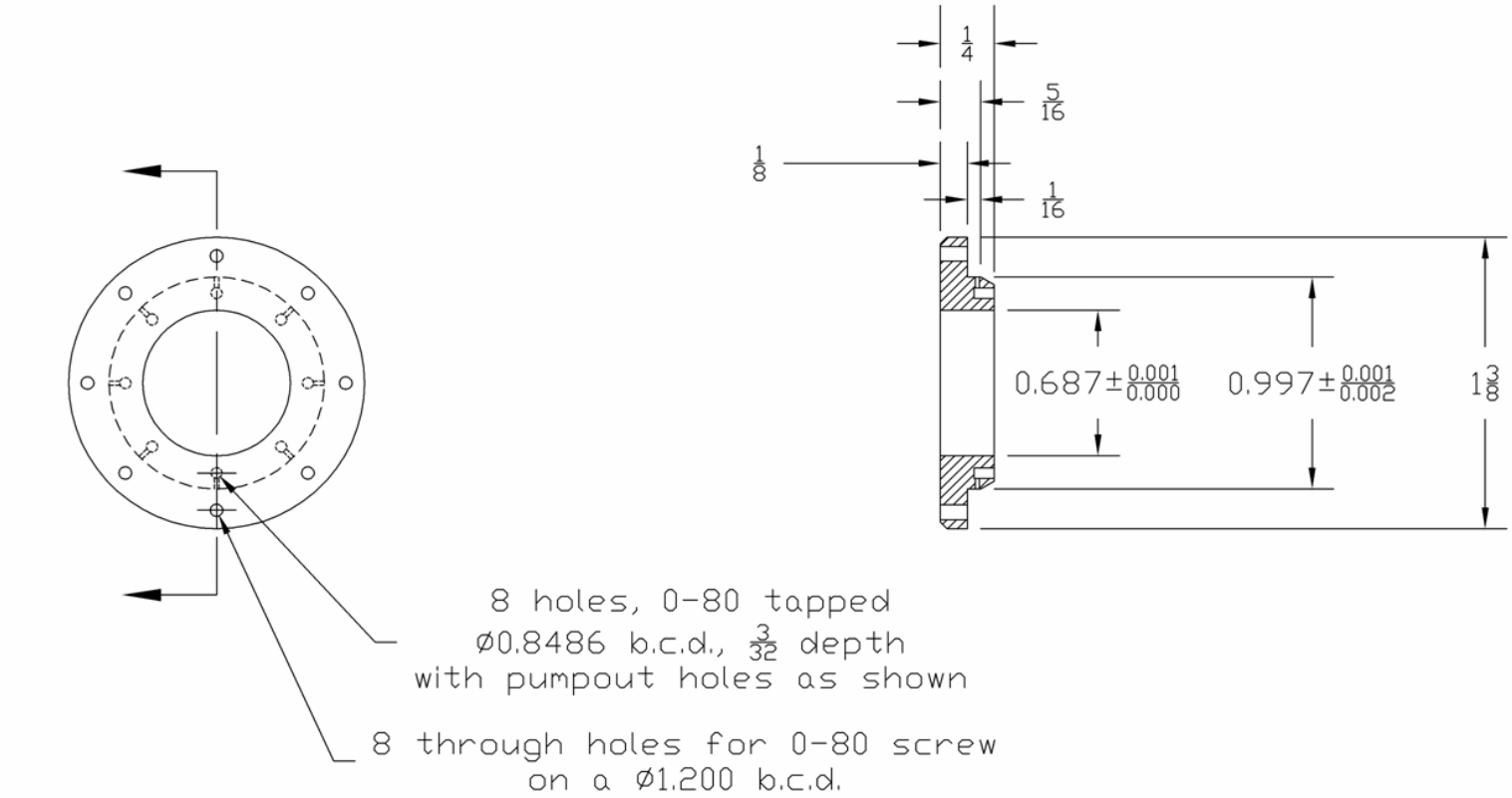

IMS-TOF Interface – Lens 1 (1st Revision Assembly)

Barrel Lens Design Inserted into PEEK Spacer and Closely Spaced with Skimmer

stainless steel

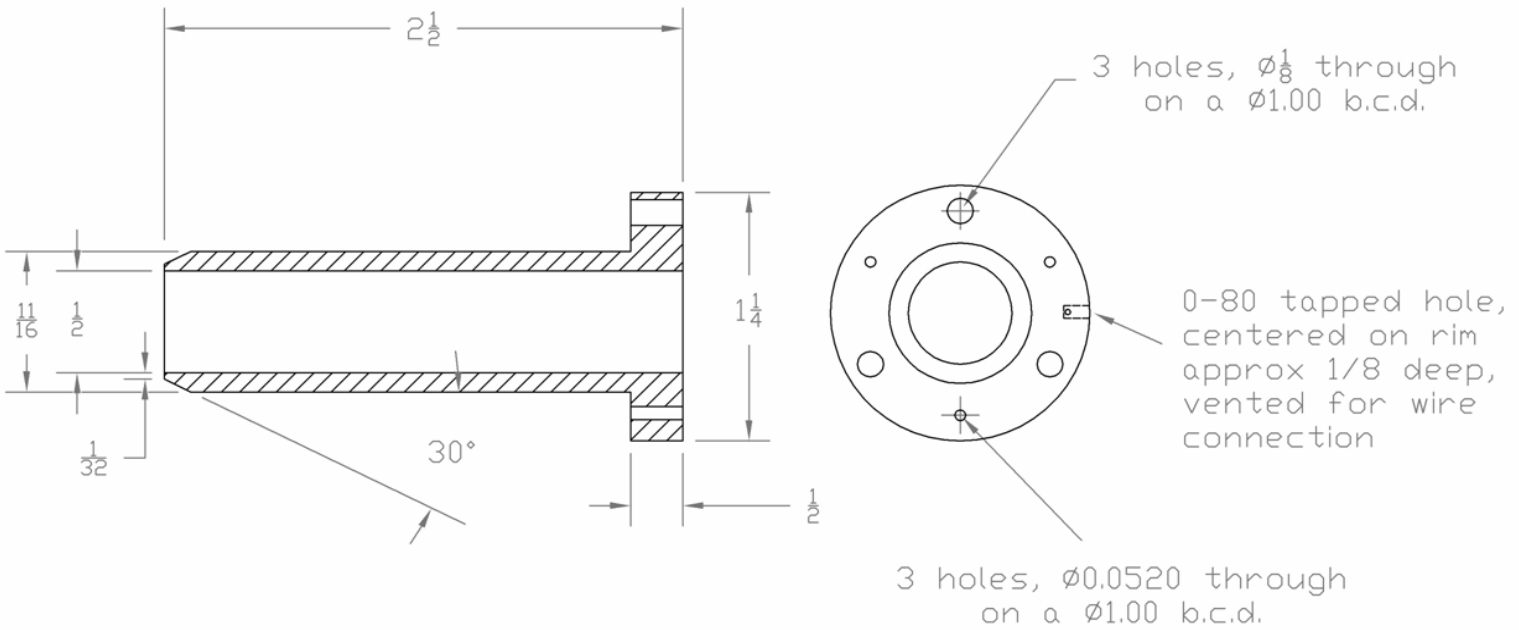

IMS-TOF Interface – Lens 2 (1st Revision Assembly)

Barrel Lens Design – Sliding Adjustment with PEEK Support Ring to Allow Axial Motion of Lens Assembly

stainless steel

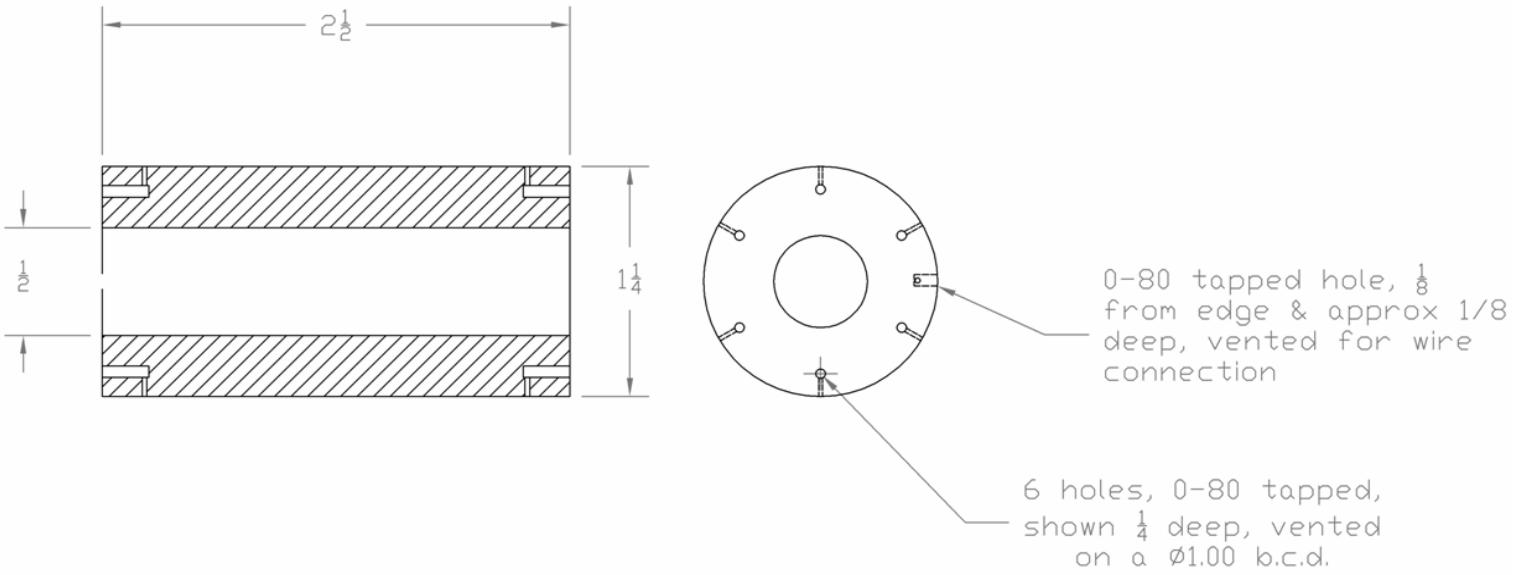

IMS-TOF Interface – Lens 3 (1st Revision Assembly)

Barrel Lens Design – Interfaces Closely to TOF Extraction Ion Optical Assembly

stainless steel

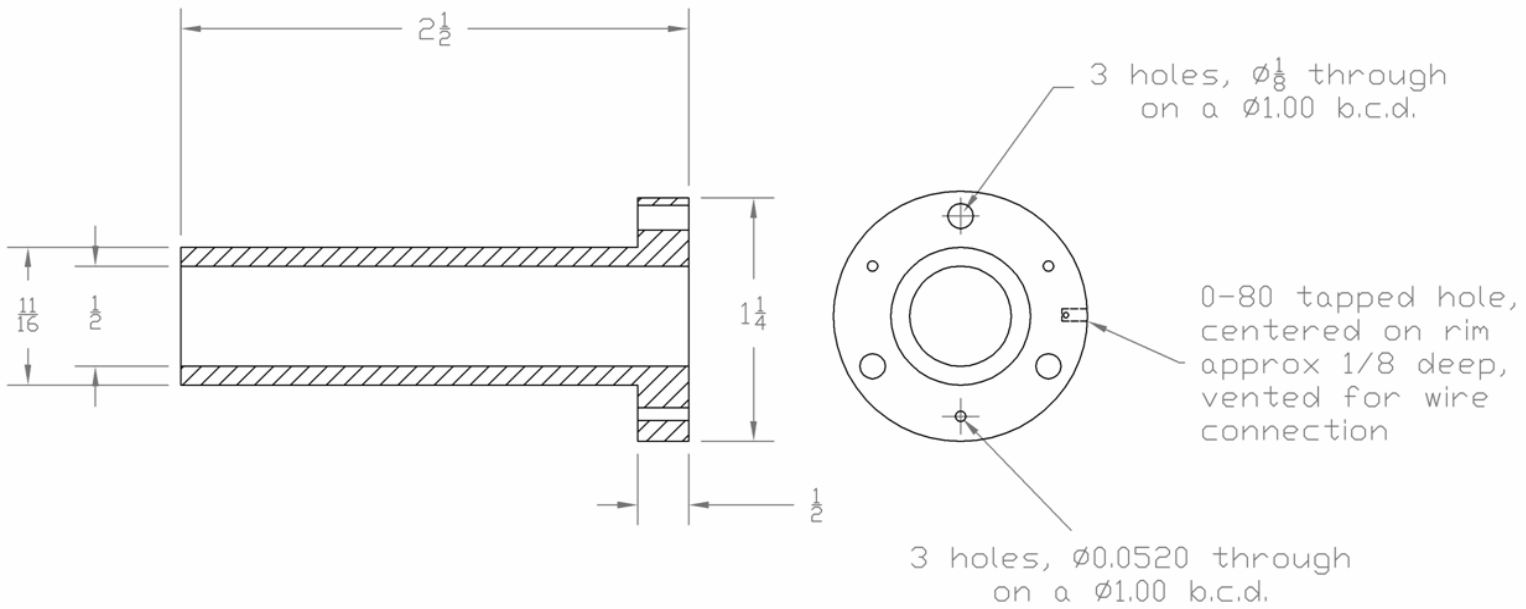

IMS-TOF Interface – Lens Ring Isolation & Sliding Support (1st Revision Assembly)

polyetheretherketone (PEEK)

Barrel Lens Design – Support Ring Allowing Axial Sliding of Lens Assembly

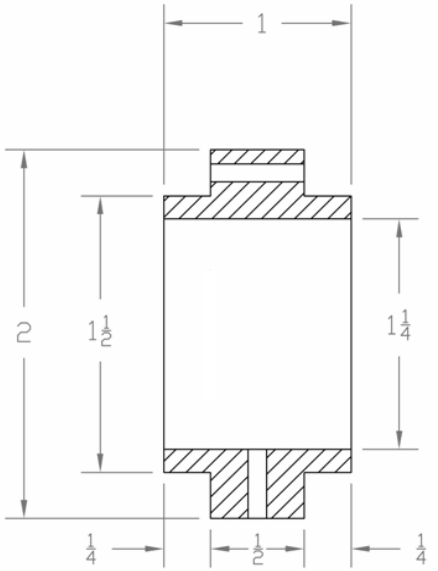

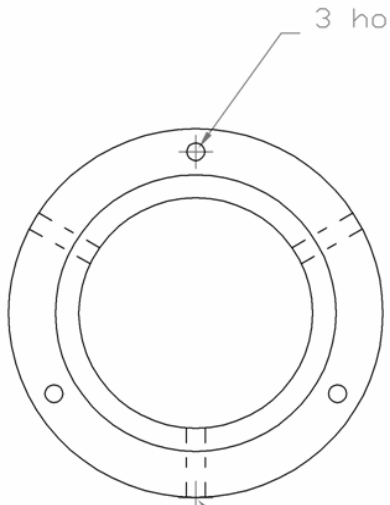

3 holes, 4-40 tapped through on a Ø1.75 b.c.d.

3 holes, 6.32 tapped through center on part radially for set screws

IMS-TOF Interface – High Conductance Lens Support
(1st Revision Assembly)

stainless steel

Barrel Lens Design – Supports Lens Assembly to Flange and Allows Free Pumping Across

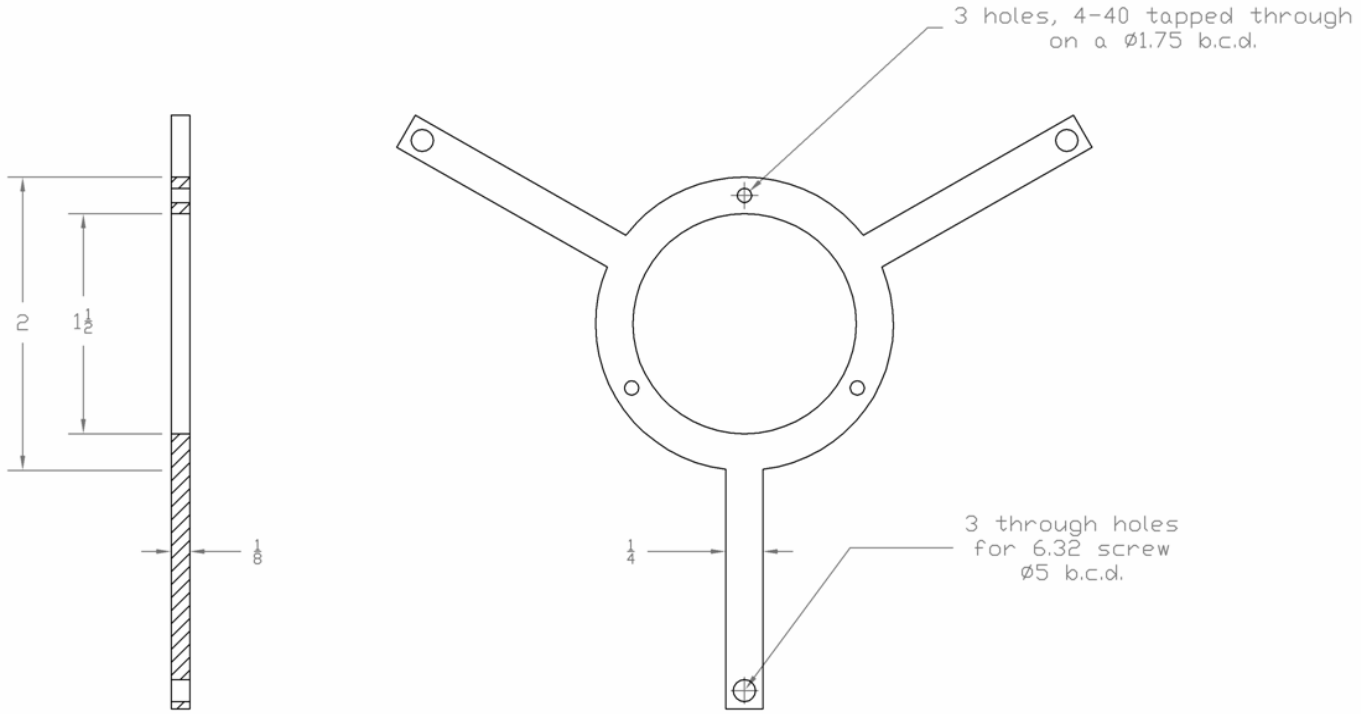

Time-of-Flight Mass Spectrometer (TOF) and Ion Detector Assemblies

Assembly Diagram

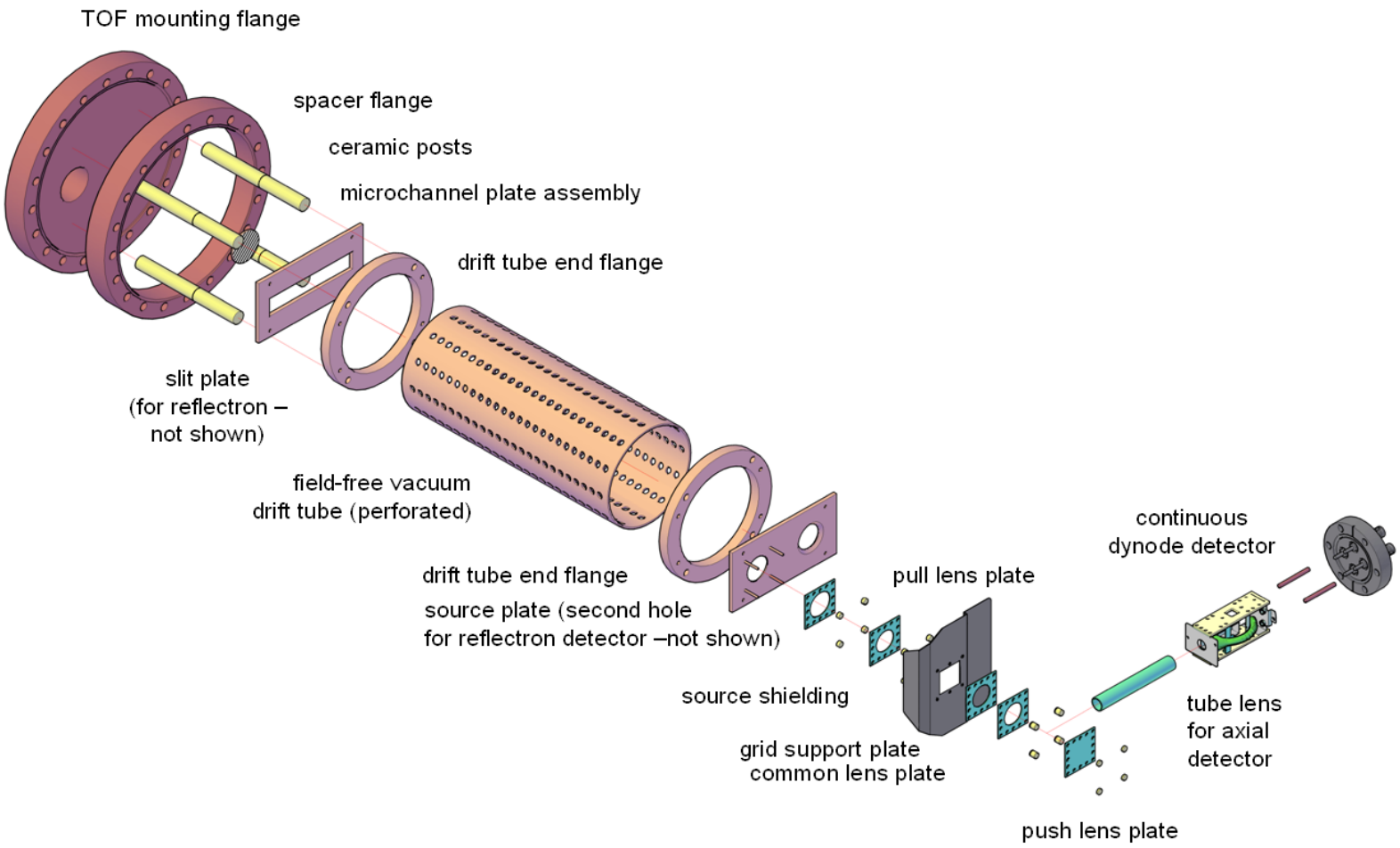

TOF Voltage Feedthrough Flange

Modified 6" CF Flange - For Mini-CF (1⅓") Feedthroughs

stainless steel

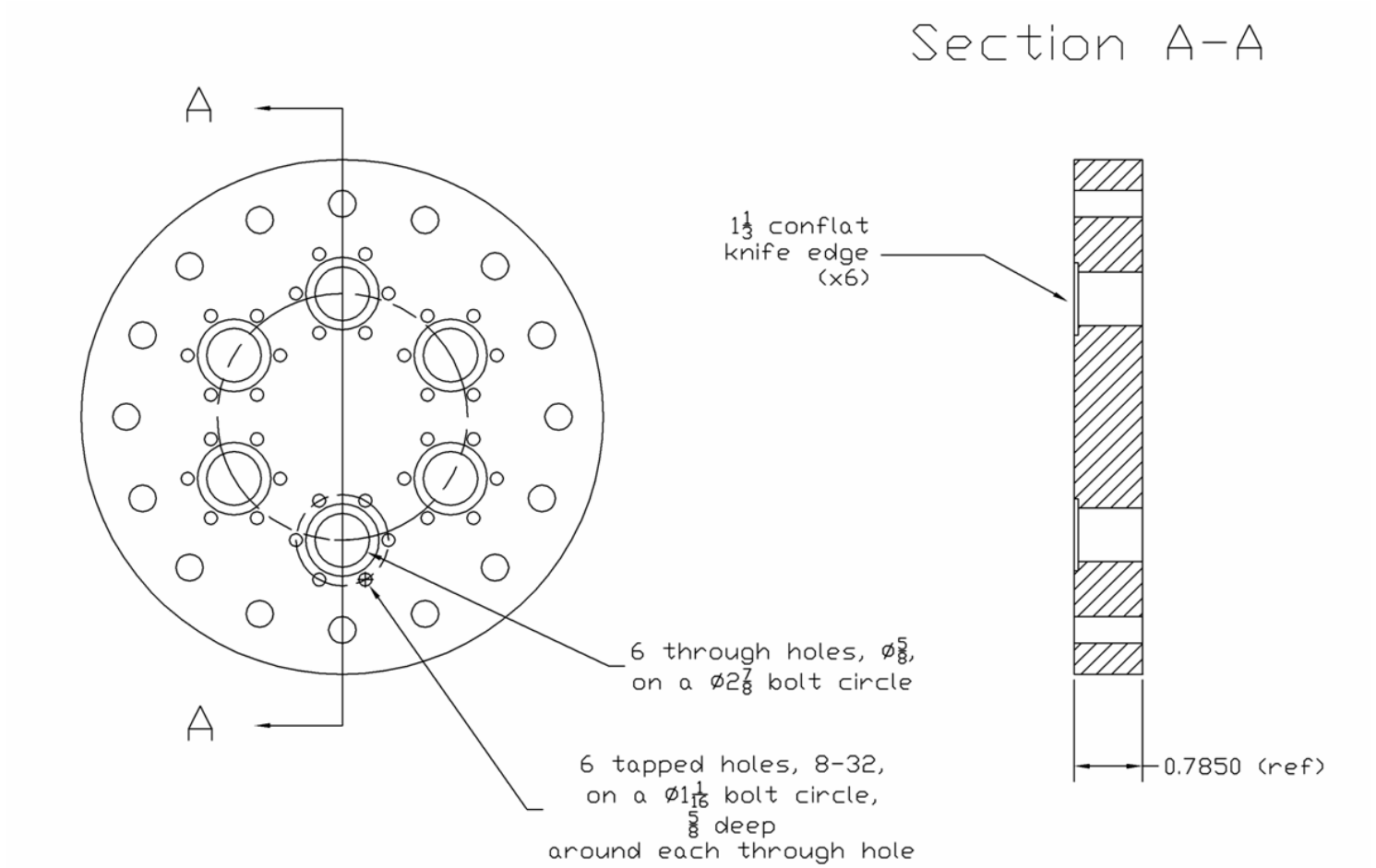

TOF Grid Retaining Rings

For Component eV Parts® System

stainless steel

NOT TO SCALE

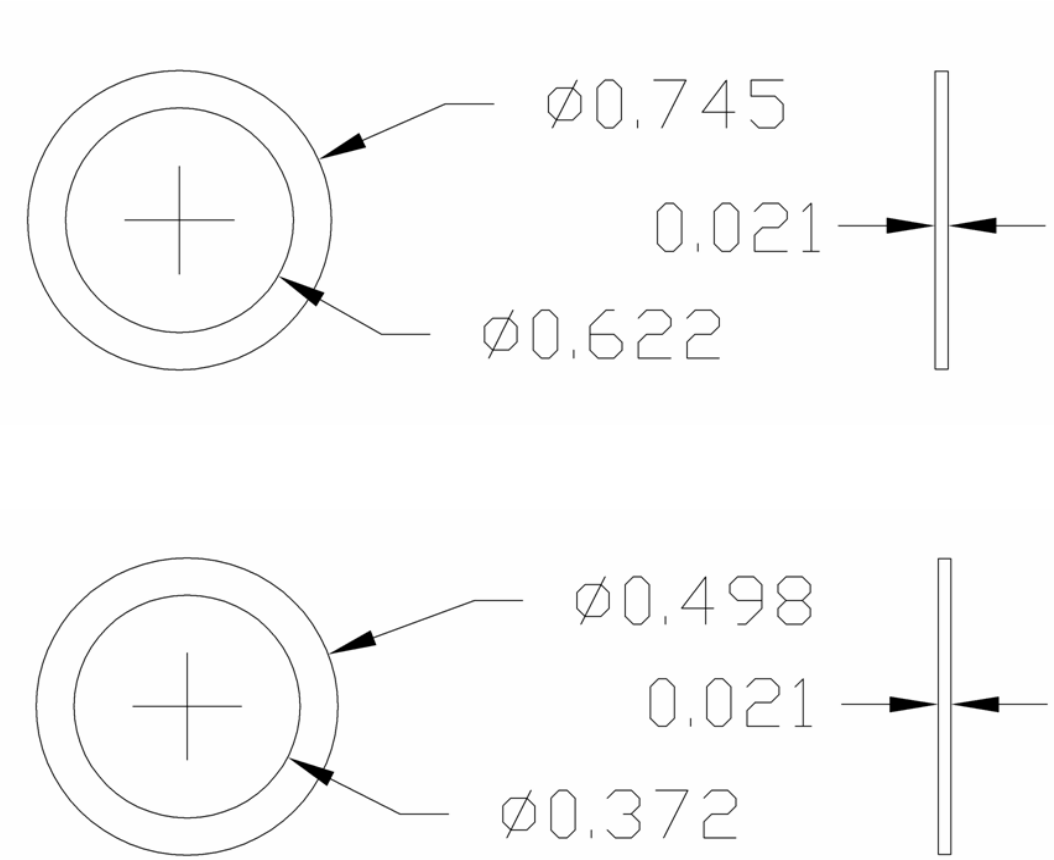

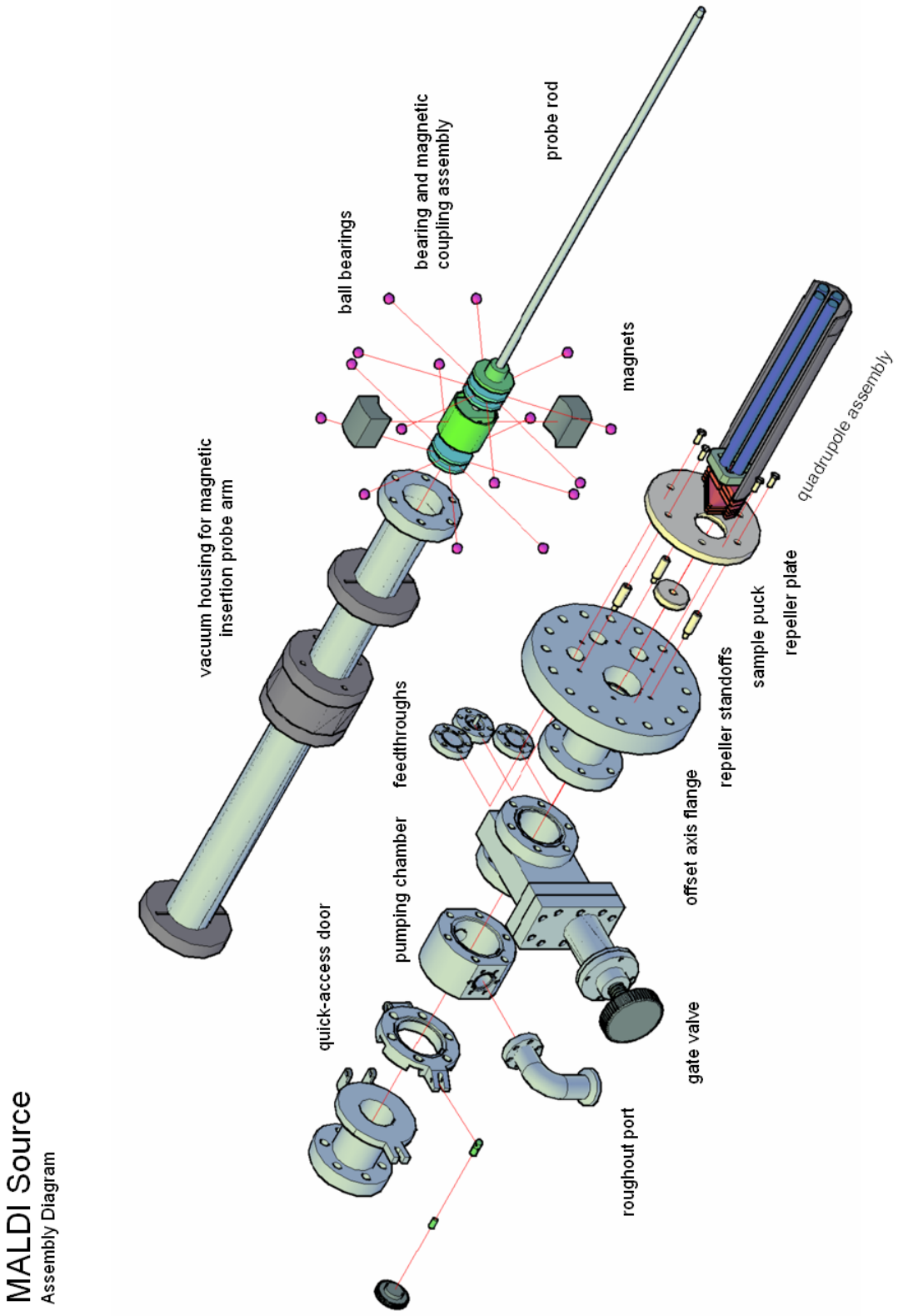
MALDI Source
Assembly Diagram
vacuum housing for magnetic insertion probe arm
ball bearings
bearing and magnetic coupling assembly
probe rod
magnets
quick-access door
pumping chamber
feedthroughs
offset axis flange
repeller standoffs
sample puck
repeller plate
quadrupole assembly
gate valve
roughout port

MALDI Source – Source Chamber Laser Alignment

Dimensions for Centering Sample Puck to Chamber Focal Point

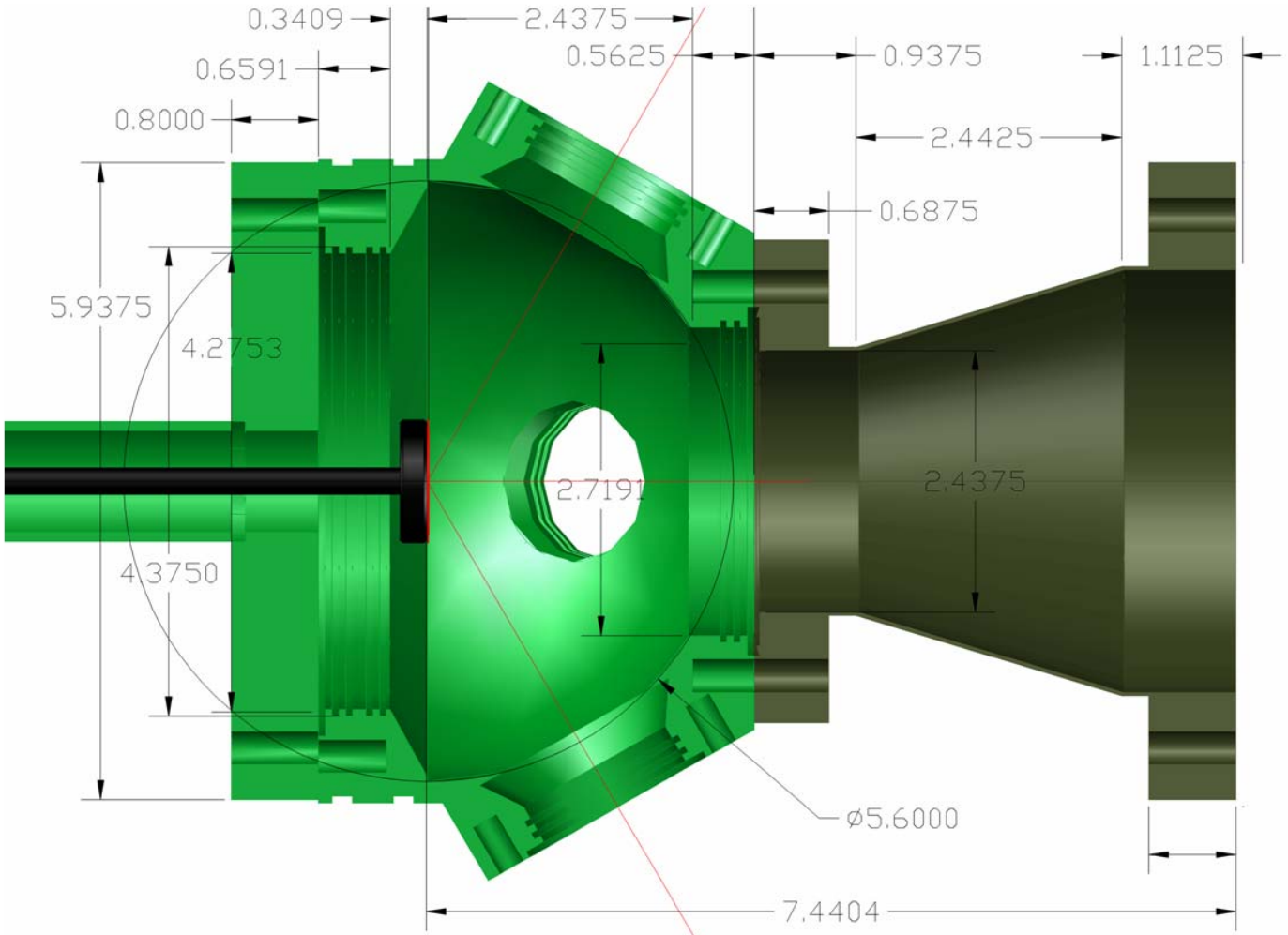

MALDI Source Magnetic Insertion Probe Parts

Probe Flange – Modified from 2¾" CF Flange

stainless steel

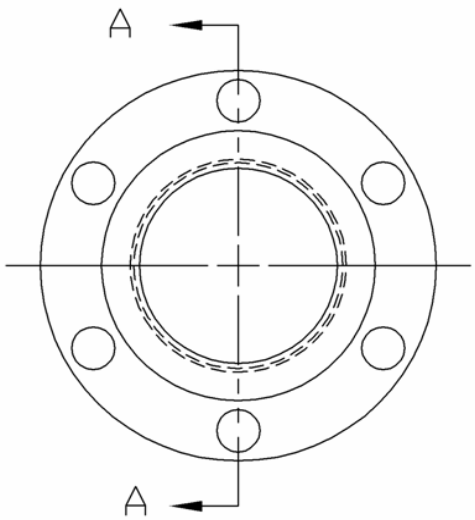

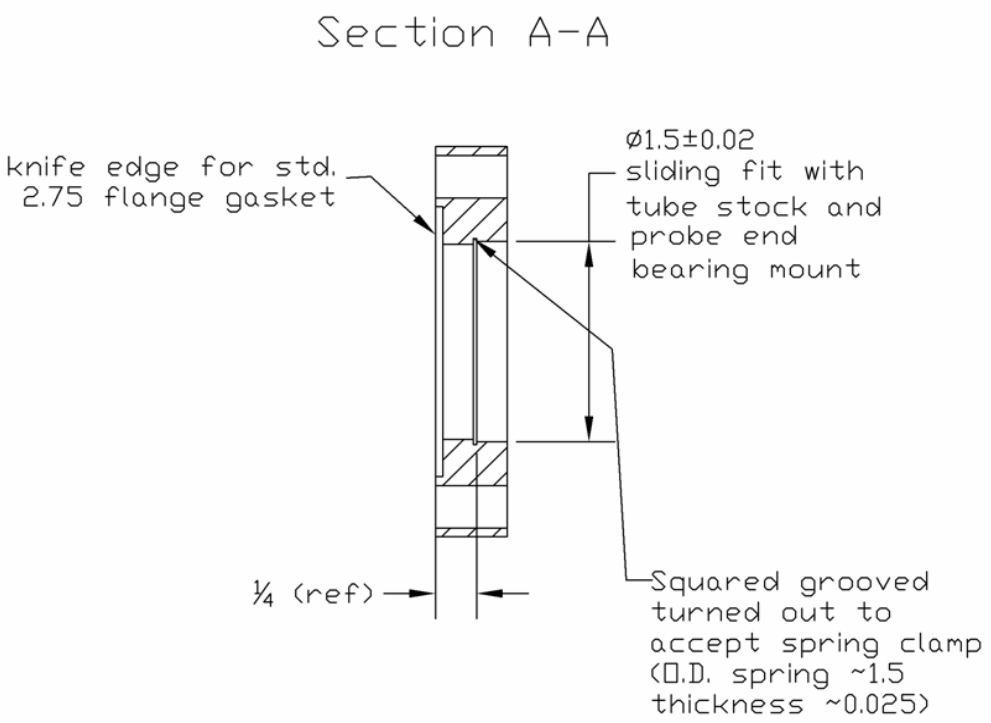

MALDI Source Magnetic Insertion Probe Parts

Slide Bearing Ring Holder – Bearings Seat Along Perimeter Groove

stainless steel

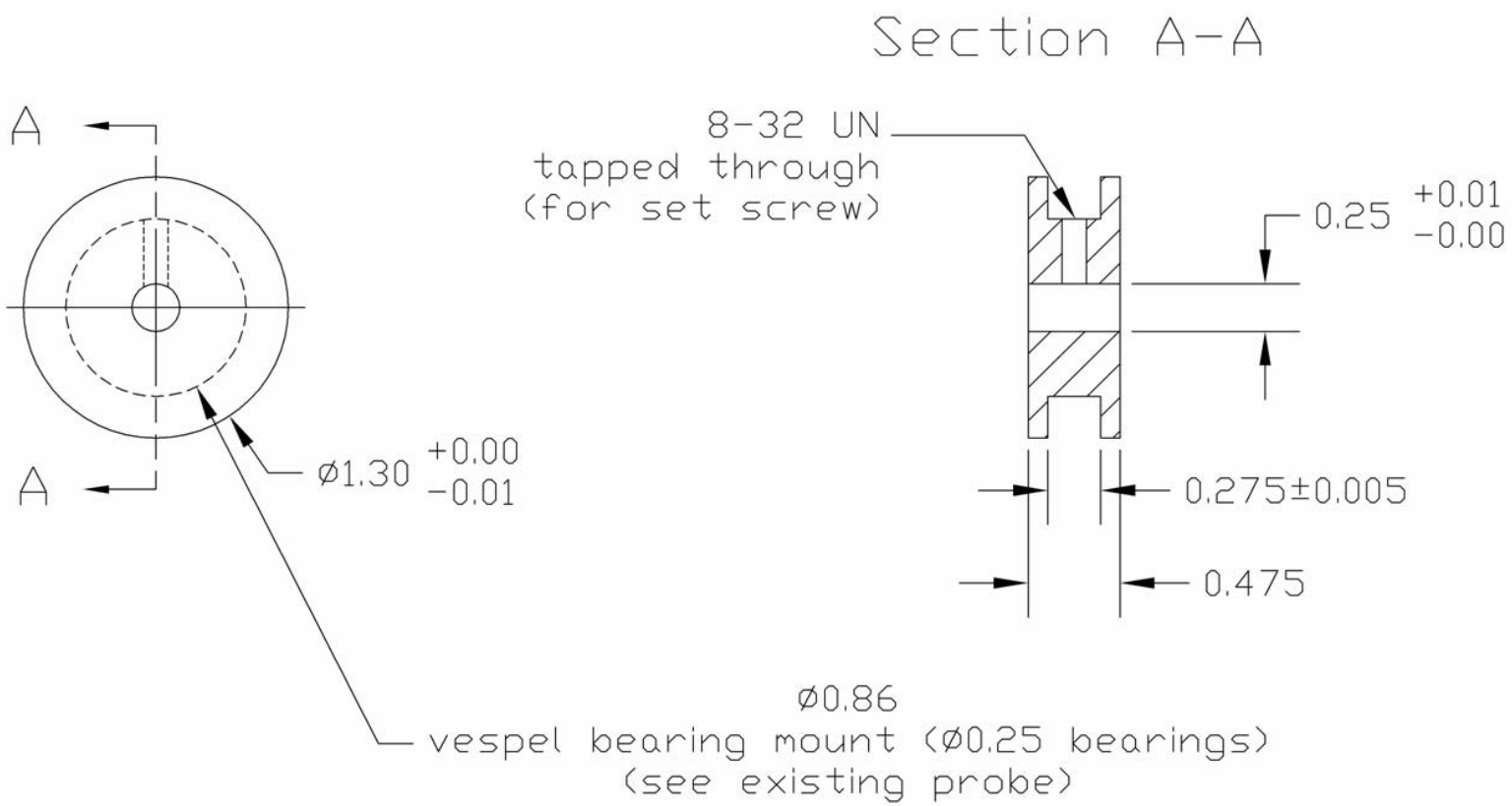

MALDI Source Magnetic Insertion Probe Parts

Magnetic Slug for Coupling – Accepts Rod Arm

magnetic steel

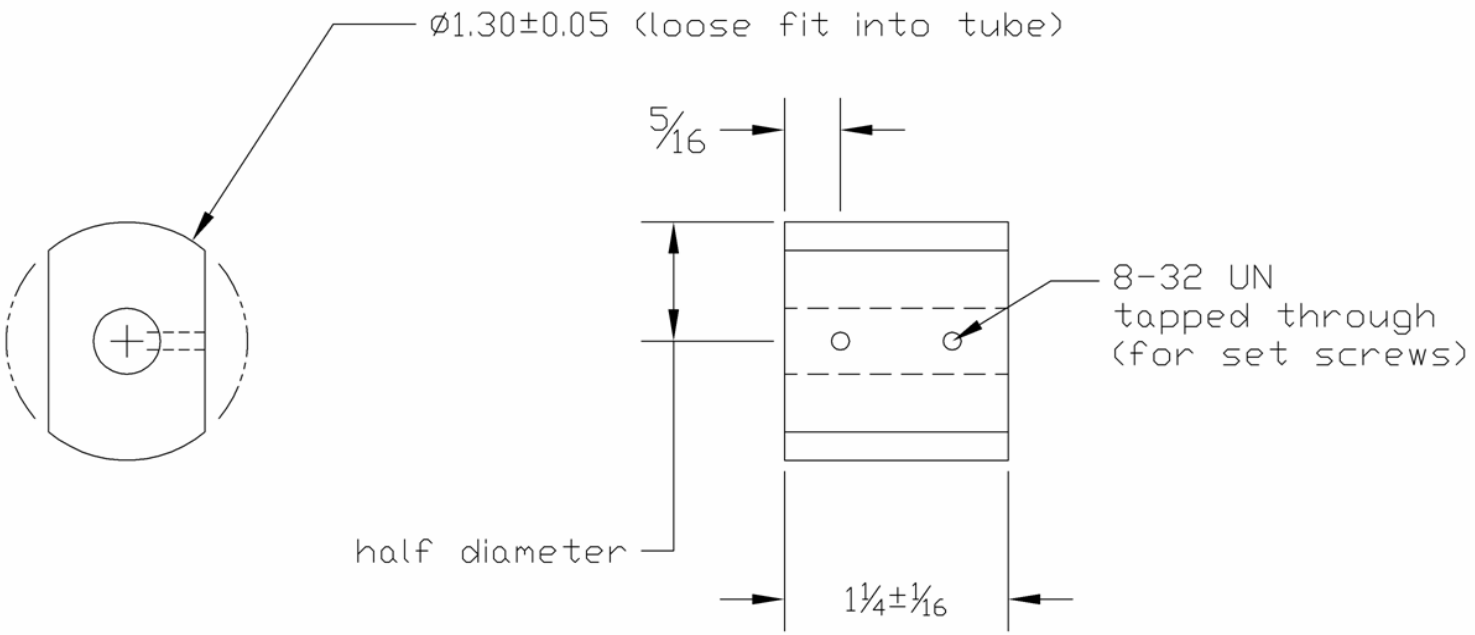

MALDI Source Insertion Probe Rod Parts

Main Insertion Rod & Insulating Segment

stainless steel
polyamide-imide (Torlon®)

NOT TO SCALE

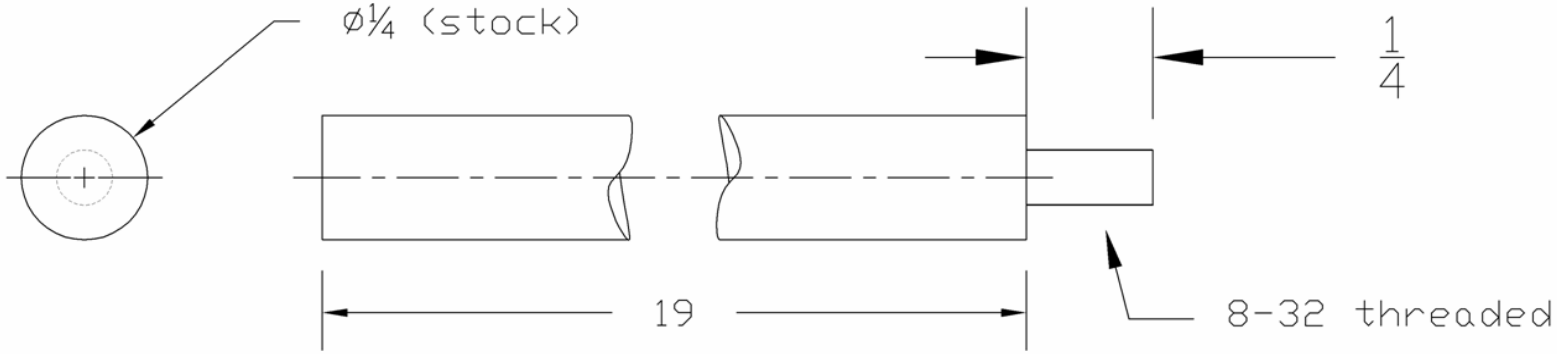

Probe Rod

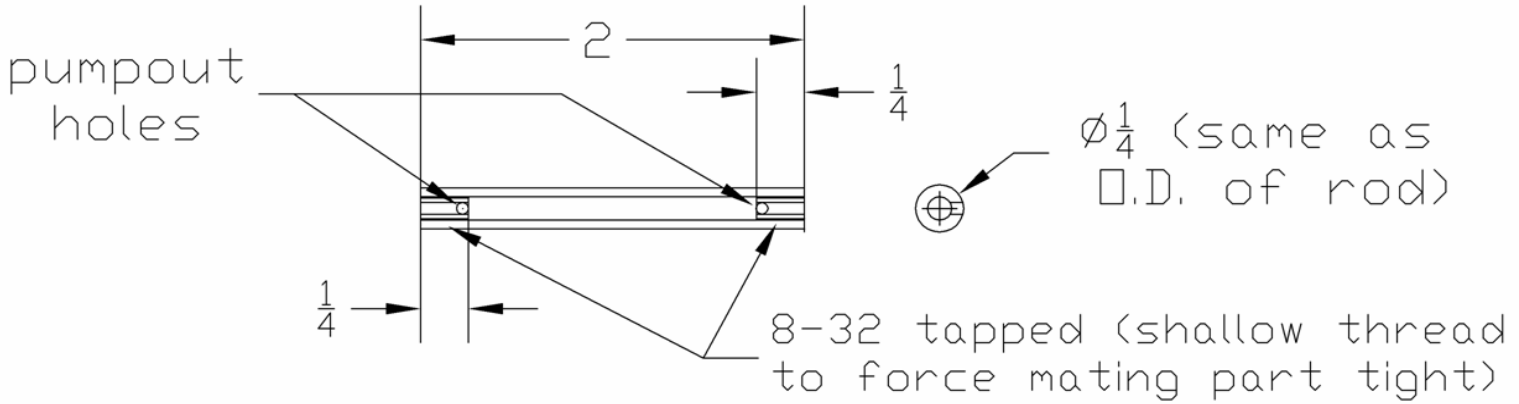

Insulating Section (Torlon®)

MALDI Source Sample Puck Parts
Repeller Plate Insulating Posts

Rotating Sample Puck & Attachment Arm; Mounting Posts for Repeller Plate

stainless steel
polyamide-imide (Torlon®)

NOT TO SCALE

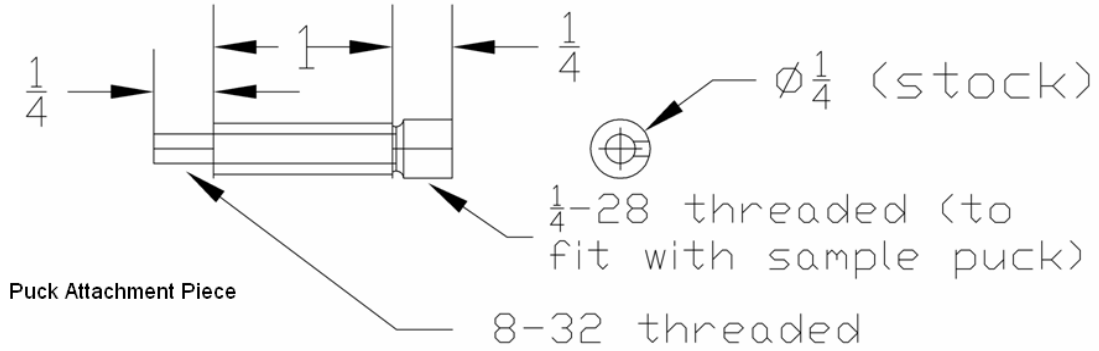

Puck Attachment Piece

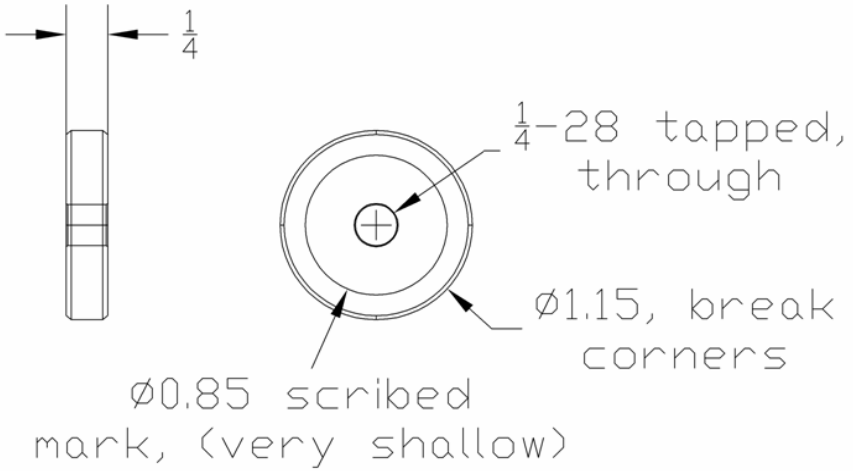

Sample Puck

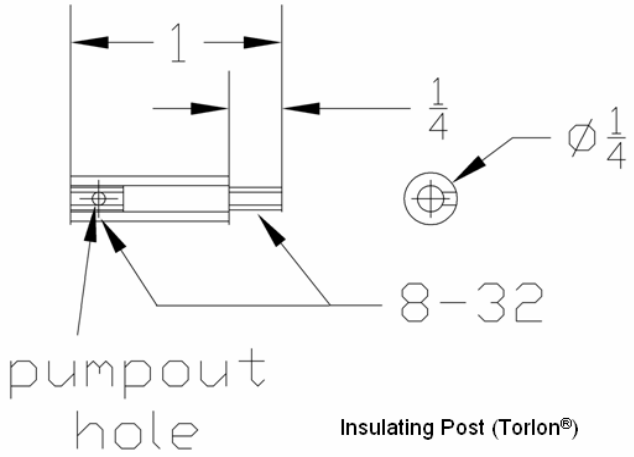

Insulating Post (Torlon®)

MALDI Source Insertion Probe Pumpout Chamber

Low Profile 2 ¾" x 1⅓ " Conflat® Compatible Cross

stainless steel

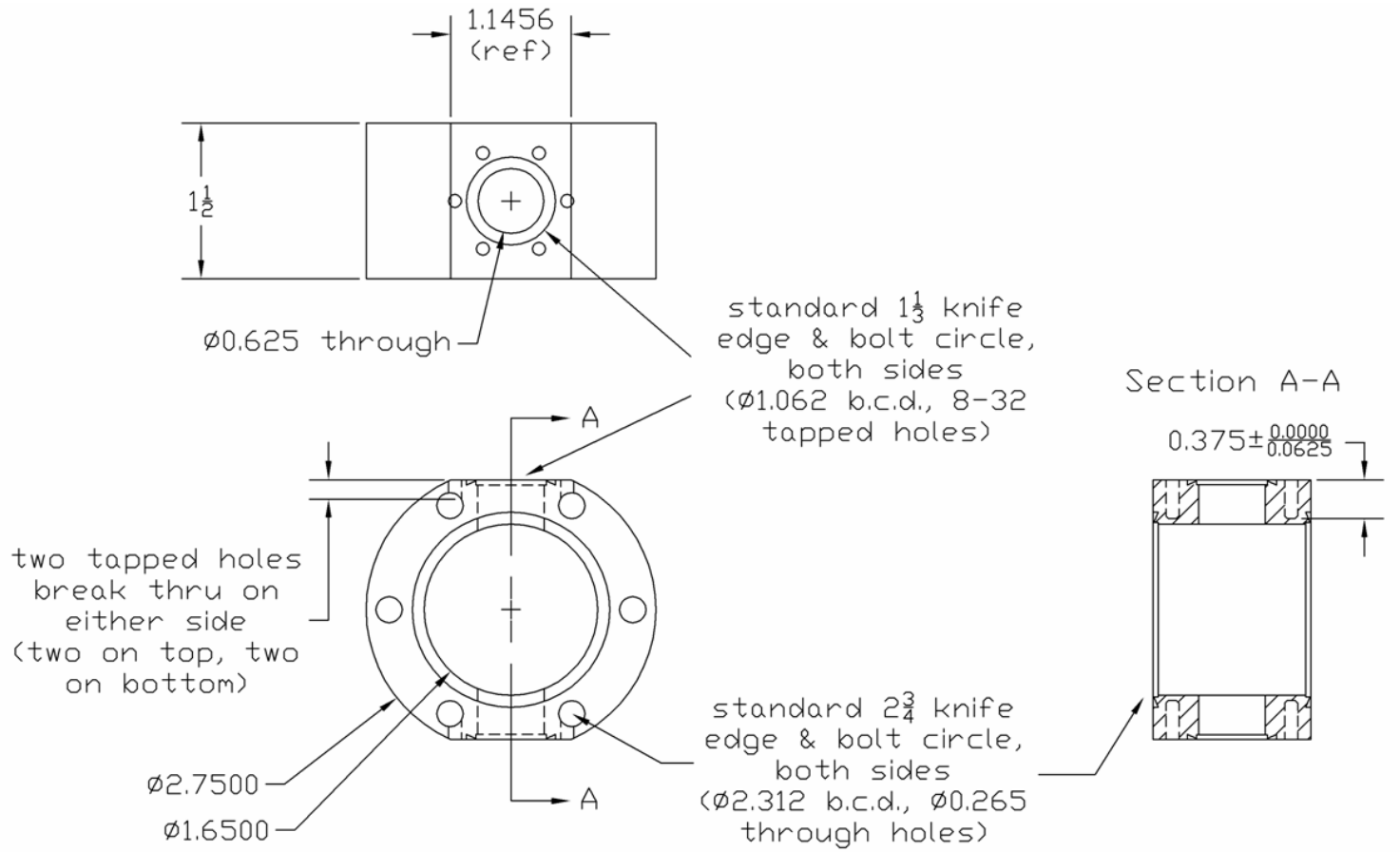

MALDI Source Repeller Plate

Allows Flush Insertion & Electrical Connection of Sample Puck

stainless steel

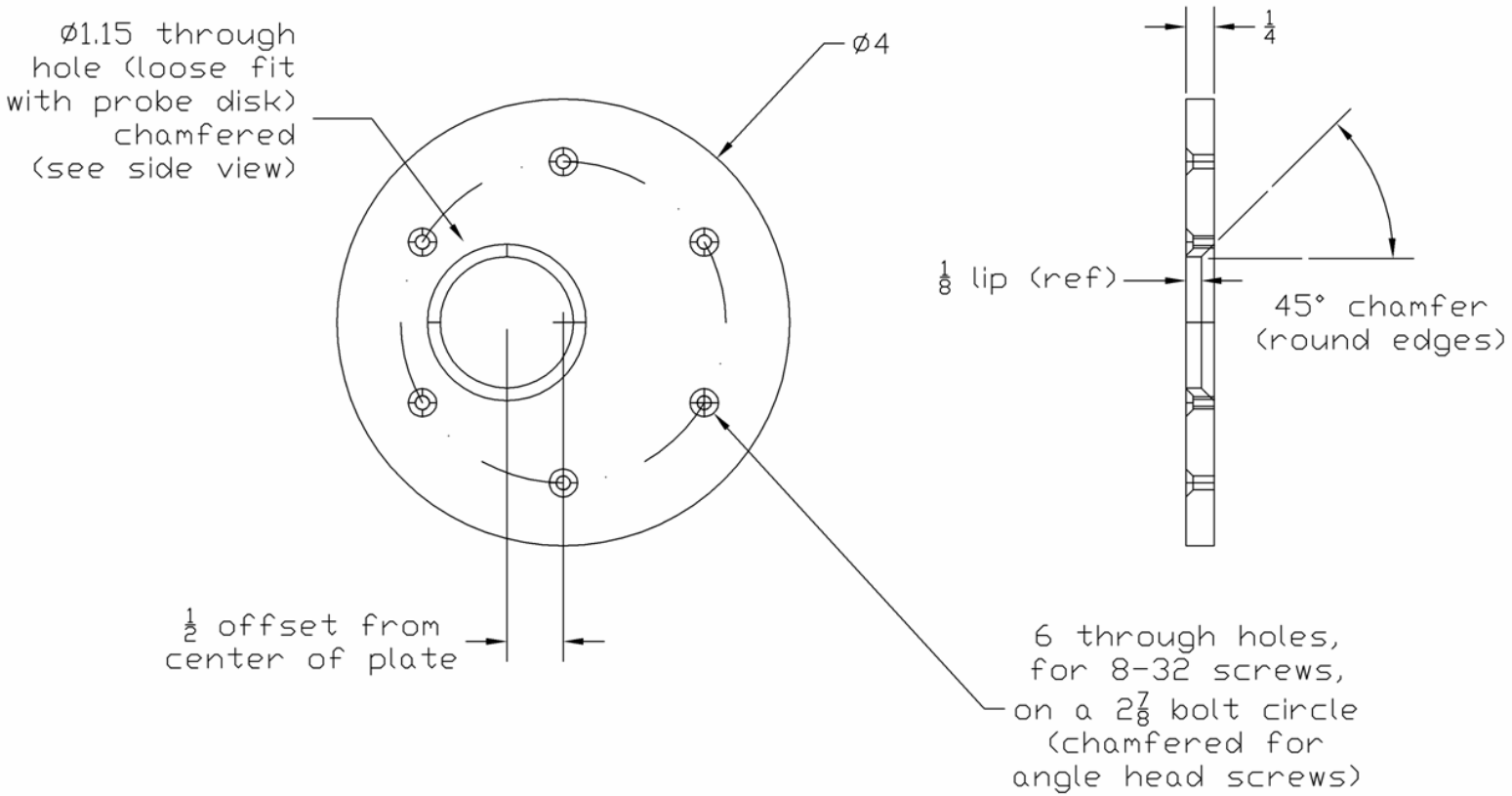

MALDI Source Laser Neutral Density Filter Slides

Custom Mounting System for Stand-Alone NDF Elements – Enables Precise Selection of Density

aluminum

NOT TO SCALE

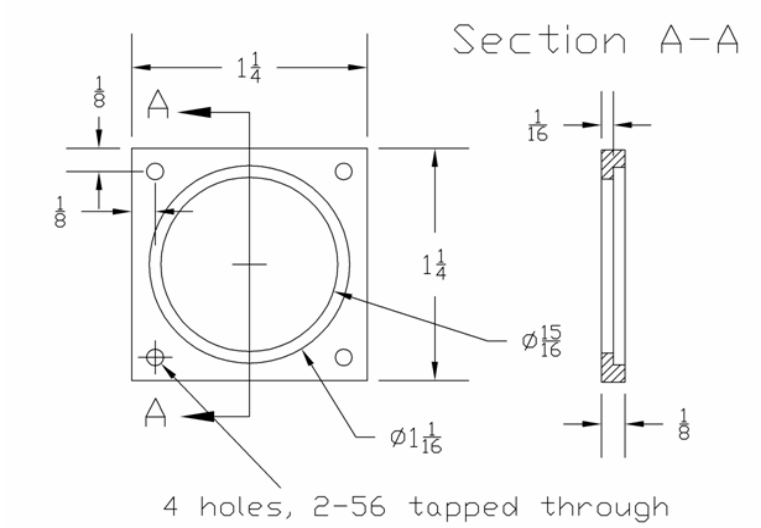

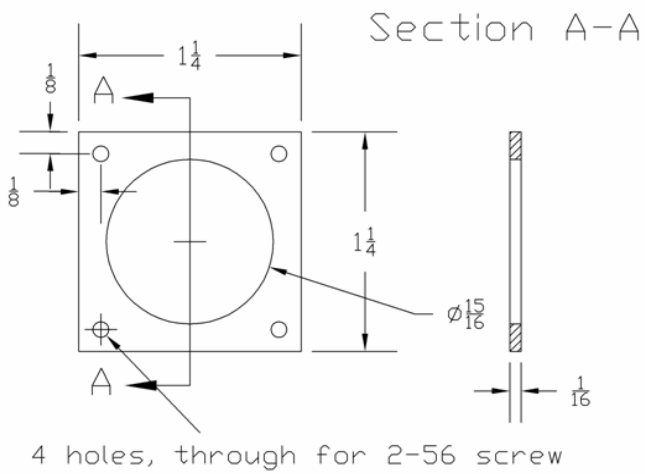

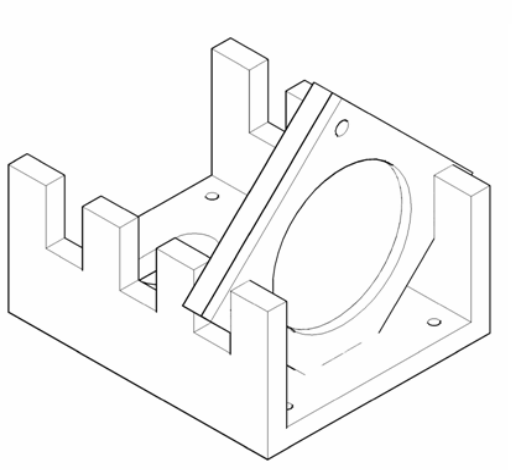

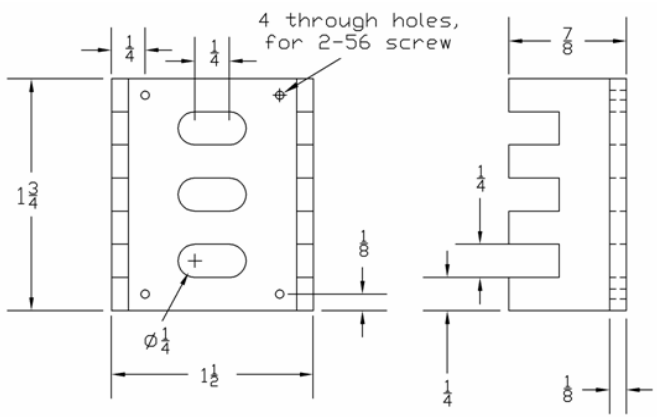

MALDI Source Laser Lens Mounting Cap

Slides onto Existing 2¾" Conflat® Viewing Port

aluminum

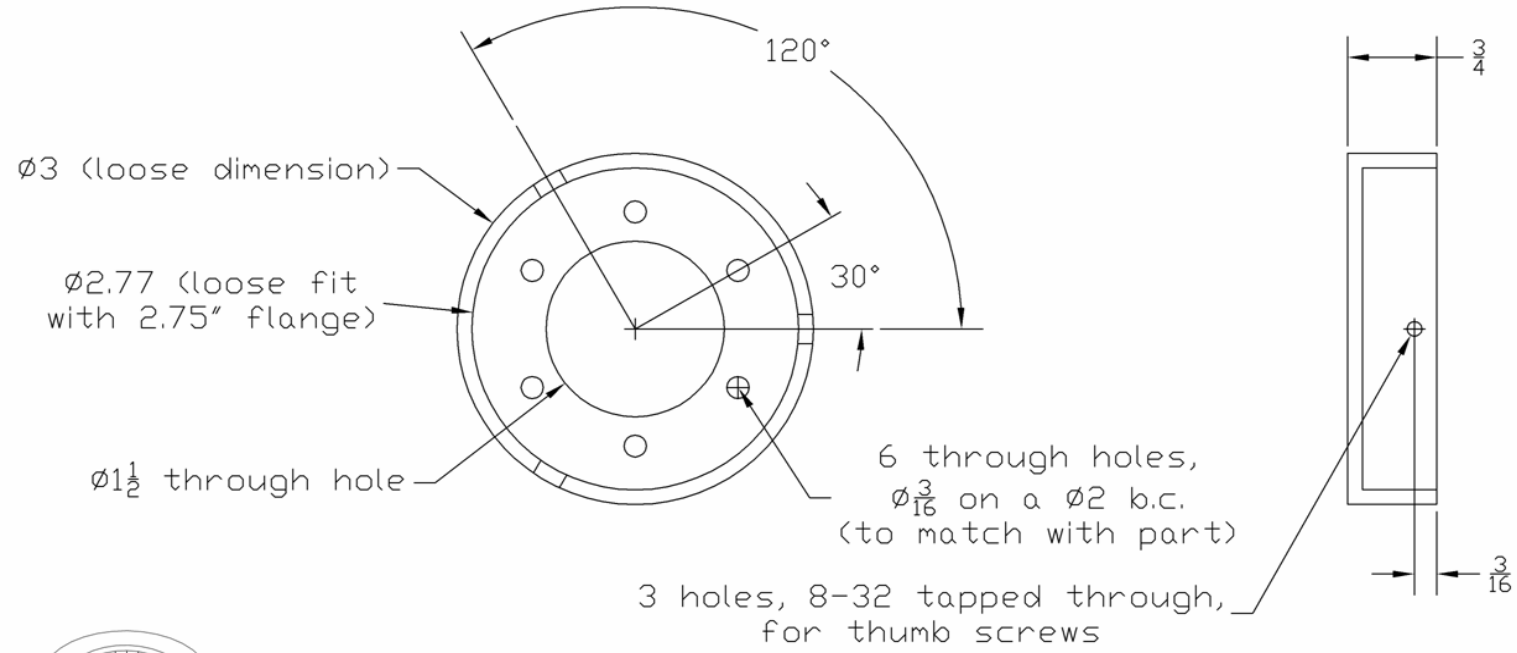

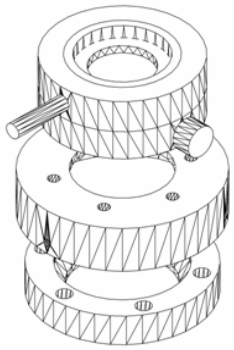

lens adjustment assembly

mounting cap (shown above)

viewport

ESI-Ion Funnel Source

Assembly Diagram

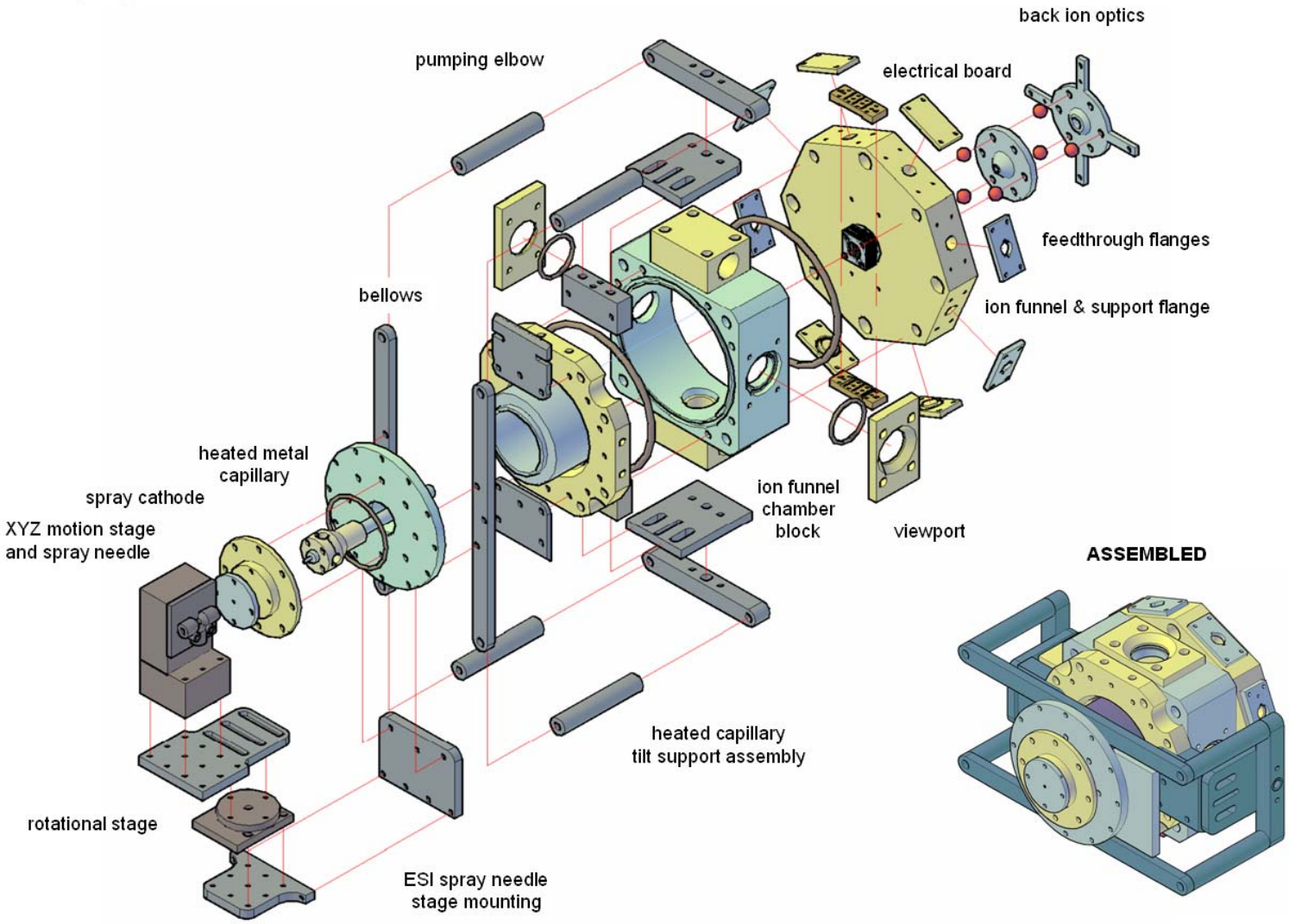

ESI Source – Spray Needle XYZ Stage Support

Mounts XYZ Stage with Bread Board and Rotational Stage with Slotted Holes

aluminum

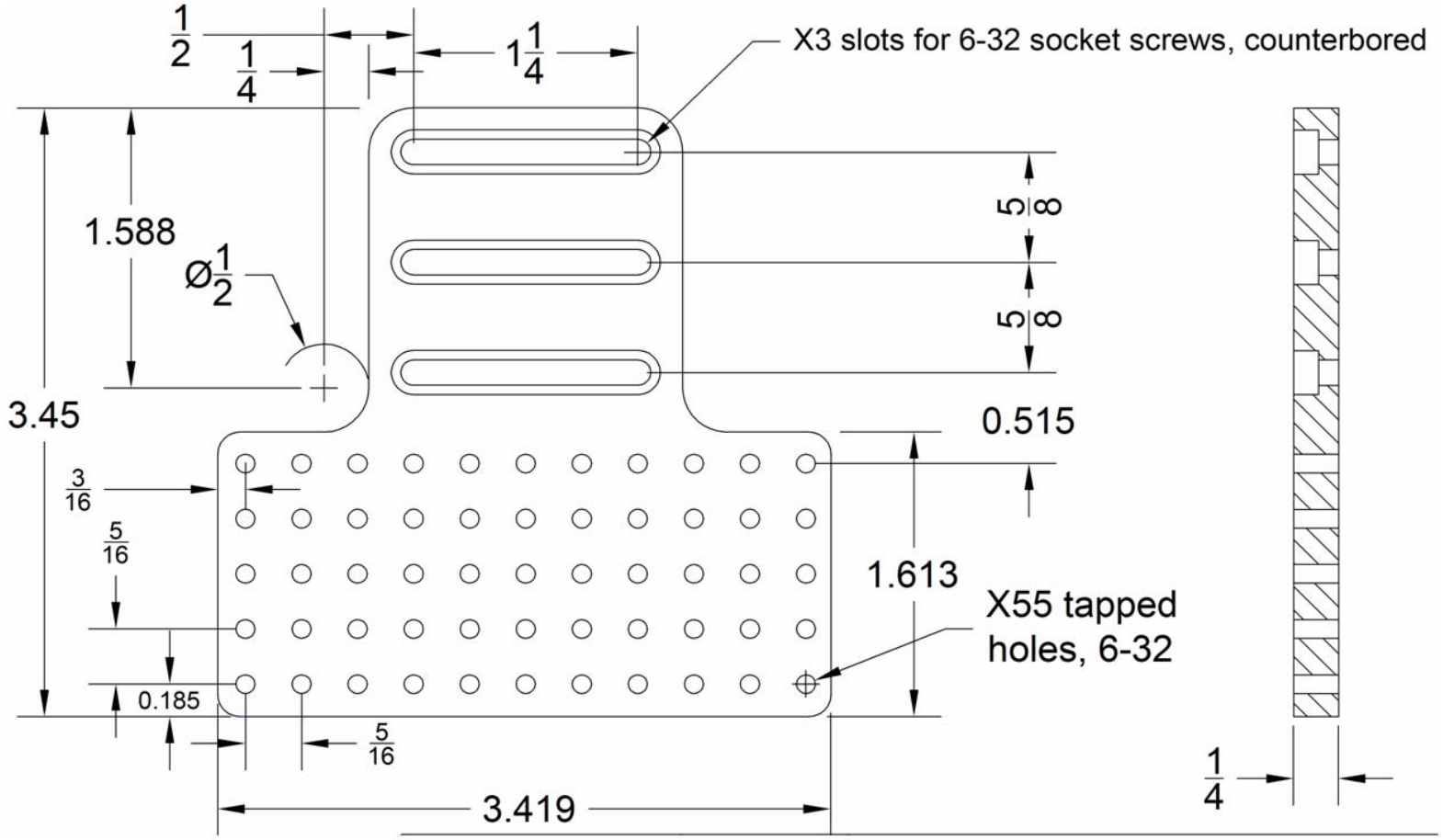

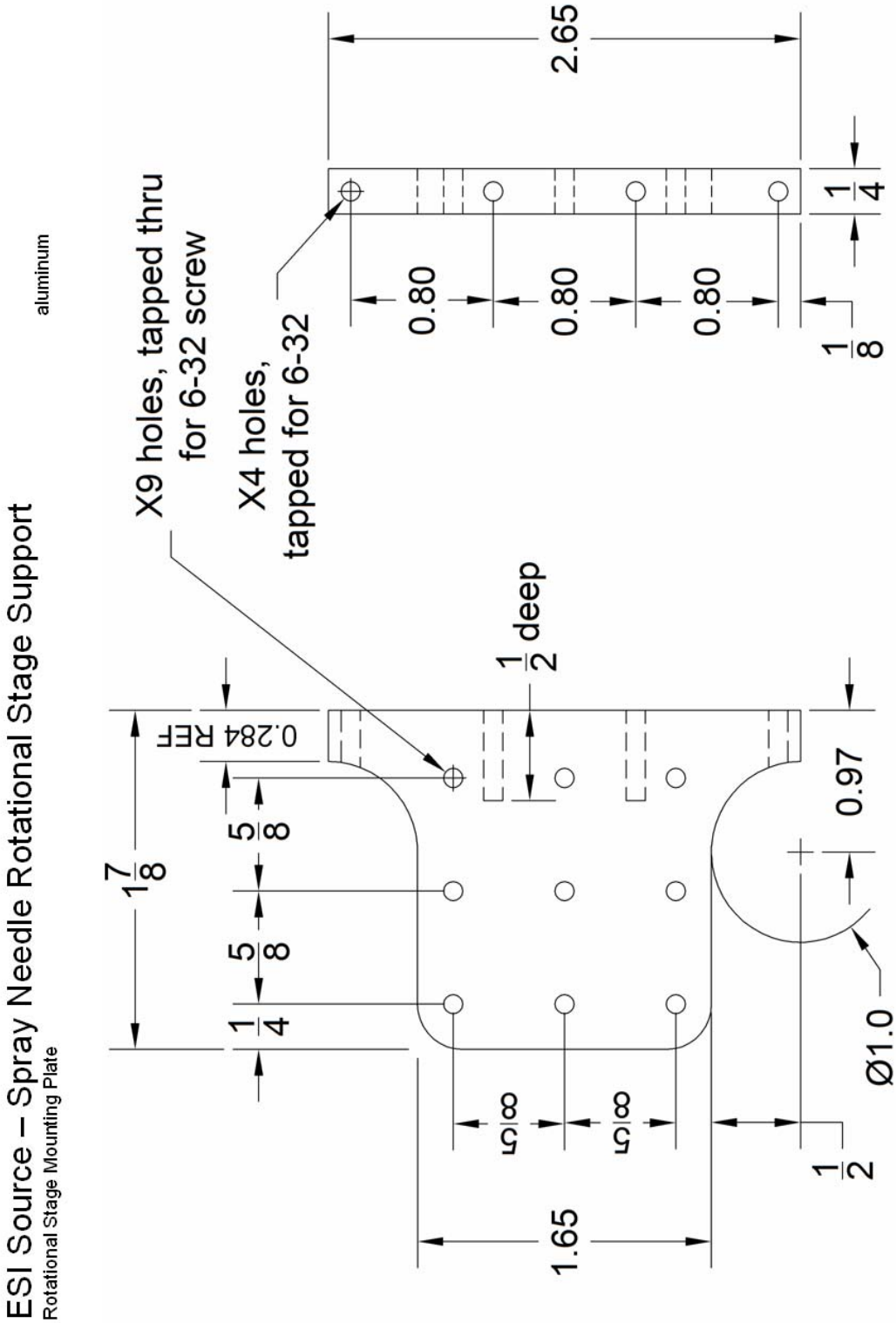
ESI Source – Spray Needle Rotational Stage Support
Rotational Stage Mounting Plate
aluminum
X9 holes, tapped thru for 6-32 screw
X4 holes, tapped for 6-32
2.65
0.80
0.80
0.80
1/4
1/8
1/2 deep
0.284 REF
1 7/8
5/8
5/8
1/4
0.97
Ø1.0
1/2
1.65

ESI Source – Spray Needle to ESI Flange Plate

Mounts Motion Stage Assembly to Main Source Body

aluminum

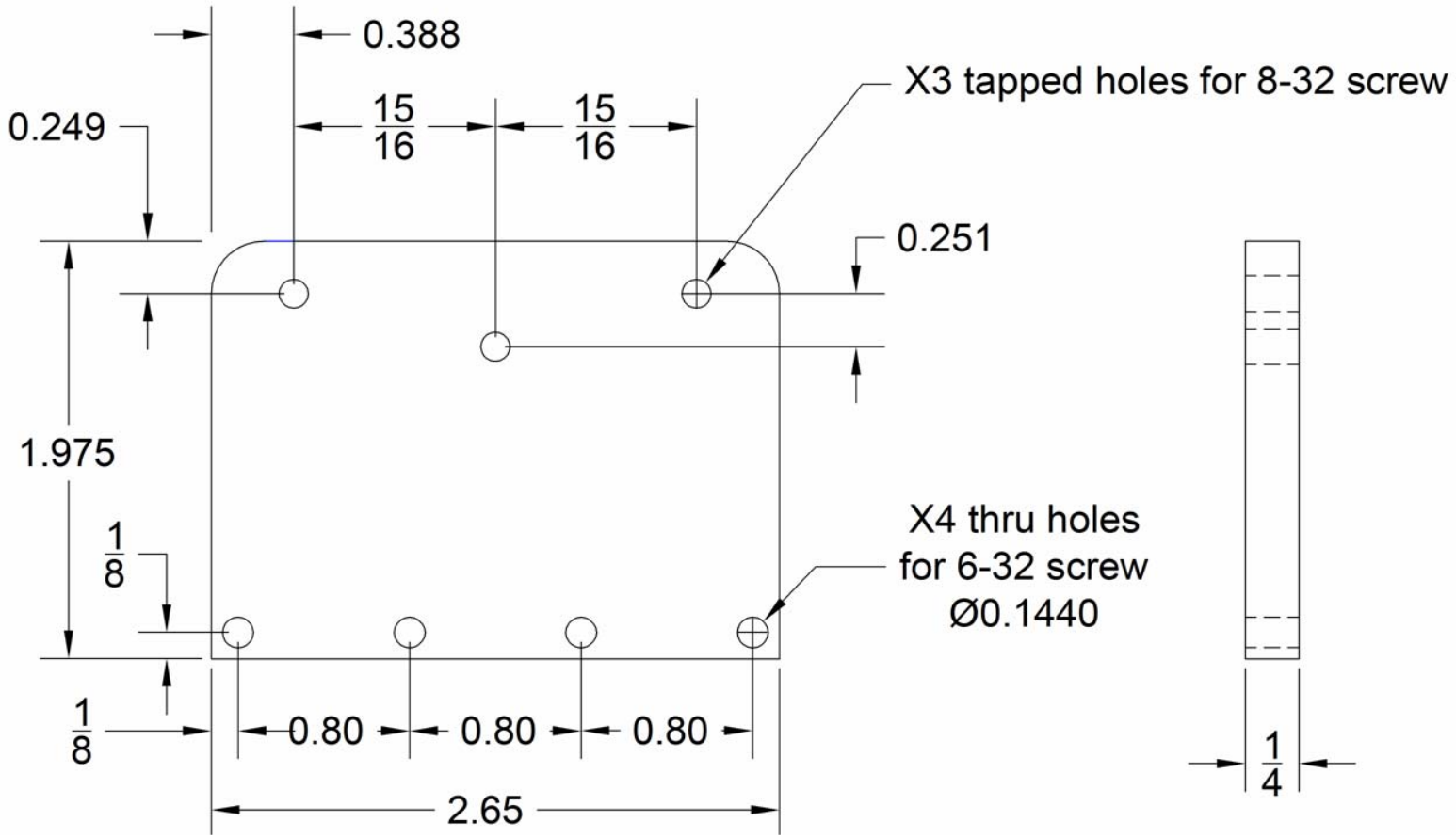

ESI Source – Spray Needle Cathode Disk

Cathode Electrode for Spray – Insert Hole for Heated Capillary Cartridge

stainless steel

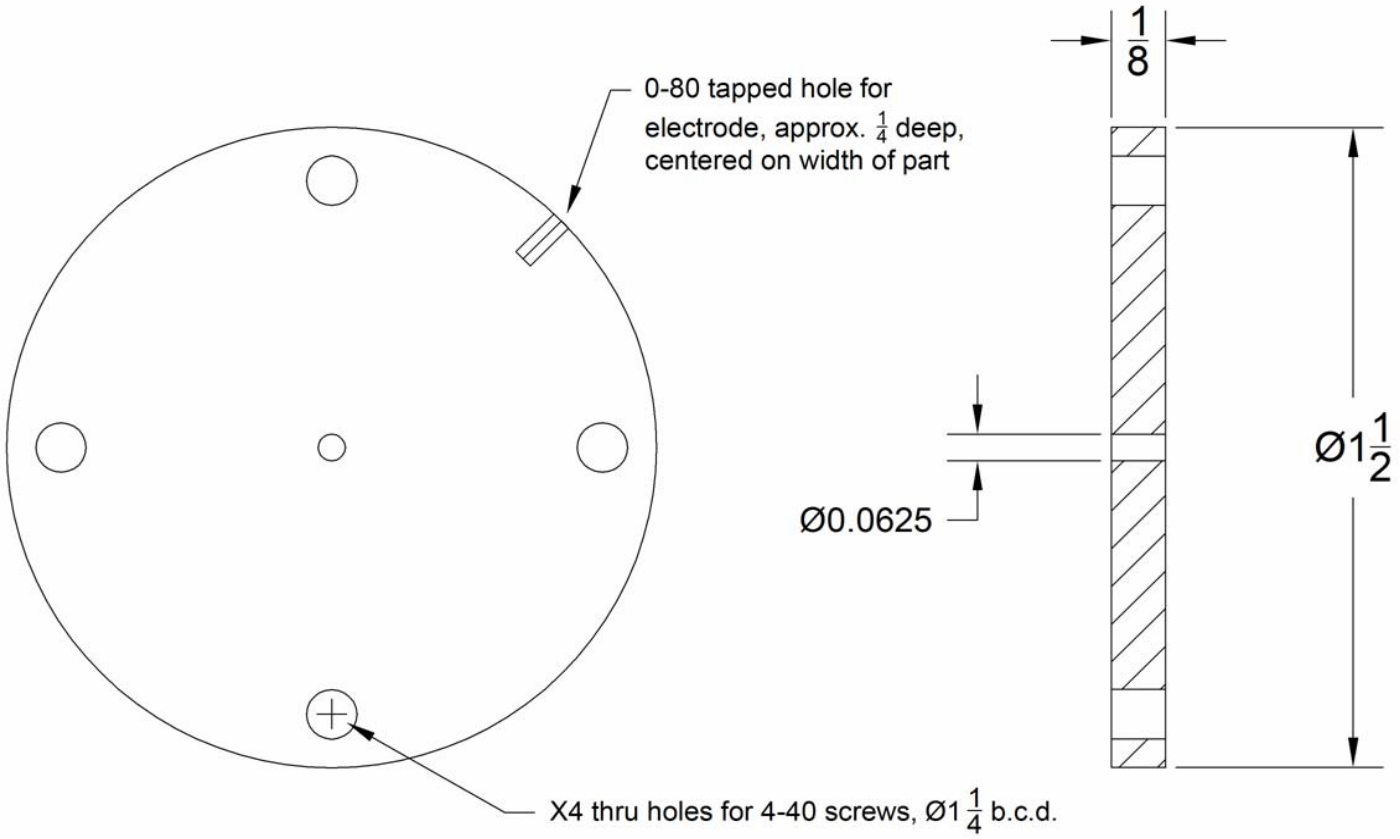

ESI Source – Heated Capillary Compression Flange

Flange to Electrically Isolate Spray Cathode and Apply Compressive Force to Capillary Assembly

polyoxymethylene (Delrin®)

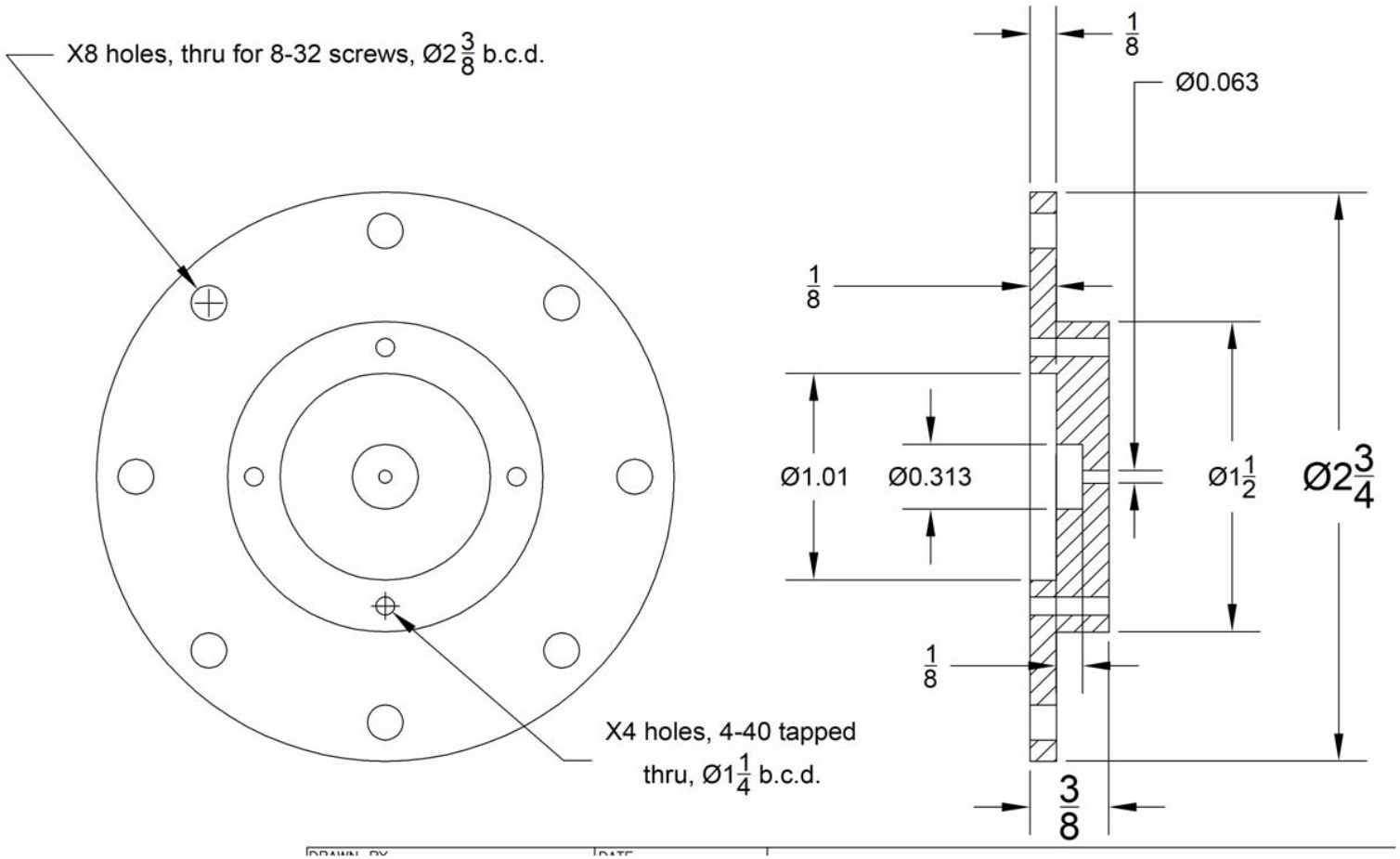

ESI Source – Heated Capillary Compression Flange 2

Modification to Compression Flange to Access Capillary Housing Screws

polyoxymethylene (Delrin®)

modify existing part as shown

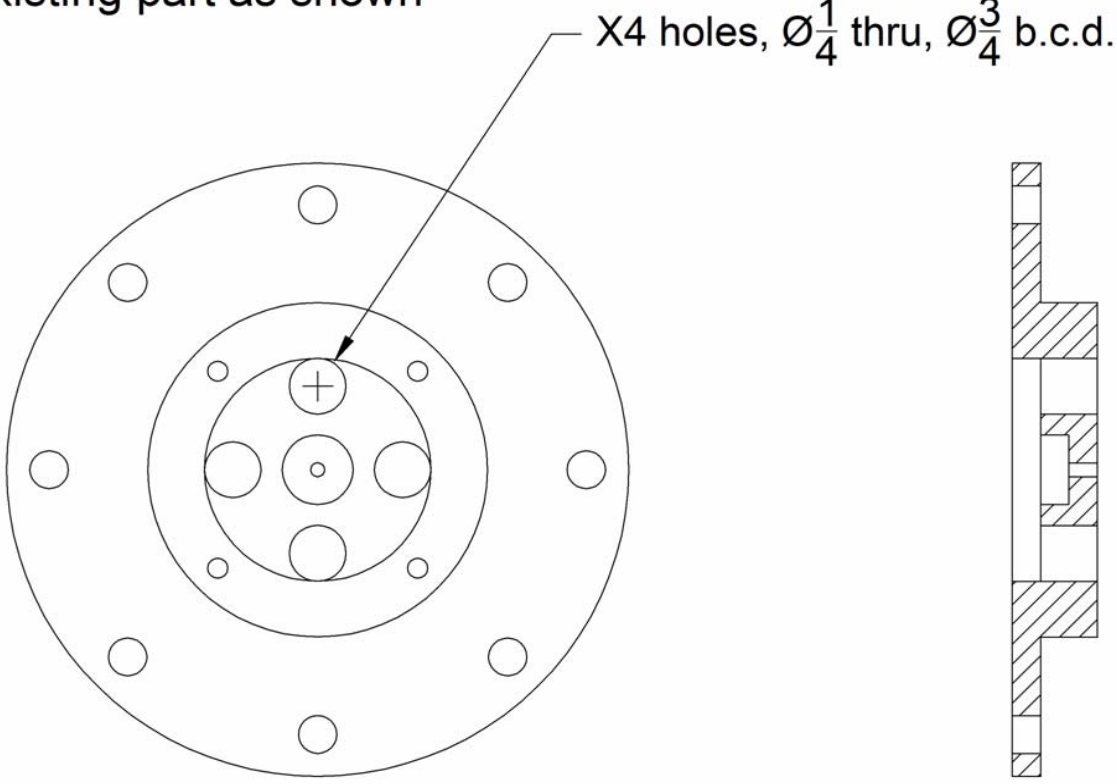

ESI Source – Heated Capillary Thermal Cap

Endcap to Aid in Thermally Isolating Capillary End

polytetrafluoroethylene (PTFE Teflon®)

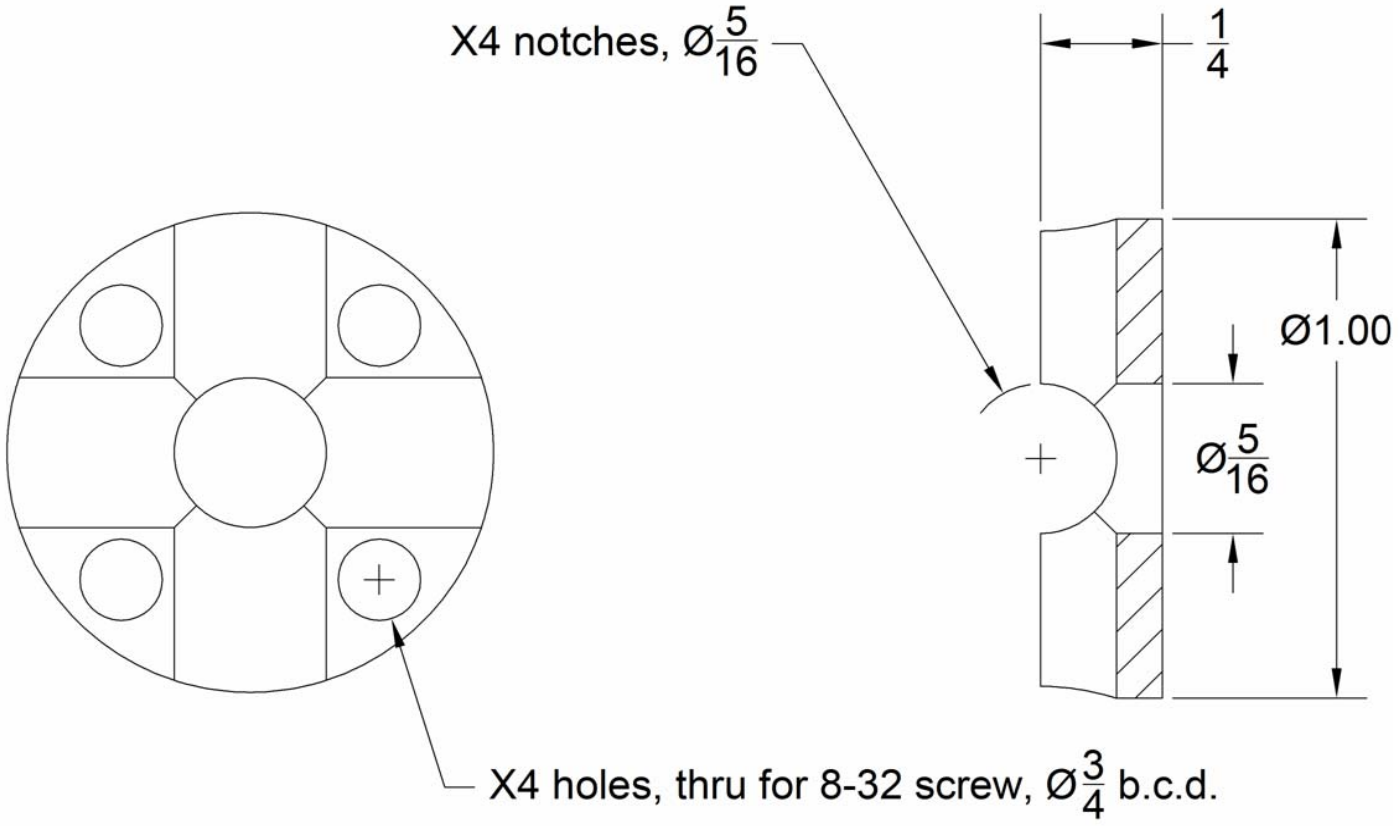

ESI Source – Heated Capillary Thermal Tube

Tube for Thermally Isolating Capillary and Provides Pressure Assisted Sealing of Chamber

polytetrafluoroethylene (PTFE Teflon®)

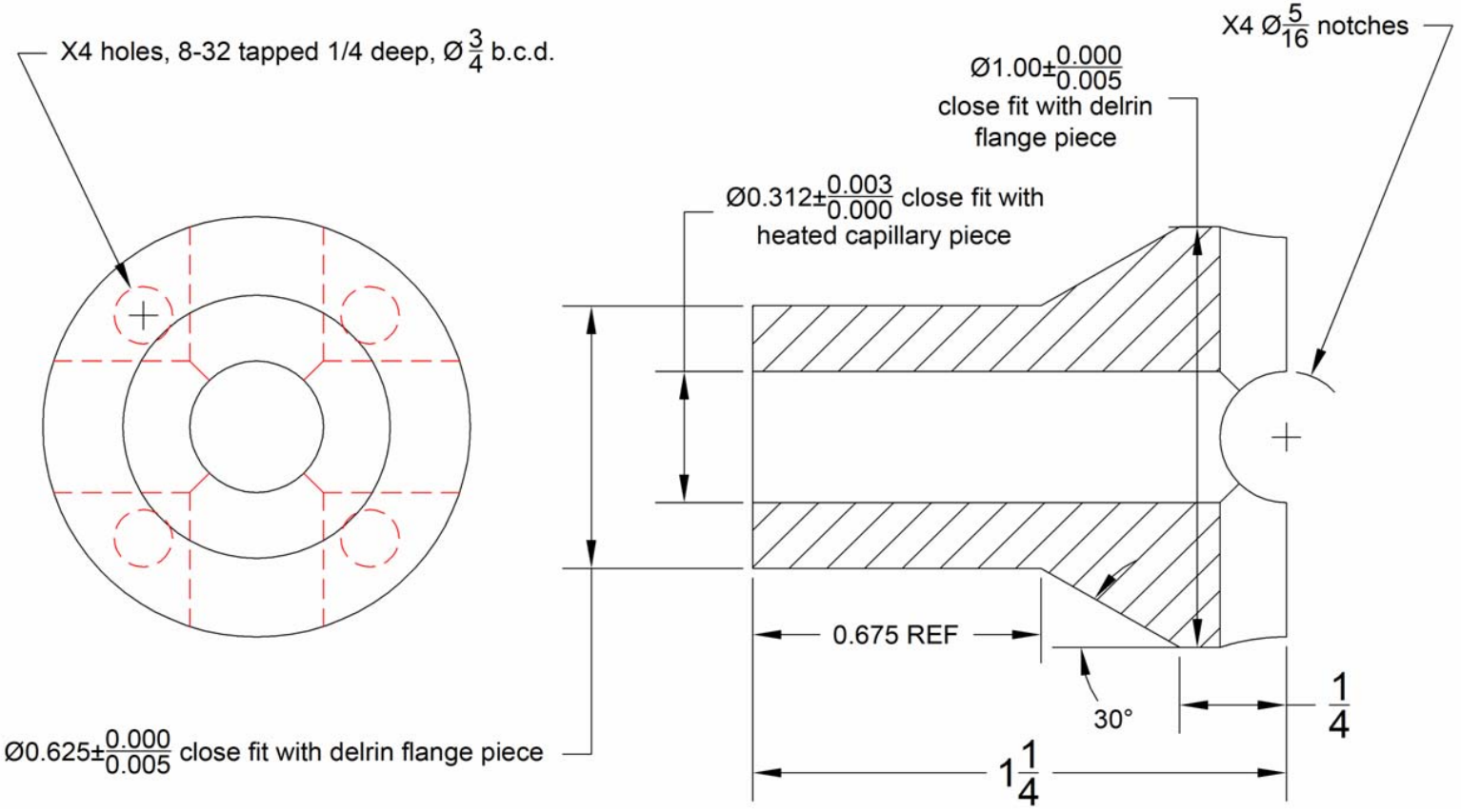

ESI Source – Heated Capillary Bellows Flange - Small

End Flange for Stainless Steel Bellows – Tapped Holes to Compress Capillary Assembly

stainless steel

NOTE: flanges must align relative to one another when welded onto bellows piece

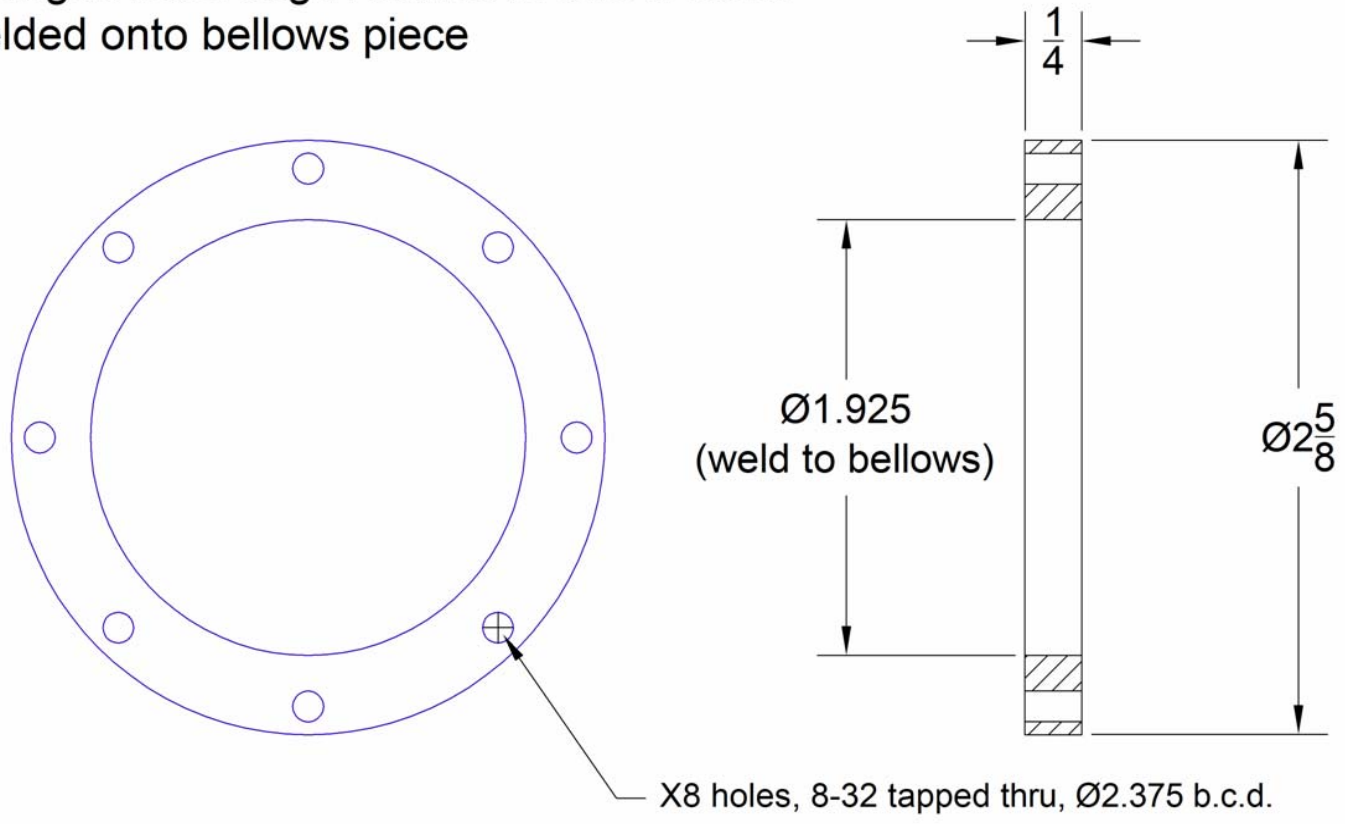

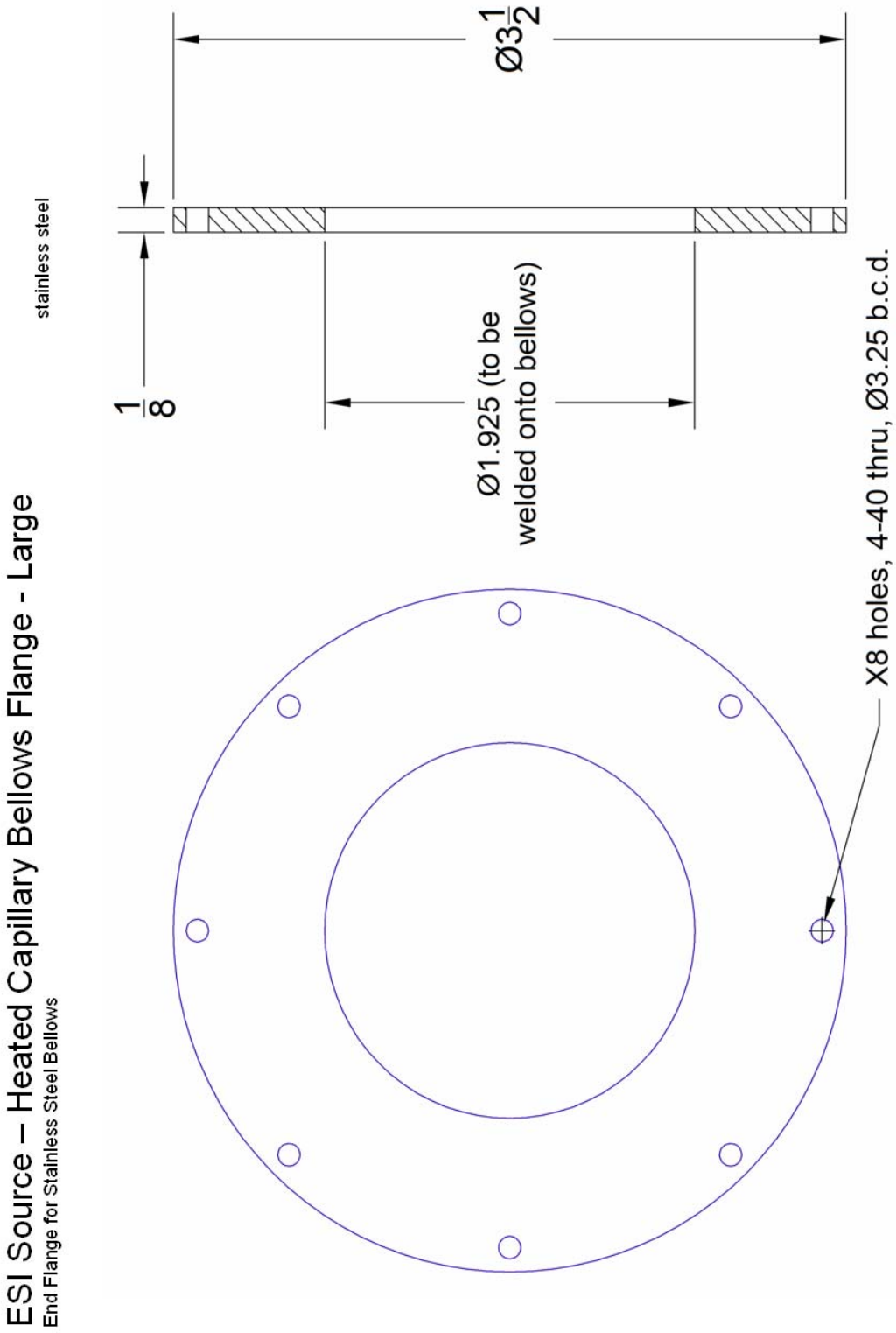
ESI Source – Heated Capillary Bellows Flange - Large
End Flange for Stainless Steel Bellows
stainless steel
1/8
Ø1.925 (to be welded onto bellows)
Ø3 1/2
X8 holes, 4-40 thru, Ø3.25 b.c.d.

ESI Source – Heated Capillary Support Flange

Supporting Flange for the Heated Capillary Assembly

aluminum

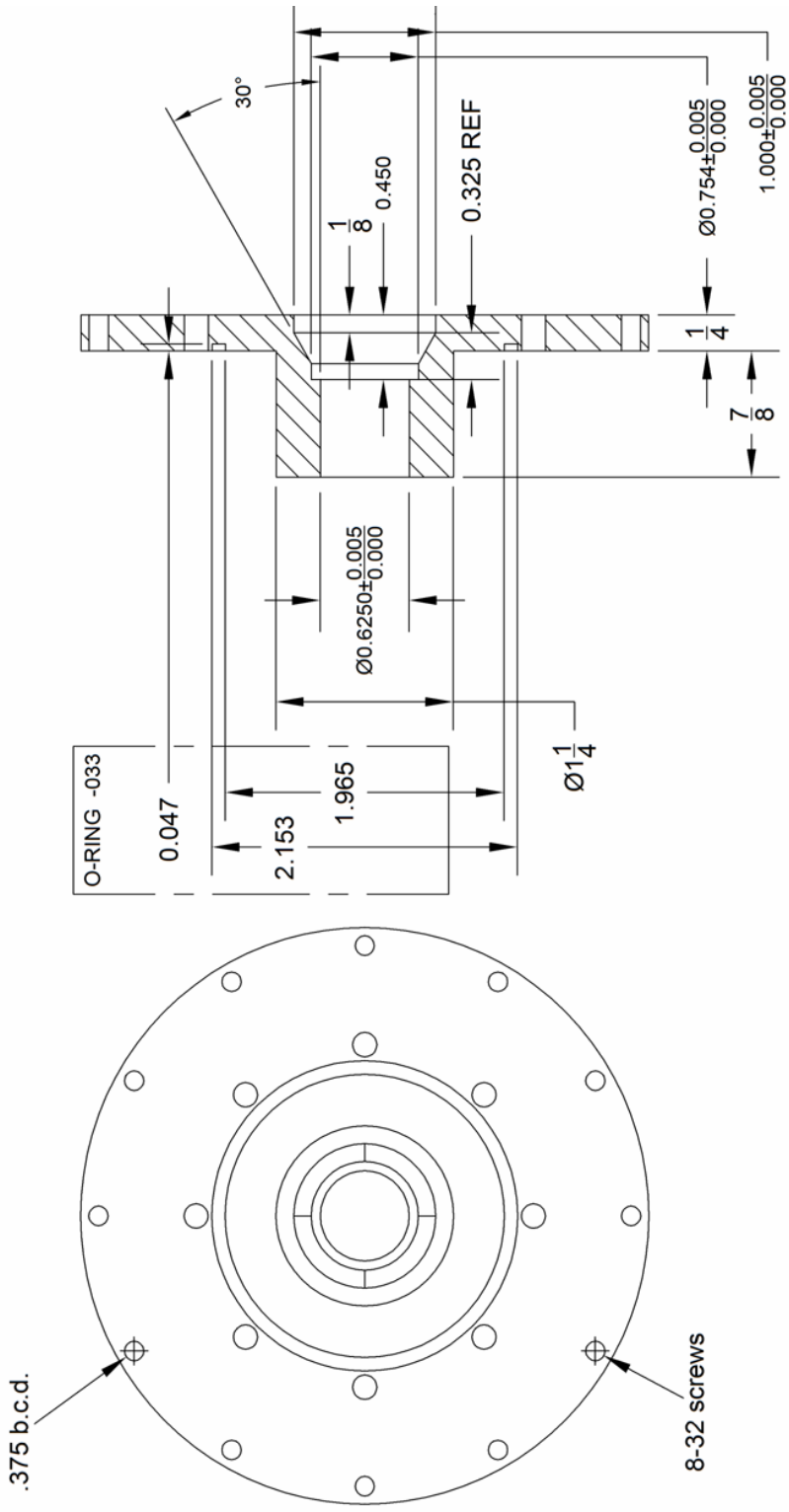

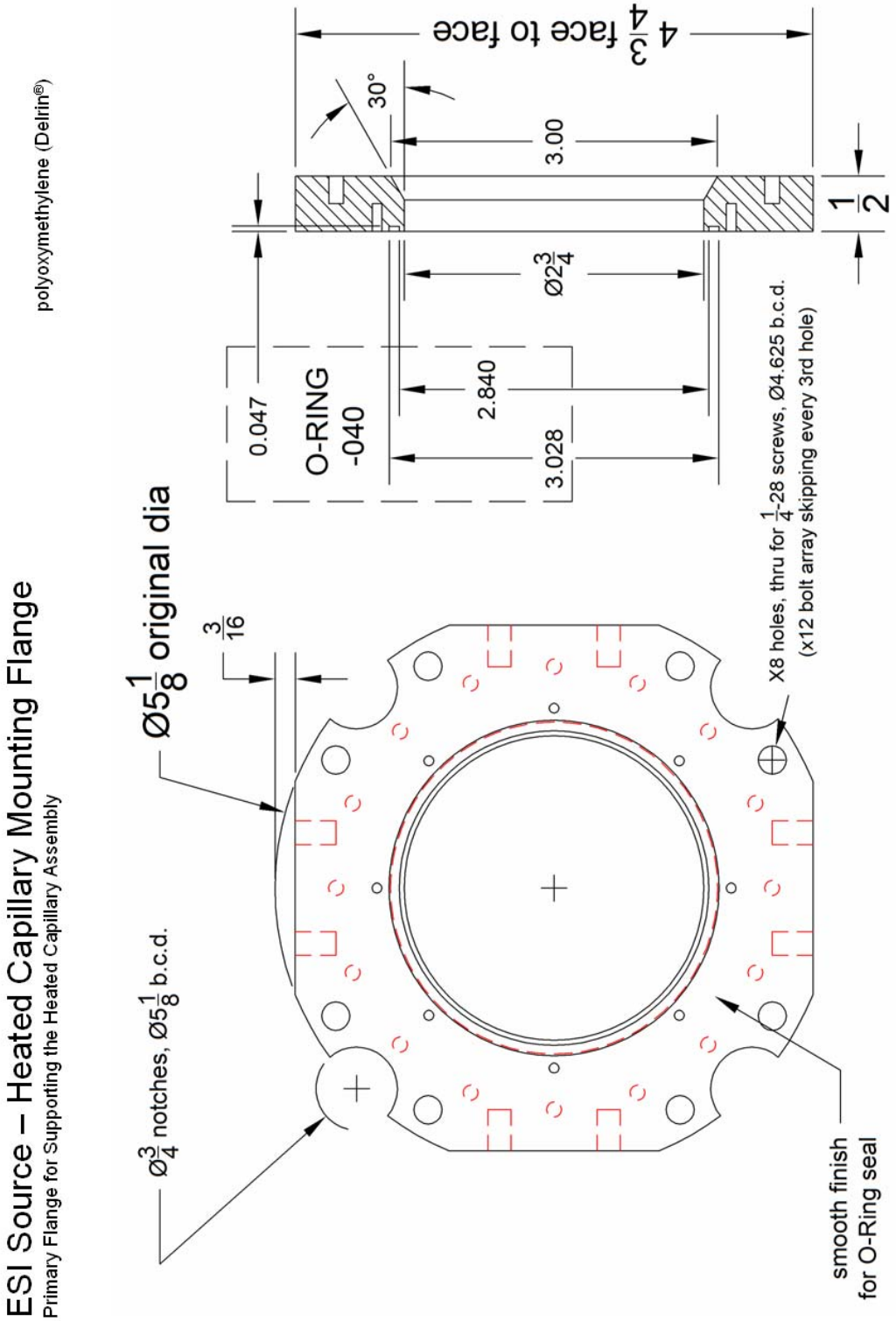
ESI Source – Heated Capillary Mounting Flange
Primary Flange for Supporting the Heated Capillary Assembly
polyoxymethylene (Delrin®)
4 3/4 face to face
30°
3.00
1/2
0.047
O-RING
-040
2.840
3.028
Ø2 3/4
Ø5 1/8 original dia
3/16
Ø3/4 notches, Ø5 1/8 b.c.d.
X8 holes, thru for 1/4-28 screws, Ø4.625 b.c.d.
(x12 bolt array skipping every 3rd hole)
smooth finish
for O-Ring seal

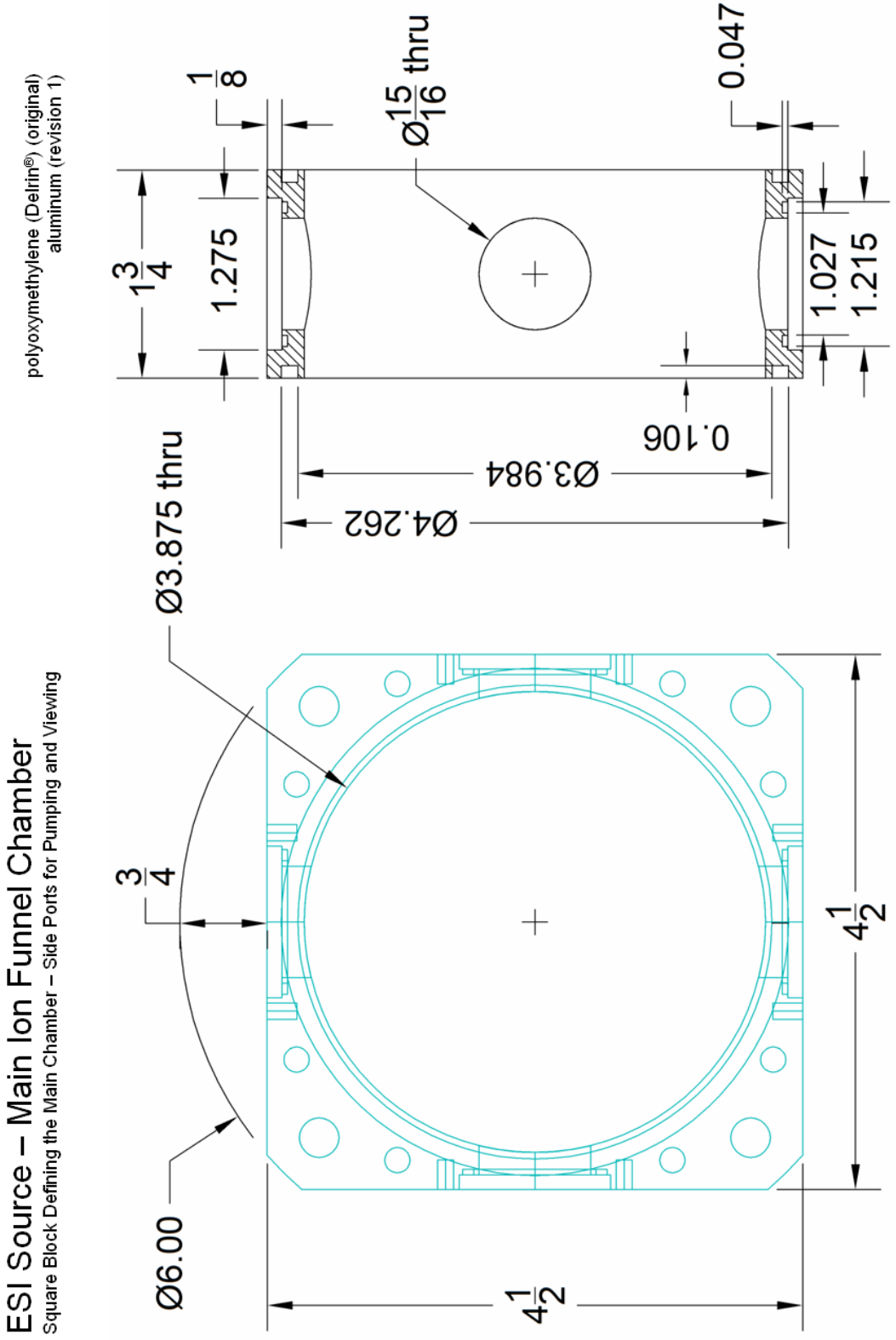
ESI Source – Main Ion Funnel Chamber
Square Block Defining the Main Chamber – Side Ports for Pumping and Viewing
polyoxymethylene (Delrin®) (original)
aluminum (revision 1)
Ø6.00
Ø3.875 thru
3/4
4 1/2
4 1/2
1 3/4
1.275
1/8
Ø15/16 thru
0.047
1.027
1.215
0.106
Ø3.984
Ø4.262

ESI Source – Main Ion Funnel Chamber – Additional Dimensions

Bolt Hole Dimensions

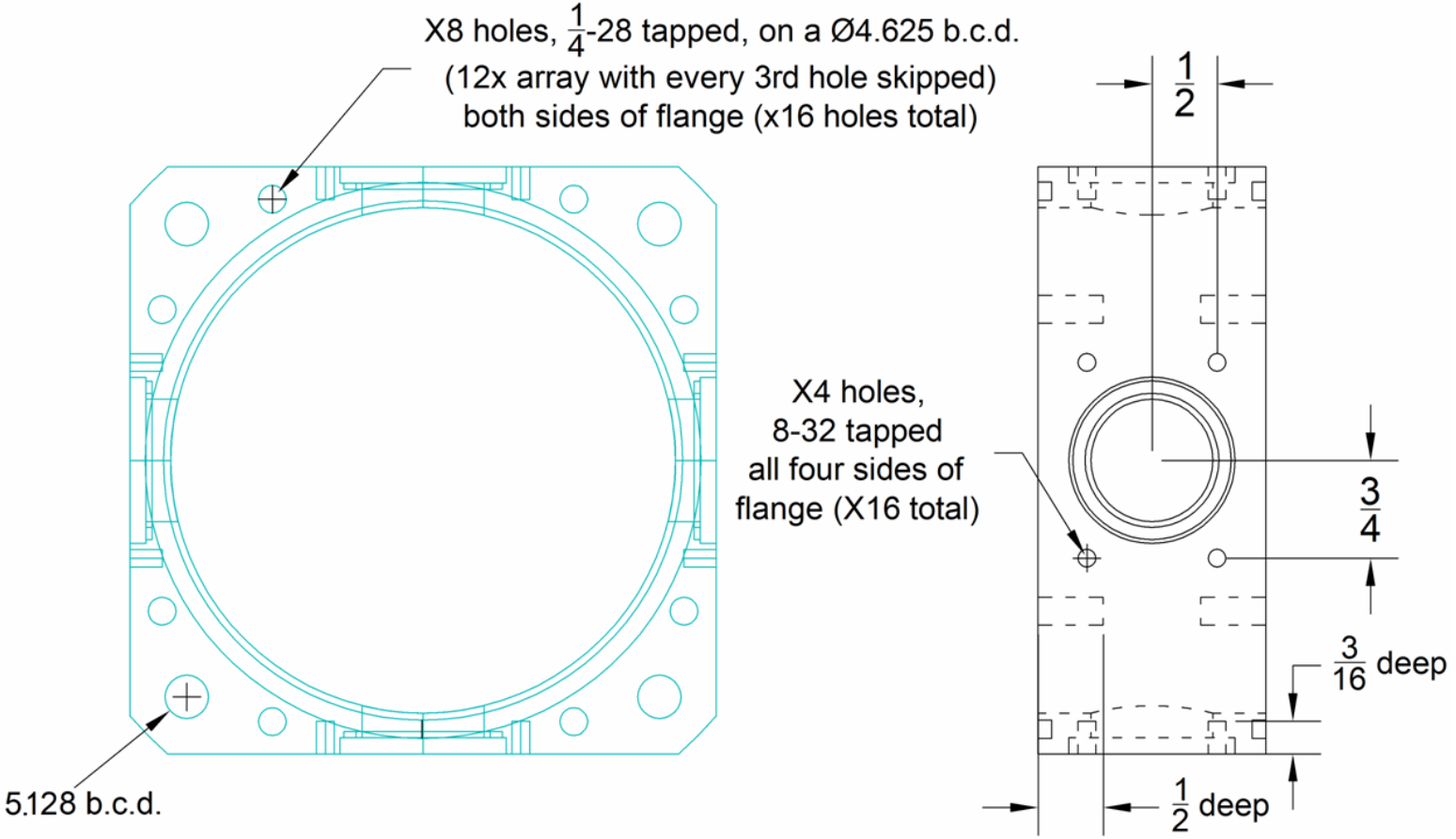

ESI Source – Chamber Block Shielding Cage

Metal Cage Lining to Terminate Field Lines and Prevent Charging of the Viewports and Plastic Block (Original Design)

stainless steel

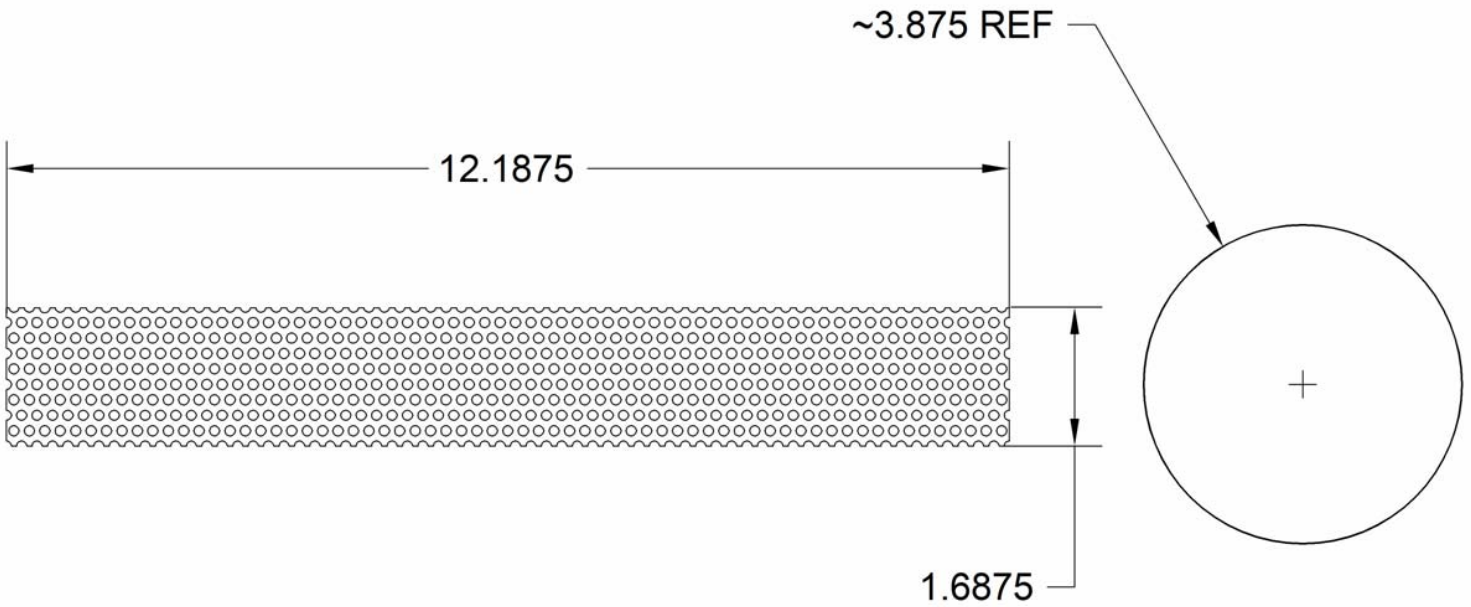

Cut Perforated SST Sheet to dimensions as shown
NOTE: these dimensions correspond to cutting thru centers of perforations

Bend strip into a clean circle as shown above.

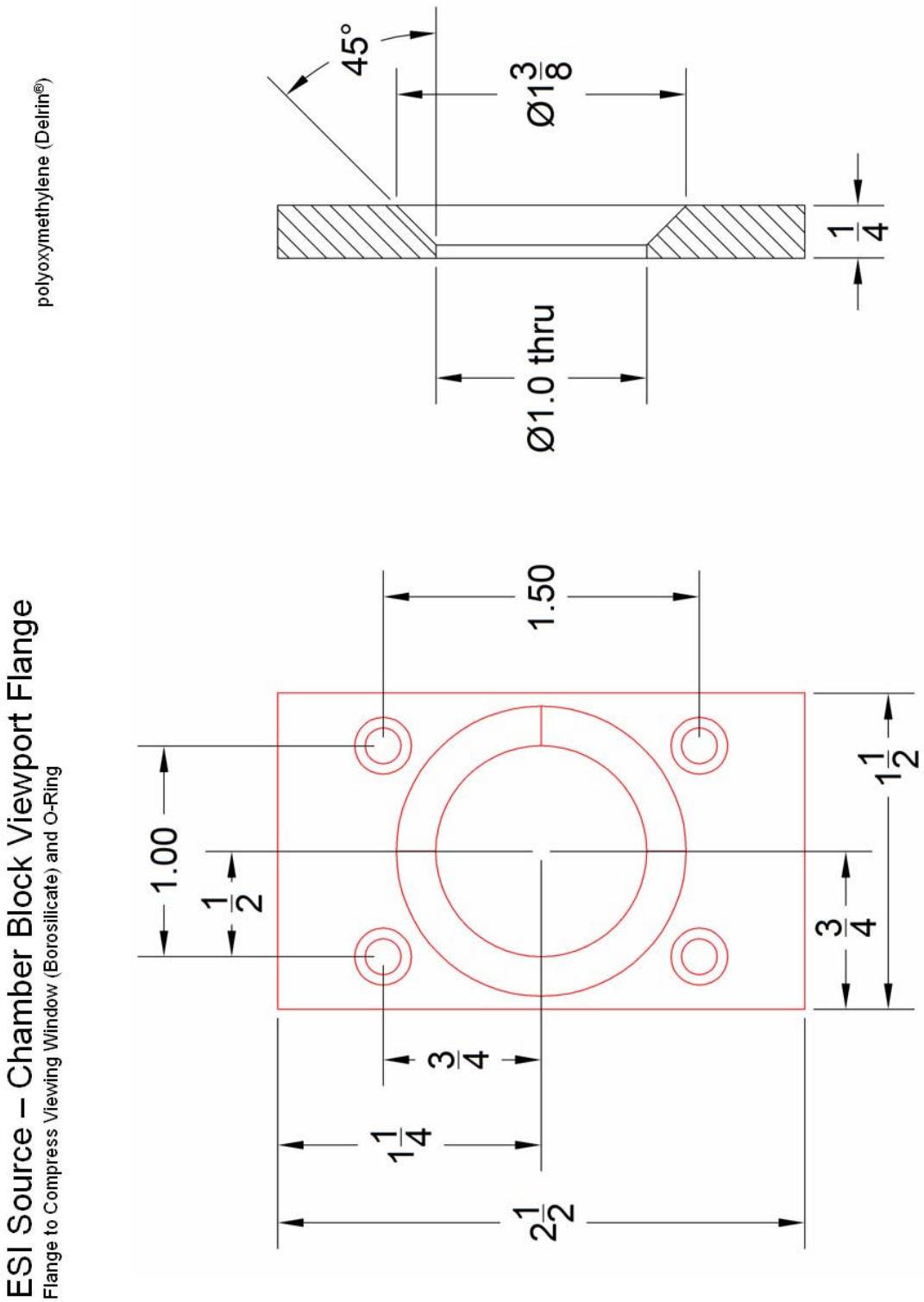
ESI Source – Chamber Block Viewport Flange
Flange to Compress Viewing Window (Borosilicate) and O-Ring
polyoxymethylene (Delrin®)
45°
Ø1 3/8
Ø1.0 thru
1/4
1.00
1/2
1.50
1 1/4
3/4
2 1/2
3/4
1 1/2

ESI Source – Chamber Block Pumping Adapter 90° Bend

Adapter Piece to Attach to Viewport Flange, Converting it to a Pumping Port

polyoxymethylene (Delrin®)

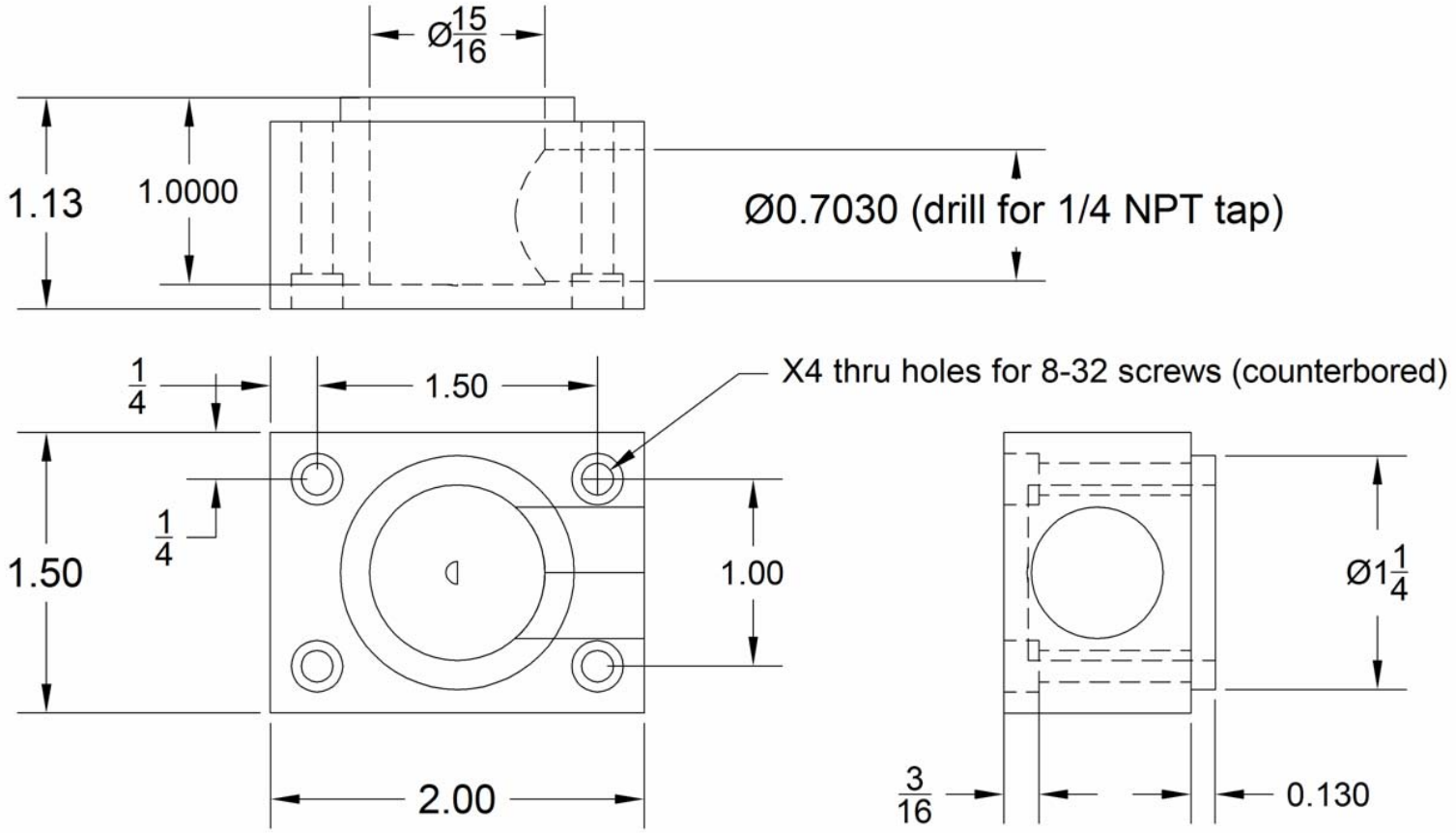

ESI Source – Ion Funnel Support Flange

Primary Support Flange for Ion Funnel Assembly and Voltage Breakouts

polyoxymethylene (Delrin®)

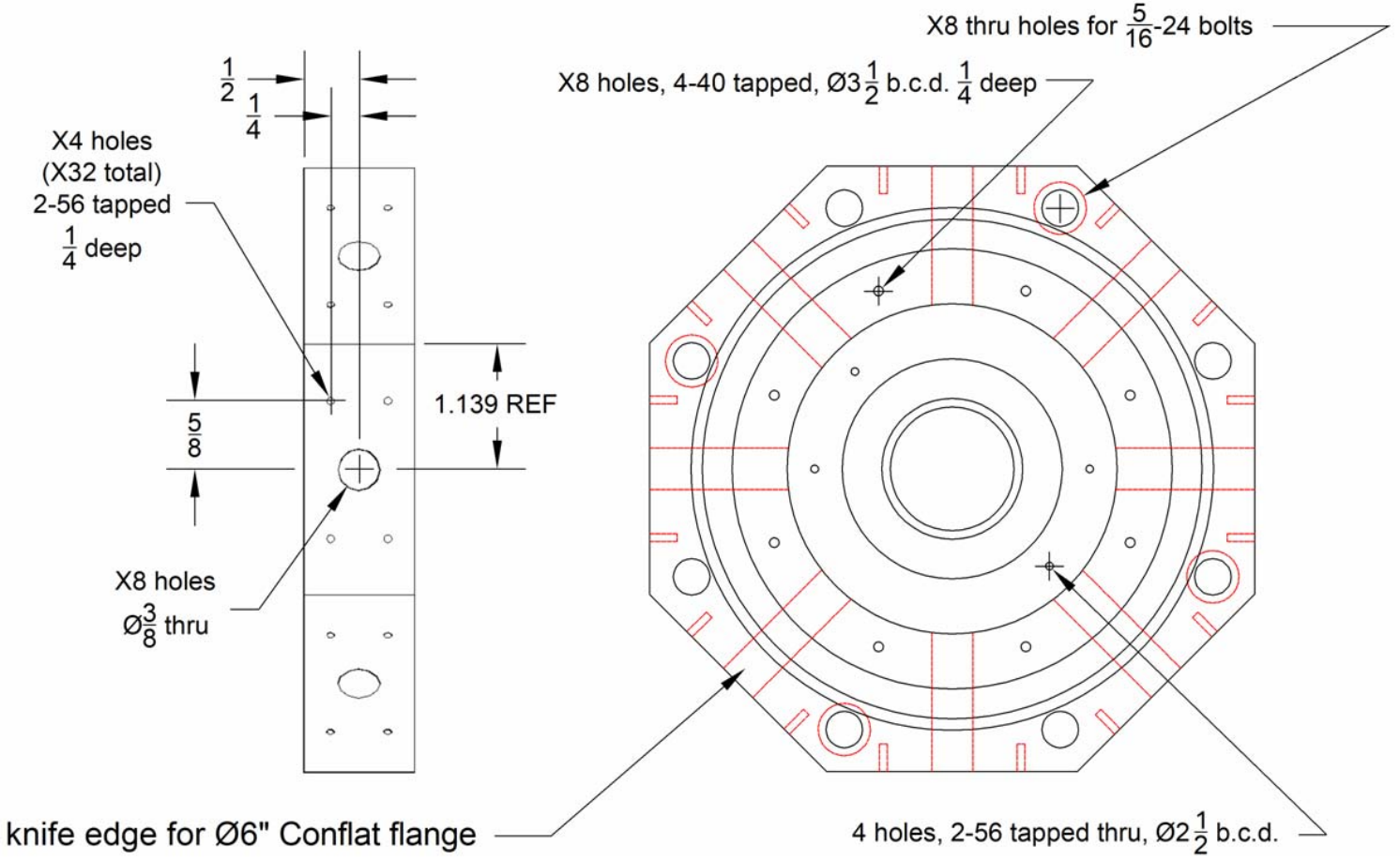

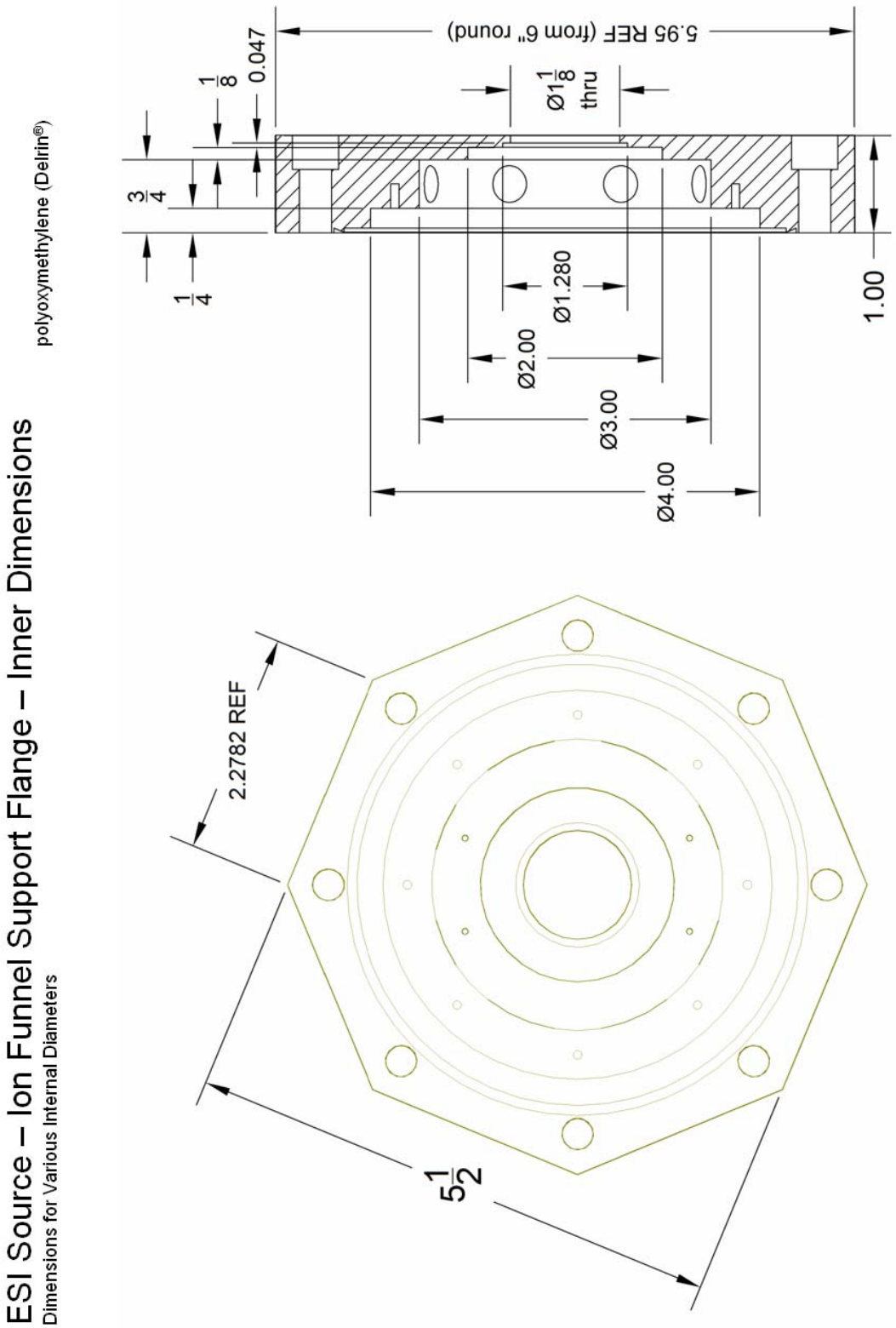
ESI Source – Ion Funnel Support Flange – Inner Dimensions
Dimensions for Various Internal Diameters
polyoxymethylene (Delrin®)
5.95 REF (from 6" round)
Ø1 1/8 thru
1/8
0.047
3/4
1/4
Ø1.280
Ø2.00
Ø3.00
Ø4.00
1.00
2.2782 REF
5 1/2

ESI Source – Ion Funnel Feedthrough Flanges

Flanges to Compress Coaxial Feedthroughs Equipped with O-Rings

polyoxymethylene (Delrin®) (original)
aluminum (revision 1)

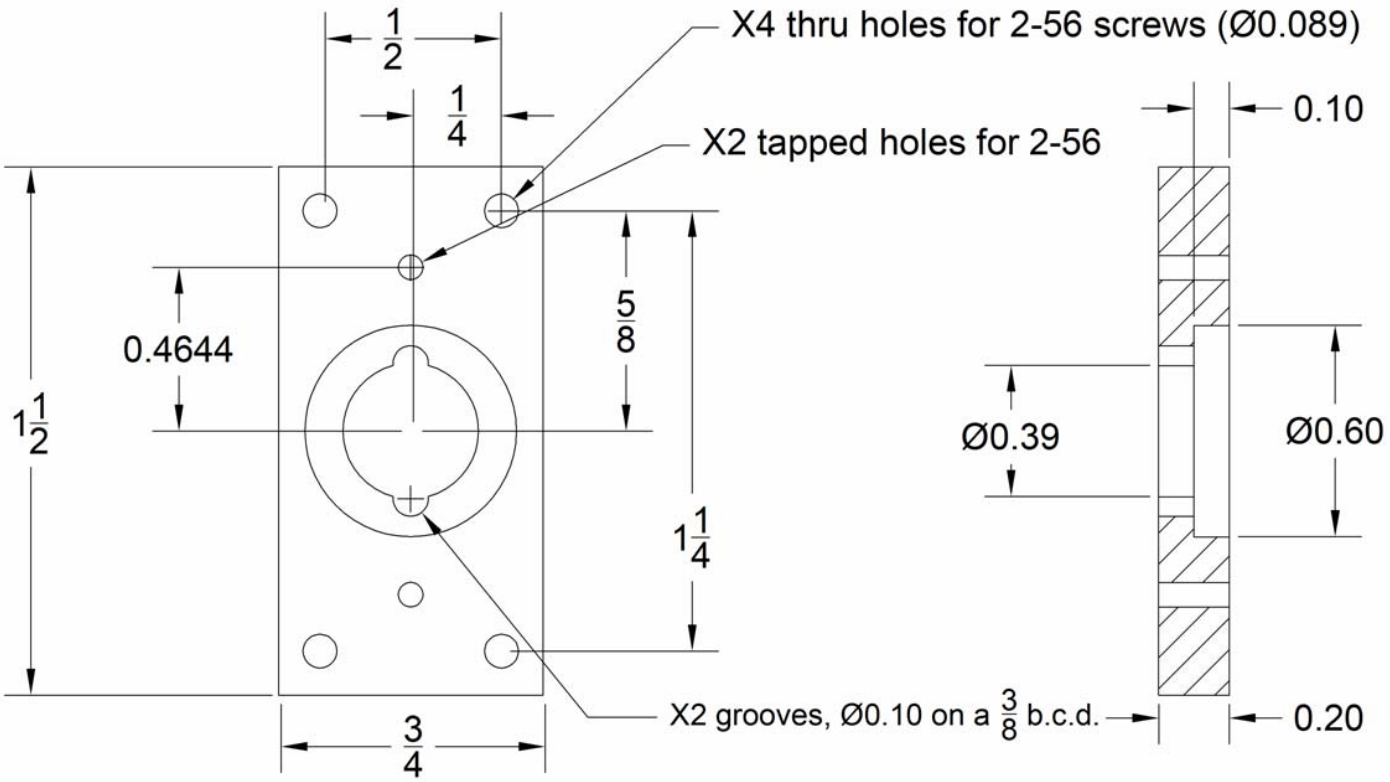

ESI Source – Ion Funnel Blank Flanges

Flanges to Blank Off Feedthrough Ports

polyoxymethylene (Delrin®)

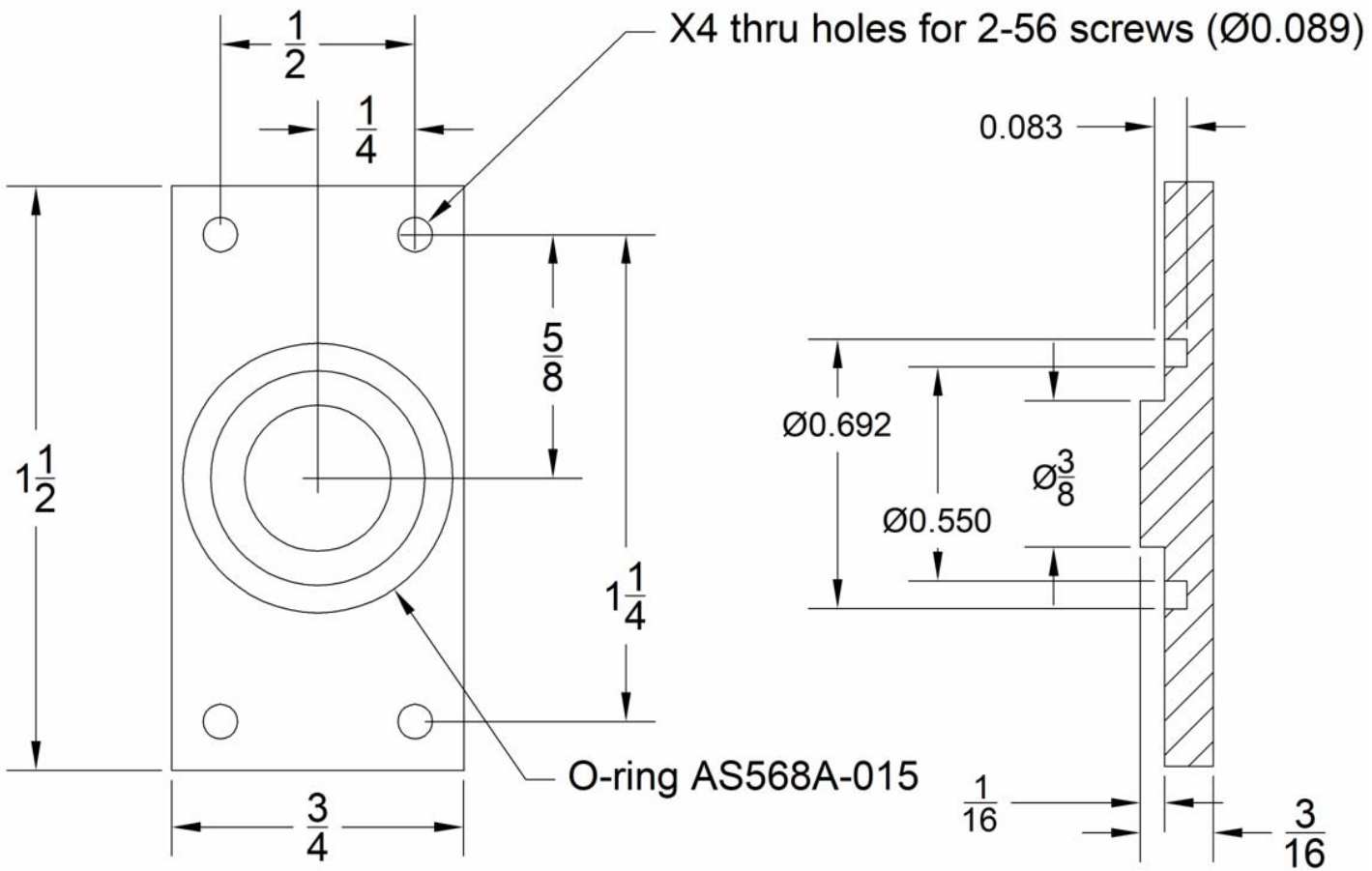

ESI Source – Ion Funnel Electrodes

Modified from Off the Shelf eV Parts® - Nonstandard I.D.'s Shown Here.

stainless steel

NOT TO SCALE

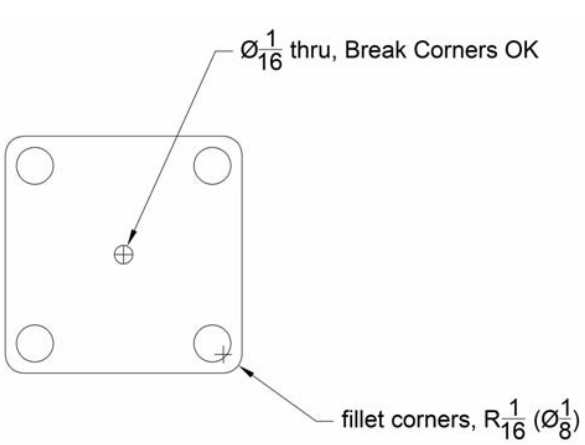

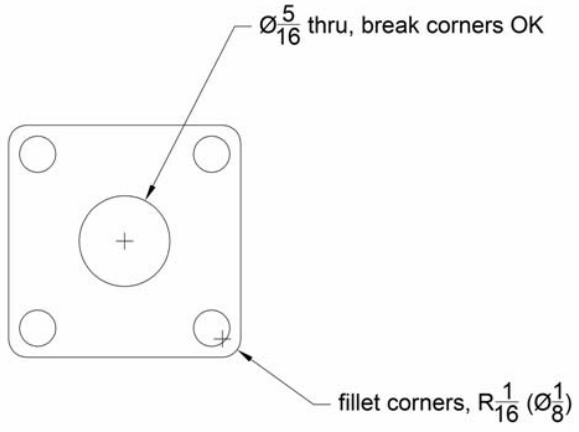

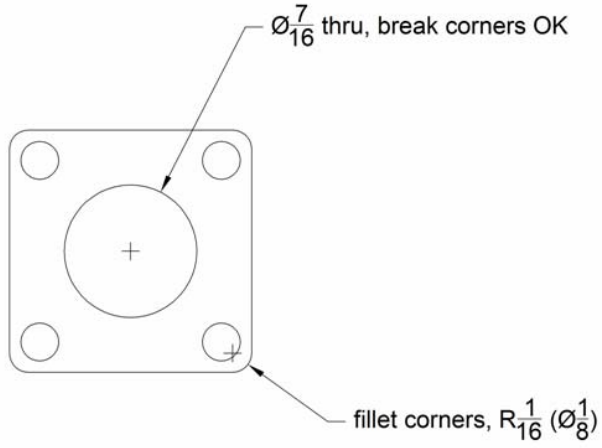

ESI Source – Ion Funnel Support/ DC Aperture Plate

Inner Diameter Tapped Holes Accept Electrode Plates – Outer Diameter Accepts Mobility Rings

stainless steel

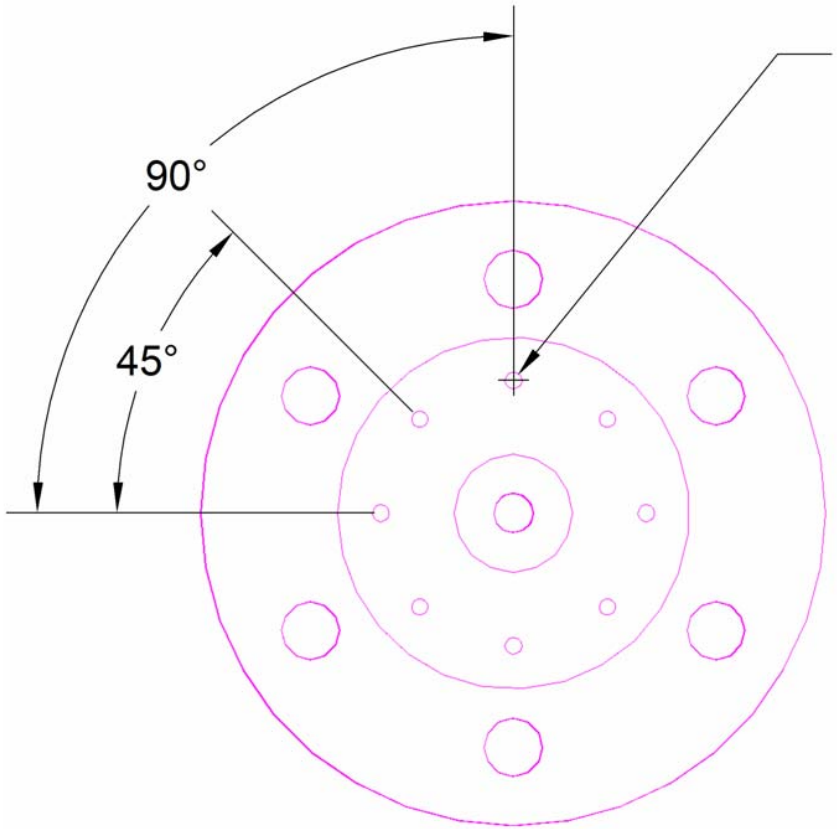

X8 Holes, 0-80 tapped, on a Ø0.8486 b.c.d. (to align with existing square plate parts, provided), approx $\frac{1}{16}$ deep

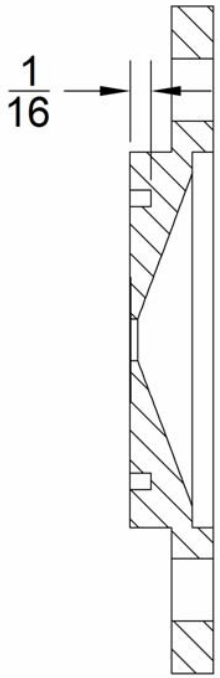

ESI Source – Ion Funnel Electrode Connector

Aligns with Individual Funnel Electrodes – Supports Capacitor/Resistor Circuitry

polyetheretherketone (PEEK)

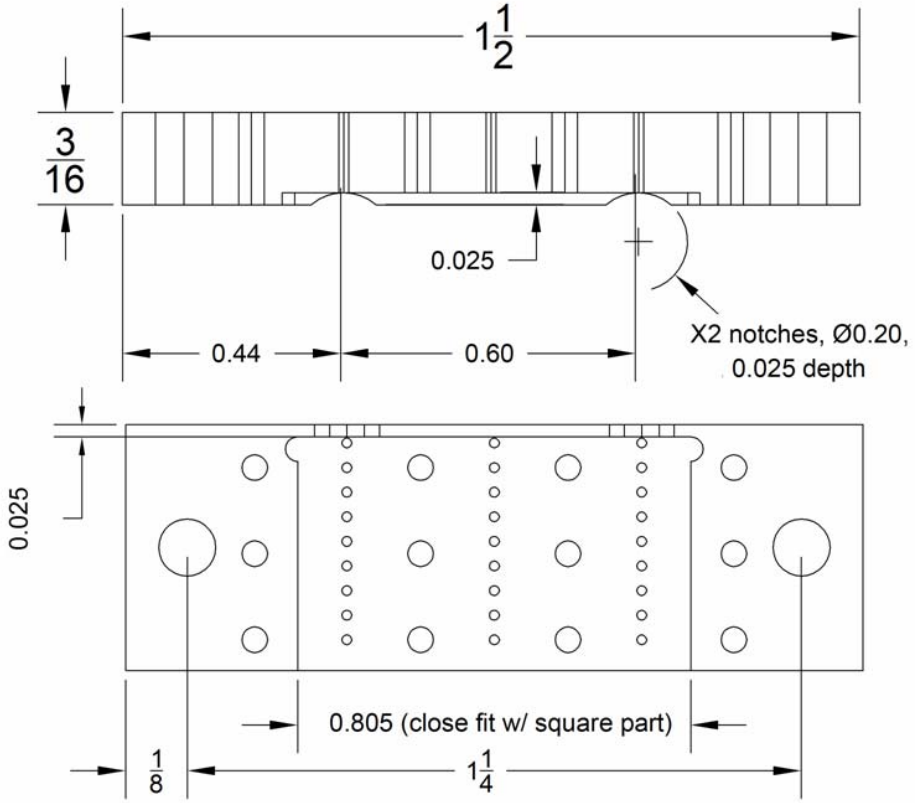

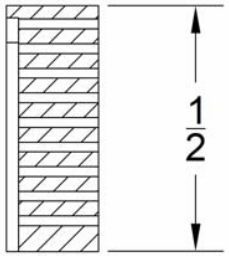

ESI Source – Ion Funnel Electrode Connector – Additional Dimensions

polyetheretherketone (PEEK)

Dimensioning for Hole Details

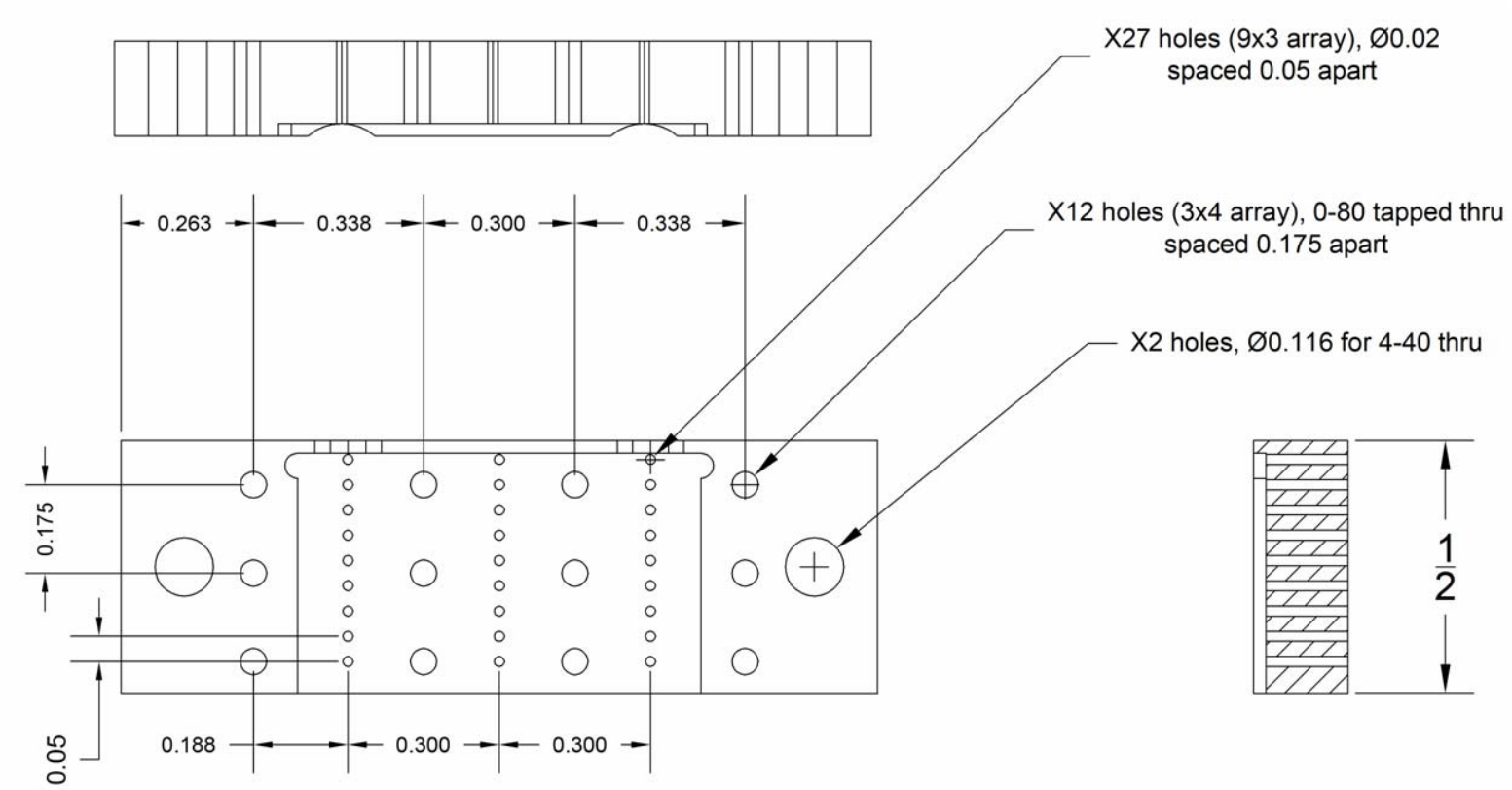

ESI Source – Back End Ion Optics – Lens 1

First Ion Optic Following the Ion Funnel Aperture – Transitions into the Periodic Field Geometry

stainless steel

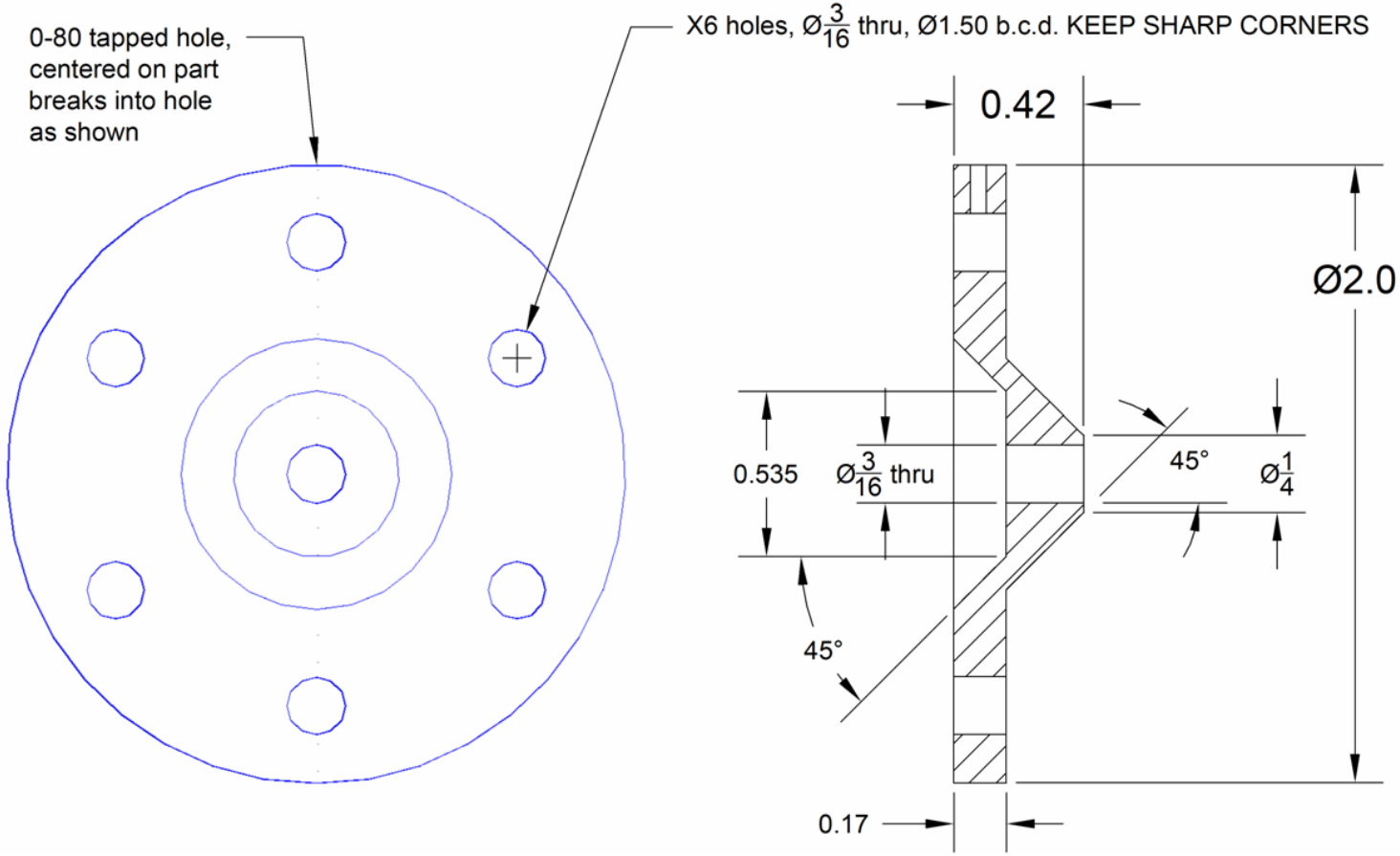

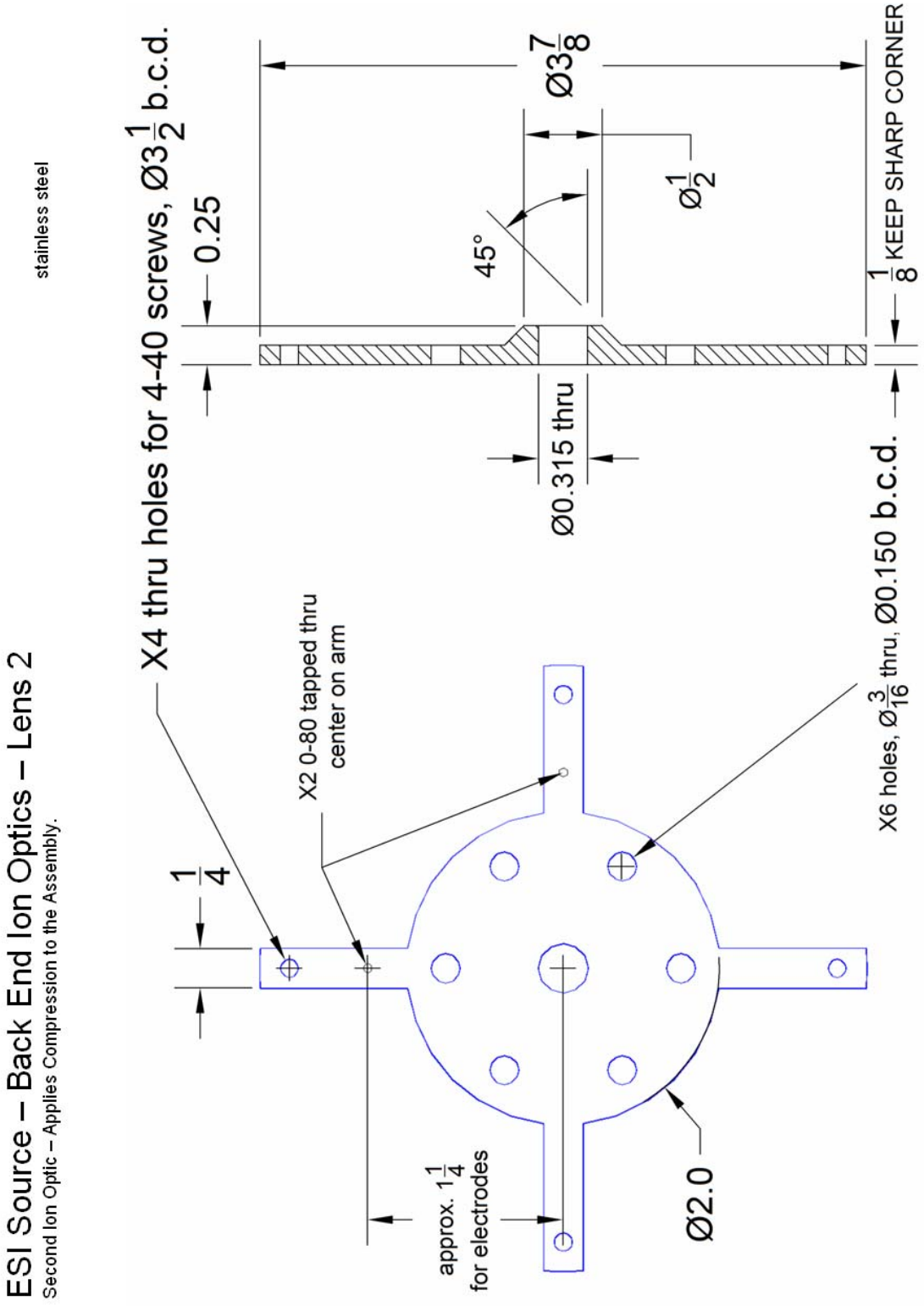
ESI Source – Back End Ion Optics – Lens 2
Second Ion Optic – Applies Compression to the Assembly.
stainless steel
X4 thru holes for 4-40 screws, Ø3 1/2 b.c.d.
0.25
Ø3 7/8
45°
Ø1/2
Ø0.315 thru
1/8 KEEP SHARP CORNER
1/4
X2 0-80 tapped thru center on arm
X6 holes, Ø3/16 thru, Ø0.150 b.c.d.
approx. 1 1/4 for electrodes
Ø2.0

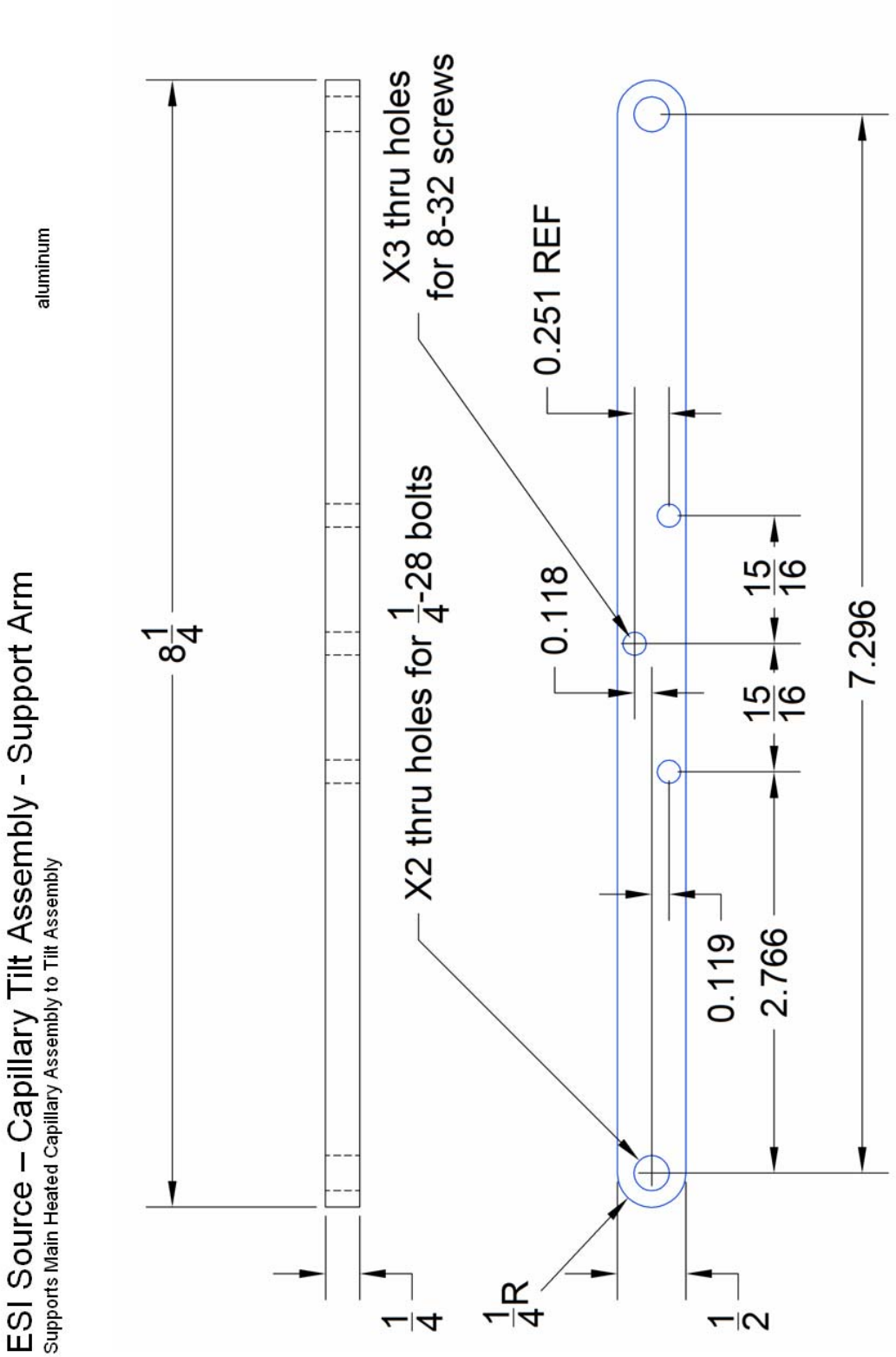
ESI Source – Capillary Tilt Assembly - Support Arm
Supports Main Heated Capillary Assembly to Tilt Assembly
aluminum
8 1/4
X3 thru holes for 8-32 screws
X2 thru holes for 1/4-28 bolts
0.251 REF
0.118
15/16
15/16
7.296
0.119
2.766
1/4
1/4R
1/2

ESI Source – Capillary Tilt Assembly - Rods

Attaches Support Arm to Rotating Bar

aluminum

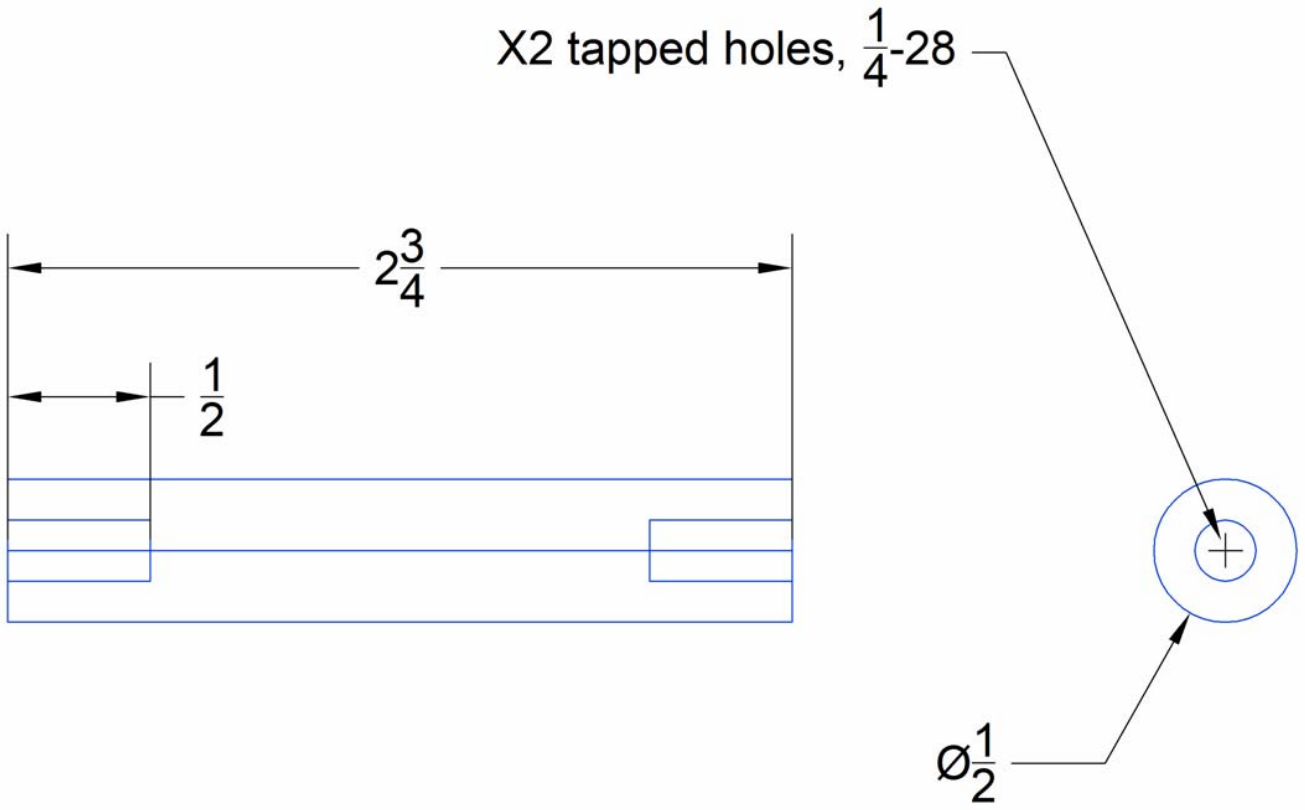

ESI Source – Capillary Tilt Assembly – Rotating Bar

Main Rotational Bar

aluminum

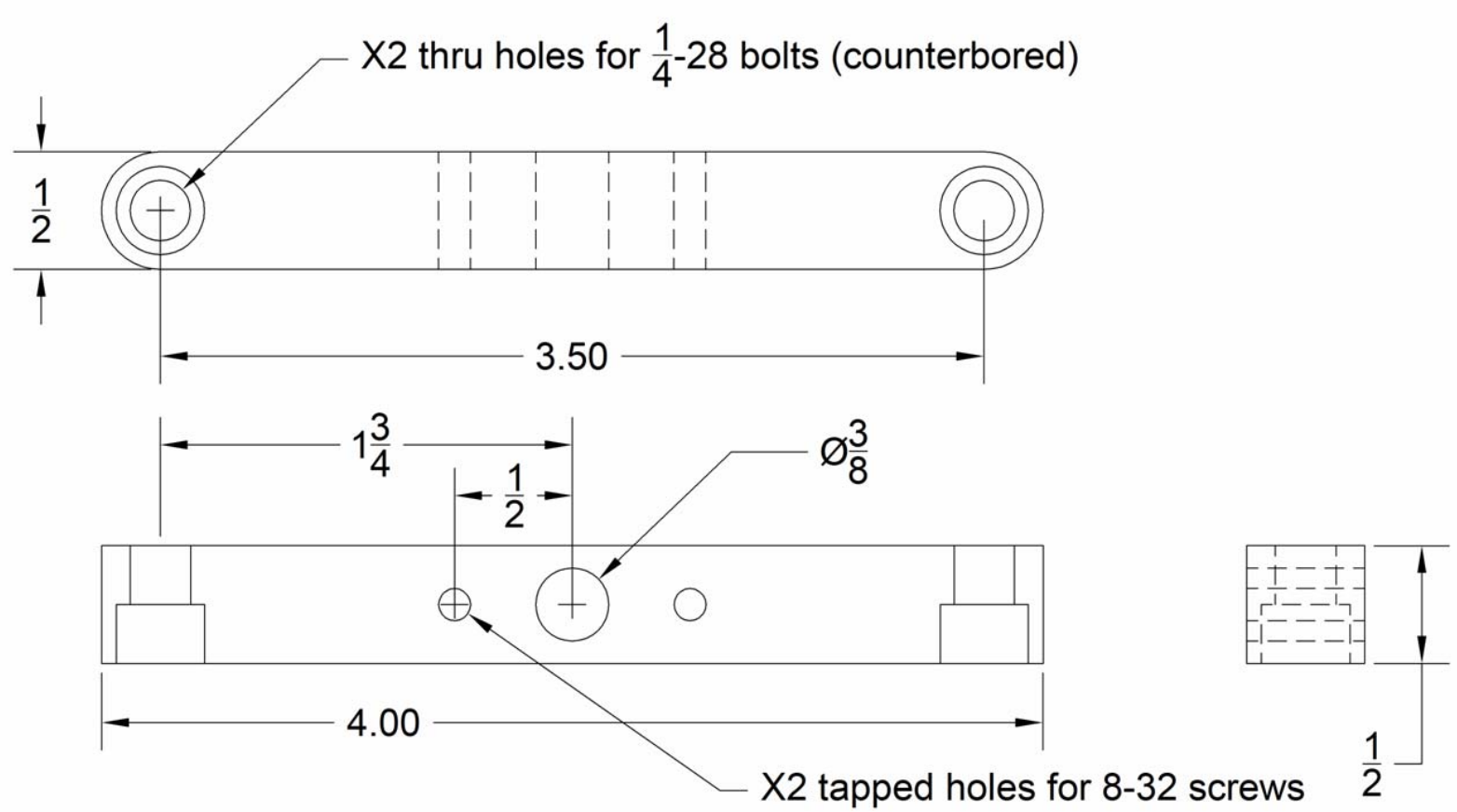

ESI Source – Capillary Tilt Assembly – Sleeve Bearing

Custom Sleeve Bearing for Rotating Tilt Assembly

Filled PTFE (Rulon J®)

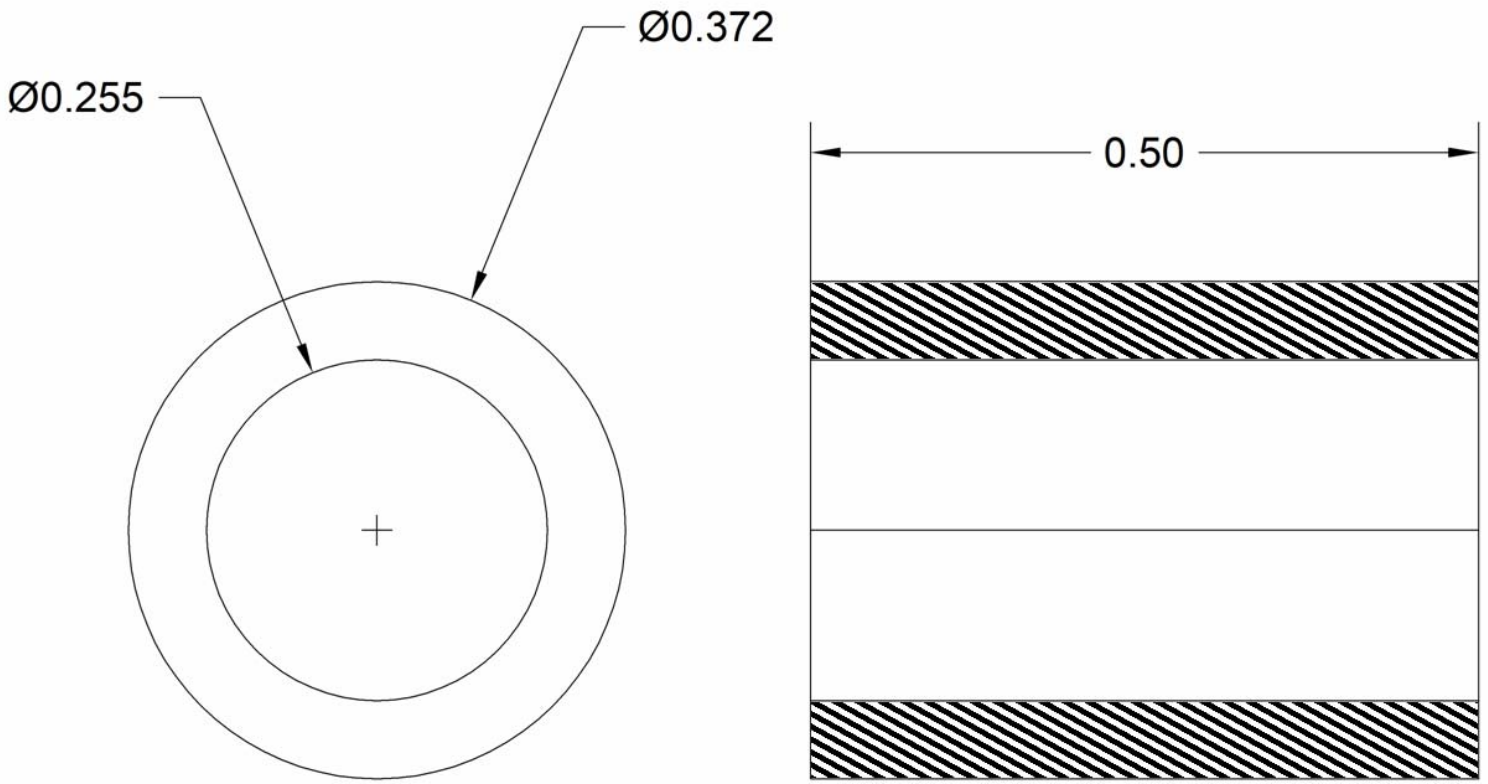

ESI Source – Capillary Tilt Assembly – Slotted Plate

Slotted Plate Allowing Fine Adjustment of Depth of Capillary Insertion into Ion Funnel

aluminum

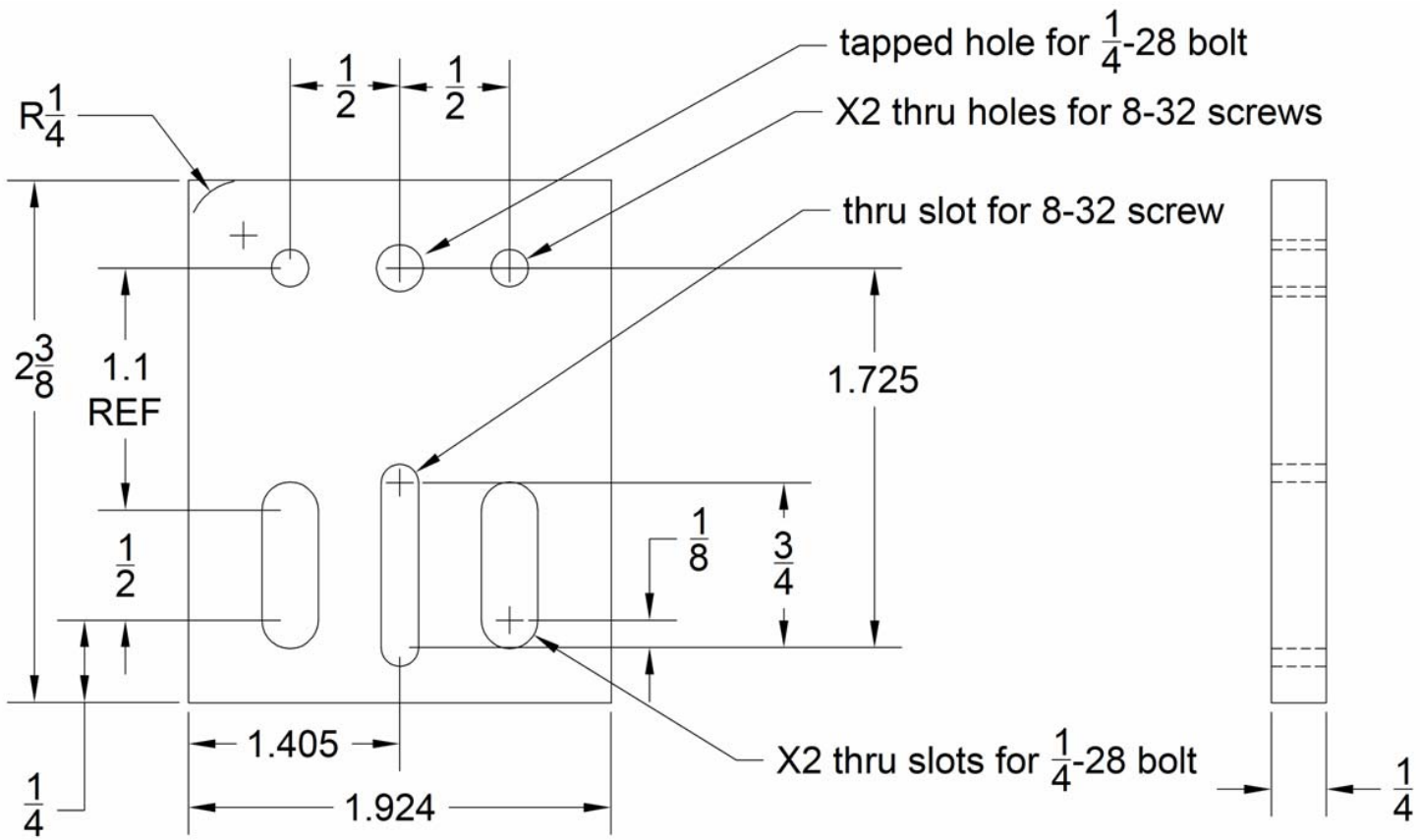

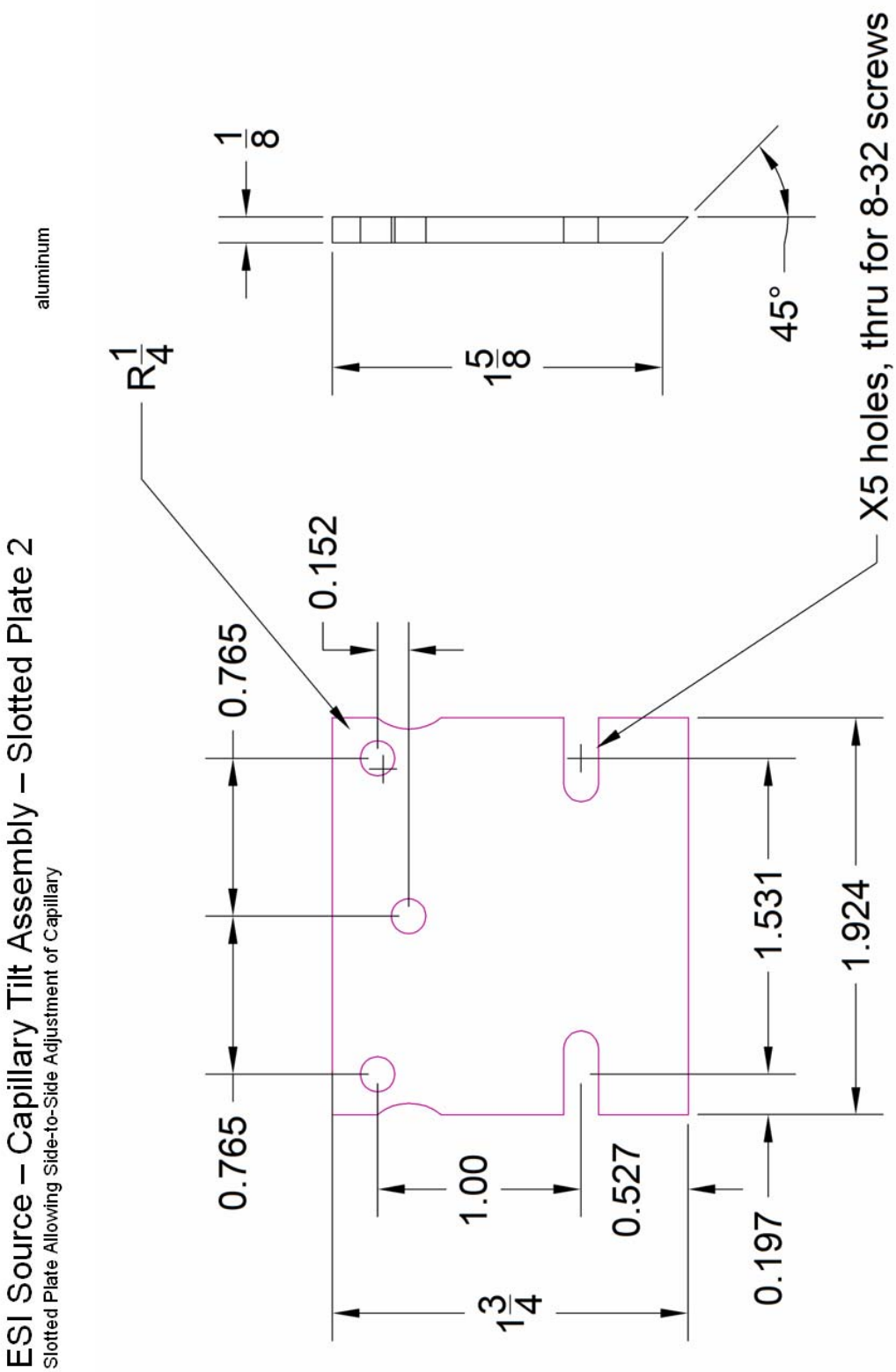
ESI Source – Capillary Tilt Assembly – Slotted Plate 2
Slotted Plate Allowing Side-to-Side Adjustment of Capillary
aluminum
R 1/4
0.765
0.152
0.765
1 3/4
1.00
0.527
0.197
1.531
1.924
1 5/8
45°
1/8
X5 holes, thru for 8-32 screws

ESI Source – Capillary Tilt Assembly – Slotted Plate 2 Modifications

Modifications to Slotted Plate Allowing More Side-to-Side Motion and Fit With Existing Bolts

aluminum

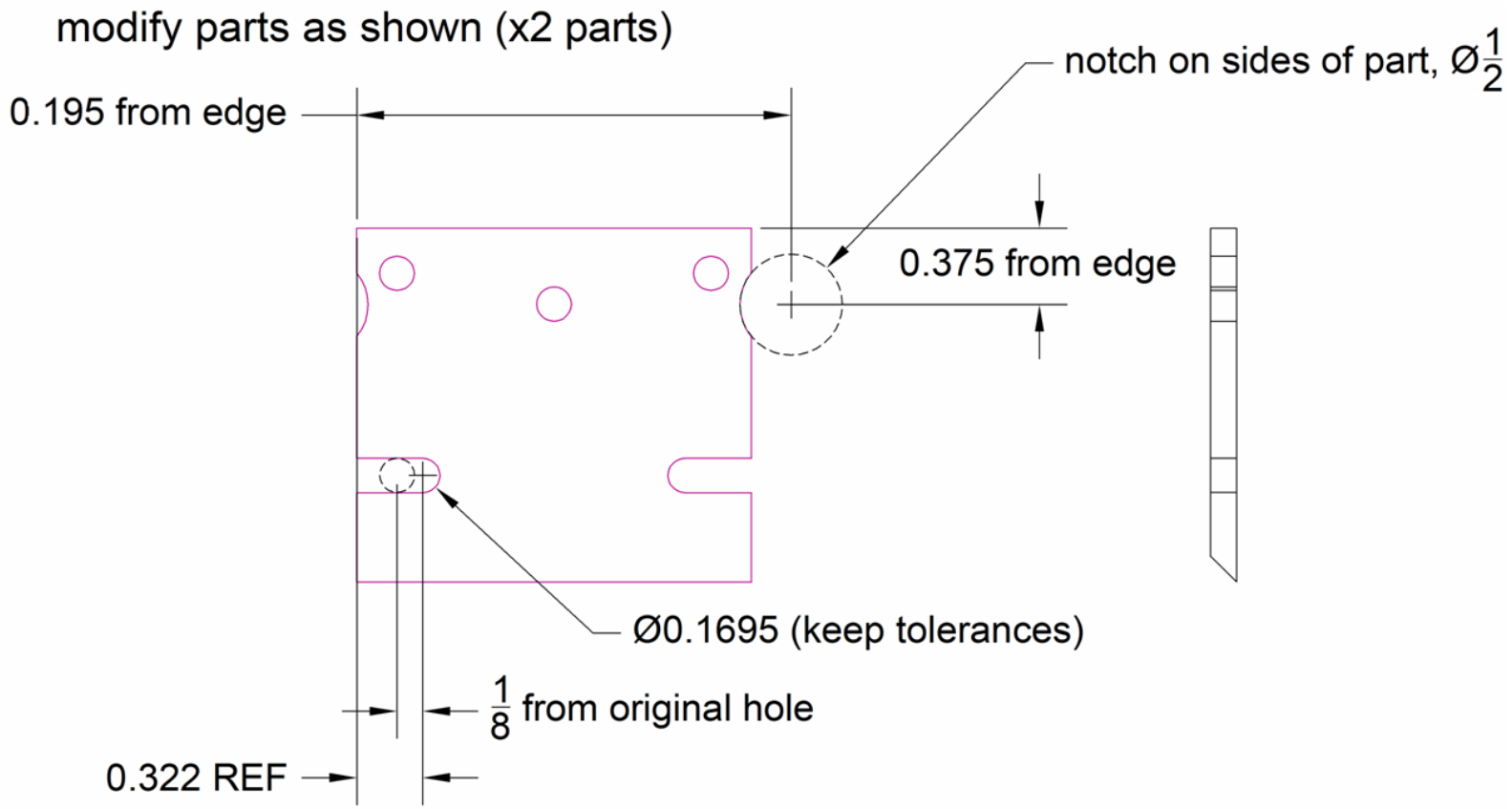

ESI Source – Capillary Tilt Assembly – Support Plate

Plate to Support Tilt Assembly to Chamber Block

aluminum

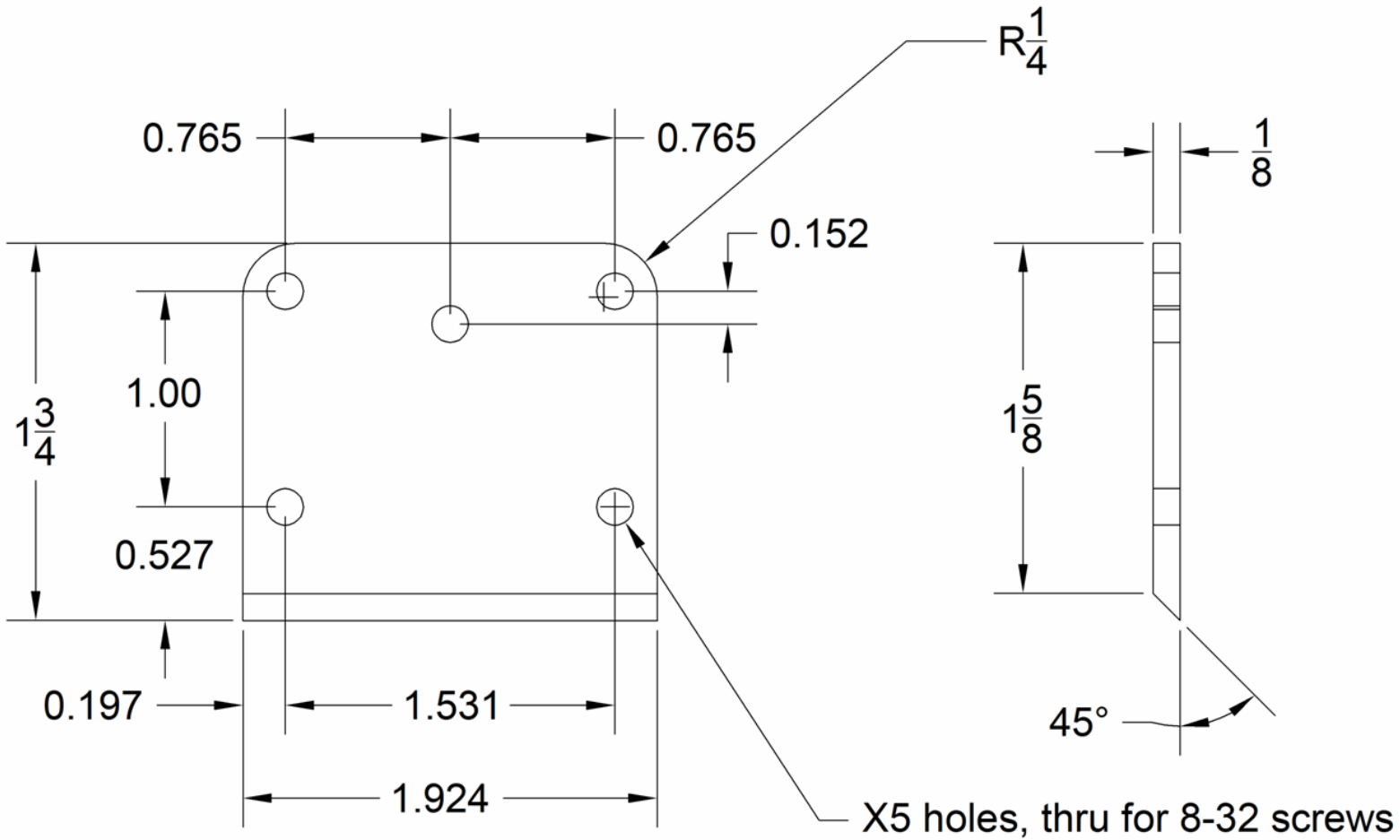

ESI Source – Capillary Tilt Assembly – Tapped Block

Tapped Block to Couple Both Slotted Plates

aluminum

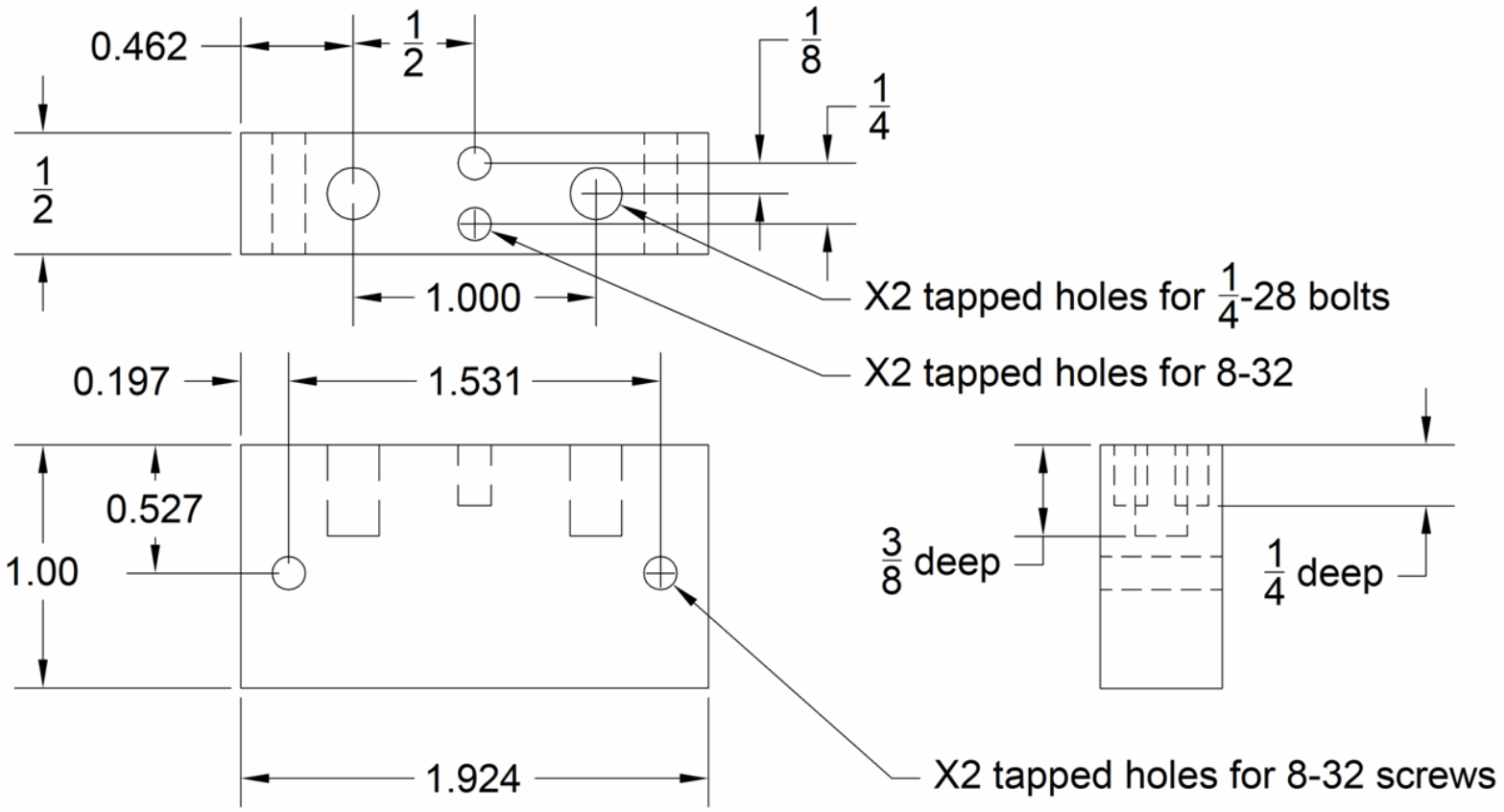

APPENDIX C

CIRCUIT DIAGRAMS FOR SELECT

ELECTRONIC COMPONENTS

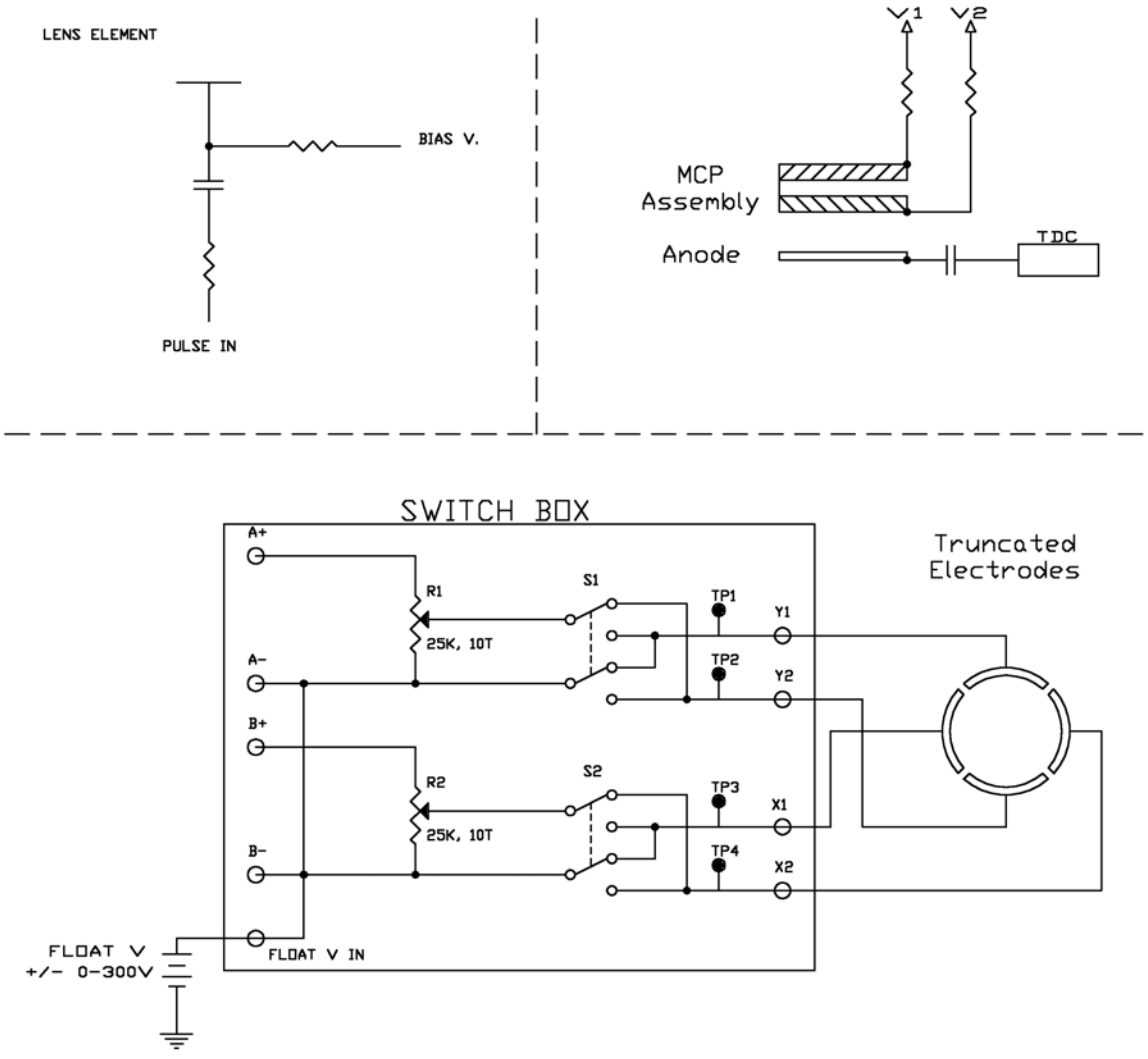

APPENDIX D

MATHCAD WORKSHEET CALCULATIONS

FOR VARIOUS INSTRUMENT PARAMETERS

Define Variables Here: $m_{ion} := 52 \cdot \frac{gm}{mol}$ $z := 1$

TOF - Initial Variable Setup

Defined Variabled & Units

$m_{ion1} := \frac{m_{ion}}{N_A}$ $N_A := 6.022 \cdot 10^{23} \cdot mol^{-1}$ $q := 1.602 \cdot 10^{-19} \cdot C$

$m_{ion1} = 8.635 \times 10^{-23}\ gm$ $eV := 1.602 \cdot 10^{-19} \cdot J$ $usec := 10^{-6} \cdot s$

TOF Voltages

$V_{push} := 550 \cdot V$

$V_{common} := -301.7 \cdot V$ $V_{push1} := V_{push} + V_{common}$ $V_{push1} = 248.3\ V$

$V_{pull} := -488 \cdot V$ $V_{pull1} := -(V_{pull} - V_{common})$ $V_{pull1} = 186.3\ V$

$E_{src1} := (V_{push1}) \cdot q \cdot z$ $E_{src1} = 3.978 \times 10^{-17}\ J$

$E_{src2} := (V_{pull1}) \cdot q \cdot z$ $E_{src2} = 2.985 \times 10^{-17}\ J$

$V_{stage1} := V_{push1} + V_{pull1}$ $V_{stage1} = 434.6\ V$

$E_{stage1} := E_{src1} + E_{src2}$ $E_{stage1} = 6.962 \times 10^{-17}\ J$

$V_{TOF\_bias} := -5000 \cdot V$ $E_{stage2} := -(V_{TOF\_bias} - V_{pull}) \cdot q \cdot z$ $E_{stage2} = 7.228 \times 10^{-16}\ J$

$E_{TOF} := E_{stage1} + E_{stage2}$ $E_{TOF} = 7.924 \times 10^{-16}\ J$

$V_{stage2} := -(V_{TOF\_bias} - V_{pull})$ $V_{stage2} = 4.512 \times 10^{3}\ V$

TOF dimensions

$V_{TOF} := V_{stage1} + V_{stage2}$ $V_{TOF} = 4.947 \times 10^{3}\ V$

$d_{src1} := 0.2 \cdot in$

$d_{src2} := 0.15 \cdot in$ $d_{stage1} := d_{src1} + d_{src2}$ $d_{stage1} = 0.35\ in$

$d_{stage2} := 0.15 \cdot in$

$EF_{src1} := \frac{V_{push1}}{d_{src1}}$ $EF_{src1} = 488.78 \frac{V}{cm}$ If the electric field in src1 is close to the field in src2, then your 1st TOF stage is optimal.

$d_{TOF\_region} := 10.998 \cdot in$

$d_{TOF\_path} := 11.536 \cdot in$ $EF_{src2} := \frac{V_{pull1}}{d_{src2}}$ $EF_{src2} = 488.976 \frac{V}{cm}$

TOF - Initial Variable Setup

TOF - Ion Velocities & Transit Times

$E = \frac{1}{2} \cdot m \cdot v^2$ $v_{ion\_src1} := \frac{1}{m_{ion1}} \cdot \sqrt{2} \cdot (m_{ion1} \cdot E_{src1})^{\frac{1}{2}}$ $v_{ion\_src2} := \frac{1}{m_{ion1}} \cdot \sqrt{2} \cdot (m_{ion1} \cdot E_{src2})^{\frac{1}{2}}$

$v_{ion\_src1} = 3.035 \times 10^{4} \frac{m}{s}$ $v_{ion\_src1} = 30.353 \frac{mm}{usec}$ Ion velocity from PUSH PLATE to COMMON GRID

$t_{src1} := \frac{d_{src1}}{v_{ion\_src1}}$

$t_{src1} = 0.167\ usec$ time it takes ion to transit the SRC1 region (PUSH to COMMON)

$v_{ion\_src2} = 2.629 \times 10^{4} \frac{m}{s}$ $v_{ion\_src2} = 26.292 \frac{mm}{usec}$ Ion velocity from COMMON GRID to PULL GRID

$t_{src2} := \frac{d_{src2}}{v_{ion\_src2}}$

$t_{src2} = 0.145\ usec$

$t_{stage1} := t_{src1} + t_{src2}$ $t_{stage1} = 0.312\,usec$ time it takes ion to transit STAGE 1 (PUSH PLATE to PULL GRID)

$$v_{ion\_stage2} := \frac{1}{m_{ion1}} \cdot \sqrt{2} \cdot \left(m_{ion1} \cdot E_{stage2}\right)^{\frac{1}{2}}$$

$v_{ion\_stage2} = 1.294 \times 10^5 \frac{m}{s}$ $v_{ion\_stage2} = 129.39 \frac{mm}{usec}$ ion velocity post STAGE 2 (TOF velocity)

$$t_{stage2} := \frac{d_{stage2}}{v_{ion\_stage2}}$$

$t_{stage2} = 0.029\,usec$ time it takes ion to transit STAGE 2 (PULL GRID to TOF GRID)

$t_{stage1} + t_{stage2} = 0.342\,usec$ time it takes ion to enter TOF region from PUSH PLATE

$$t_{TOF\_region} := \frac{d_{TOF\_region}}{v_{ion\_stage2}}$$

$t_{TOF\_region} = 2.159\,usec$ time it takes ion to transit TOF field free region from TOF GRID

$t_{TOF} := t_{stage1} + t_{stage2} + t_{TOF\_region}$

$t_{TOF} = 2.501\,usec$ total TOF time (PUSH PLATE to DETECTOR)

TOF - Ion Velocities & Transit Times

TOF - Ion Injection V for Optimal Detector Coincidence

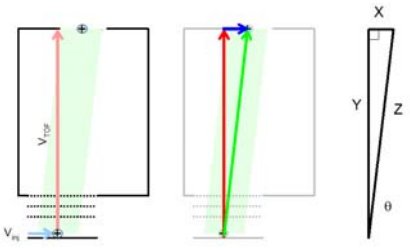

$X := 1.3 \cdot in$

$Y := 11.4425 \cdot in$

$Z := \sqrt{X^2 + Y^2}$ $Z = 11.516\,in$

$\tan(\theta) = \frac{X}{Y}$

$\theta := \operatorname{atan}\left(\frac{X}{Y}\right)$ $\theta = 0.113$

$V_{inj\_avg1} := \tan(\theta) \cdot V_{TOF}$ $V_{inj\_avg2} := \left(\frac{1.3}{11.4425}\right) \cdot V_{TOF}$ These two values represent the average injection voltage magnitude for the entire transit...

$V_{inj\_avg1} = 561.991\ V$ $V_{inj\_avg2} = 561.991\ V$

Since there are two fields in the TOF experiment, it is necessary to only consider the injection for the first stage (PUSH to PULL)

$V_{inj\_stage1} := \tan(\theta) \cdot V_{stage1}$

A rough approximation can be made by using the variables in stage1 only for the calculation.

$V_{inj\_stage1} = 49.376\ V$

TOF - Ion Injection V for Optimal Detector Coincidence

TOF - Space Focus Plane (2-Stage)

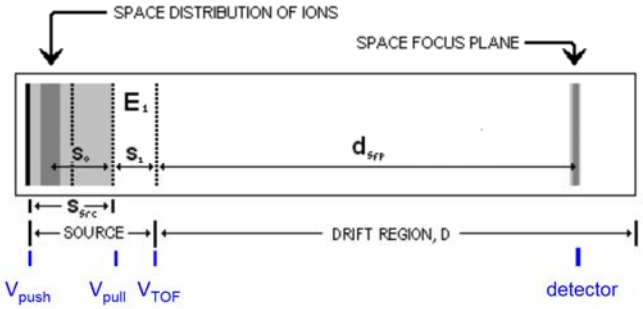

$$EF_{stage1} := \frac{EF_{src1} + EF_{src2}}{2} \qquad EF_{stage1} = 488.878\ \frac{V}{cm}$$

Electric field averaged across source region (PUSH to PULL)

$$EF_{stage2} := \frac{V_{stage2}}{d_{stage2}} \qquad EF_{stage2} = 1.184 \times 10^{4}\ \frac{V}{cm}$$

Electric field STAGE 2 (PULL to TOF)

$$d_{ion\_origin} := \frac{1}{2}\cdot d_{src1} + d_{src2} \qquad d_{ion\_origin} = 0.25\ in$$

Ion origin assumed to be directly between PUSH and COMMON

$$d_{sfp} := \frac{2\cdot\left(d_{ion\_origin} + \frac{EF_{stage2}}{EF_{stage1}}\cdot d_{stage2}\right)^{\frac{3}{2}}}{\sqrt{d_{ion\_origin}}} \qquad d_{sfp} = 30.613\ in$$

space focus plane

▲ TOF - Space Focus Plane (2-Stage)

TOF Calculation Summary:

$d_{TOF\_path} = 11.536\ in$

$t_{TOF} = 2.501\ usec$ Time of Flight

$d_{sfp} = 30.613\ in$ distance of space focus plane from source

$V_{inj\_stage1} = 49.376\ V$ orthogonal injection energy needed for detector coincidence

^{132}Xe Calculated TOF = 3.43
Simion Calculated TOF = 3.27
Experimental TOF = 3.70

▼ IM - Initial Variable Setup

$P_{gas} := 2.09\cdot torr$

$T_{gas} := 299\cdot K$

$m_{gas} := 4\cdot\frac{gm}{mol}$

$V_{IM} := 210\cdot V$

$d_{IM} := 30.157\cdot cm$

$(T_{gas} - 273\cdot K)\cdot\frac{C}{K} = 26\ C$

$Td := 10^{-17}\cdot V\cdot cm^{2}$

$R_{gas} := 8.314\cdot\frac{J}{mol\cdot K}$

$k_b := 1.381\cdot 10^{-23}\cdot\frac{J}{K}$

$N_{gas} := \frac{P_{gas}\cdot N_A}{R_{gas}\cdot T_{gas}} \qquad N_{gas} = 6.75 \times 10^{16}\ \frac{1}{cm^3}$

Buffer gas density (molecules/L)

$\mu_{iongas} := \frac{m_{ion}\cdot m_{gas}}{m_{ion} + m_{gas}}\cdot\frac{1}{N_A} \qquad \mu_{iongas} = 6.168 \times 10^{-27}\ kg$

Ion-gas reduced mass

$EF_{IM} := \frac{V_{IM}}{d_{IM}} \qquad EF_{IM} = 6.964\ \frac{V}{cm}$

Average E Field across IM cell

$E_{0P} := \frac{EF_{IM}}{P_{gas}} \qquad E_{0P} = 3.332\ \frac{V}{cm\cdot torr}$

E/P

$E_{0N} := \frac{EF_{IM}}{N_{gas}} \qquad E_{0N} = 10.316\ Td$

E/N in Td

▲ IM - Initial Variable Setup

▼ IM - MFP, Relative Velocity, Thermal Energy

Table of collision diameters (VDW):

$pm := 10^{-12} \cdot m$

$d_{He} := 280 \cdot pm$ $d_{Ne} := 308 \cdot pm$ $d_{Ar} := 376 \cdot pm$ $d_{Kr} := 404 \cdot pm$ $d_{Xe} := 432 \cdot pm$

$d_{N2} := 218 \cdot pm$ $d_{NO} := 300 \cdot pm$ $d_{CO2} := 407 \cdot pm$

$d_{CH3OH} := 184.33 \cdot pm$ $d_{CH2OH2} := 190.82 \cdot pm$

$d_{coll} := d_{Xe} + d_{He}$ Sum of the ion and bath gas diameters

$\lambda_{MFP} := \frac{R_{gas} \cdot T_{gas}}{\sqrt{2} \cdot \pi \cdot d_{coll}^{2} \cdot N_A \cdot P_{gas}}$ $\lambda_{MFP} = 6.578 \times 10^{-6}\ m$ Mean Free Path

$\lambda_{MFP} = 6.578 \times 10^{-3}\ mm$

$v_r := \sqrt{\frac{8 \cdot k_b \cdot T_{gas}}{\pi \cdot \mu_{iongas}}}$ $v_r = 1.306 \times 10^{3}\ \frac{m}{s}$ Relative (thermal) velocity

$Z_{CF} := \frac{v_r}{\lambda_{MFP}}$ $Z_{CF} = 1.985 \times 10^{8}\ \frac{1}{s}$ Collision Frequency (at thermal velocities)

$Z_{CF} = 198.504\ \frac{1}{usec}$

$MPS_{gas} := \sqrt{\frac{2 \cdot k_b \cdot T_{gas}}{m_{gas} \cdot \frac{1}{N_A}}}$ $MPS_{gas} = 1.115 \times 10^{3}\ \frac{m}{s}$ most probable (thermal) speed

$E_{thermal} := \frac{5}{2} \cdot k_b \cdot T_{gas}$ $E_{thermal} = 0.064\ eV$ Boltzmann (thermal) energy

IM - MFP, Relative Velocity, Thermal Energy

IM - Drift Velocity, # of Collisions, CM Velocity, total KE, Teff

$t_{IM} := 600 \cdot usec$ Experimentally measured IM drift time (uncorrected)

$t_{IM\_corr} := t_{IM} - 14.8 \cdot usec$

$t_{IM\_corr} = 585.2\ usec$ Non IM flight time correction (estimated from vacuum experiments)

$v_d := \frac{d_{IM}}{t_{IM\_corr}}$ $v_d = 515.328\ \frac{m}{s}$ IM drift velocity (empirically measured)

$\alpha_d := \frac{q \cdot EF_{IM}}{\mu_{iongas}}$ $\alpha_d = 1.809 \times 10^{10}\ \frac{m}{s^2}$ IM drift acceleration (W. Harries)

$\tau_{MFP} := \sqrt{\frac{2\lambda_{MFP}}{\alpha_d}}$ $\tau_{MFP} = 0.027\ usec$ ion drift time between collisions

$v_{d2} := \frac{\lambda_{MFP}}{\tau_{MFP}}$ $v_{d2} = 243.892\ \frac{m}{s}$ IM drift velocity (assumes ion starts from rest after each collision, W Harries)

$K_{ion} := \frac{v_d}{EF_{IM}}$ $K_{ion} = 7.4 \times 10^{3}\ \frac{cm^2}{V \cdot s}$ Mobility constant

$Z_{CF\_IM} := \frac{v_d}{\lambda_{MFP}}$ $Z_{CF\_IM} = 7.835 \times 10^{7}\ \frac{1}{s}$ Collision Frequency in Drift Field

$Z_{total} := Z_{CF\_IM} \cdot t_{IM\_corr}$ $Z_{total} = 4.585 \times 10^{4}$ Total number of IM collisions

$v_{CM} := \frac{m_{ion} \cdot v_d + m_{gas} \cdot v_r}{m_{ion} + m_{gas}}$ $v_{CM} = 571.781\ \frac{m}{s}$ Center-of-mass Frame velocity

$KE_1 := \frac{1}{2} \cdot \frac{m_{ion}}{N_A} \cdot v_d^2$ $KE_1 = 0.072\ eV$ average KE/collision based on ion mass

$KE_{total} := \frac{1}{2} \cdot \mu_{iongas} \cdot v_r^2 + \frac{1}{2} \cdot \left(\frac{m_{ion} + m_{gas}}{N_A} \right) \cdot v_{CM}^2$

$KE_{total} = 0.128\ eV$ average KE/collision based on CM (Houston)

$E_{Tion} := \left(\frac{m_{ion}}{m_{gas}} + \frac{m_{gas}}{m_{ion}} \right) \cdot q \cdot EF_{IM} \cdot \lambda_{MFP}$ $E_{Tion} = 0.06\ eV$ total energy calculated via another approach (energy gained between collisions)

$E_{cm} := \frac{3}{2} \cdot k_b \cdot T_{gas} + \frac{1}{2} \cdot \frac{m_{gas}}{N_A} \cdot v_{CM}^2$ $E_{cm} = 0.045\ eV$ Average center-of-mass collision energy (Wannier's Equation)

$E_{lab} := \left(\frac{m_{ion} + m_{gas}}{m_{gas}} \right) \cdot E_{cm}$ $E_{lab} = 0.636\ eV$

$T_{eff} := T_{gas} + \frac{m_{gas} \cdot v_d^2}{3 \cdot k_b \cdot N_A}$ $T_{eff} = 341.577\ K$

▲ IM - Drift Velocity, # of Collisions, CM Velocity, total KE, Teff

▼ IM - Max Resolving Power

$R_{low1} := \sqrt{\frac{EF_{IM} \cdot d_{IM} \cdot z \cdot q}{16 \cdot k_b \cdot T_{gas} \cdot \ln(2)}}$ $R_{low1} = 27.104$ Maximum Theoretical IM Resolution (low field, diffusion limited) (H. Hill),

$R_{low2} := 32.3417 \cdot \left(\frac{s}{m} \cdot \sqrt{\frac{K \cdot C}{kg}} \right) \cdot \sqrt{\frac{d_{IM} \cdot EF_{IM} \cdot z}{T_{gas}}}$ $R_{low2} = 27.104$ Guido's simplification (note the coefficient term is shown with units here)

$t_{gate} := 4usec$ $R_{gate} := \frac{t_{IM}}{t_{gate}}$ $R_{gate} = 150$ Ion gate limited resolution

▲ IM - Max Resolving Power

IM Calculation Summary:

$E_{thermal} = 0.064\ eV$ Thermal Energy

$KE_{total} = 0.128\ eV$ Ion Energy (three theories)

$E_{Tion} = 0.06\ eV$

$E_{lab} = 0.636\ eV$

$Z_{total} = 4.585 \times 10^4$ Total Number of Collisions

$E_{0P} = 3.332\ \frac{V}{cm \cdot torr}$ Electric Field

$E_{0N} = 10.316\ Td$ Electric Field (Td)

$R_{low1} = 27.104$ Diffusion Limited Resolving Power

$R_{gate} = 150$ Ion Gate Limited Resolving Power

▶ Injection Energy

Effective Ion Temperature

Initial Variables

$N_A := 6.022 \cdot 10^{23} \cdot \frac{1}{mol}$ $k_b := 1.38 \cdot 10^{-23} \cdot \frac{J}{K}$ $e_{charge} := 1.6022 \cdot 10^{-19} \cdot C$ $usec := 10^{-6} \cdot sec$

$eV := 1.602 \cdot 10^{-19} \cdot J$

Initial Variables

Post IMS Drift Time - Calculated

$m_{gas} := 4 \cdot \frac{gm}{mol}$ $m_{gas\_corr} := \frac{m_{gas}}{N_A}$ $\mu_{mass} := \frac{m_{ion\_corr} \cdot m_{gas\_corr}}{m_{ion\_corr} + m_{gas\_corr}}$

$T_{gas} := 270 \cdot K$ $T_{gas} = -3.15\,°C$

$\mu_{mass} = 6.168 \times 10^{-27}\,kg$

$d_{drift} := 30.157 \cdot cm$

$t_{drift} := 436.91 \cdot usec$ $t_{drift\_corr} := t_{drift} - t_{corr}$ Post IMS drift time correction

$v_{drift} := \frac{d_{drift}}{t_{drift\_corr}}$ $v_{drift} = 727.13\,\frac{m}{s}$ Drift Velocity (average)

$T_{ion} := T_{gas} + \frac{m_{gas\_corr}}{3 \cdot k_b} \cdot v_{drift}^2$

$T_{ion} = 354.829\ K$

Wannier's Eqn - Total Ion Energy

$E_K := \frac{1}{2} \cdot m_{ion\_corr} \cdot v_{drift}^2 + \frac{1}{2} \cdot \mu_{mass} \cdot v_{drift}^2 + \frac{3}{2} \cdot k_b \cdot T_{gas}$ $E_{thermal} := \frac{3}{2} \cdot k_b \cdot T_{gas}$

$E_K = 0.188\,eV$

$E_{thermal} = 0.035\,eV$

Wannier's Eqn - Total Ion Energy

Reduced Mobility

$V_{drift} := 210 \cdot V$ $E_{drift} := \frac{V_{drift}}{d_{drift}}$ $E_{drift} = 6.964\,\frac{V}{cm}$

$P_{gas} := 2.12 \cdot torr$

$K_0 := \frac{d_{drift}}{t_{drift} \cdot E_{drift}} \cdot \frac{P_{gas}}{760 \cdot torr} \cdot \frac{273.15 \cdot K}{T_{gas}}$ $K_0 = 27.972\,\frac{cm^2}{V \cdot sec}$

Reduced Mobility

VITA

Jody Christopher May received his Bachelor of Science degree in chemistry from The University of Central Arkansas in 2000. He entered the Chemistry program at Texas A&M University in August 2001 under the tutelage of Prof. David Russell. His research interests include instrumentation development and operational principles for the mass spectrometry and ion mobility techniques as applied to chemical and biological detection technologies. He enjoys the hands on aspects of scientific instrumentation development with particular emphasis on component machining and electronic interfacing—interests which were cultivated in his graduate career by the department of chemistry support staff and facilities. He plans on continuing his work in the development of analytical methods for mass spectrometry and has accepted a postdoctoral research appointment at Vanderbilt University in Nashville, TN where he will be developing new ion mobility technologies and methods to address specific research problems in structural biology, glycomics and medical diagnostic research. Jody moonlights as a graphics design artist.

Jody can be contacted at Vanderbilt University, 7330 Stevenson Center, Station B 351822, Nashville, TN 37235. His email address is jodymay@gmail.com.